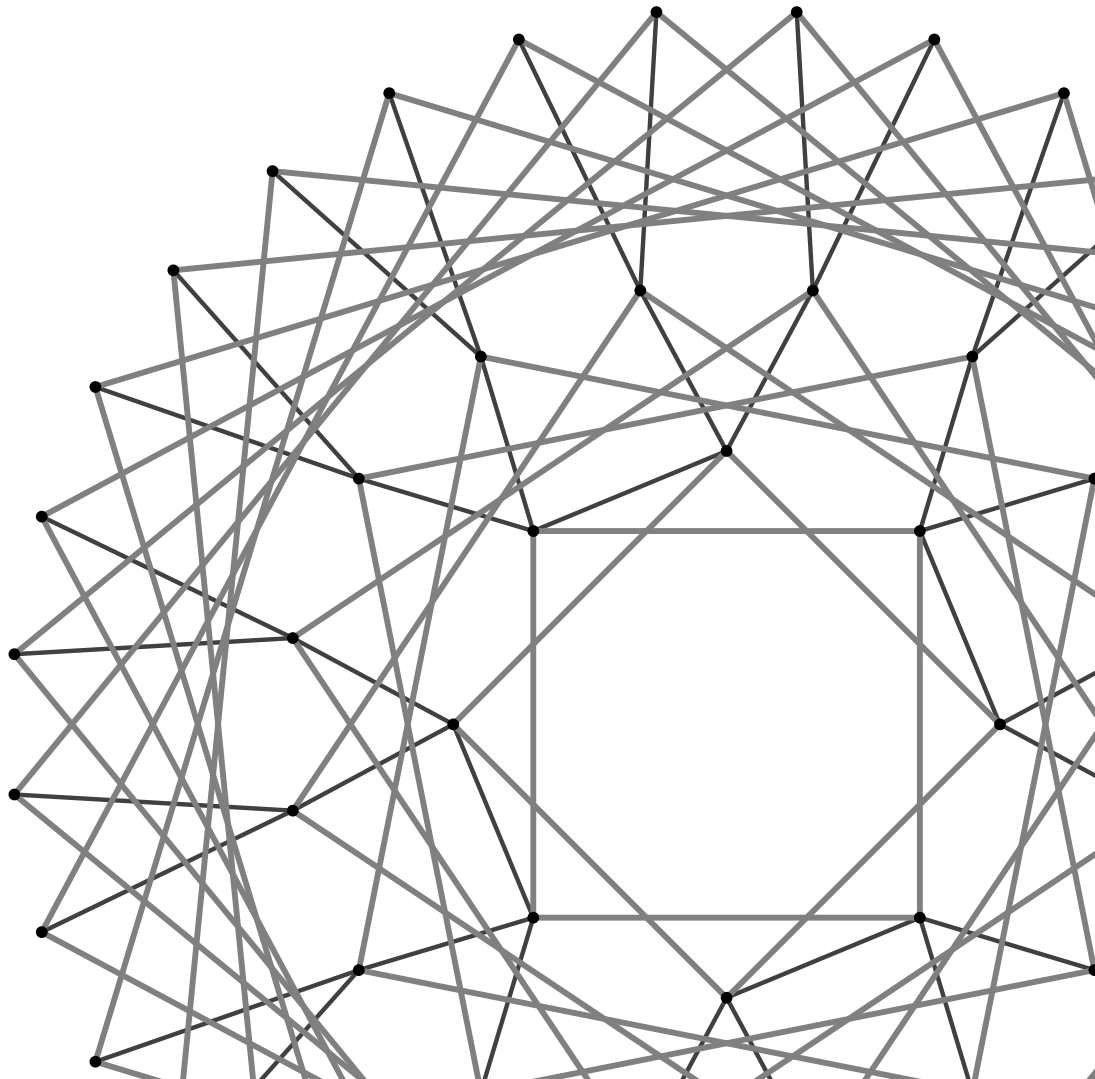


CLUSTER DYNAMICAL MEAN-FIELD THEORY OF STRONGLY CORRELATED
SUPERCONDUCTIVITY & MAGNETISM

DISSERTATION
WITH THE AIM OF ACHIEVING A DOCTORAL DEGREE
AT THE FACULTY OF MATHEMATICS, INFORMATICS AND NATURAL SCIENCES
DEPARTMENT OF
PHYSICS
OF
UNIVERSITÄT HAMBURG
BY
MALTE HARLAND

HAMBURG
2019



Gutachter der Dissertation: Prof. Dr. Alexander I. Lichtenstein
Prof. Dr. Michael Potthoff

Zusammensetzung der
Prüfungskommission: Prof. Dr. Alexander I. Lichtenstein
Prof. Dr. Michael Potthoff
Prof. Dr. Daniela Pfannkuche
Prof. Dr. Nils Huse
Prof. Dr. Ludwig Matthey

Vorsitzende der
Prüfungskommission: Prof. Dr. Daniela Pfannkuche

Datum der Disputation: 25.05.2020

Vorsitzender Fach-
Promotionsausschusses Physik: Prof. Dr. Michael Potthoff

Leiter des Fachbereichs Physik: Prof. Dr. Wolfgang Hansen

Dekan der Fakultät MIN: Prof. Dr. Heinrich Graener

Kurzfassung

Verschiedene bedeutsame Gittermodelle stark korrelierter Systeme werden mittels der dynamischen Molekularfeldtheorie von Zellen untersucht. Dabei werden alle Korrelationen in einem endlichen Teilgitter, der Zelle, exakt beschrieben. Darin sind auch Korrelationen von Temperaturfluktuationen eingeschlossen. Das Phänomen der Hochtemperatursupraleitung in Kupferoxiden wird im Rahmen des effektiven, mikroskopischen Hubbard Modells behandelt. Die Vielteilchenkorrelationen innerhalb einer zwei-mal-zwei Zelle, der Plaquette, ist ausreichend um Mott-isolierende, supraleitende und antiferromagnetische Zustände zu studieren. Im Phasendiagramm der isolierten Plaquette wird ein hochgradig entarteter Punkt bei 25% Lochdotierung identifiziert. In diesem Punkt kreuzen sich die Energien der Grundzustände verschiedener Teilchenzahlen. Es werden unterschiedliche Gitterumgebungen für die Plaquette entwickelt und ihre Phasen werden im Kontext des entarteten Punktes und seiner Vielteilchenstruktur analysiert. Es wird vorgeschlagen, dass die Entartung im Energiespektrum starke Quantenfluktuationen unterstützt, die zu einem quantenkritischen Punkt führen, falls Plaquettekorrelationen die Eigenschaften des Quadratgitters im entsprechenden Parameterbereich bestimmen. Eine spezielle Umgebung entspricht dem vierfachen Bethe-Gitter, das aus Plaquetten gekoppelt in unendlich vielen Dimensionen besteht und ein exakt lösbares Modell der Supraleitung mit $d_{x^2-y^2}$ Symmetrie repräsentiert. Des Weiteren wird das lokale Kraft Theorem angewandt, um das korrelierte Hubbard Modell zum effektiven Josephson Gitter zu vergrößern. Letzteres ist ein vereinfachtes XY Modell von supraleitenden Phasenfluktuationen zwischen Plaquetten. Es ermöglicht Abschätzungen bezüglich der London Eindringtiefe und deutet darauf hin, dass Phasenfluktuationen die Übergangstemperatur in Kupferoxiden vermindern können. Außerdem wird das lokale Kraft Theorem in seinem ursprünglichen Kontext untersucht, das heißt als Abbildung zum Heisenberg Modell, welches Spinaustausch Kopplung beschreibt. Es wird gezeigt, dass bei hinreichend kalten Temperaturen, bei denen sich gut definierte lokale magnetische Momente formen, die hergeleitete Wechselwirkung mittels Einteilchen-Korrelationsfunktionen ausgedrückt werden kann. Der Formalismus der effektiven Heisenberg Abbildungen wird zu allgemeinen nichtlokalen Elektron-Elektron Wechselwirkungen erweitert. Weiterhin wird gezeigt, dass magnetische Eigenschaften in komplexen Materialien von der multiorbitalen Struktur der Übergangsmetallatomen beeinflusst werden. Interorbitaler Coulombaustausch lässt ferromagnetische Spinkopplung entstehen und verstärkt Korrelationseffekte. Im Gegensatz dazu können stark überlappende Orbitale von verschiedenen Übergangsmetallatomen Dimere bilden, die die Elektronen in Molekülorbitalzustände vom Spintyp Singulett binden. Schließlich wird herausgefunden, dass der Wettstreit zwischen dem Molekülorbitalzustand und dem Hund's Kopplung getriebenen Doppelaustauschzustand zu Übergängen im Spinzustand führen kann. Dieser Übergang besitzt die kritische Eigenschaft des Spineinfrierens. Konsequenzen für Theorien von Supraleitung und Magnetismus in Materialien werden diskutiert.

Abstract

Various important lattice models of strongly correlated systems are investigated by means of the cluster dynamical mean-field theory, which describes all correlations within a cellular scheme exactly, including temperature fluctuations. The phenomenon of high-temperature superconductivity in copper oxides is discussed in the framework of the effective microscopic Hubbard model. The many-body correlations within a two-by-two cluster, the plaquette, are sufficient to study Mott-insulating, superconducting and antiferromagnetic states. A highly degenerate point is identified at 25% hole doping in the phase diagram of the isolated plaquette. At this point ground states of different particle numbers cross. Different lattice environments for the plaquette are developed, and their phases are analyzed in the context of the plaquette's degenerate point and its many-body structure. It is suggested that the degeneracy of the energy spectrum supports strong quantum many-body fluctuations that lead to a quantum critical point, if plaquette correlations determine the properties of the square lattice in a respective parameter regime. A special environment corresponds to the quadruple Bethe lattice which consists of plaquettes coupled in infinite dimensions and represents an exactly solvable model of superconductivity with $d_{x^2-y^2}$ symmetry. Moreover, the local force theorem is applied to coarse grain the correlated Hubbard model to the effective Josephson lattice, a simplified XY model of superconducting phase fluctuations between plaquettes. It provides estimates for the London penetration depth and indicates that phase fluctuations can diminish the transition temperature in copper oxide superconductors. Furthermore, the local force theorem is examined in its original context as the map to the Heisenberg model of spin exchange coupling. It is shown that at sufficiently cold temperatures, at which well-defined local magnetic moments form, the derived interaction can be expressed by single-particle correlation functions. The formalism of effective Heisenberg mapping is extended to general non-local electron-electron interactions. It is shown that magnetic properties of complex materials can be affected by the multiorbital structure of the transition metal atoms. Interorbital Coulomb exchange gives rise to ferromagnetic spin coupling and can enhance correlation effects. In contrast, strong overlapping between orbitals of different transition metal atoms can cause dimer formation that binds the electrons into a molecular orbital state of spin-singlet type. It is found that the competition between the molecular orbital and the Hund's coupling-driven double exchange state can lead to spin-state transitions with a crossover regime which exhibits the critical property of spin freezing. Implications for theories of superconductivity and magnetism in real materials are discussed.

Contents

1	Introduction	1
1.1	Strong electronic correlations	1
1.2	Notation & units	5
2	Computational condensed matter methods	6
2.1	Tightbinding	7
2.2	Mean-field theory	8
2.3	Dynamical mean-field theory	11
2.3.1	Bethe lattice	15
2.4	Cluster dynamical mean-field theory	18
2.5	Analytic continuation	22
2.5.1	Numerical approaches	24
2.5.2	Stochastic optimization method*	26
3	Strongly correlated superconductivity	46
3.1	Copper oxides	47
3.2	Hubbard model	51
3.3	Mott insulator	53
3.4	Pseudogap	56
3.5	Two-by-two plaquette	57
3.5.1	Six-fold degenerate point of the plaquette*	59
3.5.2	Exactly solvable model*	69
3.5.3	Complex network analysis*	86
3.6	Superconducting phase fluctuations	112
3.6.1	Condensate wave function and London penetration depth	112
3.6.2	Two-dimensional phase fluctuations	115
3.6.3	Josephson lattice model*	117
4	Strongly correlated magnetism	131
4.1	Antiferromagnetism of the hypercubic lattice	132
4.2	Local force theorem for magnetism	136
4.2.1	Effective Heisenberg exchange of the extended Hubbard model*	138
4.3	Multiorbital effects	160
4.3.1	Correlations from Hund's coupling	160

4.3.2	Competing orders in multiorbital dimers*	161
4.4	Exotic magnetism	176
4.4.1	Triple Bethe lattice	176
5	Conclusion	186
	Bibliography	188
	List of Publications	209
	List of Figures	211
	Acknowledgements	213

* *includes a publication*

Chapter 1

Introduction

1.1 Strong electronic correlations

A solid state consists of periodically aligned building blocks that contain many atoms. The cores of these atoms create potentials for their electrons and such an electron can change its state by absorbing energy and thereby change its orbit around the atomic core, or it can also change its atom and move through the lattice. In particular the outermost electrons on the atom are the ones which are most likely to change the atom as these transitions require energies that can occur in the everyday life by, e.g., heat or radiation. These transitions and their respective energies define the relevant scale for solid state, or condensed matter, phenomena. More precisely, the itinerant electrons of a solid state form a common quantum many-body state for that, strictly speaking, it is impossible to assign single electrons to their atomic cores as the considered electrons behave like waves that are everywhere in the solid and fundamentally indistinguishable. In this regard, the atomic cores are well-described by point masses, whereas the electrons can be thought of as strings, or membranes, that are stretched between these points and the vibrations are the states of these electrons. In that analogy, only resonant vibrations are valid states for the electrons. Therefore, electronic states belong to discrete energies and can be characterized by their direction and wavelength. This is the main idea behind band theory [1, 2] that can distinguish metals and insulators by the electronic band structure, in which bands are discrete energy levels. If the energetically highest band is only partially occupied by electrons, then the material is predicted to be a metal. If the band is fully occupied (or empty), then it is an insulator.

The assumption of the band structure model neglects interactions between the electrons which can be reasonable in some cases, but if the bandwidth of certain states is of similar magnitude as the interaction between the electrons, then competing effects between the kinetic and potential energies of the electrons can occur. This can lead to metal insulator transitions in materials of partially filled bands due to electron-electron couplings [3, 4]. Such interelectronic effects are summarized under the notion of strong electronic correlations that manifest in a diverse range of phenomena. Materials of such phenomena are transition metal compounds [5] with the transition metals being the elements of partially

filled atomic d and f shells. Transitions of valence electrons in these shells define the low-energy properties of correlated materials.

Strong correlations can occur between same orbitals of different sites or can also involve different orbitals, e.g. in the rare earths and actinides the f electrons tend to be more localized forming local magnetic moments. The screening of this local moment by conduction electrons can occur upon cooling and is known as the Kondo effect [6] which also causes an anomaly in the temperature dependence of the system's conductance. Usually, conduction electrons scatter on the local magnetic moments, but at the Kondo temperature they resonate and form a spin singlet state. Thus, the local moments become screened which leads to a minimum in the resistance. It was measured in impurity systems in which the magnetic impurity is embedded in a metallic host. But the screening effect occurs not only in impurity setups, but also in lattices that have competing interactions.

One of the early approaches to describe interaction effects has been by perturbation theory. If the correlation effects are sufficiently small, then the system can be described as a Fermi gas with renormalized masses, a Fermi liquid. The validity of Fermi liquid theory depends on the one-to-one correspondence, or adiabatic continuity, to the particles of the noninteracting system. But in strongly correlated systems the low-energy excitations can be different from renormalized electrons, and Fermi liquid theory can, at best, only describe the system's state up to the transition point to a different phase. In some systems the electron masses are renormalized to a thousand times heavier due to strong correlations, such systems are termed heavy fermion compounds [7].

A hallmark example for strong electronic correlations is the Mott insulating phase [8, 9]. The corresponding metal-insulator transition is paramagnetic and has a band gap which is proportional to the electron-electron interaction, the screened Coulomb repulsion [10, 11]. In proximity of the Mott transition the electrons localize and turn from wave-like into particle-like. The intuition behind this idea is that of electrons being in a traffic jam, they are blocking each other and thus can not support an electrical current. Materials such as Nickel oxide [12], vanadates (VO_2 , SrVO_3) and titanates (LaTiO_3 , YTiO_3) [13] exhibit properties that agree with the concept of strong electronic correlations and Mottness. The correlated electrons stem from the highest occupied orbital, i.e. close to Fermi level, of the transition metals (V, La, Y). The d electrons extend from the core of the atom so that the highest d levels of the transition metals can hybridize with their ligands, e.g. with p orbitals of neighboring oxygen atoms which is often the case for the common crystal structure of the perovskites where each transition metal atom is coordinated by an octahedron of oxygen atoms on its corners. Besides crystal field splitting of the d levels, the ligands of the transition metals also support the tunneling of electrons between the transition metal atoms via the superexchange mechanism [14], which causes the delocalization of the correlated electrons. The tunneling amplitude is defined by the bonding-antibonding splitting of the hybridization with the ligands. In contrast, localization is promoted by the double occupation of a transition metal atom. Importantly, Non-trivial effects can occur because a many-body wavefunction can be a quantum superposition of doubly/empty and singly occupied sites of the lattice.

The minimal model to describe the Mott insulator is the Hubbard model [15]. It

describes the electrons moving through a lattice and minimizing the systems energy by tunneling from site to site, and if two electrons meet at the same site, they raise the energy of system resembling the Coulomb repulsion. Details of the atom's orbital structure and the interatomic tunneling of the electrons are considered effectively only. The Hubbard model is minimal in the sense that it can describe the bands of freely moving electrons, but it combines it with the simplest energetic structure of an atom for the description of a site. Thus, a solution of the Hubbard model considers the effects of the lattice geometry as well as the quantum many-body structure of a, so-called, Hubbard atom that can be occupied by zero to two electrons. Depending on the parameters of the model, the low-energy physics of the system can be dominated by properties of the lattice or of the atomic structure. Moreover, new phenomena can emerge by the complex competition between the two [16, 17].

Especially by computational techniques, it has been found that the Hubbard model, or related models, can describe crucial features of these materials. Albeit the results also depend on the approximation. Numerical approaches are still being developed and have to converge to a consistent and complete picture. Computational approaches to strongly correlated electrons have focused on finite-size studies [18] and mean-field techniques. Regarding the Hubbard model there, are two outstanding achievements which are exact solutions. First, the Bethe ansatz that works only in one dimension [19], i.e. for chains. The quantum character of such systems becomes evident as spin and charge of an electron can be separated meaning that excitations can carry only fractions of the electron's properties which originally are the many-body wavefunction's constituents. And second, the dynamical mean-field theory that solves the Hubbard model exactly, but only in infinite dimensions [20, 21]. Further, it is used to construct approximations for finite dimensions. The number of dimensions, in the context of lattices, is basically the coordination number. It turned out that in certain aspects, e.g. regarding orderings, three dimensional structures are more similar to infinite dimensions than to one dimension. However, the case of two dimensions, for superconducting copper oxides, is special [22, 23] and current approaches have to be improved.

Properties of the copper oxides belong to the most notable experimental findings in condensed matter physics that remain to be fully understood. In 1986, the historically first copper oxide compound was identified as a high-temperature superconductor [24]. The superconducting state is interesting on one hand for technologies as it can conduct without resistance and exhibits the Meissner effect of expelling magnetic fields [25], and on the other hand it is a macroscopic quantum state in that a huge number of electrons, which originally are fermions, have condensed into the same wavefunction which is conceptually appealing for theorists. The superconducting state is realized by cooling certain materials.

The Bardeen-Cooper-Schrieffer (BCS) theory of conventional (non-copper oxide) superconductors uses electron-phonon coupling as an explanation for the effective attractive force, the "glue", between electrons that makes them pair into Cooper pairs [26] which obey bosonic statistics. Depending on the mechanism, superconductors are divided into conventional and unconventional superconductors. Most of the elemental superconductors are conventional, e.g. Nb and Hg. Their transition temperatures lie in a range up to 20 K.

Therefore, the relatively high transition temperatures found in copper oxides have been an intriguing finding. Besides the copper oxides, there are also superconducting iron pnictides and heavy fermion superconductors, rare earth compounds. It is unclear whether all unconventional superconductors have a common pairing mechanism [27]. It would be subtle, because the iron pnictides and heavy fermion compounds are suspected to exhibit multiple atomic orbitals which are correlated, whereas the copper oxides are usually modeled using a single atomic orbital.

A popular example of the copper oxide family, also known as cuprates, is yttrium barium copper oxide with a transition temperature of 93 K [28]. Whereas the formalism and perhaps some elements of BCS theory can be adapted for a theory of high temperature superconductivity (HTSC), the phonons at such high temperatures are rather incoherent and thus as an explanation not straight-forwardly applicable to HTSC. The copper oxide superconductors consist of quasi-two dimensional copper oxide planes that are separated by relatively large spacers, e.g. yttrium atoms. A lot of theoretical progress [29, 30, 31, 32, 33] has been achieved by modeling these planes using the two-dimensional Hubbard model, or the very similar t - J model [34, 35], indicating that electronic correlations play an important role in the HTSC mechanism.

The copper oxides planes have to be hole doped in order to turn superconducting. Hole dopings means to effectively remove electrons from the strongly correlated copper oxide planes. The realization of the doping process depends on the compound, e.g. for $\text{La}_{2-x}\text{Sr}_x\text{Cu}_4\text{O}$ the transition metal La, with one d valence-electron, is replaced by the earth metal Sr which has no d valence-electrons. At half-filling, the copper oxides are insulating and at sufficiently low temperatures antiferromagnetic. Whereas the mechanism of strongly correlated superconductivity remains puzzling, in contrast, the relation of antiferromagnetism to Mottness is better understood. The defining energy scale of this kind of antiferromagnetism, i.e. Heisenberg antiferromagnetism, is the nearest-neighbor spin exchange “ J ” [36] which can be derived from the Hubbard model as a prime example for the notion of emergence. An intuitive picture of the Mottness behind the Heisenberg antiferromagnetism can be gained by imagining localized electrons on a Hubbard lattice. The quantum mechanical character of the state allows for a very weak delocalization of the electrons to the neighboring sites at the same time, so-called virtual state contributions. Due to the fermionic nature of the electrons, the only way to tunnel to a neighboring site without changing the spin configuration is, if the spins are antiferromagnetically aligned. Thus, the localized state of the electrons serves as a starting point, but the nearest neighbor spatial correlation is crucial for understanding the Heisenberg antiferromagnetism based on the Hubbard model.

In this sense, superconductivity and magnetism are intimately connected by their common origin of strong electronic correlations. The correlated substructures of strongly correlated materials can be diverse and are usually formed by low-energy states of d and f (valence-)electrons. In theory, the correlated substructure can exhibit finer resolution of the atom, such as the intra-atomic Hund’s coupling, or certain spatial degrees of freedom. Hund’s coupling is commonly associated with the ferromagnetic coupling of local spins in different orbitals of the same atom. However, strong correlations can change the impact

of this coupling dramatically, due to the competition with the electron's itineracy it can cause heavily renormalized quasiparticles [37].

Quantitative descriptions of correlated materials are challenging and computational approaches are popular in this field. One of the most common numerical ab initio methods is the density functional theory [38, 39]. It allows to calculate the groundstate wavefunction of one-particle theories. However, strong correlations require extensions [40, 41, 42, 43] that account for quantum many-body effects. The dynamical mean-field theory (DMFT) treats the lattice and the atomic quantum many-body structures on equal footing and thereby allows for an unbiased prediction on the outcome of the competition between the two. The Mott insulator is the simplest example where this becomes important. More complex correlated atomic structures make the theory computationally more demanding, but are feasible in principle. The theory is applicable for problems of finite temperatures and infinite-size systems, but it neglects spatial correlations beyond the atom. This approximation is very reasonable for lattices with large coordination numbers.

In contrast for, e.g., the quasi two-dimensional copper oxides spatial correlations beyond the atom are important and extensions of the DMFT have been developed that capture these effects. The cluster dynamical mean-field theory (CDMFT) includes the spatial correlations of finite-size clusters within the lattice and since the size of the correlated subspace grows exponentially with the sites of the cluster, a vast number of correlated degrees of freedom become available for the search of new competing effects. Mean-field theories rely on the solution of implicit equations, that are solved by "good" initial guesses followed by the iterative application of the implicit equation until, ideally, a convergence to an attractive fixpoint is reached. This has to be done numerically which is a reason for the rapid progress of computational approaches in this field [44, 45]. In particular quantitative predictions that need to take into account many properties and effects often can only be solved with computational methods. Moreover, computational methods [46, 47, 48] provide useful tools to get an overview and intuition of quantum systems and give insights that can be improved upon by purely analytical approaches.

1.2 Notation & units

Throughout this thesis frequencies and temperatures are provided in units of energy using $\hbar = 1$ and $k_B = 1$ if not stated differently explicitly. According to conventions of research on the Hubbard model, the amplitude of the nearest neighbor hopping $|t|$ is taken as the unit of energy. However, in this work, the sign is chosen so that $t < 0$. Thus, another energy of different sign would be, e.g., $t' = 0.3$, but $t'/t = -0.3$. This convention absorbs the signs into the actual parameters and the hamiltonian of the model can be written without any concerns about the signs. Nevertheless, since this work contains publications to which different authors have contributed, the convention that are applied differ, but this is stated explicitly in the respective works. In particular, publications that discuss features of materials more closely provide energies in electronvolts (eV) or even restore the original physical dimensions. Finally, the term "plaquette" is used for the description of the quadratic two-by-two cluster.

Chapter 2

Computational condensed matter methods

This chapter introduces the cluster dynamical mean-field theory (CDMFT). The method builds upon other techniques that are not related to CDMFT entirely, so they can be introduced separately. The CDMFT is a mean-field theory, that maps an interacting lattice to an interacting cluster in a renormalized, non-interacting bath. The latter setup can be described by the multiorbital Anderson impurity model. The non-interacting solution is obtained by the tightbinding method. The mapping to a cluster is an extension of the mapping to a single site. The case of a single site is solved by the dynamical mean-field theory (DMFT). The theory becomes exact in the limit of infinite dimensions which can be taken on e.g. the Bethe lattice. Finally, at finite temperatures and depending on the numerical impurity solver, an analytic continuation from Matsubara frequencies to real frequencies has to be done. It produces correlation functions on real frequencies from correlation functions on Matsubara frequencies. The former are necessary to compare the calculations with experimental results from e.g. photoemission spectroscopy.

The cluster extension of DMFT is developed for the purpose of capturing spatial correlations which are non-local on the microscopic scale, i.e. short-ranged. In contrast, other descriptions aim to describe long-range effects, e.g. the Ginzburg-Landau field theory [49] and the effect of Goldstone modes in low dimensions [22]. Systems are described on macroscopic scales including an infinite number of atoms or sites. Short-range effects can also be addressed by solving the matrix presentation of finite-size systems numerically, a popular example is the density matrix renormalization group [46, 50]. The latter can be used to study correlation lengths which is interesting for the detection of second order phase transitions. However, the finite-size property can always be subjected to introduce artifacts stemming from the boundaries. The CDMFT includes spatial correlations within the cluster, but neglects those beyond the cluster, because the environment of the cluster is summarized into a mean-field. Importantly, the CDMFT aims to describe a system in the thermodynamic limit, but only effectively, i.e. without spatial correlations beyond the cluster. In particular this means that the CDMFT can be expected to give more reliable results in systems of large coordination, or similarly, of large temperatures where the correlation

lengths tend to be shorter.

2.1 Tightbinding

Lattices break the continuous translational symmetry of the vacuum down to discrete space group symmetries. The tight binding method uses the translational symmetry of the lattices in order to determine the spectrum of the electrons. The model describes electrons hopping over the lattice sites i, j optimizing their kinetic energies described by the parameters of the hopping amplitudes t_{ij} . Therefore the Hamiltonian reads

$$H = \sum_{ij} c_i^\dagger t_{ij} c_j. \quad (2.1)$$

Each electron contributes independently, which leads to a hamiltonian of only single-particle processes. The fermionic character is described by the fermionic creation c^\dagger and annihilation operators c .

The success of this method originates from the overlaps of atomic orbitals in solids. They allow for tunneling processes of the electrons between the atoms. The electrons move through the potentials given by the atoms of the solid and only hopping processes between close neighbours occur. The least localized electrons are in the outer shells of the atoms and often only those are considered as they determine the low-energy properties of the solid. The lattice unit cell need not be only a single atom, but can also consist of more complex structures.

The strategy of solving the model is based on the fact that the hopping

$$t_{ij} = t(r_i, r_j) = t(r_i - r_j) \quad (2.2)$$

depends only on translations $r_i - r_j$ and has only a finite number of non-zero entries in that representation due to the tight-binding of the electrons. Therefore the sum over i, j effectively becomes finite in an infinite-spatially extended lattice. Because of the periodicity the momentum k is a good quantum number and plane waves are the corresponding eigenstates. Then, the diagonalization of t_{ij} requires a Fourier transform

$$c_i^\dagger = \sum_k w_k c_k^\dagger e^{-ikr_i}, \quad c_i = \sum_k w_k c_k e^{ikr_i}. \quad (2.3)$$

A more complicated situation with more atomic degrees of freedom can be treated e.g. with Bloch waves [2]. For the calculation of local properties, e.g. the local density of states

$$D(\omega) = \sum_k w_k \delta(\omega - t_k), \quad (2.4)$$

one has to perform the sum over k . The normalization is treated by w_k . Often the weights are equal to the number of k -points of the full Brillouin zone $w_k = 1/N_k$. However, in some cases it is reasonable to take into account additional symmetries of the lattice basis, e.g. reflection or rotation, that reduce the summation over the full Brillouin zone to a sum

over a irreducible wedge, i.e. a part that contains all the different points of the Brillouin zone. The corners and edges of the irreducible wedge have different weights w_k than the interior. Finally, as a matter of convention it shall be noted that the Fourier transform of t_{ij} is usually denoted as $\varepsilon(k)$.

2.2 Mean-field theory

A first introduction to the dynamical mean-field theory [20] can be well understood in the context of the related static mean-field theory. The mean-field theory can be used to approximate different models by simplifying a quartic interaction into an effective quadratic one. For example, the self-consistent Hartree-Fock perturbation theory for the quartic interaction U_{ijkl} can be regarded as a mean-field approximation, i.e.

$$\begin{aligned} H &= c_i t_{ij} c_j^\dagger + c_i c_j U_{ijkl} c_k^\dagger c_l^\dagger \\ &\simeq (t_{il} + \underbrace{(U_{ijlk} - U_{ijkl}) G_{jk}}_{\Sigma_{il}^{HF}}) c_i c_l^\dagger, \end{aligned} \quad (2.5)$$

using fermion operators (c^\dagger , c), the sum convention for indices which occur twice and the definition of the Green function

$$G_{ij} = -\langle c_i c_j^\dagger \rangle. \quad (2.6)$$

Importantly, the quadratic auxiliary problem ($U_{ijkl} = 0$) can be solved analytically with the solution of G^0 . Σ^{HF} is the self-energy that occurs in perturbation theory and can be defined via the Dyson equation

$$\Sigma = (G^0)^{-1} - G^{-1}, \quad (2.7)$$

which closes the self-consistency. Technically, this approximation of Eq. (2.5) is obtained by partial Wick contractions, that keep track of the different exchange processes and lead to the Hartree and Fock -terms of Σ^{HF} . It is important to note, that the remaining creation and annihilation operators are still acting on the Hilbert space and G is the substituted expectation value. Thus there is still the full one-particle problem to be solved in each mean-field iteration. There are different ways to solve the one-particle problem, that also depend on the system under consideration. In the framework of density functional theory [38] the interpretation of the self-energy as a one-particle effective potential has lead to successful first principle theories [41].

As a popular example of mean-field theory is the Ising model, that is discussed in the following of this section in the context of (Weiss) mean-field theory. In a system of classical spins S , the Ising model, with interaction J and external magnetic field h the Hamilton

operator reads

$$\begin{aligned}
H &= - \sum_{ij} J_{ij} S_i S_j - h \sum_i S_i, \\
&\simeq - \sum_j \left(\sum_i J_{ij} m_i + h \right) S_j \\
&= -h_{eff} S_0.
\end{aligned} \tag{2.8}$$

h_{eff} is the effective field, that acts on a single local spin S_0 and effectively accounts for the whole environment. The second equation of Eq. (2.8) is the mean-field approximation $S_i \mapsto m_i = \langle S_i \rangle$, where quantum correlations of the term $S_i S_j$ are neglected by the replacement of the operator S with its expectation value, the magnetization m . More formally mean-field approximations can be defined as expansions in the fluctuations $\delta S = S - m$, this would add a trivial term $\sim m^2$. In the last equation of Eq. (2.8) also the translation invariance of the lattice has been used, such that all sites i, j become equivalent. The the magnetization can be calculated as

$$m = \tanh(\beta h + \beta z J m), \tag{2.9}$$

where J_{ij} has been reduced to interaction between nearest neighbours J and each site has z nearest neighbors. Eq. (2.9) resembles the typical mean-field character in terms of implicit equations, that can not be solved analytically, but numerically instead. E.g. a guess for m is used to initialize the iterative calculation of Eq. (2.9) and hopefully this series converges.

The introduction of the mean-field approximation in Eq. (2.8) was rather informal and ad-hoc. It means, that it remains unclear whether the representability of the chosen auxiliary system is guaranteed. In order to understand the approximation or even control it, it is necessary to find a formalism that allows a derivation of the weiss field's construction [51, 52, 21]. Reminding that a system of interacting spins with non-local interaction shall be represented by a local spin, it is reasonable to introduce an additional parameter that interpolates between the local and the non-local systems

$$H = \alpha \sum_{ij} J_{ij} S_i S_j. \tag{2.10}$$

Next, the local magnetization is introduced as a parameter by means of the Legendre transform

$$\begin{aligned}
\Gamma_\alpha(m_i) &= -\beta^{-1} \ln \text{Tr} e^{-\beta(H_\alpha + \sum_i \lambda_i (S_i - m_i))} \\
&= -\beta^{-1} \ln \text{Tr} e^{-\beta(H_\alpha + \sum_i \lambda_i S_i)} + \sum_i \lambda_i m_i,
\end{aligned} \tag{2.11}$$

with the constraint

$$\langle S_i \rangle = m_i \tag{2.12}$$

enforced by the Lagrange multipliers λ_i , that are determined by m_i via Eq. (2.12) and thus $\lambda_i = \lambda_i(m_i)$, which also means that Γ depends only on m_i . The evaluation of the new

functional for the chosen local reference system of $\alpha = 0$ becomes

$$\Gamma_0(m_i) = \sum_i \left(-\beta^{-1} \ln \cosh \beta \lambda_i + m_i \lambda_i \right), \quad (2.13)$$

whose minimum with respect to λ_i determines the latter (for $\alpha = 0$)

$$\lambda_i(m_i) = \beta^{-1} \tanh^{-1} m_i \quad (2.14)$$

and shows that λ_i is indeed the Weiss field. The explicit form of the functional thus reads

$$\begin{aligned} \Gamma_0(m_i) &= \beta^{-1} \sum_i \left(\frac{1+m_i}{2} \ln \frac{1+m_i}{2} + \frac{1-m_i}{2} \ln \frac{1-m_i}{2} \right) \\ &= \beta^{-1} \sum_{i\sigma} P_{i\sigma} \ln P_{i\sigma} \end{aligned} \quad (2.15)$$

in that for the elimination of λ_i the identity $2 \tanh^{-1}(x) = \ln(1+x) - \ln(1-x)$ is used. Further, the term resembles the entropy of free Ising spins with the probability distribution $P_{i\sigma} = (1+\sigma m_i)/2$ and $\sigma \in +1, -1$ for spin-up and -down configurations. In the case of Ising spins $m_i \in \{-1, 1\}$ it is clear that Eq. (2.14) holds and the representability is guaranteed, i.e. the Weiss field λ_i always exists.

Returning to the original system of $\alpha = 1$ the functional $\Gamma \equiv \Gamma_{\alpha=1}$ can be obtained starting from Γ_0 by an integration over the coupling constant

$$\Gamma(m_i) = \Gamma_0(m_i) + \int_0^1 d\alpha \frac{d\Gamma_\alpha}{d\alpha}(m_i). \quad (2.16)$$

From Eq. (2.11) it can be seen that the calculation of the derivative is straight forward and gives

$$\frac{d\Gamma_\alpha}{d\alpha} = - \sum_{ij} J_{ij} \langle S_i S_j \rangle. \quad (2.17)$$

The insertion of constraint Eq. (2.12) finally gives

$$\Gamma(m_i) = \underbrace{\Gamma_0(m_i) - \sum_{ij} J_{ij} m_i m_j}_{\Gamma_{MFT}} - \underbrace{\sum_{ij} J_{ij} \langle (S_i - m_i)(S_j - m_j) \rangle}_{\Gamma_{corr}}. \quad (2.18)$$

The minimization of Γ_{MFT} well reproduces the Weiss mean-field (Eq. (2.9), here without external field for convenience) and the correlated part Γ_{corr} is neglected in this approach. Furthermore it is possible to write the exact mean-field of the equilibrium as

$$h_i^{eff} = \sum_j J_{ij} m_j - \frac{d\Gamma_{corr}}{dm_i}. \quad (2.19)$$

In the course of the functional derivation the distinction between the choice of reference system (Eq. (2.14)) and the approximation (Eq. (2.19)) is clearly shown. Additionally,

the functional framework offers opportunities to improve systematically the Weiss field approximation. E.g. it is possible to expand $\beta\Gamma$ in β , i.e. a high temperature expansion [52]. The latter turns out to be similar in its mathematical structure to an expansion in the coordination number z with nearest neighbor interaction $J_{ij} \sim zJ$.

The expansion in z is particularly interesting because it shows that in the limit of infinite coordination, or equivalently dimensions, the mean-field approach becomes exact. This expansion requires to rescale the interaction proportional to $1/z$ in order to keep the energy density E/N constant. Thus by the choice of $J = 1/(2z)$, the free energy expands as [52]

$$\begin{aligned}
-\frac{\beta A}{N} = & - \left(\frac{1+m}{2} \ln \frac{1+m}{2} + \frac{1-m}{2} \ln \frac{1-m}{2} \right) \\
& + \frac{\beta}{2z} z m^2 \\
& + \frac{1}{2} \left(\frac{\beta}{2z} \right)^2 z (1-m^2)^2 \\
& + \mathcal{O}(1/z)^3.
\end{aligned} \tag{2.20}$$

The first two terms can be recognized as the mean-field contributions. The third term is of higher order ($1/z$) and vanishes as $z \rightarrow \infty$. Therefore, Eq. (2.20) shows an example of how mean-field theory becomes exact in the limit of infinite dimensions. Further this expansion can also work at lower temperatures. Using mean-field theory in finite dimensions in the context of the Ising model, it can predict magnetic phases. However, even if the mean-field approximation at finite dimensions predicts a broken symmetry phase correctly, quantities such as the critical temperature or critical exponents still have to be questioned.

2.3 Dynamical mean-field theory

In static mean-field theory, presented in Sec. 2.2, not only non-local correlations are neglected but also local correlations of fluctuations. Because, in the course of solving the local reference problem of a site in a mean-field, the operators are replaced by expectation values. It is possible to improve upon that, by mapping to a different auxiliary setup that includes such effects. The considered interaction can contain a non-local quadratic term and an arbitrary, but local, term

$$H = \sum_{ij\sigma} t_{ij} c_{i\sigma}^\dagger c_{j\sigma} + H_{loc}, \tag{2.21}$$

where c^\dagger and c , create and annihilate fermions of spin σ , respectively and t is the hopping between the sites i, j of a lattice. Thereby it defines the symmetries of the lattice. Further, it can be diagonalized in Fourier space. The Green function will contain all local correlations and thus it depends on imaginary time

$$G_{i\sigma, j\sigma}(\tau - \tau') = - \left\langle \mathbf{T}_\tau c_{i\sigma}(\tau) c_{j\sigma}^\dagger(\tau') \right\rangle \tag{2.22}$$

with imaginary time τ and τ ordering operator T_τ . The imaginary time propagation of one-particle processes described by $G(\tau)$ contains information about the local fluctuations and their correlations.

Then, the DMFT [20, 53, 42, 21, 54] maps lattice models with local interactions H_{loc} to the effective Anderson impurity model

$$\begin{aligned} H_{AIM} &= H_{loc} + H_{bath} + H_{hyb}, \\ H_{bath} &= \sum_{l\sigma} \epsilon_l^a a_{l\sigma}^\dagger a_{l\sigma}, \\ H_{hyb} &= \sum_{l\sigma} \left(V_l a_{l\sigma}^\dagger c_\sigma + \text{h.c.} \right), \end{aligned} \quad (2.23)$$

with bath fermions a and impurity fermions c . There are different bath levels l but only one impurity level of different spins σ . In principle, the impurity can also have a multiorbital structure, but this is omitted here for convenience. This model is numerically solvable, e.g. by Monte-Carlo techniques [44], and the correlation function $G_{imp}(\tau)$ has information about all local one-particle correlations. For example, a bath electron can tunnel from the bath onto the impurity, remain there for some imaginary time and tunnel back. Another bath electron could do the same, and if two meet, then the system experiences an energy gain by U . These correlations are dynamical as they depend on τ .

The DMFT separates the lattice of Eq. (2.21) into a single site (impurity) and the remaining environment (bath). The bath, according to Eq. (2.23), has only single-particle transitions, whereas the original environment has H_{loc} on each site. Thus, the DMFT describes a self-consistency that adjusts the bath so that it effectively models an environment of interacting sites. The effective action of the impurity setup for the paramagnetic case reads

$$S_{imp} = - \int_0^\beta d\tau \int_0^\beta d\tau' \sum_\sigma c_\sigma^\dagger(\tau) \mathcal{G}^{-1}(\tau - \tau') c_\sigma(\tau') + \int_0^\beta d\tau H_{loc}(\tau) \quad (2.24)$$

with the dynamical mean-field (bath Green function)

$$\mathcal{G}^{-1}(i\omega_n) = i\omega_n + \mu - \underbrace{\sum_l \frac{|V_l|^2}{i\omega_n - \epsilon_l^a}}_{\Delta(i\omega_n)}, \quad (2.25)$$

written in Matsubara frequency ω_n representation. $\Delta(i\omega_n)$ is the hybridization function that results from the integration over the bath degree of freedoms of the impurity setup (Eq. (2.23)) and characterizes the effective bath. $\Delta(i\omega_n)$ has the same matrix-structure as $\mathcal{G}(i\omega_n)$, however V can become a non-square matrix since the bath parameters l need not be of the same number as the single-particle orbitals as $\Delta_{\alpha\beta} \propto \sum_l V_{\alpha l} V_{l\beta}^\dagger$. It has its poles at ϵ_l^a with the weights defined by V_l . Depending on the implementation these two quantities or, equivalently, $\Delta(i\omega_n)$ have to converge in the course of the self-consistency.

The self-consistency is obtained if

$$G_{loc}(i\omega_n) = \sum_k G(k, i\omega_n) = \int_{-\infty}^{\infty} d\epsilon \frac{N_0(\epsilon)}{i\omega_n + \mu - \Sigma(i\omega_n) - \epsilon} = G_{imp}(i\omega_n), \quad (2.26)$$

the local lattice Green function G_{loc} equals the impurity Green function G_{imp} . The local Green function can be obtained by the summation over the Brillouin zone of the wave-vector k dependent lattice Green function

$$G^{-1}(k, i\omega_n) = i\omega_n + \mu - \epsilon_k - \Sigma(k, i\omega_n), \quad (2.27)$$

where ϵ_k is the Fourier transform of t_{ij} and $\Sigma(k, i\omega_n)$ the self-energy. However, the integral need not be performed over k , but more generically it can also be written as an integral over energies ϵ using the non-interacting density of states of the considered system $N_0(\epsilon)$.

The reformulation is complete and the local lattice Green function is represented with an impurity setup. The term ‘‘dynamical’’ is not related to non-equilibrium physics, but stresses the mean-field extension by imaginary times or Matsubara frequencies in $\mathcal{G}(i\omega_n)$. It allows the DMFT to include different energy scales in the excitation spectrum at equilibrium. Next, the approximation can be introduced within the obtained framework. In the Dyson equation the self-energy has k -dependence and the latter is neglected in the following approximation

$$\Sigma_{ij}(i\omega_n) \simeq \delta_{ij} \Sigma_{imp}(i\omega_n), \quad (2.28)$$

where the impurity self-energy

$$\Sigma_{imp} = \mathcal{G}^{-1} - G_{imp}^{-1} \quad (2.29)$$

obeys a Dyson-like equation. Thus, the approximation is to consider a purely local self-energy with all non-local entries being zero. In principle, the self-energy could be eliminated from the expressions above and instead the approximation can be formulated with the hybridization function only. However, it is useful to introduce the self-energy as it can be used to prove conservation properties of the DMFT [55, 56, 57].

The DMFT has the non-interacting limit $H_{loc} = 0$, for that $G(i\omega_n) = \mathcal{G}(i\omega_n)$, which also means that $\Sigma(i\omega_n) = 0$, i.e. the self-energy has no k -dependence and thereby this limit is well described by the DMFT. The solution basically reduces to the Fourier transform of the hopping $t_{ij} \mapsto \epsilon_k$ and thus the electrons are very itinerant and of wave-type. The opposite limit is the atomic limit of $t_{ij} = 0$ which gives $\Delta(i\omega_n)$ and corresponds to a lattice of disconnected atoms. Then, the electrons are localized particles on those atoms and the atomic structure alone determines the properties of the lattice. Hence, both limits are reproduced by the DMFT and additionally it can interpolate between them. It also stresses the non-perturbative character of the DMFT.

The DMFT is accurate if intersite correlations are small or negligible. For example this is the case for lattices with a large coordination number and dimensionality or at high temperatures. Further, short-range correlations can be caused by orbital degeneracies or frustration, e.g. by the geometry of the lattice. In contrast long-correlation length as in the proximity of second order phase transitions are not described by the DMFT and its results

become questionable. Finally, H_{loc} has not been specified and the introduction above is rather abstract in this regard. In that context it shall be pointed out that the lattice can also be presented more abstractly in the framework of DMFT. For example, the single-particle transition energies can also be provided by density functional theory [39, 58] where a correlated subspace has to be selected and this subspace enters the DMFT calculation.

Different techniques have been developed to derive or motivate the DMFT equations [20, 42]. One of them is the coupling constant integration [21] analogous to Eq. (2.16). For the construction of such a functional, the non-local hopping part of Eq. (2.21) is rescaled. Then, regarding the Legendre transform, the constraint is $G_{ij}(\tau - \tau') = -c_i(\tau)c_j^\dagger(\tau')$ with the Lagrange multiplier being the hybridization function $\Delta(\tau - \tau')$. $\Delta(\tau - \tau')$ depends on imaginary time τ which is the important difference to static mean-field theory, and the local, auxiliary problem can be of many-body type. Again, this formalism stresses the distinction between representation and approximation, and can also show the exact limit in infinite dimensions. However, it results in a functional that depends only on G as Δ is not an independent variable but expressed by a coupling constant integration over G [21].

The exactness of the DMFT equations in the limit of infinite dimensions (coordination) is closely related to the self-energy becoming local $\Sigma_{ij}(i\omega_n) \propto \delta_{ij}\Sigma(i\omega_n)$. An important detail is that one has to require a finite total kinetic energy, or equivalently bandwidth, while that limit is performed. Examples [20] are the Bethe lattice with the density of states $A(\epsilon) = \sqrt{4t^2 - \epsilon^2}/(2\pi t^2)$ for $|\epsilon| < 2t$ and the hypercubic lattice with $A(\epsilon) = \exp(-\epsilon^2/(2t^2))/\sqrt{2\pi t^2}$, where t is the nearest neighbor hopping. Both require the rescaling of the hopping

$$t \mapsto \frac{t}{\sqrt{d}}, \quad (2.30)$$

as the dimensionality $d \rightarrow \infty$. Considering a perturbation theory for a small local interaction, i.e. weak coupling, the non-interacting propagator obeys

$$G_{ij}^0 \sim \mathcal{O}\left(1/d^{|r_i - r_j|/2}\right), \quad (2.31)$$

with position vectors r_i and r_j , similar to the hopping. In real space the interaction is represented by a four-leg vertex. All diagrams for that two internal vertices can be connected by more than two paths vanish as $d \rightarrow \infty$ except for $i = j$ [59]. The contributing diagrams can be summarized by a skeleton expansion of the self-energy for that the non-interacting propagators are replaced by full propagators. This groups internal corrections to non-interacting propagators together into a single diagram of full propagators. The skeleton diagrams can be generated using the Luttinger-Ward functional [55, 60] Φ ,

$$\Sigma = \frac{\delta\Phi}{\delta G}, \quad (2.32)$$

and in particular for infinite dimensions

$$\Phi = \sum_i \phi[G_{ii}], \quad (2.33)$$

which gives the exact relation of Eq. (2.28), i.e. a local self-energy. However, the self-energy exhibits still the full dynamics in the sense of the Matsubara frequency dependence. Numerical calculations [59] indicate that the physics of three and infinite dimensions can be similar, whereas in one dimension it is well-known to be very different [19].

Eq. (2.32) and Eq. (2.33) suggest the application of the Baym-Kadanoff functional framework [56, 60, 42]. For that, the free energy

$$\Omega[G, \Sigma] = -\text{Tr} \ln(G_0^{-1} - \Sigma) - \text{Tr} \Sigma G + \Phi, \quad (2.34)$$

depends on the Green function and the self-energy. G_0 is the non-interacting Green function. This framework is not restricted to the infinite-dimensionality problem but is more generic and can be applied in the context of many perturbation theories. It is especially useful for proving the conserving property of approximations. It provides the value of the free energy of a system at its stationary point. The variation with respect to G gives Eq. (2.32) and the variation with respect to Σ gives the Dyson equation

$$\Sigma = G_0^{-1} - G^{-1}, \quad (2.35)$$

which coincides with the expression for the lattice Green function Eq. (2.27). However, it shall be stressed that G_0 must not be confused with \mathcal{G} as the latter also depends on the hybridization. Moreover, the so-called Dyson-like equation of Eq. (2.29) includes only the local (impurity) Green function rather than the lattice Green function so that there is no contradiction but only a required consistence of local and lattice quantities that has to be found.

2.3.1 Bethe lattice

The Bethe lattice is a self-similar structure, and strictly speaking it is not a lattice in the sense of translational invariance, but importantly it is understood how it can be constructed in infinite dimensions. The starting point for its construction are Cayley trees. These are simple trees consisting of vertices and branches. A Cayley tree is defined by its coordination number z , i.e. number of nearest neighbors, and its recursion number k . The tree has a root vertex and the number of branches that are being transversed by going to the edge of the tree gives the recursion depth, see Fig. 2.1. Such a tree has no loops. The Bethe lattice is a Cayley tree with infinite vertices $k = \infty$, i.e. sites, and thus it does not have a root. It was considered for the first time in the context of disordered systems in large dimensions [61]. In the DMFT of the Bethe lattice, the lattice is defined by the hopping energies and its symmetries. Graphical representations can vary because different bond lengths represent the same hopping values and they differ only for illustrational purposes. The existence of the infinite-dimensional limit crucially depends on the rescaling of the hopping $t \rightarrow t/\sqrt{d}$ so that the bandwidth remains finite.

The action S of the Bethe lattice can be derived from the cavity construction method [20]. The starting point is the separation of the lattice into a cavity (S_0), the remaining

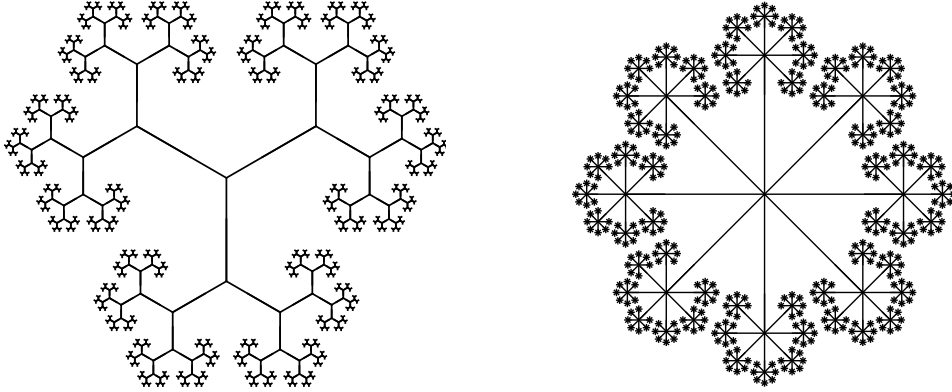


Figure 2.1: Cayley trees with coordination $z = 3$, recursion depth $k = 8$ (left) and $z = 8$, recursion depth $k = 3$ (right). Vertices present sites and branches nearest neighbor hopping connections. Different branch lengths are only for illustrational purposes and do not reflect hopping amplitudes.

environment ($S^{(0)}$) and processes between the two (ΔS)

$$S = S^{(0)} + \Delta S + S_0, \quad (2.36)$$

with

$$S_i = \int_0^\beta d\tau \sum_\sigma c_{i\sigma}^\dagger (\partial_\tau - \mu) c_{i\sigma} + H_{loc,i} \quad (2.37)$$

$$\Delta S = - \int_0^\beta d\tau \sum_{\sigma, i \neq 0} t_{i0} (c_{i\sigma}^\dagger c_{0\sigma} + c_{0\sigma}^\dagger c_{i\sigma}). \quad (2.38)$$

Since all sites are equivalent S_i describes the action on the cavity and also each site of the environment. ∂_τ is the imaginary time derivative and σ denotes the spin. In ΔS there is a distinction between the cavity $i = 0$ and its nearest neighbors i . $S^{(0)}$ includes the full environment with the cavity removed. Thus, it contains not only the sum over S_i , but also hoppings between the sites. The next step is to assume that the environment can be integrated over and gives a Green function of the environment $G^{(0)}$. The remaining degree of freedom is that of the cavity with an effective action

$$S_{eff} = - \sum_{n=1}^{\infty} \sum_{i_1 \dots j_n} c_0^\dagger t_{0i_1} \dots c_{i_n}^\dagger t_{i_n i_{n-1}} \dots t_{j_1 0} c_0 \dots t_{j_n 0} c_0 \underbrace{\langle T_\tau c_{i_1} \dots c_{i_n} c_{j_1}^\dagger \dots c_{j_n}^\dagger \rangle^{(0)}}_{-G_{i_1 \dots i_n j_1 \dots j_n}^{(0)}} + S_0, \quad (2.39)$$

where each operator has its own imaginary time argument, but this is omitted for conve-

nience. The expansion of S_{eff} can be simplified using similar arguments as in Eq. (2.31). However, the difference is that the cavity construction is not a perturbation theory in the sense that we disturbed with a small parameter and $G^{(0)}$ is the full Green function of the environment. Only the local $n = 0$ and the smallest term, that obeys the total particle number, $n = 2$ remain as $d \rightarrow \infty$ and these two terms are concluded in the dynamical mean-field

$$\mathcal{G}^{-1}(i\omega_n) = i\omega_n + \mu - \sum_{ij} t_{0i} G^{(0)}(i\omega_n) t_{j0}. \quad (2.40)$$

A further simplification in $d \rightarrow \infty$ is that properties of a site do not change if a neighbor is removed as there are infinitely many, i.e.

$$d \rightarrow \infty : \quad G_{ii}^{(0)} = G_{ii}, \quad (2.41)$$

where Eq. (2.41) holds for the infinite dimensional limit of the Bethe lattice only. Then, the self-consistency of the Bethe lattice in infinite dimensions reads

$$\mathcal{G}^{-1}(i\omega_n) = i\omega_n + \mu - t^2 G_{00}(i\omega_n) \quad (2.42)$$

and is an exact equation of the local Green function G_{00} that can be solved self-consistently for any local interaction by numerically solving the auxiliary problem of Eq. (2.24).

Rather than directly taking the limit of infinite dimensions, it is also possible to gradually approach this limit with the goal to resolve the local density for the non-interacting Bethe lattice at large, but finite, z . Considering the non-interacting, i.e. tightbinding, case it is possible to perform the integration of the action over all sites except for the cavity. This gives

$$G_{00}^{-1}(i\omega_n) = i\omega_n + \mu - \frac{t^2}{z} \sum_{0,i} G_{ii}^{(0)}(i\omega_n) \quad (2.43)$$

$$= i\omega_n + \mu - t^2 G_{ii}^{(0)}(i\omega_n), \quad (2.44)$$

where the summation goes over the cavity 0 and its nearest neighbors i . Rather than removing the cavity and integrating over its neighbors, one can also remove the nearest neighbors i and integrate over their nearest neighbors j . Since the cavity 0 has already been removed, each i has only $(z - 1)$ neighbors j left. Therefore

$$\left(G_{ii}^{(0)}\right)^{-1} = i\omega_n + \mu - (z - 1) \frac{t^2}{z} G_{jj}^{(0,i)}(i\omega_n), \quad (2.45)$$

where $G_{jj}^{(0,i)}$ is the Green function of the cavity's next-nearest neighbors j with the cavity and its nearest neighbors i removed. By the arguments above, of $d \rightarrow \infty$, $G_{ii}^0 = G_{jj}^{0,i}$ and Eq. (2.45) can be solved for the local Green function

$$G(\zeta) = \frac{(z - 2)\zeta - z\sqrt{\zeta^2 - 4(z - 1)t^2/z}}{2(zt^2 - \zeta^2)}, \quad (2.46)$$

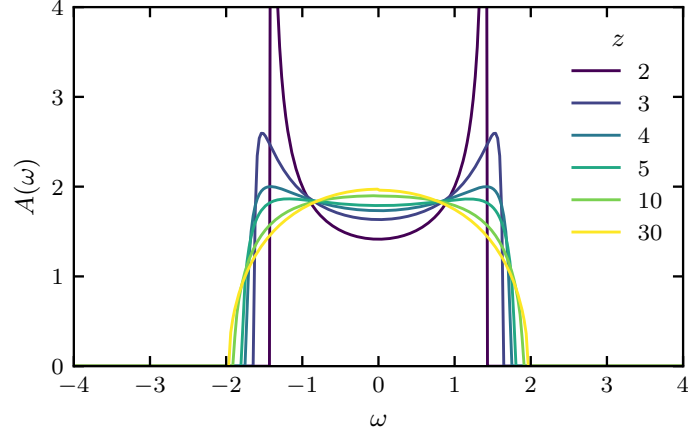


Figure 2.2: Density of states $A(\omega)$ of the non-interacting Bethe lattice for different coordination numbers z .

for $\zeta = i\omega_n + \mu$. The non-interacting version of Eq. (2.42), i.e. with $\mathcal{G} = G$, is the large- z limit of Eq. (2.45). The more elaborated derivation extends the prior results by $1/z$ effects.

The analytical continuation of $\zeta = \omega + i\epsilon$ for infinitesimal ϵ gives the retarded Green function whose imaginary part defines the local density of states that is shown in Fig. 2.2. It can provide an intuition of what finite Bethe lattice coordination number gives similar behavior to the infinite-dimensional limit. The local density of states for $z = 30$ looks like a semicircular with the radius of $2t$, which is the infinite-dimensional limit of the Bethe lattice. $z = 10$ is almost converged and looks similar to $z = 30$. Around $z = 5$ the semicircular becomes a rectangle with rounded corners and for even smaller z , it develops a local minimum around its center and maxima on the edges. At $z = 2$ the local density of states diverges at the edges. Thus, from the non-interacting analysis of the Bethe lattice, $d = 10$ is well approximated by $d \rightarrow \infty$ and the approximation probably fails for $z = 2$.

2.4 Cluster dynamical mean-field theory

Cluster methods extend the single-site analogues by clusters. The framework for their description is a partitioning of the original sites into clusters [62]. This can be achieved by writing the position of a site r as

$$r = \tilde{r} + R, \quad (2.47)$$

that divides the original lattice description using r into a lattice of clusters with a new unit cell, i.e. the cluster, see Fig. 2.3. The sites within the new unit cell are located at R and the translation vector corresponding to the same physical lattice described by a new basis is \tilde{r} . The corresponding Fourier transform maps to wave vectors \tilde{k} of the reduced Brillouin zone. Analogously the wave vector of the original Brillouin zone k can be decomposed into

$$k = \tilde{k} + K, \quad (2.48)$$

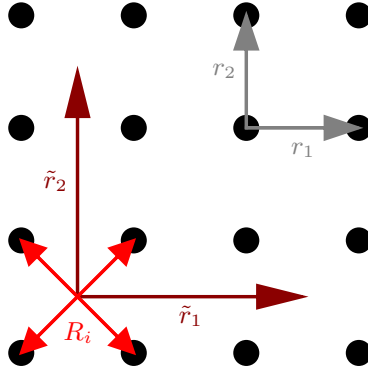


Figure 2.3: Two different descriptions of the same (square) lattice: The translation vectors r_i describe the full translational invariance and its unit cell consists of a single site (black dot). The translation vectors \tilde{r}_i describe a reduced translational symmetry with a larger unit cell of four sites R_i , the cluster. Shown are only 16 out of infinitely many sites.

where K is the cluster-momentum that corresponds to the Fourier transform of R . The reduced Brillouin zone is smaller than the original one. This embodies the reduced translational symmetry used by the new description of the cluster-lattice. It is also possible to apply a mixed description, e.g. cluster-lattice wave vectors \tilde{k} together with clusters defined in real space R . The local order parameters allow for a description of more complex orders, particularly those that depend on the bonds such as d -wave superconductivity. “Local” is meant as being within the cluster, because there is still the distinction to non-local in a sense of macroscopic effects, that can be described by effective field theories.

The difference between intra- and inter-cluster quantities is emphasized by the cluster perturbation theory [63, 64, 65, 62] (CPT) that can be derived by taking the cluster with intra-cluster hopping as the solvable reference system and perturbing it by inter-cluster hopping $\delta t(\tilde{k})$. The formalism to derive it is the locator expansion. More generally, it perturbs not only the hopping but also the self-energy. However, CPT considers only the intra-cluster self-energy, intra-cluster hopping and first-order perturbation in inter-cluster hopping. The Green function of the isolated cluster

$$G_c^{iso}(z) = (z + \mu)\mathbb{1} - t_c - \Sigma_c(z) \quad (2.49)$$

is a matrix over the cluster sites and depends on frequencies, real or imaginary, z . The cluster is assumed to be solvable, e.g. by exact diagonalization. Then the CPT approximation reads

$$G(\tilde{k}, z) = \left(G_c^{iso}(z) - \delta t(\tilde{k}) \right)^{-1}. \quad (2.50)$$

The quantities of Eq. (2.50) are matrices in intracluster degrees of freedom. This can be either cluster sites R or cluster momenta K . The intercluster effects stem from $\delta t(\tilde{k})$ which has no frequency dependency. The self-energy Σ_c is restricted to the cluster, therefore

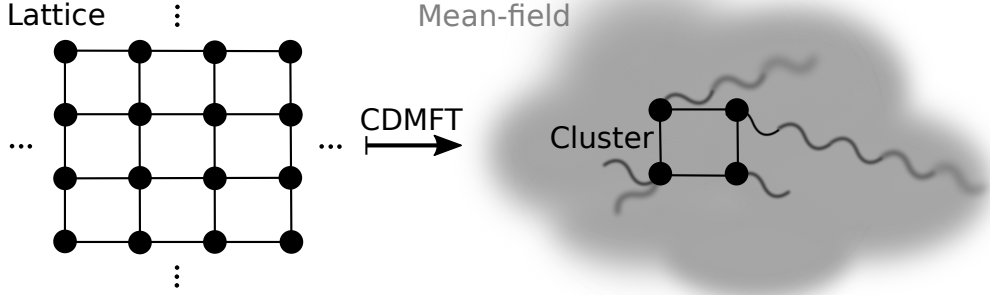


Figure 2.4: Illustration of the cluster dynamical mean-field theory. The infinitely extended lattice (left) is mapped to an auxiliary (impurity) problem of a cluster coupled to a mean-field (right). Curvy lines depict effective interactions of the mean-field with the cluster.

this quantity breaks the translational symmetry which can be seen as a drawback of the method. The Green function of the isolated cluster G_c^{iso} can be calculated via the Lehmann after the eigenstates have been obtained. A mean-field mapping to an auxiliary model as in the DMFT is not part of the CPT and neither is a self-consistency condition.

Cluster dynamical mean-field theories (CDMFT) extend the DMFT by including certain, but not all, spatial correlations. The lattice is mapped to an impurity setup which consists of a cluster coupled to a bath which is defined by the mean-field, see Fig. 2.4. Importantly, the environment of the cluster has some feedback on the cluster self-energy. A CDMFT should have a single-site limit at that it reduces to the DMFT, but that condition still leaves space for ambiguities in the generalization of DMFT to CDMFT. Thus, several CDMFTs have been developed that differ in important criteria. The CDMFT, DCA and PCDMFT [66, 62] have an effective action that can be understood in terms of the DMFT action combined with the cluster formulation

$$S_{imp} = - \int_0^\beta d\tau \int_0^\beta d\tau' \sum_{\sigma\sigma'RR'} c_{\sigma R}^\dagger(\tau) \mathcal{G}_{\sigma R, \sigma' R'}^{-1}(\tau - \tau') c_{\sigma' R'}(\tau') + \int_0^\beta d\tau H_c(\tau), \quad (2.51)$$

where H_c is the interaction that must not extend beyond the cluster. The effective action for the impurity setup S_{imp} takes into account the couplings between the cluster sites R and also other spin (or orbital) degrees of freedom σ . The solution of Eq. (2.51) gives the impurity Green function that by the self-consistency condition equals the local part of the lattice Green function whereat “local” here means “on the cluster”. The self-consistency can be defined via the definition of the Weiss field. In particular for the Cellular-DMFT (C-DMFT) it reads

$$\mathcal{G}^{-1}(i\omega_n) = \left(\sum_{\tilde{k}} \frac{1}{(i\omega_n + \mu)\mathbb{1} - t_c(\tilde{k}) - \Sigma_c(i\omega_n)} \right)^{-1} + \Sigma_c(i\omega_n) \quad (2.52)$$

which looks very similar to the self-consistency of the DMFT (Eq. (2.29)), but with the important difference that the quantities are matrices in the cluster sites R and the summation goes over the momentum vectors of the reduced Brillouin zone \tilde{k} . The self-energy of C-DMFT has finite values only within the cluster and beyond that it is neglected by this approximation. In that sense it describes a “free” cluster, because in terms of many-body correlations of the self-energy, this method does not consider an environment, i.e. $(\Sigma_c)_{\tilde{r}\tilde{r}'} = \delta_{\tilde{r}\tilde{r}'}$. A consequence of the latter is the violation of momentum conservation of C-DMFT which can be used in the formulation of the approximation in terms of the Luttinger-Ward functional

$$\Phi \simeq \sum_{\tilde{r}} \phi[G_{\tilde{r}\tilde{r}}] = \Phi(R, R'), \quad (2.53)$$

where the sum consists of independent terms corresponding to different clusters \tilde{r} . This problem of the violation of momentum conservation has been approached in different ways, e.g. the momentum conservation can be enforced during the self-consistency, which is discussed below, or the interpretation of the resulting correlation functions is adjusted such that C-DMFT is an approximation for the calculation of local quantities only, and for k -dependent observables it is unsuitable.

The dynamical cluster approximation [67, 68, 69] (DCA) looks similar to the C-DMFT, its self-consistency condition reads

$$\mathcal{G}^{-1}(i\omega_n, K) = \left(\sum_{\tilde{k}} \frac{1}{i\omega_n + \mu - t(\tilde{k} + K) - \Sigma_c(i\omega_n, K)} \right)^{-1} + \Sigma_c(i\omega_n, K). \quad (2.54)$$

In contrast to the case of the C-DMFT, the quantities are not matrices in the cluster sites, instead there is an additional cluster momentum dependency K . Importantly, the self-energy is coarse-grained in momentum space, i.e. it consists of constant patches that cover the Brillouin zone. Each patch is a constant value of the self-energy at a certain point within this patch, thus it is a zero-order interpolation of the self-energy in k -space. More sophisticated interpolations have also been developed, e.g. in the framework of the DCA⁺ [70, 69]. The momenta K are conserved as by construction there is no coupling between them, particularly because the interaction is coarse-grained as well $U_{ijkl} \mapsto U(K)$ and therefore the Luttinger-Ward functional approximation of the DCA

$$\Phi \simeq \Phi(K), \quad (2.55)$$

depends only on the cluster momenta K . In contrast to the C-DMFT, the translation invariance of the DCA self-energy allows for its consideration as a lattice self-energy and thus the lattice Green function becomes available naturally within the DCA, i.e. without further approximations, also maintaining its conserving property from the functional derivation of Eq. (2.55).

The issue of the breaking of translational invariance of the C-DMFT scheme motivates the PCDMFT. The main idea is to impose the constraint of the self-energy’s translational

invariance

$$\Sigma_{lat}(i\omega_n, k) = \sum_r e^{ikr} \left(\Sigma_{lat}^{TB}[\Sigma_c(i\omega_n)] \right)_r, \quad (2.56)$$

where Σ_{lat}^{TB} is constructed analogous to the tightbinding scheme, in that hopping amplitudes within and between unit cells are described by matrices. These unit cells become the cluster in the case of PCDMFT. The entries of the self-energy effectively renormalize the hopping with real- and imaginary part. It is important to note that the translational symmetry is enforced and not derivable within this scheme and this is reflected by the manual construction of Σ_{lat}^{TB} from entries of Σ_c . It is imposed within the self-consistency cycle, such that the approximated (local) Green function can inherit the translational invariance via the Dyson equation and becomes the translationally invariant full lattice Green function. In fact, the historically first CDMFT variant applied to the problem of superconductivity and magnetism includes this additional constraint [30]. This method has been discussed extensively in the context of causality violation [66, 62], which corresponds to a positive imaginary part of the (traced) self-energy on Matsubara frequencies. An important part are the weights of the cluster self-energy withing the tightbinding-like construction of the lattice self-energy [71].

The periodization process [72] has also been applied subsequently to the C-DMFT loops which is rather ad-hoc and uncontrolled, but probably the easiest way to extract k -dependent quantities from C-DMFT calculations. Further, the periodization process can not only be applied to the self-energy, but also to the cluster Green function or the so-called cumulant [73], which is the Green function with the hopping removed. The idea behind the latter is that only local quantities shall be periodized and the “very non-local” hopping exhibits translational invariance already. The ultimate answer to such approximate post-processings is in principle to be found by cluster-size studies, but practically compromises have to be made [72].

The cluster extensions of the DMFT have in common that the choice of cluster size and shape has to be made a priori. This introduces a bias to the calculations. In particular if the system is unstable to orders that are commensurable with the infinite lattice, but can be incommensurable, or biased, by the choice of shape and size of the cluster. This issue is addressed by the nested cluster scheme [66, 74] that focuses on taking into account different clusters of the same lattice in a consistent matter that is derived by the Luttinger-Ward functional formalism. This requires the process of solving coupled impurity problems and can be numerically expensive. So far, this method has been used to show unphysical minima in the Luttinger-Ward formulation of the free energy [74]. In regard of the cluster choice, also the variational cluster approximation [75, 54] has been developed. It can be seen as an extension of the CPT that provides a criterion for the best cluster setup.

2.5 Analytic continuation

Analytic continuation [76] describes the mathematical operation of the change of domain of the Correlation function from e.g. imaginary time to real time $-i\tau \mapsto t$ or from imaginary frequencies to real frequencies. Modern numerical Many-body techniques particularly in

the field of strong electronic correlations make use of the imaginary domain of correlation functions as it simplifies calculations and makes them more efficient. Static observables are straight forward to obtain from a correlation function of an imaginary domain. However, dynamic response functions require analytic continuation. Even in an equilibrium system these dynamics contain information of the low-energy excitations. Those response functions are measured in experiments such as spectroscopy, transport measurements. Despite a lot of effort and progress the analytic continuation is still an open problem, that receives attention [77, 78, 79, 80].

In order to understand the necessity and origin of this problem it is useful to remind from where imaginary time originates in first place. By the laws of thermodynamics it is possible to calculate every observable of an ensemble if an analytical expression of the partition function

$$Z = \text{Tr} e^{-\beta H} \quad (2.57)$$

is known. However, the exponential depends on the inverse temperature β and the Hilbert-space Hamilton operator. In a finite system Z could be calculated by solving the eigenproblem of H and executing the matrix exponential. But Hilbert-space grows exponentially fast with the number of states involved. Therefore methods that do not rely on the calculation of the eigenfunctions are desirable.

The problem can be circumvented by inserting an infinite amount of unities in the basis of coherent states. The eigenvalues of the coherent states are in the case of fermions Grassmann numbers (fermionic fields) and the Hamilton operator becomes a function of those. Further, because of the normalization of the coherent states the argument of the exponential effectively gets Legendre transformed and the partition function becomes finally a functional integral of an action

$$Z = \int_{\substack{\psi^*(0)=\zeta\psi^*(\beta) \\ \psi(0)=\zeta\psi(\beta)}} D(\psi^*, \psi) e^{-\int_0^\beta d\tau L} \quad (2.58)$$

with the Lagrangian L and fermionic ($\zeta = -1$) or bosonic ($\zeta = 1$) boundary conditions. Eq. (2.58) looks very similar to the action formalism of (real-)time propagation, but with a missing imaginary unit i at the front of the exponential's argument. Thus it is straight forward to interpret $\tau = it$ as an imaginary time and real and imaginary time propagators are connected via the Wick rotation. The expression of the partition function in the basis of coherent states thus allows for an application of the Green function perturbation theory also in this context of thermodynamics.

Further advantages can be gained by (anti-)periodizing, i.e. extending the domain, the fields and thereby also correlation functions

$$G(\tau) = \zeta G(\tau + \beta), \quad (2.59)$$

which also introduces a discontinuity at $\tau = 0$. This allows for a Fourier representation of

discrete frequencies, so-called Matsubara frequencies,

$$G(i\omega_n) = \int_0^\beta d\tau e^{i\omega_n\tau} G(\tau) \quad (2.60)$$

with the fermionic frequency $\omega_n = (2n+1)\pi/\beta$ or the bosonic frequency $\omega_n = 2n\pi/\beta$. The boundary conditions of Eq. (2.58) are implicitly included in the definition of those frequencies. At this point the simplest way to compare the theory to experiments would probably be by static observables, i.e. summing the Green function over Matsubara frequencies or equivalently evaluating it at $\tau = 0$.

However, in some experiments, e.g. photoemission spectroscopy, it is also possible to measure dynamic quantities, that contain important information about the low-energy excitations of a system. The quantity of interest is then the one-particle spectral function

$$A(\omega) = -\frac{1}{\pi} \text{Im} G^{ret}(\omega) \quad (2.61)$$

with the retarded Green function

$$G^{ret}(\omega) = G(\omega + i0^+), \quad (2.62)$$

where 0^+ is an infinitesimal that ensures convergence. Thus the spectral function is related to the Green function of Eq. (2.60), whose domain has been extended to the whole complex plane, by a Wick (back-)rotation. For an analytical expression $i\omega_n \mapsto \omega + i0^+$ can easily be performed (note, that this technically requires the Green function to be analytic). However, for numerical data this is clearly not as trivial.

2.5.1 Numerical approaches

The Padé method aims to fit a rational polynomial function

$$G(z) = \frac{\sum_{i=1}^{k+1} a_i z^{i-1}}{\sum_{i=1}^r b_i z^{i-1} + z^r} \quad (2.63)$$

of complex z and coefficients a_i and b_i . The asymptotic behavior is determined by a_{k+1} . Thus $k = r - 1$ for the correct high-frequency tail of a Green function $\sim 1/z$ and $a_r = 1$. Then the coefficients can be used to apply the fitted function to the domain of real frequencies $G(\omega)$. There are different variants of this method that follow different strategies in terms of fitting the coefficients [81, 82]. The Padé method is known to be reliable for data with relatively small noise. Moreover, it works best at small frequencies around the Fermi level and finally, it is also fast compared to most other methods.

Besides the Padé method, other methods make use of the fact, that Eq. (2.61) can be rewritten as an integral with the useful relation of the Hilbert transform

$$G(i\omega_n) = - \int_{-\infty}^{\infty} d\omega \frac{\zeta}{i\omega_n - \omega} A(\omega), \quad (2.64)$$

including a principal value integral. The kernel of that integral can vary depending on the observable or basis of G . Eq. (2.64) outlines the issue that is addressed by most modern numerical analytic continuation methods. The inverse operation of that integral is analytically not available. Therefore the only option left is to guess A such that it produces the correct G . But this procedure is obviously not unambiguous and thereby ill-defined. The ambiguity suggests to incorporate additional information or criteria to select a particular solution.

The discrete version of Eq. (2.64) is written in terms of a G and A -vector and a kernel matrix K ,

$$G = KA. \quad (2.65)$$

It is introduced for numerical purposes and also for convenience. A straight forward optimization scheme to find A then is

$$\min_{0 \leq A} |G - KA|^2, \quad (2.66)$$

which is known as the nonnegative least squares method and the generic setup appears in many problems [83]. Unfortunately, for the analytic continuation this type of optimization alone is not well suited as it exhibits so-called sawtooth noise. It stems from overfitting of the statistical errors of the input. This type of noise can be reduced by the introduction of a constraint, that suppresses large values of A , i.e.

$$\min_{0 \leq A} |G - KA|^2 + |\lambda A|^2, \quad (2.67)$$

known as Tikhonov regularization, where λ controls the strength of the regularization. λ is a parameter to smoothen A . In principle λ can also be a matrix that suppresses different entries of A (corresponding to ω) differently.

One of the most popular methods is the maximum entropy method [84, 76]. It regularizes by means of a default model, that is a chosen reference and known a priori to be similar to an anticipated solution. The optimization problem reads

$$\min_{0 \leq A} |G - KA|^2 + \lambda S[A], \quad (2.68)$$

with the entropy $S = A \log(A/\tilde{A})$, where \tilde{A} is the spectral function of the reference model. Thus the entropy part of Eq. (2.68) is optimized for $A = \tilde{A}$. However, it is still far from ideal, that this method relies strongly on the default model. Especially in cases, in that new features are searched. λ controls how strong the entropy term is taken into account in the optimization. Algorithms can try to find reasonable values for λ , but the choice of the default model remains an issue [85].

Non-overfitting alternatives to the maximum entropy method, that do not depend on a default model are stochastic methods [86, 76]. The idea is to obtain a final solution by taking into account many different particular solutions that are weighted by a deviation

measure. Written in a functional form the spectral function is

$$A = \int d\tilde{A} P[\tilde{A}|G] \tilde{A}. \quad (2.69)$$

\tilde{A} is a particular solution and $P[\tilde{A}|G]$ is the likelihood (conditional probability) of that particular solution given G . The explicit form of the likelihood requires a deviation measure that can vary for different methods. Despite the lack of a formal proof the stochastic nature of this approach smoothens features of certain particular solution with a small deviation measure, but with overfitting. It stems from the averaging process and can be seen as a form of implicit regularization. The formulation of Eq. (2.69) of an average depending on a probability distribution in a high-dimensional setup suggests a solution via the Metropolis sampling algorithm. The original form of the probability distribution is

$$P[\tilde{A}|G] = \exp\left(-|G - K\tilde{A}|^2/\mathcal{T}\right), \quad (2.70)$$

similar to a Boltzmann distribution of a fictitious temperature \mathcal{T} . It is possible to formulate also other methods in terms of likelihood functions and then to combine them with the stochastic method, this has been done e.g. for the maximum entropy method [87].

2.5.2 Stochastic optimization method

The stochastic optimization method [76, 79] can be classified as a stochastic method. However, it has an important difference, i.e. it denies the assumption of a certain underlying probability distribution such as the Boltzmann distribution. This usage has the problem that it suggests a certain fictitious temperature and correspondingly also energy. The stochastic optimization uses the stochastic component to find particular solutions, but they are not weighted accordingly, i.e.

$$A(\omega) = \sum_{i=1}^L \xi_i \tilde{A}_i(\omega). \quad (2.71)$$

i labels the particular solutions \tilde{A} , that are averaged ($\xi_i = 1/L$) for the final solution A . Certainly, a different ξ can be introduced, but it's not a probability distribution, but e.g. a threshold that selects only particular solutions of a certain quality. The stochastic part of this method still has the benefit of diminishing overfits by means of the average and it uses less a priori knowledge. The method can be implemented such that the spectral function is generated by e.g. rectangles on a continuous mesh. Thus there is no discretization error from a finite mesh resolution. Then after a small change (move) the deviation function $D = |G - K\tilde{A}|$ is evaluated and compared to the prior and by that states are rejected or accepted for the continuation of the algorithm. However, in this Markov-chain is in practice a lot of fine tuning involved as one the one hand optimization is desired, but on the other hand ergodicity is necessary as well.

A detailed algorithm will be presented below. However, a picture representation of the rough outline can help to understand the algorithm better. Fig. 2.5 presents a simplified

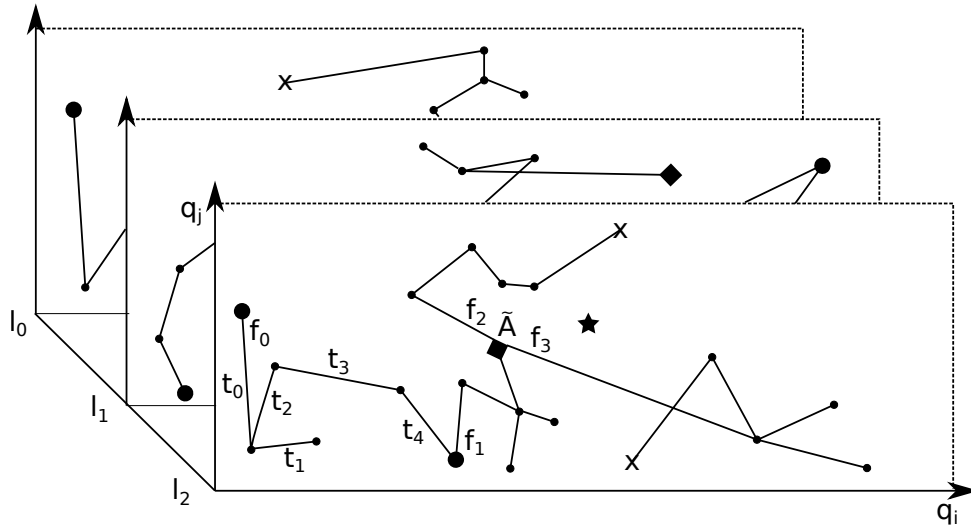


Figure 2.5: Illustration of the (simplified) sampling procedure of the SOM algorithm. Three (l_i) particular solutions \tilde{A} (square) are calculated each with four global (f_i) and five elementary (t_i) moves. Ideally \tilde{A} lies at the true solution (star).

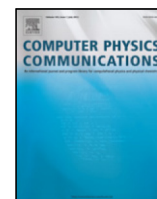
overview of the optimization procedure. A particular solution l_i is obtained by starting from a random configuration of rectangles. Then starts a Markov chain t_i that is governed by the Metropolis algorithm of the transition probability

$$P_{t \rightarrow t+1} = \begin{cases} 1, & D_{t+1} \leq D_t \\ (D_t/D_{t+1})^d, & D_{t+1} > D_t \end{cases}. \quad (2.72)$$

Dependent on the parameter d there is a probability for accepting a state, that is according to the deviation measure D worse. This shall improve ergodicity. Fig. 2.5 is simplified as e.g. it does not illustrate that d can change. In order to enhance the ergodicity even further d can be used to increase the probability $P_{t \rightarrow t+1}$ at the beginning of the Markov chain and later it can be reduced. The changes of the t_i -labeled configurations are called elementary updates. There are also global updates corresponding to the Markov chain of f_i , which is a Markov chain of Markov chains. But in contrast the global updates are not governed by the Metropolis algorithm, instead it is simply

$$P_{f \rightarrow f+1} = \begin{cases} 1, & D_{f+1} < D_f \\ 0, & D_{f+1} \geq D_f \end{cases}. \quad (2.73)$$

The numbers of global and elementary updates and particular solutions are parameters of the algorithm, that usually converge. In the following an implementation based on the TRIQS library [45] is presented [88].



TRIQS/SOM: Implementation of the stochastic optimization method for analytic continuation[☆]

Igor Krivenko^{*}, Malte Harland

I. Institut für Theoretische Physik, Uni. Hamburg, Jungiusstraße 9, 20355 Hamburg, Germany

ARTICLE INFO

Article history:

Received 5 August 2018

Received in revised form 21 January 2019

Accepted 27 January 2019

Available online 18 February 2019

Keywords:

Quantum Monte Carlo

Analytic continuation

Stochastic optimization

Python

ABSTRACT

We present the TRIQS/SOM analytic continuation package, an efficient implementation of the Stochastic Optimization Method proposed by Mishchenko et al. (2000). TRIQS/SOM strives to provide a high quality open source (distributed under the GNU General Public License version 3) alternative to the more widely adopted Maximum Entropy continuation programs. It supports a variety of analytic continuation problems encountered in the field of computational condensed matter physics. Those problems can be formulated in terms of response functions of imaginary time, Matsubara frequencies or in the Legendre polynomial basis representation. The application is based on the TRIQS C++/Python framework, which allows for easy interoperability with TRIQS-based quantum impurity solvers, electronic band structure codes and visualization tools. Similar to other TRIQS packages, it comes with a convenient Python interface.

Program summary

Program Title: TRIQS/SOM

Program Files doi: <http://dx.doi.org/10.17632/fcjzyhrwpw.1>

Licensing provisions: GNU General Public License (GPLv3)

Programming language: C++/Python

External routines/libraries: TRIQS 1.4.2, Boost >=1.58, cmake.

Nature of problem: Quantum Monte Carlo methods (QMC) are powerful numerical techniques widely used to study quantum many-body effects and electronic structure of correlated materials. Obtaining physically relevant spectral functions from noisy QMC results in the imaginary time/Matsubara frequency domains requires solution of an ill-posed analytic continuation problem as a post-processing step.

Solution method: We present an efficient C++/Python open-source implementation of the stochastic optimization method for analytic continuation.

Additional comments: Project homepage <http://krivenko.github.io/som/>.

© 2019 Elsevier B.V. All rights reserved.

1. Introduction

Quantum Monte Carlo methods (QMC) [1] are one of the most versatile classes of numerical tools used in quantum many-body theory and adjacent fields. When applied in combination with the dynamical mean field theory (DMFT) [2–4] and an electronic structure calculation method, such as the density functional theory (DFT), they also allow to assess diverse effects of electronic correlations in real materials [5].

In spite of a considerable progress in development of real time quantum Monte Carlo solvers [6–10], QMC methods formulated in the imaginary time [11–17] remain a more practical choice in most situations. Such algorithms have a fundamental limitation as they calculate dynamical response functions in the imaginary time/Matsubara frequency representation, or in a basis of orthogonal polynomials in more recent implementations [18]. Getting access to the spectral functions that are directly observable in the experiment requires solution of the infamous analytic continuation problem. The precise mathematical statement of the problem varies between response functions in

[☆] This paper and its associated computer program are available via the Computer Physics Communication homepage on ScienceDirect (<http://www.sciencedirect.com/science/journal/00104655>).

^{*} Correspondence to: Department of Physics, University of Michigan, Ann Arbor, MI 48109, USA.

E-mail addresses: ikrivenk@physnet.uni-hamburg.de (I. Krivenko), mharland@physnet.uni-hamburg.de (M. Harland).

question and representations chosen to measure them. However, all formulations amount to the solution of an inhomogeneous Fredholm integral equation of the first kind w.r.t. to the spectral function $A(\epsilon)$ and with an approximately known left hand side $O(\xi)$,

$$O(\xi) = \int_{\epsilon_{\min}}^{\epsilon_{\max}} d\epsilon K(\xi, \epsilon)A(\epsilon). \quad (1)$$

Such equations are known to be ill-posed by Hadamard, i.e. neither existence nor uniqueness of their solutions is guaranteed [19]. Moreover, behaviour of the solution is unstable w.r.t. the changes in the LHS. This last feature makes the numerical treatment of the problem particularly hard as the LHS is known only up to the stochastic QMC noise. There is little hope that a general solution of the problem of numerical analytic continuation can be attained. Nonetheless, the ongoing effort to develop useful continuation tools has given rise to dozens of diverse methods.

One of the earliest continuation methods, which is still in use, is based on construction of Padé approximants of the input data [20–22]. In general, its applicability is strongly limited to the cases with high signal-to-noise ratio of the input.

Variations of the Maximum Entropy Method (MEM) currently represent the *de facto* standard among tools for numerical analytic continuation [23,24]. While not being computationally demanding, they allow to obtain reasonable results for realistic input noise levels. There are high quality open source implementations of MEM available to the community, such as TRIQS/maxent [25,26], Ω Maxent [27] together with its compatibility layer OmegaMaxEnt_TRIQS [28], and a package based on the ALPSCORE library [29]. The typical criticism of the MEM targets its bias towards the specified default model [30].

Another group of approaches, collectively dubbed stochastic continuation methods, exploit the idea of random sampling of the ensemble of possible solutions (spectral functions). The method of A. Sandvik is one of the most well-known members of this family [31]. It can be shown that the MEM is equivalent to the saddle-point approximation of the statistical ensemble considered by Sandvik [32].

The Stochastic Optimization Method (SOM) [33,34], also referred to as Mishchenko method, is a stochastic algorithm that demonstrates good performance in practical tests [35]. It is bias-free in the sense that it does not favour solutions close to a specific default model, or those possessing special properties beyond the standard non-negativity and normalization requirements. It also features a continuous-energy representation of solutions, which is more natural than the traditional projection on a fixed energy mesh. The price to pay for SOM's advanced features is its relatively high CPU time demands. In some cases, running SOM simulations may require as much time as running a QMC solver for producing input data.

The lack of a high quality open source implementation of such a well-established and successful method urged us to write the program package called SOM. Besides, until the very recent releases of TRIQS/maxent and OmegaMaxEnt_TRIQS there were no good analytic continuation tool compatible with otherwise powerful Toolbox for Research on Interacting Quantum Systems (TRIQS) [36], so we decided to fill this gap. (TRIQS Green's function library features only a simplistic and very limited implementation of the Padé method).

There are other continuation methods that are worth mentioning. Among these are the average spectrum method [37], the method of consistent constraints (MCC) [38], stochastic methods based on the Bayesian inference [30,39], the Stochastic Optimization with Consistent Constraints protocol (SOCC, a hybrid between SOM and MCC that allows for characterization of the result accuracy) [34], and finally the recent and promising sparse modelling approach [40].

This paper is organized as follows. In Section 2 we recapitulate the Stochastic Optimization Method. Section 3 gives a brief description of the performance optimizations devised in our implementation of SOM. We proceed in Section 4 with instruction on how to use the program. Section 5 contains some illustrational results of analytic continuation with SOM. Practical information on how to obtain and install the program is given in Section 6. Section 7 summarizes and concludes the paper. Some technical details, which could be of interest to authors of similar codes, can be found in the appendices.

2. Stochastic optimization method

We will now briefly formulate the analytic continuation problem, and summarize Mishchenko's algorithm [41] as implemented in SOM.

2.1. Formulation of problem

Given a function $O(\xi)$ (referred to as *observable* throughout the text), whose numerical values are approximately known at M discrete points ξ_m , we seek to solve a Fredholm integral equation of the first kind,

$$O(\xi_m) = \int_{\epsilon_{\min}}^{\epsilon_{\max}} d\epsilon K(\xi_m, \epsilon)A(\epsilon), \quad (2)$$

w.r.t. spectral function $A(\epsilon)$ defined on interval $[\epsilon_{\min}; \epsilon_{\max}]$. The observable O is usually obtained as a result of QMC accumulation, and therefore known with some uncertainty. It is also assumed that values of $O(\xi_m)$ for different m are uncorrelated. The definition domain of $A(\epsilon)$ as well as the explicit form of the integral kernel $K(\xi, \epsilon)$ vary between different kinds of observables and their representations (choices of ξ). The sought spectral function is required to be smooth, non-negative within its domain, and is subject to normalization condition

$$\int_{\epsilon_{\min}}^{\epsilon_{\max}} d\epsilon A(\epsilon) = \mathcal{N}, \quad (3)$$

where \mathcal{N} is a known normalization constant.

Currently, SOM supports four kinds of observables. Each of SOM can be given as a function of imaginary time points on a regular grid $\tau_m = \beta \frac{m}{M-1}$ (β is the inverse temperature), as Matsubara components, or as coefficients of the Legendre polynomial expansion [18]. This amounts to a total of 12 special cases of Eq. (2). Here is a list of all supported observables.

Table 1

List of supported integral kernels $K(\xi, \epsilon)$. The zero temperature correlator admits two frequency representations. $i_\ell(x)$ is the modified spherical Bessel function of the first kind.

Observable kind	Kernel in representation ξ		
	Imaginary time, τ	Matsubara frequency, ω_n/ν_n	Legendre polynomials, P_ℓ
Green's function of fermions	$-\frac{e^{-\tau\epsilon}}{1+e^{-\beta\epsilon}}$	$\frac{1}{i\omega_n - \epsilon}$	$-\frac{\beta\sqrt{2\ell+1}(-\text{sgn}(\epsilon))^\ell i_\ell(\beta \epsilon /2)}{2\cosh(\beta\epsilon/2)}$
Correlator of boson-like operators	$\frac{1}{\pi} \frac{\epsilon e^{-\tau\epsilon}}{1-e^{-\beta\epsilon}}$	$\frac{1}{\pi} \frac{-\epsilon}{i\nu_n - \epsilon}$	$\frac{1}{\pi} \frac{\beta\epsilon\sqrt{2\ell+1}(-\text{sgn}(\epsilon))^\ell i_\ell(\beta \epsilon /2)}{2\sinh(\beta\epsilon/2)}$
Autocorrelator of a Hermitian operator	$\frac{1}{\pi} \frac{\epsilon(e^{-\tau\epsilon} + e^{-(\beta-\tau)\epsilon})}{1-e^{-\beta\epsilon}}$	$\frac{1}{\pi} \frac{2\epsilon^2}{\nu_n^2 + \epsilon^2}$	$\frac{1+(-1)^\ell}{2\pi} \frac{\beta\epsilon\sqrt{2\ell+1}i_\ell(\beta\epsilon/2)}{\sinh(\beta\epsilon/2)}$
Zero temperature correlator	$-e^{-\tau\epsilon},$ $\tau \in [0; \tau_{\max}]$	$\frac{1}{i\pi(2n+1)/\tau_{\max} - \epsilon}$ $\frac{1}{i2\pi n/\tau_{\max} - \epsilon}$	$\tau_{\max} \frac{(-1)^{\ell+1} \sqrt{2\ell+1} \times}{i_\ell\left(\frac{\epsilon\tau_{\max}}{2}\right)} \exp\left(-\frac{\epsilon\tau_{\max}}{2}\right)$

1. Finite temperature Green's function of fermions, $G_{\alpha\alpha}(\tau) = -\langle \mathbb{T}_\tau c_\alpha(\tau) c_\alpha^\dagger(0) \rangle$. $G(\tau)$ must fulfil the anti-periodicity condition $G(\tau + \beta) = -G(\tau)$. The off-diagonal elements $G_{\alpha\beta}(\tau)$ are not supported, since they are not in general representable in terms of a non-negative $A(\epsilon)$. It is possible to analytically continue similar anti-periodic functions, such as fermionic self-energy Σ . For the self-energies, it is additionally required that (a) the constant contribution $\Sigma(i\infty)$ is subtracted from $\Sigma(i\omega_n)$, and (b) the zeroth spectral moment \mathcal{N} is known *a priori* (for an example of how \mathcal{N} can be computed, see [42]).¹
2. Finite temperature correlation function of boson-like operators B and B^\dagger , $\chi_B(\tau) = \langle \mathbb{T}_\tau B(\tau) B^\dagger(0) \rangle$. $\chi_B(\tau)$ must be β -periodic, $\chi_B(\tau + \beta) = \chi_B(\tau)$. Typical examples of such functions are Green's function of bosons $G_b(\tau) = \langle \mathbb{T}_\tau b(\tau) b^\dagger(0) \rangle$ and the transverse spin susceptibility $\chi_{+-}(\tau) = \langle \mathbb{T}_\tau S_+(\tau) S_-(0) \rangle$.
3. Autocorrelator of a Hermitian operator.
The most widely used observables of this kind are the longitudinal spin susceptibility $\chi_{zz}(\tau) = \langle S_z(\tau) S_z(0) \rangle$ and the charge susceptibility $\chi(\tau) = \langle N(\tau) N(0) \rangle$. This is a special case of the previous observable kind with $B = B^\dagger$, and its use is in general preferred due to the reduced $A(\epsilon)$ definition domain (see below).
4. Correlation function of operators at zero temperature.
Strictly speaking, the imaginary time argument τ of a correlation function is allowed to grow to positive infinity in the limit of $\beta \rightarrow \infty$. Therefore, one has to choose a fixed cutoff τ_{\max} up to which the input data is available. Similarly, in the zero temperature limit spacing between Matsubara frequencies vanishes. Neither periodicity nor antiperiodicity property makes sense for observables at $\beta \rightarrow \infty$, so one can opt to use fictitious Matsubara frequencies with any of the two possible statistics and with the spacing equal to $2\pi/\tau_{\max}$.

The spectral function $A(\epsilon)$ is defined on $(-\infty, \infty)$ for observables (1)–(2), and on $[0, \infty)$ for observables (3)–(4).

The Matsubara representation of an imaginary time function $F(\tau)$ is assumed to be

$$F(iz_n) = \int_0^{\tilde{\beta}} d\tau e^{iz_n\tau} F(\tau), \quad (4)$$

with $\tilde{\beta}$ being β in the cases (1)–(3) and τ_{\max} in the case (4), z_n are fermionic Matsubara frequencies $\omega_n = \pi(2n+1)/\beta$ in the case (1), bosonic Matsubara frequencies $\nu_n = 2\pi n/\beta$ in the cases (2)–(3), and fictitious frequencies $\pi(2n+1)/\tau_{\max}$ (or $2\pi n/\tau_{\max}$) in the case (4). The Legendre polynomial representation is similar for all four observables.

$$F_\ell = \sqrt{2\ell+1} \int_0^{\tilde{\beta}} d\tau P_\ell[\chi(\tau)] F(\tau), \quad \chi(\tau) = 2\tau/\tilde{\beta} - 1. \quad (5)$$

Supported observables and their respective integral kernels $K(\xi, \epsilon)$ are summarized in Table 1.

2.2. Method

The main idea of the Stochastic Optimization Method is to use Markov chain sampling to minimize an objective function

$$D[A] = \sum_{m=1}^M |\Delta(m)|, \quad \Delta(m) = \frac{1}{S(m)} \left[\int_{\epsilon_{\min}}^{\epsilon_{\max}} d\epsilon K(\xi_m, \epsilon) A(\epsilon) - O(\xi_m) \right] \quad (6)$$

with respect to the spectrum $A(\epsilon)$. $\Delta(m)$ is the deviation function for the m th component of the observable. The weight factor $S(m)$ can be set to QMC error-bar estimates (if available) to stress importance of some input data points $O(\xi_m)$. In contrast to most other analytic

¹ An alternative approach to continuation of self-energies consists in constructing an auxiliary Green's function $G_{\text{aux}}(z) = [z + \mu - (\Sigma(z) - \Sigma(i\infty))]^{-1}$ on the Matsubara axis, performing a SOM run for $G_{\text{aux}}(i\omega_n)$ with $\mathcal{N} = 1$ and recovering $\Sigma(\epsilon)$ from $G_{\text{aux}}(\epsilon)$ [25].

continuation methods, $S(m)$ should not, however, be identified with the error-bars. Multiplication of all $S(m)$ by a common scalar would result in an equivalent objective function, i.e. only the relative magnitude of different components of $S(m)$ matters.

The integral equation (2) is not guaranteed to have a unique solution, which means $D[A]$ has in general infinitely many minima. Most of these minima correspond to non-smooth spectra containing strong sawtooth noise. SOM addresses the issue of the sawtooth instability in the following way. At first, it generates L particular solutions \tilde{A} using a stochastic optimization procedure. Each generated solution \tilde{A}_j is characterized by a value of the objective function $D[\tilde{A}_j]$. A subset of relevant, or “good” solutions is then isolated by picking only those \tilde{A}_j that satisfy $D[\tilde{A}_j]/D_{\min} \leq \alpha_{\text{good}}$. D_{\min} is the absolute minimum among all computed particular solutions, and α_{good} is a deviation threshold factor (usually set to 2). The final solution is constructed as a simple average of all good solutions, and has the sawtooth noise approximately cancelled out from it. In mathematical form, this procedure summarizes as

$$A(\epsilon) = \frac{1}{L_{\text{good}}} \sum_{j=1}^L \theta(\alpha_{\text{good}} \min\{D[\tilde{A}_j]\} - D[\tilde{A}_j]) \tilde{A}_j(\epsilon), \quad (7)$$

$$L_{\text{good}} = \sum_{j=1}^L \theta(\alpha_{\text{good}} \min\{D[\tilde{A}_j]\} - D[\tilde{A}_j]).$$

SOM features a special way to parametrize spectra $\tilde{A}(\epsilon)$ as a sum of possibly overlapping rectangles with positive weights.

$$\tilde{A}(\epsilon) = \sum_{k=1}^K R_{\{c_k, w_k, h_k\}}(\epsilon), \quad (8)$$

$$R_{\{c_k, w_k, h_k\}}(\epsilon) = h_k \theta(\epsilon - (c_k - w_k/2)) \theta((c_k + w_k/2) - \epsilon). \quad (9)$$

$\{c_k, w_k, h_k\}$ stand for centre, width and height of the k th rectangle, respectively. The positivity constraint is enforced by requiring $w_k > 0$, $h_k > 0$ for all k , while the normalization condition (3) translates into

$$\sum_{k=1}^K h_k w_k = \mathcal{N}. \quad (10)$$

Sums of rectangles offer more versatility as compared to fixed energy grids and sums of delta-peaks (as in [32]). They are well suited to represent both large scale structures, as well as narrow features of the spectra.

The optimization procedure used to generate each particular solution is organized as follows. In the beginning, a random configuration C_0 (sum of $K > 0$ rectangles) is generated and height-normalized to fulfil Eq. (10). Then, a fixed number F of global updates $C_f \rightarrow C_{f+1}$ are performed. Each global update is a short Markov chain of elementary updates governed by the Metropolis–Hastings algorithm [43,44] with acceptance probability

$$P_{t \rightarrow t+1} = \begin{cases} 1, & D[C_{t+1}] \leq D[C_t], \\ (D[C_t]/D[C_{t+1}])^{d+1}, & D[C_{t+1}] > D[C_t]. \end{cases} \quad (11)$$

The global update is only accepted if $D[C_{f+1}] < D[C_f]$. SOM implements all seven types of elementary updates proposed by Mishchenko et al. [41].

1. Shift of rectangle;
2. Change of width without change of weight;
3. Change of weight of two rectangles preserving their total weight;
4. Adding a new rectangle while reducing weight of another one;
5. Removing a rectangle while increasing weight of another one;
6. Splitting a rectangle;
7. Glueing two rectangles.

To further improve ergodicity, the Markov chain of T elementary updates is split into two stages. During the first T_1 elementary updates, large fluctuations of the deviation measure are allowed by setting $d = d_1 \in (0; 1]$. d is then changed to $d_2 \in [1; d_{\max}]$ for the rest of the Markov chain, so that chances to escape a local minimum are strongly suppressed during the second stage. $T_1 \in [0; T]$, d_1 and d_2 are chosen randomly and anew at the beginning of a global update. Introduction of global updates helps accelerate convergence towards a deep minimum of the objective function D , whereas MC evolution within each global update ensures possibility to escape a shallow local minimum.

An insufficient amount of global updates may pose a serious problem and result in particular solutions \tilde{A} that fit (2) poorly. Mishchenko suggested a relatively cheap way to check whether a given F is large enough to guarantee good fit quality [41] (see Appendix F for a detailed description of this recipe for real- and complex-valued observables). Although SOM can optionally try to automatically adjust F , this feature is switched off by default. From practical calculations, we have found that the F -adjustment procedure may fail to converge for input data with a low noise level.

Another important calculation parameter is the number of particular solutions to be accumulated. Larger L lead to a smoother final solution $A(\epsilon)$ but increases computation time as $O(L)$. Setting L manually to some value from a few hundred to a few thousand range gives reasonably smooth spectral functions in most cases. Nonetheless, SOM can be requested to dynamically increase L until a special convergence criterion is met. This criterion can be formulated in terms of a frequency distribution (histogram) of the objective function $D[A]$. L is considered sufficient if the histogram is peaked near $D_{\min} = \min\{D[\tilde{A}_j]\}$. In addition to α_{good} we define $\alpha_{\text{very good}} < \alpha_{\text{good}}$ (4/3 by default), and count those good solutions, which also satisfy $D[\tilde{A}_j]/D_{\min} < \alpha_{\text{very good}}$. If nearly all good solutions (95% or more) are very good, the histogram is well localized in the vicinity of D_{\min} , and all \tilde{A}_j included in the final solution provide a good fit. It is worth noting, however, that simple increase of L does not in general guarantee localization of the histogram.

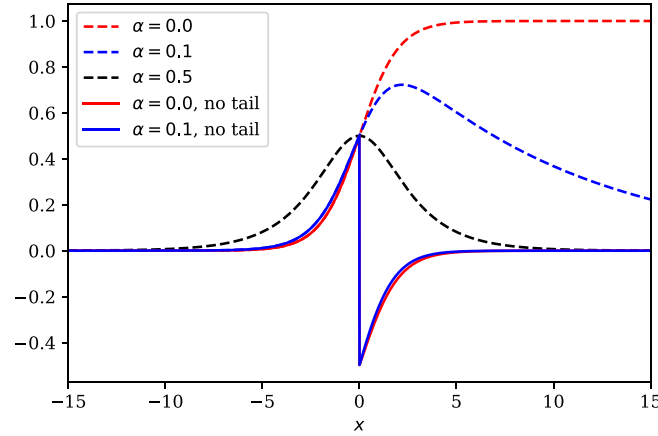


Fig. 1. Illustration of $\Lambda(\tau, \Omega)$ evaluation problem. Dashed lines: Integrand from (13) for different values of $\alpha = \tau/\beta$. Solid lines: The same integrand with the tail contribution $t_\alpha(x)$ subtracted.

3. Performance optimizations

The most computationally intensive part of the algorithm is evaluation of integral (2) for a given configuration $C = \{c_k, w_k, h_k\}$,

$$\int_{\epsilon_{\min}}^{\epsilon_{\max}} d\epsilon K(\xi_m, \epsilon) \tilde{A}(\epsilon) = \sum_{k=1}^K \int_{\epsilon_{\min}}^{\epsilon_{\max}} d\epsilon K(\xi_m, \epsilon) R_{\{c_k, w_k, h_k\}}(\epsilon) = \sum_{k=1}^K h_k [\Lambda(\xi_m, c_k + w_k/2) - \Lambda(\xi_m, c_k - w_k/2)], \tag{12}$$

where an integrated kernel $\Lambda(\xi_m, \Omega) = \int_{\epsilon_{\min}}^{\Omega} K(\xi_m, \epsilon) d\epsilon$ has been introduced. The integral over one rectangle runs from $c_k - w_k/2$ to $c_k + w_k/2$, but is computed as a difference of two integrals: from some fixed constant (ϵ_{\min}) to $c_k + w_k/2$ and from the same constant to $c_k - w_k/2$. The lower integration limit in the definition of $\Lambda(\xi_m, \Omega)$ is irrelevant and can be set to an arbitrary number, e.g. 0. This has the benefit that only one integral needs to be known/evaluated for all possible upper limits.

In the Matsubara representation, the integrated kernels $\Lambda(\xi_m, \Omega)$ are simple analytic functions (see Appendix B). For the imaginary-time and Legendre representations, however, there are no closed form expressions for $\Lambda(\xi_m, \Omega)$. Doing the integrals with a numerical quadrature method for each rectangle and upon each proposed elementary update would be prohibitively slow. SOM boasts two major optimizations that strongly alleviate the problem.

At first, it uses pre-computation and special interpolation schemes to quickly evaluate $\Lambda(\xi_m, \Omega)$. As an example, let us consider the kernel for the fermionic GF in the imaginary time (for definition of kernel $K(\tau, \epsilon)$ see the upper left cell of Table 1),

$$\Lambda(\tau; \Omega) = -\frac{1}{\beta} \int_0^{\beta\Omega} \frac{e^{-(\tau/\beta)x}}{1 + e^{-x}} dx \tag{13}$$

(ϵ has been substituted by x/β , the lower integration limit is set to 0). The integral on the right hand side is analytically doable only for a few values of $\alpha = \tau/\beta$, namely $\alpha = 0, 1/2, 1$. For all other $\alpha \in (0; 1/2) \cup (1/2; 1)$ it has to be done numerically and approximated using a cubic spline interpolation. The spline interpolation would be easy to construct if the integrand were localized near $x = 0$ for all α . Unfortunately, this is not the case. The integrand develops a long “tail” on the positive/negative half-axis as α approaches 0/1 respectively. The length of this tail scales as α^{-1} (or $(1 - \alpha)^{-1}$), which would require an excessively large number of spline knots needed to construct a reliable approximation. This issue is solved by subtracting an exponential tail contribution $t_\alpha(x)$ from the integrand, such that the difference is well localized, and an integral of $t_\alpha(x)$ is trivial (Fig. 1).

$$\Lambda(\tau; \Omega) = -\frac{1}{\beta} [\theta(-\Omega) S_\alpha^-(\beta\Omega) + \theta(\Omega) S_\alpha^+(\beta\Omega) + T_\alpha(\beta\Omega)], \tag{14}$$

$$S_\alpha^-(z) = -\int_z^0 \left[\frac{e^{-\alpha x}}{1 + e^{-x}} - t_\alpha(x) \right] dx, \quad S_\alpha^+(z) = \int_0^z \left[\frac{e^{-\alpha x}}{1 + e^{-x}} - t_\alpha(x) \right] dx, \tag{15}$$

$$T_\alpha(z) = \int_0^z t_\alpha(x) dx. \tag{16}$$

For each $\alpha_m = \tau_m/\beta$, the integrals $S_\alpha^-(z)$ and $S_\alpha^+(z)$ are expressed in terms of special functions or rapidly convergent series and are precomputed on a uniform grid with a fixed number of z -points. The precomputed values provide data to construct the cubic spline interpolation between those points, and $T_\alpha(z)$ are simple analytical functions that are quick to evaluate. The length of the segment, on which the splines are defined, is chosen such that functions $S_\alpha^\pm(z)$ can be considered constant outside it. Appendix C contains relevant expressions and necessary implementation details for all observable kinds.

A somewhat similar approach is taken to evaluate integrated Legendre kernels. Once again, let us take the fermionic GF as an example (upper right cell of Table 1),

$$\Lambda(\ell; \Omega) = - \int_0^{\Omega} \frac{\beta \sqrt{2\ell+1} (-\text{sgn}(\epsilon))^\ell i_\ell\left(\frac{\beta|\epsilon|}{2}\right)}{2 \cosh(\beta\epsilon/2)} d\epsilon = (-\text{sgn}(\Omega))^{\ell+1} \sqrt{2\ell+1} \int_0^{|\Omega|\beta/2} \frac{i_\ell(x)}{\cosh(x)} dx, \quad (17)$$

where $i_\ell(x)$ is the modified spherical Bessel function of the first kind [45]. The integrand $\frac{i_\ell(x)}{\cosh(x)}$ is rather inconvenient for numerical evaluation, because both the Bessel function and the hyperbolic cosine grow exponentially. Moreover, the integral itself grows logarithmically for $|\Omega|\beta \rightarrow \infty$, which makes naive pre-computation and construction of a spline infeasible. This time, our evaluation scheme is based on the following expansion of the integrand,

$$\frac{i_\ell(x)}{\cosh(x)} = \frac{e^x}{e^x + e^{-x}} \sum_{n=0}^{\ell} (-1)^n \frac{a_n(\ell+1/2)}{x^{n+1}} + \frac{e^{-x}}{e^x + e^{-x}} \sum_{n=0}^{\ell} (-1)^{\ell+1+n} \frac{a_n(\ell+1/2)}{x^{n+1}}, \quad (18)$$

with $a_n(\ell+1/2)$ being coefficients of the Bessel polynomials [46],

$$a_n(\ell+1/2) = \frac{(\ell+n)!}{2^n n! (\ell-n)!}. \quad (19)$$

For large x (high-energy region), the integrand can be approximated as

$$\frac{i_\ell(x)}{\cosh(x)} \approx \sum_{n=0}^{\ell} (-1)^n \frac{a_n(\ell+1/2)}{x^{n+1}}. \quad (20)$$

In the low-energy region we do the integral $F^<(z) \equiv \int_0^z \frac{i_\ell(x)}{\cosh(x)} dx$ on a fixed z -mesh, $z \in [0; x_0]$, using the adaptive Simpson's method. Results of the integration are used to construct a cubic spline interpolation of $F^<(z)$. For each ℓ the boundary value x_0 between the low- and high-energy regions is found by comparing values of (18) and (20). In the high-energy region we use the asymptotic form (20) to do the integral,

$$F^>(z)|_{z>x_0} = F^<(x_0) + \left\{ \log(x) + \sum_{n=1}^{\ell} (-1)^{n+1} \frac{a_n(\ell+1/2)}{x^n n} \right\} \Big|_{x_0}^z. \quad (21)$$

Implementation details for other Legendre kernels can be found in Appendix D.

The second optimization implemented in SOM consists in aggressive caching of rectangles' contributions to the integral (2). As it is seen from (12), the integral is a simple sum over all rectangles in a configuration. Thanks to the fact that elementary updates affect at most two rectangles at once, it makes sense to store values of every individual term in the sum. In the proposal phase of an update, evaluation of the integrated kernel is then required only for the affected rectangles. If the update is accepted, contributions of the added/changed rectangles are stored in a special cache and can be reused in a later update. Since the size of a configuration does not typically exceed 100, and $M \leq 1000$, the cache requires only a moderate amount of memory.

Besides the two aforementioned optimizations, SOM can take advantage of MPI parallel execution. Generation of particular solutions is “embarrassingly parallel”, because every solution is calculated in a completely independent manner from the others. When a SOM calculation is run in the MPI context, the accumulation of particular solutions is dynamically distributed among available MPI ranks.

4. Usage

4.1. Basic usage example

Running SOM to analytically continue input data requires writing a simple Python script. This usage method is standard for TRIQS applications. We refer the reader to Section 9.3 of [36] for instructions on how to execute Python scripts in the TRIQS environment. Details of the script will vary depending on the physical observable to be continued, and its representation. Nonetheless, a typical script will have the following basic parts.

- Import TRIQS and SOM Python modules.

```
# Green's function containers used to store input and output data.
from pytriqs.gf.local import *
# HDFArchive interface to HDF5 files.
from pytriqs.archive.hdf_archive import HDFArchive, HDFArchiveInert
# HDF5 archives must be modified only by one MPI rank.
# is_master_node() checks we are on rank 0.
from pytriqs.utility.mpi import is_master_node
# bcast() broadcasts its argument from the master node to all others
from pytriqs.utility.mpi import bcast
# Main SOM class.
from pytriqs.applications.analytical_continuation.som import Som
```

- Load the observable to be continued from an HDF5 archive.

```
# On master node, open an HDF5 file in read-only mode.
arch = HDFArchive('input.h5', 'r') if is_master_node() else HDFArchiveInert()
# Read input Green's function and broadcast it to all nodes.
# arch['g'] must be an object of type GfImTime, GfImFreq or GfLegendre.
g = bcast(arch['g'])
```

This step can be omitted or modified if the input data comes from a different source. For instance, it could be loaded from text files or generated in the very same script by a quantum Monte-Carlo impurity solver, such as TRIQS/CTHYB [47]. Only the values stored in the `g.data` array will be used by SOM, while any high frequency expansion information (`g.tail`) will be disregarded. If `g` is matrix-valued (or, in TRIQS's terminology, has a target shape bigger than 1×1), SOM will only construct analytic continuation of the diagonal matrix elements.

- Set the importance function $S(m)$

```
# Create a container for 'S' by copying 'g'.
S = g.copy()
# Set all elements of 'S' to a constant.
S.data[:] = 1.0
```

In this example we assume that all elements of $g(m)$ are equally important. Alternatively, one could read the importance function from an HDF5 archive or another source.

- Construct `Som` object.

```
# Create Som object
cont = Som(g, S, kind = "FermionGf", norms = 1.0)
```

The argument `kind` must be used to specify the kind of the physical observable in question. Its recognized values are `FermionGf` (Green's function of fermions), `BosonCorr` (correlator of boson-like operators), `BosonAutoCorr` (autocorrelator of a Hermitian operator), `ZeroTemp` (zero temperature correlator). The optional argument `norms` is a list containing expected norms \mathcal{N} (Eq. (3)) of the spectral functions to be found, one positive real number per one diagonal element of `g`. Instead of setting all elements of norms to the same constant `x`, one may simply pass `norms = x`. By default, all norms are set to 1, which is correct for the fermionic Green's functions. However, adjustments would normally be needed for self-energies and bosonic correlators/autocorrelators.

- Set simulation parameters.

```
# Dictionary containing all simulation parameters
params = {}
# SOM will construct a spectral function
# within this energy window (mandatory)
params['energy_window'] = (-5.0, 5.0)
# Number of particular solutions to accumulate (mandatory).
params['l'] = 1000
# Set verbosity level to the maximum on MPI rank 0,
# and silence all other ranks
params['verbosity'] = 3 if is_master_node() else 0
# Do not auto-adjust the number of particular solutions to accumulate
# (default and recommended).
params['adjust_l'] = False
# Do not auto-adjust the number of global updates (default and recommended).
params['adjust_f'] = False
# Number of global updates per particular solution.
params['f'] = 200
# Number of local updates per global update.
params['t'] = 500
# Accumulate histogram of the objective function values,
# useful to analyse quality of solutions.
params['make_histograms'] = True
```

In Section 4.2 we provide a table of main accepted simulation parameters.

- Run simulation.

```
cont.run(**params)
```

This function call is normally the most expensive part of the script.

- Extract solution and reconstructed input.

```
# Evaluate the solution on a real frequency mesh.
g_w = GfReFreq(window = (-5.0, 5.0), n_points = 1000, indices = g.indices)
g_w << cont
# Imaginary time/frequency/Legendre data reconstructed from the solution.
g_rec = g.copy()
g_rec << cont
```

Table 2
Main run() parameters.

Parameter Name	Python type	Default value	Meaning
energy_window	(float,float)	N/A	Lower and upper bounds of the energy window. Negative values of the lower bound will be reset to 0 in <code>BosonAutoCorr</code> and <code>ZeroTemp</code> modes.
max_time	int	-1 (unlimited)	Maximum run() execution time in seconds.
verbosity	int	2 on MPI rank 0, 0 otherwise	Verbosity level (maximum level — 3).
t	int	50	Number of elementary updates per global update (T). Bigger values may improve ergodicity.
f	int	100	Number of global updates (F). Bigger values may improve ergodicity. Ignored if <code>adjust_f=True</code> .
adjust_f	bool	False	Adjust the number of global updates automatically.
l	int	2000	Number of particular solutions to accumulate (L). Bigger values reduce the sawtooth noise in the final solution. Ignored if <code>adjust_l=True</code> .
adjust_l	bool	False	Adjust the number of accumulated particular solutions automatically.
make_histograms	bool	False	Accumulate histograms of objective function values.

g_w is the retarded fermionic Green's function of the real frequency corresponding to the input g . Its imaginary part is set to $-\pi A(\epsilon)$, whereas the real part is computed semi-analytically using the Kramers–Kronig relations (there are closed form expressions for a contribution of one rectangle to the real part). The relation between g_w and $A(\epsilon)$ slightly varies with the observable type; relevant details are to be found in the online documentation.

The high frequency expansion coefficients will be computed from the sum-of-rectangles representation of $A(\epsilon)$ and written into g_w as well. If g_w is constructed with a wider energy window compared to that from `params`, $A(\epsilon)$ is assumed to be zero at all “excessive” energy points.

The reconstructed function g_{rec} is the result of the substitution of $A(\epsilon)$ back into the integral equation (2). The correctness of results should always be controlled by comparing g with g_{rec} .

- Save results to an HDF5 archive.

```
# On master node, save results to an archive
if mpi.is_master_node():
    with HDFArchive("results.h5", 'w') as ar:
        ar['g'] = g
        ar['g_w'] = g_w
        ar['g_rec'] = g_rec
    # Save histograms for further analysis
    ar['histograms'] = cont.histograms
```

The output archive can be read by other TRIQS scripts and outside utilities, in order to analyse, post-process and visualize the resulting spectra. More elaborate examples of SOM Python scripts can be found on the official documentation page, <http://krivenko.github.io/som/documentation.html>.

4.2. Simulation parameters

Table 2 contains main simulation parameters understood by `run()` method of class `Som`. More advanced parameters intended for experienced users are listed in [Appendix A](#).

5. Illustrational results

5.1. Testing methodology

We apply SOM to a few synthetic test cases where the exact spectral function is known. These tests serve as an illustration of SOM's capabilities and as guidance to the prospective users. Being based on a Markov chain algorithm with a fair number of adjustable parameters,

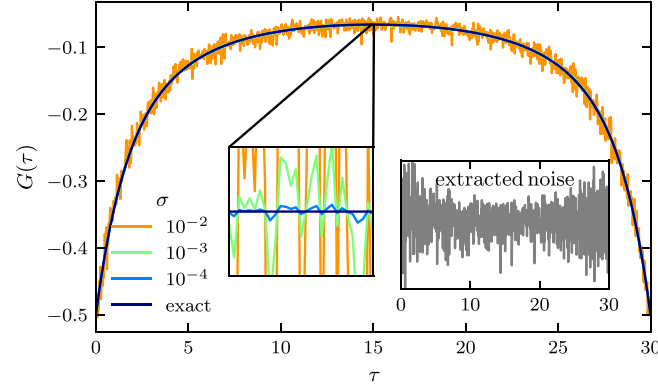


Fig. 2. Extraction of noise from the imaginary time Green's function $G(\tau)$ computed by TRIQS/CTHYB QMC solver, and its subsequent rescaling.

SOM may suffer from ergodicity problems and produce characteristic spectral artefacts if the parameters are not properly chosen. It is therefore instructive to consider analytic continuation problems that can potentially pose difficulty to SOM, and study the effect of the various input parameters on the quality of the solution. Throughout this section, we use arbitrary units for all energies and frequencies ($\hbar = 1$), while imaginary time τ and inverse temperature β are measured in $[a.u.^{-1}]$.

To perform most of the tests, we have devised a special procedure allowing to model stochastic noise characteristic to fermionic Green's functions $G(\tau)$ measured by QMC solvers. The procedure involves running a single-loop DMFT [4] calculation for a non-interacting single-band tight-binding model on a Bethe lattice using the TRIQS/CTHYB solver. The exact Green's function of this model $G_{\text{Bethe}}^{\text{ex}}(\tau)$ is easily computed from the well known semi-elliptic spectral function. The impurity solver will introduce some noise $\tilde{\eta}(\tau)$ that can easily be estimated from the accumulation result $G_{\text{Bethe}}^{\text{MC}}(\tau)$ as

$$\tilde{\eta}(\tau) = G_{\text{Bethe}}^{\text{MC}}(\tau) - G_{\text{Bethe}}^{\text{ex}}(\tau), \quad (22)$$

and normalized according to

$$\eta(\tau) = \tilde{\eta}(\tau) / \sqrt{\frac{1}{M} \sum_m \left(\tilde{\eta}(\tau_m) - \frac{1}{M} \sum_{m'} \tilde{\eta}(\tau_{m'}) \right)^2}. \quad (23)$$

We ensure that values of the noise are uncorrelated between different time slices τ_m by taking a sufficiently large number of Monte Carlo updates per measurement. Eventually, the extracted and normalized noise is rescaled and added to a model Green's function to be continued with SOM (Fig. 2),

$$G_{\sigma}^{\text{noisy}}(\tau) = G^{\text{ex}}(\tau) + \sigma \eta(\tau). \quad (24)$$

By using the described procedure, we hope to reproduce a more realistic noise distribution and its dependence on τ observed in QMC runs, as compared to a synthetically generated Gaussian noise with a fixed dispersion.

In the case of a susceptibility (two-pole model, see below), we simply add Gaussian noise to $\chi(i\nu_m)$. It is independently generated for each ν_m with zero mean and equal dispersion σ .

5.2. Comparison of model spectra

Results of tests with four model spectra and various levels of added noise are shown in Fig. 3. In all tests presented in that figure, the inverse temperature has been set to $\beta = 30$ ($\tau_{\text{max}} = 30$ for the zero-temperature kernel). All curves have been calculated from the imaginary time input data on a grid with 500 τ -points ($G^{\text{ex}}(\tau)$ are computed from analytically known spectral functions via (2)). The importance function has been chosen to be a constant in all simulations. The number of global updates is set to $F = 1500$ and the number of elementary updates is $T = 250$. The remaining parameters are set to SOM defaults, if not stated otherwise.

The model studied first is the single Hubbard atom with the Coulomb repulsion strength $U = 2$ at half-filling. Its spectral function comprises two discrete levels at $\pm U/2$ corresponding to excitations through empty and doubly occupied states. For a general complex frequency z , the Green's function of the Hubbard atom reads

$$G(z) = \frac{1/2}{z + U/2 + i\delta} + \frac{1/2}{z - U/2 + i\delta}, \quad (25)$$

where $\delta = 0.1$ is the resonance broadening term. The analytic continuation with SOM shows that strong noise smears the calculated spectral function, the peak height is diminished and the spectral weight is spread asymmetrically around the peak. The smearing at large frequencies is more pronounced. The peak position converges correctly to the exact solution as σ decreases.

The second model is the non-interacting double Bethe lattice [48],

$$G(z) = \zeta(z - t_{\perp}) + \zeta(z + t_{\perp}), \quad (26)$$

$$\zeta(z) = \frac{z - i \operatorname{sign} \Im(z) \sqrt{4t_b^2 - z^2}}{2t_b^2}. \quad (27)$$

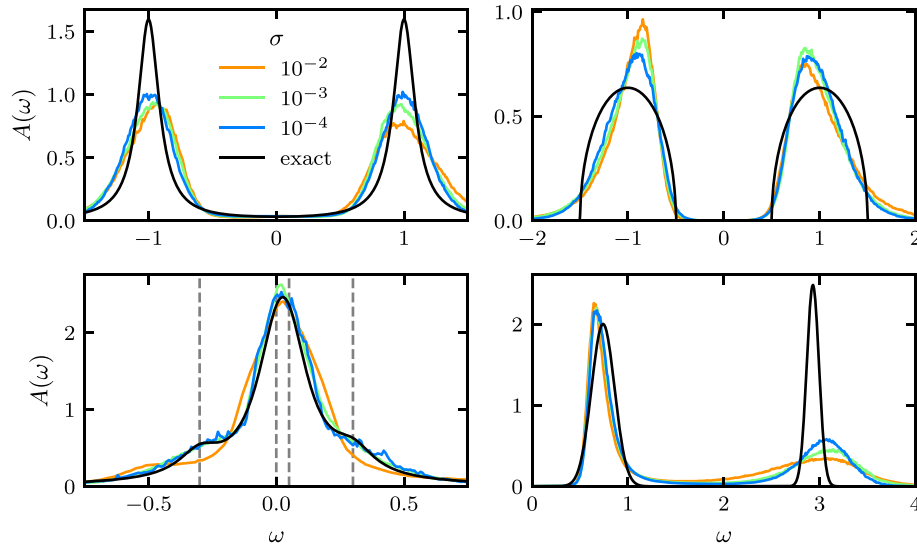


Fig. 3. Spectral functions produced by SOM with $F = 1500$ depending on the input noise level σ . The corresponding models are the Hubbard atom (top left), the double Bethe lattice (top right), an asymmetric metal (bottom left), and the zero-temperature Fermi polaron (bottom right). The frequency positions of the asymmetric metal's superposed Lorentzians are marked by dashed lines.

The specific feature of this model is a gapped symmetric spectrum with sharp band edges. Splitting between the semi-elliptic bands is given by $|2t_{\perp}| = 2$, and their bandwidths are $4t_b = 1$. Top right part of Fig. 3 shows that at large σ the particle–hole asymmetry introduced by the noise can also break the symmetry of the solution. As the noise level goes down, the SOM solution approaches the exact one, but the shape of the bands remains somewhat Lorentzian-like, which leads to an underestimated gap.

As an example of a gapless spectrum (Fig. 3, bottom left), we take a Green's function that produces a sum of four Lorentzian peaks, i.e.

$$G(z) = \sum_i \frac{c_i}{z - b_i + i\delta} \quad (28)$$

with $c = (0.1, 0.4, 0.4, 0.1)$, $b = (-0.3, 0, 0.05, 0.3)$ and $\delta = 0.1$. The Lorentzians overlap and form a single peak that has two shoulders. The peak doesn't have a mirror symmetry with respect to the vertical axis and its centre is not at the Fermi level. The shoulders are not resolved for the largest noise level of $\sigma = 10^{-2}$, but for smaller noise levels $\sigma \in \{10^{-3}, 10^{-4}\}$ both shoulders are correctly detected by SOM. The spectra with $\sigma \in \{10^{-3}, 10^{-4}\}$ look notably more noisy. The origin of this effect is SOM's ability to find the best particular solution that is a very good fit to the input data (with a very small D_{\min}). With a fixed $D[A]/D_{\min}$ threshold, only a few particular solutions are considered for inclusion in the final solution. Hence, the less smooth curves.

The fourth model (Fig. 3, bottom right) appears in the context of the Fermi polaron problem, and it has previously been used in [34] to assess performance of other continuation methods. It consists of two peaks modelled via Gaussians,

$$G(z) = \frac{1}{N} \sum_i c_i e^{-\frac{(z-a_i)^2}{b_i}} \quad (29)$$

with $c = (0.62, 0.41)$, $a = (0.74, 2.93)$ and $b = (0.12, 0.064)$. N is used to set the spectral norm to 1. Here, we apply the zero-temperature imaginary time kernel with $\tau_{\max} = 30$. This case is difficult as it contains sharp features over a broad energy range. We observe that the low-energy peak can be relatively well resolved. However, the high-energy peak is strongly broadened with the width dependent of the noise level. Positions of both peaks are reproduced with a reasonable accuracy of $\sim 5\%$.

5.3. Effect of F

We have observed in practical calculations that the choice of the amount of global updates F can drastically affect ergodicity of SOM Markov chains and, eventually, the output spectra. Fig. 4 shows evolution of SOM spectral functions with F for the Fermi polaron model. Parameters other than F are kept at their default values, i.e. $T = 50$, $L = 2000$, and the noise level is set to $\sigma = 10^{-4}$. The Fermi polaron spectra obtained from the imaginary time representation (Fig. 4, left) demonstrates that SOM has generally no problem resolving the low-energy peak regardless of F . The high-energy peak, however, significantly changes its shape and position as F grows, slowly approaching the reference curve.

The situation is rather different, when the Legendre representation is used (Fig. 4, right). As before, the noise is created and added to the Green's function in the imaginary time representation. Subsequently, it is transformed to the Legendre basis and passed to SOM. The number of Legendre coefficients used here is $N_{\ell} = 50$. Positions of both peaks do not change much with F . For sufficiently large F , their width and height are visibly closer to the exact solution as compared to the imaginary time results. A likely cause of this difference is the truncation of the Legendre expansion and the corresponding noise filtering. In contrast, for small F the peaks contain relatively strong noise. This effect has been found with the asymmetric metal model for large σ , too. It occurs when the final solution is dominated by a few particular solutions with very small D , i.e. when Markov chains suffer from poor ergodicity and struggle to escape an isolated deep minimum of the objective function.

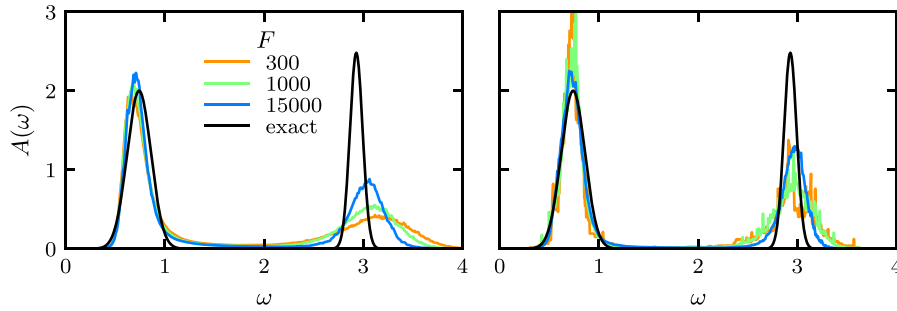


Fig. 4. Effect of the number of global updates F on the spectral functions produced by SOM. Shown are spectral functions for the Fermi polaron model obtained from the imaginary time (left) and Legendre (right) input data.

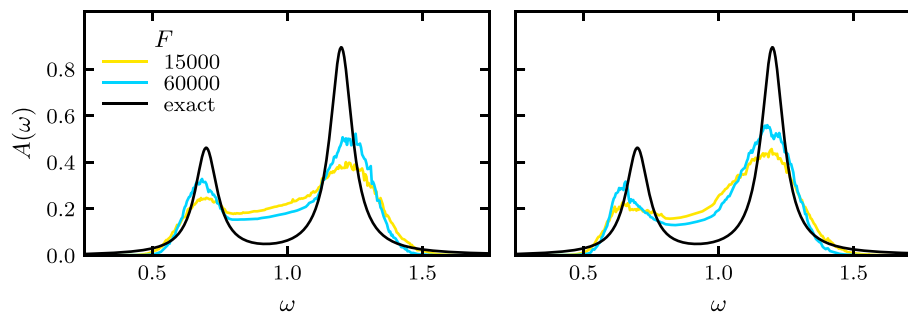


Fig. 5. Effect of the number of global updates F on the spectral functions produced by SOM. Shown are spectral functions for the two-pole model obtained from the Matsubara frequency (left) and Legendre (right) input data.

In Fig. 5, a similar comparison is presented for the two-pole susceptibility model [35],

$$\chi(z) = \frac{1}{\chi_0} \sum_i \frac{c_i}{z^2 - b_i^2}, \quad (30)$$

$$\chi_0 = - \sum_i \frac{c_i}{b_i^2},$$

with $c = (0.1, 0.335663)$, $b = (0.7, 1.2)$. We use the Hermitian autocorrelator kernel for Matsubara frequencies and add uncorrelated Gaussian noise with the standard deviation $\sigma = 10^{-4}$. Other parameters are $\beta = 50$, $T = 50$ and $L = 2000$. For the same number of global updates, we obtain a double-peak structure (Fig. 5, left) similar to that shown in Fig. 2 of [35]. Additionally, we transform the same set of noisy input data into the Legendre representation ($N_\ell = 50$) and apply the corresponding kernel (Fig. 5, right). As in the case of the Fermi polaron, use of the Legendre basis results in slightly more pronounced peaks. However, their positions are reproduced slightly better by the Matsubara kernel.

5.4. Diagnostics

After a solver run, SOM does not only provide the continued function, but also the reconstructed input function as well as a histogram of the objective function. These features are mainly for debugging purposes and for an estimation of result's quality. It is obvious that the reconstructed Green's function should ideally be a smooth version of the input Green's function. In the upper left part of Fig. 6 we plot the difference between the exact Green's function of the Fermi polaron model and its SOM reconstruction after an imaginary time simulation (the corresponding spectrum is shown in Fig. 4). First of all, we observe that the difference shrinks with increasing F . Furthermore, the main difference comes from the small imaginary times. The Green's function has its largest values there, and so does the noise. At larger τ -points it has less pronounced features or is even featureless. However, τ_{\max} has to be set sufficiently large, i.e. the result should converge and be independent of its actual value.

The Legendre basis has been identified as a useful tool to filter noise by cutting off large expansion coefficients[18]. In Fig. 6 (bottom left) we provide a similar comparison of exact and reconstructed Green's functions in the Legendre representation. They lie on top of each other everywhere except for large-order Legendre coefficients. This kind of plots may give a hint at how many Legendre polynomial coefficients should be retained to filter out the noise without losing relevant information in the input data.

The objective function histogram helps determine whether the choice of F and T is adequate. The histogram is usually stretched when T and/or F are too small, and should converge to a sharper peak shape for larger values. Objective function histograms for both used kernels are plotted in the right part of Fig. 6. It is clearly seen that increased F lead to localization of the histograms and, as a result, to more efficient accumulation of particular solutions.

5.5. Final remarks

In conclusion, we would like to make some remarks about the rest of the main simulation parameters. The energy window must be chosen such that the entire spectral weight fits into it, but within the same order of magnitude with the bandwidth. Extremely wide energy

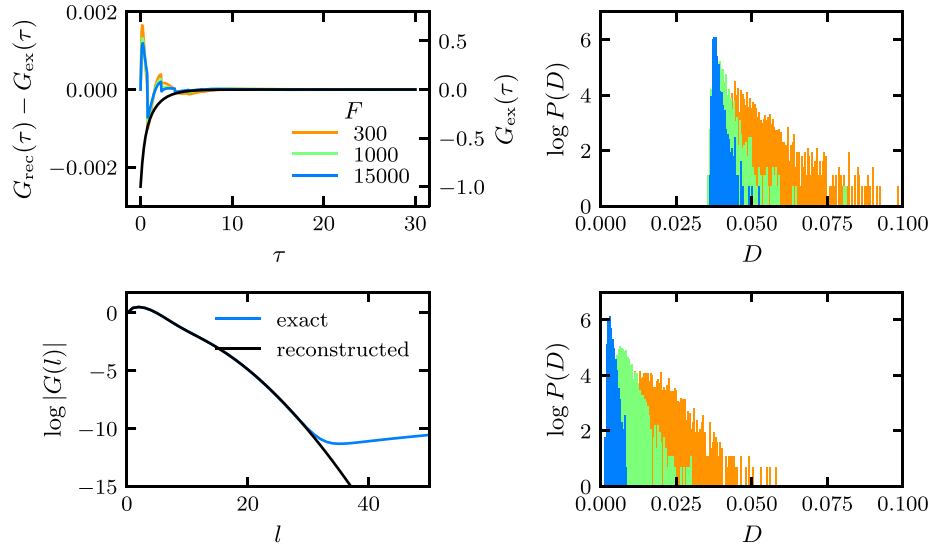


Fig. 6. Top, left: Colourful lines/left axis show the difference of the SOM-reconstructed Green's function and the exact Green's function of the Fermi polaron model, continued using the imaginary time kernel. Black curve/right axis shows the exact Green's function itself. Bottom, left: The reconstructed Green's function and the exact Green's function in the Legendre basis (same model, $F = 15000$). Right: Corresponding histograms of objective function values.

windows may be wasteful as they are likely to cause low acceptance rates in the Markov chains. The effect of increased L has not been explicitly studied here, but it is similar to that of a moving average noise filter. It is, however, not recommended to post-process (smoothen) SOM-generated spectra using such a filter, because it can cause artefacts that also depend on the moving frame size. Regarding efficiency, it is worth noting that simulations with the Legendre kernels typically require less CPU time, mainly because of the different dimensions of the input data arrays (a few dozen Legendre coefficients versus $10^2 - 10^3$ τ -points/Matsubara frequencies). To give the reader a general idea of how expensive SOM simulations are, we roughly estimated the CPU time required to produce some plots in this section. It took 136 core-hours to obtain one spectral curve for the Hubbard atom, the double Bethe lattice, and the asymmetric metal (Fig. 3). The Fermi polaron simulations were a lot cheaper, 19 core-hours. The most expensive curve ($F = 15000$) in Fig. 4 took 20 core-hours with the imaginary time kernel, and 8 core-hours with the Legendre kernel. Similarly, the $F = 60000$ curve of Fig. 5 required 25 and 14 core-hours with the imaginary time and the Legendre kernels respectively. The required run time scales nearly linearly with F .

6. Getting started

6.1. Obtaining SOM

The SOM source code is available publicly and can be obtained from a GitHub repository located at <https://github.com/krivenko/som>. It is recommended to always use the 'master' branch of the repository, as it contains the most recent bug fixes and new features being added to SOM.

6.2. Installation

The current version of SOM requires the TRIQS library 1.4.2 as a prerequisite. An installation procedure of TRIQS is outlined in Section 9.2 of [36]. More detailed step-by-step instructions are available on the TRIQS documentation website (<https://triqs.github.io/triqs/1.4/install.html>). It is of crucial importance to check out the version tag 1.4.2 before compiling and installing TRIQS. This can be done by running the following shell command

```
$ git checkout 1.4.2
```

in the cloned source directory of the TRIQS library. It is also important to make sure that TRIQS is compiled against a recent version of the Boost C++ libraries, 1.58 or newer.

Installing SOM is similar to that of other TRIQS-based applications. Assuming that TRIQS 1.4.2 has been installed at `/path/to/TRIQS/install/dir` SOM is simply installed by issuing the following commands at the shell prompt:

```
$ git clone https://github.com/krivenko/som som_src
$ mkdir som_build && cd som_build
$ cmake -DTRIQS_PATH=/path/to/TRIQS/install/dir ../som_src
$ make
$ make test
$ make install
```

This will install SOM in the same location as TRIQS. Further installation instructions are given in the online documentation.

6.3. Citation policy

TRIQS/SOM is provided free of charge. We kindly ask to help us with its continued maintenance and development by citing the present paper, as well as the accompanying paper to the TRIQS library [36], in any published work using the SOM package. We also strongly recommend to cite [33] as the original work where the Stochastic Optimization Method was first introduced.

6.4. Contributing

TRIQS/SOM is an open source project and we encourage feedback and contributions from the user community. Issues should be reported via the GitHub website at <https://github.com/krivenko/som/issues>. For contributions, we recommend to use the pull requests on the GitHub website. It is recommended to coordinate with the TRIQS/SOM developers before any major contribution.

7. Summary

We have presented the open-source TRIQS/SOM package that implements the Stochastic Optimization Method for analytic continuation. On a set of practical examples, we demonstrated the versatility of TRIQS/SOM, as well as its potential to become a viable alternative to various implementations of the Maximum Entropy Method, the current *de facto* standard in the field of computational condensed matter physics. The algorithm contains a number of performance optimizations that significantly reduce overall computation costs.

Our plans for future releases include porting the code base to more recent versions of the TRIQS library and adding support for more integral kernels, such as kernels for superconducting correlators [29]. Another interesting addition would be the ability to compute the two-point correlators of particular solutions $\sigma_{mm'}$ as defined in [34]. Following the methodology of Goulko et al., one could use the accumulated correlators to characterize the accuracy of the output spectral functions.

Acknowledgements

Authors are grateful to Alexander Lichtenstein and Olga Goulko for fruitful discussions, to Roberto Mozara for his valuable comments on the usability of the code, and to Andrey Mishchenko for giving access to the original FORTRAN implementation of the SOM algorithm. We would also like to thank Vladislav Pokorný and Hanna Terletska, who stimulated writing of this paper. I.K. acknowledges support from Deutschen Forschungsgemeinschaft (DFG) via project SFB668 (subproject A3, “Electronic structure and magnetism of correlated systems”). M.H. acknowledges financial support by the DFG, Germany in the framework of the SFB925. The computations were performed with resources provided by the North-German Supercomputing Alliance (HLRN).

Appendix A. Advanced simulation parameters

See [Tables A.3](#) and [A.4](#).

Appendix B. Evaluation of integrated Matsubara kernels

See [Table B.5](#).

Appendix C. Evaluation of integrated imaginary time kernels

The spline interpolation procedure used to evaluate the integrated kernels is outlined in Section 3. Here we only give the observable-specific details. Throughout this Appendix, we denote dimensionless imaginary time and energy arguments by $\alpha = \tau/\beta = 1 - \bar{\alpha}$ and $z = \Omega\beta$ respectively. $T_\alpha(z) = \int_0^z t_\alpha(x)dx$ denotes the integrated tail contribution. All series found in the tables below are rapidly (exponentially) convergent. $\text{Li}_2(x)$ is the dilogarithm (Spence’s function), $\psi(x) = \frac{d}{dx} \log \Gamma(x)$ is the digamma function, $\psi^{(1)}(x) = \frac{d^2}{dx^2} \log \Gamma(x)$ is the trigamma function, $\Psi(x) = \frac{1}{2}[\psi(\frac{1+x}{2}) - \psi(\frac{x}{2})]$.

C.1. Green’s function of fermions

$$A(\tau; \Omega) = -\frac{1}{\beta} \int_0^z \frac{e^{-\alpha x}}{1 + e^{-x}} dx = -\frac{1}{\beta} [\theta(-z)S_\alpha^-(z) + \theta(z)S_\alpha^+(z) + T_\alpha(z)], \quad (\text{C.1})$$

$$S_\alpha^-(z) = -\int_z^0 \left[\frac{e^{-\alpha x}}{1 + e^{-x}} - t_\alpha(x) \right] dx, \quad S_\alpha^+(z) = \int_0^z \left[\frac{e^{-\alpha x}}{1 + e^{-x}} - t_\alpha(x) \right] dx. \quad (\text{C.2})$$

Table A.3
Fine tuning run() parameters.

Parameter Name	Python type	Default value	Meaning
random_seed	int	34788+928374*MPI.rank	Seed for pseudo-random number generator.
random_name	str	"mt19937" (Mersenne Twister 19937 generator)	Name of pseudo-random number generator. Other supported values are mt11213b, ranlux3 and variants of lagged_fibonacci PRNG (see documentation of Boost.Random for more details).
max_rects	int	60	Maximum number of rectangles to represent a configuration (K).
min_rect_width	float	1e-3	Minimal allowed width of a rectangle, in units of the energy window width.
min_rect_weight	float	1e-3	Minimal allowed weight of a rectangle, in units of the requested solution norm \mathcal{N} .
distrib_d_max	float	2.0	Maximal parameter of the power-law distribution function for the Metropolis algorithm (d_{\max}).
gamma	float	2.0	Proposal probability parameter γ (see Appendix E).
adjust_l_good_d	float	2.0	Maximal ratio D/D_{\min} for a particular solution to be considered good, α_{good} (see Section 2.2).
hist_max	float	2.0	Right boundary of the histograms, in units of D_{\min} (left boundary is always set to D_{\min}).
hist_n_bins	int	100	Number of bins for the histograms.

Table A.4
run() parameters for F - and L -adjustment procedures (see Appendix F and Section 2.2 respectively).

Parameter Name	Python type	Default value	Meaning
adjust_f_range	(int,int)	(100,5000)	Search range for the F -adjustment procedure (see Appendix F).
adjust_f_l	int	20	Number of particular solutions used in the F -adjustment procedure (see Appendix F).
adjust_f_kappa	float	0.25	Limiting value of κ used in the F -adjustment procedure (see Appendix F).
adjust_l_range	(int,int)	(100,2000)	Search range for the L -adjustment procedure (see Section 2.2).
adjust_l_verygood_d	float	4.0/3	Maximal ratio D/D_{\min} for a particular solution to be considered very good, $\alpha_{\text{very good}}$ (see Section 2.2).
adjust_l_ratio	float	0.95	Critical ratio $L_{\text{very good}}/L_{\text{good}}$ that stops the L -adjustment procedure (see Section 2.2).

Table B.5

Integrated kernels in the Matsubara representation. Respective kernels $K(\xi_n, \epsilon)$ are defined in the second column of Table 1. $R_{\{c,w,h\}}(\epsilon)$ is the rectangle function defined in (9).

Observable kind, O	Integrated kernel, $\int_{\epsilon_{\min}}^{\epsilon_{\max}} d\epsilon K(\xi_n, \epsilon) R_{\{c,w,h\}}(\epsilon)$
Green's function of fermions	$h \log \left(\frac{i\omega_n - c + w/2}{i\omega_n - c - w/2} \right)$
Correlator of boson-like operators	$\frac{hw}{\pi} + \frac{hiv_n}{\pi} \log \left(\frac{iv_n - c - w/2}{iv_n - c + w/2} \right)$
Autocorrelator of a Hermitian operator	$\frac{2hw}{\pi} + \frac{2hiv_n}{\pi} \left(\text{atan} \left(\frac{c - w/2}{v_n} \right) - \text{atan} \left(\frac{c + w/2}{v_n} \right) \right)$
Zero temperature correlator	$h \log \left(\frac{iz_n - c + w/2}{iz_n - c - w/2} \right)$, with $z_n = \pi(2n + 1)/\tau_{\max}$ or $2\pi n/\tau_{\max}$

Segments to construct the splines on:

$$S_{\alpha}^{-}(z) : z \in [-z_0, 0], \quad S_{\alpha}^{+}(z) : z \in [0; z_0], \quad z_0 = -2 \log(\text{tolerance}). \tag{C.3}$$

α	$t_{\alpha}(x)$	$T_{\alpha}(z)$	$S_{\alpha}^{-}(z)$	$S_{\alpha}^{+}(z)$
0	$\theta(x)$	$\theta(z)z$	$\log(1 + e^z) - \log(2)$	$\log(1 + e^{-z}) - \log(2)$
(0; 1/2)	$\theta(x)e^{-\alpha x}$	$\theta(z)\frac{e^{-\alpha z}-1}{-\alpha}$	$\sum_{n=0}^{\infty} (-1)^n \frac{e^{(n+\bar{\alpha})z}}{(n+\bar{\alpha})} - \Psi(\bar{\alpha})$	$-\sum_{n=0}^{\infty} (-1)^n \frac{e^{-(n+1+\alpha)z}}{-(n+1+\alpha)} - \Psi(1+\alpha)$
1/2	0	0	$2 \text{atan}(e^{z/2}) - \pi/2$	$-2 \text{atan}(e^{-z/2}) + \pi/2$
(1/2; 1)	$\theta(-x)e^{\bar{\alpha}x}$	$\theta(-z)\frac{e^{\bar{\alpha}z}-1}{\bar{\alpha}}$	$-\sum_{n=0}^{\infty} (-1)^n \frac{e^{(n+1+\bar{\alpha})z}}{(n+1+\bar{\alpha})} + \Psi(1+\bar{\alpha})$	$\sum_{n=0}^{\infty} (-1)^n \frac{e^{-(n+\alpha)z}}{-(n+\alpha)} + \Psi(\alpha)$
1	$\theta(-x)$	$\theta(-z)z$	$-\log(1 + e^z) + \log(2)$	$-\log(1 + e^{-z}) + \log(2)$

C.2. Correlator of boson-like operators

$$\Lambda(\tau; \Omega) = \frac{1}{\pi \beta^2} \int_0^z \frac{x e^{-\alpha x}}{1 - e^{-x}} dx = \frac{1}{\pi \beta^2} [\theta(-z)S_{\alpha}^{-}(z) + \theta(z)S_{\alpha}^{+}(z) + T_{\alpha}(z)], \tag{C.4}$$

$$S_{\alpha}^{-}(z) = - \int_z^0 \left[\frac{x e^{-\alpha x}}{1 - e^{-x}} - t_{\alpha}(x) \right] dx, \quad S_{\alpha}^{+}(z) = \int_0^z \left[\frac{x e^{-\alpha x}}{1 - e^{-x}} - t_{\alpha}(x) \right] dx. \tag{C.5}$$

Segments to construct the splines on:

$$S_{\alpha}^{-}(z) : z \in [-z_0, 0], \quad S_{\alpha}^{+}(z) : z \in [0; z_0]. \tag{C.6}$$

Factor x in the kernel tends to strengthen its delocalization, so it makes sense to choose z_0 slightly larger, for instance, $z_0 = -2.3 \log(\text{tolerance})$.

α	$t_{\alpha}(x)$	$T_{\alpha}(z)$	$S_{\alpha}^{-}(z)$	$S_{\alpha}^{+}(z)$
0	$\theta(x)x$	$\theta(z)z^2/2$	$-\pi^2/6 + z \log(1 - e^z) + \text{Li}_2(e^z)$	$\pi^2/6 + z \log(1 - e^{-z}) - \text{Li}_2(e^{-z})$
(0; 1/2)	$\theta(x)xe^{-\alpha x}$	$\theta(z)\frac{1-e^{-\alpha z}(1+z\alpha)}{\alpha^2}$	$\sum_{n=0}^{\infty} \frac{e^{(n+\bar{\alpha})z}[1-z(n+\bar{\alpha})]}{(n+\bar{\alpha})^2} - \psi^{(1)}(\bar{\alpha})$	$-\sum_{n=1}^{\infty} \frac{e^{-(n+\alpha)z}[1+z(n+\alpha)]}{(n+\alpha)^2} + \psi^{(1)}(1+\alpha)$
1/2	0	0	$-\pi^2/2 + z \log(\tanh(-z/4)) - \text{Li}_2(e^z) + 4\text{Li}_2(e^{z/2})$	$\pi^2/2 + z \log(\tanh(z/4)) + \text{Li}_2(e^{-z}) - 4\text{Li}_2(e^{-z/2})$
(1/2; 1)	$\theta(-x)(-x)e^{\bar{\alpha}x}$	$\theta(-z)\frac{e^{\bar{\alpha}z}(1-z\bar{\alpha})-1}{(\bar{\alpha})^2}$	$\sum_{n=1}^{\infty} \frac{e^{(n+\bar{\alpha})z}[1-z(n+\bar{\alpha})]}{(n+\bar{\alpha})^2} - \psi^{(1)}(1+\bar{\alpha})$	$-\sum_{n=0}^{\infty} \frac{e^{-(n+\alpha)z}[1+z(n+\alpha)]}{(n+\alpha)^2} + \psi^{(1)}(\alpha)$
1	$\theta(-x)(-x)$	$\theta(-z)(-z^2/2)$	$-\pi^2/6 + z \log(1 - e^z) + \text{Li}_2(e^z)$	$\pi^2/6 + z \log(1 - e^{-z}) - \text{Li}_2(e^{-z})$

C.3. Autocorrelator of a Hermitian operator

$$\Lambda(\tau; \Omega) = \frac{1}{\pi \beta^2} \int_0^z \frac{x(e^{-\alpha x} + e^{-\bar{\alpha}x})}{1 - e^{-x}} dx = \frac{1}{\pi \beta^2} [S_\alpha(z) + T_\alpha(z)], \tag{C.7}$$

$$S_\alpha(z) = \int_0^z \left[\frac{x(e^{-\alpha x} + e^{-(1-\alpha)x})}{1 - e^{-x}} - t_\alpha(x) \right] dx. \tag{C.8}$$

(The upper integration limit can be only positive, which eliminates the need for two splines). Segment to construct the spline on is $z \in [0; z_0], z_0 = -2.3 \log(\text{tolerance})$.

α	$t_\alpha(x)$	$T_\alpha(z)$	$S_\alpha(z)$
0,1	$x(1 + e^{-x})$	$1 + z^2/2 - e^{-z}(1 + z)$	$-1 + \pi^2/3 + 2z \log(1 - e^{-z}) - 2\text{Li}_2(e^{-z}) + e^{-z}(1 + z)$
$(0; 1/2) \cup (1/2; 1)$	$x(e^{-\alpha x} + e^{-\bar{\alpha}x})$	$\frac{1 - e^{-\alpha z}(1 + z\alpha)}{\alpha^2} + \frac{1 - e^{-\bar{\alpha}z}(1 + z\bar{\alpha})}{(\bar{\alpha})^2}$	$-\sum_{n=1}^{\infty} \frac{e^{-(n+\alpha)z}[1 + z(n+\alpha)]}{(n+\alpha)^2} + \psi^{(1)}(1+\alpha) - \sum_{n=1}^{\infty} \frac{e^{-(n+\bar{\alpha})z}[1 + z(n+\bar{\alpha})]}{(n+\bar{\alpha})^2} + \psi^{(1)}(1+\bar{\alpha})$
1/2	$2xe^{-x/2}$	$4(2 - e^{-z/2}(2 + z))$	$-8 + \pi^2 + 4e^{-z/2}(2 + z) + 2z \log \tanh(z/4) - 8\text{Li}_2(e^{-z/2}) + 2\text{Li}_2(e^{-z})$

C.4. Zero temperature correlator

$$\int_0^{+\infty} d\epsilon K(\tau, \epsilon) R_{\{c, w, h\}}(\epsilon) = \begin{cases} -hw, & \tau = 0, \\ \frac{h}{\tau}(e^{-\tau(c+w/2)} - e^{-\tau(c-w/2)}), & \text{otherwise.} \end{cases} \tag{C.9}$$

Appendix D. Evaluation of integrated Legendre kernels

The spline interpolation procedure used to evaluate the integrated kernels is outlined in Section 3.

D.1. Green's function of fermions

$$\Lambda(\ell; \Omega) = (-\text{sgn}(\Omega))^{\ell+1} \sqrt{2\ell + 1} \int_0^{|\Omega|^{1/\beta/2}} \frac{i_\ell(x)}{\cosh(x)} dx. \tag{D.1}$$

Asymptotic form of the integrand ($x \rightarrow \infty$),

$$\begin{aligned} \frac{i_\ell(x)}{\cosh(x)} &= \frac{e^x}{e^x + e^{-x}} \sum_{n=0}^{\ell} (-1)^n \frac{a_n(\ell + 1/2)}{x^{n+1}} + \frac{e^{-x}}{e^x + e^{-x}} \sum_{n=0}^{\ell} (-1)^{\ell+1+n} \frac{a_n(\ell + 1/2)}{x^{n+1}} \\ &\approx \sum_{n=0}^{\ell} (-1)^n \frac{a_n(\ell + 1/2)}{x^{n+1}}. \end{aligned} \tag{D.2}$$

Integral $F(z) = \int_0^z \frac{i_\ell(x)}{\cosh(x)} dx$ in the high-energy limit,

$$F^>(z)|_{z>x_0} = F^<(x_0) + \left\{ \log(x) + \sum_{n=1}^{\ell} (-1)^{n+1} \frac{a_n(\ell + 1/2)}{x^n n} \right\} \Big|_{x_0}^z. \tag{D.3}$$

D.2. Correlator of boson-like operators

$$\Lambda(\ell; \Omega) = -(-\text{sgn}(\Omega))^{\ell+1} \frac{2\sqrt{2\ell + 1}}{\pi \beta} \int_0^{|\Omega|^{1/\beta/2}} \frac{i_\ell(x)x}{\sinh(x)} dx. \tag{D.4}$$

Asymptotic form of the integrand ($x \rightarrow \infty$),

$$\begin{aligned} \frac{i_\ell(x)x}{\sinh(x)} &= \frac{e^x}{e^x - e^{-x}} \sum_{n=0}^{\ell} (-1)^n \frac{a_n(\ell + 1/2)}{x^n} + \frac{e^{-x}}{e^x - e^{-x}} \sum_{n=0}^{\ell} (-1)^{\ell+1+n} \frac{a_n(\ell + 1/2)}{x^n} \\ &\approx \sum_{n=0}^{\ell} (-1)^n \frac{a_n(\ell + 1/2)}{x^n}. \end{aligned} \tag{D.5}$$

Integral $F(z) = \int_0^z \frac{i_\ell(x)x}{\sinh(x)} dx$ in the high-energy limit,

$$F^>(z)|_{z>x_0} = F^<(x_0) + \left\{ x - \frac{\ell(\ell + 1)}{2} \log(x) + \sum_{n=1}^{\ell-1} (-1)^n \frac{a_{n+1}(\ell + 1/2)}{x^n n} \right\} \Big|_{x_0}^z. \tag{D.6}$$

D.3. Autocorrelator of a Hermitian operator

$$A(\ell; \Omega) = (1 + (-1)^\ell) \frac{2\sqrt{2\ell + 1}}{\pi\beta} \int_0^{\Omega\beta/2} \frac{i_\ell(x)x}{\sinh(x)} dx. \tag{D.7}$$

This integral is evaluated in full analogy with the previous kernel.

D.4. Zero temperature correlator

$$A(\ell; \Omega) = (-1)^{\ell+1} \sqrt{2\ell + 1} \int_0^{\Omega\tau_{max}/2} 2e^{-x} i_\ell(x) dx. \tag{D.8}$$

Asymptotic form of the integrand ($x \rightarrow \infty$),

$$2e^{-x} i_\ell(x) = \sum_{n=0}^{\ell} (-1)^n \frac{a_n(\ell + 1/2)}{x^n} + e^{-2x} \sum_{n=0}^{\ell} (-1)^{\ell+1} \frac{a_n(\ell + 1/2)}{x^n} \approx \sum_{n=0}^{\ell} (-1)^n \frac{a_n(\ell + 1/2)}{x^n}. \tag{D.9}$$

Integral $F(z) = \int_0^z 2e^{-x} i_\ell(x) dx$ in the high-energy limit,

$$F^>(z)|_{z>x_0} = F^<(x_0) + \left\{ \log(x) + \sum_{n=1}^{\ell} (-1)^{n+1} \frac{a_n(\ell + 1/2)}{x^n n} \right\} \Big|_{x_0}^z. \tag{D.10}$$

Appendix E. Probability density function for the parameter change

Every proposed elementary update is parametrized by a real number $\delta\xi \in [\delta\xi_{min}; \delta\xi_{max}]$. A concrete meaning of $\delta\xi$ depends on the elementary update in question. For instance, $\delta\xi$ can be a shift of the centre of an existing rectangle, or the weight of a rectangle to be added. In general, $\delta\xi$ are defined so that larger $|\delta\xi|$ correspond to more prominent changes in the configuration. SOM randomly generates values of $\delta\xi$ according to the following probability density function,

$$\mathcal{P}(\delta\xi) = N \exp\left(-\gamma \frac{|\delta\xi|}{X}\right), \quad X \equiv \max(|\delta\xi_{min}|, |\delta\xi_{max}|), \tag{E.1}$$

$$N = \frac{\gamma}{X} [\text{sign}(\delta\xi_{min})(e^{-\gamma|\delta\xi_{min}|/X} - 1) + \text{sign}(\delta\xi_{max})(1 - e^{-\gamma|\delta\xi_{max}|/X})]^{-1}. \tag{E.2}$$

User can change parameter $\gamma > 0$ to control non-uniformity of the PDF (E.1).

Appendix F. Fit quality criterion and choice of F

Mishchenko introduced a special quantity κ that characterizes the fit quality of a given particular solution $A(\epsilon)$ [41].

$$\kappa = \frac{1}{M-1} \sum_{m=2}^M \theta(-\Delta(m)\Delta(m-1)). \tag{F.1}$$

The observable O and, therefore, deviation $\Delta(m)$ (Eq. (6)) are assumed to be real-valued here. κ measures the degree to what adjacent deviation values $\Delta(m)$ are anti-correlated. Since input data points $O(\xi_m)$ are expected to be statistically independent, deviations $\Delta(m)$ should rapidly fluctuate changing sign between adjacent points. Conversely, if the solution $A(\epsilon)$ gives a systematic deviation from the input points $O(\xi_m)$, products $\Delta(m)\Delta(m-1)$ are more likely to be positive, which results in a smaller κ . Ideally, κ must approach 1/2, but in practice values as small as 1/4 signal satisfactory fit quality.

A similar expression can be written for complex-valued observables, such as functions of Matsubara frequencies. Our generalization consists in replacing

$$\begin{aligned} \theta(-\Delta(m)\Delta(m-1)) &\mapsto \frac{1}{2} \left[1 - \frac{\Re[\Delta(m)\Delta^*(m-1)]}{|\Delta(m)\Delta^*(m-1)|} \right] \\ &= \frac{1}{2} [1 - \cos[\arg(\Delta(m)) - \arg(\Delta(m-1))]]. \end{aligned} \tag{F.2}$$

According to the modified definition, two adjacent values of Δ are considered anti-correlated, if the complex phase shift between them exceeds $\pm\pi/2$. In the case of real-valued quantities the phase shift is always either 0, or π .

SOM has an option to automatically adjust the number of global updates F used in a calculation. Starting from $F = F_{min}$ it finds a few (20 by default) particular solutions $\hat{A}(\epsilon)$ and checks that $\kappa \geq \kappa_{min}$ (1/4 by default) for at least a half of them. If this is not the case, the test is repeated with an increased F . This procedure stops upon a successful κ -test or when F_{max} is reached, whichever happens first.

References

- [1] E. Gull, A.J. Millis, A.I. Lichtenstein, A.N. Rubtsov, M. Troyer, P. Werner, *Rev. Modern Phys.* 83 (2011) 349–404, <http://dx.doi.org/10.1103/RevModPhys.83.349>, <https://link.aps.org/doi/10.1103/RevModPhys.83.349>.
- [2] W. Metzner, D. Vollhardt, *Phys. Rev. Lett.* 62 (3) (1989) 324–327, <http://dx.doi.org/10.1103/PhysRevLett.62.324>, <http://journals.aps.org/prl/abstract/10.1103/PhysRevLett.62.324>.
- [3] A. Georges, G. Kotliar, *Phys. Rev. B* 45 (12) (1992) 6479–6483, <http://dx.doi.org/10.1103/PhysRevB.45.6479>, <http://journals.aps.org/prb/abstract/10.1103/PhysRevB.45.6479>.
- [4] A. Georges, G. Kotliar, W. Krauth, M. Rozenberg, *Rev. Modern Phys.* 68 (1) (1996) 13–125, <http://dx.doi.org/10.1103/RevModPhys.68.13>, <http://journals.aps.org/rmp/abstract/10.1103/RevModPhys.68.13>.
- [5] G. Kotliar, S. Savrasov, K. Haule, V. Oudovenko, O. Parcollet, C. Marianetti, *Rev. Modern Phys.* 78 (3) (2006) 865–951, <http://dx.doi.org/10.1103/RevModPhys.78.865>, <http://link.aps.org/doi/10.1103/RevModPhys.78.865>.
- [6] L. Mühlbacher, E. Rabani, *Phys. Rev. Lett.* 100 (2008) 176403, <http://dx.doi.org/10.1103/PhysRevLett.100.176403>, <https://link.aps.org/doi/10.1103/PhysRevLett.100.176403>.
- [7] P. Werner, T. Oka, A.J. Millis, *Phys. Rev. B* 79 (2009) 035320, <http://dx.doi.org/10.1103/PhysRevB.79.035320>, <https://link.aps.org/doi/10.1103/PhysRevB.79.035320>.
- [8] P. Werner, T. Oka, M. Eckstein, A.J. Millis, *Phys. Rev. B* 81 (2010) 035108, <http://dx.doi.org/10.1103/PhysRevB.81.035108>, <https://link.aps.org/doi/10.1103/PhysRevB.81.035108>.
- [9] H.-T. Chen, G. Cohen, D.R. Reichman, *J. Chem. Phys.* 146 (5) (2017) 054105, <http://dx.doi.org/10.1063/1.4974328>.
- [10] H.-T. Chen, G. Cohen, D.R. Reichman, *J. Chem. Phys.* 146 (5) (2017) 054106, <http://dx.doi.org/10.1063/1.4974329>.
- [11] A.N. Rubtsov, V.V. Savkin, A.I. Lichtenstein, *Phys. Rev. B* 72 (2005) 035122, <http://dx.doi.org/10.1103/PhysRevB.72.035122>, <https://link.aps.org/doi/10.1103/PhysRevB.72.035122>.
- [12] P. Werner, A.J. Millis, *Phys. Rev. B* 74 (2006) 155107, <http://dx.doi.org/10.1103/PhysRevB.74.155107>, <https://link.aps.org/doi/10.1103/PhysRevB.74.155107>.
- [13] E. Gull, P. Werner, O. Parcollet, M. Troyer, *Europhys. Lett.* 82 (5) (2008) 57003, <http://stacks.iop.org/0295-5075/82/i=5/a=57003>.
- [14] J. Otsuki, H. Kusunose, P. Werner, Y. Kuramoto, *J. Phys. Soc. Japan* 76 (11) (2007) 114707, <http://dx.doi.org/10.1143/JPSJ.76.114707>.
- [15] N. Prokofev, B. Svistunov, *Phys. Rev. Lett.* 99 (2007) 250201, <http://dx.doi.org/10.1103/PhysRevLett.99.250201>, <https://link.aps.org/doi/10.1103/PhysRevLett.99.250201>.
- [16] N.V. Prokofev, B.V. Svistunov, *Phys. Rev. B* 77 (2008) 125101, <http://dx.doi.org/10.1103/PhysRevB.77.125101>, <https://link.aps.org/doi/10.1103/PhysRevB.77.125101>.
- [17] R. Blankenbecler, D.J. Scalapino, R.L. Sugar, *Phys. Rev. D* 24 (1981) 2278–2286, <http://dx.doi.org/10.1103/PhysRevD.24.2278>, <https://link.aps.org/doi/10.1103/PhysRevD.24.2278>.
- [18] L. Boehnke, H. Hafermann, M. Ferrero, F. Lechermann, O. Parcollet, *Phys. Rev. B* 84 (2011) 075145, <http://dx.doi.org/10.1103/PhysRevB.84.075145>, <https://link.aps.org/doi/10.1103/PhysRevB.84.075145>.
- [19] C. Groetsch, *J. Phys. Conf. Ser.* 73 (1) (2007) 012001, <http://stacks.iop.org/1742-6596/73/i=1/a=012001>.
- [20] H.J. Vidberg, J.W. Serene, *J. Low Temp. Phys.* 29 (1977) 179–192, <http://dx.doi.org/10.1007/BF00655090>.
- [21] X. Zhu, G. Zhu, *J. Comput. Appl. Math.* 148 (2) (2002) 341–348, [http://dx.doi.org/10.1016/S0377-0427\(02\)00554-X](http://dx.doi.org/10.1016/S0377-0427(02)00554-X), <http://www.sciencedirect.com/science/article/pii/S037704270200554X>.
- [22] K.S.D. Beach, R.J. Gooding, F. Marsiglio, *Phys. Rev. B* 61 (2000) 5147–5157, <http://dx.doi.org/10.1103/PhysRevB.61.5147>, <https://link.aps.org/doi/10.1103/PhysRevB.61.5147>.
- [23] M. Jarrell, J. Gubernatis, *Phys. Rep.* 269 (3) (1996) 133–195, [http://dx.doi.org/10.1016/0370-1573\(95\)00074-7](http://dx.doi.org/10.1016/0370-1573(95)00074-7), <http://www.sciencedirect.com/science/article/pii/S0370157395000747>.
- [24] R.K. Bryan, *Eur. Biophys. J.* 18 (3) (1990) 165–174, <http://dx.doi.org/10.1007/BF02427376>.
- [25] G.J. Kraberger, R. Triebl, M. Zingl, M. Aichhorn, *Phys. Rev. B* 96 (2017) 155128, <http://dx.doi.org/10.1103/PhysRevB.96.155128>, <https://link.aps.org/doi/10.1103/PhysRevB.96.155128>.
- [26] G.J. Kraberger, M. Zingl, *MaxEnt*, <https://github.com/TRIQS/maxent>.
- [27] D. Bergeron, A.-M.S. Tremblay, *Phys. Rev. E* 94 (2016) 023303, <http://dx.doi.org/10.1103/PhysRevE.94.023303>, <https://link.aps.org/doi/10.1103/PhysRevE.94.023303>.
- [28] D. Bergeron, TRIQS Interface to the OmegaMaxEnt Code, https://github.com/TRIQS/omegamaxent_interface.
- [29] R. Levy, J. LeBlanc, E. Gull, *Comput. Phys. Comm.* 215 (2017) 149–155, <http://dx.doi.org/10.1016/j.cpc.2017.01.018>, <http://www.sciencedirect.com/science/article/pii/S0010465517300309>.
- [30] K. Vafayi, O. Gunnarsson, *Phys. Rev. B* 76 (2007) 035115, <http://dx.doi.org/10.1103/PhysRevB.76.035115>, <https://link.aps.org/doi/10.1103/PhysRevB.76.035115>.
- [31] A.W. Sandvik, *Phys. Rev. B* 57 (1998) 10287–10290, <http://dx.doi.org/10.1103/PhysRevB.57.10287>, <https://link.aps.org/doi/10.1103/PhysRevB.57.10287>.
- [32] K.S.D. Beach, Identifying the maximum entropy method as a special limit of stochastic analytic continuation, 2004, [arXiv:cond-mat/0403055](https://arxiv.org/abs/cond-mat/0403055).
- [33] A.S. Mishchenko, N.V. Prokofev, A. Sakamoto, B.V. Svistunov, *Phys. Rev. B* 62 (2000) 6317–6336, <http://dx.doi.org/10.1103/PhysRevB.62.6317>, <https://link.aps.org/doi/10.1103/PhysRevB.62.6317>.
- [34] O. Gouliko, A.S. Mishchenko, L. Pollet, N. Prokofev, B. Svistunov, *Phys. Rev. B* 95 (2017) 014102, <http://dx.doi.org/10.1103/PhysRevB.95.014102>, <https://link.aps.org/doi/10.1103/PhysRevB.95.014102>.
- [35] J. Schött, E.G.C.P. van Loon, I.L.M. Locht, M.I. Katsnelson, I. Di Marco, *Phys. Rev. B* 94 (2016) 245140, <http://dx.doi.org/10.1103/PhysRevB.94.245140>, <https://link.aps.org/doi/10.1103/PhysRevB.94.245140>.
- [36] O. Parcollet, M. Ferrero, T. Ayril, H. Hafermann, I. Krivenko, L. Messio, P. Seth, *Comput. Phys. Comm.* 196 (2015) 398–415, <http://dx.doi.org/10.1016/j.cpc.2015.04.023>, <http://www.sciencedirect.com/science/article/pii/S0010465515001666>.
- [37] O.F. Syljuåsen, *Phys. Rev. B* 78 (2008) 174429, <http://dx.doi.org/10.1103/PhysRevB.78.174429>, <https://link.aps.org/doi/10.1103/PhysRevB.78.174429>.
- [38] N.V. Prokofev, B.V. Svistunov, *JETP Lett.* 97 (11) (2013) 649–653, <http://dx.doi.org/10.1134/S002136401311009X>.
- [39] S. Fuchs, M. Jarrell, T. Pruschke, *J. Phys. Conf. Ser.* 200 (1) (2010) 012041, <http://stacks.iop.org/1742-6596/200/i=1/a=012041>.
- [40] J. Otsuki, M. Ohzeki, H. Shinaoka, K. Yoshimi, *Phys. Rev. E* 95 (2017) 061302, <http://dx.doi.org/10.1103/PhysRevE.95.061302>, <https://link.aps.org/doi/10.1103/PhysRevE.95.061302>.
- [41] A.S. Mishchenko, in: E. Pavarini, E. Koch, F. Anders, M. Jarrell (Eds.), *Correlated Electrons: From Models To Materials*, in: *Schriften des Forschungszentrums Jülich. Reihe Modeling and simulation*, 2, Forschungszentrum Jülich GmbH, Jülich, 2012, <http://user.fz-juelich.de/record/136393>.
- [42] M. Potthoff, T. Wegner, W. Nolting, *Phys. Rev. B* 55 (1997) 16132–16142, <http://dx.doi.org/10.1103/PhysRevB.55.16132>, <https://link.aps.org/doi/10.1103/PhysRevB.55.16132>.
- [43] N. Metropolis, A.W. Rosenbluth, M.N. Rosenbluth, A.H. Teller, E. Teller, *J. Chem. Phys.* 21 (6) (1953) 1087–1092, <http://dx.doi.org/10.1063/1.1699114>.
- [44] W.K. Hastings, *Biometrika* 57 (1) (1970) 97–109, <http://dx.doi.org/10.1093/biomet/57.1.97>.
- [45] M. Abramowitz, I.A. Stegun, *Handbook of Mathematical Functions with Formulas, Graphs, and Mathematical Tables*, Dover, New York, 1972, pp. 443–445.
- [46] L. Carlitz, *Duke Math. J.* 24 (2) (1957) 151–162, <http://dx.doi.org/10.1215/S0012-7094-57-02421-3>.
- [47] P. Seth, I. Krivenko, M. Ferrero, O. Parcollet, *Comput. Phys. Comm.* 200 (2016) 274–284, <http://dx.doi.org/10.1016/j.cpc.2015.10.023>, <http://www.sciencedirect.com/science/article/pii/S001046551500404X>.
- [48] G. Moeller, V. Dobrosavljević, A.E. Ruckenstein, *Phys. Rev. B* 59 (1999) 6846–6854, <http://dx.doi.org/10.1103/PhysRevB.59.6846>, <https://link.aps.org/doi/10.1103/PhysRevB.59.6846>.

Chapter 3

Strongly correlated superconductivity

The phenomenon of superconductivity has been found in different classes of materials, e.g. in cuprates, iron pnictides, iron chalcogenides and heavy fermion materials. An understanding of unconventional superconductivity requires insights on how such different materials support the superconducting phase, and it can be suspected that all these materials have something in common regarding the pairing mechanism [27]. In particular, antiferromagnetism is a feature that is found often in the phase diagram of superconducting materials in proximity to the superconducting phase. It indicates that spin fluctuations are likely to have crucial impact on the superconducting properties. Moreover, in terms of their structure these materials have in common that they consist of quasi-two-dimensional layers that are relatively widely separated. The correlated electrons stem from partially filled d or f shells of copper (Cu), iron (Fe) or cerillium (Ce) atoms of the layer which are coordinated by anionic ligands. The stacking of the layers differs depending on the compound and its stoichiometry, but still very different stackings lead to superconductivity. However, the critical temperature changes depending on the stackings.

In iron pnictides the iron atoms are sufficiently close to support direct tunneling of the correlated electrons which renders the system metallic. The heavy fermion compounds contain rather localized f electrons which can become delocalized by their coupling to the conduction band of the ligands. The name “heavy fermion” already clarifies that the material is metallic with strongly renormalized conduction electrons stemming from interaction effects. In contrast, the cuprates are insulators if the CuO planes are undoped. The phases found in these materials are diverse, e.g. but for each material its the same electrons that define these phases. Moreover, theoretical approaches have found descriptions of these phases by considering these electrons only. Therefore it is reasonable to summarize such materials under the notion of strong electronic correlations.

Whereas in cuprates the superconducting correlations are most often suspected to be described by an effective one-band model, in iron pnictides Hund’s coupling can be essential and thus a multiorbital description is necessary as Hund’s coupling basically is interorbital Coulomb exchange that can lead to parallel spin alignment. Based on spin fluctuations

Compound	T_c^{\max} [K]	Ref.
HgBa ₂ Ca ₂ Cu ₃ O _{8+x}	135	[90]
HgBa ₂ CaCu ₂ O _{6+x}	128	[90]
HgBa ₂ CuO _{4+x}	94	[90]
Bi ₂ Sr ₂ Ca ₂ Cu ₃ O _{10+x}	105	[91]
Bi ₂ Sr ₂ CaCu ₂ O _{8+x}	95	[91]
Bi ₂ Sr ₂ CuO _{6+x}	22	[91]
YBa ₂ Cu ₃ O _{7-x}	93	[28]
La _{2-x} Sr _x Cu ₄ O	38	[92]
La _{2-x} Ba _x CuO ₄	35	[24]

Table 3.1: A selection of Superconducting copper oxide compounds and their respective highest critical temperatures T_c^{\max} .

there has been studies that suggest a unified description of superconductivity in cuprates and in iron pnictides by relating copper-intersite and iron-multiorbital correlations to each other [89].

3.1 Copper oxides

The superconducting properties, i.e. zero electrical resistance, of the copper oxides have been discovered in the year 1986 [24] and it was a very surprising discovery as the copper oxides are ceramics that are rather bad conductors at temperatures above the superconducting transition temperature T_c , particularly in the context of the previously discovered conventional (BCS) superconductors which are metallic and have a large density of states at Fermi level. The discovery was rewarded with the Nobel price for Bednorz and Müller in 1987. They found superconductivity in the material La_{2-x}Ba_xCuO₄ which at that time was the material with the highest $T_c = 35$ K. This finding triggered further research on high- T_c superconductivity in copper oxides, also known as cuprates. A list of subsequent findings is provided in Tab. 3.1. This list is not a complete list of all superconducting copper oxides, but shows some intensively investigated representatives and provides an overview.

The crystal structure of most copper oxides is tetragonal, but other structures are also possible YBa₂Cu₃O₇, e.g., can be orthorhombic depending on its stoichiometry. YBa₂Cu₃O₇ is the first discovered superconductor that enters the superconducting state at temperatures above the melting temperature of liquid nitrogen. Its unit cell contains a double layer of CuO planes, in which the copper atoms (d^9 configuration) are in octahedral coordination of oxygen ligands, similar to perovskite structures, but with some oxygen vacancies, see Fig. 3.1. It is the CuO layers that all the superconducting copper oxides have in common. The bond between the Cu- $d_{x^2-y^2}$ orbitals and the O- p orbitals are suspected to be the crucial building block for the superconductivity [93, 94]. However, it is still actively debated whether these bonds are better described as ionic [95] or valence

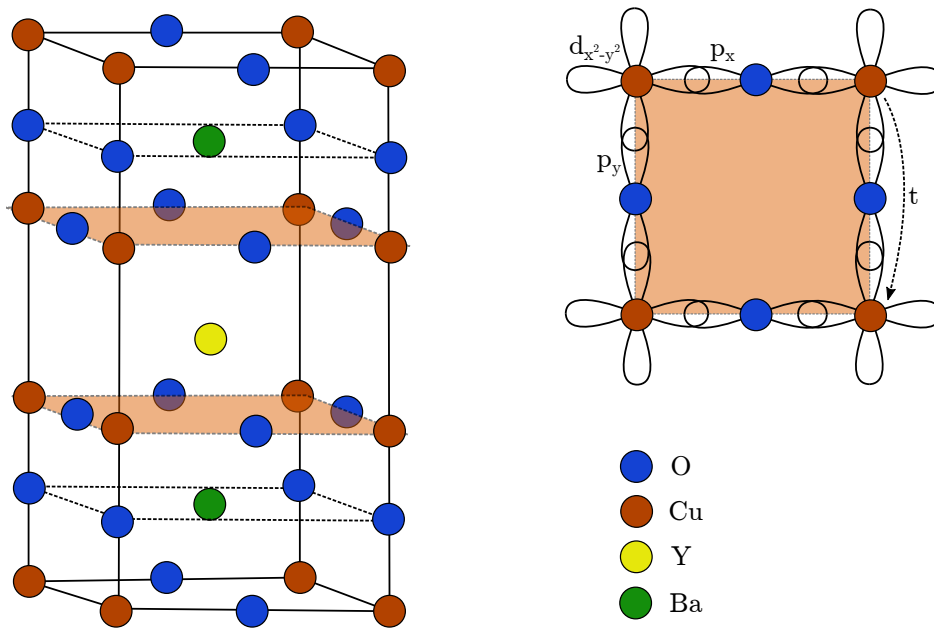


Figure 3.1: Left: Schematic unit cell of $\text{YBa}_2\text{Cu}_3\text{O}_7$ consisting of oxygen (O), copper (Cu), yttrium (Y) and barium (Ba) atoms. It contains two CuO layers of strongly correlated electrons. Right: Top-view of a strongly correlated CuO layer. $d_{x^2-y^2}$ orbitals of copper hybridize with p orbitals of oxygen and enable the superexchange tunneling mechanism of an electron from a copper atom to its nearest neighbor copper atom with effective amplitude t .

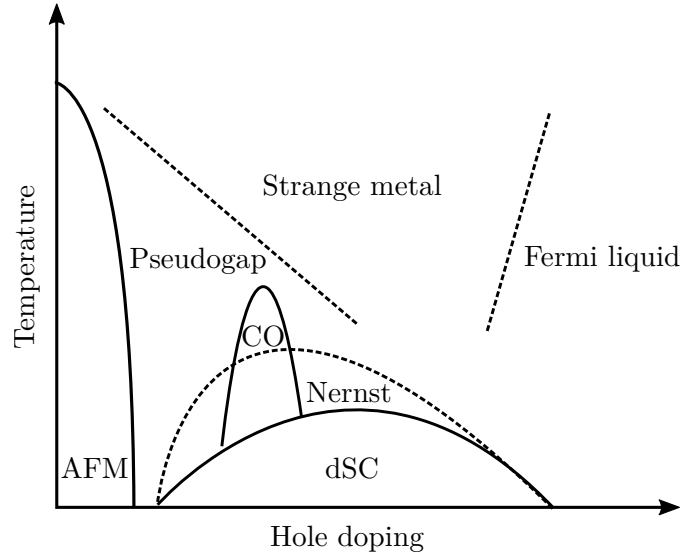


Figure 3.2: Sketch of the superconducting copper oxides' phase diagram. At low temperatures and half-filling of the CuO layers the materials are antiferromagnetic (AFM). Upon hole doping they become *d*-wave superconductors (dSC). At temperatures above the superconducting dome a Nernst signal can be detected as well as charge order (CO). Dashed lines depict crossovers. Details and features of this illustration can deviate for the individual compounds.

bonds [96]. Due to the missing oxygen between the double layer, the Cu atoms of the layers, marked in red, have only one apical oxygen each which surrounds the Ba atom. The double layer is separated by an Y atom only. The role of the layer structure together with the apical oxygens is still puzzling. Besides $\text{YBa}_2\text{Cu}_3\text{O}_7$, other layered structures have been synthesized, ranging from one to three layers. It can be controlled by the stoichiometry of the compound. The highest T_c^{max} were found for the three layer structures, e.g. $\text{HgBa}_2\text{Ca}_2\text{Cu}_3\text{O}_{8+x}$ and $\text{Bi}_2\text{Sr}_2\text{Ca}_2\text{Cu}_3\text{O}_{10+x}$. T_c^{max} decreases with the number of layers, e.g. $\text{HgBa}_2\text{CuO}_{4+x}$ corresponding to one layer, see Tab. 3.1.

The phase diagram of the copper oxides is rich and contains surprisingly many phases and crossovers. A schematic phase diagram of the copper oxides is shown in Fig. 3.2, it is meant to be universal, although details vary regarding the individual compounds. The half-filled CuO layers are antiferromagnetic (AFM) below the Néel temperature. The antiferromagnetism in the copper oxides is understood via the Mott [8] mechanism of localized electrons with well defined local moments that occupy one site each and non-local correlations with the nearest neighbors favor antiparallel spin alignment. The superconducting phase is entered by doping the CuO layers at low temperatures. Doping has to be realized depending on the compound. $\text{YBa}_2\text{Cu}_3\text{O}_{7-x}$ is hole doped by adding oxygen that has a large electronegativity and “pulls” the electrons from the CuO layers. In contrast, in $\text{La}_{2-x}\text{Sr}_x\text{Cu}_4\text{O}$ La is substituted for Sr which lacks a valence electron compared to La and thereby realizes the hole doping. The superconducting gap in copper oxides has $d_{x^2-y^2}$ symmetry [97, 98], hence the name *d*-wave superconductivity (dSC). It means, that this

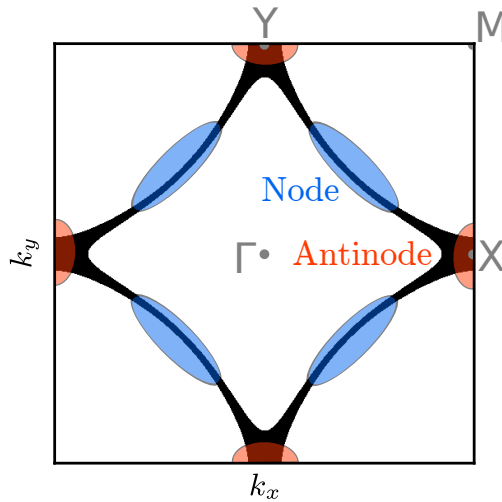


Figure 3.3: Tightbinding Fermi surface of the square lattice with the parameters $t = -1$, $t' = 0.3$ and $\mu = -1.2$. Nodal and antinodal spots are marked in blue and red, respectively. Γ , X , Y and M are the high-symmetry points of the square lattice’s Brillouin zone with the origin $\Gamma = (0, 0)$.

order parameter is defined on the bonds. Remarkably, this was predicted by theory before the actual experimental finding [29]. Considering a two-dimensional strongly correlated square lattice such as in Fig. 3.1, the d -wave gap on horizontal bonds has opposite sign than that of the vertical bonds. The superconducting dome usually spans a hole-doping range from 5% to about 25% with a maximum around 15% (optimal doping) where the notion of “percent” is normalized to the number of Cu atoms in the CuO layer. The phase diagram region of less doping than optimal doping is called “underdoped” and the region of more doping is called “overdoped”.

On top of the superconducting dome, at higher temperatures, the Nernst signal has been measured. This is interpreted as the heat transport via superconducting vortex fluctuations [99] which can be described by phase fluctuations of local dSC pairs. Though, the interpretation of the Nernst signal is not unambiguous and other excitations, e.g. quasi-particles and short-lived Cooper pairs, are discussed as well [100, 101, 102]. The shape of the Nernst region is tilted and tends to be more pronounced in the underdoped regime. The pseudogap is one of the most studied phenomena in copper oxides [103, 104] and is being investigated for over twenty years [105, 106] with remaining open questions. The problem with the high-temperature underdoped region is that so many instabilities have been measured and they have different critical temperatures [107]. For example, shown in Fig. 3.2 is the charge density wave instability, or charge order (CO). Additionally, there can be a spin density wave instability at low temperatures and between the AFM and dSC phase or a pair density wave instability below the charge density wave instability. Other orders that have been detected are stripes and nematic orders. However, none of it seems to define the onset of the pseudogap. Moreover, some instabilities have been measured in

only certain compounds which is why they might be neglected in schematic phase diagrams for all cuprates. Also, compound dependent are the endpoints of the pseudogap, it is not clear what makes the pseudogap diminish at larger hole dopings [102].

The experimental technique of angle resolved photoemission spectroscopy (ARPES) produced a detailed picture of the pseudogap. The local density of states contains a gap with spectral weight at Fermi level, hence the name “pseudogap”. The interesting feature is that the spectral weight vanishes in the so-called antinodal part, see Fig. 3.3, of the Fermi surface, but remains in the nodal part giving rise to the interpretation of nodal quasiparticles. The hole doping of the system would change the Fermi surface so that the curved lines become disconnected quarters of a circle-like object. The non-trivial part, however, is the partial vanishing of spectral weight on the Fermi surface which thereby also changes its topology. The vanishing of spectral weight occurs continuously as the temperature is lowered [108]. The remaining spectral weight at the nodes is also referred to as Fermi arcs. The possibility of a symmetry-breaking underlying the pseudogap stimulated many theorists to develop new ideas and concepts beyond the established Landau theory of phase transitions [32, 109, 110]. An early attempt is the resonating valence bond state [96] which is a quantum superposition of many entangled pairs of sites in a spin-singlet state, i.e. a valence bond. The concept describes excitations that are created by breaking up a singlet and delocalizing the spins through resonating valence bonds [111]. These excitations are called spinons, and carry only spin and no charge which renders them different from a renormalized electron and leads to spin-charge separation.

Hole-doping the pseudogap phase makes the system metallic. However, this metallic phase is very anomalous as it exhibits a resistivity that has a linear temperature dependence [112]. Originally, it has been labeled marginal “Fermi liquid” and a more recent name has become the term “strange metal”, high-energy theories have been adapted for a description of this phase [33, 113]. On further doping this linear dependence turns into a quadratic one and the full large Fermi surface [114] is restored as expected from a Fermi liquid.

3.2 Hubbard model

The low-energy effective model of the strongly correlated electronic properties in copper oxides is often assumed to be the Hubbard model [94]. Thereby is the charge transfer character of the hybridized copper and oxygen atoms neglected. The single band of the Hubbard model describes the copper atoms as sites, and between them occurs hopping of electrons, whereas a single hopping amplitude describes the tunneling of an electron from a copper atom to a neighboring copper atom through (σ -)hybridized Cu- $d_{x^2-y^2}$ and O- p orbitals. Due to the octahedral oxygen coordination, the $d_{x^2-y^2}$ orbital is the highest occupied orbital of the Cu atoms and determines the low-energy excitations of the system. Because the oxygen lies in between the copper atoms, the hopping amplitude t describes so-called superexchange. If two electrons meet on a Hubbard site, then system’s energy is raised by the interaction energy U , the screened Coulomb repulsion. From the charge-transfer point of view U can be seen as an effective description of holes with the interaction $U = E_p - E_d$ being the difference of the Cu- $d_{x^2-y^2}$ and O- p levels [32]. Thus, the one-band

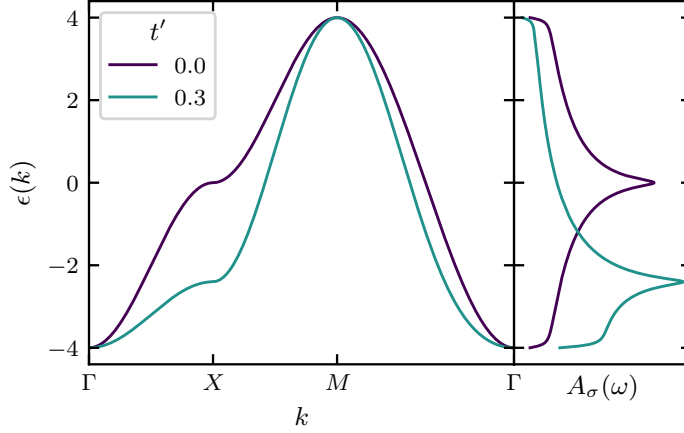


Figure 3.4: Left: Electronic band structure $\varepsilon(k)$ of the square lattice calculated via the tightbinding method with nearest neighbor hopping $t = -1$ and next-nearest neighbor hopping t' . The path along the high symmetry points Γ , X, Y and M lies within the Brillouin zone. Right: $A_\sigma(\omega)$ is the local density of states dependant on frequency ω and spin σ .

Hubbard model is defined by the hamiltonian

$$H = \sum_{ij\sigma} t_{ij} c_{i\sigma}^\dagger c_{j\sigma} - \mu \sum_{i\sigma} n_{i\sigma} + U \sum_i n_{\uparrow i} n_{\downarrow i}, \quad (3.1)$$

where c^\dagger and c , create and annihilate fermions of spin σ , respectively. They act on the many-body Fockspace and anticommute. t is the hopping between the sites i, j of a lattice, μ is the chemical potential and $n_{i\sigma} = c_{i\sigma}^\dagger c_{i\sigma}$ is the occupation number operator. The model exhibits a local charge ($U(1)$) and spin ($SU(2)$) symmetry. Moreover, on bipartite lattices it is particle-hole symmetric. The first term contains the kinetic energy and the second the potential energy of the screened Coulomb repulsion. The screening is an assumption that by far does not hold for all materials. In fact it is rather the opposite, that this situation is quite special and often used for low-temperatures only. The non-trivial correlations of the model stem from the competition of the electrons' itineracy with their localization with the constraint of the Pauli-principle which prohibits two fermions to occupy the same state.

The lattice described by t_{ij} is the square lattice, since strong coupling effects are expected to be large within the layer rather than between the relatively widely separated layers. t_{ij} alone can be solved by a k -space description using the translation symmetry of the lattice, see Sec. 2.1. The square lattice dispersion reads

$$\varepsilon(k) = 2t(\cos(k_x) + \cos(k_y)) + 4t' \cos(k_x) \cos(k_y) \quad (3.2)$$

and exhibits a bandwidth of $W = 8|t|$ which is easier to extract from other methods or experiments than the tunneling amplitudes t_{ij} . Correlation effects are expected to be pronounced, if $W \sim U$ which are of the order of magnitude of about 2 - 3 eV. The saddle points in the band structure $\varepsilon(k)$ cause divergences in the density of states $A_\sigma(\omega)$, these

are termed van Hove singularities. The energy of the van Hove singularity can be shifted by the next-nearest neighbor hopping parameter t' . For $t'/t < 0$, the van Hove singularity's energy is reduced by increasing $|t'|$. In particular for $t' = 0$ and half-filling, the van Hove singularity is at Fermi level and the system is susceptible to density wave instabilities due to nesting. However, the description of the nesting mechanism to the cuprates' problem has been applied on phenomenologically [115] since nesting alone can not account for the formation of Fermi arcs. The specific role of t' is also discussed extensively. It may be essential for a superconducting groundstate as it suppresses the competing stripe order [116]. Further, it can suppress the pseudogap [105, 117]. The comparison of tightbinding band structure calculations with experimental has shown that T_c^{\max} increases with $-t'/t$ [118].

The Coulomb term is already diagonal in the site basis and therefore the solution of isolated atoms $t_{ij} = 0$ is rather trivial. There are four eigenstates: an empty site, a doubly occupied site and the two-fold degenerate singly occupied site of spin $\sigma \in \{\uparrow, \downarrow\}$. At half-filling, the two degenerate states are the groundstates. The single-particle density of states contains two peaks, the transition from a groundstate to either the empty or the doubly occupied site. The two peaks are separated by the energy U .

The strategies of solution depend of the ratio of U/W . If U is small, then perturbation theory in U and a Fermi liquid description can be sufficient. This is considered as the weak-coupling limit. If U is large, then an expansion in t/U can be considered which, at half-filling, can lead to the Heisenberg model of an effective spin-exchange interaction $J = 4t^2/U$. The variant of the non-half-filled case is the $t-J$ model, a strong coupling limit of the Hubbard model. The model assumes well-defined local moments and its interaction favors antiferromagnetic alignment of the spins. The intermediate regime of $U \sim W$ is particularly difficult to study, but with computational methods it is possible to study localization by U versus delocalization by W on equal footing [20, 42] and a description of the Mott metal-insulator transition [3] has become available. It is a promising step towards understanding the copper oxides as they exhibit AFM as well as dSC, and strong correlations within the Hubbard model provide a consistent description of the two phases [30].

3.3 Mott insulator

The Mott insulator is a concept of an insulator that is insulating because of interacting electrons that block and keep each other from moving through the lattice [8]. The cause is the local Hubbard interaction that describes the screened Coulomb repulsion. The transition involves inherently the two energy scales of the hopping through the lattice and the local interaction. The former is mainly defined by the lattice's geometry and the latter by the atomic structure, that can also involve several orbitals [37] or small clusters [119]. The Mott transition can explain the paramagnetic metal insulator transition of material with partially filled bands. However, it is believed that the applicability of that concept is far wider than this [54], but in many cases the Mott insulator is "hidden" behind, e.g., antiferromagnetic ordering. Whereas density functional theory extensions such as LDA+U

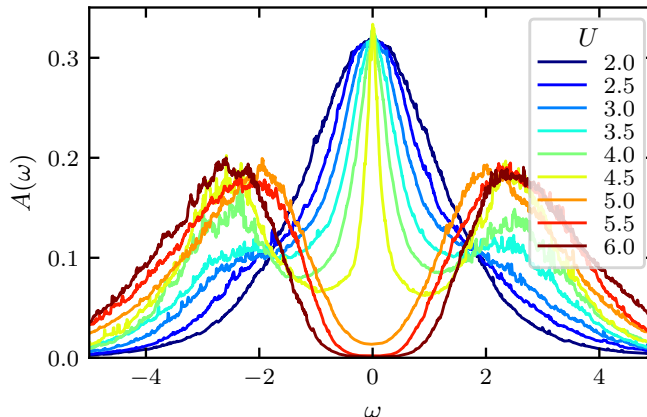


Figure 3.5: Local density of states $A(\omega)$ of the (simple) Bethe lattice for different Hubbard interactions U showing the Mott transition. Hopping $t = -1$, half-filling ($\mu = U/2$) and inverse temperature $\beta = 20$. Obtained via the stochastic optimization method.

can describe antiferromagnetism, it is questionable whether it captures the correct origin of the magnetic behavior. This is important as large- U Heisenberg antiferromagnetism, explained via Mottness, is very different from itinerant (Slater) antiferromagnetism. The strong coupling antiferromagnetism exhibits a Mott gap $\Delta \sim U$ and the gap exists at high temperatures, above the regime of long-range order that sets in around $T \sim J \sim t^2/U$. In contrast, for weak coupling, i.e. small U , itinerant (Slater) antiferromagnetism sets in simultaneously with the gap opening when cooling the system.

The dynamical mean-field theory (DMFT) [20] treats the local interaction and the itineracy through the lattice on equal footing and includes all correlations of local fluctuations in its description. This is particularly important in the strongly correlated intermediate states. The DMFT becomes an exact method for the Bethe lattice in infinite dimensions, see Sec. 2.3.1. Fig. 3.5 shows the local density of states of the paramagnetic Mott transition of the (simple) Bethe lattice [120] at half-filling, $t = -1$ and $\beta = 20$. The DMFT calculations were performed numerically [45] using 15 DMFT-loops, and for increasing U the calculation was initialized with the previous one, whereas the first was initialized by $\Sigma(i\omega_n) = \mu$. The impurity solver does the hybridization expansion [44, 121] and measures the Green function in the Legendre basis [122] using 40 coefficients and 10^6 measurements per impurity run. The analytical continuation has been performed using the stochastic optimization method [88] with 50 elementary updates, 300 global updates and the accumulation of 100 particular solutions.

The bandwidth of the Bethe lattice is $W = 4|t|$. At small $U \sim W/2$ the local density of states shows a single broad peak of a Fermi liquid. Around $U \sim W$ the system enters the strongly correlated regime developing continuously from a peak with shoulders into a three peak structure. The lower peak is the lower Hubbard band corresponding to the empty-site excitation of the atom, and the upper peak is the upper Hubbard band that corresponds to the double-occupation excitation of the atom. These two peaks are separated by $\sim U$. Close to the U -driven metal-insulator transition, the center peak is strongly renormalized

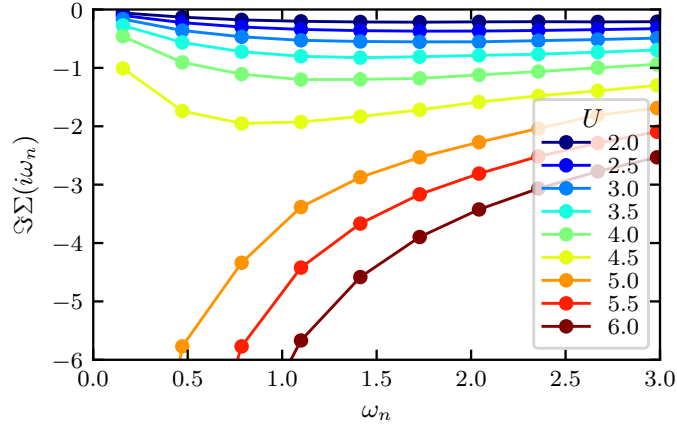


Figure 3.6: Imaginary part of the self-energy $\Sigma(i\omega_n)$ of the simple Bethe lattice for different Hubbard interactions U showing the Mott transition. ω_n are Matsubara frequencies. Hopping $t = -1$, half-filling ($\mu = U/2$) and inverse temperature $\beta = 20$.

corresponding to a quasiparticle excitation with a large mass and it vanishes abruptly. At cooler temperatures, a coexistence region can be resolved depending on whether the DMFT calculation starts from an insulating or metallic ansatz. This coexistence is the hallmark of a first order transition. The coexistence region extends on an interval of U that decreases with higher temperatures ending at a critical endpoint. The spectral weight of the U -driven transition is conserved and is transferred from the quasiparticle peak to the Hubbard bands. Examples of Mott insulators are LaTiO_3 and YTiO_3 , whereas SrVO_3 and CaVO_3 are metallic. In that case the reduced bandwidth enhanced U/W and results in insulating behavior [123].

The (simple) Bethe lattice is bipartite and thus at half-filling it is particle-hole symmetric. For the description in terms of Green functions it means that the real part of the self-energy is zero. The non-trivial part, the imaginary part, is shown in Fig. 3.6. Moreover, only the local part of the self energy is non-zero which is a special property of infinite dimensions and makes the DMFT an exact theory. A steeper negative slope of $\text{Im } \Sigma(i\omega_n)$ at small Matsubara frequencies ω_n is directly related to the mass renormalization of the low-energy quasiparticle of the system. A steeper slope means stronger renormalization. At the metal-insulator transition occurs a drastic change in the imaginary part of the self-energy, i.e. it diverges at small ω_n .

The CDMFT changes the picture of the Hubbard-Mott transition in the square lattice slightly, particularly at low temperatures the momentum resolution becomes important [124]. In the T - U phase diagram, the insulating phase at large U increases at cold temperatures towards smaller U , i.e. the critical U for the Mott transition is reduced [125]. The single-site DMFT describes an insulator of local moments that fluctuate even at low temperatures due to frustration. This state has large entropy and thus is suppressed at low temperatures. In contrast, a two-by-two cluster contains states of spin-singlets that extend over neighboring sites and therefore the paramagnetic metal-insulator transition of the CDMFT shows reentrance behavior for cooling the system close to the critical U .

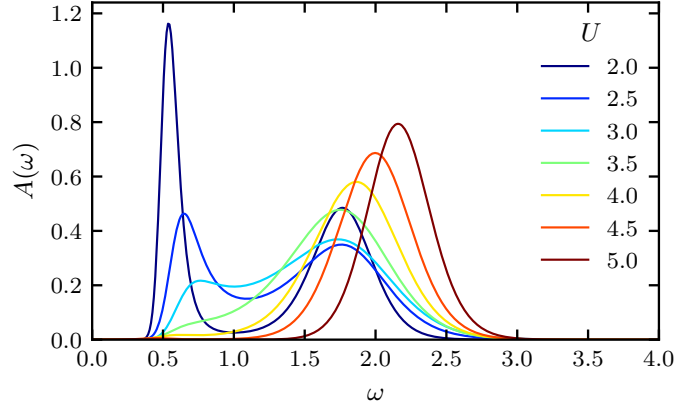


Figure 3.7: Local density of states $A(\omega)$ of the quadruple Bethe lattice for different Hubbard interactions U showing the Mott-Slater crossover. Plaquette hopping $t = -1$, Bethe lattice hopping $t_b = -0.1$, half-filling ($\mu = U/2$) and inverse temperature $\beta = 100$. Obtained via the maximum entropy method. It is particle-hole symmetric.

At low temperatures the CDMFT insulator has less entropy due to the singlet formation. However, the first-order type of the Mott transition is confirmed by the CDMFT. Moreover, the CDMFT captures antiferromagnetic spin fluctuations and the spatial resolution allows for a study of the weak/intermediate-coupling Slater to strong-coupling Mott transition which requires momentum space differentiation. The U -driven insulator-insulator crossover is shown in Fig. 3.7, the four-peak structure is identified with the Slater insulator [126] and it continuously changes to the two-peak structure of the Mott insulator. The self-consistency condition of the paramagnetic quadruple Bethe lattice is the same as of the simple Bethe lattice (Sec. 2.3.1), but with all quantities being matrices in plaquette-site space. The quadruple Bethe lattice is discussed in detail below [127, 128].

Technically, the change of the Fermi surface topology and the momentum space differentiation is encoded in the real part of the Matsubara self-energy, it shifts the poles from Fermi level [129, 117, 105] and since the self-energy has momentum resolution, so has the resulting spectral function which is used to explain angle resolved photoemission spectra [104]. Thus in CDMFT the paramagnetic metal insulator transition is not necessarily driven by a divergence in the imaginary part of the self-energy as in the single-site DMFT.

3.4 Pseudogap

The pseudogap phenomenon [104] introduced in Sec. 3.1 is challenging for theory as it appears in a region of the phase diagram of the copper oxides in which many different orders seem to compete [107]. It consists of a leading edge at about 20 – 30 meV and a broad maximum at around 100 – 200 meV. For comparison, the superconducting peak corresponds to 20 – 50 meV. Moreover, it appears at finite temperatures only and therefore its understanding requires a theory that respects temperature fluctuations. A study of

quantum oscillations of the Hall resistance as a function of an external magnetic field that suppresses the superconductivity in high-quality single crystals of YBCO [130] has shown, that a well-defined Fermi surface exists for normal-state copper oxides under the superconducting dome. The Fermi-surface is made of small Fermi pockets. Two explanations have been suggested, either it is band structure specific (YBa₂Cu₃O_{6.5}) feature, or the small pockets arise from a change of the Fermi surface's topology at a critical point that lies between $\delta = .25$ and $\delta = .1$. The Fermi arcs are then elongated Fermi pockets centered at the nodal points.

Naively speaking, many broken symmetries at finite temperatures with transitions into a continuum could produce a pseudogap-like local density of states. The special property of the pseudogap in copper oxides is the vanishing of spectral weights at the antinodes, whereas the spectral weight at the nodes remains. Since upon cooling a pseudogap material becomes superconducting, the pseudogap could be seen as some form of precursor of superconductivity. This idea is described by the resonating valence bond state [96] which has stimulated research in terms of effective theories [32, 131] and also computational approaches, especially in the framework of the CDMFT.

The spatial resolution, albeit only short-range, of the CDMFT makes the description of the pseudogap's momentum differentiation within the single-band Hubbard model possible. Discussing the CDMFT point of view and extending the picture of the single-site DMFT, new low-energy peaks have been found at half-filling associated with short-range spin fluctuations [132, 133]. The pseudogap is distinct from the superconducting gap and the two gaps also have distinct momentum differentiation, the nodal gap stems from the anomalous part of the self-energy and the antinodal gap from anomalous and normal parts of the self-energy [134]. The interplay of the two gaps have been proposed as an explanation for the "peak-dip-hump" feature of photoemission data [135]. The energy interval of the excitation gap is reduced if the system is cooled from the pseudogap state into the superconducting state. Furthermore, the critical temperature is largest at the pseudogap-onset doping [136]. Moreover, it has been clarified that the onset of the symmetry broken state within the CDMFT is to be associated with the formation of local pairs which leads not necessarily to long-range order [137].

In the pseudogap regime CDMFT predicts a momentum selective metal with large scattering rate in proximity of the Mott insulator [138] in a phase diagram with a classical finite-temperature critical point [137]. The momentum selective metal is separated from a conventional metal by a first order transition which is tied to a Lifshitz transition [117] and the pseudogap exists only for the hole-like Fermi surface [105]. The main features around the Mott transition have been shown to persist also in a three-band model considering charge transfer insulators [139].

3.5 Two-by-two plaquette

Almost all CDMFT studies of the cellular CDMFT flavor have been performed on a two-by-two cluster (plaquette) which is plausible since a cluster-size dependence study [72] has shown that the plaquette captures the important correlation effects nearby the Mott transi-

tion. This raises the question, whether the plaquette exhibits only certain symmetries and provides an effective description, or whether the superconductivity in copper oxides originates from local correlations of plaquettes. Scanning tunneling microscope measurements reveal rather inhomogeneous electronic properties on surfaces of copper oxides. A finite-size study (8×8) of coupled plaquettes with different inter- and intra-plaquette hopping using the determinant Monte Carlo method has shown that there is an optimal inhomogeneity in the hopping parameters of the one-band Hubbard model [140]. This supports the idea of strong local correlations. However, it is still investigated to what extent nematicity [141, 142, 143], the breaking of rotational symmetry on a larger scale, impacts the orderings and the pseudogap regime. It is a success of the CDMFT that it is able to simulate the symmetry broken state, albeit triggered artificially with a numerical seed, its phase diagram contains antiferromagnetism at half-filling and d -wave superconductivity upon hole doping [30, 144, 145] with a dome shape. However, the maximum of the CDMFT dome of superconductivity [146] does not coincide with the experimental finding of 15% hole doping as well as the next-nearest neighbor hopping influence on the superconductivity. Also, quantitatively the agreement can be improved, but regarding the criticism, it is worth stressing the CDMFT of the Hubbard model is an effective theory in which the estimated parameters put constraints on the accuracy of the method. Moreover, the cluster choice of the plaquette which lies in the CuO plane usually neglects interlayer effects and allows only a discussion of symmetry breaking in two dimensions in which at finite temperatures long-range order is unstable [22] due to Goldstone modes.

In regard of a microscopic theory for d -wave superconductivity in copper oxides much effort has been put into determining the relevant subspace of the plaquette and how its components interact [147, 148, 126, 149, 138, 150, 133, 127, 151, 128]. Out of the 256 many-body eigenstates of the plaquette 6, or perhaps up to about 10, have been identified to impact the effective theories around the many-body eigenstates of the plaquette the most. Whereas one path of research is to focus on how the plaquette states maintain their integrity upon embedding in square lattice-like environments [147, 152], another is to find simpler effective models that describe the interaction of the plaquette with its environment using a Hilbert space smaller than 256 states [153, 150, 89]. It is important to remind, that the plaquette itself does not experience phase transitions as it is a finite-size system. It is rather the crucial correlations which are described by the plaquette, but within the lattice, when discussing superconductivity in the context of the plaquette. The plaquette excitations have been interpreted as the microscopic origin of an effective field theory, that describes the antiferromagnetic and superconducting order parameters on equal footing by rotating them into each other [154], however, the predicted π resonance has not been proven to exist by experiments so far.

From the view of treating the plaquette as an impurity of the Anderson impurity model it has been suggested that superconductivity is the result of competing Kondo- and superexchange which causes an anomalously incoherent metal and the phase transition is the system's reaction to avoid criticality [148]. The relation to the Kondo effect could be formalized analytically into a four-level model [150], according to that the pseudogap is the result of destructive interference of the plaquette(-impurity) and its environment. Due to

the Kondo effect, the absence of degeneracy has been identified as a cause of the pseudo-gap. The Kondo mechanism is designed for resonating spins, but does not include further degeneracies, e.g. the particle number degeneracy or the spatial X/Y degeneracy of the point group of the plaquette. Thus, the notion of a Fano antiresonance [155, 156] has been suggested which describes more accurately the coupling of discrete plaquette levels to a continuum [127].

A glue, in the sense of phonons in BCS, is not necessary to explain d -wave superconductivity, because in the BCS s -wave case retardation effects cause the homogeneous effective attraction between electrons, and in contrast, for the d -wave case the spatial structure is sufficient as can be seen from a random phase approximation study [27] leading to the gap equation

$$\Delta(k) = -\frac{1}{N} \sum_{k'} \frac{\Gamma(k-k')\Delta(k')}{2\varepsilon_k} \tanh(\beta_c \varepsilon/2) \quad (3.3)$$

with momenta k, k' and normalization factor from the Fourier transform N . Γ is the particle-particle vertex in the RPA approximation, ε the electronic dispersion and β_c the inverse critical temperature. Eq. (3.3) has the non-trivial solution of a pairing gap $\Delta(k)$ with the spatial structure $\Delta(k) = \Delta_0(\cos(k_x) - \cos(k_y))$ according to $d_{x^2-y^2}$ symmetry. The momentum that connects the gap at $X = (\pi, 0)$, with that of opposite sign at $Y = (0, \pi)$, is that momentum of the antiferromagnetic wave vector $M = (\pi, \pi)$. All of these momenta are plaquette momenta, which are obtained by a Fourier transform to the cluster momentum basis. Nevertheless, the CDMFT captures also plaquette-local retardation effects, they have been related to the exchange of spin fluctuations which have been suspected to be crucial [157, 158].

3.5.1 Six-fold degenerate point of the plaquette

The low-energy subspace of the plaquette at parameters, at about which d -wave superconductivity has been calculated by CDMFT [30], contains a spin-singlet state of four electrons, i.e. half-filling, $|N, S, K\rangle = |4, 0, \Gamma\rangle$ which is a superposition of different valence bond configurations, reminiscent of the resonating valence bond state. Moreover, there is a spin-doublet of three electrons $|3, 1/2, X/Y\rangle$ and another spin-singlet, but of two electrons $|2, 0, \Gamma\rangle$. Γ , X , Y and M are plaquette momenta K , which are quantum numbers, stemming from the point group symmetry, C_{4v} , of the plaquette. $|3, 1/2, X/Y\rangle$ is four-fold degenerate because it is a spin doublet and has the degenerate plaquette momenta X/Y . Considering a chemical potential at which $|4, 0, \Gamma\rangle$ is the groundstate, then the system propagating through $|3, 1/2, X/Y\rangle$ describes a fermionic hole excitation with momentum X/Y [147]. Similarly, $|2, 0, \Gamma\rangle$ would be a two-hole excitation and $|4, 1, M\rangle$ a (antiferro-)magnon. Investigating superconducting correlations in non-superconducting system, it is reasonable to focus on the groundstates of particle number sectors as the particle number sectors will be mixed in the symmetry-broken state. The states are depicted in Fig. 3.8.

The transition between $|4, 0, \Gamma\rangle$ and $|2, 0, \Gamma\rangle$, the two-hole boson, has been found to keep its integrity in the full square lattice [147]. Although in that calculation the model has been mapped to an effective bosonic model. Thus, the fermionic part has been neglected. Fig. 3.9

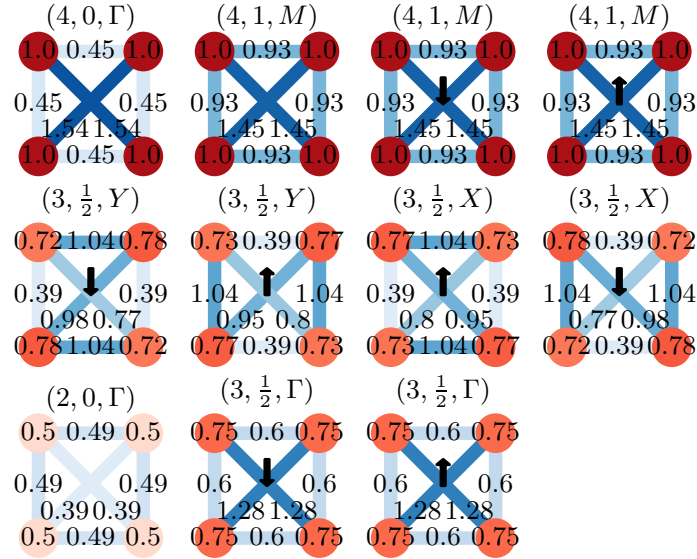


Figure 3.8: Local particle number (red) and neighboring spin-spin correlation (blue) observables of eigenstates of the isolated plaquette. The states are the main contributors to one-particle transitions in proximity of the plaquette degenerate point. The states $|N, S, K\rangle$ are labeled by their quantum numbers of the plaquette- particle number, spin and momentum, respectively. Spin-multiplet states are \uparrow - \downarrow degenerate depicted by black arrows.

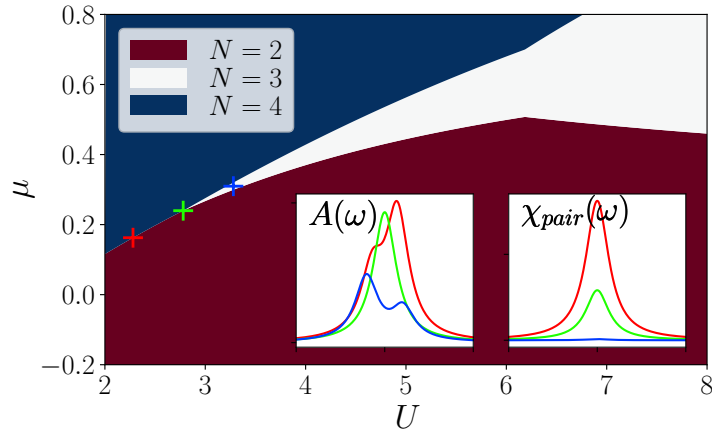


Figure 3.9: Particle number N sectors of the isolated plaquette with Hubbard interaction U and chemical potential μ ($t = -1$, $t' = 0.3$, $\beta = 400$). The particle number sectors meet at a degenerate point of the plaquette (green +). Insets show the spectral function $A(\omega)$ and the pairing susceptibility $\chi_{pair}(\omega)$ calculated using the Lehmann representation.

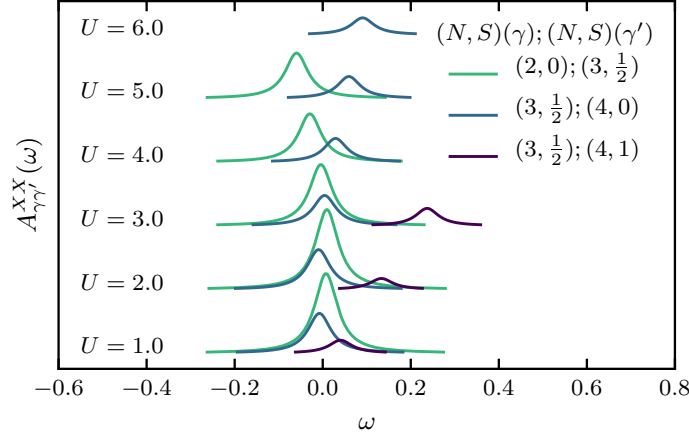


Figure 3.10: The pseudoparticle spectral function $A_{\gamma\gamma'}^{XX}(\omega)$ of single-particle excitations of plaquette momentum sector X propagating the system through many-body plaquette eigenstates γ and γ' for different Hubbard interactions U along the $N = 2, 4$ crossover ($t = -1$, $t' = 0.3$, $\beta = 30$).

shows the plaquette degenerate point (PDP) at which the sectors $N = 2, 3, 4$ cross. This point exhibits a sharp peak in the (fermionic) one-particle spectral function at Fermi level whereas in its proximity the spectral function contains a pseudogap-like structure. The $N = 2, 4$ crossover is a groundstate crossover for $U < U_{PDP}$ and becomes a crossover of excited states for $U_{PDP} < U$, which is located above the $N = 3$ groundstate region, centered with respect to μ . Sharp peaks at Fermi level are interesting features as they represent many low-energy transitions that can enhance interaction effects and lead to instabilities.

The sharp peak can be understood further by considering the pseudoparticle spectral function

$$G_{\gamma\gamma'}^{KK'}(z) = \frac{\langle \gamma | c_K | \gamma' \rangle \langle \gamma' | c_K^\dagger | \gamma \rangle (e^{-\beta E_\gamma} + e^{-\beta E_{\gamma'}})}{Z (z + E_\gamma - E_{\gamma'})}, \quad (3.4)$$

$$A_{\gamma\gamma'}^{KK'}(\omega) = -\frac{1}{\pi} \text{Im} G_{\gamma\gamma'}^{KK'}(\omega + i\varepsilon),$$

which resolves the many-body eigenstate (γ) contributions to the spectral function. The low-energy peaks are determined by the one-particle transitions between $|4, 0, \Gamma\rangle$, $|3, 1/2, X/Y\rangle$ and $|2, 0, \Gamma\rangle$, see Fig. 3.10. The pairs are expected to be similar to BCS-pairs in the sense that they contain two electrons and have even parity. The plaquette states that contribute to the superconducting state and define the low-energy pairs within the CDMFT are $|4, 0, \Gamma\rangle$ and $|2, 0, \Gamma\rangle$, and transitions involving $|3, 1/2, X/Y\rangle$ define the single-particle gap [148].

Transforming $A(\omega)$ to its real-space representation (Fig. 3.11) shows that the nearest neighbor transitions are entirely absent at low transition energies. Moreover, the two low-energy peaks of the local spectral function are mirrored on the ω -axis in the next-nearest neighbor spectral function. Negative spectral weight occurs only on off-diagonal entries of the Green function. Since the temperature of Fig. 3.11 is rather high, the center peak is a

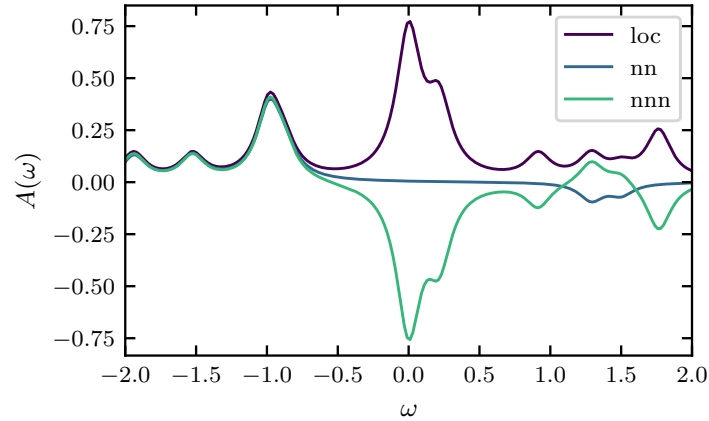


Figure 3.11: Real-space spectral function $A(\omega)$ at the degenerate point of the plaquette ($t = -1$, $t' = 0.3$, $U = 2.784$, $\mu = 0.24$, $\beta = 30$) for local (loc), nearest neighbor (nn) and next-nearest neighbor (nnn) transitions.

peak of two transitions, see Fig. 3.10, and the shoulder is the transition involving $|4, 1, M\rangle$.

Often the PDP is labeled quantum critical point (QCP) of the plaquette. Precisely, a QCP can exist only in an infinite extended lattice as only in such it can exhibit its scale invariance. However, the idea is that the PDP develops into the QCP of the square lattice and it is the challenge to find a model and formalism to continuously embed the PDP into a square lattice environment. The following work [127] presents a bottom-up approach to the description of a QCP in superconducting copper oxides. The discrete eigenstates of the plaquette are coupled to different environments and continua. The high degeneracy of the plaquette eigenstates of different particle-, spin- and momentum- quantum numbers suggest strong quantum fluctuations at low temperatures [159, 160].

Plaquette valence bond theory of high-temperature superconductivity

Malte Harland

Institut für Theoretische Physik, Universität Hamburg, Jungiusstraße 9, 20355 Hamburg, Germany

Mikhail I. Katsnelson

Radboud University, Institute for Molecules and Materials, Heyendaalseweg 135, 6525AJ Nijmegen, The Netherlands

Alexander I. Lichtenstein

*The Hamburg Centre for Ultrafast Imaging, Luruper Chaussee 149, Hamburg 22761, Germany
and Institut für Theoretische Physik, Universität Hamburg, Jungiusstraße 9, 20355 Hamburg, Germany*

(Received 10 April 2016; revised manuscript received 26 July 2016; published 19 September 2016)

We present a strong-coupling approach to the theory of high-temperature superconductivity based on the observation of a quantum critical point in the plaquette within the t, t' Hubbard model. The crossing of ground-state energies in the $N = 2-4$ sectors occurs for parameters close to the optimal doping. The theory predicts the maximum of the $d_{x^2-y^2}$ -wave order parameter at the border between localized and itinerant electron behaviors and gives a natural explanation for the pseudogap formation via the soft-fermion mode related to local singlet states of the plaquette in the environment. Our approach follows the general line of resonating valence-bond theory stressing a crucial role of singlets in the physics of high- T_c superconductors but focuses on the formation of *local* singlets, similar to phenomena observed in *frustrated* one-dimensional quantum spin models.

DOI: [10.1103/PhysRevB.94.125133](https://doi.org/10.1103/PhysRevB.94.125133)**I. INTRODUCTION**

After the 30-year history of extremely intensive experimental [1–4] and theoretical [5–10] studies of the high-temperature superconductivity (HTSC) in copper oxides we are still far from understanding the basic mechanism of this fascinating phenomenon. Taking into account the enormous number of researchers involved in this field, one can assume that almost all possible ideas were expressed and that the main problem is just to select the basic simple concepts from the pile of available theoretical results. The most ambitious attempt was made by Anderson who emphasized with his resonating valence-bond (RVB) theory the crucial importance of strong electron correlations, the tendency for singlet spin state formation, and the non-Fermi-liquid character of the normal phase [6]. Unfortunately, details of his original approach, such as suppression of interlayer hopping in the normal phase as the main factor of superconductivity, seem to contradict experimental data [11]. The latest version of the RVB theory is presented in Ref. [12]. We believe that the main assumption of the strongly correlated limit as the base of understanding the high-temperature superconductivity is correct as well as emphasizing a crucial role of spin singlet states but important details were missing. Below we present arguments for the thesis that the minimal object of HTSC theory is the plaquette in the so-called effective t, t' Hubbard model [13,14] rather than the conventional atomic limit typical for the theory of Mott insulators [6,9]. The best practical realization of this atomic-based theory is the dynamical mean-field theory (DMFT) [15]. The obvious minimal generalization in the case of $d_{x^2-y^2}$ -wave pairing is a cluster DMFT (CDMFT) scheme [16,17].

Since the first plaquette CDMFT calculation of $d_{x^2-y^2}$ -wave superconducting order together with antiferromagnetic fluctuations [16], there have been many calculations for different cluster sizes and geometries based on continuous-time

quantum Monte Carlo (CTQMC) or exact diagonalization solvers [17–35]. Unfortunately, the basic qualitative feature of the many-body states in the plaquette were hidden in the computational details. The main aim of this paper is to present a simple and transparent strong-coupling theory of the $d_{x^2-y^2}$ -wave superconductivity, i.e., a *minimal* consistent many-body model, based on the plaquette energy spectrum peculiarity, namely, the “quantum critical point” that merges two singlets and two doublets. These states of the doped plaquette are different from those discussed in the resonating valence-bond theory [6,12]. The main point is that the quantum critical point discussed here is related to the formation of *local* valence bonds in the *frustrated* quantum spin model [36]. Therefore, the optimal superconducting states are located on the border between localized and delocalized resonating plaquette valence bonds. Here we follow a bottom-up approach starting with an isolated plaquette and building stepwise a more complex environment.

An important theoretical problem is to find a minimal and generic electronic-structure model of cuprate superconductors. From band-structure calculations [13,14] we can safely reduce it to an effective one-band model with nearest- and next-nearest-neighbor hopping. We use a standard parametrization of the tight-binding model for $\text{YBa}_2\text{Cu}_3\text{O}_7$ [13,14] with the next-nearest-neighbor hopping: $t'/t = -0.3$ and t as units of our energies. The local Hubbard interaction parameter U is on the order of the bandwidth $W = 8t$. Then, the t, t' Hubbard model on the square lattice reads

$$H = - \sum_{ij} t_{ij} c_{i\sigma}^\dagger c_{j\sigma} + \sum_i U n_{i\uparrow} n_{i\downarrow}, \quad (1)$$

where t_{ij} is an effective hopping and U is the local Coulomb interaction. The operators $c_{i\sigma}^\dagger, c_{i\sigma}$ create and annihilate fermions, respectively, at site i with spin $\sigma = \uparrow(+), \downarrow(-)$, and the

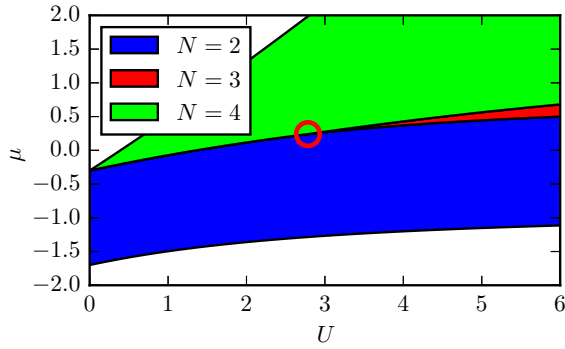


FIG. 1. Zero-temperature phase diagram of the isolated plaquette as a function of the Hubbard U and chemical potential μ in the proximity of the quantum critical point (circle) for $t'/t = -0.3$.

occupation operator is $n_{i\sigma} = c_{i\sigma}^\dagger c_{i\sigma}$; furthermore we will use t as the energy unit.

II. ISOLATED PLAQUETTE

We start the discussion with electronic states in the isolated Hubbard plaquette. The optimal doping for high-temperature superconductivity is on the order of 15% of holes per site for almost all cuprate materials. This gives us an average number of electrons per site of 0.85 and results in 3.4 fermions per four-site plaquette in the crystal. We argue that this is related to three-electron states of the isolated plaquette since particle-hole asymmetry introduced by the next-nearest-neighbor hopping t' with moderate values of U and certain fixed chemical potentials (μ) result in an occupation per plaquette of the crystal, that is very close to the optimal value of 3.4 electrons.

The Hamiltonian of the isolated plaquette reads

$$H_p = \sum_{(i,j)=1\dots 4} h_{ij}^0 c_{i\sigma}^\dagger c_{j\sigma} + \sum_{i=1\dots 4} U n_{i\uparrow} n_{i\downarrow},$$

$$-\hat{h}_0 = \begin{pmatrix} \mu & t & t' & t \\ t & \mu & t & t' \\ t' & t & \mu & t \\ t & t' & t & \mu \end{pmatrix}. \quad (2)$$

We include the chemical potential in the diagonal part of h_{ij}^0 . The energy spectrum of the isolated plaquette near the three-electron filling is very unusual. We present in Fig. 1 regions in the $U - \mu$ space, whose ground states have an occupation of three plus-minus one electrons. The one-electron spectrum possesses four states with the energies: $\pm 2t - t' - \mu$ and double-degenerate $t' - \mu$. At zero interaction $U = 0$, there is no stable ground state with three electrons in the sense that one can add or remove one electron without changing the thermodynamic potential. Starting from some critical interaction strength $U \approx 3$ there is a small region in that the plaquette ground state with $N = 3$ electrons is separated by energy gaps from the states with $N = 2$ and $N = 4$, see Fig. 1. Importantly, this $N = 3$ ground state is fourfold degenerate consisting of two doublets in the sectors $(2_\uparrow, 1_\downarrow)$ and $(1_\uparrow, 2_\downarrow)$, which we label X and Y , according

to their symmetry. Moreover, there is a critical point (circle in Fig. 1) where all three sectors with two through four electrons have the same ground-state energy and form a sixfold degenerate ground-state multiplet consisting of two singlets of the sectors $(1_\uparrow, 1_\downarrow)$ and $(2_\uparrow, 2_\downarrow)$ together with two doublets of the three-electron sectors. This critical point has the coordinates $U = 2.78$, $\mu = 0.24$ for the standard value of $t'/t = -0.3$. We think that this critical point of the plaquette has crucial importance for the physics of the strong-coupling $d_{x^2-y^2}$ -wave superconductivity. The importance of these three many-body states of the plaquette CDMFT has been discussed first for the t - J model [19]. In that case an additional triplet state in the $N = 4$ sector appeared without formation of the single quantum critical point. The crossing of different many-body states has been investigated in the valence-bond DMFT [20], the checkerboard Hubbard model [37], and in the plaquette CDMFT [27,33]. The idea of a quantum critical point and nematicity has also been discussed in Refs. [23,31,32]. Here, we demonstrate via a bottom-up approach that this is the key ingredient of a consistent minimal picture of HTSC.

If we approach this critical point from the region with the $N = 3$ ground state, then the one-electron density of states (DOS) at the Fermi energy diverges for both electron and hole sides due to transitions from the fourfold degenerate $N = 3$ ground state to singlets of $N = 2$ (hole side) and $N = 4$ (electron side) with zero excitation energy. The corresponding spectral weights with normalization of the δ functions are equal to 0.46 and 0.23 for the hole and electron sides, respectively. Thus, it introduces an important electron-hole asymmetry. We see below that this plaquette quantum critical point results in a formation of a soft-fermion mode, i.e., a DOS peak at the Fermi energy when investigating it in a crystal of plaquettes. We argue that these soft fermions favor the formation of the $d_{x^2-y^2}$ -wave superconducting pairing at low temperatures and of the pseudogap at high temperatures. At smaller t' this critical point shifts to larger U , and at $t'/t = 0$ its coordinates are $U = 4.58$, $\mu = 0.72$. It is worthwhile to point out that at optimal values of t' antiferromagnetic order is suppressed due to frustrations. As soon as we add a fermionic bath to the plaquette within the spirit of CDMFT or density-matrix embedding theory (DMET) [38] with only four bath sites, a stable singlet solution forms with an almost equal mixture of all $N = 2-4$ sectors, which again is favorable for the superconducting state as is shown below.

III. PLAQUETTE IN THE BATH

The appearance of the DOS peak at the Fermi energy leads to a universal instability in the sense that the susceptibility diverges in many different channels (magnetic, superconducting, charge-density wave, etc.). From the weak-coupling point of view this was discussed in the framework of the van Hove scenario of HTSC [39–41]. In order to study the interplay of different instability channels from the strong-coupling perspective we introduce a simple model of an embedded plaquette in the spirit of DMET [38]. To this aim we add to the plaquette's Hamiltonian a hybridization with four fermionic bath states, one bath state per corner of the plaquette, see Fig. 2(a). We use an exact diagonalization technique, namely, the Lanczos scheme with a Hilbert space size of 2^{16}

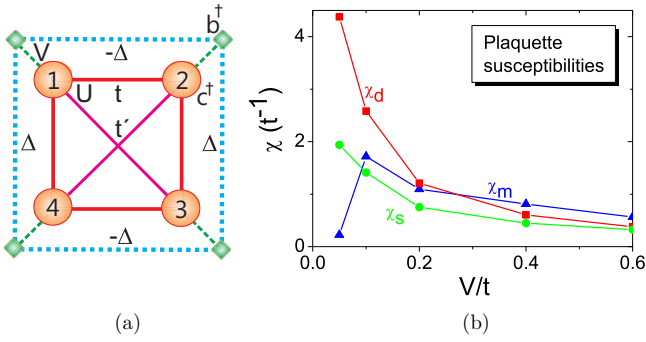


FIG. 2. (a) Sketch of the plaquette in the four-site bath with the $d_{x^2-y^2}$ -wave order parameter. (b) Superconducting (χ_d), singlet bond order (χ_s), and antiferromagnetic (χ_m) susceptibilities of the plaquette in a bath as a function of the hybridization V for $U = 3$ and $\mu = 0.27$.

without any symmetry restrictions. Furthermore, we introduce different symmetry-breaking fields acting on the bath fermions $b_{i\sigma}^\dagger, b_{j\sigma}$, i.e., $d_{x^2-y^2}$ -wave pairing, singlet magnetic states on the bonds, and the conventional Néel antiferromagnetic state,

$$h_d = \sum_{\sigma=\uparrow,\downarrow, i=1\dots 4} (-1)^i \sigma \Delta_d (b_{i,\sigma} b_{i+1,-\sigma} + \text{H.c.}), \quad (3)$$

$$h_s = \sum_{\sigma=\uparrow,\downarrow, i=1\dots 4} (-1)^i \sigma \Delta_s (b_{i,\sigma}^\dagger b_{i+1,-\sigma} + \text{H.c.}), \quad (4)$$

$$h_m = \frac{1}{2} \sum_{\sigma=\uparrow,\downarrow, i=1\dots 4} (-1)^i \sigma \Delta_m b_{i,\sigma}^\dagger b_{i,\sigma}. \quad (5)$$

Here we assume periodic boundary conditions, that means for $i = 4$, we define $i + 1 = 1$. We switch on small fields $\Delta_d = \Delta_s = \Delta_m = 0.01t$ simultaneously and calculate numerically their associated susceptibilities of the plaquette. The hybridization V between fermions $c_{i\sigma}^\dagger$ and $b_{j\sigma}^\dagger$ breaks the sixfold degeneracy of the plaquette's quantum critical point, and without external fields it results in a singlet ground state, see Fig. 2(a). The $d_{x^2-y^2}$ -wave superconducting [Eq. (3)] and the magnetic bond-singlet [Eq. (4)] external fields respect quantum entanglement of the singlet character of the ground state, whereas the Néel field Eq. (5) destroys it. Being classical in its nature, the Néel state is expected to be the most stable for sufficiently strong coupling with the environment V [42] or high temperatures [43]. For an infinite system different types of order can be found by studying divergences of susceptibilities. Since in DMET we deal with finite systems, the susceptibilities remain finite up to zero temperature, and we assume that the largest susceptibility of the cluster, shown in Fig. 2(a), signals the corresponding order of the crystal. The computational results are shown in Fig. 2(b) as a function of the hybridization parameter V . One can see that the $d_{x^2-y^2}$ -wave superconducting pairing always wins in comparison with the singlet bond pairing and is more favorable than the Néel order for $V \leq 0.2$. The self-consistent plaquette-Bethe DMFT for the cluster case (see below) with optimal HTSC parameters corresponds to $V = 0.1$. The singlet ground state near the plaquette's quantum critical point favors $d_{x^2-y^2}$ -wave superconductivity rather than magnetic ordering. This result

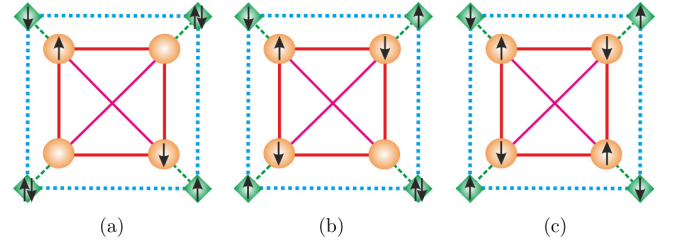


FIG. 3. The main contributions to the plaquette's singlet ground state in a four-site bath with the $d_{x^2-y^2}$ -wave order parameter is the hybridization $V = 0.2\Delta_d = 0.05$ for $U = 3$ and $\mu = 0.27$. (a) Sector $N = 2$ with coefficient = 0.05 and four antisymmetric contributions. (b) Sector $N = 3$ with coefficient = 0.06 and eight antisymmetric contributions. (c) Sector $N = 4$ with coefficient = 0.08 and two antisymmetric contributions.

agrees well with large-scale CDMFT calculations for optimal doping [28,29].

In order to elucidate important properties of the plaquette singlet in the superconducting bath we visualize the main contributions to the ground-state singlet in Figs. 3(a)–3(c). There are three main contributions by the single-plaquette sectors with $N = 2$ –4 electrons, which have almost equal spectral weights. In particular, it means a strong mixture of states that differ by two electrons, i.e., by a local Cooper pair on the bond. This is understood as an important detail for superconductivity since the degenerate quantum critical point (circle in Fig. 1) consists of states with the same total number of electrons ($N_{\text{tot}} = 8$), but none of those show a double occupation on the plaquette. It occurs only on bath sites that have no Hubbard interaction, see Figs. 3(a)–3(c). The degeneracy of the quantum critical point splits into four states for $N = 2$, eight states for $N = 3$, and two states for $N = 4$. Taking into account the total number of these states and including all their antisymmetric singlet combinations, we observe that 85% of the ground-state components are related to the quantum critical point. This means that the system *as a whole* perfectly screens the strong Coulomb interactions (Hubbard U is about 70% of the bandwidth), and the plaquette states with $N = 2$ –4 electrons contribute equally to the ground-state singlet of the total system. The fact that there are no double occupied states inside the plaquette and only on the bath sites with no Hubbard interactions was expected to occur only in the limit $U \gg W$, obtained by the perfect Gutzwiller projector. The crucial role of the Gutzwiller projector for the physics of high- T_c superconductivity was emphasized by Anderson [12]. We see that the situation is much more subtle: A specific symmetry of the ground state at the plaquette's quantum critical point increases effectively the *single-site* U by suppressing double occupations on plaquette sites. But, at the same time, it decreases the effective U for the plaquette in a sense that one does not have to pay an additional energy for adding two more electrons to the plaquette as a whole. This situation is very nontrivial; it demonstrates clearly that discussions of strong correlations for the high- T_c cuprates would be based on a rather four-orbital Hubbard model, corresponding to a lattice built from plaquettes, than on an initial single-band Hubbard model for copper sites.

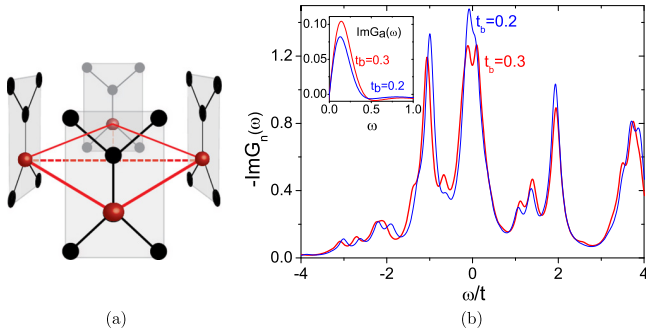


FIG. 4. (a) Sketch of the plaquette-Bethe lattice with connectivity $q = 2$. Only one plaquette is shown for simplicity. (b) Local part of the normal Green's function of the $d_{x^2-y^2}$ -wave solution in the plaquette-Bethe lattice near optimal values of t_b for $U = 3$ and $n = 0.85$ and (the inset) the nonlocal part of the anomalous Green's function.

IV. PLAQUETTE-BETHE LATTICE

As a next step towards a more realistic description of the cuprate crystal, we consider a plaquette-Bethe model with all sites arranged in quadrupole Bethe “planes” and interconnected in a plaquettelike manner, see Fig. 4(a). The plaquette CDMFT becomes exact for this model when the connectivity of the Bethe sublattice q tends to infinity. We obtain similar results as for the double-Bethe model for a two-site cluster [42,44]. The bath Green's function in Nambu representation for this model reads

$$\hat{G}^{-1}(i\omega) = i\omega\mathbb{1} + (\mu - \hat{h}_0)\sigma_z - t_b\sigma_z\hat{G}(i\omega)\sigma_z t_b, \quad (6)$$

where σ_z is the Pauli matrix and including site degrees of freedom $\hat{G}(i\omega)$ is an 8×8 matrix of the superconducting Green's function for the plaquette in the bath. We discretize the bath Green's function with only four states similar to the DMET approach using the Lanczos scheme in order to find the matrix Green's function of the superconducting states [28,29]. As mentioned above, there is a sixfold degenerate ground state for $t_b = 0$ at the quantum critical point. At sufficiently small hybridizations, i.e., small t_b in the plaquette-Bethe model, the system becomes metallic with a slightly broadened peak in the DOS at the Fermi energy. The ground state is $d_{x^2-y^2}$ -wave superconducting at low temperatures [28,29]. However, when t_b increases a quantum phase transition occurs with the destruction of the singlet states and a formation of the energy gap in the single-electron excitation spectrum. The latter can be observed in the normal part of the one-electron Green's function at $t_b = 0.3$, see Fig. 4(b). The energy gap of the states can be estimated at $0.2t$, that is, an order of magnitude larger than the superconducting gap. For $t = 0.25$ eV [13] this results in a pseudogap on the order of 50 meV, which is observed experimentally [45]. In regard to the double-Bethe model this corresponds to a transition of a quantum entangled singlet state to a classical Néel state [42]. Importantly, the anomalous (superconducting) part of the Green's function has a maximum exactly at this transition, see the right inset in Fig. 4(b). Similar behavior has been observed recently experimentally for the maximum of the superconducting order parameter at the localized-delocalized transition point in the strongly correlated

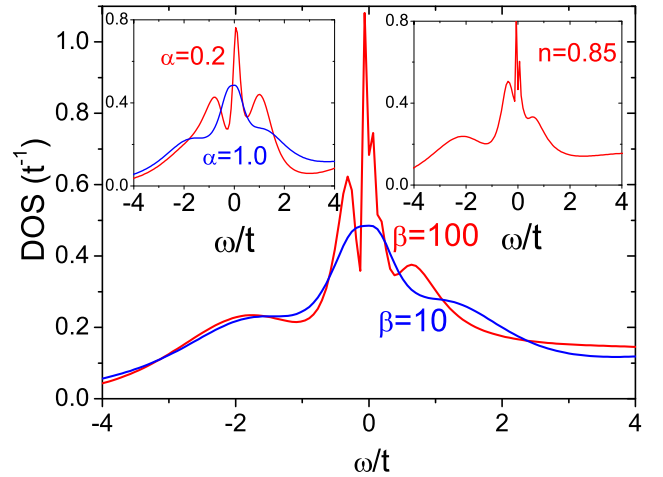


FIG. 5. Density of states for both spins of the plaquette CDMFT for $U = 6$ and $\mu = 0.54$ for different temperatures, (the left inset) with plaquette-lattice hoppings scaled by a factor of α at $\beta = 10$ and (the right inset) for optimal doping $n = 0.85$ at $\beta = 100$.

organic superconductors [46] as well as for the BCS-BEC crossover in cold-atom systems [47].

V. PLAQUETTE CDMFT

Finally, we perform the standard CDMFT calculations using a strong-coupling continuous-time quantum Monte Carlo solver [48,49] in the normal state. Since a transition to the periodic plaquette in the crystal increases the bandwidth by a factor of 2 due to doubling of the coordination numbers compared to the isolated plaquette, we increase the values of U and μ by the factor of 2. Note, that the natural energy unit is the bandwidth W rather than the hopping t . Furthermore, we use the value of $U/t = 6$, which approximately describes real cuprate materials [50].

The calculated local DOS obtained by maximum-entropy analytic continuation [51] is shown in Fig. 5. We observe that for sufficiently high temperatures there is a broad peak at the Fermi energy originating from the plaquette quantum critical point. This relation is illustrated in the inset of Fig. 5. We artificially scaled the hopping between plaquettes by a factor of α ranging from 0 to the physical value 1.

At lower temperatures a pseudogap is formed. It is well known in all HTSC materials and considered as one of its most striking features [45]. Sometimes this pseudogap is also considered to be the precursor of the superconducting gap (formation of incoherent Cooper pairs above T_c) or as a smeared antiferromagnetic gap (shadow bands) [45]. However, both interpretations have problems when they get compared to experiments [45]. Within our scheme it is natural to interpret this pseudogap as a pseudohybridization gap similar to that arising in Kondo lattices [52] or intermediate valence semiconductors [53]. From this point of view the pseudogap in HTSC materials originates from the Fano antiresonance due to embedding of the soft-fermion mode of the plaquette (discussed above) into a continuous band spectrum of the lattice. Indeed, from the degeneracy between the states with $N = 3$ and $N = 3 \pm 1 = 2, 4$ of the isolated plaquette

immediately follows by the Lehmann spectral representation that the atomic Green's function of the plaquette has a pole at $E = 0$. In a lattice built from plaquettes this pole is mixed by hopping with the other spectral components of the Green's function, which otherwise would form a regular strongly correlated band. However, the mixture with the $E = 0$ peak leads to a singularity in the self-energy and thus to the gap opening. The broadening of the $E = 0$ peak transforms the gap into the pseudogap. A similar effect is produced by the Kondo peak in the periodic Anderson model [52] but with the important difference that the spectral weight of the Kondo peak is proportional to the Kondo temperature and therefore small, whereas in the model discussed here the soft fermion has a noticeable spectral weight. It leads to a much larger energy scale of the pseudogap compared to the Kondo lattices. The singularity in the self-energy and the gap opening in systems with flat bands has been discussed recently from the point of view of phenomenological Fermi-liquid theory [54].

The role of soft-fermion modes, the hidden fermion, has been discussed in Refs. [55–57]. However, it was not done in the context of the quantum critical point of the plaquette. This relation is the main message of our paper.

The density of states for optimal doping $n = 0.85$ in the self-consistent CDMFT calculations is shown in the right inset of Fig. 4(b). Its chemical potential converges to a value of $\mu = 1.2$, which is very similar to that of the fixed μ of the quantum critical point in the isolated plaquette. Furthermore, we have calculated a low-temperature superconducting state with CDMFT, a Lanczos solver, eight-bath sites, and with a CTQMC cluster solver and found similar results to many other calculations [17–35].

VI. CONCLUSIONS

To conclude, we developed a picture of HTSC based on the existence of a quantum critical point at the crossing of the ground-state energies in the $N = 2-4$ sectors within the plaquette for parameters close to the optimal doping, t' being of crucial importance. Contrary to the original RVB theory of Anderson [6], we start with the *local* valence-bond formation in the doped plaquette. The difference can be illustrated

by comparison with the exactly solvable one-dimensional quantum spin model [36]. The prototype state for the RVB is the Bethe ansatz solution for the antiferromagnetic $S = 1/2$ Heisenberg model in the nearest-neighbor approximation. For the model with first- and second-nearest-neighbor interactions $J_2/J_1 = 1/2$, the ground state is known exactly too. It can be represented as a product state of local valence-bond singlets [36]. For the two-dimensional J_1, J_2 model [58,59] recent calculations show the formation of a plaquette valence-bond state with a tendency towards the d -wave superconductivity for the $t - J_1, J_2$ model [60]. The second-nearest-neighbor hopping t' seems to play a similar role in the Hubbard model. The optimal superconducting region is related to a localized-delocalized transition of plaquette valence-bond states in the plaquette. It would be interesting to describe the formation of global singlet states with plaquette valence-bond states using the matrix product scheme [61] since the CDMFT scheme breaks translational symmetry.

Formation of the soft-fermion mode near the optimal doping has an analog in the weak-coupling theory within the van Hove scenario of HTSC [62]. Due to the formation of flat bands of many-body origin [62,63] there is a whole region of parameters t', U, μ in that the Fermi-liquid description is broken. However, we believe that the strong-coupling description presented here is more relevant for real HTSC materials, which are characterized by large values of U [50].

ACKNOWLEDGMENTS

We thank B. L. Altshuler, O. K. Andersen, P. W. Anderson, A. Georges, A. Millis, M. Potthoff, T. Wehling, and J. Wiebe for helpful discussions as well as T. Berberich and M. Valentyuk for their assistance with the figures, L. Boehnke for the MAXENT code, and S. Okamoto for the LANZOS-SC code. A.I.L. acknowledges support from the DFG Grant No. SFB-668 and The Hamburg Centre for Ultrafast Imaging, M.I.K. acknowledges financial support from ERC (Project No. 338957 FEMTO/NANO) and from NWO via the Spinoza Prize. Computations have been performed at the NIC, Forschungszentrum Jülich, under Project No. HHH26.

-
- [1] J. G. Bednorz and K. A. Müller, *Z. Phys. B: Condens. Matter* **64**, 189 (1986).
 - [2] A. Damascelli, Z. Hussain, and Z.-X. Shen, *Rev. Mod. Phys.* **75**, 473 (2003).
 - [3] J. Orenstein, and A. J. Millis, *Science* **288**, 468 (2000).
 - [4] M. H. Hamidian, S. D. Edkins, C. K. Kim, J. C. Davis, A. P. Mackenzie, H. Eisaki, S. Uchida, M. J. Lawler, E.-A. Kim, S. Sachdev, and K. Fujita, *Nat. Phys.* **12**, 150 (2016).
 - [5] P. W. Anderson, *Adv. Phys.* **46**, 3 (1997).
 - [6] P. W. Anderson, *The Theory of Superconductivity in the High- T_c Cuprates* (Princeton University Press, Princeton, 1997).
 - [7] D. J. Scalapino, *Rev. Mod. Phys.* **84**, 1383 (2012).
 - [8] J. Schmalian, D. Pines, and B. Stojkovic, *Phys. Rev. Lett.* **80**, 3839 (1998).
 - [9] M. Imada, A. Fujimori, and Y. Tokura, *Rev. Mod. Phys.* **70**, 1039 (1998).
 - [10] E. Dagotto, *Rev. Mod. Phys.* **66**, 763 (1994).
 - [11] H. J. A. Molegraaf, C. Presura, D. van der Marel, P. H. Kes, and M. Li, *Science* **295**, 2239 (2002).
 - [12] P. W. Anderson, *Int. J. Mod. Phys. B* **25**, 1 (2011).
 - [13] O. K. Andersen, A. I. Liechtenstein, O. Jepsen, and F. Paulsen, *J. Phys. Chem. Solids* **56**, 1573 (1995).
 - [14] E. Pavarini, I. Dasgupta, T. Saha-Dasgupta, O. Jepsen, and O. K. Andersen, *Phys. Rev. Lett.* **87**, 047003 (2001).
 - [15] A. Georges, G. Kotliar, W. Krauth, and M. J. Rozenberg, *Rev. Mod. Phys.* **68**, 13 (1996).
 - [16] A. I. Liechtenstein and M. I. Katsnelson, *Phys. Rev. B* **62**, R9283(R) (2000).

- [17] T. Maier, M. Jarrell, T. Pruschke, and M. H. Hettler, *Rev. Mod. Phys.* **77**, 1027 (2005).
- [18] T. A. Maier, M. S. Jarrell, and D. J. Scalapino, *Phys. Rev. Lett.* **96**, 047005 (2006).
- [19] K. Haule and G. Kotliar, *Phys. Rev. B* **76**, 104509 (2007).
- [20] M. Ferrero, P. S. Cornaglia, L. De Leo, O. Parcollet, G. Kotliar, and A. Georges, *Europhys. Lett.* **85**, 57009 (2009).
- [21] M. Ferrero, P. S. Cornaglia, L. De Leo, O. Parcollet, G. Kotliar, and A. Georges, *Phys. Rev. B* **80**, 064501 (2009).
- [22] E. Gull, M. Ferrero, O. Parcollet, A. Georges, and A. J. Millis, *Phys. Rev. B* **82**, 155101 (2010).
- [23] E. Khatami, K. Mielson, D. Galanakis, A. Macridin, J. Moreno, R. T. Scalettar, and M. Jarrell, *Phys. Rev. B* **81**, 201101(R) (2010).
- [24] E. Gull, O. Parcollet, and A. J. Millis, *Phys. Rev. Lett.* **110**, 216405 (2013).
- [25] D. Senechal, P.-L. Lavertu, M.-A. Marois, and A.-M. S. Tremblay, *Phys. Rev. Lett.* **94**, 156404 (2005).
- [26] M. Aichhorn, E. Arrigoni, M. Potthoff, and W. Hanke, *Phys. Rev. B* **76**, 224509 (2007).
- [27] E. Gull, P. Werner, X. Wang, M. Troyer, and A. J. Millis, *Europhys. Lett.* **84**, 37009 (2008).
- [28] M. Civelli, *Phys. Rev. Lett.* **103**, 136402 (2009).
- [29] S. S. Kancharla, B. Kyung, D. Senechal, M. Civelli, M. Capone, G. Kotliar, and A.-M. S. Tremblay, *Phys. Rev. B* **77**, 184516 (2008).
- [30] S. Okamoto and T. A. Maier, *Phys. Rev. Lett.* **101**, 156401 (2008).
- [31] G. Sordi, K. Haule, and A.-M. S. Tremblay, *Phys. Rev. B* **84**, 075161 (2011).
- [32] S. Okamoto, D. Sénéchal, M. Civelli, and A.-M. S. Tremblay, *Phys. Rev. B* **82**, 180511 (2010).
- [33] G. Sordi, P. Sémon, K. Haule, and A.-M. S. Tremblay, *Sci. Rep.* **2**, 547 (2012).
- [34] X. Chen, J. P. F. LeBlanc, and E. Gull, *Phys. Rev. Lett.* **115**, 116402 (2015).
- [35] L. Fratino, P. Sémon, G. Sordi, and A.-M. S. Tremblay, *Sci. Rep.* **6**, 22715 (2016).
- [36] I. Affleck, *J. Phys.: Condens. Matter* **2**, 405 (1990).
- [37] H. Yao, W.-F. Tsai, and S. A. Kivelson, *Phys. Rev. B* **76**, 161104(R) (2007).
- [38] B.-X. Zheng and G. K.-L. Chan, *Phys. Rev. B* **93**, 035126 (2016).
- [39] V. Y. Irkhin, A. A. Katanin, and M. I. Katsnelson, *Phys. Rev. B* **64**, 165107 (2001).
- [40] A. P. Kampf and A. A. Katanin, *Phys. Rev. B* **67**, 125104 (2003).
- [41] W. Metzner, M. Salmhofer, C. Honerkamp, V. Meden, and K. Schönhammer, *Rev. Mod. Phys.* **84**, 299 (2012).
- [42] H. Hafermann, M. I. Katsnelson, and A. I. Lichtenstein, *Europhys. Lett.* **85**, 37006 (2009).
- [43] J. Otsuki, H. Hafermann, and A. I. Lichtenstein, *Phys. Rev. B* **90**, 235132 (2014).
- [44] G. Moeller, V. Dobrosavljevic, and A. E. Ruckenstein, *Phys. Rev. B* **59**, 6846 (1999).
- [45] M. Hashimoto, I. M. Vishik, R.-H. He, T. P. Devereaux, and Z.-X. Shen, *Nat. Phys.* **10**, 483 (2014).
- [46] R. H. Zadik, Y. Takabayashi, G. Klupp, R. H. Colman, A. Y. Ganin, A. Potočník, P. Jeglič, D. Arčon, P. Matus, K. Kamarás, Y. Kasahara, Y. Iwasa, A. N. Fitch, Y. Ohishi, G. Garbarino, K. Kato, M. J. Rosseinsky, and K. Prassides, *Sci. Adv.* **1**, e1500059 (2015).
- [47] C. A. Regal, M. Greiner, and D. S. Jin, *Phys. Rev. Lett.* **92**, 040403 (2004).
- [48] E. Gull, A. J. Millis, A. I. Lichtenstein, A. N. Rubtsov, M. Troyer, and P. Werner, *Rev. Mod. Phys.* **83**, 349 (2011).
- [49] P. Seth, I. Krivenko, M. Ferrero, and O. Parcollet, *Comput. Phys. Commun.* **200**, 274 (2016).
- [50] B. Dalla Piazza, M. Mourigal, M. Guarise, H. Berger, T. Schmitt, K. J. Zhou, M. Grioni, and H. M. Ronnow, *Phys. Rev. B* **85**, 100508(R) (2012).
- [51] M. Jarrell and J. E. Gubernatis, *Phys. Rep.* **269**, 133 (1996).
- [52] R. Bulla, T. A. Costi, and T. Pruschke, *Rev. Mod. Phys.* **80**, 395 (2008).
- [53] V. Y. Irkhin and M. I. Katsnelson, *Zh. Eksp. Teor. Fiz.* **90**, 1080 (1986) [*Sov. Phys. JETP* **63**, 631 (1986)].
- [54] V. A. Khodel, *Pis'ma Zh. Eksp. Teor. Fiz.* **103**, 795 (2016).
- [55] S. Sakai, M. Civelli, and M. Imada, *Phys. Rev. Lett.* **116**, 057003 (2016).
- [56] S. Sakai, Y. Motome, and M. Imada, *Phys. Rev. B* **82**, 134505 (2010).
- [57] S. Sakai, S. Blanc, M. Civelli, Y. Gallais, M. Cazayous, M.-A. Méasson, J. S. Wen, Z. J. Xu, G. D. Gu, G. Sangiovanni, Y. Motome, K. Held, A. Sacuto, A. Georges, and M. Imada, *Phys. Rev. Lett.* **111**, 107001 (2013).
- [58] L. Capriotti and S. Sorella, *Phys. Rev. Lett.* **84**, 3173 (2000).
- [59] S.-S. Gong, W. Zhu, D. N. Sheng, O. I. Motrunich, and M. P. A. Fisher, *Phys. Rev. Lett.* **113**, 027201 (2014).
- [60] D. Poilblanc, P. Corboz, N. Schuch, and J. I. Cirac, *Phys. Rev. B* **89**, 241106(R) (2014).
- [61] F. Verstraete, J. I. Cirac, and V. Murg, *Adv. Phys.* **57**, 143 (2008).
- [62] V. Y. Irkhin, A. A. Katanin, and M. I. Katsnelson, *Phys. Rev. Lett.* **89**, 076401 (2002).
- [63] D. Yudin, D. Hirschmeier, H. Hafermann, O. Eriksson, A. I. Lichtenstein, and M. I. Katsnelson, *Phys. Rev. Lett.* **112**, 070403 (2014).

3.5.2 Exactly solvable model

The next study [128] presents the quadruple Bethe (or plaquette-Bethe) lattice in detail, especially its broken-symmetry phases. It consists of four Bethe lattices of which equivalent sites are interconnected into plaquettes. The symmetry-broken d -wave superconducting states exist in infinite dimensions which is a complementary insight to the two-dimensional approximation of the CDMFT. “Exactly” is meant in the numerical sense, importantly the solution is calculated with arbitrary precision depending on the computational effort, but no limitations due to assumptions. The quadruple Bethe lattice has an additional hopping parameter, the hopping within the Bethe lattices. The optimal Bethe hopping is rather small, i.e. $t_b \sim 0.1t$ of the plaquette. The superconducting state seems to have its origin, its crucial correlations, in the plaquette. Antiferromagnetism is different as it occurs also in the (simple) Bethe lattice and requires larger Bethe hoppings ($t_b \sim 0.4t$). Although the two-dimensional CDMFT approximation includes the square lattice’s band structure in the calculation, it is probably more complicated to isolate the microscopic mechanism than in the quadruple Bethe lattice. It is shown that the Bethe hopping can be used to isolate the relevant plaquette eigenstates, i.e. those crossing at the PDP/QCP of the plaquette, that describe the superconducting state. Remarkably, these states produce superconductivity with the optimal doping of $\sim 0.15\%$, which is found in many experiments.

However, the degenerate point of the plaquette does not translate directly into the optimal configuration for the superconductivity of the quadruple Bethe lattice. To get an intuition why this is the case it is important to consider the non-interacting lattice which has a different chemical potential for a certain filling than the plaquette. The chemical potential converges with the CDMFT loops and, moreover, the real part of the self-energy at low energies produces an effective quasiparticle energy. This can impact how single plaquette eigenstates contribute to the total state of the system. A strategy chosen in the following is to start from a superconducting state and continuously disconnect the plaquettes by decreasing the Bethe hopping. At a certain finite value the superconductivity vanishes but a linear extrapolation can be performed and it points to the degenerate point of the plaquette.

Exactly solvable model of strongly correlated d -wave superconductivity

Malte Harland,¹ Sergey Brener,¹ Mikhail I. Katsnelson,² and Alexander I. Lichtenstein¹

¹*Institute of Theoretical Physics, University of Hamburg, Jungiusstraße 9, 20355 Hamburg, Germany*

²*Institute for Molecules and Materials, Radboud University, 6525AJ, Nijmegen, the Netherlands*

(Dated: May 30, 2019)

We present an infinite-dimensional lattice of two-by-two plaquettes, the quadruple Bethe lattice, with Hubbard interaction and solve it exactly by means of the cluster dynamical mean-field theory. It exhibits a d -wave superconducting phase that is related to a highly degenerate point in the phase diagram of the isolated plaquette at that the groundstates of the particle number sectors $N = 2, 3, 4$ cross. The superconducting gap is formed by the renormalized lower Slater peak of the correlated, hole-doped Mott insulator. We engineer parts of the interaction and find that pair hoppings between X/Y -momenta are the main two-particle correlations of the superconducting phase. The suppression of the superconductivity in the overdoped regime is caused by the diminishing of pair hopping correlations and in the underdoped regime by charge blocking. The optimal doping is ~ 0.15 at which the underlying normal state shows a Lifshitz transition. The model allows for different intra- and inter-plaquette hoppings that we use to disentangle superconductivity from antiferromagnetism as the latter requires larger inter-plaquette hoppings.

I. INTRODUCTION

High-temperature superconductivity in cuprates¹ can persist at temperatures up to $T \sim 100\text{K}$, which makes an understanding of their pairing mechanism non-trivial in the context of conventional theory of superconductivity and very interesting for theoretical and practical purposes. The large transition temperature is not the only peculiar characteristic of such materials. They are unconventional also by their anisotropic superconducting gap², small superfluid density³, and competing orders⁴. Cuprates share a common quasi two-dimensional structure of layered copper-oxide compounds that are insulating and become superconducting upon doping with charge carriers⁵. The different compounds of that family share a d -wave character of superconducting gap and antiferromagnetic order in the undoped insulating state. Furthermore, at larger hole doping and temperatures above the critical temperature they exhibit a very incoherent metal behavior characterized in particular by a linear temperature dependence of the resistivity⁶ and by a pseudogap formation⁷.

The Cu atoms of the stacked Cu-planes form a square lattice. On their bonds are oxygen atoms whose p -orbitals mediate electronic transitions from one Cu d -orbital to its nearest neighbor's d -orbital. This process is modeled by effective $d-d$ hopping with the amplitude t that competes with the local screened Coulomb repulsion U . Further hoppings also exist, but they are smaller in their amplitude. The bandwidth of the d -orbitals is comparable to the interaction energy U . The broadly accepted minimal model to account for these competing electronic effects is the Hubbard model⁸⁻¹⁰. Despite its simple appearance that model in two and three dimensions can be solved by approximations only, contrary to the one-dimensional case that is exactly solvable by Bethe Ansatz¹¹.

A simple but powerful approximation is the dynamical mean-field theory (DMFT)¹² which accounts only

for the local correlations by including only the local self-energy from an effective impurity model. The DMFT provides an exact solution in the formal limit of infinite dimensions but is questionable for two dimensions (2D). Phenomena such as the Mott transition¹³ and itinerant antiferromagnetism¹⁴ (Slater physics) are captured by the infinite-dimensional DMFT, but are severely overestimated in low dimensions.

The DMFT can be extended by restricting the self-energy not to a single site, but to a cluster of several sites. Hence, this extension is called cluster DMFT (CDMFT)¹⁵⁻¹⁷. The generalization to clusters is not unique and still debated^{18,19}. Regardless of the particular choice of CDMFT-"flavor" it was found that intersite correlations within the cluster are sufficient to obtain a symmetry-broken d -wave superconducting (dSC) state. The minimal cluster is the two-by-two cluster (plaquette), since dSC order is defined on the bonds according to $d_{x^2-y^2}$ -wave symmetry¹⁵. In 2D CDMFT is an approximation and long-range correlations beyond the cluster can be important for a correct description of the dSC state in cuprates^{20,21}. Therefore in the dSC state CDMFT aims to describe only the local formation of Cooper pairs. For example, CDMFT gives coexisting antiferromagnetic (AFM) and dSC orders¹⁵, whereas in cuprates these phases do not coexist. The reason is that CDMFT does not distinguish between long-range and short-range AFM order if the corresponding correlation length is much larger than the lattice constant. Thereby, it also neglects the stripe order phase of cuprates which has been found to be suppressed by the next-nearest neighbor hopping within the Hubbard model^{22,23}.

In this work we present a detailed analysis of the infinite dimensional quadruple Bethe lattice model within the CDMFT. Similar to the well-known Mott transition found in the simple Bethe lattice^{12,24-26} and the correlated Peierls insulator transition in the double Bethe lattice²⁷⁻²⁹, we find the dSC transition in the strong-coupling quadruple Bethe lattice³⁰. This choice of setup

is complementary to prior studies in the sense that we investigate a less accurate model of infinite dimensionality but in return obtain an exact solution. Compared to the simple Bethe lattice the local Hilbert-space size is increased, from 4 of the Hubbard site to 256 of the Hubbard plaquette. This opens up new degrees of freedom that can interact with the mean-field environment. In particular, we focus on those plaquette eigenstates^{31–35}, that define the dSC and cross at a quantum critical point³⁰ (QCP) of the plaquette. This point is particularly interesting as quantum critical behavior^{19,36,37} has been found for the square lattice by CDMFT studies of the pseudogap phenomenon that has been suggested to originate from negative interference of hybridizing plaquette states^{30,38–40}.

In this paper we start with a presentation of the quadruple Bethe lattice and the single-particle basis we use in Sec. II. In Sec. III we provide an overview of the isolated cluster's Hilbert space, that is the auxiliary system of our CDMFT mapping. The opposite limit of non-interacting Bethe lattices is presented in Sec. IV. In Sec. V we analyse the dependence of the dSC order parameter on the screened Coulomb repulsion and the chemical potential for small Bethe lattice hoppings, i.e. plaquette hybridizations, for that the dSC order is dominant and other orders are less pronounced. In Sec. VI we show how different components of the two-particle interaction promote or interfere with the dSC order. Dynamical properties, such as quasiparticle characterization and spectral functions are presented in Sec. VII. Finally, larger Bethe lattice hoppings yield more pronounced antiferromagnetic order, see Sec. VIII, and an extended Bethe lattice hopping allows us to tune the non-interacting density of states more similar to a van-Hove singularity, that is presented in Sec. IX.

II. MODEL & METHOD

As stated above, the correlated d -electrons of the copper-oxide planes are described by the Hubbard model

$$H = \sum_{ij\sigma} t_{ij} c_{i\sigma}^\dagger c_{j\sigma} + U \sum_i c_{i\uparrow}^\dagger c_{i\uparrow} c_{i\downarrow}^\dagger c_{i\downarrow}, \quad (1)$$

with fermionic creation/annihilation operators c^\dagger/c , sites i, j and spins σ . It contains a hopping term $t_{i,j}$ that for lattice structures becomes diagonal in k -space and therefore promotes delocalization of the charge. Albeit, the quadruple Bethe lattice is only a pseudolattice in that regard since it does not exhibit translational invariance. But still, its sites are equivalent due to its self-similar structure. The screened local Coulomb repulsion U is diagonal in site-space and promotes charge localization. The chemical potential μ can be written explicitly, or it can be absorbed into the diagonal, local part of t_{ij} .

The quadruple Bethe lattice is constructed from four Bethe lattices, that are plaquette-wise connected, see

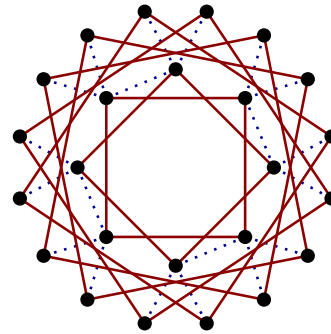


FIG. 1. Quadruple Bethe lattice, four Bethe lattices (dotted lines) interconnected via plaquettes (solid lines). The coordination number for each Bethe lattice of this figure is set to $z = 3$, and six sites of each Bethe lattice are depicted. An entire Bethe lattice exhibits an infinite number of sites with self-similar structure. Next-nearest neighbor hoppings of the plaquette are omitted for convenience.

Fig. 1, i.e. equivalent sites of the four Bethe lattices form a two-by-two plaquette. The coordination number of the Bethe-lattices is set to $z = \infty$ corresponding to infinite dimensions. We introduce three types of hopping. The first hopping t connects sites of the Bethe-lattice with equivalent points of two neighboring Bethe-lattices, i.e. within plaquettes. We use $t = -1$ throughout, and its absolute value defines our energy unit. The second hopping t' connects with equivalent points of the one remaining Bethe-lattice and thus occurs on the next-nearest neighbor bond of the plaquette. The third hopping t_b connects sites within the Bethe-lattices, i.e. between plaquettes. We write the plaquette hopping matrix in site basis as

$$t^p = \begin{pmatrix} -\mu & t & t & t' \\ t & -\mu & t' & t \\ t & t' & -\mu & t \\ t' & t & t & -\mu \end{pmatrix}. \quad (2)$$

Then, we can decompose the kinetic energy H_t , the first term of Eq. (1), into hopping within plaquettes and between plaquettes, i.e. within Bethe lattices

$$H_t = t_b \sum_{\langle r, r' \rangle R\sigma} c_{r'R\sigma}^\dagger c_{rR\sigma} + \sum_{rRR'} t_{RR'}^p c_{r'R\sigma}^\dagger c_{rR\sigma}. \quad (3)$$

The original site label i has been rewritten as a position within the Bethe lattice r and position within the plaquette R . The summation over $\langle r, r' \rangle$ is performed over nearest neighbors. In principle the Bethe hopping can also be a matrix, but since we focus mostly on the case of a scalar t_b , we will restrict the following derivation to it. The generalization to a matrix Bethe hopping is straight forward, and we apply it in Sec. IX only.

We apply a discrete Fourier transform to diagonalize the hopping of the plaquette from site space into the plaquette-momentum basis of momenta K which can

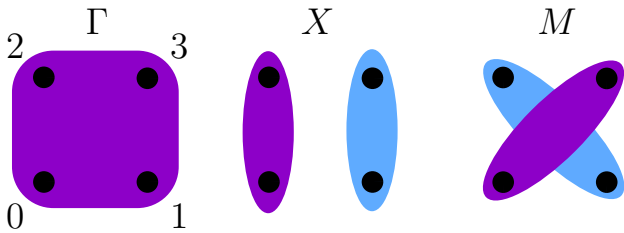


FIG. 2. Illustration of the plaquette orbitals/momenta Γ, X, M (Y omitted), i.e. the basis that diagonalizes the hopping in plaquette-site space $(0, 1, 2, 3)$. Colors denote symmetries of the orbitals.

take four possible values, Γ, M, X, Y . The transformation applied to plaquette-site space reads

$$T = \frac{1}{2} \begin{pmatrix} e^{i\Gamma R_0} & \dots & e^{i\Gamma R_3} \\ e^{iM R_0} & \dots & e^{iM R_3} \\ e^{iX R_0} & \dots & e^{iX R_3} \\ e^{iY R_0} & \dots & e^{iY R_3} \end{pmatrix} \quad (4)$$

$$= \frac{1}{2} \begin{pmatrix} 1 & 1 & 1 & 1 \\ 1 & -1 & -1 & 1 \\ 1 & -1 & 1 & -1 \\ 1 & 1 & -1 & -1 \end{pmatrix}$$

with

$$(R_0, \dots, R_3) = \begin{pmatrix} 0 & 1 & 0 & 1 \\ 0 & 0 & 1 & 1 \end{pmatrix} a, \quad (5)$$

$$(\Gamma, M, X, Y) = \begin{pmatrix} 0 & 1 & 1 & 0 \\ 0 & 1 & 0 & 1 \end{pmatrix} \frac{\pi}{a}$$

with a unit length a . Due to the symmetry of the site-space, we can diagonalize the quadratic parts of the Hamiltonian H in plaquette-momentum space. At this point the quadruple Bethe lattice can be regarded as a multiorbital simple Bethe lattice, see Fig. 2.

The interaction has to be transformed to K basis as well. From the fact that it is local in site basis, one can already expect many terms in the plaquette-momentum basis. We apply the rank-2 tensor transformation $U \mapsto TTUT^\dagger T^\dagger$ also using plaquette-momentum conservation and obtain

$$H_U = \sum_{rK_1 \dots K_4} U_{K_1 \dots K_4} c_{rK_1 \uparrow}^\dagger c_{rK_2 \uparrow} c_{rK_3 \downarrow}^\dagger c_{rK_4 \downarrow} \quad (6)$$

with the Hubbard interaction tensor $U_{K_1 \dots K_4} = U \delta_{K_1+K_3, K_2+K_4}^{(2\pi/a)}/4$, where $\delta_{K_1, K_2}^{(2\pi/a)} = 1$, when $K_1 - K_2 =$

$2\pi n/a$ with integer n and $= 0$ otherwise. Depending on the relative values of the four plaquette momenta $K_1 \dots K_4$ we can classify the terms of $U_{K_1 \dots K_4}$ into intra-orbital ($\times 4$, e.g. U_{XXXX}), inter-orbital ($\times 12$, e.g. U_{XXYY}), pair-hopping ($\times 12$, e.g. U_{XYXY}), spin-flip ($\times 12$, e.g. $U_{XY YX}$), and correlated hopping ($\times 24$ with all four momenta pairwise distinct).

Regarding the superconducting order we use the Nambu spinor basis for its description

$$\tilde{c}_r^\dagger = \left(c_{r\Gamma\uparrow}^\dagger c_{r\Gamma\downarrow} c_{rM\uparrow}^\dagger c_{rM\downarrow} c_{rX\uparrow}^\dagger c_{rX\downarrow} c_{rY\uparrow}^\dagger c_{rY\downarrow} \right). \quad (7)$$

It can be constructed efficiently by particle-hole transforming the spin- \downarrow part of the conventional spinor representation. This is sufficient if no other than $S_z = 0$ spin-structures are considered for the pairing. Next, we address the Hubbard-Hamiltonian in Nambu basis. We apply the Nambu spinor construction and examine how t_{ij} , μ and U transform. This is done by using the anti-commutation rules. We obtain

$$\begin{aligned} \tilde{t}_\sigma^p &= t^p (\delta_{\sigma\uparrow} - \delta_{\sigma\downarrow}), \\ \tilde{\mu}_\sigma &= (\mu + U) \delta_{\sigma\uparrow} - \mu \delta_{\sigma\downarrow}, \\ \tilde{U} &= -U, \end{aligned} \quad (8)$$

where \uparrow and \downarrow denote the indices of the Nambu spinor entries, i.e. spin- \uparrow particles and spin- \downarrow holes. The Bethe hopping t_b transforms under the Nambu spinor construction in the same way as the plaquette hopping t^p .

We use the CDMFT^{12,15-17,41} to map the lattice problem to the Anderson impurity model of an impurity, i.e. the cluster, with (quartic) interaction and a bath of non-interacting, but potentially renormalized, particles. The environment is defined by the dynamical mean-field (bath Green function) $\mathcal{G}(i\omega_n)$. In particular for the quadruple Bethe lattice with infinite coordination of the Bethe lattices, the CDMFT becomes exact as the self-energy

$$\Sigma(i\omega_n) = \mathcal{G}^{-1}(i\omega_n) - G^{-1}(i\omega_n) \quad (9)$$

exists only within the plaquettes and not between them. Eq. (9) is the Dyson equation and relates Σ to the local Green function G and the bath Green function \mathcal{G} . They depend on Matsubara frequencies $\omega_n = \pi(2n+1)/\beta$ with inverse temperature β . In this study we use for the quadruple Bethe lattice calculations $\beta = 100$ throughout (though for calculations on the isolated plaquette we also use $\beta = 30$). The self-consistency condition to treat AFM and dSC order reads

$$G_{AK\sigma, AK'\sigma'}^{-1}(i\omega_n) = i\omega_n \delta_{KK'} \delta_{\sigma\sigma'} + (\mu \delta_{KK'} - t_{KK'}^p) \sigma_{\sigma\sigma'}^z - t_b^2 \sum_{\tau\tau'} \sigma_{\sigma\tau}^z G_{BK\tau, BK'\tau'}(i\omega_n) \sigma_{\tau'\sigma'}^z - \Sigma_{AK\sigma, K'j\sigma'}(i\omega_n). \quad (10)$$

K, K' are labels for the plaquette momenta. $\sigma, \sigma', \tau, \tau'$

label the Nambu-space, i.e. spin- \uparrow electrons or spin- \downarrow

holes. The Nambu representation also requires a transformation of the single-particle energies (Eq. (8)), the chemical potential μ , the matrix of plaquette-hoppings t^p and the scalar Bethe hopping t_b . For that reason the third Pauli matrix σ^z appears in Eq. (10).

The fact that the Bethe lattice is bipartite allows us to additionally consider the possibility of AFM symmetry breaking. We can divide the lattice into two sublattices of which we know how to transform their local Green functions into each other analytically. We describe the AFM of the sublattices A and B with Nambu-Green functions as

$$G_{BK\sigma, BK'\sigma'}(i\omega_n) = - \sum_{\tau\tau'} R_{\sigma\tau} G_{AK\tau, AK'\tau'}^*(i\omega_n) R_{\tau'\sigma'}^\dagger \quad (11)$$

with the rotation matrix

$$R = e^{i\pi\sigma^y/2}. \quad (12)$$

Eq. (11) describes a spin-flip accompanied by a particle-hole transformation due to the Nambu spinor formalism. For the diagonal entries of the Green function there is no difference in using the first (σ_x) or the second (σ_y) Pauli matrix for the rotation of Eq. (12). In contrast, off-diagonal (anomalous) entries obtain an additional minus sign from σ_y . We use this Berry phase in order not to change the dSC order for the Bethe sublattices A and B . σ_x would change the dSC according to an X/Y -flip. Thus, Eq. (11) defines staggered spin, but homogenous dSC order.

The spin order within the plaquette can still be diverse for different solutions. A/B sublattices not only support AFM order, but also a spin order that is ferromagnetic within the plaquette and antiferromagnetic with respect to the Bethe sublattices A/B . We will refer to the latter as plaquette antiferromagnetism (PAFM).

The dynamical mean-field is constructed as

$$\begin{aligned} \mathcal{G}_{AK\sigma, AK'\sigma'}^{-1}(i\omega_n) &= i\omega_n \delta_{KK'} \delta_{\sigma\sigma'} + (\mu \delta_{KK'} - t_{KK'}^p) \sigma_{\sigma\sigma'}^z \\ &\quad - t_b^2 \sum_{\tau\tau'} \sigma_{\sigma\tau}^z G_{BK\tau, BK'\tau'}(i\omega_n) \sigma_{\tau'\sigma'}^z. \end{aligned} \quad (13)$$

Together with the local interaction, \mathcal{G} defines the impurity setup. Eq. (13) shows that the mean-field of sublattice A is constructed from the local properties of sublattice B . In the following we drop the Bethe lattice index $r = A/B$ for convenience. The numerical solution of the impurity Green function is obtained by the hybridization expansion continuous time quantum Monte-Carlo method⁴²⁻⁴⁶ (CTHYB). The self-consistency is closed with the Dyson equation and by demanding that the local lattice Green function equals the impurity Green function which is inserted into the right-hand side of Eq. (10) until convergence is reached. In our implementation Eq. (10) is also used to iteratively find μ in the case of a certain filling is set as a parameter rather than μ directly.

The numerics can be implemented efficiently using symmetries and blockstructure of the Green function. For our setup the Matsubara-Green function has the structure

$$G = \begin{pmatrix} \Gamma & M & X & Y \\ \left(\begin{array}{cc|cc} \gamma & 0 & a & 0 \\ 0 & -\gamma^* & 0 & a^* \\ \hline a & 0 & m & 0 \\ 0 & a^* & 0 & -m^* \end{array} \right) & 0 & \left(\begin{array}{cc|cc} x & -d & \tilde{a} & \pi \\ -d & -x^* & -\pi & \tilde{a}^* \\ \hline \tilde{a} & -\pi & y & d \\ \pi & \tilde{a}^* & d & -y^* \end{array} \right) \end{pmatrix}. \quad (14)$$

It contains the two-by-two Nambu blocks of spin- \uparrow particles and spin- \downarrow holes and additionally four-by-four blocks in plaquette momentum basis, the ΓM - and the XY -blocks. d and a/\tilde{a} stand for dSC and AFM orders, respectively. AFM breaks the plaquette point-group symmetry in such a way, that Γ , M and X, Y are pairwise coupled. In the plaquette momentum basis AFM order is reflected by non-zero a/\tilde{a} off-diagonals. Furthermore, dSC order breaks the plaquette symmetries so that the X - Y degeneracy is lifted, but off-diagonals are introduced only in Nambu-space, d and $-d$. The diagonal-part of the X/Y -block is not affected by the dSC symmetry breaking, and thus $y = x$. The entries of π describe spin-triplet superconductivity πSC which we study in Sec. VIII. The anomalous part of the Green function has non-zero elements only in the XY -block. It can be written as

$$F = \begin{pmatrix} -d & \pi \\ -\pi & d \end{pmatrix}, \quad (15)$$

for that the entries of π show the symmetry $F_{XY}^{\uparrow\downarrow} = -F_{YX}^{\uparrow\downarrow} = F_{XY}^{\downarrow\uparrow}$ and hence also the spin-triplet pairing. In contrast $d = F_{XX}^{\uparrow\downarrow} = -F_{XX}^{\downarrow\uparrow}$ which is a spin-singlet structure. Note, that in the present study non-zero entries for π occur only simultaneously with the coexistence of dSC and AFM.

DMFT calculations of broken symmetries can be done efficiently by introducing seeds with the proper symmetry for the first DMFT-iteration and subsequently running additional loops until convergence. For example regarding dSC, we initialize the anomalous Green function with

$$d^{\text{init}}(i\omega_n) = \frac{d_0\beta}{2} (\delta_{n,-1} + \delta_{n,0}) \quad (16)$$

for some small d_0 . This function transforms into a cosine in imaginary time that is symmetric and real.

III. TWO-BY-TWO PLAQUETTE

The low-energy many-body states of the Hubbard two-by-two plaquette, around $\langle N \rangle = 3$ filling, have been con-

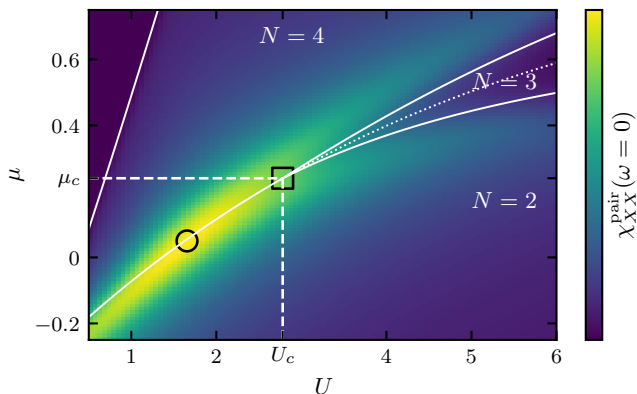


FIG. 3. Retarded pairing susceptibility $\chi^{\text{pair}}(\omega)$ of pairs with plaquette momentum X in the isolated plaquette dependent on the screened Coulomb repulsion U and chemical potential μ . The groundstate sectors $N = 2, 3, 4$ (solid lines) cross at a quantum critical point (square) with $U_c = 2.78$ and $\mu_c = 0.24$. The maximum of $\chi^{\text{pair}}(\omega)$ (black circle) lies at the $N = 2, 4$ crossover that becomes a non-groundstate crossover at $U_c < U$ (dotted line).

considered as an essential element of the description of superconductivity in cuprates. Prior investigations have shown^{30–32}, that the relevant low-energy subspace of the 256 plaquette-states contains 6 states: a $N = 2$ spin-singlet with the symmetry of the plaquette- Γ orbital $|2, 0, \Gamma\rangle$, two $N = 3$ spin-doublets with X/Y symmetries $|3, \frac{1}{2}, \frac{X}{Y}\rangle$ and a $N = 4$ spin-singlet of Γ symmetry $|4, 0, \Gamma\rangle$. Note, that we use the notation of $|3, \frac{1}{2}, \frac{X}{Y}\rangle$ for the sector of the four degenerate states. In addition to these most important 6 states there are also a $N = 4$ spin-triplet $|4, 1, M\rangle$ and a $N = 3$ spin-quadruplet $|3, \frac{3}{2}, M\rangle$, that become important for large U ($t - J$ -limit). In this section we use $t' = 0.3$. Calculations for $t' = 0$ show qualitatively similar results although the QCP is shifted to larger values of μ and U .

The instability towards dSC order can be observed already in the isolated plaquette using exact diagonalization. The pairing susceptibility

$$\chi_{XX}^{\text{pair}}(\tau) = \left\langle T_\tau c_{X\uparrow}(\tau) c_{X\downarrow}(\tau) c_{X\downarrow}^\dagger(0) c_{X\uparrow}^\dagger(0) \right\rangle, \quad (17)$$

with imaginary time (τ) ordering operator T_τ can be calculated using the Lehmann representation. The retarded pairing susceptibility at Fermi level $\chi^{\text{pair}}(\omega = 0)$ shows large values in the μ/U -phase diagram at the boundary of $N = 2, 4$, see Fig. 3. In the $N = 4$ sector, where $|4, 0, \Gamma\rangle$ is the groundstate, $|2, 0, \Gamma\rangle$ describes a bosonic two-hole excitation³¹. χ_{XX}^{pair} has its maximum close to $U = 2$. Moreover, in this phase diagram the quantum critical point where 6 many-body states of the sectors $N = 2, 3, 4$ cross can be seen at $U_c = 2.78$ and $\mu_c = 0.24$.

To get a view on the low-energy subspace of the plaquette we present in Fig. 4 the energy dependence of the states as a function of μ for constant $U = U_c$. Addition-

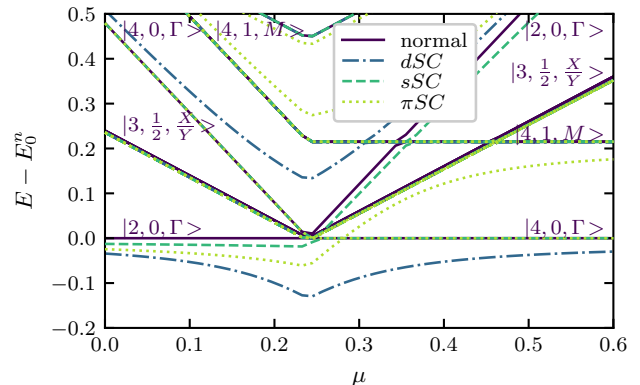


FIG. 4. Plaquette eigenenergies E as functions of the chemical potential μ around $\mu = 0.24, U = 2.78$ at that $N = 2, 3, 4$ cross. All energies are plotted relative to the groundstate-energy of the normal state E_0^n . The kets label the normal states particle number N , spin number S and plaquette momentum K . The superconducting (SC) fields are $\Delta_x = 0.1$ for the different orders x : d -wave dSC , s -wave sSC and spin-triplet πSC .

ally, we add different N -symmetry breaking fields

$$\begin{aligned} h_{dSC} &= \Delta_{dSC}(c_{\uparrow X} c_{\downarrow X} - c_{\uparrow Y} c_{\downarrow Y}) + \text{h.c.}, \\ h_{sSC} &= \Delta_{sSC}(c_{\uparrow X} c_{\downarrow X} + c_{\uparrow Y} c_{\downarrow Y}) + \text{h.c.}, \\ h_{\pi SC} &= \Delta_{\pi SC}(c_{\uparrow X} c_{\downarrow Y} + c_{\downarrow X} c_{\uparrow Y}) + \text{h.c.} \end{aligned} \quad (18)$$

of spin-singlet s -wave (sSC), spin-singlet d -wave (dSC) and spin-triplet (πSC) symmetries. The groundstate energy lowering by the dSC order is the largest at the critical point $\mu_c \sim 0.24$, see Fig. 4. Different absolute values of the slopes in Fig. 4 correspond to different particle number sectors of the normal state. The small- μ and large- μ part have $|2, 0, \Gamma\rangle$ and $|4, 0, \Gamma\rangle$ as groundstates, respectively. The dSC -groundstate is a superposition of mainly these two and there crossing is avoided by the symmetry breaking. A contribution of $N = 3$ to the dSC groundstate is excluded since Cooper-pairs contain two electrons and therefore the groundstate has even parity, i.e. it is a superposition of particle number sectors of even particle numbers.

Regarding Δ_{sSC} , only the $|2, 0, \Gamma\rangle$ is lowered in energy, but not due to mixing with the low-energy $|4, 0, \Gamma\rangle$ of the normal state as this one is unaffected. For the πSC field, the degeneracy of the spin-triplet $|4, 1, M\rangle$ is lifted as only the $S^z = 0$ -state mixes with $|2, 0, \Gamma\rangle$. The splitting of the two is visible, whereas one state is lowered in energy, the other is increased relative to the corresponding normal state. Without field, i.e. in the normal state, $|2, 0, \Gamma\rangle$ and $|4, 1, M\rangle$ cross around $\mu = 0.35$, this crossing is avoided in the πSC state. Among the considered symmetry breakings, the energy splitting of low-energy states with dSC -field is the largest. It is noticeable, that the main instability in the many-body physics of the Hubbard two-by-two plaquette is towards dSC order as it lowers the energy the most.

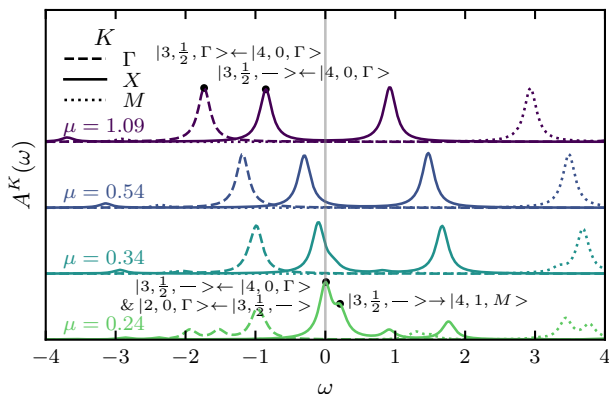


FIG. 5. Plaqueette momentum K resolved Spectral function $A^K(\omega)$ of the isolated plaquette for different chemical potentials μ . The peaks are identified with single-particle transitions of the plaquette eigenstates. $U = 2.78$, $t' = 0.3$, $\beta = 30$ and Lorentzian broadening $\epsilon = \pi/\beta$.

In addition to the transition of pairs we investigate also single-particle transitions of the isolated plaquette, see Fig. 5. At half-filling ($\mu = 1.09$) we observe a four-peak structure of the spectral function. Since we are interested in hole-doping, we focus on the transitions below Fermi-level. The lowest has plaquette momentum Γ and is a transition of the groundstate, $|4, 0, \Gamma\rangle \rightarrow |3, \frac{1}{2}, \Gamma\rangle$. The second lowest and closest to Fermi level has plaquette momentum X/Y and corresponds to $|4, 0, \Gamma\rangle \rightarrow |3, \frac{1}{2}, \frac{X}{Y}\rangle$. Thus, $|3, \frac{1}{2}, \frac{X}{Y}\rangle$ describes the low-energy, one-particle excitation of plaquette momentum X/Y of the $N = 4$ system with groundstate $|4, 0, \Gamma\rangle$.

Upon reducing μ the system gets hole-doped and the lower peak of $A^K(\omega)$ crosses Fermi-level. At $\mu = 0.24$ is a groundstate crossover, the QCP, and therefore other transitions become active. At the QCP the transitions $|4, 0, \Gamma\rangle \rightarrow |3, \frac{1}{2}, \frac{X}{Y}\rangle$ and $|3, \frac{1}{2}, \frac{X}{Y}\rangle \rightarrow |2, 0, \Gamma\rangle$ occur on the same ω . Furthermore, the peak has a pronounced shoulder from the transition $|3, \frac{1}{2}, \frac{X}{Y}\rangle \rightarrow |4, 1, M\rangle$. Thus in total around the QCP three prominent one-particle transitions exist close to Fermi level.

IV. NON-INTERACTING QUADRUPLE BETHE LATTICE

For the non-interacting case ($U = 0$, $\Sigma = 0$) the Green function $G(i\omega_n)$ of Eq. (10) becomes the bare Green function $G^0(i\omega_n)$. Thus, we can solve Eq. (10) analytically and obtain

$$G_K^0(i\omega_n) = \frac{2\sigma_z}{\xi_K - \sqrt{\xi_K^2 - 4t_b^2}}, \quad (19)$$

$$\xi_K = i\omega_n \sigma_z + (\mu - t_K^p) \mathbb{1}.$$

The third Pauli matrix σ_z stems from the particle hole transformation of the hoppings and acts on Nambu space. The derivation of the analytical solutions depends on the

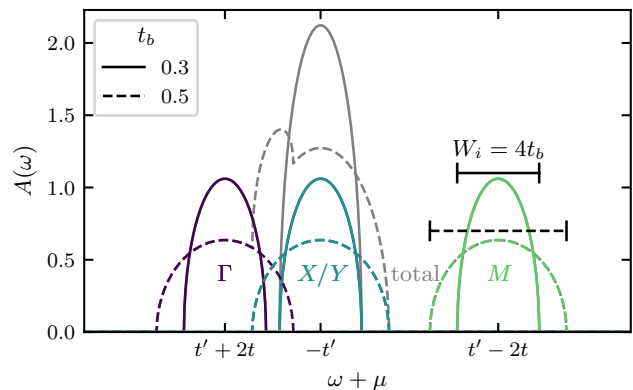


FIG. 6. Semicircular densities of states of the non-interacting ($U = 0$) quadruple Bethe lattice for the different orbitals/momenta and bethe-lattice hoppings t_b ($t' = 0.3$). The semicirculars have the same width W_i for scalar t_b .

fact, that all quantities can be diagonalized in spinor and K -space by a unitary transformation.

The spectral function corresponding to $G^0(i\omega_n)$ is shown in Fig. 6. It consists of four semicirculars of that two are degenerate corresponding to X and Y . The semicirculars have a bandwidth of $W = 4t_b$ each. The positions of the semicirculars are defined by the eigenvalues of the hopping within the plaquette. Therefore, we have the lowest momentum/orbital Γ at $\omega_\Gamma = t' + 2t - \mu$, the highest M at $\omega_M = t' - 2t - \mu$ and X/Y at $\omega_{X/Y} = -t' - \mu$. The model is particle-hole symmetric for $t' = 0$ and large values of t' or t_b can make the orbitals overlap.

The dependence of the filling on the chemical potential and the Bethe-hopping are shown in Fig. 7. In order to relate states of the isolated plaquette to solutions of the quadruple Bethe lattice, it can be useful to know the effect of t_b . From the non-interacting case we can learn how t_b and μ change the filling. For small t_b and $0.5 < \langle n \rangle < 1$, t_b reduces the particle occupation. There are mainly two effects that define this dependence. First, the semicircular at Fermi-level broadens, depending on whether its maximum is above or below Fermi-level it increases or decreases the filling. Second, an additional semicircular can broaden enough to also touch the Fermi-level and thereby change the filling.

V. μ - U PHASE DIAGRAM

In order to get an overview of the phases of the quadruple Bethe lattice and their relation to the states of the isolated plaquette, Fig. 8 presents several phase diagrams in the μ - U -plane for different plaquette next-nearest-neighbor hoppings t' and Bethe hoppings t_b . The orders described by the selfconsistency condition of Eq. (10), that exist for small t_b , are dSC, AFM and PAFM. Their

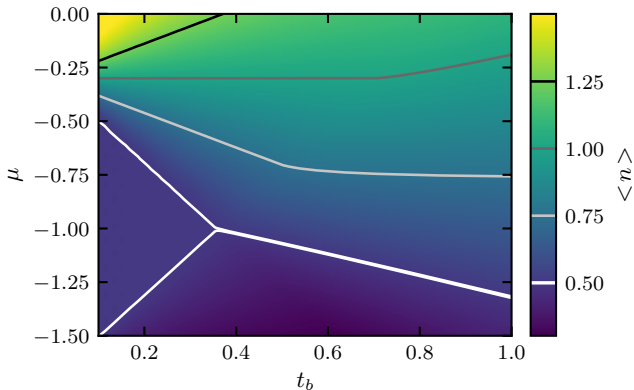


FIG. 7. Filling $\langle n \rangle$ dependence on the chemical potential μ and the Bethe hopping t_b for the non-interacting ($U = 0$) quadruple Bethe lattice ($t' = 0.3$).

order parameters are defined as

$$\begin{aligned} \Psi_{dSC} &= \frac{1}{4^2} \sum_{RR'} (\cos[X(R - R')] - \cos[Y(R - R')]) \\ &\quad \times \langle c_{R\uparrow} c_{R'\downarrow} - c_{R\downarrow} c_{R'\uparrow} \rangle, \\ \Psi_{AFM} &= \frac{1}{4} \sum_R e^{iMR} \langle S_R^z \rangle, \\ \Psi_{PAFM} &= \frac{1}{4} \sum_R e^{i\Gamma R} \langle S_R^z \rangle, \end{aligned} \quad (20)$$

with the local spin along quantization axis $S_R^z = (n_{R\uparrow} - n_{R\downarrow})/2$. By the symmetries of Eq. (14) and Eq. (15) we obtain $\Psi_{dSC} = \text{Tr}_{i\omega_n} F_{XX}(i\omega_n)$. The order parameters are calculated broad region around the QCP, where the groundstates $|2, 0, \Gamma\rangle$, $|3, \frac{1}{2}, \frac{X}{Y}\rangle$ and $|4, 0, \Gamma\rangle$ cross. We stress that Fig. 8 combines information of two different systems, i.e. the phase boundaries of the isolated plaquette ($t_b = 0, T = 0$) and order parameters of the quadruple Bethe lattice ($t_b > 0, T = 0.01$).

The most dominant order in that region for all t' and t_b of Fig. 8 is the dSC. For small t_b the dSC region is relatively narrow as a function of μ . It broadens, and its maximum Ψ_{dSC}^{max} decreases with increasing t_b , as if it is smeared. t_b increases the width of the semicircular density of states keeping its area constant and thereby decreases its height. Thus, t_b increases the energy window for fluctuations, i.e. more plaquette eigenstates from higher energies contribute to the solution of the quadruple Bethe lattice, but at the same time the amplitudes of the quantum fluctuations can become smaller. This gives at least an intuition of t_b 's effect, the quantitative details are hidden in the CDMFT self-consistency.

The QCP of the plaquette shifts to smaller μ and smaller U as t' is increased. For $t' = 0.3$, we also find an additional crossover from the spin-doublet $|3, \frac{1}{2}, \frac{X}{Y}\rangle$ to the spin-quadruplet $|3, \frac{3}{2}, M\rangle$, that is recognized by a kink in the phase boundaries around $U \sim 6$. In the quadruple Bethe lattice, at $t_b = 0.2$, in that region PAFM

t'	$\mu_{24}(U_c) = \mu_c$	$\mu_{opt}^{(1)}$	$U_{opt}^{(0)}$	$U_{opt}^{(1)}$
0	0.72	0.51 ± 0.02	2.93	1.79
0.3	0.24	0.62 ± 0.05	1.82	5.04

TABLE I. Fit-coefficients of the linear- t_b models for the optimal chemical potential μ_{opt} and optimal Hubbard interaction U_{opt} for different next-nearest-neighbor hoppings t' . The offset of μ_{opt} , i.e. μ_{24} , is calculated in the isolated plaquette, it is the chemical potential at that $|2, 0, \Gamma\rangle$ and $|4, 0, \Gamma\rangle$ of the isolated plaquette cross.

order is observed. It is spin-3/2 antiferromagnetism of plaquette “supersites”, i.e. a quadruple Bethe lattice of ferromagnetic plaquettes and antiferromagnetic Bethe lattices. The cuprates show many competing orders near the dSC dome, such as stripes and spin/charge density waves, that have also been investigated in the framework of the Hubbard model or its limit, the t - J model. However, it is unclear how the PAFM order found here could be related to those.

AFM is found for $t' = 0.3, t_b = 0.3$ at large μ , close to half-filling, with a relatively small order parameter, but in the considered parameters of Fig. 8 AFM is mostly absent. Heisenberg AFM is promoted by double occupations of sites that occur at half-filling. The effective spin exchange J appears in the strong coupling regime of the Hubbard model, i.e. for large U ^{47,48}. Therefore the predominant absence of AFM within the phase diagrams of Fig. 8 seems reasonable as t_b is small and U has intermediate values. The fact that it appears only at $t' = 0.3$ suggests that t' can cause an effectively enhanced U . A more detailed view on the AFM order will be provided below, in Sec. VIII where we discuss larger t_b .

In the following we locate and study the optimal parameter set $(\mu_{opt}, U_{opt}, t_b^{opt})$ that corresponds to Ψ_{dSC}^{max} using linear fits for fixed $t' = 0$ and $t' = 0.3$. The optimal chemical potential μ_{opt} , that corresponds to Ψ_{dSC}^{max} as a function of U is found on a line in μ - U -plane that is parallel to the line μ_{24} of the plaquette's $|2, 0, \Gamma\rangle$ - $|4, 0, \Gamma\rangle$ -crossing, even if these two are not the groundstates. Fig. 8 shows this for small $0.1 \leq t_b \leq 0.3$. In Fig. 7 we see a linear t_b -dependence of μ at constant filling. We write the linear model to fit the optimal chemical potential for a constant t'

$$\mu_{opt}(U, t_b) \simeq \mu_{24}(U) + \mu_{opt}^{(1)} t_b. \quad (21)$$

$\mu_{24}(U)$ is calculated on the isolated plaquette and the coefficient of the linear shift by t_b , namely $\mu_{opt}^{(1)}$, is fitted to the numerical results of the quadruple Bethe lattice, see Tab. I for the coefficients. The maxima in the doping-dependence of the dSC order parameter $\Psi_{dSC}(\delta)$ have been calculated via quadratic fits to the largest values. The data is presented in Fig. 9 (insets). Fig. 9 shows, that the t_b -dependence of the Ψ_{dSC}^{max} is indeed linear. Furthermore, the extrapolation to $t_b = 0$ points to μ_{24} of the isolated plaquette, that for $U = 4.59, t' = 0$

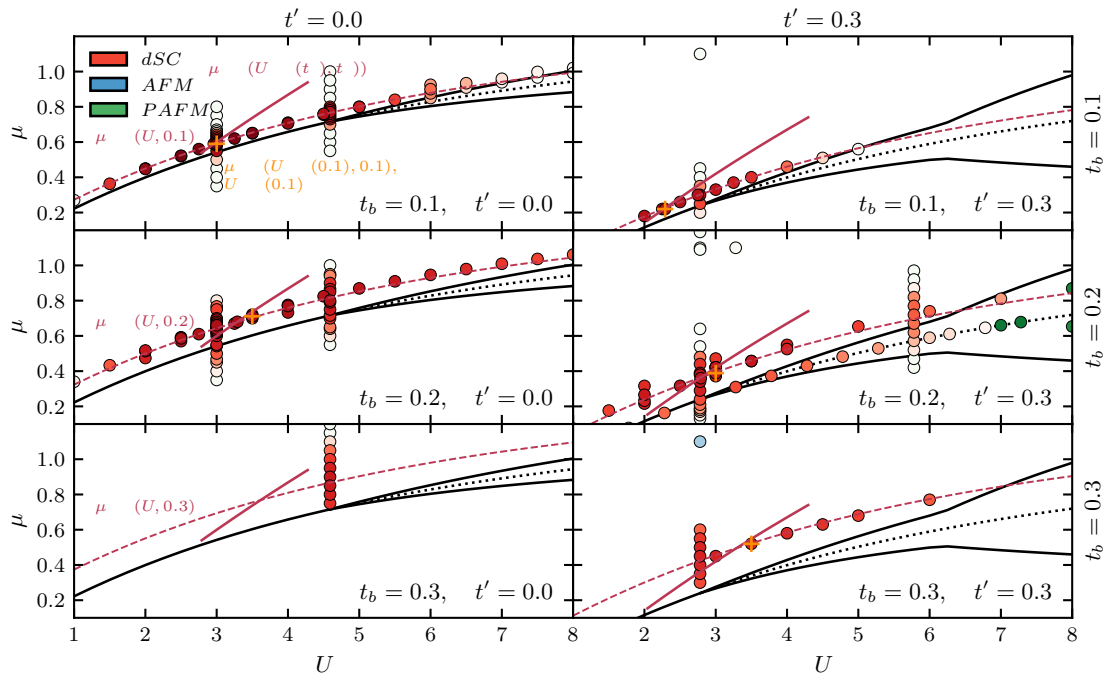


FIG. 8. Phase diagrams of the quadruple Bethe lattice dependent on the chemical potential μ and Hubbard interaction U for several next-nearest-neighbor hoppings t' and Bethe hoppings t_b . Considered spontaneously broken symmetries are d -wave superconductivity (dSC), antiferromagnetism (AFM) and plaquette antiferromagnetism (PAFM). The black lines denote the groundstate crossovers of the regions $N = 2, 3, 4$ (bottom to top) of the isolated plaquette. The dotted black line marks the crossing of the $N = 2, 4$ sector-groundstates of the isolated plaquette. The maximum dSC order value per diagram is marked by “+”. The dashed and solid colored lines correspond to $\mu_{opt}(U, t_b)$ and $U_{opt}(t_b)$ fits corresponding to Ψ_{dSC}^{max} , respectively.

and $U = 2.78$, $t' = 0.3$ is the QCP. Ψ_{dSC}^{max} at $t_b = 0.1$ is very similar for $t' = 0$ and $t' = 0.3$. For very small t_b the quadruple Bethe lattice turns into isolated plaquettes and dSC vanishes.

So far, we have focused on a description in terms of energies and thus on μ rather than the observable hole doping δ . In Fig. 9 (insets) we present Ψ_{dSC} depending on the doping. For small t_b $t' = 0$ and $t' = 0.3$ share a maximum around $\delta \sim 0.15$, that is the optimal doping of cuprates⁵. In particular, for the data of $t' = 0.3$, at that we have also calculated solutions of $t_b = 0.5$, Ψ_{dSC}^{max} shifts towards half-filling. It is remarkable, that the maximum at $\delta \sim 0.15$ is such a stable feature for different t' and U at small $t_b \sim 0.1$, i.e. weakly hybridized plaquettes. Larger t_b make the dSC dome results similar to 2D CDMFT studies at larger temperatures, where the dSC dome is closer to half-filling. In the 2D approximation of CDMFT the hybridization is solely determined by the self-consistency condition and there is no analogue to t_b . The present context can raise the question whether long-range correlations that are neglected by 2D CDMFT can effectively turn the system into more weakly hybridized plaquettes.

With the fit of $\mu_{opt}(U, t_b)$ we can predict optimal doping, next we fit a linear model for optimal Hubbard in-

teraction

$$U_{opt}(t_b) \simeq U_{opt}^{(0)} + U_{opt}^{(1)} t_b, \quad (22)$$

to find the optimal $U_{opt}(t_b)$ that maximizes Ψ_{dSC} along the line described by $\mu_{opt}(U, t_b)$ in the $\mu - U$ phase diagram. But contrary to $\mu_{opt}(U, t_b)$, we need to fit the slope $U_{opt}^{(1)}$ and the offset $U_{opt}^{(0)}$. Furthermore, there is no motivation from the non-interacting case as in the μ_{opt} -fit. We use it only to estimate the position of the maximum Ψ_{dSC}^{max} within the $\mu - U$ phase diagram, also for different t_b . Fig. 10 (top) shows the linear fit of U_{opt} , though only few points are taken into account. The fitted models predict the position, (μ_{opt}, U_{opt}) , of Ψ_{dSC}^{max} dependent on t_b in the $\mu - U$ plane, see Fig. 8.

Along the line of t_b -dependent (U_{opt}, μ_{opt}) the dSC order parameter exhibits a maximum at $t_b = 0.1$, see Fig. 10 (bottom), that is an order of magnitude larger than the temperature $T = 0.01$ and smaller than the plaquette hopping $|t| = 1$. The steep slope of Ψ_{dSC} in Fig. 10 (bottom) at small t_b is difficult to resolve accurately since the filling is very sensitive and small errors in the μ_{opt} -estimate can cause strong noise. The steep slope is caused by the transition of the quadruple Bethe lattice into disconnected plaquettes. The t_b dependence of $U_{opt}(t_b)$ is stronger for $t' = 0.3$ than for $t' = 0$ (Tab. I).

In order to sum up the numerical calculations shown

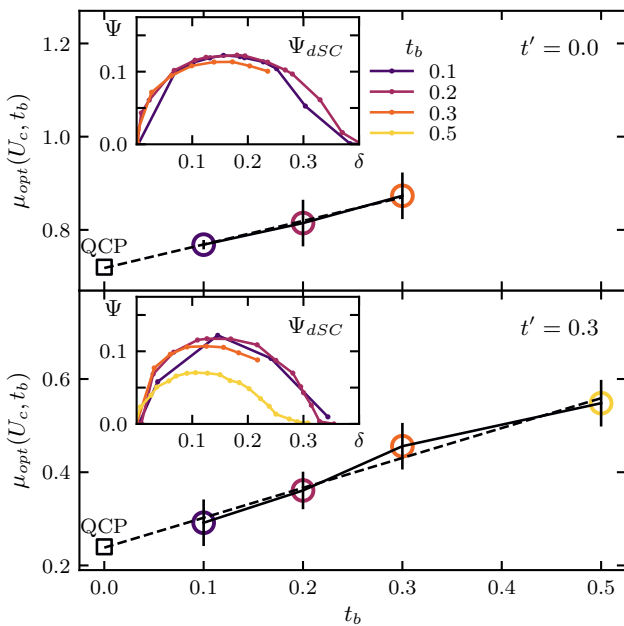


FIG. 9. Chemical potential μ_{opt} , that maximizes the d -wave superconducting order parameter Ψ_{dSC} as a function of the Bethe hopping t_b , $U = U_c$. Linear fits (dashed) are performed for the next-nearest neighbor hoppings $t' = 0$ (top) and $t' = 0.3$ (bottom) separately and are extrapolated to $t_b = 0$. The quantum critical point (QCP) of the isolated plaquette is shown, too. Ψ_{dSC} is also shown as a function of the hole doping δ (insets) for different t_b (color-coded).

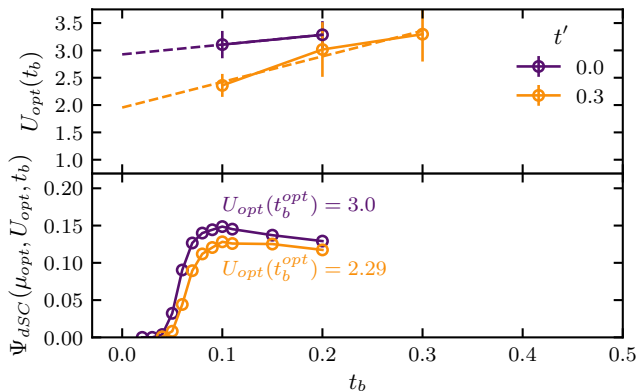


FIG. 10. Top: Linear fit (dashed) of the optimal Hubbard interaction U_{opt} as a function of the Bethe hopping t_b at optimal doping (μ_{opt}). The fit is performed for different next-nearest-neighbor hoppings t' separately. Bottom: d -wave superconducting order parameter along the optimal μ - U -line as a function of t_b .

in this section we present an overview of the fitted models of the quadruple Bethe lattice's μ_{opt} and U_{opt} in the context of the isolated plaquette groundstate phase diagram, see Fig. 11. At small U the plaquette exhibits a transition from $|2, 0, \Gamma\rangle$ to $|4, 0, \Gamma\rangle$ at μ_{24} . For $U > U_c$ this crossover is not a groundstate crossover. However,

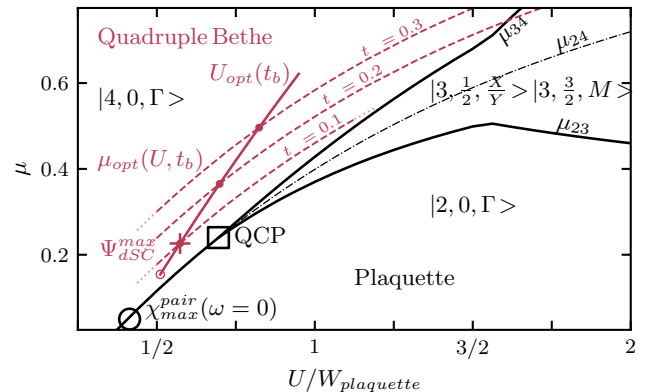


FIG. 11. Chemical potential μ , Hubbard interaction U - phase diagram of the isolated plaquette (black, solid) with the groundstates $|N, S, K\rangle$ ($t = 0.3$). $W_{plaquette}$ is the energy range of the plaquette-hopping. The crossover of $|2, 0, \Gamma\rangle$ and $|4, 0, \Gamma\rangle$ is also shown for $U > U_{QCP}$, where it is not a groundstate crossover (black, dash-dotted). The highly degenerate quantum critical point (QCP) and the maximum of the retarded pairing susceptibility $\chi_{max}^{pair}(\omega = 0)$ of the plaquette are marked. Linear fits of $\mu_{opt}(U, t_b)$ (red, dashed) and $U_{opt}(t_b)$ (red, solid) of the quadruple Bethe lattice are shown. The maximum Ψ_{dSC}^{max} corresponding to the parameter set $(\mu_{opt}, U_{opt}, t_b^{opt})$ is marked by +.

μ_{opt} of the quadruple Bethe lattice is parallel to it, indicating that the optimal plaquette state superposition for dSC requires a certain, t_b -proportional, gapsize between $|2, 0, \Gamma\rangle$ and $|4, 0, \Gamma\rangle$. Upon varying t_b , Ψ_{dSC}^{max} of the quadruple Bethe lattice stays in the $\mu - U$ diagram closer to the QCP than to the maximum of the pairing susceptibility of the isolated plaquette.

The quadruple Bethe lattice effectively provides an environment for the states of the isolated plaquette. Neither of the two distinct points, QCP and χ_{dSC}^{max} , in $\mu - U$ diagram of the isolated plaquette is the optimal parameter set for the maximum of the dSC order parameter of the quadruple Bethe lattice Ψ_{dSC}^{max} . This is due to effective environment shifting dependent on t_b the crucial properties of the QCP, in particular the spectral density peak (Fig. 5), to different values of μ and U . The peak at the Fermi level is due to the $N = 2, 3, 4$ degeneracy at the QCP. We will investigate how this feature is related to Ψ_{dSC}^{max} in Sec. VII. The qualitative behavior around the QCP for different t' are very similar despite the QCP being at different (μ, U) . Thus, at least for small $t_b \sim 0.1$, the dSC properties are governed by the proximity of the QCP. Large $t_b > 0.3$ make the description of the dSC more complicated as transitions between plaquette states other than $|2, 0, \Gamma\rangle$, $|3, \frac{1}{2}, \frac{X}{Y}\rangle$ and $|4, 0, \Gamma\rangle$ become active. Those will also change the optimal doping as shown in Fig. 9.

In Fig. 11 we choose to present U with respect to the energy range of the plaquette hopping $W_{plaquette} = 4|t|$. This ratio is interesting in a sense that the square lattice, that is more accurately applied as a description for

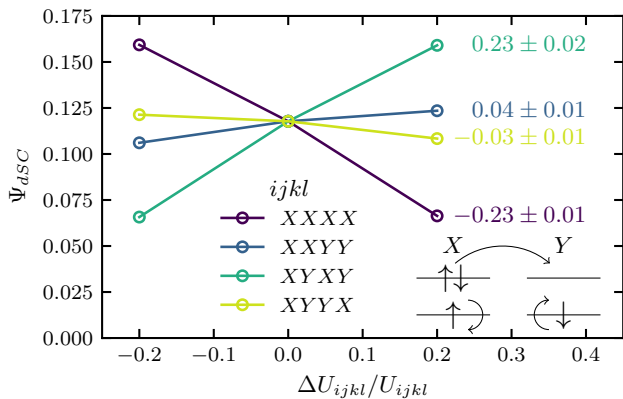


FIG. 12. d -wave superconducting order parameter Ψ_{dSC} as a function of the change in different entries of the Hubbard-interaction ΔU_{ijkl} normalized by its initial value U_{ijkl} ($t' = 0.3$, $t_b = 0.2$, $\delta = 0.15$ and $U = 2.78$). Further shown are slopes of linear fits (right) and an illustration (bottom, right) of the two-particle fluctuations, i.e. pair hopping and spin flip.

the cuprates, has a bandwidth of $W_{2d} = 8|t|$ and this estimated factor of $2 = W_{2d}/W_{\text{plaque}}t$ puts our result in a context with U -induced correlations of Mott physics studied before with (C)DMFT. With this normalization the QCP lies at $U/W_{\text{plaque}} \approx 0.75$ and the maximum dSC order parameter at $U/W_{\text{plaque}} \approx 0.5$, which can be regarded as intermediate coupling strengths⁴⁹.

VI. COMPONENT ANALYSIS OF THE HUBBARD INTERACTION

In Eq. (6) we transform the local interaction U into the plaquette-momentum/orbital basis and observe the existence of many two-particle couplings between the plaquette momenta^{38,40}, that we classify into intra-orbital repulsion, inter-orbital repulsion, spin-flip, pair-hop and correlated hopping terms. In this section we investigate the effect of those on the dSC order, but we restrict the discussion to the X/Y -orbitals, that are close to Fermi level and describe the dSC order parameter.

Regarding the notation we introduce the tensor U_{ijkl} for convenience. Initially all of its values are either “0” or “ $U/4$ ”, see Eq. (6). In Fig. 12 we change U_{ijkl} by 20% ($\Delta U_{ijkl}/U_{ijkl} = \pm 0.2$) and observe its effect on the dSC order parameter. Throughout, we change all terms falling into the same class, e.g. a reduction of U_{XXXX} means also a reduction of U_{YYXX} . The terms of U_{ijkl} , shown in Fig. 12, have the same degeneracy. Also, we adjust μ so that $\delta = 0.15$. Changing certain parts of U_{ijkl} , we can decrease as well as increase Ψ_{dSC} . Whereas pair hoppings (U_{XYXY}) and inter-orbital repulsion (U_{XYYX}) promote the dSC, spin flips (U_{XYYX}) and intra-orbital repulsion (U_{XXXX}) diminish it. By the magnitude of the change in Ψ_{dSC} , we can identify two competitions in

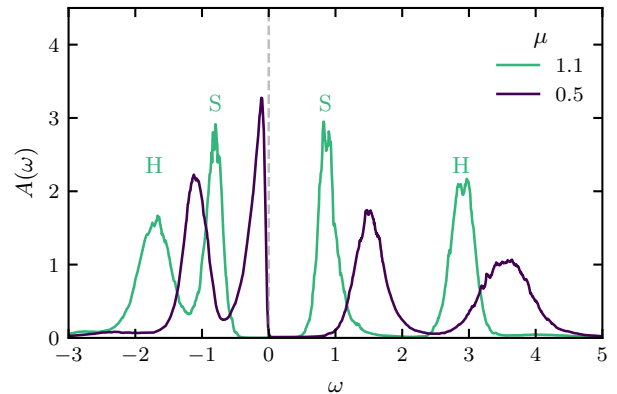


FIG. 13. Spectral function $A(\omega)$ for different chemical potentials μ at approximately half-filling $\delta \approx 0$. For $\mu = 0.5$ we label the one-particle excitations Hubbard (H) and Slater (S) peaks ($t' = 0.3$, $t_b = 0.2$, $U = 2.78$). The analytic continuation is obtained by the stochastic optimization method⁵⁴⁻⁵⁶.

the two-particle processes. First, the pair hopping has the same slope as the negative slope of the intra-orbital repulsion ($U\Delta\Psi_{dSC}/\Delta U \sim 0.23$) and second, the spin flip has the same slope as the negative slope of the inter-orbital repulsion ($U\Delta\Psi_{dSC}/\Delta U \sim 0.04$).

Fig. 12 shows that at $\delta = 0.15$ the fluctuations are characterized by pair hopping and intra-orbital repulsion rather than spin flips and inter-orbital repulsion. Both competitions occur between a density-density and a fluctuation term. The dominant contribution to the dSC stems from the pair hoppings that compete with the intra-orbital repulsion. The two-particle interaction terms in the plaquette orbital basis reminds of the Kanamori interaction of a multi-orbital atom with peculiar values of the Hund’s exchange coupling. Indeed, a supersite formed by only the next-nearest neighbors of the plaquette has been proposed for a unified description of the superconductivity in cuprates and pnictides.⁵⁰

VII. SPECTRAL PROPERTIES & DOPING DEPENDENCE

The cuprates become superconducting upon doping whereas at half-filling they are insulating. The insulating state is of interest as it can exhibit crucial correlations, but without free charge carriers. The theoretical concepts of the quantum spin liquid and the resonating valence bond state originate from this insulating behavior^{51,52}. At low temperatures this insulator is hidden behind antiferromagnetic ordering. Antiferromagnetic correlations and insulating behavior at half-filling can be explained by the Mott insulator and the DMFT¹². The Mott insulator is characterized by a divergence in the mass renormalization of the quasiparticles and has also been suspected to affect the dSC⁵³.

The value of the Hubbard interaction U to model the

cuprates is known only approximately⁴⁹, and it is debatable whether dSC is a weak- or strong-coupling phenomenon. In Fig. 13 we present the density of states of the quadruple Bethe lattice at $\delta \approx 0$. It is obtained by the stochastic optimization analytic continuation^{54–56} of the (impurity) Green function. At $\mu = 1.1$ we observe almost symmetric gap edges formed by two Slater peaks, and with decreasing μ , but still within the gap, so that $\delta \approx 0$, an asymmetry develops. The hole excitation peak becomes sharper and shifts towards Fermi level. A structure similar to this four-peak structure of two Slater peaks within the Hubbard gap has been found in a prior study for $t' = 0$, and is characteristic of Slater physics that include short-range singlet correlations^{33,57,58}. Correlated singlets also appear in the double Bethe lattice^{28,29}, and define the low-energy excitations at intermediate coupling strengths.

The hole-doped copper-oxide superconductors have a peculiar phase of the pseudogap at underdoping and temperatures above T_c . CDMFT studies have shown that its opening can be related to a topological Lifshitz transition at that the Fermi surface turns from electron- to hole-like^{59,60}. It can be defined as the point at that the renormalized quasiparticle energy of the $K = X/Y$ points

$$\tilde{\epsilon}_K = Z_K(t_K^p + \text{Re} \Sigma_K(0)) \quad (23)$$

cross the Fermi level. Z_K is the quasiparticle residue. The importance of a particle-hole symmetry has also been pointed out in the dSC state³². Particularly for the Bethe lattice model we can also define a renormalized band model for the semicircular density of states²⁹

$$\tilde{W}_K = Z_K 4t_b. \quad (24)$$

We compare the plaquette momenta of the quadruple Bethe lattice to the high-symmetry points of the Brillouin zone of the square lattice, and thus the Lifshitz transition is defined by $\tilde{\epsilon}_{X/Y}$.

Fig. 14 shows the evolution of the quasiparticle residue Z and the renormalized quasiparticle bands ($\tilde{W}, \tilde{\epsilon}$) with decreasing μ . We use it to continuously tune the insulator into the hole-doped regime. The approximate half-filling region $\delta \approx 0$ on the hole-doped side extends over a large region of $1.1 > \mu > 0.5$. The role of μ is here reminiscent of a field effect transistor experiment in that the spectral properties of the hole excitations change due to the gate voltage.

The Mott phase¹² is found near $\mu = 1.1$, in the center of the gap, where the quasiparticle residue vanishes $Z_X \approx 0$. The system restores coherence in the plaquette orbital X with decreasing μ . The renormalized band model assumes that the self-energy makes only small contributions and renormalizes the quasiparticles of the non-interacting system. For the Mott insulator this assumption is not fulfilled. But for $\mu \lesssim 0.8$ we observe that the renormalized band model agrees with the spectral function from analytic continuation (Fig. 13) as both describe the low-energy hole excitation that shifts towards Fermi

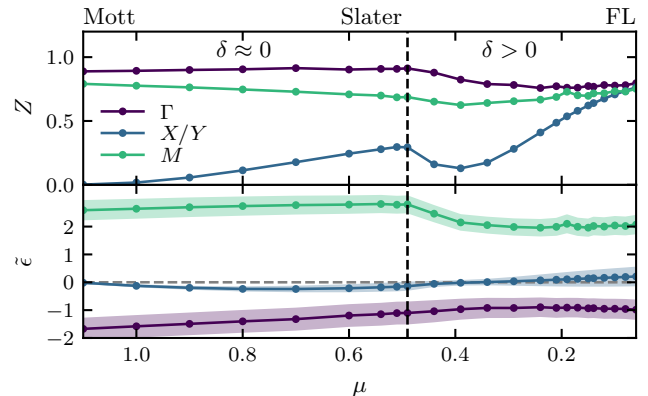


FIG. 14. Quasiparticle residue Z (top) and renormalized quasiparticle energy $\tilde{\epsilon}$ and bandwidth \tilde{W} (bottom) of the normal state as functions of the chemical potential μ , that at a certain value (dashed vertical line) hole dopes δ the system. The K -differentiation of Z is absent in the Fermi liquid (FL) ($t' = 0.3$, $t_b = 0.2$ and $U = 2.78$).

level. According to the renormalized band model, the spectral properties change and the Mott insulator develops a correlated Slater peak.

In the hole-doped regime $\delta > 0$, we have performed calculations of the normal state for that dSC order is suppressed (Fig. 14). Thereby we can investigate quasiparticles and their contribution to the dSC mechanism. Z_X has a local minimum at the Lifshitz transition^{59,60}, at that $\tilde{\epsilon}_X = 0$. It is related to a strong scattering rate and suggests an avoided criticality³² mechanism of dSC. In the overdoped region the Fermi surface is electron-like and for large hole dopings the plaquette momentum differentiation in Z_K is lifted. In this case, a DMFT description of a (site-)local self-energy can be sufficient for a description, and the system enters the Fermi liquid regime.

In Fig. 15 we show the plaquette-momentum resolved spectral function. It is obtained by analytic continuation of the (local lattice) Green function and shown also for the symmetry-broken dSC state. The Slater peaks describe excitations with momentum X/Y . The splitting of upper peaks and lower peaks is of the order of U . Decreasing the chemical potential shifts the lower Slater peak to Fermi level, and the dSC order originates from the lower Slater peak, i.e. the dSC gap appears with the doping of the Slater peak, see Fig. 15. The spectral function of Fig. 15 looks very similar to Fig. 5, so that it is possible to relate the plaquette transitions $|4, 0, \Gamma\rangle \rightarrow |3, \frac{1}{2}, \frac{X}{Y}\rangle$ and $|4, 0, \Gamma\rangle \rightarrow |3, \frac{1}{2}, \Gamma\rangle$ to the lower Slater and Hubbard peaks, respectively. It points out the crucial part of $|3, \frac{1}{2}, \frac{X}{Y}\rangle$, that provides low-energy transitions for the electrons that will form the dSC pairs. Further does $|3, \frac{1}{2}, \frac{X}{Y}\rangle$ provide a single-particle transition to $|2, 0, \Gamma\rangle$ and the pairs are formed by the latter and $|4, 0, \Gamma\rangle$ (Fig. 3).

Fig. 16 (a) shows the doping dependence of the dSC

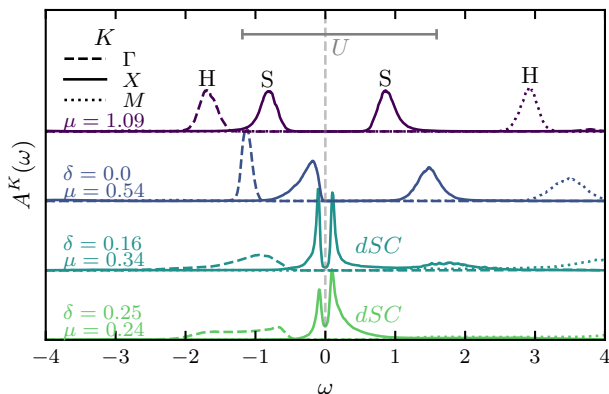


FIG. 15. Momentum resolved spectral function $A^K(\omega)$ for different dopings δ (corresponding to chemical potentials μ) showing a four-peak structure at half-filling ($\delta = 0$) of Hubbard (H) and Slater (S) peaks and for hole-dopings δ the d -wave superconducting gap ($t' = 0.3$, $t_b = 0.2$, $U = 2.78$). The analytic continuation is obtained by the stochastic optimization method^{54–56}.

order for $t_b = 0.2$. We characterize the maximum and the endpoints by features in the correlation functions of the normal state with suppressed dSC order (Fig. 16 (b)-(d)). At half-filling we find the two different solutions of insulators as discussed in Fig. 14. In the underdoped regime the single-particle excitations are hole-like and the quasiparticle bandwidth W_X is strongly renormalized. The renormalization is particularly strong at the Lifshitz transition at that the Fermi surface changes from hole-like to particle-like. At this point is also the maximum of the dSC dome. At overdoping the quasiparticle of the X -orbital becomes more Fermi liquid-like and the quasiparticle energy shifts away from Fermi level. The renormalized bandwidth broadens and quasiparticle states remain at Fermi level at the overdoping end of the dSC dome.

In the overdoped regime the dynamics of the single-particle correlations do not show any peculiar feature. In order to understand this regime better we present the static two-particle correlation functions in Fig. 16 (c). In Eq. (6) we have discussed the transformation of the local Coulomb repulsion into plaquette momentum basis. The fluctuation terms between X and Y only, i.e. pair hopping and spinflip terms, appear symmetrically in the interaction, but the dependence of Ψ_{dSC} is stronger on the pair hopping part of the interaction, see Sec. VI. At the overdoping end of the dSC dome pair hopping and spin flip correlations between X and Y are equally weak.

Due to the small Bethe hopping (hybridization) the dSC phase is mostly governed by a few low-energy cluster eigenstates. Fig. 16 (d) shows that the dSC order occurs only where the Boltzmann weights of $|3, \frac{1}{2}, \frac{X}{Y}\rangle$ and $|2, 0, \Gamma\rangle$ are non-zero. The large pair hopping correlations stem mostly from $|4, 0, \Gamma\rangle$. Only a combination of both, $|3, \frac{1}{2}, \frac{X}{Y}\rangle$ which produces a peak at Fermi level and pair hopping correlations, results in the non-trivial dome-like

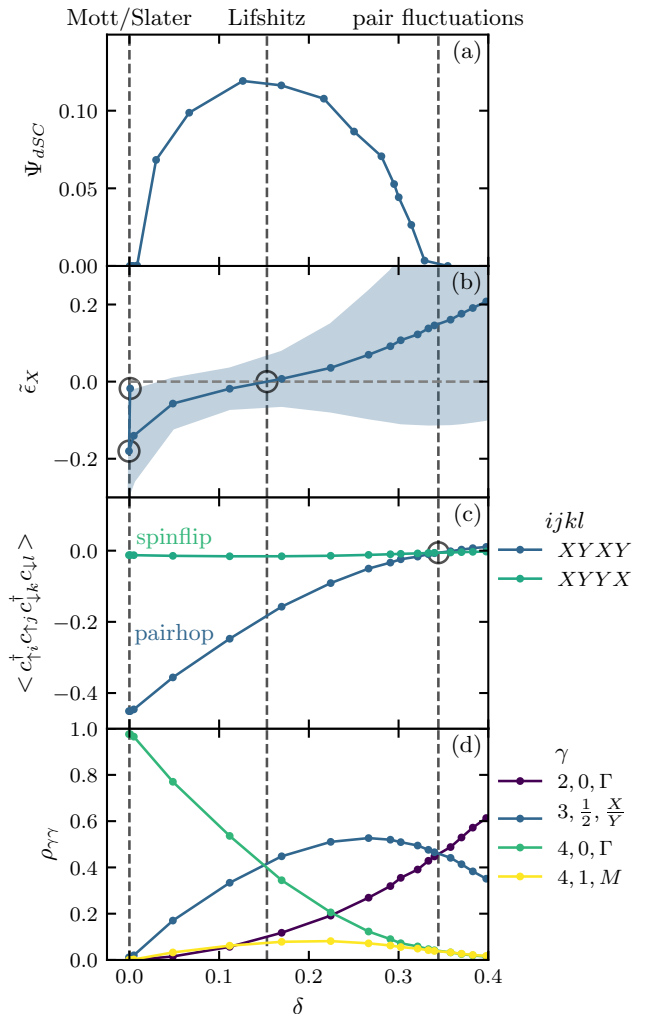


FIG. 16. d -wave superconducting order parameter Ψ_{dSC} of the symmetry-broken state (a), renormalized quasiparticle band(width) $\bar{\epsilon}_X$ of the normal state (b), static two-particle correlation functions $\langle \dots \rangle$ of the normal state (c) and reduced density matrix of the normal state ρ with plaquette many-body state indices γ (d) as functions of hole-doping δ . Points of certain features in the doping dependence are marked by circles. $t' = 0.3$, $t_b = 0.2$, $U = 2.78$.

structure of the dSC order. At the overdoping end of the dSC dome the Boltzmann weight of the spin-triplet $|4, 1, M\rangle$ exceeds that of $|4, 0, \Gamma\rangle$, and pair hoppings correlations vanish which suppresses the dSC.

Fig. 17 is a detailed view of Fig. 15 with more values for δ . It shows the dSC gap of the one-particle spectral function. Finite hole doping and dSC order set in with a sharp peak below Fermi level and a small peak above. The latter grows until at optimal doping the dSC gap is approximately particle-hole symmetric. From optimal doping to overdoping the peak of hole excitations shifts through the Fermi level increasing spectral weight at Fermi level until the gap is closed and dSC order is absent. In contrast to the lower edge the upper edge of

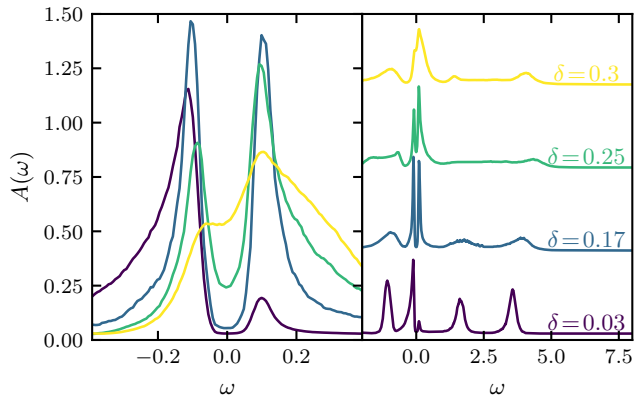


FIG. 17. Local density of states for different hole-dopings δ in the dSC state ($t' = 0.3$, $t_b = 0.2$, $U = 2.78$). The color code in the zoom-in (left) is the same as in the overview (right). The analytic continuation is obtained by the stochastic optimization method^{54–56}.

the dSC gap does not shift with doping. It suggests that two distinct mechanisms contribute to the formation of the dSC gap in the one-particle spectral function⁶¹.

VIII. SUPERCONDUCTIVITY & ANTIFERROMAGNETISM

Using a two-by-two plaquette as cluster, we can describe AFM and dSC order on equal footing, and both are relevant for the phase diagram of the cuprates. In Fig. 18 we observe that it is largest at half-filling, at that according to experimental findings, the Néel temperature is also largest. In contrast to the hole doped cuprates we find coexistence^{62,63} of AFM and dSC order up to $\delta = 0.25$ which is a well-known feature of CDMFT^{15,64–66} and is expected to arise from the neglecting of long-ranged correlations. In fact, already an eight-site cluster can suppress dSC in proximity of half-filling⁶⁷.

The maximum value of the AFM order parameter is $\Psi_{AFM} = 0.25$, which is only half the magnitude of the plaquette’s full magnetization. This is the case, because two electrons are locked in the singlet of the Γ -orbital, that is fully occupied and doesn’t touch the Fermi-level, see Fig. 6. Finite values for Ψ_{AFM} we find only for $t_b \geq 0.3$, it increases sharply as function of t_b and saturates around $t_b = 0.4$ at $\Psi_{AFM} = 0.25$. This is very different from the dSC order parameter, that has its maximum around $t_b = 0.1$ (Fig. 11). It seems, that for the AFM it is necessary to have a certain minimal spin exchange interaction not only within but also between plaquettes. In contrast, dSC requires a certain plaquette eigenstate configuration and a much weaker plaquette hybridization. To some extent this asymmetry can be understood regarding the non-interacting density of states (Fig. 6 and Eq. (14)). While dSC occurs entirely within X and Y , AFM order couples also Γ and M , which are split and farther from the Fermi level.

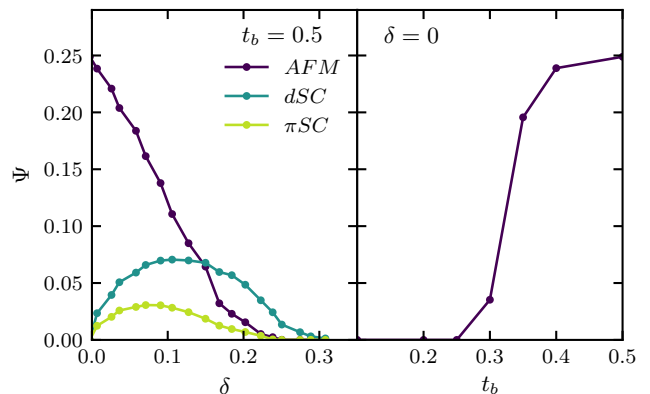


FIG. 18. Order parameters Ψ of antiferromagnetism (AFM), d -wave superconductivity (dSC) and spin-triplet superconductivity (π SC) dependent on hole doping δ for Bethe hopping $t_b = 0.5$ (left) and dependent on t_b for half-filling $\delta = 0$ (right) ($U = 2.78$, $t' = 0.3$).

Moreover, we observe spin-triplet superconductivity^{66,68} (π SC) with the order parameter

$$\Psi_{\pi SC} = \frac{1}{4^2} \sum_{RR'} (\cos[X(R-R')] - \cos[Y(R-R')]) \times e^{iMR'} \langle c_{R\uparrow} c_{R'\downarrow} + c_{R\downarrow} c_{R'\uparrow} \rangle. \quad (25)$$

It is described by entries of the correlation functions that are off-diagonal in Nambu and plaquette-momentum space, see Eq. (14). Further, a comparison with Eq. (20) shows also that it is a combination of AFM and dSC as it breaks the spatial symmetries of the plaquette according to AFM and dSC. Finally, the symmetry upon spin-exchange can be seen explicitly in Eq. (25) and stresses the spin-triplet character. We find non-zero values for $\Psi_{\pi SC}$ only at dopings for the the quadruple Bethe lattice also shows coexistence of dSC and AFM. Thus π SC is a result of the interplay between dSC and AFM.

IX. EXTENDED BETHE LATTICE HOPPING

To this point the Bethe hopping exists only within one Bethe lattice and is represented by a scalar. In this section we introduce the Bethe-hopping matrix in plaquette-site space

$$\underline{t}_b = \begin{pmatrix} t_b & 0 & 0 & t'_b \\ 0 & t_b & t'_b & 0 \\ 0 & t'_b & t_b & 0 \\ t'_b & 0 & 0 & t_b \end{pmatrix} \quad (26)$$

with the extended Bethe-lattice hopping t'_b , that appears in entries, that in the case of the plaquette hopping matrix t_b are occupied by the next-nearest neighbor hopping. It means, that for t'_b the transition between plaquettes is accompanied by a transition to the next-nearest

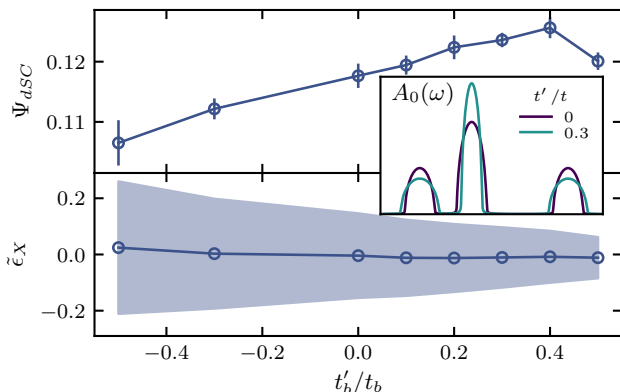


FIG. 19. Superconducting order parameter Ψ_{dSC} (top) and renormalized quasiparticle energy $\tilde{\epsilon}_X$ (bottom) as functions of the extended Bethe lattice hopping at $\delta = 0.15$ ($U = 2.78$, $t' = 0.3$, $t_b = 0.2$). The colored area marks the renormalized quasiparticle bandwidth \tilde{W} . Non-Interacting semicircular density of states for different next-nearest neighbor Bethe lattice hoppings (inset).

neighbor of the target plaquette. The effect of the non-diagonal terms in the \underline{t}_b -matrix is the finetuning of the widths of the semicirculars independently. The nearest neighbor components would affect only the widths of the Γ and M bands, so we have set them to zero for simplicity.

The CDMFT self-consistency becomes

$$G^{-1}(i\omega_n) = (i\omega_n + \mu) \mathbb{1} - t^p - \underline{t}_b G(i\omega_n) \underline{t}_b \quad (27)$$

with the quantities being matrices in plaquette site space (Nambu degrees of freedom are omitted for convenience), and the last term are matrix products of \underline{t}_b and G .

The transformation Eq. (4) must be applied to \underline{t}_b , too. Thus it gets diagonalized. The non-interacting semicircular density of states changes so that the width and height of G , M differ from those of X , Y , but they remain semicirculars, see Fig. 19 (inset). Depending on the sign of t'_b/t_b the height increases and the width decreases or vice versa. Despite the absence of a real divergence the effect of an increased density of states of X and Y can be interesting in the context of the van Hove singularity^{69,70} in the square lattice.

Fig. 19 shows that the dSC order parameter increases with a decreasing quasiparticle bandwidth. The doping is set to $\delta = 0.15$ that remains independent of t'_b related to the Lifshitz transition, i.e. the quasiparticle energy $\tilde{\epsilon}_X$ is almost constant. The change in Ψ_{dSC} is small, and therefore in Fig. 19 we also present errorbars, that are calculated as the largest absolute deviation of eight values of two CDMFT-loops with local Green functions that by symmetry have four entries of the order parameter. The quasiparticle residue of the presented calculations only weakly depends on t'_b , i.e. stays $Z_X = 0.38 \pm 0.02$. Therefore the change of the quasiparticle's bandwidth with t'_b is almost entirely due to the renormalization of the non-interacting X/Y -band.

The modification of the semicircular density of states by t'_b is small and finite, but it already shows an enhancing effect on Ψ_{dSC} . The van Hove singularity corresponds to an infinite density of states and can potentially enhance that effect much more. The role of the next-nearest neighbor hopping t' in the cuprates is cumbersome. Whereas a comparison of bandstructure calculations with experiments show a finite value for t' as the optimal one⁷¹, calculations in the framework of strong correlations are not able to confirm this by including only local correlations. First, we observe that t' shifts the quantum critical point of the plaquette, which in the quadruple Bethe lattice is in proximity to the maximum Ψ_{dSC} , to smaller U . And second, we find that a hopping similar to t' , i.e. t'_b , can have an enhancing effect on Ψ_{dSC} . It reduces effectively the bandwidth of X towards the optimal value $t_b \approx 0.1$ (Fig. 10). Finally, it is important to note that the diminishing effect of the next-nearest neighbor hopping in CDMFT studies of the square lattice is not necessarily a contradiction with bandstructure calculations on cuprates, since it may also indirectly support dSC by suppressing other, competing, orders e.g. stripes²³.

X. CONCLUSION

We have formulated the CDMFT self-consistency, Eq. (10), that solves the quadruple Bethe lattice exactly, also in the d -wave superconducting state. An analysis of the isolated two-by-two cluster has shown that this plaquette is even without an environment unstable towards dSC order. The coupling to other plaquettes in the infinite dimensional quadruple Bethe lattice allows for the spontaneous symmetry breaking. dSC order is found in proximity of a QCP of the plaquette in the μ - U diagram, where the plaquette eigenstates $|2, 0, \Gamma\rangle$, $|3, \frac{1}{2}, \frac{X}{Y}\rangle$ and $|4, 0, \Gamma\rangle$ cross. The optimal value for the parameter that controls the hybridization of plaquettes is $t_b = 0.1$ with the optimal doping $\delta = 0.15$. The latter has also been measured in experiments on the cuprates.

The dSC dome of the doping phase diagram lies next to a half-filling state with a vanishing quasiparticle residue, characteristic of the Mott insulator. Moreover, at half-filling the renormalized quasiparticle picture shows a crossover to an insulator with a correlated Slater peak with decreasing μ . The hole excitations corresponding to the Slater peak occur around the energy of the $|4, 0, \Gamma\rangle \rightarrow |3, \frac{1}{2}, \frac{X}{Y}\rangle$ -transition of the isolated plaquette. At hole doping this hole excitation forms the superconducting gap. The small density of states at Fermi level restricts the local pair formation in the underdoped regime, a Lifshitz transition occurs at optimal doping, and at overdoping the superconductivity is suppressed by the vanishing of the two-particle pair-hopping correlations.

For large $t_b = 0.5$ the model exhibits AFM that coexists with dSC order. Since the AFM does not exist at $t_b = 0.1$ this additional parameter allows for a disentangled

glement of these two orders. It can be used to model effects beyond the cluster effectively, e.g. by an increase of the non-interacting density of states at Fermi level, reminiscent of a van Hove singularity. The latter can enhance the dSC. Additionally, in the coexistence regime of dSC and AFM exists a spin-triplet type of superconductivity, π SC. Whereas AFM is staggered within each of the four Bethe lattices of the quadruple Bethe lattice, dSC and π SC are homogenous in those.

ACKNOWLEDGMENTS

We thank A. Georges and A. Millis for discussions. MH, SB and AIL acknowledge support by the Cluster of Excellence 'Advanced Imaging of Matter' of the Deutsche Forschungsgemeinschaft (DFG) - EXC 2056 - project ID 390715994 and by the DFG SFB 925. MIK acknowledges financial support from NWO via Spinoza Prize. The computations were performed with resources provided by the North-German Supercomputing Alliance (HLRN).

- ¹ J. G. Bednorz and K. A. Müller, *Zeitschrift für Physik B Condensed Matter* **64**, 189 (1986).
- ² D. A. Wollman, D. J. Van Harlingen, W. C. Lee, D. M. Ginsberg, and A. J. Leggett, *Phys. Rev. Lett.* **71**, 2134 (1993).
- ³ V. J. Emery and S. A. Kivelson, *Nature* **374**, 434 EP (1995).
- ⁴ E. Fradkin, S. A. Kivelson, and J. M. Tranquada, *Rev. Mod. Phys.* **87**, 457 (2015).
- ⁵ A. Damascelli, Z. Hussain, and Z.-X. Shen, *Rev. Mod. Phys.* **75**, 473 (2003).
- ⁶ M. Gurvitch and A. T. Fiory, *Phys. Rev. Lett.* **59**, 1337 (1987).
- ⁷ C. Renner, B. Revaz, J.-Y. Genoud, K. Kadowaki, and O. Fischer, *Phys. Rev. Lett.* **80**, 149 (1998).
- ⁸ J. Hubbard, *Proceedings of the Royal Society of London A: Mathematical, Physical and Engineering Sciences* **276**, 238 (1963).
- ⁹ F. C. Zhang and T. M. Rice, *Phys. Rev. B* **37**, 3759 (1988).
- ¹⁰ E. Dagotto, *Rev. Mod. Phys.* **66**, 763 (1994).
- ¹¹ E. H. Lieb and F. Y. Wu, *Phys. Rev. Lett.* **20**, 1445 (1968).
- ¹² A. Georges, G. Kotliar, W. Krauth, and M. J. Rozenberg, *Rev. Mod. Phys.* **68**, 13 (1996).
- ¹³ M. Imada, A. Fujimori, and Y. Tokura, *Rev. Mod. Phys.* **70**, 1039 (1998).
- ¹⁴ M. Fleck, A. I. Liechtenstein, A. M. Oleś, L. Hedin, and V. I. Anisimov, *Phys. Rev. Lett.* **80**, 2393 (1998).
- ¹⁵ A. I. Liechtenstein and M. I. Katsnelson, *Phys. Rev. B* **62**, R9283 (2000).
- ¹⁶ T. Maier, M. Jarrell, T. Pruschke, and M. H. Hettler, *Rev. Mod. Phys.* **77**, 1027 (2005).
- ¹⁷ G. Kotliar, S. Y. Savrasov, K. Haule, V. S. Oudovenko, O. Parcollet, and C. A. Marianetti, *Rev. Mod. Phys.* **78**, 865 (2006).
- ¹⁸ G. Biroli, O. Parcollet, and G. Kotliar, *Phys. Rev. B* **69**, 205108 (2004).
- ¹⁹ J. Vučićević, N. Wentzell, M. Ferrero, and O. Parcollet, *Phys. Rev. B* **97**, 125141 (2018).
- ²⁰ E. Gull, M. Ferrero, O. Parcollet, A. Georges, and A. J. Millis, *Phys. Rev. B* **82**, 155101 (2010).
- ²¹ S. Sakai, G. Sangiovanni, M. Civelli, Y. Motome, K. Held, and M. Imada, *Phys. Rev. B* **85**, 035102 (2012).
- ²² B.-X. Zheng, C.-M. Chung, P. Corboz, G. Ehlers, M.-P. Qin, R. M. Noack, H. Shi, S. R. White, S. Zhang, and G. K.-L. Chan, *Science* **358**, 1155 (2017).
- ²³ H.-C. Jiang and T. P. Devereaux, *arXiv e-prints*, arXiv:1806.01465 (2018).
- ²⁴ M. J. Rozenberg, R. Chitra, and G. Kotliar, *Phys. Rev. Lett.* **83**, 3498 (1999).
- ²⁵ R. Bulla, T. A. Costi, and D. Vollhardt, *Phys. Rev. B* **64**, 045103 (2001).
- ²⁶ M. Eckstein, M. Kollar, K. Byczuk, and D. Vollhardt, *Phys. Rev. B* **71**, 235119 (2005).
- ²⁷ G. Moeller, V. Dobrosavljević, and A. E. Ruckenstein, *Phys. Rev. B* **59**, 6846 (1999).
- ²⁸ H. Hafermann, M. I. Katsnelson, and A. I. Liechtenstein, *EPL (Europhysics Letters)* **85**, 37006 (2009).
- ²⁹ O. Nájera, M. Civelli, V. Dobrosavljević, and M. J. Rozenberg, *Phys. Rev. B* **97**, 045108 (2018).
- ³⁰ M. Harland, M. I. Katsnelson, and A. I. Liechtenstein, *Phys. Rev. B* **94**, 125133 (2016).
- ³¹ E. Altman and A. Auerbach, *Phys. Rev. B* **65**, 104508 (2002).
- ³² K. Haule and G. Kotliar, *Phys. Rev. B* **76**, 092503 (2007).
- ³³ E. Gull, P. Werner, X. Wang, M. Troyer, and A. J. Millis, *EPL (Europhysics Letters)* **84**, 37009 (2008).
- ³⁴ M. Ferrero, P. S. Cornaglia, L. De Leo, O. Parcollet, G. Kotliar, and A. Georges, *Phys. Rev. B* **80**, 064501 (2009).
- ³⁵ G. Sordi, K. Haule, and A.-M. S. Tremblay, *Phys. Rev. Lett.* **104**, 226402 (2010).
- ³⁶ K. Mielson, E. Khatami, D. Galanakis, A. Macridin, J. Moreno, and M. Jarrell, *Phys. Rev. B* **80**, 140505 (2009).
- ³⁷ N. S. Vidhyadhiraja, A. Macridin, C. Şen, M. Jarrell, and M. Ma, *Phys. Rev. Lett.* **102**, 206407 (2009).
- ³⁸ J. Merino and O. Gunnarsson, *Phys. Rev. B* **89**, 245130 (2014).
- ³⁹ O. Gunnarsson, T. Schäfer, J. P. F. LeBlanc, E. Gull, J. Merino, G. Sangiovanni, G. Rohringer, and A. Toschi, *Phys. Rev. Lett.* **114**, 236402 (2015).
- ⁴⁰ O. Gunnarsson, J. Merino, T. Schäfer, G. Sangiovanni, G. Rohringer, and A. Toschi, *Phys. Rev. B* **97**, 125134 (2018).
- ⁴¹ T. Maier, M. Jarrell, T. Pruschke, and J. Keller, *Phys. Rev. Lett.* **85**, 1524 (2000).
- ⁴² P. Werner and A. J. Millis, *Phys. Rev. B* **74**, 155107 (2006).
- ⁴³ P. Werner, A. Comanac, L. de' Medici, M. Troyer, and A. J. Millis, *Phys. Rev. Lett.* **97**, 076405 (2006).
- ⁴⁴ E. Gull, A. J. Millis, A. I. Liechtenstein, A. N. Rubtsov, M. Troyer, and P. Werner, *Rev. Mod. Phys.* **83**, 349 (2011).
- ⁴⁵ O. Parcollet, M. Ferrero, T. Ayrál, H. Hafermann, I. Krivenko, L. Messio, and P. Seth, *Computer Physics Communications* **196**, 398 (2015).
- ⁴⁶ P. Seth, I. Krivenko, M. Ferrero, and O. Parcollet, *Computer Physics Communications* **200**, 274 (2016).

- ⁴⁷ W. F. Brinkman and T. M. Rice, Phys. Rev. B **2**, 1324 (1970).
- ⁴⁸ T. Pruschke and R. Zitzler, Journal of Physics: Condensed Matter **15**, 7867 (2003).
- ⁴⁹ A. Comanac, L. de' Medici, M. Capone, and A. J. Millis, Nature Physics **4**, 287 EP (2008).
- ⁵⁰ P. Werner, S. Hoshino, and H. Shinaoka, Phys. Rev. B **94**, 245134 (2016).
- ⁵¹ P. A. Lee, N. Nagaosa, and X.-G. Wen, Rev. Mod. Phys. **78**, 17 (2006).
- ⁵² B. Kyung and A.-M. S. Tremblay, Phys. Rev. Lett. **97**, 046402 (2006).
- ⁵³ G. Sordi, P. Sémon, K. Haule, and A.-M. S. Tremblay, Phys. Rev. Lett. **108**, 216401 (2012).
- ⁵⁴ I. Krivenko and M. Harland, Computer Physics Communications **239**, 166 (2019).
- ⁵⁵ A. S. Mishchenko, N. V. Prokof'ev, A. Sakamoto, and B. V. Svistunov, Phys. Rev. B **62**, 6317 (2000).
- ⁵⁶ E. Pavarini, E. Koch, F. Anders, and M. E. . Jarrell, *Correlated electrons: from models to materials*, Schriften des Forschungszentrums Jülich. Reihe Modeling and simulation, Vol. 2 (Forschungszentrum Jülich GmbH, Jülich, 2012) p. getr. Paginierung, record converted from JUWEL: 18.07.2013.
- ⁵⁷ H. Park, K. Haule, and G. Kotliar, Phys. Rev. Lett. **101**, 186403 (2008).
- ⁵⁸ A. Go and A. J. Millis, Phys. Rev. Lett. **114**, 016402 (2015).
- ⁵⁹ W. Wu, M. S. Scheurer, S. Chatterjee, S. Sachdev, A. Georges, and M. Ferrero, Phys. Rev. X **8**, 021048 (2018).
- ⁶⁰ H. Bragança, S. Sakai, M. C. O. Aguiar, and M. Civelli, Phys. Rev. Lett. **120**, 067002 (2018).
- ⁶¹ M. Civelli, M. Capone, A. Georges, K. Haule, O. Parcollet, T. D. Stanescu, and G. Kotliar, Phys. Rev. Lett. **100**, 046402 (2008).
- ⁶² E. Demler, W. Hanke, and S.-C. Zhang, Rev. Mod. Phys. **76**, 909 (2004).
- ⁶³ D. E. Almeida, R. M. Fernandes, and E. Miranda, Phys. Rev. B **96**, 014514 (2017).
- ⁶⁴ M. Capone and G. Kotliar, Phys. Rev. B **74**, 054513 (2006).
- ⁶⁵ S. S. Kancharla, B. Kyung, D. Sénéchal, M. Civelli, M. Capone, G. Kotliar, and A.-M. S. Tremblay, Phys. Rev. B **77**, 184516 (2008).
- ⁶⁶ A. Foley, S. Verret, A. M. S. Tremblay, and D. Sénéchal, ArXiv e-prints , arXiv:1811.12363 (2018), arXiv:1811.12363 [cond-mat.str-el].
- ⁶⁷ E. Gull, O. Parcollet, and A. J. Millis, Phys. Rev. Lett. **110**, 216405 (2013).
- ⁶⁸ X. Chen, J. P. F. LeBlanc, and E. Gull, Phys. Rev. Lett. **115**, 116402 (2015).
- ⁶⁹ R. Markiewicz, Journal of Physics and Chemistry of Solids **58**, 1179 (1997).
- ⁷⁰ A. Piriou, N. Jenkins, C. Berthod, I. Maggio-Aprile, and Ø. Fischer, Nature Communications **2**, 221 EP (2011), article.
- ⁷¹ E. Pavarini, I. Dasgupta, T. Saha-Dasgupta, O. Jepsen, and O. K. Andersen, Phys. Rev. Lett. **87**, 047003 (2001).

3.5.3 Complex network analysis

Following the idea of a bottom-up approach for a theory of high-temperature superconductivity based on the two-by-two plaquette, a reasonable step is to couple several plaquettes. In order to preserve the X/Y point group symmetry of the two-by-two plaquette, the smallest finite size system of coupled two-by-two plaquettes is the four-by-four cluster (for this part the term “plaquette” is reserved for the two-by-two case for convenience). The question that is addressed by this setup is how do the environmental plaquettes change the properties of a plaquette. For a plaquette theory of high-temperature superconductivity the crucial correlations of the plaquette have to persist in the lattice. The correlations of the plaquette’s quantum critical point are particularly important as they lead to the superconducting state in the case of the quadruple Bethe lattice and plaquette-impurity environments. Technically, the difficulty lies in the fact that the quantum critical point in the plaquette has been identified using many-body states and there is no correspondence from a four-site cluster with a 4^4 -size Fockspace to a sixteen-site cluster with a 4^{16} -size Fockspace.

A key component of the resonating valence bond state is the quantum superposition of many valence bond configurations, which by themselves are already superpositions. The quantum superpositions are contained in the wavefunction, precise information on the nature of these entanglement properties get lost to some extent in the calculation of observables, although they have an impact on the observables. The coefficients of the wavefunction depend on the single-particle basis that is chosen to formulate a setup. In contrast, the observables are basis independent. The goal is to find a quantity, or quantities, that map the inter-plaquette correlations including entanglement properties to a single number, at best basis independent. This has been approached by the use of tools from information theory, such as mutual information, disparity and others [161, 162]. It has been shown that using tools from information theory can help detect quantum criticality, albeit in the context of one-dimensional spin chains [163, 164].

The starting point for the definition of many such quantities is the von Neumann entropy $S_A = -\text{Tr} \rho^A \ln \rho^A$ that measures uncertainty of a (quantum) system A and is well-known from thermodynamics. But in contrast to the maximum entropy principle that applies to the whole system, it is necessary to access information within and between plaquettes that is quantified via entropies of subsystems. Let $|n\rangle$ be an eigenstate of some system that can be decomposed into subsystem A and subsystem B with states $|i\rangle \in A$ and $|j\rangle \in B$, then

$$|n\rangle = \sum_{ij} c_{ij}^n (|i\rangle |j\rangle), \quad (3.5)$$

with coefficients c_{ij} , which practically are obtained by formulating a many-body problem using the basis $|i\rangle |j\rangle \in A \otimes B$ and solving it for its eigenstates. Then, the reduced density

matrix of subsystem A

$$\begin{aligned}\rho^A &= \text{Tr}_B \rho \\ &= \sum_j (\mathbb{1}_A \otimes \langle j|) \rho (\mathbb{1}_A \otimes |j\rangle)\end{aligned}\quad (3.6)$$

acts on the focksubspace of A as the subspace of B is integrated out. The integration is performed using $(\mathbb{1}_A \otimes \langle j|)$, the identity of subspace A and the orthonormal basis $|j\rangle$ of subsystem B . The identity $\mathbb{1}$ can be used to evaluate Eq. (3.6) further. It can be written as

$$\begin{aligned}\mathbb{1} &= \sum_n |n\rangle \langle n| \\ &= \sum_n \left[\sum_{i_1 j_1} c_{i_1 j_1}^n (|i_1\rangle |j_1\rangle) \right] \left[\sum_{i_2 j_2} (c_{i_2 j_2}^n)^* (\langle i_2| \langle j_2|) \right] \\ &= \sum_{ni_1 i_2 j_1 j_2} c_{i_1 j_1}^n (c_{i_2 j_2}^n)^* (|i_1\rangle |j_1\rangle) (\langle i_2| \langle j_2|),\end{aligned}\quad (3.7)$$

and is inserted twice into Eq. (3.6), once on the left-hand side of ρ (simple-index notation) and once on the right-hand side of ρ (prime-index notation)

$$\begin{aligned}\rho^A &= \sum_{jnn'i_1 j_1 i_2 j_2 i'_1 j'_1 i'_2 j'_2} c_{i_1 j_1}^n (c_{i_2 j_2}^n)^* c_{i'_1 j'_1}^{n'} (c_{i'_2 j'_2}^{n'})^* \\ &\quad \times \underbrace{(\mathbb{1}_A \langle j|) (|i_1\rangle |j_1\rangle)}_{|i_1\rangle \delta_{j j_1}} \underbrace{(\langle i_2| \langle j_2|) \rho (|i'_1\rangle |j'_1\rangle)}_{\rho_{nn} \delta_{nn'} \delta_{i_2 i'_1} \delta_{j_2 j'_1}} \underbrace{(\langle i'_2| \langle j'_2|) (\mathbb{1}_A |j\rangle)}_{\delta_{j'_2 j} \langle i'_2|} \\ &= \sum_{jn i_1 i'_2} c_{i_1 j}^n (c_{i'_2 j}^n)^* \rho_{nn} |i_1\rangle \langle i'_2| \sum_{i_2 j_2} |c_{i_2 j_2}^n|^2 \\ &= \sum_{jn i i'} c_{i j}^n (c_{i' j}^n)^* \rho_{nn} |i\rangle \langle i'|.\end{aligned}\quad (3.8)$$

As expected, the result contains summations of the full fockspace (n) and the subsystem B (j) and returns a matrix in the focksubspace of A (i, i'). The full density matrix is diagonal in the basis $|n\rangle$ whose non-zero entries are $\rho_{nn} = \langle n| \rho |n\rangle$. The summation simplifies for a non-degenerate groundstate in the zero-temperature limit in which only the groundstate $|n_0\rangle$ contributes $\rho_{T=0} = |n_0\rangle \langle n_0|$ and therefore the summation over n can be dropped.

Finally, it is important to point out that in the derivation above, the normal order of the fockspace of the full system had already separated the subsystems A and B . In general, the subspace A is chosen according to certain single-particle basis states, e.g. four sites, a plaquette, out of the sixteen-site cluster. Then, in order to apply Eq. (3.8), the eigenstates $|n\rangle$ have to be transformed into the correct order $|i\rangle |j\rangle$ by the application of pairwise permutations. Importantly, those permutations generate minus signs if two permuted states are occupied by fermions.

By means of the density matrix and its reduced density matrices, it is possible to

conveniently introduce the quantum mutual information of subsystem A and subsystem B as

$$\mathcal{I}_{AB} = S_A + S_B - S_{AB}. \quad (3.9)$$

The term “quantum mutual information” is already descriptive on its own and Eq. (3.9) shows that the mutual information is the difference of the sum of the distinct subsystem’s entropies and the entropy of the merged subsystems. It is intuitive that this difference can contain some non-local information between A and B which is one of the outstanding properties of quantum entanglement. However, a more accurate interpretation of this quantity states that the mutual information is the minimal amount of noise that would be necessary to add in order to decorrelate A from B entirely [165]. “Entirely” means that the correlations stemming from quantum entanglement and also from so-called secret classical correlations are erased from the state.

For example, considering a system in the entangled state

$$|\pm\rangle = \frac{1}{\sqrt{2}} (|0\rangle|0\rangle \pm |1\rangle|1\rangle) \quad (3.10)$$

characterized by the density matrix

$$\rho_0 = |+\rangle\langle+|, \quad (3.11)$$

with the shorthand notation of $|0\rangle|0\rangle = |0\rangle \otimes |0\rangle$ which is bipartite and can be attributed, e.g., to the Hilbert spaces of Alice and Bob. Then, Alice can apply noise to the system by a local unitary transformation

$$\begin{pmatrix} |0\rangle \\ |1\rangle \end{pmatrix} \mapsto \sigma_z \begin{pmatrix} |0\rangle \\ |1\rangle \end{pmatrix} = \begin{pmatrix} |0\rangle \\ -|1\rangle \end{pmatrix} \quad (3.12)$$

which is applied only at a probability of 50%, i.e. at the remaining probability of 50% the identity transformation is applied. Thus, the pure state of ρ_0 becomes a mixed state

$$\begin{aligned} \rho_1 &= \frac{1}{2} (|+\rangle\langle+| + |-\rangle\langle-|) \\ &= \frac{1}{2} (|0\rangle\langle 0| \otimes |0\rangle\langle 0| + |1\rangle\langle 1| \otimes |1\rangle\langle 1|), \end{aligned} \quad (3.13)$$

in which the quantum entanglement of Alice and Bob has been erased, but they are still correlated in the classical sense as ρ_1 is a mixed state. This mixed appeared only upon the removal of the quantum entanglement and therefore the classical correlations are termed “secret”. Next, Alice adds additional noise, but this time using the transformation

$$\begin{pmatrix} |0\rangle \\ |1\rangle \end{pmatrix} \mapsto \sigma_x \begin{pmatrix} |0\rangle \\ |1\rangle \end{pmatrix} = \begin{pmatrix} |1\rangle \\ |0\rangle \end{pmatrix}, \quad (3.14)$$

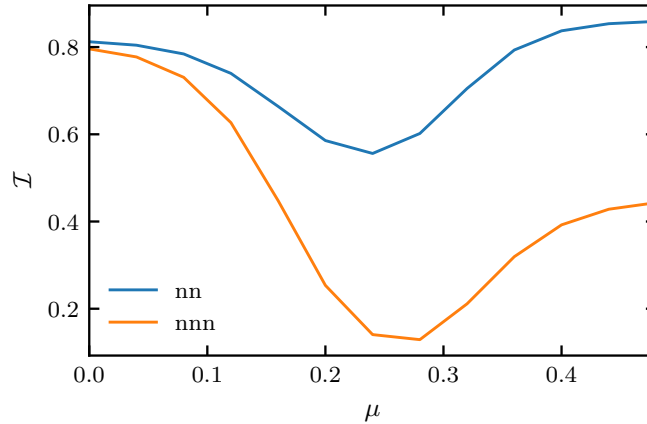


Figure 3.12: Quantum mutual information of the two-by-two plaquette for nearest neighbors (nn) and next-nearest neighbors (nnn). $\beta = 30$, $t = -1$, $t' = 0.3$, $U = 2.78$.

which transforms ρ_1 to

$$\begin{aligned} \rho_2 &= \frac{1}{4} (|0\rangle\langle 0| \otimes |0\rangle\langle 0| + |1\rangle\langle 1| \otimes |0\rangle\langle 0| + |0\rangle\langle 0| \otimes |1\rangle\langle 1| + |1\rangle\langle 1| \otimes |1\rangle\langle 1|) \\ &= \frac{1}{4} \mathbb{1} \otimes \mathbb{1}. \end{aligned} \quad (3.15)$$

ρ_2 is again a pure state, but contrary to the initial ρ_0 without entanglement. Thus, quantum and classical correlations between Alice's and Bob's Hilbert spaces have been erased by adding noise twice, two local unitary operations on the Hilbert space of Alice. This “two” should be obtained by the calculation of the mutual information between Alice and Bob. Indeed, the reduced density matrices read

$$\rho_0^A = \frac{1}{2} (|0\rangle_A \langle 0|_A + |1\rangle_A \langle 1|_A), \quad (3.16)$$

$$\rho_0^B = \frac{1}{2} (|0\rangle_B \langle 0|_B + |1\rangle_B \langle 1|_B), \quad (3.17)$$

and evaluate to $S_A^{(2)} = S_B^{(2)} = 1$ and $S_{AB}^{(2)} = 0$. The superscript (2) means that the logarithm of base 2 has been used. This gives the mutual information $\mathcal{I}_{AB} = 2$ in agreement with the amount of noise that Alice had added. This relation has been proved also for the generic case [165].

Based on the quantum mutual information further quantities, such as the disparity, clustering and Pearson correlations, which will be introduced in detail below, have been defined. These quantities show distinct features on the critical points of quantum phase transitions in 1D systems [166, 167]. This has been investigated by means of the density matrix renormalization group method which is efficient for one-dimensional systems and can confirm the finite-size scaling properties of such systems, but the study of large two-dimensional systems is much more difficult.

Fig. 3.12 shows the quantum mutual information of the nearest neighbors and the next-

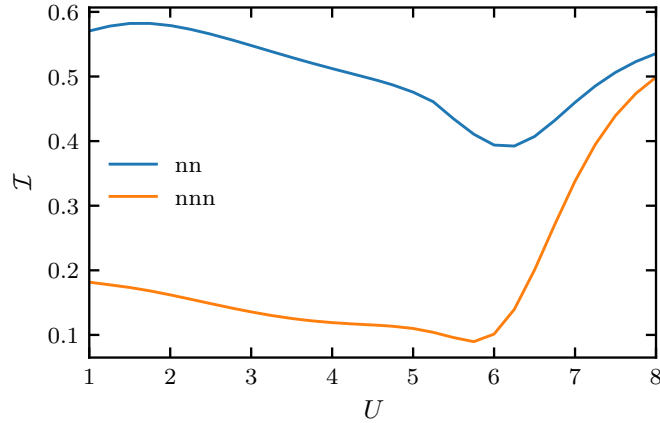


Figure 3.13: Quantum mutual information of the two-by-two plaquette for nearest neighbors (nn) and next-nearest neighbors (nnn). $\mu = \mu_{24}(U)$, that is the chemical potential along the crossover of the $N = 2$ -groundstate and the $N = 4$ -groundstate. $\beta = 30$, $t = -1$, $t' = 0.3$.

nearest neighbors of the two-by-two plaquette with Hubbard interaction. Since $t' = 0.3$ and $U = 2.78$, $\mu_c = 0.24$ is the QCP of the isolated plaquette with the $N = 2, 3, 4$ degeneracy. Thus, for $\mu < \mu_c$ the groundstate stems from the particle number sector $N = 2$ and for $\mu > \mu_c$ it stems from the sector $N = 4$. Regarding the $N = 2$ region, the mutual information of nearest neighbors and next-nearest neighbors are very similar. the $N = 2$ spin-singlet groundstate has almost the same mutual information between all the sites, furthermore, the small difference could stem from the finite temperature $\beta = 30$. With increasing μ the QCP is approached and the mutual information shows a local minimum for the nearest and next-nearest neighbors. This can be related to the spin-doublet character of the four-fold degenerate $N = 3$ groundstates. The intuitive picture is that double occupations are excluded due to the interaction U and mutual information originates from spin-singlet formation of electrons on different sites, just as a valence bond. Then, a spin-doublet counteracts this scenario with a local, unpaired spin. Remarkably, around the QCP the nearest neighbor mutual information is about three times as large as the next-nearest neighbor mutual information. This factor changes from three to two for $\mu_c < \mu$ with the $N = 4$ spin-singlet groundstate. This suggests a half-filled resonating valence bond state which has larger entanglement contributions from nearest-neighbor valence bonds than next-nearest neighbor valence bonds.

The U -dependence of the same quantities is shown in Fig. 3.13 with a varying chemical potential μ , so that the graphs correspond to the crossover of the $N = 2$ -groundstate and the $N = 4$ -groundstate which are not necessarily the groundstates of the whole system. Indeed, since the QCP is at $U_c = 2.78$, for $U_c < U$ the groundstates are the four-fold degenerate $N = 3$ states. The mutual information of nearest neighbors is three times as large as the next-nearest neighbor mutual information and it shows a local maximum around $U = 2$, which is notably close to the global maximum of the quadruple Bethe lattice's superconducting order parameter (Sec. 3.5.2). The mutual information decreases for larger

U up to the groundstate crossover in the $N = 3$ sector from a spin-doublet to a spin-quadruplet between $U = 6$ and $U = 7$. With further increasing U the mutual information of nearest and next-nearest neighbors approach similar values. In comparison with the study of the quadruple Bethe lattice (Sec. 3.5.2) one can suspect that the occurrence of superconductivity is related to the strong differentiation of the nearest neighbor and next-nearest neighbor mutual information of the Hubbard two-by-two plaquette. The following article [168] presents a study of the four-by-four cluster with Hubbard interaction using quantum information tools based on mutual information. This can show that properties of the QCP persist with finite-size scaling and indicates its impact on the full Hubbard lattice that is frequently used to model copper oxides.

Detecting the quantum critical point in high-temperature superconducting cuprates via complex network theory

Andrey A. Bagrov^{1,*†}, Mikhail Danilov^{2,†}, Sergey Brener², Malte Harland², Alexander I. Lichtenstein²
& Mikhail I. Katsnelson¹

¹*Radboud University, Institute for Molecules and Materials, 6525AJ Nijmegen, The Netherlands*

²*Institute of Theoretical Physics, University of Hamburg, 20355 Hamburg, Germany*

**Email: abagrov@science.ru.nl*

†These authors equally contributed

The current understanding of high- T_c superconductivity in cuprates assumes a crucial role of strong electron correlations¹⁻⁴. There is a popular view that a single-band $t - t'$ Hubbard model⁵ is the minimal model to catch the main relevant physics but even this oversimplified model is too complicated to be treated accurately and convincingly. It has been thoroughly studied numerically, and a number of valuable results have been obtained⁶⁻¹¹. On the other hand, a considerable success in phenomenological description of high- T_c superconductors has been achieved within the paradigm of Quantum Critical Point^{12,13} (QCP) - a parental state of a variety of exotic phases that is characterized by dense entanglement and absence of well-defined quasiparticles. However, the microscopic origin of the critical regime in real materials remains an open question. Here, we suggest that emergence of the QCP is tightly connected with entanglement in real space and identify its location on the phase diagram of the hole-doped $t - t'$ Hubbard model. To detect the QCP we study a weighted graph of

inter-site quantum mutual information within a four-by-four plaquette that is solved by exact diagonalization. We demonstrate that certain characteristics of such a graph, viewed as a complex network, exhibit peculiar behavior around a point on the phase diagram corresponding to the onset of pseudogap in $\text{YBa}_2\text{Cu}_3\text{O}_7$. This method allows us to overcome difficulties caused by finite size effects and to identify the transition point even on a small lattice, where long-range asymptotics of correlation functions cannot be accessed.

The phenomenon of high-temperature superconductivity (HTSC) still remains very puzzling after more than thirty years since the discovery of superconducting copper-oxide compounds¹⁴. Serious hopes for the understanding of this phenomenon are related to the concept of a quantum critical point (QCP)¹³, - an exotic state of matter that exhibits scale invariance and lacks long-lived quasiparticles, and thus cannot be described by means of conventional Fermi-liquid theory. Contemporary discussions of observed properties of HTSC are frequently organized around this concept^{15,16}. From the theoretical side, focus on QCP requires a change of basic mathematical tools. The diagrammatic approach, the main apparatus of quantum many-body theory during the last sixty years^{17,18}, is very well fitted to the description of quasiparticles; microscopic justification of the Landau Fermi-liquid theory remains probably its main success. A paradigmatic shift in studying strongly coupled systems near the QCP has occurred when it was realized that the anti de Sitter/Conformal field theory (holographic) correspondence¹⁹ can be used to analyze certain universal phenomenological properties of correlated electronic matter in the regime where the traditional Fermi-liquid picture breaks down^{20,21}. With regard to the high-temperature superconductors, this allowed to resolve within a relatively short time frame a number of puzzles that

remained perplexing for decades¹. The correspondence provided an explanation for the linear- T scaling of DC resistivity in the normal state of cuprates²² (known as strange metals), relating it to general hydrodynamic properties of systems with minimal viscosity proportional to the thermodynamic entropy²³. It was shown²⁴ that the Hall angle, - the temperature dependent ratio of the Hall and DC conductivities, $\tanh \theta_H = \sigma_{xy}/\sigma_{xx} \sim 1/T^2$, can be naturally interpreted in terms of a two-constituent quantum liquid, where the regular quasiparticles and the critical sectors give independent contributions to the conductivity, leading to an anti-Matthiessen rule for transport. A new mechanism of the interaction-driven metal-insulator transition that causes anisotropic localization has been suggested²⁵, and it appears to be fully in line with the localization of conducting electron gas in two-dimensional CuO planes, while the conductivity in the orthogonal direction is suppressed. Other phenomena, such as the formation of Fermi arcs seen in the angle-resolved photoemission spectra of high- T_c compounds, or charge density waves also fit pretty naturally into the context of quantum criticality²⁶.

The main problem of this approach is its purely phenomenological character. It cannot explain by itself why the high- T_c compounds, contrary to the most of interesting condensed matter systems, do not behave as the Fermi liquid but instead are characterized by minimal quantum viscosity and other fancy properties. Such an explanation requires an analysis of electronic structure of specific materials.

In an attempt to proceed along this path, we shall focus on a particular minimal model that was formulated⁵ on the basis of the density functional band structure of cuprates, - the single-band

$t - t'$ Hubbard model on a square lattice given by the Hamiltonian

$$H = -t \sum_{\langle i,j \rangle, \sigma} c_{i,\sigma}^\dagger c_{j,\sigma} - t' \sum_{\langle\langle l,k \rangle\rangle, \sigma} c_{l,\sigma}^\dagger c_{k,\sigma} + h.c. + U \sum_i n_{i,\uparrow} n_{i,\downarrow}, \quad (1)$$

where, the first sum is taken over the pairs $\langle i, j \rangle$ of nearest neighbors, the second one - over the pairs $\langle\langle l, k \rangle\rangle$ of next-to-nearest (diagonal) neighbors, $c_{i,\sigma}$ is the electron annihilation operator, and the on-site occupation operator is $n_{i,\sigma} = c_{i,\sigma}^\dagger c_{i,\sigma}$. Correlation effects beyond the band structure approximation in this model have been thoroughly analyzed with different methods, and there are a number of good indications that it captures all the relevant features of cuprate superconductors. In a series of papers²⁷⁻³², perturbative renormalization group studies of the model have been conducted, and the emergence of the superconducting order parameter and the competition between superconductivity and antiferromagnetism were demonstrated. In particular³¹, it was argued that the next-to-nearest neighbor hopping t' plays a crucial role in the stabilization of superconductivity. A complementary approach is based on the cluster dynamical mean-field studies which consider a 2-by-2 plaquette as an elementary unit³³. Recently¹¹, it was noticed that this plaquette has a very special electronic structure for the parameters t and the electron occupation number typical for the optimal doping regime in $\text{YBa}_2\text{Cu}_3\text{O}_7$ ($t'/t = -0.3$, $U/t \simeq 6$), with an ‘‘accidental’’ degeneracy of many-electron energy levels and formation of the soft fermion mode due to this degeneracy. The pseudogap forms via this mode by a mechanism of the Fano antiresonance, and the superconducting d-wave susceptibility dominates over other instability channels. This behavior was interpreted in terms of formation of a local plaquette valence bond state. On a larger scale, the ground state of the model has been analyzed by means of density matrix renormalization group³⁴ (DMRG) (see also³⁵ for the related studies of its cousin, $t - J$ -model), and additional arguments in

favor of stabilization of superconductivity by the next-to-nearest neighbor hopping were provided. In turn, at temperatures above the superconducting phase transition, determinantal Monte Carlo computations³⁶ demonstrated that the DC resistivity exceeds the Mott-Ioffe-Regel limit and scales linearly with temperature.

The search for the QCP in the $t-t'$ Hubbard model has been performed within the dynamical cluster approximation⁸, and its existence has been proven by studying thermodynamics properties of the model at finite temperature and their further extrapolation to $T = 0$. However, it is tempting to get a deeper insight into the microscopics of the QCP and demonstrate its emergence due to interactions of electrons at low temperatures.

Since large scale simulations of the fermionic Hubbard model away from half-filling are challenging because of the sign problem, it is natural to ask whether we can extract any information about the tendency to form critical states out of small cluster solutions obtained by means of exact diagonalization. At first, this goal does not seem realistic since studying systems in the critical regime unavoidably requires dealing with long-range correlations, while all the microscopic precursors of the transition on small lattices would be washed out by the finite-size effects. However, it is useful to bear in mind that, in the context of many-body quantum dynamics, the concept of entanglement and the phenomenon of collective emergence go hand in hand. An archetypical example of such relation is the Cooper pairs in the BCS theory of superconductivity: while the ground state wavefunction has a form of a product state of the Cooper pairs, each pair itself is a two-body entangled system. Therefore it is natural to expect that major transitions in phenomono-

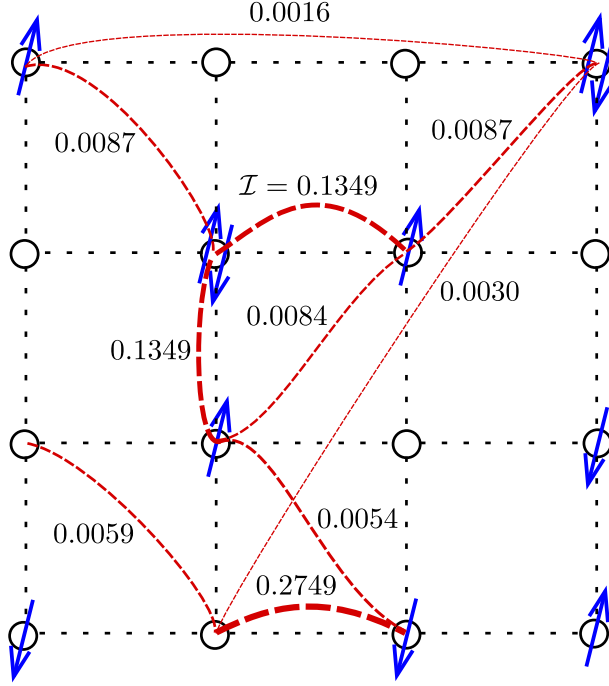


Figure 1: An artistic view of the mutual information complex network defined on the Hubbard lattice. While the network is fully connected, for illustrative purposes, only some of the network links are shown. The shown values of inter-site mutual information correspond to the case of non-periodic boundary conditions, (6, 6) sector, $U = 7.5$.

logical properties of many-body systems would be reflected in the patterns of entanglement, and quantum criticality should leave its fingerprint on all scales, not only in the deep infrared limit.

Recently, a novel approach to phase transitions in quantum lattice models based on complex network theory has been suggested^{37,38}. It was noticed that a particular structure that can be computed with relative ease and appears to be very sensitive to reconfigurations of the quantum state is the network of quantum mutual information. The mutual information between two subsystems

A and B of a larger systems is defined as

$$\mathcal{I}_{AB} = S_A + S_B - S_{A \cup B}, \quad (2)$$

where $S_A = -\text{Tr} \rho_A \log \rho_A$ is the von Neumann entropy, and $\rho_A = \text{Tr}_{\bar{A}} \rho$ is the density matrix of subsystem A . Then we can associate a weighted graph with a state of a quantum lattice system, e.g. the Hubbard model, by considering the lattice sites $i = 1 \dots N$, where N is the number of sites, as nodes of the graph, and the values of pairwise inter-site mutual information I_{ij} play the role of weights on the graph links (see Fig. 1). This representation is appealing for the following reason. Once a wave function on the lattice is known, it is easy to compute the entanglement entropy of a pair of sites and thus the mutual information. At the same time, such a network by design contains information of multi-partite quantum correlations which could be very important to understand the dynamics of strongly correlated systems. In the cases of the 1d Ising model in a transverse field and the 1d Bose-Hubbard model, it was demonstrated that certain characteristics of the mutual information network can be used to detect quantum phase transitions^{37,38}. Namely, behavior of the following functions upon changing parameters of the models has been studied:

- **Clustering** of a weighted graph is defined as

$$C = \frac{\text{Tr} \mathcal{I}^3}{\sum_{j \neq i}^N \sum_{i=1}^N [\mathcal{I}^2]_{ij}}, \quad (3)$$

where N is the total number of sites in the lattice, and \mathcal{I} is the $N \times N$ matrix of inter-site mutual information. One can see that this quantity maximizes on graphs with a lot of three-link loops with high weights. For the cases studied in Ref.³⁷, it was shown that it serves as sensitive detector that exhibits a clear dip at the phase transition point.

- **Disparity** of a single node in a network is defined as a measure to capture how non-uniformly weights on the links attached to this node are distributed:

$$Y_i = \frac{\sum_{j=1}^N (\mathcal{I}_{ij})^2}{\left(\sum_{j=1}^N \mathcal{I}_{ij}\right)^2} \quad (4)$$

For example, if the node has the same value of mutual information with all the other nodes of the network, its disparity would be $Y_i = 1/(N - 1)$, while if it correlates only with one neighbor, the disparity maximizes as $Y_i = 1$. Physically speaking, high disparity of a lattice site means that it tends to correlate only with a few other sites, and “factorize out” of the rest of the system. In the context of quantum many-body physics such a behavior would be typical for states that can be nearly decomposed into product states. On the other hand, low disparity means that the site correlates with a large number of degrees of freedom.

- **Density** is an overall characteristic of a network given by

$$D = \frac{1}{N(N-1)} \sum_{i,j=1}^N \mathcal{I}_{ij}, \quad (5)$$

i.e. it is the averaged fraction of all the weights (mutual information values) of the network.

To gain more intuition on what properties of the many-body quantum state it reflects, we shall estimate an upper bound on this measure. If site i of the network is maximally entangled with the rest of the system, its entanglement entropy equals $S_i = \ln d = \ln 4$, where $d = 4$ is dimension of the local on-site Hilbert space in Hubbard model. On the other hand, mutual information monogamy theorem implies that $S_i \geq \sum_{j \neq i} \mathcal{I}_{ij}$. From that we readily conclude

$$D \leq \frac{1}{N(N-1)} \sum_{i=1}^N S_i \leq \frac{\ln 4}{N-1} \xrightarrow{N \rightarrow \infty} 0 \quad (6)$$

i.e. the mutual information network is generally sparse even if the system is highly entangled. Note that bound (6) can be saturated in physically very distinct cases. D is maximal if either each single site is maximally entangled with just one partner site, and the state as a whole decomposes into a product of Bell pairs, or if the entanglement between the site and the rest of the system is homogeneously scrambled over all the sites. To distinguish between such configurations one has to refer to the disparity which we defined above.

- **Pearson correlations** measure how much two nodes i and j of a network differ from each other:

$$r_{ij} = \frac{\sum_{k=1}^N (\mathcal{I}_{ik} - \langle \mathcal{I}_i \rangle) (\mathcal{I}_{jk} - \langle \mathcal{I}_j \rangle)}{\sqrt{\sum_{k=1}^N (\mathcal{I}_{ik} - \langle \mathcal{I}_i \rangle)^2} \sqrt{\sum_{k=1}^N (\mathcal{I}_{jk} - \langle \mathcal{I}_j \rangle)^2}}, \quad (7)$$

$$\langle \mathcal{I}_i \rangle = \frac{1}{N} \sum_{j=1}^N \mathcal{I}_{ij}$$

In Ref.³⁷ Pearson correlations of neighboring nodes were shown to develop a cusp around the phase transition point.

For one-dimensional Ising and Bose-Hubbard models³⁷, this approach to detecting quantum phase transitions points was successfully applied for systems of $\sim 10^2$ sites, and was demonstrated to be very robust upon finite-size effects. In the two-dimensional case, we are limited by much smaller system sizes (we perform exact diagonalization for a 4-by-4 plaquette), and should not expect our results to be free from finite-size artifacts. Still, as we shall see in the next section, the network measures exhibit clearly distinguishable features at certain values of parameters of the $t-t'$ Hubbard model close to the level-crossing point observed in a 2-by-2 plaquette¹¹.

Results. We have computed the complex network measures discussed above across the space of parameters of the $t - t'$ Hubbard model. We have studied 4-by-4 plaquette adopting both the non-periodic and periodic boundary conditions. We take $t'/t = -0.3$, which is estimated to be the value of next-neighbor hopping in the Hubbard model of YBCO compounds, consider the system in the canonical ensemble, and within each fixed particles number sector compute the network measures scanning over $U \in [0, 12]$. The temperature is fixed to $1/T = \beta = 100$ (all energies are expressed in the units of $|t|$).

We assume that a transition point is evident if all the measures exhibit some clear features around the same point. Accepting this criterion, we can claim with a high confidence that for $t'/t = -0.3$ a phase transition is seen in the $(6, 6)$ quantum number sector (6 electrons with spin up, 6 electrons with spin down), which corresponds to the hole doping of $\delta = 25\%$. Within this sector, there is a point where clustering, density, the Pearson coefficients between neighboring sites, and disparity (the latter – only in the non-periodic case), considered as functions of the Coulomb repulsion U , – all have a clear cusp. Concrete value of Coulomb repulsion U seems to be dependent on the choice of boundary conditions, - it is $U \simeq 7.5$ for the open cluster, and $U \simeq 9.5 - 10$ for the periodic one. That is not unexpected since we perform the small-scale analysis and cannot eliminate the finite-size effects.

At the same time, in the density of states (d.o.s.) the transition point is (almost) invisible. Some minor peculiarity at the quantum critical point is visible in the density of states at $t'/t = -0.3$ for non-periodic boundary conditions. Around the transition point identified by means of

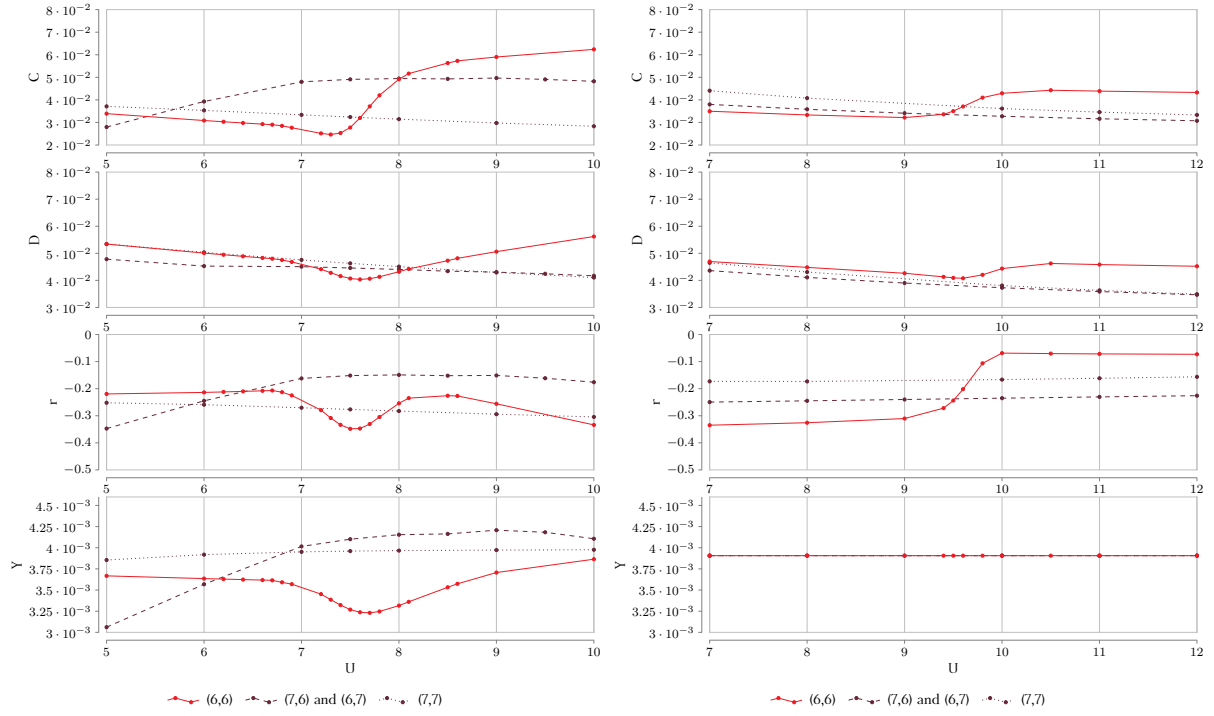


Figure 2: Characteristics of the mutual information complex network, – clustering C , density D , Pearson correlation r between neighboring sites in the middle of the 4-by-4 plaquette, and disparity Y of a site in the middle of the plaquette, – as functions of the on-site Coulomb repulsion U computed in different sectors for non-periodic (left panel) and periodic (right panel) boundary conditions. The hopping is $t'/t = -0.3$, the inverse temperature is $\beta = 100$.

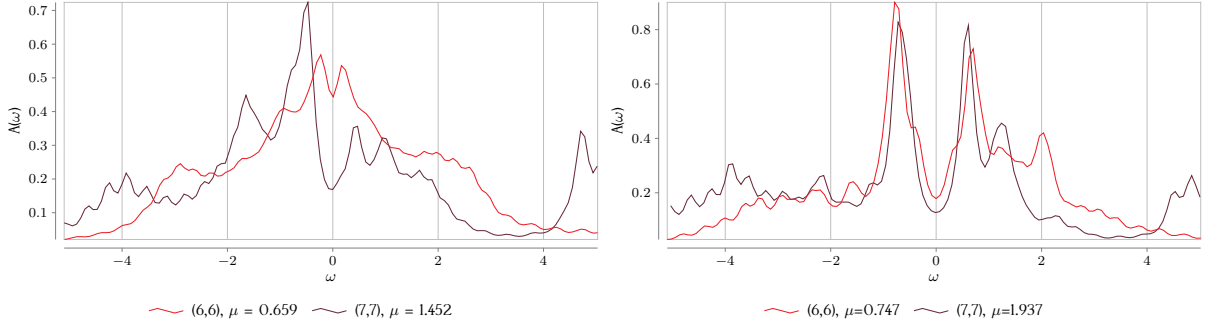


Figure 3: The density of states computed with non-periodic (left) and periodic boundary conditions. Whereas the comparison of different boundary shows that quantitatively the finite-size effects are important, qualitatively, in both schemes one can see the pseudogap formation near the quantum critical point. Its interpretation in terms of the Fano antiresonance due to formation of a “soft fermion” mode was given in Ref.¹¹

the complex network theory ($U = 7.5$, sector (6,6)) the peak in the d.o.s. starts splitting and the pseudogap emerges, see Fig. 3. Further decrease of the hole doping leads to enhancement of the gap. The particular role of U in this transition is less clear, as the d.o.s. profile varies very mildly upon changing U . The only peculiarity one can spot is that the emerged peaks become symmetric when passing the $U \simeq 7.5$ point in the (6,6) sector. However, since the d.o.s. for the other choice of boundary conditions do not reveal any specific features, it would be safer to claim that the low-order correlation functions are not sensitive to the discussed quantum phase transition. Ideologically, this situation is somewhat similar to the Anderson localization in disordered systems which is a clear example of a phenomenon that cannot be detected on the level of the average Green’s functions³⁹.

Discussion. By associating the quantum state of the $t-t'$ Hubbard model with a weighted network of inter-site mutual information, for different values of the next-neighbor hopping t'/t , we have found a transition point where characteristics of the network have a clearly distinguishable cusp. Such a behavior was previously shown to be an indication of a quantum phase transition in different one-dimensional models^{37,38}. Strikingly, this cusp is located exactly in the sector where onset of the pseudogap is expected to occur. The modern experimental understanding of the putative QCP in cuprates tells that it indeed must be associated with the emergence of the pseudogap phase¹⁵. Experimentally, for YBCO compounds the onset of pseudogap was demonstrated to happen at hole doping $\delta \simeq 22\%$ ⁴⁰. The hole doping $\delta = 25\%$ is the closest value one can get for a 4-by-4 cluster (the (6, 6) sector), and that's precisely the point where we observe the phase transition. The particular values of the on-site Coulomb doping is affected by the finite size effects, and estimated to be in the range $U \simeq 7 - 10$, dependent on the adopted boundary conditions. At the same time, no peculiarity is seen in the density of states at the transition point which might be a good indication that the low-order correlation functions that define the spectral and the response properties of the system could be blind to restructuring of many-body quantum states, and does not contain enough information on the role of quantum correlations behind phase transitions in electron systems.

Methods. In this section we give the relevant technical details of the calculation of the entanglement measures defined above. The first step is to diagonalize the Hubbard model (1) for a 4-by-4 cluster. This can be done either for a periodic or a non-periodic model. The diagonalization is performed using the Lanczos algorithm with 200 Krylov basis vectors⁴¹. The particle number and

spin conservation laws are used so that the diagonalization can be restricted to a sector with a fixed number of up- and down-spins. Those eigenstates with the corresponding eigenvectors are then used to calculate the reduced density matrices for each possible pair of sites as well as for each single site.

The reduced density matrix is computed using its definition that can be symbolically written as:

$$\rho_A(a, a') = \frac{1}{Z} \sum_n e^{-\beta E_n} \text{Tr}_{\bar{A}} |\psi_{n,(a,\bar{a})}\rangle \langle \psi_{n,(a',\bar{a})}|. \quad (8)$$

Here a, a' denote the many-particle (Fock) basis states describing the subsystem A we calculate the density matrix for, \bar{a} stands for the many-particle basis state of the complementary subsystem \bar{A} , thus a couple of those (a, \bar{a}) denotes a basis Fock state for the whole cluster explicitly split into two parts. As before, n stands for a particular eigenvector, the density matrices for given eigenstates are weighted with the Boltzmann factors corresponding to their energies. In a given sector for a given set of parameters we use the Boltzmann factor cut-off of 1% meaning $e^{(E_0 - E_i)\beta} > 10^{-2}$, where E_0 is the ground state energy and E_i is the energy of the highest (i th) level taken into account. Note that while performing the partial trace over \bar{A} one has to correctly account for the fermionic commutation relations. To this aim one has to effectively change the numeration of sites so that the sites for which we calculate the density matrix stand first. Explicitly it means that each component of an eigenvector, corresponding to a given basis state of the cluster, gets a factor determined as the parity acquired while "dragging" the occupied sites of A to the beginning past the occupied states of \bar{A} . In other words for each basis vector one takes each occupied site

from A and for each occupied spin component counts the number of same spin occupied sites from \bar{A} standing before the considered site in the original numeration. Summing up the parities of those numbers for all occupied sites and spins from A one gets the parity that is assigned to a given basis vector with respect to the subsystem A . Having multiplied the eigenvector components with the acquired parities one finally performs the partial trace over the complementary subset \bar{A} .

Given the reduced density matrix we first calculate the von Neumann entropy of a given subsystem and then, with (2) the mutual information for each pair of sites, that serves as the basis for our network.

The ω -dependent Green function is given by:

$$G_{i,\sigma}(\omega) = \frac{1}{Z} \sum_{m,n} \frac{|\langle m | c_{i,\sigma}^\dagger | n \rangle|^2}{\omega + E_n - E_m} (e^{-\beta E_n} + e^{-\beta E_m}). \quad (9)$$

Here m, n denote the eigenstates of the system, i and σ denote a given site and spin (in the paramagnetic case the answer is spin-independent), E_n is the energy of the n -th state, and $Z = \sum_m e^{-\beta E_m}$ is the partition function. Note that m and n necessarily belong to different sectors.

The Green function is used to calculate the density of states. The delta-peaks are broadened with $\delta = \pi/\beta$.

Acknowledgements. Authors thank Lincoln Carr for inspiring discussions.

Competing Interests. The Authors declare no Competing Financial or Non-Financial Interests.

Author contributions. A.A.B., M.I.K. and A.I.L. designed the project and directed it with the help of

S.B., M.D. and M.H. performed the calculations. A.A.B., M.I.K. and S.B. wrote the manuscript. All authors contributed to discussions.

Funding. A.A.B. and M.I.K. would like to thank the support of NWO via Spinoza Prize and of ERC Advanced Grant 338957 FEMTO/NANO.

Data Availability. The data that support the findings of this study are available from the corresponding author upon reasonable request.

1. P.W. Anderson, *The Theory of Superconductivity in the High- T_c Cuprates* (Princeton University Press, Princeton, 2007).
2. E. Dagotto, Correlated electrons in high-temperature superconductors, *Rev. Mod. Phys.* **66**, 763-840 (1994).
3. J. Orenstein, and A.J. Millis, Advances in the physics of high-temperature superconductivity, *Science* **288**, 468-474 (2000).
4. D.J. Scalapino, A common thread: The pairing interaction for unconventional superconductors, *Rev. Mod. Phys.* **84**, 1383-1417 (2012).
5. O.K. Andersen, A.I. Liechtenstein, O. Jepsen, F. Paulsen LDA energy bands, low-energy hamiltonians, t' , t'' , $t_{\perp}(k)$, and J_{\perp} , *Journal of Physics and Chemistry of Solids*, **56**, 1573–1591 (1995).
6. Th. Maier, M. Jarrell, Th. Pruschke, and M. H. Hettler, Quantum cluster theories, *Rev. Mod. Phys.* **77**, 1027 (2005)

7. K. Haule and G. Kotliar, Strongly correlated superconductivity: A plaquette dynamical mean-field theory study, *Phys. Rev. B* **76**, 104509 (2007)
8. E. Khatami, K. Mielson, D. Galanakis, A. Macridin, J. Moreno, R. T. Scalettar, and M. Jarrell, Quantum criticality due to incipient phase separation in the two-dimensional Hubbard model, *Phys. Rev. B* **81**, 201101(R) (2010)
9. E. Gull, O. Parcollet, and A. J. Millis, Superconductivity and the Pseudogap in the Two-Dimensional Hubbard Model, *Phys. Rev. Lett.* **110**, 216405 (2013)
10. M. Civelli, Evolution of the Dynamical Pairing across the Phase Diagram of a Strongly Correlated High-Temperature Superconductor, *Phys. Rev. Lett.* **103**, 136402 (2009)
11. M. Harland, M.I. Katsnelson, A.I. Lichtenstein Plaquette valence bond theory of high-temperature superconductivity, *Phys. Rev. B* **94**, 125133 (2016).
12. S. Sachdev, H.D. Scammell, M.S. Scheurer, and G. Tarnopolsky, Gauge theory for the cuprates near optimal doping, arXiv:1811.04930.
13. S. Sachdev, *Quantum Phase Transitions*, second edition (Cambridge University Press, Cambridge, 2011).
14. J.G. Bednorz and K.A. Müller, Possible high-T_c superconductivity in the BaLaCuO system, *Z. Phys. B: Condens. Matter* **64**, 189-193 (1986).
15. N.E. Hussey, J. Buhot, and S. Licciardello, A tale of two metals: contrasting criticalities in the pnictides and hole-doped cuprates, *Rep. Prog. Phys.* **81**, 052501 (2018).

16. B. Michon et al., Thermodynamic signatures of quantum criticality in cuprate superconductors, *Nature* **567**, 218222 (2019)
17. A.A. Abrikosov, L.P. Gorkov, and I.E. Dzialoshinski, *Methods of Quantum Field Theory in Statistical Physics* (Dover, New York, 1975).
18. G.D. Mahan, *Many-Particle Physics*, third edition (Springer, New York, 2000).
19. J. Maldacena, The large-N limit of superconformal field theories and supergravity, *Int. j. of theor. phys.* **38**, 1113–1133 (1999).
20. J. Zaanen, Y. Liu, Y.W. Sun, K. Schalm, *Holographic Duality in Condensed Matter Physics*, (Cambridge University Press, Cambridge, 2015).
21. S.A. Hartnoll, A. Lucas, and S. Sachdev, *Holographic Quantum Matter* (MIP Press, Cambridge Mass., 2018).
22. A. Legros et al., Universal T-linear resistivity and Planckian dissipation in overdoped cuprates, *Nature Physics* **15**, 142147 (2019)
23. R.A. Davison, K. Schalm, J. Zaanen, Holographic duality and the resistivity of strange metals, *Phys. Rev. B* **89**, 245116 (2014).
24. M. Blake, A. Donos, Quantum critical transport and the Hall angle in holographic models, *Phys. Rev. Lett.* **114**, 021601 (2015).
25. A. Donos, S. Hartnoll, Interaction-driven localization in holography, *Nature Physics* **9**, 649–655 (2013).

26. T. Andrade, A. Krikun, K. Schalm, J. Zaanen, Doping the holographic Mott insulator, *Nature physics* **14**, 1049–1055 (2018).
27. V.Y. Irkhin, A.A. Katanin, and M.I. Katsnelson, Effects of van Hove singularities on magnetism and superconductivity in the t - t' Hubbard model: A parquet approach, *Phys. Rev. B* **64**, 165107 (2001).
28. C.J. Halboth, W. Metzner, Renormalization-group analysis of the two-dimensional Hubbard model, *Phys. Rev. B* **61**, 7364–7377 (1999).
29. A. Neumayr, W. Metzner, Renormalized perturbation theory for Fermi systems: Fermi surface deformation and superconductivity in the two-dimensional Hubbard model, *Phys. Rev. B* **67**, 035112 (2003).
30. J. Reiss, D. Rohe, W. Metzner, Renormalized mean-field analysis of antiferromagnetism and d -wave superconductivity in the two-dimensional Hubbard model, *Phys. Rev. B* **75**, 075110 (2007).
31. A. Eberlein, W. Metzner, Superconductivity in the two-dimensional $t - t'$ -Hubbard model, *Phys. Rev. B* **89**, 035126 (2014).
32. M. Oshadnik, C. Honerkamp, T.M. Rice, and M. Sigrist, Breakdown of Landau Theory in Overdoped Cuprates near the Onset of Superconductivity, *Phys. Rev. Lett.* **101**, 256405 (2008).
33. A.I. Lichtenstein and M.I. Katsnelson, Antiferromagnetism and d -wave superconductivity in cuprates: A cluster dynamical mean-field theory, *Phys. Rev. B* **62**, R9283-R9286 (R) (2000).

34. H.C. Jiang, T.P. Devereaux, Superconductivity in the doped Hubbard model and its interplay with charge stripes and next-nearest hopping t' , arXiv: 1806.01465.
35. H.C. Jiang, Z.Y. Weng, S.A. Kivelson Superconductivity in the doped $t - J$ model: results for four-leg cylinders, *Phys. Rev. B* **98**, 140505 (2018).
36. E.W. Huang, R. Sheppard, B. Moritz, T.P. Devereaux, Strange metallicity in the doped Hubbard model, arXiv: 1806.08346.
37. M.A. Valdez, D. Jaschke, D.L. Vargas, L.D. Carr, Quantifying Complexity in Quantum Phase Transitions via Mutual Information Complex Networks, *Phys. Rev. Lett.* **119**, 225301 (2017).
38. B. Sundar, M.A. Valdez, L.D. Carr, K.R.A. Hazzard, A complex network description of thermal quantum states in the Ising spin chain, *Phys. Rev. A* **97**, 052320 (2018).
39. I.M. Lifshitz, S.A. Gredeskul, L.A. Pastur, *Introduction to the Theory of Disordered Systems* (Wiley, New York, 1988).
40. Y. Sato et al. Thermodynamic evidence for nematic phase transition at the onset of pseudogap in $\text{YBa}_2\text{Cu}_3\text{O}_y$, *Nature Physics* **13**, 1074-1078 (2017).
41. S. Iskakov, M. Danilov, Many-body physics, Exact diagonalization, Hubbard model, Anderson impurity model, *Comp. Phys. Commun.* **225**, 128 (2018).

3.6 Superconducting phase fluctuations

The superconductivity is mediated by Cooper pairs, even for unconventional superconductors this is commonly believed. Such a pair obeys quantum mechanical laws just as electrons, but with different statistics since they are bosonic. But still, their wavefunction has also a wave character and thus can be described by an amplitude and a phase. This section shows a study of the impact of this phase [169]. Theoretically, local pairs can form without macroscopic superconductivity. The superconducting state on the macroscopic scale can be inhibited by wave interference of the pairs, i.e. they can not move coherently through the lattice. A lot of attention has been devoted to the formation of the pairs as it is certainly intriguing how two fundamentally repellent electrons bind together, but this does not necessarily mean that an understanding of this mechanism provides a quantitative theory of the transition temperature. It is suspected that at least in parts of the copper oxide phase diagrams phase fluctuations have a strong impact on the critical temperature and that phase disorder prevents the macroscopic superconductivity at higher temperatures. This is different from conventional superconductivity as in that case the pairing defines the critical temperature as it occurs only at very low temperatures at which disorder effects are absent.

The difference in the phase can be thought of as a difference in an electric potential that makes supercurrents flow. This can be understood by the inspection of the gauge degree of freedom as will be shown below. Conventional type I superconductors exhibit the Meissner effect [25], i.e. they expel external magnetic flux. If magnetic fields are applied to the superconductor it develops circular supercurrents that shield it. This effect requires macroscopic quantum coherence, that is suspected to be less pronounced in the case of unconventional superconductors. In unconventional (type II) superconductors magnetic flux can penetrate the superconductor to an extent that creates small local circular supercurrents around these fluxlines, the Abrikosov vortices [170]. The London penetration depth of conventional superconductors are much smaller, $\lambda^{\text{Pb}} \approx 0.4 \mu\text{m}$, than in (unconventional) copper oxides, $\lambda_c^{\text{YBCO}} \lesssim 7.8 \mu\text{m}$, where c is the direction perpendicular to the CuO plane and the value of λ^{YBCO} also depends on the oxygen doping [169, 171]. In particular between the layers, the phase fluctuations are often considered to be important for a dimensional crossover [172] that is important for macroscopic superconductivity and the Meissner effect.

3.6.1 Condensate wave function and London penetration depth

The interference of preexisting pairs can occur by their wave-like nature that manifests in phase fluctuations in the wave function of pairs [173]

$$\psi(r, t) = \sqrt{n_s} e^{i\theta(r, t)}. \quad (3.18)$$

n_s is a real scalar constant, that describes the uniform particle density of the superconducting state, the particles being Cooper pairs. In order to define a current, i.e. a flow of the probability of such particles, one has to consider the local conservation of the wave

function's probability density

$$\frac{\partial P}{\partial t} = -\nabla \cdot J_s \quad (3.19)$$

with the probability density $P = \psi^* \psi$. The time-derivative acting on the probability density can be evaluated on the wave functions. Their dynamics are described by the Schrödinger equation (and its conjugate)

$$\frac{\partial P}{\partial t} = -\frac{i}{\hbar} (\psi^* H \psi - \psi H \psi^*) \quad (3.20)$$

with the hamilton operator H . The superfluid has kinetic energy and is coupled to a (real) three-dimensional electromagnetic gauge field A . By assumption only the charge couples to A , which in the case of superconductivity is very reasonable, as Cooper pairs are spin-singlet bosons. Furthermore only the first order multipole is considered. This leads to the minimal coupling, that is defined by the substitution of the kinematic momentum by the generalized momentum

$$p \mapsto p - qA \quad (3.21)$$

with charge q . Then, inserting the Hamilton operator

$$H = \frac{1}{2m} (p - qA)^2 \quad (3.22)$$

into Eq. (3.20), replacing one p by its explicit spatial-derivative form and comparing with Eq. (3.19) gives the probability current

$$J_s = \frac{1}{2m} (\psi^* p \psi - \psi p \psi^* - 2qA |\psi|^2). \quad (3.23)$$

Strictly speaking this is the current of the probability density. The probability is that of finding a particle at certain point. It is related to the interpretation of the wavefunction, which by itself is not an observable and thus, e.g. for electrons not an observable continuous charge distribution. Only in the limit of many particles being in the same state this picture becomes correct. In the case of macroscopically many Cooper pairs it is possible to identify the probability current as the current of electrical charge

$$J = qJ_s. \quad (3.24)$$

Boson statistics permit many particles to be in the same state, fermions in contrast do not by the Pauli principle. In that sense, the superconductivity is a peculiar phenomenon of a macroscopic quantum state that consists of electrons, that “circumvent” the fermion statistics by forming pairs. The trial wavefunction of Eq. (3.18) gives the probability current

$$J_s = \frac{n_s}{m} (\hbar \nabla \theta - qA). \quad (3.25)$$

The corresponding electric current of Cooper pairs is

$$J = qJ_s \quad (3.26)$$

with $q = 2e$ since each pair carries twice the electron charge. With the electric current the Maxwell equations can be applied further

$$\text{rot}B = \mu_0 J \quad (3.27)$$

with the magnetic flux $B = \text{rot}A$ being the curl (rot) of A and the vacuum permeability μ_0 . This equation describes the boundary current induced by a magnetic flux that penetrates its interior. Taking the curl on both sides of Eq. (3.27) gives

$$\nabla(\nabla \cdot B) - \nabla^2 B = -\frac{\mu_0 q^2 n_s}{m} B \quad (3.28)$$

in that the first term vanishes as the magnetic flux has no divergence $\nabla \cdot B = 0$ and the term proportional to θ vanishes since the curl of a gradient gives always zero. The second term is the Laplace operator ∇^2 . The solution of this differential equation is an exponential decaying B -field for that the (London) penetration depth can be written as the decay length

$$\lambda^{-2} = \frac{\mu_0 q^2 n_s}{m}. \quad (3.29)$$

The superconducting stiffness is a quantity that associates changes in the phase θ with a raise in the energy of the system. It can be related to the penetration depth. To this end one has to evaluate the energy(-density) of the wave function of Eq. (3.18) assuming that A is only supposed to probe the penetration depth and does not affect the phase fluctuations of ψ ,

$$\begin{aligned} E &= \psi^* H_{A=0} \psi \\ &= \frac{n_s \hbar^2}{2m} (\nabla \theta)^2 \\ &\equiv \frac{I}{2} (\nabla \theta)^2, \end{aligned} \quad (3.30)$$

that can be used to define the superconducting stiffness I . For the total energy an integration over space has to be performed. Thus, in three space dimensions I has the dimensions energy over length, whereas in two space dimensions it is energy. Inserting Eq. (3.30) into Eq. (3.29) gives an expression for the penetration depth in terms of I ,

$$\lambda^{-2} = \frac{4e^2 \mu_0}{\hbar^2} I. \quad (3.31)$$

The unit-system used here is the international system of units (SI). By the use of the Gaussian (CGS) unit-system the Hamilton operator (Eq. (3.22)) and the Maxwell equation

(Eq. (3.27)) change as

$$q \mapsto \frac{q}{c}, \quad \mu_0 \mapsto \frac{4\pi}{c}, \quad (3.32)$$

respectively. Thus Eq. (3.31) becomes [169, 109]

$$\lambda^{-2} = \frac{16\pi e^2}{\hbar^2 c^2} I. \quad (3.33)$$

3.6.2 Two-dimensional phase fluctuations

The description of the copper oxides using two-dimensional models can be reasonable as at temperatures around the critical temperature the copper layer may be coherent only within the planes. This idea is motivated by the layered structure, in which the distance of copper atoms within a layer is smaller than between layers. If this is the case, then the phase transition into the superconducting state can be defined by the Kosterlitz-Thouless (KT) transition [23, 174]. At the KT temperature vortex-antivortex pairs unbind and lead to phase disorder.

The vortex excitation can be understood starting from a two-dimensional model of rotors. These rotors can represent spins that rotate within the plane or the superconducting phase $\theta(\vec{r})$ at position \vec{r} . Importantly, the rotation is that of a moment within the plane, around a single angle ($U(1)$). A global phase does not change the physics by gauge invariance. Locally varying phase differences, however, can cause interesting effects. The kinetic energy of a pair wave function of Eq. (3.18) motivates the effective XY model

$$H = \frac{I}{2} \int d^2r (\nabla\theta(\vec{r}))^2, \quad (3.34)$$

with I defining the energy of rotor configurations. The energy can be minimized by the trivial solution of the homogeneous state $\theta(\vec{r}) = \text{const.}$ or by $\theta(\vec{r})$ being only curl of the rotor vector field. The vortex is an excitation that is a source of divergence in the rotor vector field. It can be quantified by the topological invariant, the vorticity,

$$v = \frac{1}{2\pi} \oint_C d\vec{r} \cdot \nabla\theta(\vec{r}) \quad (3.35)$$

that counts the number of vortex centers within the contour C , whereas the orientation matters and the vorticity can become negative and it can cancel with other vortex centers within the contour. With the vortex creation the system enters a different topological phase. Topological phases are characterized by the topological invariant, it formalizes the fact that the rotor configurations can not be continuously deformed into the different topological phases. The popular everyday life example is the cup which can be continuously deformed into a donut, but not into a pancake. The important difference is the hole of the cup, or donut, that can not be created in a continuous manner. The role of this hole is taken by the vortex in the 2D XY model.

Assuming vortices described by Eq. (3.35), i.e. that give a constant vorticity and also that they are rotationally invariant, it follows that the gradient-field of the rotor angles

reads $|\nabla\theta(\vec{r})| = vr^{-1}$. Thus, a single vortex excitation exhibits the energy

$$E_v = \frac{I}{2} \int d^2r r^{-2} = I\pi \int_a^L dr r^{-1} = I\pi \ln \frac{L}{a}, \quad (3.36)$$

where a is a short distance cutoff that is required to avoid the divergence at the origin and is reasonable also from the physics perspective as this model is a field theory modeling the solid as a continuum. However, on length scales smaller than a details of the discrete lattice structure have to be taken into account. Thus, the region within the circle of radius a is considered the core of the vortex that may add some contribution to the total energy that is not discussed in detail at this point.

The other end of the vortex is defined by the system size L . According to Eq. (3.36), for macroscopic system sizes the energy of a single vortex seems to diverge, but vortices are excited in pairs of $v = \pm 1$ and therefore at long distances from the cores the two contributions will cancel up to a constant. The characteristic length is then the distance between the two cores r and the energy of such a vortex/antivortex pair is

$$E_v^{pair} = 2I\pi \ln \frac{r}{a}. \quad (3.37)$$

The KT transition is the temperature at which the vortex-antivortex pairs unbind and the vortices exist independently. This occurs if the entropy term equals the energy term of the free energy. The entropy can be estimated by the number of positions that a vortex can take within the solid, i.e. L^2/a^2 . Thus, the free energy of a vortex is

$$F = I\pi \ln \frac{L}{a} - T \ln \frac{L^2}{a^2}, \quad (3.38)$$

and the transition occurs at the temperature

$$T_{KT} = \frac{\pi}{2}I. \quad (3.39)$$

The transition temperature lies in between two phases of which one is at large temperatures and disordered, and the other, at low temperatures, is ordered. The correlation length of the phases at low temperatures decays algebraically [175]

$$\left\langle e^{i(\theta(r)-\theta(0))} \right\rangle_{\text{low-}T} \sim |r|^{-\frac{T}{2\pi I}} \quad (3.40)$$

which is a rare and renders the two-dimensional case special. In contrast, a high-temperature expansion gives exponential decay of the correlation length

$$\left\langle e^{i(\theta(r)-\theta(0))} \right\rangle_{\text{high-}T} \sim e^{-r \ln \frac{2T}{I}}. \quad (3.41)$$

Thus, the phase disorder introduced by high temperatures decorrelates the rotors at large distances.

Above, in Eq. (3.30), it is shown that the stiffness I is linear to the superfluid density. Therefore, the transition temperature depends linearly to the superfluid density [176] and

this relation has been measured in the (uncharged) superfluid phase of liquid helium [177]. Superconductors are charged and therefore, the vortices and antivortices may interact via magnetic flux lines. In principle, the vortices can interact not only within a layer, but also between layers [178]. This has been investigated mostly via phenomenological theories and it remains unclear to what extent these effects are important. The crucial component regarding the KT transition is the logarithmic dependence of the vortices' interaction on the vortex-antivortex distance and screening effects provide an explanation for a similarity of superconductors to neutral superfluids [179]. Experiments on copper oxides have indeed confirmed a linear relation between superfluid density and the critical temperature, but only for the underdoped copper oxides [180]. Thus the KT transition could provide an explanation for the transition temperature of the underdoped copper oxides whereas for the overdoped copper oxides a (BCS-like) mean-field description has been suggested [169], but even the latter remains an open question [181].

The vortices have also been attempted to be measured via the Nernst-effect [99]. The application of a heat gradient to the system makes the vortices move to the cold, low-entropy, place. This is done in the presence of an orthogonal magnetic field and since the vortices in a superconductor are charged, a perpendicular electric field appears according to the Hall effect. The study was performed on the materials YBCO and LSCO, and the onset of the Nernst signal does not occur at the same temperature at which the onset of the pseudogap in photoemission spectroscopy has been observed [104]. Rather, the onset of the Nernst signal lies half way in between the superconducting transition temperature and the pseudogap temperature.

3.6.3 Josephson lattice model

The Josephson effect [182] has originally been observed in a setup of two superconducting electrodes that have a distance $d = R - L$, the tunneling junction, in between. Depending on the distance and an applied gauge field through the tunneling junction, the supercurrent in between the electrodes can be diminished or augmented in a periodic manner, which shows the wave-like interference of the superconductors. It can be described [183] by bosonic pairs of the left φ_L and right φ_R electrodes tunneling with an amplitude V

$$H = V\varphi_L\varphi_R^\dagger e^{-ia} + V\varphi_R\varphi_L^\dagger e^{ia} \quad (3.42)$$

with the phase a given by the gauge field $A(x)$

$$a(t) = \int_L^R dx A(x) = -\phi t \quad (3.43)$$

that contains the voltage difference between the electrodes ϕ . The pair fields can be decomposed into an amplitude-phase description $\varphi_i = |\varphi_i|e^{i\theta_i}$. Then, the superconducting

current through the junction is given by

$$\begin{aligned}
 \langle j \rangle &= -\partial_a H \\
 &= iV(\varphi_L \varphi_R^\dagger e^{-ia} - \varphi_R \varphi_L^\dagger e^{ia}) \\
 &= 2V|\varphi_L||\varphi_R| \sin(\theta - a(t)),
 \end{aligned} \tag{3.44}$$

where θ is the phase difference of the two condensates in the left and right electrodes. The tunneling of pairs at zero voltage $\phi = 0$ occurs only if the condensates in the two electrodes have a finite phase difference $\theta \neq n\pi$ with integer n .

The Josephson lattice model presented in the following is an effective XY model of plaquettes [184]. The local moments, the rotors, belong to plaquettes and are created by the strongly correlated pairing mechanism described by CDMFT. The mapping starts from local correlation functions of the CDMFT and uses perturbation theory, the local force theorem, to derive the effective Josephson coupling parameters of the XY model. The Josephson coupling is the (free) energy cost of phase differences between the plaquette condensates, in that sense, the plaquettes are coupled like Josephson junctions and small phase fluctuations can cause local supercurrents between them. Although the idea of a suppression in the underdoped region of copper oxides by phase fluctuations is not entirely new [169], it can be an important step towards a quantitative theory of high-temperature superconductivity. A limiting component remains, i.e. the uncertainty of the precise values of the Hubbard model parameters, thus the Josephson lattice model is not applied as an *ab initio* method. Nevertheless, the results show a reasonable order of magnitude and the Josephson lattice model provides new opportunities to support XY model calculations regarding the 2D/3D crossover [172, 185] or driven superconductivity in non-equilibrium states [186, 187].

Josephson lattice model for phase fluctuations of local pairs in copper oxide superconductors

Malte Harland,¹ Sergey Brener,¹ Alexander I. Lichtenstein,¹ and Mikhail I. Katsnelson²

¹*Institute of Theoretical Physics, University of Hamburg, Jungiusstraße 9, 20355 Hamburg, Germany*

²*Institute for Molecules and Materials, Radboud University, 6525AJ, Nijmegen, The Netherlands*



(Received 4 November 2018; revised manuscript received 18 February 2019; published 17 July 2019)

We derive an expression for the effective Josephson coupling from the microscopic Hubbard model. It serves as a starting point for the description of phase fluctuations of local Cooper pairs in $d_{x^2-y^2}$ -wave superconductors in the framework of an effective XY model of plaquettes, the Josephson lattice. The expression for the effective interaction is derived by means of the local-force theorem, and it depends on local symmetry-broken correlation functions that we obtain using the cluster dynamical mean-field theory. Moreover, we apply the continuum limit to the Josephson lattice to obtain an expression for the gradient term in the Ginzburg-Landau theory and compare predicted London penetration depths and Kosterlitz-Thouless transition temperatures with experimental data for $\text{YBa}_2\text{Cu}_3\text{O}_{7-x}$.

DOI: [10.1103/PhysRevB.100.024510](https://doi.org/10.1103/PhysRevB.100.024510)

I. INTRODUCTION

Since the discovery of High- T_c superconductivity [1] many types of competing orders have been considered [2–9] which could have strong effects on the superconducting critical temperature. It is generally recognized that in the underdoped copper-oxide superconductors the Kosterlitz-Thouless (KT) physics [10] is crucial due to strong phase fluctuations [11–16]. Important progress in the nonperturbative [17] treatment of the antiferromagnetism and d -wave superconductivity (dSC) in the Hubbard model is related to the cluster dynamical mean-field theory (CDMFT) [18–30]. It yields a local d -wave superconducting order parameter, but it neglects spatial correlations beyond the cluster. Recently, large-scale DMRG calculations [31,32] confirmed the existence of long-range superconducting correlations in the Hubbard and t - J models. The CDMFT prediction for the superconducting critical temperature T_c , however, is too high, and long-range corrections are required for a realistic description.

In this work, we apply a truncated description, coarse graining, which is a very general and powerful tool that allows for a replacement of a microscopic by a macroscopic description with microscopically defined parameters. The prototype procedure in the theory of magnetism has opened the way to a quantitative theory of magnetism for real materials [33–35]. We map the CDMFT solution of the Hubbard model onto the Josephson lattice model assuming a separation of energy scales that correspond to the dSC phase (Goldstone) and amplitude (Higgs) fluctuations. We start from a numerically exact solution of the minimal CDMFT problem with the two-by-two plaquette in a superconducting bath as an effective impurity, and we obtain a local cluster dSC order parameter. Subsequently, we introduce long-range perturbations in the dSC-phase and derive the effective coupling of the Josephson lattice model that describes phase fluctuations.

II. THEORY: FROM HUBBARD TO JOSEPHSON

The one-band Hubbard model [36], which is widely accepted to capture the essential physics of cuprates [3–5], reads

$$H = - \sum_{k\sigma} t(k) c_{k\sigma}^\dagger c_{k\sigma} + U \sum_r n_{r\uparrow} n_{r\downarrow}, \quad (1)$$

where $t(k)$ are the Fourier-transformed hopping parameters and U is the interelectron Coulomb repulsion parameter on site r . $c_{r\sigma}^\dagger$ and $c_{r\sigma}$, ($c_{k\sigma}^\dagger$ and $c_{k\sigma}$) are electron creation and annihilation operators in site (momentum) representation, respectively, and $n_{r\sigma} = c_{r\sigma}^\dagger c_{r\sigma}$. We use the nearest-neighbor hopping of the square lattice $|t|$ as energy unit and for the next-nearest-neighbor hopping $t'/t = -0.3$ for $\text{YBa}_2\text{Cu}_3\text{O}_{7-x}$ [37].

In principle, the description of the two-dimensional (2D) square lattice defined by the dispersion

$$t^{2D}(k) = 2t[\cos(k_x) + \cos(k_y)] + 4t' \cos(k_x) \cos(k_y), \quad (2)$$

is sufficient to obtain local pairs within the strong-coupling planes. However, to calculate an effective interlayer Josephson coupling and the out-of-plane London penetration depth, it is essential to have interlayer hopping. Our three-dimensional (3D) calculations, that include interlayer hopping, use an anisotropic infinite layer model [38,39] with the dispersion

$$t^{3D}(k) = t^{2D}(k) + 2 \frac{t_\perp}{4} [\cos(k_x) - \cos(k_y)]^2 \cos(k_z), \quad (3)$$

which has interlayer hopping of $d_{x^2-y^2}$ symmetry and is generic for cuprates. For Eqs. (2) and (3), k_x , k_y , and k_z are in the Brillouin zone. Note that below we introduce a two-by-two cluster formulation that corresponds to the reduced Brillouin zone (Appendix A). This requires the choice of unit lengths $a_a, a_b, a_c = 2 \times 3.82 \text{ \AA}, 2 \times 3.82 \text{ \AA}, 3.89 \text{ \AA}$ that is twice the copper distance within the copper planes of YBCO [40,41]. Further, we choose the simplified effective hopping of $t_\perp/t = 0.15$ for YBCO and the effective tight-binding hopping $|t| = 0.35 \text{ eV}$ [27,39]. The screened Coulomb interaction is

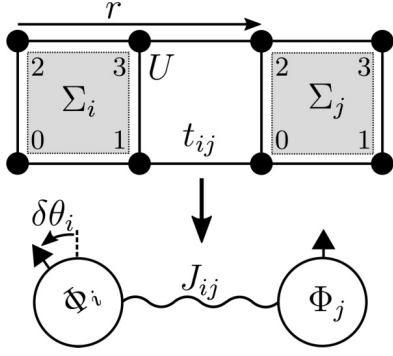


FIG. 1. Illustration of the Hubbard-plaquette lattice (t_{ij} , U) with lattice vector r , self-energies Σ_i and plaquette sites 0...3. It is mapped to the Josephson lattice model with effective coupling J_{ij} of plaquettes due to phase fluctuations $\delta\theta_i$ of the d -wave superconducting order parameter Φ_i .

set to a standard value, $U = 8|t|$, of the order of the bandwidth.

To address the specific problem of Josephson coupling in cuprates, we consider a local $U(1)$ rotation that changes the phase of the plaquette's dSC order parameter, similar to a rotation of an effective moment attributed to a two-by-two plaquette and keeps the amplitude of the local order parameter constant; see Fig. 1. We investigate macroscopic phase coherence between the plaquettes, reminiscent of the description of magnetic ordering in terms of an effective Heisenberg Hamiltonian [33,34]. The model, which can address the issue of superconducting phase ordering, is the Josephson lattice model

$$H_{\text{eff}} = - \sum_{ij} J_{ij} \cos(\theta_i - \theta_j), \quad (4)$$

i.e., an effective XY model of plaquettes. i, j are plaquette indices, and θ_i is the phase of the order parameter of plaquette i . The principal goal of our work is to obtain the Josephson coupling parameters J_{ij} based on the Hubbard model solution of the well-established CDMFT [19,21,22,26–29]. We consider the elementary plaquette in the copper layer as a supersite and introduce a superspinor $C_i^\dagger = (c_{i\alpha}^\dagger)$, where i is the index of the plaquette and $\alpha = 0\dots3$ labels the sites within the plaquette; see Fig. 1. To describe the superconducting state, we use the Nambu-Gor'kov spinor representation of the Green function, which is a 2×2 matrix. Thus, the full lattice Green function G_{ij} is an 8×8 matrix.

The explicit microscopic expressions of J_{ij} is derived by calculating the microscopic variation of the thermodynamic potential Ω of the system under small variations of the dSC

phases, and comparing the result with Eq. (4). Ω depends on the lattice Green function that we can express via the Dyson equation

$$\begin{pmatrix} G^{p\uparrow} & F \\ F & G^{h\downarrow} \end{pmatrix}_{ij}^{-1} = \begin{pmatrix} G_0^{p\uparrow} & 0 \\ 0 & G_0^{h\downarrow} \end{pmatrix}_{ij}^{-1} - \delta_{ij} \begin{pmatrix} \Sigma^{p\uparrow} & S \\ S & \Sigma^{h\downarrow} \end{pmatrix}_i, \quad (5)$$

where the last term is the local self-energy of the CDMFT (Appendix B). The superscripts p and h denote particle and hole components of the Nambu-Gor'kov representation, respectively. The anomalous parts of the self-energy S and Green function F are matrices in plaquette sites α and describe local dSC pairing via the order parameter $\Phi_{\text{dSC}}^{\text{CDMFT}} = 2T \text{Tr}_\omega F_{01}$ with $F_{01} = -F_{02}$, according to d -wave symmetry [18]. G_0 denotes the noninteracting lattice Green function. Furthermore, we consider finite temperatures T , and, therefore, the correlation functions depend on fermionic Matsubara frequencies. The last term of Eq. (5), the local self-energy Σ_i , is obtained exactly by the numerical [42–44] solution of the CDMFT.

To find the variation of the free energy

$$\begin{aligned} \Omega &= \Omega_{sp} - \Omega_{dc}, \\ \Omega_{sp} &= -\text{Tr} \ln(-G^{-1}), \\ \Omega_{dc} &= \text{Tr} \Sigma G - \Phi, \end{aligned} \quad (6)$$

with the Luttinger-Ward functional [45] Φ , we use the local-force theorem [34,46],

$$\delta\Omega \simeq \sum_{ij} \text{Tr} \left(\delta_{ij} G_{ii} \delta^* \Sigma_i + \frac{1}{2} G_{ij} \delta^* \Sigma_j G_{ji} \delta^* \Sigma_i \right), \quad (7)$$

where δ^* denotes the local variation of the self-energy Σ without taking into account its variation due to the CDMFT self-consistency, and G is the CDMFT Green function without variation. We omit matrix indices of intraplaquette and Nambu space for simplicity. Equation (7) is rigorous in the first order of the phase variations $\delta\theta_i$ [34]. However, we will use it also for the second-order terms since the first-order variation around the collinear state, $\theta_i = \text{const.}$, vanishes analytically (Appendix C). It corresponds to neglecting vertex corrections [45], which is reasonable to assume for the locally ordered phase with a well-pronounced, local order parameter [47]. Thus, near the transition, it can be used as an estimate only.

We design the variation as an infinitesimal change of the local phase $\delta\theta_i$ in a homogeneous environment. Therefore, it reads

$$\delta^* \Sigma_i = e^{i\delta\theta_i \sigma_z / 2} \Sigma_i e^{-i\delta\theta_i \sigma_z / 2} - \Sigma_i = \begin{pmatrix} \Sigma_i^{p\uparrow} & e^{i\delta\theta_i} S_i \\ e^{-i\delta\theta_i} S_i & \Sigma_i^{h\downarrow} \end{pmatrix} - \Sigma_i \simeq \begin{pmatrix} 0 & (i\delta\theta_i - \frac{(\delta\theta_i)^2}{2}) S_i \\ (-i\delta\theta_i - \frac{(\delta\theta_i)^2}{2}) S_i & 0 \end{pmatrix}, \quad (8)$$

in that the third Pauli matrix σ_z acts in the Nambu-space. This variation affects only the phases of the anomalous part of the local self-energy. We substitute Eq. (8) into Eq. (7) and the two terms of the sum become

$$G_{ii} \delta^* \Sigma_i = \begin{pmatrix} F_{ii} S_i \left(-i\delta\theta_i - \frac{(\delta\theta_i)^2}{2} \right) & G_{ii}^{p\uparrow} S_i \left(i\delta\theta_i - \frac{(\delta\theta_i)^2}{2} \right) \\ G_{ii}^{h\downarrow} S_i \left(-i\delta\theta_i - \frac{(\delta\theta_i)^2}{2} \right) & F_{ii} S_i \left(i\delta\theta_i - \frac{(\delta\theta_i)^2}{2} \right) \end{pmatrix}, \quad (9)$$

$$G_{ij}\delta^*\Sigma_j G_{ji}\delta^*\Sigma_i = \begin{pmatrix} -F_{ij}S_j F_{ji}S_i + G_{ij}^{p\uparrow}S_j G_{ji}^{h\downarrow}S_i & \dots \\ \dots & -F_{ij}S_j F_{ji}S_i + G_{ij}^{h\downarrow}S_j G_{ji}^{p\uparrow}S_i \end{pmatrix} \times \delta\theta_i\delta\theta_j. \quad (10)$$

We keep terms up to second order in $\delta\theta$, and since we are interested in the trace, we omit off-diagonals in Eq. (10). Equation (9) shows clearly that the trace makes the first order vanish. Using $\delta\theta_{ij} \equiv (\delta\theta_i - \delta\theta_j)$ and $2\delta\theta_i\delta\theta_j = -\delta\theta_{ij}^2 + \delta\theta_i^2 + \delta\theta_j^2$, we can separate local and nonlocal phase variations,

$$\delta\Omega = \sum_{ij} \text{Tr}_{\omega\alpha} (G_{ij}^{p\uparrow}S_j G_{ji}^{h\downarrow}S_i - \delta_{ij}F_{ii}S_i - F_{ij}S_j F_{ji}S_i) \delta\theta_i^2 + \frac{1}{2} \sum_{ij} \text{Tr}_{\omega\alpha} (F_{ij}S_j F_{ji}S_i - G_{ij}^{p\uparrow}S_j G_{ji}^{h\downarrow}S_i) \delta\theta_{ij}^2. \quad (11)$$

The trace goes over Matsubara frequencies and over the sites within the plaquette (α). Furthermore, the matrices form matrix-products in the α -space whereas they are diagonal in Matsubara frequencies. To obtain Eq. (11) we have also used the lattice symmetry $G_{ij} = G_{ji}$.

The term $\propto\delta\theta_i^2$ vanishes which reflects the gauge invariance of the theory (Appendix C). The remaining term is that of only nonlocal phase fluctuations $\propto\delta\theta_{ij}^2$,

$$\delta\Omega \equiv \frac{1}{2} \sum_{ij} J_{ij} \delta\theta_{ij}^2, \quad (12)$$

which by comparison with Eq. (4) defines J_{ij} . Thereby, we obtain the following expression of the Josephson lattice parameters:

$$J_{ij} = T \text{Tr}_{\omega\alpha} (-G_{ij}^{p\uparrow}S_j G_{ji}^{h\downarrow}S_i + F_{ij}S_j F_{ji}S_i), \quad (13)$$

which is essentially the main result of the present work.

III. SHORT-RANGE JOSEPHSON LATTICE PARAMETERS

Effective Josephson couplings have been applied to investigate experiments in that interplane Josephson coupling has an essential role [48,49]. We present a selection of the Josephson couplings J_r for plaquette-translations r in Fig. 2. J_r reduces sharply with increasing plaquette-translation length $|r|$, and thus the short-range components of J_r alone can give a complete description. The strongest coupling is J_{100} , followed by the interlayer coupling J_{001} . They have their maxima around $\delta = 0.05$ and $\delta = 0.1$, respectively. All couplings diminish at large dopings, $\delta > 0.1$. We observe in Sec. IV that this stems from the diminishing of the local order parameter (amplitude) of the dSC.

In the range up to $t_{\perp} = 0.45$, t_{\perp} has a diminishing effect on all in-plane J_r , shown in Fig. 2 (right). In contrast, the interlayer coupling has to increase at small t_{\perp} since there has to be $J_{001} = 0$ in a system of disconnected layers ($t_{\perp} = 0$). J_{001} becomes the second largest coupling at $t_{\perp} = 0.15$, and at $t_{\perp} = 0.2$ it reaches a maximum. For larger t_{\perp} all couplings decrease, similar to the behavior at large dopings.

The first term of Eq. (13) ($GSGS$) is negative, and the second ($FSFS$) is positive. $GSGS$ is a mixed term with normal

(G) and anomalous (S) contributions. It makes the main contribution to J ; see Fig. 3. J can be finite only if there is a superconducting gap and therefore a finite anomalous self-energy S as both terms depend on it. Regarding the largest contributions to the nearest neighbor Josephson coupling $J_{(1,0,0)}$, $GSGS$ is about three times larger than $FSFS$. However, at small dopings both terms contribute with similar magnitude, but their doping dependence can be very different. At $\delta \sim 0.05$ the first term drops sharply and $J_{(1,0,0)}$ is defined by $GSGS$. The second and third in-plane nearest neighbors have contributions from both terms and they can be of similar magnitude. However, the doping dependence have different local features, e.g., a local minimum of the second term appears in $J_{(1,1,0)}$, at a point where the first term has a maximum.

IV. SUPERCONDUCTING STIFFNESS

To study macroscopic observables of the Josephson lattice model, we take the continuum, long-wavelength limit of Eq. (4). In this limit, the interaction becomes the superconducting stiffness (Appendix D)

$$I_{ab} = \frac{T}{(2\pi)^d} \int d^d k \text{Tr}_{\omega\alpha} \times \left(-\frac{\partial G^{p\uparrow}(k)}{\partial k_a} S \frac{\partial G^{h\downarrow}(k)}{\partial k_b} S + \frac{\partial F(k)}{\partial k_a} S \frac{\partial F(k)}{\partial k_b} S \right), \quad (14)$$

with the effective Hamiltonian

$$H_{\text{eff}} = \frac{1}{2} \sum_{ab} I_{ab} \int d^d r \frac{\partial\theta}{\partial r_a} \frac{\partial\theta}{\partial r_b}. \quad (15)$$

For our model I_{ab} consists of an in-plane I_{\parallel} and a perpendicular I_{\perp} component. I_{\perp} is nonzero only in the (3D) case of interlayer hoppings $t_{\perp} > 0$. Equation (15) can be viewed as the limit of the general Ginzburg-Landau equation for the case of a constant absolute value of the superconducting order

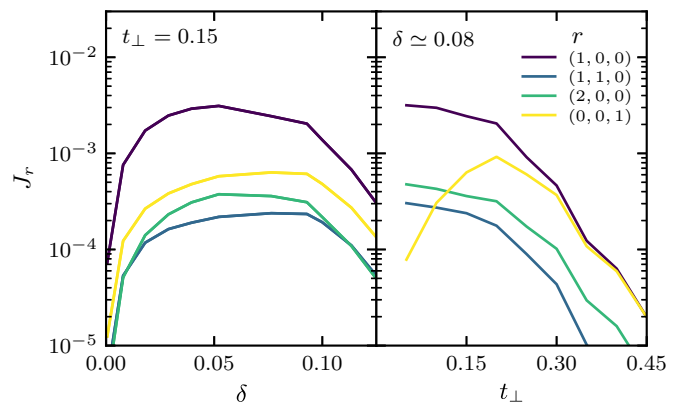


FIG. 2. Josephson coupling J_r as a function of doping δ (left) and interlayer hopping t_{\perp} (right) for different plaquette translations r at $T = 1/52$

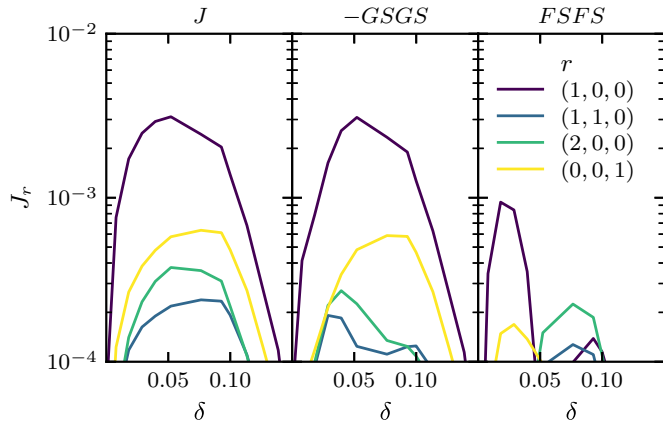


FIG. 3. Josephson coupling J_r (left) and its constituents, $GSGS$ (center) and $FSFS$ (right), as functions of doping δ and for different plaquette translations r at $T = 1/52 \sim 0.02$, $t_{\perp} = 0.15$.

parameter and negligible electromagnetic fields. The latter condition is controlled by slow spatial variations of the phase of the order parameter.

We start the discussion of the dSC stiffness for the 2D case of $t_{\perp} = 0$. The temperature dependence of the dSC stiffness can be divided into two, qualitatively different, regions depending on the hole-dopings of the copper planes δ ; see Fig. 4 (top). In the underdoped regime ($0 \lesssim \delta \lesssim 0.075$) the temperature at that I_{\parallel} becomes nonzero is constant. Furthermore, I_{\parallel} shows saturation with decreasing T only in the underdoped regime. In contrast, in the optimal- to over-doped regime ($0.1 \lesssim \delta \lesssim 0.15$), the temperature at that I_{\parallel} becomes nonzero, as well as the low-temperature ($T \sim 0.02$) value of I_{\parallel} , decrease with larger doping. The low-temperature doping dependence of I_{\parallel} qualitatively agrees with experimental studies on YBCO [50,51] (and $\text{La}_{2-x}\text{Sr}_x\text{CuO}_4$ [52]) and also with a study of the intensity of a current-current correlation function's Drude-like peak [21]. Note, that the latter method can give just a number for the superfluid density whereas our approach allows to restore the whole Hamiltonian with the nonlocal effective Josephson parameters.

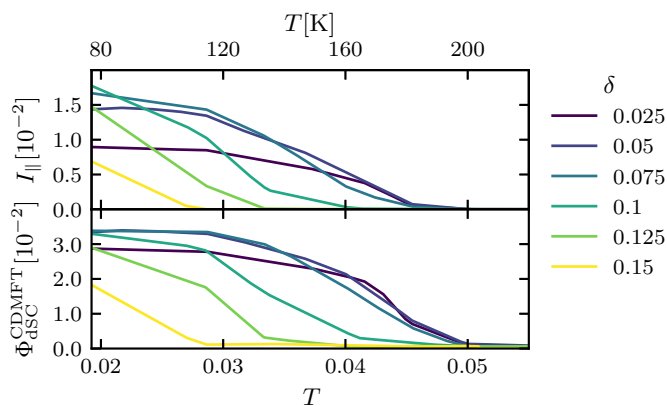


FIG. 4. Superconducting stiffness I_{\parallel} (top) and order parameter for local Cooper-pair formation $\Phi_{\text{dSC}}^{\text{CDMFT}}$ (bottom) as functions of the temperature T for various dopings δ ($t_{\perp} = 0$).

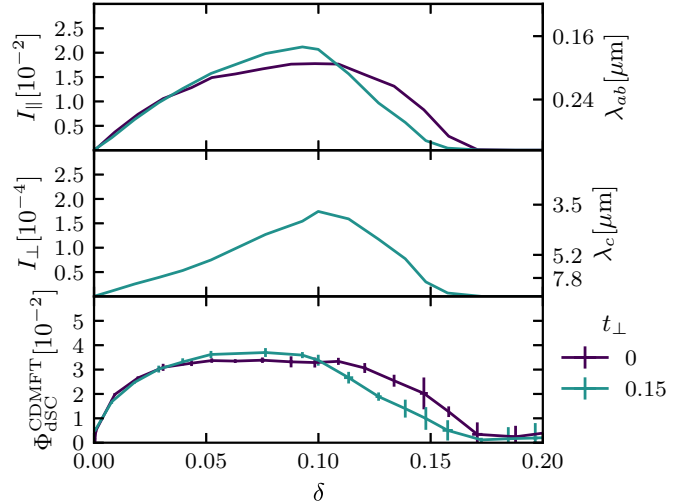


FIG. 5. In-plane superconducting stiffness I_{\parallel} (top, left), in-plane penetration depth λ_{ab} (top, right), perpendicular superconducting stiffness I_{\perp} (center, left), perpendicular penetration depth (center, right), and CDMFT dSC order parameter $\Phi_{\text{dSC}}^{\text{CDMFT}}$ (bottom) as functions of doping δ at $T = 1/52$ for different interlayer hoppings t_{\perp} .

Regarding the accuracy of the local-force theorem, it is important to check whether the saturation of the local order parameter $\Phi_{\text{dSC}}^{\text{CDMFT}}$ with respect to decreasing temperature is reached. If this is the case, then the phase fluctuations are effectively decoupled from the Higgs mode and can be considered independently. Otherwise, amplitude fluctuations of the dSC can become stronger and vertex corrections, that we neglect, become significant [47]. Our calculations show a saturation of $\Phi_{\text{dSC}}^{\text{CDMFT}}$ at $T \sim 0.02$ for dopings $\delta \lesssim 0.1$. Arbitrary low temperatures cannot be reached because of the CTQMC-fermionic sign problem [44].

In Fig. 5 we compare the in-plane/perpendicular dSC stiffness and penetration depth as well as the order parameter of local Cooper pair formation for different t_{\perp} (3D). t_{\perp} has a minor impact on I_{\parallel} which is probably related to our special choice of in-plane plaquette and to the mean-field character of the CDMFT. The perpendicular hopping $t_{\perp} = 0.15$ enhances I_{\parallel} at optimal doping ($\delta \sim 0.1$) and reduces I_{\parallel} at overdoping. At small dopings ($\delta < 0.05$), I_{\parallel} is almost independent of t_{\perp} . Furthermore, for $t_{\perp} = 0.15$, I_{\parallel} is two orders of magnitude larger than I_{\perp} (Fig. 5, center) reflecting the fact that, according to the Josephson lattice model, the superfluid is more concentrated within the strongly coupled copper planes. A comparison of $I_{\parallel/\perp}$ with $\Phi_{\text{dSC}}^{\text{CDMFT}}$ (Fig. 5, bottom) shows that $I_{\parallel/\perp}$ has a more pronounced dome shape whereas $\Phi_{\text{dSC}}^{\text{CDMFT}}$ has a plateau, up to almost half-filling. Thus, relative to $\Phi_{\text{dSC}}^{\text{CDMFT}}$ the profile of $I_{\parallel/\perp}$ is suppressed in the underdoped regime.

I is closely related to the London penetration depth [12,53] (Appendix E), i.e.,

$$\lambda^{-2} = \frac{16\pi e^2}{\hbar^2 c^2} I. \quad (16)$$

λ has been measured in several experiments on $\text{YBa}_2\text{Cu}_3\text{O}_{7-x}$, also at different oxygen dopings x . The low-temperature values lie in the range of $\lambda_{ab} = 0.1 - 0.24 \mu\text{m}$ and $\lambda_c = 0.6 - 7.8 \mu\text{m}$ [54–60]. Finite temperature effects

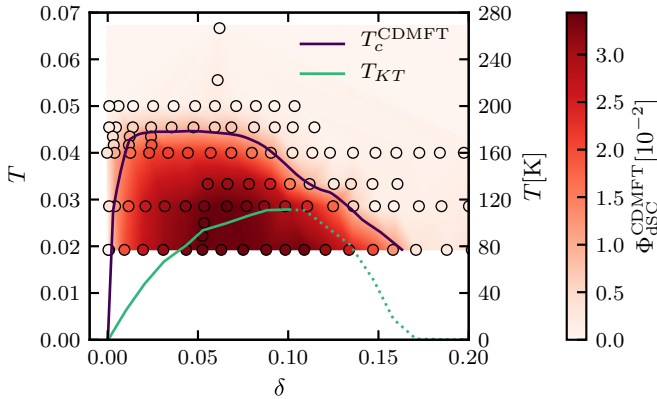


FIG. 6. Phase diagram of the local dSC order parameter $\Phi_{\text{dSC}}^{\text{CDMFT}}$ with critical temperature T_c^{CDMFT} depending on the temperature T and doping δ ($t_{\perp} = 0$). Circles denote CDMFT calculations. The transition temperature of the Josephson lattice model T_{KT} has been calculated from the superconducting stiffness at $T = 1/52$, at that $I_{\parallel}(T)$ is (not) saturated for the solid (dotted) part.

can add $\Delta\lambda_{ab} \sim 0.1 \mu\text{m}$ around $T \sim 80 \text{ K}$ [61]. In the underdoped region ($x = 0.4$), the penetration depth is $\lambda_{ab} = 0.24 \mu\text{m}$ which is within the predicted range by our theory, around $\delta \sim 0.03$. Note, that the relation between the oxygen doping of YBCO x and the hole doping of the copper-oxide planes δ is understood only qualitatively. Our largest value of $\lambda_{ab} \sim 0.16 \mu\text{m}$ is similar to the experimental result of $\lambda_{ab} = 0.15 \mu\text{m}$ for $x = 0.05$ (optimal oxygen doping). Regarding the c direction for the underdoped regime ($x = 0.3\text{--}0.5$), experiments have found $\lambda_c = 5.2\text{--}7.8 \mu\text{m}$ which we have calculated around $\delta = 0.025\text{--}0.05$. In our calculations λ is very sensitive to the details of the electronic interlayer properties (Appendix F) and the uncertainty in the interlayer hopping limits the accuracy of our predictions of λ .

In 2D, the XY model of Eq. (4) exhibits the KT transition that corresponds to the unbinding of vortex-antivortex pairs. The transition temperature reads [62]

$$T_{\text{KT}} = \frac{\pi}{2} I_{\parallel}. \quad (17)$$

This proportionality of transition temperature and dSC stiffness can explain the Uemura relation [11] that has been measured in underdoped copper-oxides, via the muon spin relaxation rate. At $T < T_{\text{KT}}$ there is no real long-range order in the system but power-law decay of the correlation function of the superconducting order parameter. In this sense, interlayer tunneling is essentially important to allow for a dimensional crossover and long-range order [63,64]. In Fig. 6 we present the transition temperatures of the CDMFT T_c^{CDMFT} , i.e., of local pair formation, and of the KT transition T_{KT} . We use I of the lowest temperature available, $T \sim 0.02$, to calculate the KT transition temperature. At $\delta \lesssim 0.1$ the low-temperature saturation of $\Phi_{\text{dSC}}^{\text{CDMFT}}$ and I_{\parallel} has been reached (Fig. 4), and thus, the application of our method is reliable. At $\delta \gtrsim 0.1$ amplitude fluctuations can change the transition temperature.

The suppression of the dSC by phase fluctuations is most pronounced at small dopings. This is where local Cooper-pairs, according to CDMFT, are well defined, up to half-filling. At half-filling the system is a Mott insulator [24,27,65]

(Appendix B), for which we have added a $T = 0$ data point of prior CDMFT studies [66]. The case of $T_c^{\text{CDMFT}} > T_{\text{KT}}$ suggests a pseudogap interpretation of preformed meta-stable pairs [12,67] in the underdoped copper-oxides. However, CDMFT supports other explanations as well [22,24,25,28]. Note, that local antiferromagnetic fluctuations are included by CTQMC, but antiferromagnetic ordering and long-ranged spin waves are not. The latter can contribute to the suppression of superconductivity in cuprates, particularly at $\delta \lesssim 0.05$ [68]. The maximum transition temperature of CDMFT is $T_c^{\text{CDMFT,max}} \sim 180 \text{ K}$, which is nearly twice as large as the experimental value [40]. In contrast, including phase fluctuations gives a major correction, as $T_{\text{KT}}^{\text{max}} \sim 120 \text{ K}$. A comparison with the critical temperature of YBCO $T_c = 93 \text{ K}$ [59] and its Nernst region, which extends over a range up to 20 K [69–71], shows that the Josephson lattice model and phase disorder can be important for a quantitative description.

V. CONCLUSION

We have derived a mapping from the Hubbard to the Josephson lattice model, i.e., Eq. (13), and obtained effective couplings that will be interesting to study further in a more realistic bilayer model for, e.g., $\text{YBa}_2\text{Cu}_3\text{O}_{7-x}$ or $\text{La}_{2-x}\text{Ba}_x\text{CuO}_4$ [7,72–74], in particular, in the framework of the XY model. At $T \sim t/50$ our theory is applicable to the underdoped regime as there the order parameter is well defined and the assumption of the separation of energy scales of amplitude and phase fluctuations is reasonable. Further, we have used analytical results of the XY model to compare predictions, based on the obtained effective couplings, to experiments on $\text{YBa}_2\text{Cu}_3\text{O}_{7-x}$. The London penetration depths have been confirmed to be reasonable estimates, and the KT transition lies closer to the experimental value than the critical temperature of the CDMFT, which can indicate long-range phase disorder effects.

ACKNOWLEDGMENTS

We thank G. Homann, L. Mathey, and A. Millis for discussions. M.H., S.B., and A.I.L. acknowledge support by the Cluster of Excellence ‘‘Advanced Imaging of Matter’’ of the Deutsche Forschungsgemeinschaft (DFG)—Grant No. EXC 2056—Project ID No. 390715994, and by the DFG SFB 925. M.I.K. acknowledges financial support from NWO via Spinoza Prize. The computations were performed with resources provided by the North-German Supercomputing Alliance (HLRN).

APPENDIX A: TIGHT-BINDING MODEL

In most strong-coupling calculations on copper-oxides theoreticians use the single-band Hubbard model as the main features are believed to exist in the square lattice symmetry. However, starting density functional calculations one can also integrate out the bands at energies distant from Fermi level and obtain an effective one-band model, which has been done for YBCO [39]. At this point we note that the complicated structure of YBCO which consists of bilayers with the intra-bilayer hopping of the order of 0.65 in units of t results in

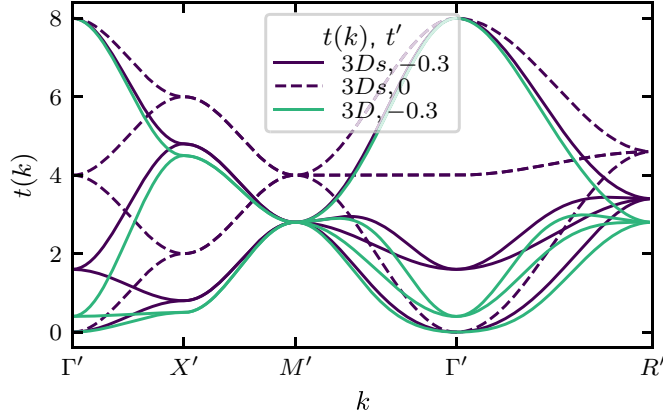


FIG. 7. Electronic tight-binding band structures of the different hopping lattices 3D and 3D* and next-nearest-neighbor hoppings t' . k is the reciprocal lattice vector in the reduced Brillouin zone. The four bands correspond to four sites within the two-by-two plaquette unit cell. With our choice of cluster the reduced Brillouin zone has the same shape as the original Brillouin zone of the square lattice. Thus, we label the high symmetry points accordingly but with a prime. $\Gamma' = (0, 0, 0)$, $X' = (1, 0, 0)$, $M' = (1, 1, 0)$, $R' = (1, 1, 1)$ in units of half of the reduced Brillouin zone.

a splitting between bonding and antibonding bands with the value of the splitting being much larger than the individual bandwidth of each of those. This is the reason why it is possible in the first approximation to consider an effective one (antibonding) band model. In this section we compare the effects of the band structures on the dSC stiffness also for a simple perpendicular hopping.

The 2D dispersion is that of the square lattice,

$$t^{2D}(k) = 2t[\cos(k_x) + \cos(k_y)] - 4t' \cos(k_x) \cos(k_y), \quad (\text{A1})$$

then, for three dimensions we can compare a simple perpendicular hopping model (3Ds),

$$t^{3Ds}(k) = t^{2D}(k) + 2t_{\perp} \cos(k_z), \quad (\text{A2})$$

with a more elaborated projection [39] (3D),

$$t^{3D}(k) = t^{2D}(k) + 2\frac{t_{\perp}}{4}[\cos(k_x) - \cos(k_y)]^2 \cos(k_z). \quad (\text{A3})$$

In Eq. (A1) to Eq. (A3) k is in the full Brillouin zone. For a cluster formulation k has to be in the reduced Brillouin zone according to the reduced translational symmetry. The band structure shown in Fig. 7 has four bands corresponding to the cluster of four sites. The hopping matrices t_r of plaquette translations r for the 3D model read

$$\begin{aligned}
 t_{(0,0,0)} &= \begin{pmatrix} 0 & t & t & t' \\ t & 0 & t' & t \\ t & t' & 0 & t \\ t' & t & t & 0 \end{pmatrix}, & t_{(1,0,0)} &= \begin{pmatrix} 0 & t & 0 & t' \\ 0 & 0 & 0 & 0 \\ 0 & t' & 0 & t \\ 0 & 0 & 0 & 0 \end{pmatrix}, & t_{(1,1,0)} &= \begin{pmatrix} 0 & 0 & 0 & t' \\ 0 & 0 & 0 & 0 \\ 0 & 0 & 0 & 0 \\ 0 & 0 & 0 & 0 \end{pmatrix}, & t_{(0,1,0)} &= \begin{pmatrix} 0 & 0 & t & t' \\ 0 & 0 & t' & t \\ 0 & 0 & 0 & 0 \\ 0 & 0 & 0 & 0 \end{pmatrix}, \\
 t_{(-1,1,0)} &= \begin{pmatrix} 0 & 0 & 0 & 0 \\ 0 & 0 & t' & 0 \\ 0 & 0 & 0 & 0 \\ 0 & 0 & 0 & 0 \end{pmatrix}, & t_{(0,0,1)} &= \begin{pmatrix} t_0 & 0 & 0 & t_2 \\ 0 & t_0 & t_2 & 0 \\ 0 & t_2 & t_0 & 0 \\ t_2 & 0 & 0 & t_0 \end{pmatrix}, & t_{(1,0,1)} = t_{(1,0,-1)} &= \begin{pmatrix} t_1 & 0 & 0 & t_2 \\ 0 & t_1 & 0 & 0 \\ 0 & t_2 & t_1 & 0 \\ 0 & 0 & 0 & t_1 \end{pmatrix}, \\
 t_{(0,1,1)} = t_{(0,1,-1)} &= \begin{pmatrix} t_1 & 0 & 0 & t_2 \\ 0 & t_1 & t_2 & 0 \\ 0 & 0 & t_1 & 0 \\ 0 & 0 & 0 & t_1 \end{pmatrix}, & t_{(1,1,1)} = t_{(1,1,-1)} &= \begin{pmatrix} 0 & 0 & 0 & t_2 \\ 0 & 0 & 0 & 0 \\ 0 & 0 & 0 & 0 \\ 0 & 0 & 0 & 0 \end{pmatrix}, & t_{(-1,1,1)} = t_{(-1,1,-1)} &= \begin{pmatrix} 0 & 0 & 0 & 0 \\ 0 & 0 & t_2 & 0 \\ 0 & 0 & 0 & 0 \\ 0 & 0 & 0 & 0 \end{pmatrix},
 \end{aligned} \quad (\text{A4})$$

with $t_0 = t_{\perp}/4$, $t_1 = t_{\perp}/16$, $t_2 = t_{\perp}/8$ and $t_{-r} = t_r^{\dagger}$. The entries correspond to the clustersites, labeled according to Fig. 1.

APPENDIX B: GREEN FUNCTIONS IN CDMFT

We solve the CDMFT [18,19,75] equation

$$\mathcal{G}^{-1}(i\omega_n) = \left(\sum_k G(i\omega_n, k) \right)^{-1} + \Sigma(i\omega_n), \quad (\text{B1})$$

$$G^{-1}(i\omega_n, k) = i\omega_n + \mu - t(k) + \Sigma(i\omega_n), \quad (\text{B2})$$

with the lattice dispersion of the reduced Brillouin zone $t(k)$ numerically [42,43] and obtain the self-consistent local lattice Green function that is the first term on the right-hand side of Eq. (B1). The chemical potential for a certain doping can

be found by solving only Eq. (B2) iteratively. But this is an additional quantity that has to converge with the CDMFT cycles. To make the CDMFT more efficient in that regard, we set a certain chemical potential μ as the parameter rather than the doping. This gives a nonuniform mesh in the temperature-doping phase diagram and requires a postprocessing of two-dimensional interpolation. CDMFT maps the lattice problem to a multiorbital Anderson impurity model, in that the different orbitals also represent the sites of the cluster. The Anderson impurity model of arbitrary local interactions can be solved exactly by the use of the continuous-time quantum Monte Carlo method (CTHYB). The bath of that model is dynamical and so is the mean field of CDMFT. But the temporal correlations exist only locally, i.e., on the cluster. Therefore, the self-energy between clusters vanishes.

Using the symmetry of the plaquette, the local Green function has the block structure

$$G_{\text{loc}} = \begin{pmatrix} G_{\Gamma} & & & \\ & G_X & & \\ & & G_Y & \\ & & & G_M \end{pmatrix}, \quad (\text{B3})$$

where we labeled the plaquette orbitals according to the same transformation properties of the high-symmetry points of the Brillouin zone of the square lattice. The transformation from site-space to plaquette orbitals is a unitary transformation with

$$U = \frac{1}{2} \begin{pmatrix} 1 & 1 & 1 & 1 \\ 1 & -1 & 1 & -1 \\ 1 & 1 & -1 & -1 \\ 1 & -1 & -1 & 1 \end{pmatrix}. \quad (\text{B4})$$

In principle, antiferromagnetic order can also be considered, but it would reduce the blockstructure of Eq. (B3) and will be computationally more expensive.

In our CDMFT approximation the self-energy exists only within the cluster and not between clusters. To obtain the lattice Green function one could try to interpolate the many-body correlations between the clusters. This procedure is ambiguous. Following the idea of strong correlations within the plaquette being crucial, we do not interpolate the self-energy. The locality of the self-energy is required for the applicability of the local force theorem. In that aspect, the CDMFT we use and the local force theorem are perfectly compatible as they make the same assumptions. Therefore, the lattice Green function reads

$$G(i\omega_n, r) = \frac{1}{N_k} \sum_k \frac{e^{ikr}}{i\omega_n + \mu - t(k) - \Sigma(i\omega_n)}, \quad (\text{B5})$$

where r are cluster-translations and $i\omega$, μ , $t(k)$, and $\Sigma(i\omega_n)$ are matrices in Nambu plaquette-orbital or site-basis. k is in the reduced Brillouin zone according to plaquette translations. For the CDMFT calculations we use 1025 Matsubara frequencies, 64 k -points per dimension, 192×10^5 Monte Carlo (MC) measurements, 200 updates per MC measurement and 3×10^3 MC warm-up cycles. The number of Legendre-coefficients for the representation of the Green function, that we measure in the Monte Carlo process, depends mostly on the temperature. A reasonable range for our calculations is 50–150. During the CDMFT loops we perform partial updates of the self-energy using a mixing parameter of 0.5. For the dSC symmetry breaking we initialized the CDMFT cycles with a symmetry breaking seed in the self-energy.

A success of the DMFT is the description of the Mott insulator, an insulator of odd-integer filling, that is gapped by local correlation effects induced by U . It can be characterized by the vanishing quasiparticle residue,

$$Z_k^{-1} = 1 - \left. \frac{\partial \text{Re} \Sigma_k(\omega)}{\partial \omega} \right|_{\omega=0}, \quad (\text{B6})$$

of that k -point, whose energy corresponds to the Fermi energy and at $T = 0$. Furthermore, we have the quasiparticle energy,

$$\tilde{\epsilon}_X = -\mu - 4t' + \text{Re} \Sigma_X(\omega = 0), \quad (\text{B7})$$

whose zeros can indicate the Lifshitz transition [29,30], at that the Fermi surface turns from particlelike to holelike. We

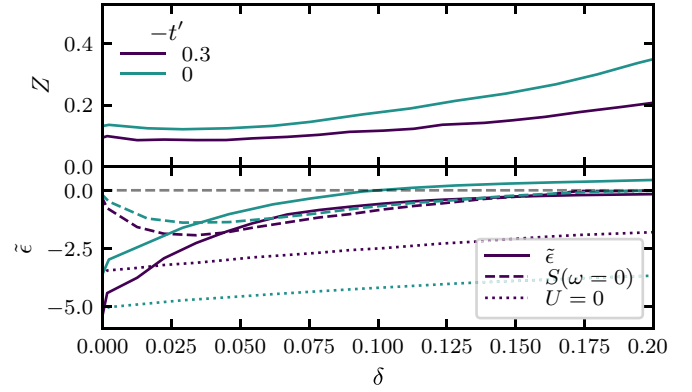


FIG. 8. The quasiparticle residue Z (top) and energy $\tilde{\epsilon}$ of $k = X$ (bottom) as functions of the hole-doping δ . The noninteraction quasiparticle energy ($U = 0$) and the anomalous part S are also shown (bottom) ($T = 1/52$, $t_{\perp} = 0$).

present these quantities for symmetry broken solutions. Thus, there is a gap and no quasiparticles. However, assuming that the feedback of a finite anomalous self-energy S on the normal parts is small and extract information on the underlying electron quasiparticles and correlations.

The quasiparticle get significantly renormalized close to half-filling resembling Mottness; see Fig. 8. The Mott insulator is known to be connected to metallic states by a first-order transition [75]. The anomalous part of the self-energy S makes an essential contribution to the Josephson coupling and the dSC stiffness. It can be seen in Fig. 8 that it becomes small at small frequencies around $\delta \sim 0.15$ at $T \sim 0.2$.

APPENDIX C: GAUGE INVARIANCE AND ITS CONSEQUENCES

Sum-rules express correlations of certain transitions in terms of sums over other transitions. We derive a set of sum-rules starting from the Dyson equation. In this section we work in the Nambu-space (omitting the spin labels for convenience), but the quantities can still be matrices of other subspaces. Therefore, we have

$$\begin{aligned} G &= \begin{pmatrix} G^p & F \\ F & G^h \end{pmatrix}, \\ G_0^{-1} &= \begin{pmatrix} (G_0^p)^{-1} & 0 \\ 0 & (G_0^h)^{-1} \end{pmatrix}, \\ \Sigma &= \begin{pmatrix} \Sigma^p & S \\ S & \Sigma^h \end{pmatrix}. \end{aligned} \quad (\text{C1})$$

We temporarily switch to the bonding-/antibonding (+, -) basis

$$2G^{\pm} = G^p + G^h, \quad 2G^{-} = G^p - G^h \quad (\text{C2})$$

and for Σ and G_0 accordingly. We expand the correlation functions in Pauli matrices:

$$\begin{aligned} G &= G^+ \mathbb{1} + (F, 0, G^-) \sigma, \\ \Sigma &= \Sigma^+ \mathbb{1} + (S, 0, \Sigma^-) \sigma, \\ G_0 &= G_0^+ \mathbb{1} + (0, 0, G_0^-) \sigma. \end{aligned} \quad (\text{C3})$$

The Dyson equation then reads

$$G^{-1} = (G_0^+ - \Sigma^+) \mathbb{1} + (S, 0, G_0^- - \Sigma^-) \sigma. \quad (\text{C4})$$

The identity

$$GG^{-1} = \mathbb{1} \quad (\text{C5})$$

leads to a set of four equations:

$$\mathbb{1} = G^+(G_0^+ - \Sigma^+) - FS + G^-(G_0^- - \Sigma^-), \quad (\text{C6})$$

$$0 = F(G_0^+ - \Sigma^+) - G^+S, \quad (\text{C7})$$

$$0 = F(G_0^- - \Sigma^-) + G^-S, \quad (\text{C8})$$

$$0 = G^+(G_0^- - \Sigma^-) + G^-(G_0^+ - \Sigma^+). \quad (\text{C9})$$

From Eqs. (C7) and (C8) directly follows

$$(G_0^+ - \Sigma^+) = F^{-1}G^+S, \quad (\text{C10})$$

$$(G_0^- - \Sigma^-) = -F^{-1}G^-S, \quad (\text{C11})$$

which we insert in Eq. (C6) also back-transforming the (+, -) basis,

$$\mathbb{1} = -FS + \frac{1}{2}(G^p F^{-1} G^h S + G^h F^{-1} G^p S). \quad (\text{C12})$$

Furthermore, we insert Eq. (C7) and (C8) into Eq. (C9), which results in

$$G^p F^{-1} G^h = G^h F^{-1} G^p. \quad (\text{C13})$$

Finally, combining Eqs. (C12) and (C13) gives an expression for the anomalous part of the self-energy:

$$S = (G^p F^{-1} G^h - F)^{-1}. \quad (\text{C14})$$

We substitute it into the coefficient of the local perturbations $\sim \delta\theta_i^2$ of Eq. (11) and analyze it in two contributions.

With Eq. (C13) the first term immediately reads

$$G^p S G^h S = [G^h F^{-1} - F(G^p)^{-1}]^{-1} [G^p F^{-1} - F(G^h)^{-1}]^{-1}. \quad (\text{C15})$$

The second involves a bit more algebra:

$$\begin{aligned} FS(1 + FS) &= (G^p F^{-1} G^h F^{-1} - 1)^{-1} [1 + (G^p F^{-1} G^h F^{-1} - 1)^{-1}] \\ &= (G^p F^{-1} G^h F^{-1} - 1)^{-1} G^p F^{-1} G^h F^{-1} (G^p F^{-1} G^h F^{-1} - 1)^{-1} \\ &= [G^h F^{-1} - F(G^p)^{-1}]^{-1} [G^p F^{-1} - F(G^h)^{-1}]^{-1}. \end{aligned} \quad (\text{C16})$$

It makes the contribution of local phase fluctuations to the variation of the thermodynamic potential vanish [see Eq. (11)], i.e.,

$$G^p S G^h S - FS - FSFS = 0, \quad (\text{C17})$$

and therefore ensures the gauge invariance.

APPENDIX D: CONTINUOUS MEDIUM LIMIT

We take the continuum limit of the Josephson lattice model to obtain a relation to the macroscopic observable, the superconducting stiffness I . Starting from the long-wavelength approximation,

$$H = \frac{1}{2} \sum_{ij} J_{ij} \theta_{ij}^2, \quad (\text{D1})$$

we assume a rather uniform spatial profile of the low-energy modes. Therefore, it is reasonable to interpolate linearly between the plaquettes (i, j) as we move them infinitesimally close together and take the continuum-limit,

$$\begin{aligned} \theta_{ij} &\rightarrow \nabla\theta(r)(r - r') \\ &= \sum_a \frac{\partial\theta}{\partial r_a} (r - r')_a. \end{aligned} \quad (\text{D2})$$

In this limit the Hamiltonian reads

$$H = \frac{1}{2} \sum_{ab} \int d^d r \frac{\partial\theta}{\partial r_a} \frac{\partial\theta}{\partial r_b} I_{ab}(r), \quad (\text{D3})$$

with the d -dimensional unit-cell volume V and the superconducting stiffness

$$I_{ab}(r) = \frac{1}{V^2} \int d^d r' J(r - r')(r - r')_a (r - r')_b. \quad (\text{D4})$$

We substitute $R = r - r'$ and insert the Fourier representation of J :

$$\begin{aligned} I_{ab} &= \frac{1}{V} \int \frac{d^d q}{(2\pi)^d} \int d^d R e^{iqR} R_a R_b J(q) \\ &= -\frac{1}{V} \partial_{q_a} \partial_{q_b} J(q) \Big|_{q=0}, \end{aligned} \quad (\text{D5})$$

with

$$J(q) = \frac{VT}{(2\pi)^d} \int d^d k \text{Tr}_{\omega\alpha} (F_k S F_{k-q} S - G_k^{p\uparrow} S G_{k-q}^{h\downarrow} S). \quad (\text{D6})$$

Next we have to evaluate the derivative. After performing the derivative with respect to q , we can substitute $k' = k - q$ and perform a partial integration that leads to

$$\begin{aligned} \partial_{q_a} \partial_{q_b} J(q) &= \frac{-VT}{(2\pi)^d} \int d^d k' \text{Tr}_{\omega\alpha} \{ (\partial_{k'_a} F_{k'-q}) S (\partial_{k'_b} F_{k'}) S \\ &\quad - (\partial_{k'_a} G_{k'-q}^{p\uparrow}) S (\partial_{k'_b} G_{k'}^{h\downarrow}) S \} \end{aligned} \quad (\text{D7})$$

and in Eq. (D5) finally to

$$\begin{aligned} I_{ab} &= \frac{T}{(2\pi)^d} \int d^d k \text{Tr}_{\omega\alpha} \\ &\quad \times \left(\frac{\partial F(k)}{\partial k_a} S \frac{\partial F(k)}{\partial k_b} S - \frac{\partial G^{p\uparrow}(k)}{\partial k_a} S \frac{\partial G^{h\downarrow}(k)}{\partial k_b} S \right), \end{aligned} \quad (\text{D8})$$

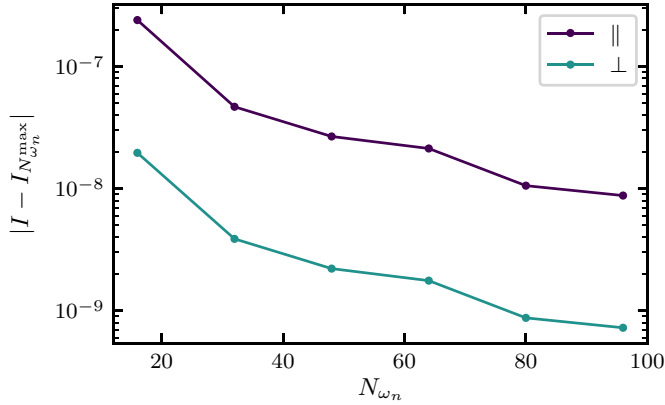


FIG. 9. Convergence of the dSC stiffness I with number of Matsubara frequencies ω_n ($N_{\omega_n}^{\max} = N_k = 128$).

with the effective Hamiltonian

$$H_{\text{eff}} = \frac{1}{2} \sum_{ab} I_{ab} \int d^d r \frac{\partial \theta}{\partial r_a} \frac{\partial \theta}{\partial r_b}. \quad (\text{D9})$$

Note that the physical units of the dSC stiffness are restored by

$$I_{\parallel} \rightarrow \frac{a_a}{a_b a_c} t I_{\parallel}, \quad I_{\perp} \rightarrow \frac{a_c}{a_a a_b} t I_{\perp}. \quad (\text{D10})$$

In particular, for numerical purposes we express the derivatives in terms of derivatives applied to inverse Green functions,

$$\partial_{k_a} G = -G(\partial_{k_a} G^{-1})G, \quad (\text{D11})$$

since it reduces the differentiation to that of the electron dispersion $G^{-1}(k) \sim t(k)$, which can be performed analytically. Regarding the number of k points per dimension and Matsubara frequencies ω_n we choose $N_k = N_{i\omega_n} = 64$, which is sufficient for an accuracy of $\sim 10^{-7}$; see Figs. 9 and 10.

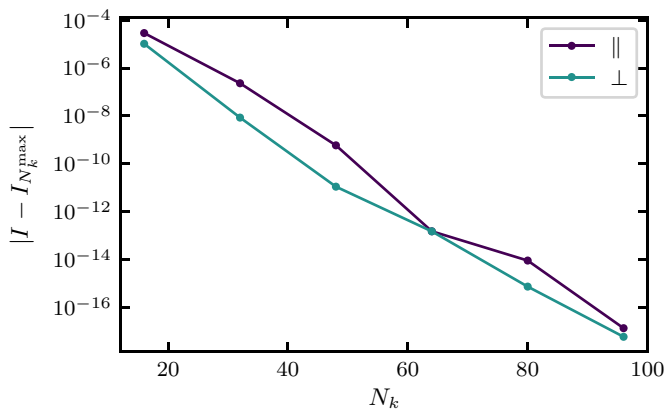


FIG. 10. Convergence of the dSC stiffness I with number of k -points per dimension ($N_k^{\max} = N_{\omega_n} = 128$).

APPENDIX E: LONDON PENETRATION DEPTH

The London penetration depth describes how far a magnetic field penetrates into the superconductor despite the Meissner effect. The superconductor expels the magnetic field by forming supercurrents. Thereby, the magnetic field decays exponentially into the superconductor. To describe the Josephson lattice model coupled to an electromagnetic field we start from the gauge-invariant minimal coupling Hamiltonian,

$$H = \frac{1}{2} \sum_{ab} I_{ab} \int d^d r \left(\frac{\partial \theta}{\partial r} - \frac{e}{\hbar c} 2A \right)_a \left(\frac{\partial \theta}{\partial r} - \frac{e}{\hbar c} 2A \right)_b. \quad (\text{E1})$$

The factor of “2” in front of the gauge field A is essential to ensure gauge invariance. The gauge transformation of the superconducting order parameter $\Phi = \langle c \rangle$ is

$$c \mapsto c e^{i \frac{e}{\hbar c} \chi}, \quad \Phi \mapsto \Phi e^{i \frac{e}{\hbar c} 2\chi}, \quad A \mapsto A + \frac{\partial \chi}{\partial r}, \quad (\text{E2})$$

for arbitrary χ . Just as in Landau-Ginzburg theory Φ can be regarded as the field of the order parameter and its phase we define as θ . According to Eq. (E2), θ transforms under a gauge transformation as $\theta \mapsto \theta + 2e\chi/\hbar c$ and hence Eq. (E1) is gauge invariant.

Next we calculate the current given by the derivative of the Hamiltonian with respect to the gauge field,

$$j_a = -c \frac{\partial H}{\partial A_a} = \frac{2e}{\hbar} \sum_b I_{ab} \int d^d r \left(\frac{\partial \theta}{\partial r} - \frac{e}{\hbar c} 2A \right)_b, \quad (\text{E3})$$

absorb $\nabla \theta$ into $A \mapsto A'$ by our choice of gauge,

$$j_a = -\frac{2e}{\hbar} \sum_b I_{ab} \int d^d r \frac{e}{\hbar c} 2A'_b, \quad (\text{E4})$$

and insert it into the Maxwell equation for the current,

$$\nabla^2 A = -\frac{4\pi}{c} j. \quad (\text{E5})$$

This gives a differential equation describing the exponential decay of the vector potential into the superconductor

$$\nabla^2 A' = \lambda^{-2} A', \quad (\text{E6})$$

with the penetration depth

$$\lambda^{-2} = \frac{16\pi e^2}{\hbar^2 c^2} I. \quad (\text{E7})$$

Note that both I and λ are matrices in Eq. (E7). Furthermore, Eq. (E5) assumes a certain geometry of the setup. The supercurrent j that expels the magnetic field $B = \text{rot} A$ inside the superconductor and B are directed along the main axes of the superconductor. The penetration depth λ describes how far the magnetic field or, equivalently, the supercurrent extent into the superconductor. Thus, the direction of the penetration depth is orthogonal to both, that of j and of B .

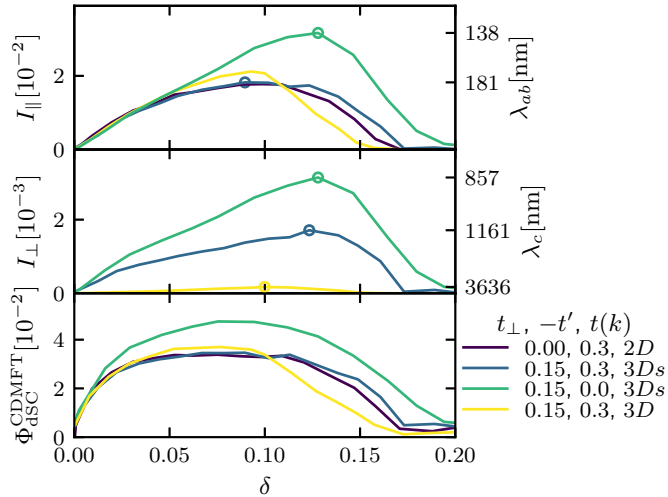


FIG. 11. In-plane superconducting stiffness I_{\parallel} (top, left), in-plane penetration depth λ_{ab} (top, right), perpendicular superconducting stiffness I_{\perp} (center, left), perpendicular penetration depth (center, right), and CDMFT dSC order parameter $\Phi_{\text{dSC}}^{\text{CDMFT}}$ (bottom) as functions of doping δ at $T = 1/52 \sim 0.02$. Quantities are shown for different interlayer hoppings t_{\perp} , next-nearest-neighbor hoppings t' , and also tight-binding lattices $t(k)$.

APPENDIX F: DETAILS OF THE STIFFNESS DEPENDENCE ON THE ELECTRONIC BAND STRUCTURE

Figure 11 presents the dSC stiffness for all three lattice dispersions. The dSC stiffness of $t^{3D}(k)$ is of similar magnitude as $t^{3Ds}(k)$. In the overdoped regime it is smaller because of the smaller local order parameter $\Phi_{\text{dSC}}^{\text{CDMFT}}$. For the underdoped to optimally doped regimes $t^{3D}(k)$ can be regarded as an effective reduction of t' in terms of the dSC stiffness. In contrast I_{\perp} is significantly suppressed by the anisotropic interplane model 3D. Its minimal value of $\lambda_c \sim 3000$ nm is still in a reasonable range compared to experiments [59]. Possibly the suppression occurs due to the more pronounced flatness of the 3D model's dispersion $t^{3D}(k)$. The derivative of Eq. (14) is thus much smaller and reduces I .

Since I can be sensitive to the lattice dispersion it is interesting to examine its dependence on the hopping parameters further. Figure 12 shows I as a function of the interplane hopping t_{\perp} . Both lattice dispersions are considered. It has to be stressed that for all the data of Fig. 12 a single CDMFT calculation is used. The parameters are varied only within the subsequent analysis of the Josephson lattice model. This allows us to isolate the effect of the hopping parameters on the phase fluctuations, neglecting the change in the strong-coupling Higgs fluctuations of the plaquette. The CDMFT calculation is performed for the 2D lattice and in the underdoped regime ($\delta \sim 0.05$) at cold temperatures ($T \sim 0.02$). This shall reduce a potential bias in the comparison between the 3Ds and 3D models. For both lattices t_{\perp} reduces I_{\parallel} and increases I_{\perp} . Furthermore, the 3D model gives smaller $I_{\parallel/\perp}$ for all values of t_{\perp} . In the 3Ds lattice I_{\perp} is more sensitive to t_{\perp} and in the 3D lattice I_{\parallel} is more sensitive to t_{\perp} .

A similar analysis is presented in Fig. 13. The single CDMFT calculation is performed at $t' = -0.3$, $\delta \sim 0.075$, $T \sim 0.02$, and $t_{\perp} = 0.15$ in the 3Ds model. Then the subsequent Josephson lattice calculations are done for different

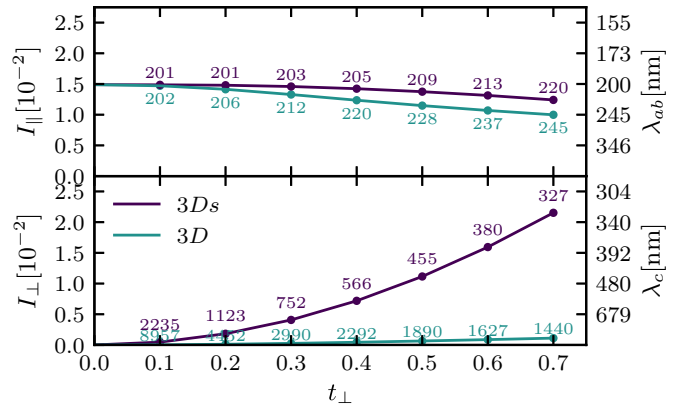


FIG. 12. Superconducting stiffness $I_{\parallel/\perp}$ and penetration depth $\lambda_{ab/c}$ as functions of the interlayer hopping t_{\perp} with in-plane next-nearest-neighbor hopping $t' = -0.3$ ($\beta = 52$, $\delta = 0.05$). Results are shown for 3Ds and 3D lattice dispersions $t(k)$. t_{\perp} changes only in the Josephson lattice model. The small numbers are values of λ .

in-plane next-nearest-neighbor hoppings t' . t' has a stronger impact on I_{\parallel} than on I_{\perp} , which is intuitive as t' and I_{\parallel} are both in-plane quantities. Also, in both cases, 3Ds and 3D, t' increases I_{\parallel} and decreases I_{\perp} . The fact that it increases I_{\parallel} is a very interesting trend, because in CDMFT t' diminishes the local order parameter of dSC $\Phi_{\text{dSC}}^{\text{CDMFT}}$. This seems as a contradiction if one interpretes T_c^{CDMFT} as the T_c of the cuprates [37], but this is clearly not the case as CDMFT takes into account only spatial correlations within the cluster. It can be speculated based on the 2D behavior of $T_{\text{KT}} \sim I_{\parallel}$, that t' has an enhancing effect on the phase fluctuations that are crucial in the underdoped regime and thus increases the critical temperature.

Figures 12 and 13 also allow us to estimate the uncertainty of our predictions on λ imposed by the hopping parameters t_{\perp} , t' , and to some extent also by the band structure. In particular in the case of $\text{YBa}_2\text{Cu}_3\text{O}_{7-x}$ it is unclear how well a single band model reflects the bilayer structure. Assuming a one-band model the uncertainty of the correct $t(k)$ and t_{\perp} translates to an estimated uncertainty of $\Delta\lambda_{ab} \sim 40$ nm and $\Delta\lambda_c \sim 7500$ nm.

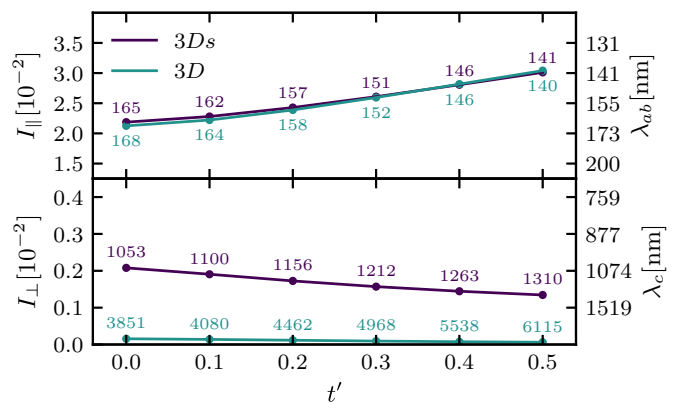


FIG. 13. Superconducting stiffness $I_{\parallel/\perp}$ and penetration depth $\lambda_{ab/c}$ as functions of the next-nearest-neighbor hopping t' with interlayer hopping $t_{\perp} = 0.15$ ($\beta = 52$, $\delta = 0.075$). Results are shown for the 3Ds lattice dispersion $t(k)$. t' changes only in the Josephson lattice model. The small numbers are values of λ .

- [1] J. G. Bednorz and K. A. Müller, *Z. Phys. B Condens. Matter* **64**, 189 (1986).
- [2] P. W. Anderson, *Science* **235**, 1196 (1987).
- [3] E. Dagotto, *Rev. Mod. Phys.* **66**, 763 (1994).
- [4] P. A. Lee, N. Nagaosa, and X.-G. Wen, *Rev. Mod. Phys.* **78**, 17 (2006).
- [5] D. J. Scalapino, *Rev. Mod. Phys.* **84**, 1383 (2012).
- [6] E. Demler, W. Hanke, and S.-C. Zhang, *Rev. Mod. Phys.* **76**, 909 (2004).
- [7] E. Berg, E. Fradkin, E.-A. Kim, S. A. Kivelson, V. Oganesyan, J. M. Tranquada, and S. C. Zhang, *Phys. Rev. Lett.* **99**, 127003 (2007).
- [8] E. Fradkin, S. A. Kivelson, and J. M. Tranquada, *Rev. Mod. Phys.* **87**, 457 (2015).
- [9] B. Keimer, S. A. Kivelson, M. R. Norman, S. Uchida, and J. Zaanen, *Nature* **518**, 179 (2015).
- [10] J. M. Kosterlitz and D. J. Thouless, *J. Phys. C: Solid State Phys.* **6**, 1181 (1973).
- [11] Y. J. Uemura, G. M. Luke, B. J. Sternlieb, J. H. Brewer, J. F. Carolan, W. N. Hardy, R. Kadono, J. R. Kempton, R. F. Kiefl, S. R. Kreitzman, P. Mulhern, T. M. Riseman, D. L. Williams, B. X. Yang, S. Uchida, H. Takagi, J. Gopalakrishnan, A. W. Sleight, M. A. Subramanian, C. L. Chien, M. Z. Cieplak, G. Xiao, V. Y. Lee, B. W. Statt, C. E. Stronach, W. J. Kossler, and X. H. Yu, *Phys. Rev. Lett.* **62**, 2317 (1989).
- [12] V. J. Emery and S. A. Kivelson, *Nature* **374**, 434 (1995).
- [13] J. V. Alvarez and C. Balseiro, *Solid State Commun.* **98**, 313 (1996).
- [14] H.-J. Kwon, A. T. Dorsey, and P. J. Hirschfeld, *Phys. Rev. Lett.* **86**, 3875 (2001).
- [15] S. G. Sharapov, H. Beck, and V. M. Loktev, *Phys. Rev. B* **64**, 134519 (2001).
- [16] L. Benfatto, A. Toschi, and S. Caprara, *Phys. Rev. B* **69**, 184510 (2004).
- [17] M. Imada, A. Fujimori, and Y. Tokura, *Rev. Mod. Phys.* **70**, 1039 (1998).
- [18] A. I. Lichtenstein and M. I. Katsnelson, *Phys. Rev. B* **62**, R9283(R) (2000).
- [19] G. Kotliar, S. Y. Savrasov, G. Pálsson, and G. Biroli, *Phys. Rev. Lett.* **87**, 186401 (2001).
- [20] T. A. Maier, M. Jarrell, T. Prushke, and M. H. Hettler, *Rev. Mod. Phys.* **77**, 1027 (2005).
- [21] K. Haule and G. Kotliar, *Phys. Rev. B* **76**, 104509 (2007).
- [22] M. Civelli, M. Capone, A. Georges, K. Haule, O. Parcollet, T. D. Stanescu, and G. Kotliar, *Phys. Rev. Lett.* **100**, 046402 (2008).
- [23] M. Ferrero, P. S. Cornaglia, L. De Leo, O. Parcollet, G. Kotliar, and A. Georges, *Phys. Rev. B* **80**, 064501 (2009).
- [24] G. Sordi, P. Sémon, K. Haule, and A.-M. S. Tremblay, *Phys. Rev. Lett.* **108**, 216401 (2012).
- [25] E. Gull, O. Parcollet, and A. J. Millis, *Phys. Rev. Lett.* **110**, 216405 (2013).
- [26] C.-D. Hébert, P. Sémon, and A.-M. S. Tremblay, *Phys. Rev. B* **92**, 195112 (2015).
- [27] L. Fratino, P. Sémon, G. Sordi, and A.-M. S. Tremblay, *Sci. Rep.* **6**, 22715 (2016).
- [28] M. Harland, M. I. Katsnelson, and A. I. Lichtenstein, *Phys. Rev. B* **94**, 125133 (2016).
- [29] H. Bragança, S. Sakai, M. C. O. Aguiar, and M. Civelli, *Phys. Rev. Lett.* **120**, 067002 (2018).
- [30] W. Wu, M. S. Scheurer, S. Chatterjee, S. Sachdev, A. Georges, and M. Ferrero, *Phys. Rev. X* **8**, 021048 (2018).
- [31] H.-C. Jiang and T. P. Devereaux, [arXiv:1806.01465](https://arxiv.org/abs/1806.01465) (2018).
- [32] H.-C. Jiang, Z.-Y. Weng, and S. A. Kivelson, *Phys. Rev. B* **98**, 140505(R) (2018).
- [33] A. Liechtenstein, M. Katsnelson, V. Antropov, and V. Gubanov, *J. Magn. Magn. Mater.* **67**, 65 (1987).
- [34] M. I. Katsnelson and A. I. Lichtenstein, *Phys. Rev. B* **61**, 8906 (2000).
- [35] O. Eriksson, A. Bergman, L. Bergqvist, and J. Hellsvik, *Atomistic Spin Dynamics: Foundations and Applications* (Oxford University Press, Oxford, 2017), p. 272.
- [36] J. Hubbard, *Proc. R. Soc. London A* **276**, 238 (1963).
- [37] E. Pavarini, I. Dasgupta, T. Saha-Dasgupta, O. Jepsen, and O. K. Andersen, *Phys. Rev. Lett.* **87**, 047003 (2001).
- [38] S. Chakravarty, A. Sudbø, P. W. Anderson, and S. Strong, *Science* **261**, 337 (1993).
- [39] O. Andersen, A. Liechtenstein, O. Jepsen, and F. Paulsen, *J. Phys. Chem. Solids* **56**, 1573 (1995).
- [40] M. K. Wu, J. R. Ashburn, C. J. Torng, P. H. Hor, R. L. Meng, L. Gao, Z. J. Huang, Y. Q. Wang, and C. W. Chu, *Phys. Rev. Lett.* **58**, 908 (1987).
- [41] R. J. Cava, B. Batlogg, R. B. van Dover, D. W. Murphy, S. Sunshine, T. Siegrist, J. P. Remeika, E. A. Rietman, S. Zahurak, and G. P. Espinosa, *Phys. Rev. Lett.* **58**, 1676 (1987).
- [42] O. Parcollet, M. Ferrero, T. Ayal, H. Hafermann, I. Krivenko, L. Messio, and P. Seth, *Comput. Phys. Commun.* **196**, 398 (2015).
- [43] P. Seth, I. Krivenko, M. Ferrero, and O. Parcollet, *Comput. Phys. Commun.* **200**, 274 (2016).
- [44] E. Gull, A. J. Millis, A. I. Lichtenstein, A. N. Rubtsov, M. Troyer, and P. Werner, *Rev. Mod. Phys.* **83**, 349 (2011).
- [45] J. M. Luttinger and J. C. Ward, *Phys. Rev.* **118**, 1417 (1960).
- [46] E. A. Stepanov, A. Huber, A. I. Lichtenstein, and M. I. Katsnelson, *Phys. Rev. B* **99**, 115124 (2019).
- [47] E. A. Stepanov, S. Brener, F. Krien, M. Harland, A. I. Lichtenstein, and M. I. Katsnelson, *Phys. Rev. Lett.* **121**, 037204 (2018).
- [48] J.-i. Okamoto, A. Cavalleri, and L. Mathey, *Phys. Rev. Lett.* **117**, 227001 (2016).
- [49] J.-i. Okamoto, W. Hu, A. Cavalleri, and L. Mathey, *Phys. Rev. B* **96**, 144505 (2017).
- [50] Y. J. Uemura, V. J. Emery, A. R. Moodenbaugh, M. Suenaga, D. C. Johnston, A. J. Jacobson, J. T. Lewandowski, J. H. Brewer, R. F. Kiefl, S. R. Kreitzman, G. M. Luke, T. Riseman, C. E. Stronach, W. J. Kossler, J. R. Kempton, X. H. Yu, D. Opie, and H. E. Schone, *Phys. Rev. B* **38**, 909 (1988).
- [51] B. Boyce, J. Skinta, and T. Lemberger, *Physica C: Superconductivity* **341-348**, 561 (2000).
- [52] C. Panagopoulos, B. D. Rainford, J. R. Cooper, W. Lo, J. L. Tallon, J. W. Loram, J. Betouras, Y. S. Wang, and C. W. Chu, *Phys. Rev. B* **60**, 14617 (1999).
- [53] S. Sachdev, *Quantum Phase Transitions* (Cambridge University Press, Cambridge, 2011).
- [54] D. N. Basov, R. Liang, D. A. Bonn, W. N. Hardy, B. Dabrowski, M. Quijada, D. B. Tanner, J. P. Rice, D. M. Ginsberg, and T. Timusk, *Phys. Rev. Lett.* **74**, 598 (1995).
- [55] C. Homes, T. Timusk, D. Bonn, R. Liang, and W. Hardy, *Physica C: Superconductivity* **254**, 265 (1995).

- [56] C. C. Homes, D. A. Bonn, R. Liang, W. N. Hardy, D. N. Basov, T. Timusk, and B. P. Clayman, *Phys. Rev. B* **60**, 9782 (1999).
- [57] H. L. Liu, M. A. Quijada, A. M. Zibold, Y.-D. Yoon, D. B. Tanner, G. Cao, J. E. Crow, H. Berger, G. Margaritondo, L. Forró, B.-H. O, J. T. Markert, R. J. Kelly, and M. Onellion, *J. Phys.: Condens. Matter* **11**, 239 (1999).
- [58] T. Pereg-Barnea, P. J. Turner, R. Harris, G. K. Mullins, J. S. Bobowski, M. Raudsepp, R. Liang, D. A. Bonn, and W. N. Hardy, *Phys. Rev. B* **69**, 184513 (2004).
- [59] C. C. Homes, S. V. Dordevic, M. Strongin, D. A. Bonn, R. Liang, W. N. Hardy, S. Komiyama, Y. Ando, G. Yu, N. Kaneko, X. Zhao, M. Greven, D. N. Basov, and T. Timusk, *Nature* **430**, 539 (2004).
- [60] S. V. Dordevic, D. N. Basov, and C. C. Homes, *Sci. Rep.* **3**, 1713 (2013).
- [61] S. Kamal, R. Liang, A. Hosseini, D. A. Bonn, and W. N. Hardy, *Phys. Rev. B* **58**, R8933 (1998).
- [62] D. R. Nelson and J. M. Kosterlitz, *Phys. Rev. Lett.* **39**, 1201 (1977).
- [63] N. D. Mermin and H. Wagner, *Phys. Rev. Lett.* **17**, 1133 (1966).
- [64] L. Benfatto, C. Castellani, and T. Giamarchi, *Phys. Rev. Lett.* **98**, 117008 (2007).
- [65] G. Sordi, K. Haule, and A.-M. S. Tremblay, *Phys. Rev. Lett.* **104**, 226402 (2010).
- [66] S. S. Kancharla, B. Kyung, D. Sénéchal, M. Civelli, M. Capone, G. Kotliar, and A.-M. S. Tremblay, *Phys. Rev. B* **77**, 184516 (2008).
- [67] Q. Chen, J. Stajic, S. Tan, and K. Levin, *Phys. Rep.* **412**, 1 (2005).
- [68] A. Damascelli, Z. Hussain, and Z.-X. Shen, *Rev. Mod. Phys.* **75**, 473 (2003).
- [69] M. Zeh, H.-C. Ri, F. Kober, R. P. Huebener, A. V. Ustinov, J. Mannhart, R. Gross, and A. Gupta, *Phys. Rev. Lett.* **64**, 3195 (1990).
- [70] H.-C. Ri, R. Gross, F. Gollnik, A. Beck, R. P. Huebener, P. Wagner, and H. Adrian, *Phys. Rev. B* **50**, 3312 (1994).
- [71] Y. Wang, L. Li, and N. P. Ong, *Phys. Rev. B* **73**, 024510 (2006).
- [72] S. A. Kivelson, I. P. Bindloss, E. Fradkin, V. Oganesyan, J. M. Tranquada, A. Kapitulnik, and C. Howald, *Rev. Mod. Phys.* **75**, 1201 (2003).
- [73] A. Wollny and M. Vojta, *Phys. Rev. B* **80**, 132504 (2009).
- [74] S. Rajasekaran, J. Okamoto, L. Mathey, M. Fechner, V. Thampy, G. D. Gu, and A. Cavalleri, *Science* **359**, 575 (2018).
- [75] A. Georges, G. Kotliar, W. Krauth, and M. J. Rozenberg, *Rev. Mod. Phys.* **68**, 13 (1996).

Chapter 4

Strongly correlated magnetism

The probably most popular form of magnetism is ferromagnetism such as it occurs at room temperature in iron, cobalt and nickel. In this case the origin of the magnetism can be understood by the atomic multiorbital structure giving rise to the Hund's rules [188, 37]. These three rules give a construction rule for the electronic (d -shell) states of the atom. They state that first of all the total spin multiplicity S should be maximized. Then, secondly, the angular momentum L is to be maximized and finally the total angular momentum $J = L + S$ should be the highest for more than half-filling of the outermost shell and otherwise the lowest J is to be chosen. Whereas the latter assumes weak spin-orbit coupling. The Hund's rules consider the Coulomb interaction of a single atom. Nevertheless, it alone can not create a consistent understanding of magnetic and electronic properties of solids. The metallic character of those ferromagnets suggests a band description rather than an atomic one. The effective description of the Weiss mean-field theory [189], which can describe the temperature-dependence of the magnetic susceptibility $\chi(T) \sim (T - T_c)^{-1}$, has been a breakthrough, but assumes local magnetic moments and needs microscopic justification. Treating the atomic- and the band picture on equal footing has become available by means of the DMFT and semiquantitative studies of ferromagnetism have been performed successfully [190].

A more subtle, but also very prominent type of magnetism is antiferromagnetism [191] which occurs, e.g., in the copper oxides (Sec. 3.1). Also this case can raise the question whether its microscopic origin is itinerant or localized. One form of antiferromagnetism can be understood in the framework of the Heisenberg model as an emerging property from the Hubbard model. Considering the half-filling sector of a Hubbard dimer [76]

$$H = \begin{pmatrix} 0 & 0 & -t & -t \\ 0 & 0 & t & t \\ -t & t & U & 0 \\ -t & t & 0 & U \end{pmatrix}, \quad (4.1)$$

with the basis of $(|\uparrow, \downarrow\rangle, |\downarrow, \uparrow\rangle, |\uparrow\downarrow, \cdot\rangle, |\cdot, \uparrow\downarrow\rangle)$. In the limit of large U solution of Eq. (4.1) gives a low-energy gap determined by a spin-singlet state $|\uparrow, \downarrow\rangle - |\downarrow, \uparrow\rangle$ and a spin-triplet state $|\uparrow, \downarrow\rangle + |\downarrow, \uparrow\rangle$ of the energy $J = 4t^2/U$. In a lattice the relation $J = 2t^2/U$ was

found due to normalization constraints [36]. Further, this energy is the interaction of the Heisenberg model

$$H = - \sum_{ij} J_{ij} S_i \cdot S_j, \quad (4.2)$$

of local spin vectors S_i on sites i, j . This is considered as the strong coupling limit of the Hubbard model at half-filling. Thus, the energy gap has the origin of the Coulomb repulsion, i.e. electronic interactions. In that sense, the antiferromagnetic gap is determined by Mottness.

This is to be contrasted by itinerant antiferromagnetism which can be obtained by (static) mean-field theory of the Hubbard hamiltonian [192], see also Sec. 2.2. This weak-coupling limit

$$H = \sum_{k\sigma} (\varepsilon(k) + I \langle n_{-\sigma} \rangle) c_{k\sigma}^\dagger c_{k\sigma}, \quad (4.3)$$

with the simplified interaction I and electronic dispersion $\varepsilon(k)$ predicts a transition according to the Stoner criterion $IA(\omega = 0) > 1$. Thus, a large density of states at Fermi level promotes the transition towards magnetic ordering. In this case the material is understood by the band picture and the transition is driven by I as opposed to the Heisenberg case for which the ordering is driven by kinetic energy. Finally, both types of magnetism can be calculated using the DMFT and the U -driven transition between them is a smooth crossover [193].

4.1 Antiferromagnetism of the hypercubic lattice

Besides the Bethe lattice, the hypercubic lattice is also an exactly solvable model in infinite dimensions within the framework of the DMFT [59, 20]. The solution depends in the case as well on the locality of the self-energy. Then, the intersite coupling can be solved analytically as it is derived below. It contains the two k -points of $(0, 0, \dots)$ and (π, π, \dots) , which allows for a description of ferromagnetic and antiferromagnetic orderings [193]. The order studied in this section is the antiferromagnetism based on the Hubbard model. Therefore, the local moment formation and the long-range ordering can be investigated.

Starting from the lattice dispersions of the one-dimensional chain, the two-dimensional square lattice and the three-dimensional cubic lattice it is straightforward to generalize the expression for the electronic dispersion to a hypercubic lattice of dimension d and hopping amplitude t by

$$\varepsilon(k) = -\frac{2t}{N} \sum_{i=1}^d \cos(k_i). \quad (4.4)$$

A reasonable constraint for normalization N is introduced to require the bandwidth to converge to a finite value in the limit of infinite dimensions $d \rightarrow \infty$. Since hypercubic lattices have orthogonal lattice vectors, each dimension must contribute equally and for evaluation of the density of states the central limit theorem can be applied. Therefore, in infinite dimensions the density of states becomes a normal distribution. In order to obtain

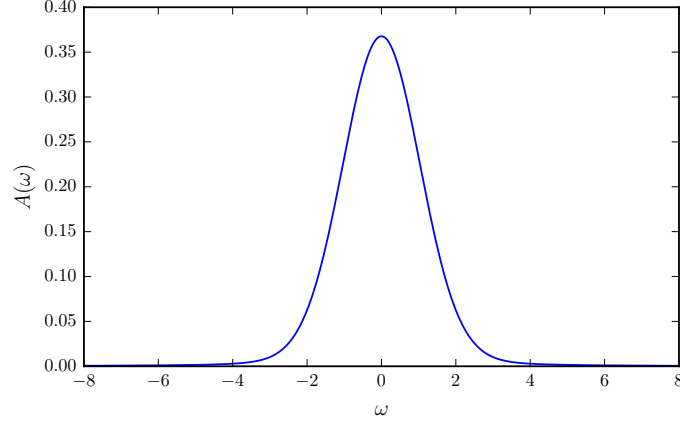


Figure 4.1: Non-interacting density of states of the hypercubic lattice. Obtained through the Padé method of analytic continuation.

the parameters of that distribution the mean and the variance of the lattice dispersion have to be calculated

$$\langle \varepsilon(k) \rangle = \int \frac{d^d k}{(2\pi)^d} \varepsilon(k) = 0, \quad (4.5)$$

$$\langle \varepsilon^2(k) \rangle = \frac{4t^2}{N^2} d \int_{-\pi/2}^{\pi/2} \frac{dk}{(2\pi)} \cos^2(k) = \frac{t^2 d}{N^2}. \quad (4.6)$$

Therefore, $N = \sqrt{d}$ will result in a finite bandwidth, which has as a free parameter only the hopping t . The latter sets the standard deviation of the normal distribution and the density of states reads

$$\rho(\omega) = \frac{\exp\left(-\frac{\omega^2}{2t^2}\right)}{t\sqrt{2\pi}}. \quad (4.7)$$

The following choice of $t = 1$ relates to a bandwidth of $W = 4$, see Fig. 4.1.

In order to describe the hypercubic lattice in the antiferromagnetic state, one has to make use of the fact, that it is a bipartite lattice, which can be divided it into two sublattices A and B

$$H_0 = \sum_{k \in \text{RBZ}} \begin{pmatrix} c_{Ak\uparrow} \\ c_{Bk\uparrow} \\ c_{Ak\downarrow} \\ c_{Bk\downarrow} \end{pmatrix}^\dagger \begin{pmatrix} -\mu + h & \varepsilon(k) & 0 & 0 \\ \varepsilon(k) & -\mu + h & 0 & 0 \\ 0 & 0 & -\mu - h & \varepsilon(k) \\ 0 & 0 & \varepsilon(k) & -\mu - h \end{pmatrix} \begin{pmatrix} c_{Ak\uparrow} \\ c_{Bk\uparrow} \\ c_{Ak\downarrow} \\ c_{Bk\downarrow} \end{pmatrix}. \quad (4.8)$$

with wave vector k . h is an external magnetic field and $\varepsilon(k)$ the electronic dispersion. The external field h is only used as a numerical seed for a single DMFT-cycle and then switched off in order to allow the numerics to leave the potentially metastable paramagnetic state. Using the local self-energy $\Sigma(i\omega_n)$ and $\zeta = i\omega_n + \mu - \Sigma(i\omega_n)$ the inverse of the local green

function can be written as

$$G^{-1}(i\omega_n) = \begin{pmatrix} \zeta_{A\uparrow} & -\varepsilon(k) & 0 & 0 \\ -\varepsilon(k) & \zeta_{B\uparrow} & 0 & 0 \\ 0 & 0 & \zeta_{A\downarrow} & -\varepsilon(k) \\ 0 & 0 & -\varepsilon(k) & \zeta_{B\downarrow} \end{pmatrix}. \quad (4.9)$$

The antiferromagnetic symmetry on a bipartite lattice relates $\Sigma_{\alpha\sigma} = \Sigma_{\bar{\alpha}\bar{\sigma}}$ and allows to calculate the inverse

$$G(i\omega_n) = \begin{pmatrix} 1 & 0 \\ 0 & 0 \end{pmatrix} \otimes \frac{1}{\zeta_{A\uparrow}\zeta_{A\downarrow} - \varepsilon(k)^2} \begin{pmatrix} \zeta_{A\downarrow} & \varepsilon(k) \\ \varepsilon(k) & \zeta_{A\uparrow} \end{pmatrix} \quad (4.10)$$

$$+ \begin{pmatrix} 0 & 0 \\ 0 & 1 \end{pmatrix} \otimes \frac{1}{\zeta_{A\downarrow}\zeta_{A\uparrow} - \varepsilon(k)^2} \begin{pmatrix} \zeta_{A\uparrow} & \varepsilon(k) \\ \varepsilon(k) & \zeta_{A\downarrow} \end{pmatrix} \quad (4.11)$$

with the kronecker product \otimes for convenience and in order to obtain the same block-structure of Eq. (4.9). A and B can be transformed into each other analytically, both are important for the auxiliary setup, the impurity problem. The antiferromagnetic self-consistency equation places the impurity into a mean-field of opposite spin. However, a paramagnetic self-consistency equation can lead to the same solution, but the local spin will flip with the DMFT iterations. The $\varepsilon(k)$ of the off-diagonals are absorbed into the mean-field and all non-local parts can be integrated over.

Results for the hypercubic lattice in its symmetry-broken phase are shown in Fig. 1 of “Effective Heisenberg Model and Exchange Interaction for Strongly Correlated Systems” for the phase diagram. The main features are the expected U -dependence of the Néel temperature $T_N \sim 1/U$ at strong coupling $5 < U$. At weak coupling $U < 5$ exponential behavior is expected, but the resolution is not sufficient, but seems reasonable due to the steep slope, and the maximum of the Néel temperature is found around $U \sim 5$. More details are shown in Fig. 4.2. At large temperatures, the paramagnetic metallic phase is tuned into an antiferromagnetic by increasing U rather quickly as the spectral weight of the local density of states drops to zero from $U = 3$ to $U = 4$. The energy defining the gap is then U , i.e. the systems is defined by localization and Mottness. At colder temperatures, however, the symmetry-breaking sets in at smaller U , at which the state remains metallic. This is characteristic of itinerant Slater antiferromagnetism. Diverging self-energies are obtained only at large temperatures $\beta = 6$.

In Fig. 4.3 can be observed that the paramagnetic metal-insulator transition, i.e. the Mott transition, occurs around $U = 5$ ($\beta = 10$). The phase transition towards the antiferromagnetic state can be artificially suppressed by enforcing the spin symmetry. In this study no check for coexistence has been performed as it is expected from the first order Mott transition. It seems consistent that the underlying Mott transition separates the Slater and the Heisenberg antiferromagnetic phases. Interestingly, the largest Néel temperature is also found at the point at which the antiferromagnetism changes from itinerant to localized. However, it shall be stressed that the resolution in U is rather coarse.

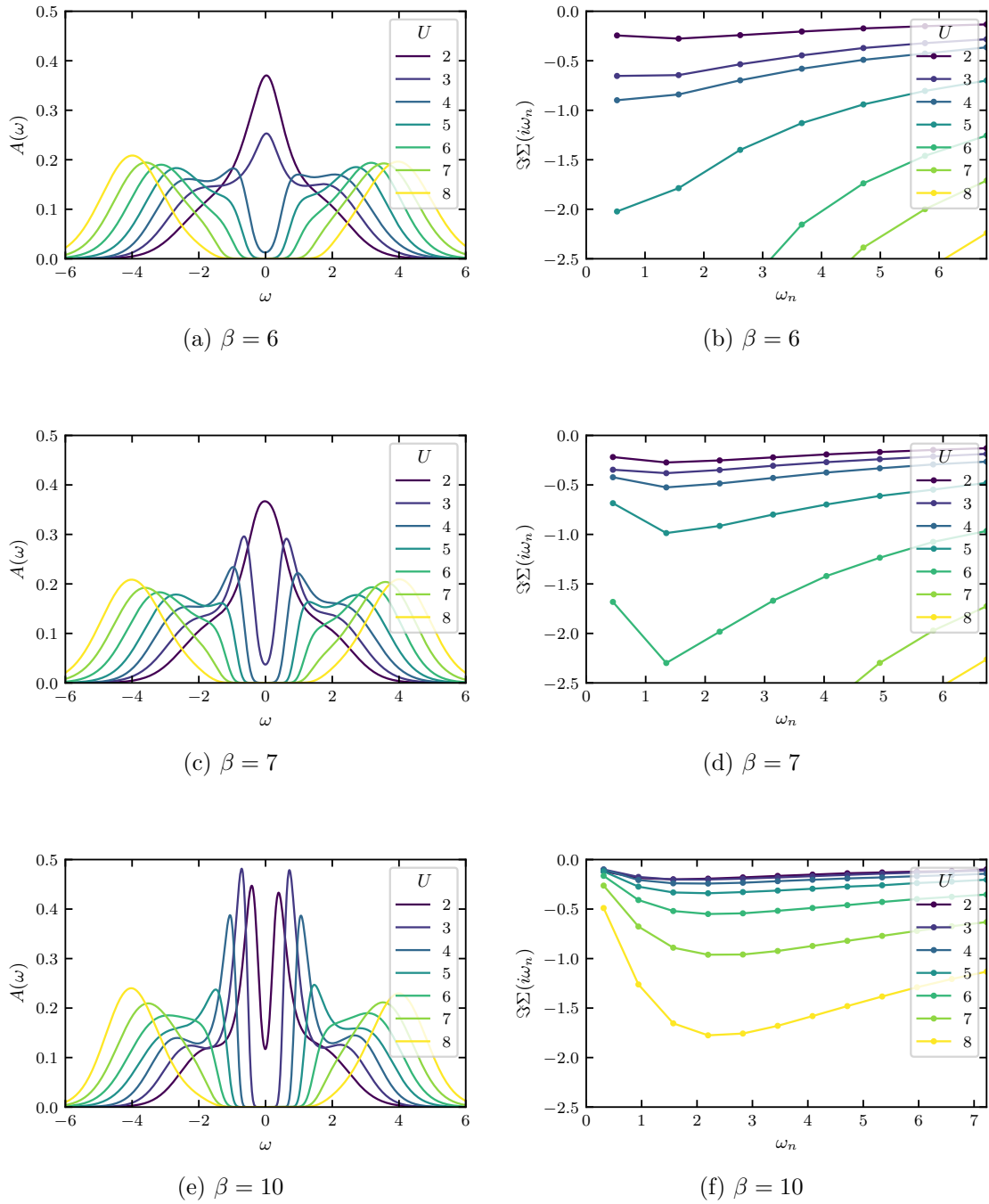


Figure 4.2: Left: Local density of states $A(\omega)$ of the antiferromagnetic hypercubic lattice for different Hubbard interactions U and inverse temperatures $\beta = 6$ (top), $\beta = 7$ (center) and $\beta = 10$ (bottom). Obtained using the maximum entropy method ($t = 1$). Right: Corresponding imaginary parts of the self-energies $\text{Im}\Sigma$ on Matsubara frequencies ω_n .

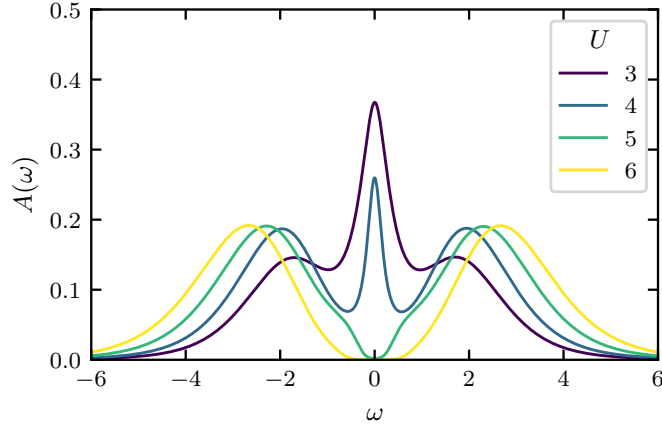


Figure 4.3: Hubbard U -driven paramagnetic metal-insulator transition of the hypercubic lattice at $\beta = 10$ ($t = 1$). Obtained via the maximum entropy method.

4.2 Local force theorem for magnetism

Ab initio density functional theory considers itinerant electrons and can produce spin symmetry-broken solutions on a mean-field basis. However, it can be questioned as it can not capture the correct origin of the magnetic behavior particularly in the case of Mottness. Originally, the idea of the local force theorem was introduced to account for spin fluctuations of well-defined moments in density functional theory, labeled as the local spin density functional approach [194, 195]. It was supposed to explain the magnetic properties of, e.g., nickel above its transition temperature. The challenge is to describe a state of local magnetic moments without long-range ordering. The local force theorem assumes a separation of energy scales that can be treated separately during the calculation. One is the formation of the local moments, which can, to some extent, be provided by density functional calculation. And the other are the fluctuations around the groundstate which can be introduced subsequently via the local perturbations on the exchange potential, which is performed via the local force theorem.

The local force theorem has been translated from the density functional framework to that of Matsubara Green functions [196]. In this form it is applicable to results of the DMFT. In particular, because the DMFT works based on a local self-energy, the local force theorem matches neatly as a postprocessing to include local perturbations on the self-energy which causes non-local correlation effects. The starting point is the free energy written in terms of correlation functions

$$\Omega = -\ln -G^{-1} - \text{Tr} \Sigma G + \phi, \quad (4.12)$$

with the Luttinger-Ward functional ϕ which generates the vertex functions, e.g. $\delta_G \phi = \Sigma$. In analogy with the local force theorem from density functional theory the first term is labeled single-particle term $\Omega_{sp} = -\ln -G^{-1}$ and the second the double-counting term $\Omega_{dc} = \text{Tr} \Sigma G - \phi$. Thus, $\Omega = \Omega_{sp} - \Omega_{dc}$. The perturbation, which is applied to the free

energy, is split into two parts. The first, δ^* , can be regarded as an external perturbation, but without taking into account the self-consistency. The latter is treated by δ_1 . In the following derivation the Dyson equation is applied $G^{-1} = G_0^{-1} - \Sigma$. Thus,

$$\begin{aligned}
\delta\Omega &= \delta^*\Omega_{sp} + \delta_1\Omega_{sp} - \delta\Omega_{dc} \\
&= -\delta^* \text{Tr} \ln -G^{-1} - \text{Tr} \left(\Sigma - G_0^{-1} \right)^{-1} \delta_1 \Sigma - \text{Tr} \Sigma \delta G - (\delta \Sigma) G + \text{Tr} \delta_G \phi \delta G \\
&= -\delta^* \text{Tr} \ln -G^{-1} + \text{Tr} G \delta_1 \Sigma - \text{Tr} \Sigma \delta G - \text{Tr} G \delta \Sigma + \text{Tr} \Sigma \delta G \\
&= -\delta^* \text{Tr} \ln \left(\Sigma - G_0^{-1} \right).
\end{aligned} \tag{4.13}$$

The expression reduces to the perturbation without taking into account the change due to the self-consistency. The perturbation can either be applied to the self-energy or to G_0 . In the case of a perturbation of an external magnetic field on spins this corresponds to changing the spin configuration in the external field or to change the external field with respect to the fixed spin, respectively. The change in the free energy will be affected in the same way. Continuing the case of spin, the magnetic moment is assumed to be sufficiently well described and the aim is to consider rotations. Regarding the formalism it is convenient to separate spin and charge of the correlation functions by expanding it using Pauli matrices $G_\tau^s = \text{Tr}_\tau G \sigma_\tau / 2$ with Pauli matrix σ and spin index τ . Together with the identity the Pauli matrices form a complete basis. Hence, G^c corresponds to the identity. Furthermore, \vec{G}^s can be seen as a vector. The local perturbation of spin rotations is designed as [196]

$$\delta^*\Omega_{sp} = 2 \text{Tr} \vec{\Sigma}_i^s \times \vec{G}_{ii}^s \delta\varphi_i, \tag{4.14}$$

with site index i and infinitesimal angle φ_i . The resulting expression is interpreted as a new effective problem which due to its minimization would also minimize the change in the free energy. The general expression for the effective spin-rotation

$$H_{\text{eff}} = - \sum_{ij} \text{Tr} \{ (\vec{G}_{ij}^s \vec{\Sigma}_j^s) (\vec{G}_{ji}^s \vec{\Sigma}_j^s) - \vec{\Sigma}_i^s \vec{G}_{ij}^c \vec{\Sigma}_j^s \vec{G}_{ji}^c - i (\vec{\Sigma}_i^s \times \vec{G}_{ij}^c \vec{\Sigma}_j^s) \vec{G}_{ji}^s \} \tag{4.15}$$

simplifies for the non-relativistic and collinear case to

$$\begin{aligned}
H_{\text{eff}} &= - \sum_{ij} J_{ij} \vec{e}_i \vec{e}_j, \\
J_{ij} &= - \text{Tr} \{ \Sigma_i^s G_{ij}^\uparrow \Sigma_j^s G_{ji}^\downarrow \},
\end{aligned} \tag{4.16}$$

where the correlation functions are written in terms of their components and $\Sigma^s = (\Sigma^\uparrow - \Sigma^\downarrow)/2$. As for the superconducting case (Sec. 3.6.3), the continuum limit can be applied and the stiffness can be calculated. The local force theorem, together with the local density approximation (a density functional approach) and DMFT, could improve the description of the spinwave stiffness in iron with $D = 260 \text{ meV}/A^2$ compared to the experimental value of $D = 280 \text{ meV}/A^2$ [197].

4.2.1 Effective Heisenberg exchange of the extended Hubbard model

In the Hubbard model the interaction is only local. This is a reasonable approximation and can be justified with screening effects. However, if the screening process itself has to be studied, then long-range interactions beyond the Hubbard model have to be considered [198, 54]. The generalized extended Hubbard model

$$H = \sum_{k\sigma} c_{k\sigma}^\dagger (\varepsilon_k - \mu) c_{k\sigma} + U \sum_i n_{i\uparrow} n_{i\downarrow} + \sum_{ij} V_{ij} n_{i\uparrow} n_{j\downarrow} - \sum_{ij} J_{ij} \vec{S}_i \vec{S}_j \quad (4.17)$$

contains long-range charge and spin interactions of two-particle type. The first two terms of Eq. (4.17) corresponds to the original Hubbard model of screened and local Coulomb repulsion U . The non-local Coulomb repulsion V_{ij} can promote, e.g., charge ordering and long-range spin interactions J_{ij} are formulated using the spin operators $\vec{S}_i = \sum_{\tau\tau'} c_{i\tau}^\dagger \vec{\sigma}_{\tau\tau'} c_{i\tau'}$. In systems of long-range effects, e.g. V_{ij} , those do not necessarily make the original Hubbard model invalid, but are important to consider in connection with ab initio calculations in which the effective U can be renormalized by V , i.e. $U \mapsto U - \bar{V}$ with an averaged \bar{V} [199]. The latter has been considered for studies on graphene, silicene and benzene. In the following study [200] a generalization of the local force theorem is presented in the sense that the effective exchange interaction is obtained from the extended Hubbard model. However, for the description of the non-local parts the formalism has to be substantially extended using dual boson techniques [201]. A further insight is regarding the accuracy very important for the application of the local force theorem. It is shown that the neglect of vertex corrections is reasonable if the local moments are well-defined meaning that their amplitude fluctuations can be neglected. From the computational view this is very important as the calculation of the effective interaction reduces to single-particle correlation functions.

Effective Heisenberg Model and Exchange Interaction for Strongly Correlated SystemsE. A. Stepanov,^{1,2} S. Brener,³ F. Krien,³ M. Harland,³ A. I. Lichtenstein,^{3,2} and M. I. Katsnelson^{1,2}¹*Radboud University, Institute for Molecules and Materials, 6525AJ Nijmegen, Netherlands*²*Theoretical Physics and Applied Mathematics Department, Ural Federal University, Mira Street 19, 620002 Ekaterinburg, Russia*³*Institute of Theoretical Physics, University of Hamburg, 20355 Hamburg, Germany*

(Received 27 February 2018; published 20 July 2018)

We consider the extended Hubbard model and introduce a corresponding Heisenberg-like problem written in terms of spin operators. The derived formalism is reminiscent of Anderson's idea of the effective exchange interaction and takes into account nonlocal correlation effects. The results for the exchange interaction and spin susceptibility in the magnetic phase are expressed in terms of single-particle quantities. This fact not only can be used for realistic calculations of multiband systems but also allows us to reconsider a general description of many-body effects in the most interesting physical regimes, where the physical properties of the system are dominated by collective (bosonic) fluctuations. In the strongly spin-polarized limit, when the local magnetic moment is well defined, the exchange interaction reduces to a standard expression of the density functional theory that has been successfully used in practical calculations of magnetic properties of real materials.

DOI: [10.1103/PhysRevLett.121.037204](https://doi.org/10.1103/PhysRevLett.121.037204)

The theory of magnetism is one of the most attractive and discussed areas of physics. Additional interest in this topic is heated up by the theoretical prediction [1] and experimental observation [2–4] of topologically stable Skyrmionic spin textures that are intensively studied now in the context of spintronics and magnetic data storage [5–7]. Also, a correct accounting of spin excitations is important for realization of the Kitaev spin model [8,9] and its practical application in Majorana quantum computers [10–15]. A quantitative description of the mentioned effects requires knowledge of the exchange interaction between two spins. However, this problem is challenging when applied to many magnetic materials that are, by definition, strongly correlated quantum systems.

Originally, the development of the theory of exchange interactions in solids and molecules was based on the Heitler-London theory of the hydrogen molecule [16]. It was demonstrated, however, in the early 1960s by Freeman and Watson [17] that this theory, being applied to ferromagnetic transition metals, gives a completely wrong order of magnitude and even an incorrect sign of the exchange parameters. For magnetic insulators, a semiempirical theory of exchange interactions was developed in the 1950s, known as the Goodenough-Kanamori-Anderson rules [18–21]; however, it was not quantitative. An analysis of “superexchange” in particular compounds always assumed some model considerations, that is, the importance and nonimportance of specific intermediate states. When the density functional theory (DFT) became the base of microscopic quantum theory of molecules and crystals [22–24], the most straightforward way to estimate the exchange interactions was simply the calculation of the

total energy difference between ferromagnetic and antiferromagnetic phases. This assumes the applicability of the Heisenberg model, which is frequently not the case, especially for itinerant electron systems [24–27].

A general, model-independent and parameter-free method to calculate exchange interactions within DFT was suggested in Refs. [28–30] based on the “magnetic local force theorem.” It is based on the consideration of second-order variations of the total energy with respect to small rotations of magnetic moments starting from equilibrium ground states. Later, this approach was generalized to strongly correlated systems [31,32] [within the framework of dynamical mean-field theory (DMFT) [33,34]], magnetic systems out of equilibrium [35], and relativistic magnetic interactions, such as the Dzyaloshinskii-Moriya interaction [36–38]. This theory was successfully used for many calculations of real systems, such as magnetic semiconductors [39], molecular magnets [40,41], ferromagnetic transition metals [42,43], and half-metallic ferromagnets [44].

Despite the success of this approach, its conceptual status remains unclear. Indeed, a mapping from DFT or from a Hubbard model to the Heisenberg model is, in general, impossible; exchange interactions obtained from the magnetic force theorem are classical and dependent on the magnetic configuration (see, e.g., Ref. [45]). Their relation to observables is not very clear; strictly speaking, only the spin-wave stiffness constant in ferromagnets is a well-defined quantity since we can be sure that in the limit of slow times and large spatial scales the phenomenological Landau-Lifshitz equations are correct. This was emphasized already in a previous paper [28]. Observables are

directly related to the dynamic magnetic susceptibility, but to establish relations between the magnetic local force approach and the standard language of response functions is not an easy problem to solve. It was solved only within the local spin-density approximation in DFT [46] and within the time-dependent mean-field approach in the Hubbard model [47]. However, most of the interesting magnetic materials are strongly correlated systems, and these approximations seem to be insufficient (or, at least, not completely justified) to describe spin dynamics.

In this Letter we show that the extended Hubbard Hamiltonian can be mapped onto an effective Heisenberg model. Inspired by the Dual Boson (DB) formalism [48–51], we construct a bosonic model whose interaction is reminiscent of Anderson’s superexchange mechanism [52,53]. Importantly, the derived formalism remains applicable not only in the strongly localized regime and allows the description of every magnetic system with a well-defined local magnetic moment. Moreover, the presence of the latter allows us to reveal a general way of the description of a complicated quantum many-body problem in terms of single-particle quantities with the use of Ward identities [54,55].

Effective s - d model.—We consider the action of the extended Hubbard model for correlated electrons,

$$\begin{aligned} S = & - \sum_{\mathbf{k}, \nu, \sigma} c_{\mathbf{k}\nu\sigma}^* [i\nu + \mu - \varepsilon_{\mathbf{k}}] c_{\mathbf{k}\nu\sigma} \\ & + U \sum_{\mathbf{q}, \omega} n_{\mathbf{q}\omega\uparrow}^* n_{\mathbf{q}\omega\downarrow} + \frac{1}{2} \sum_{\mathbf{q}, \omega, \zeta} \rho_{\mathbf{q}\omega}^{*\zeta} [V_{\mathbf{q}}]_{\zeta\zeta} \rho_{\mathbf{q}\omega}^{\zeta}. \end{aligned} \quad (1)$$

Here, $c_{\mathbf{k}\nu\sigma}^*$ ($c_{\mathbf{k}\nu\sigma}$) are Grassmann variables corresponding to creation (annihilation) of an electron with momentum \mathbf{k} , fermionic Matsubara frequency ν , and spin σ labels. The label $\zeta = \{c, \mathbf{s}\}$ depicts charge c and spin $\mathbf{s} = \{x, y, z\}$ degrees of freedom (d.o.f.), so U corresponds to local Coulomb interaction, $[V_{\mathbf{q}}]_{cc} = V_{\mathbf{q}}$ and $[V_{\mathbf{q}}]_{ss} = -J_{\mathbf{q}}^d/2$ describe nonlocal Coulomb and direct ferromagnetic exchange interactions, respectively. Here, we also introduce bosonic variables: $\rho_{\mathbf{q}\omega}^{\zeta} = n_{\mathbf{q}\omega}^{\zeta} - \langle n_{\mathbf{q}\omega}^{\zeta} \rangle$, where $n_{\mathbf{q}\omega}^{\zeta} = \sum_{\mathbf{k}\nu\sigma\sigma'} c_{\mathbf{k}\nu\sigma}^* \sigma_{\sigma\sigma'}^{\zeta} c_{\mathbf{k}+\mathbf{q}, \nu+\omega, \sigma'}$ is the charge ($\zeta = c$) and spin ($\zeta = s$) density of electrons with the momentum \mathbf{q} , bosonic frequency ω , and Pauli matrices $\sigma^{\zeta} = \{\mathbb{1}, \sigma^s\}$.

Expressing the effective exchange interaction in terms of correlation functions is a nontrivial task since it is not an observable. Furthermore, in the strongly correlated regime charge and spin fluctuations are entangled in a complicated way. Both challenges can be approached within the dual boson formalism [48–51] since it naturally separates charge and spin d.o.f. by representing them in terms of bosonic fields entering an effective action. To this aim, one splits the lattice action (1) into the local impurity problem of the extended dynamical mean-field theory (EDMFT [56–61]) and the remaining nonlocal part, which is a bilinear function of $c^*(c)$ and ρ variables. Within the DB approach

this remaining part is decoupled by two Hubbard-Stratonovich transformations, thus introducing *dual* fermionic $f^*(f)$ and bosonic ϕ fields. Then, the initial fermionic d.o.f. $c^*(c)$ can be integrated out, leading to the interaction part $\tilde{W}[f, \phi]$ of the resulting dual action being expressed in terms of the full vertex functions of the local impurity problem (for details see the Supplemental Material [62]). Thus, by construction, local correlations are already embedded in the bare propagators and interactions of the DB problem, which is very convenient for practical calculations. In the following we restrict ourselves to the lowest order terms in $\tilde{W}[f, \phi]$ stemming from the four-point $\tilde{\gamma}_{\nu\nu\omega}$ and three-point $\gamma_{\nu\omega}$ vertices [62].

Dual fields $f^*(f)$ and ϕ have no direct physical interpretation, but this fact does not represent a significant obstacle for the calculation of physical observables since there is an exact connection between dual and lattice quantities [48–51]. However, for our goal of deriving an effective bosonic model that describes initial (lattice) d.o.f., it is crucial to formulate the problem in terms of bosonic fields that have a clear physical meaning. To remedy this problem, we perform the reverse Hubbard-Stratonovich transformation for the bosonic variables ϕ introducing fields $\bar{\rho}$. In this we were inspired by the works of Dupuis [63–65], where a similar trick was performed for fermionic d.o.f. After integrating over dual bosonic fields ϕ , one gets the following action reminiscent of the s - d model [62]:

$$S_{s-d} = - \sum_{\mathbf{k}, \nu, \sigma} f_{\mathbf{k}\nu\sigma}^* \tilde{G}_0^{-1} f_{\mathbf{k}\nu\sigma} - \frac{1}{2} \sum_{\mathbf{q}, \omega, \zeta(\prime)} \bar{\rho}_{\mathbf{q}\omega}^{*\zeta} [X_E]_{\zeta\zeta}^{-1} \bar{\rho}_{\mathbf{q}\omega}^{\zeta} + W. \quad (2)$$

Here, X_E is the EDMFT susceptibility and \tilde{G}_0 is the nonlocal part of the EDMFT Green’s function. Importantly, after all transformations the field $\bar{\rho}$ indeed has the same physical meaning as the original *composite* bosonic field ρ of the lattice problem (1), as shown in Ref. [62]. The decisive advantage of the variable $\bar{\rho}$ is that it can now be treated as the *elementary* bosonic field that has a well-defined propagator and is independent of fermionic d.o.f. $c^*(c)$. Remarkably, $W[f, \bar{\rho}]$ keeps the practical form of the dual interaction $\tilde{W}[f, \phi]$ with the replacement of bosonic variable $\phi \rightarrow \bar{\rho}$, although the four-fermionic term is modified under these transformations. As we argue in Ref. [62] and numerically check below, in the case of well-developed bosonic fluctuations, this modification results in the corresponding contribution to the interaction $W[f, \rho]$ becoming negligibly small, and the latter takes the simple form $W[f, \rho] \simeq \sum_{\mathbf{k}, \mathbf{q}} \sum_{\nu, \omega, \zeta} \tilde{\gamma}_{\nu\nu\omega}^{\zeta} \rho_{\mathbf{q}\omega}^{*\zeta} J_{\mathbf{k}\nu\sigma}^* f_{\mathbf{k}+\mathbf{q}, \nu+\omega, \sigma'}$. At last, we mention that the fermionic d.o.f. are kept in the dual space, which will prove to be useful to discriminate between local and nonlocal contributions to the lattice susceptibility.

Magnetic susceptibility.—In order to design an effective Heisenberg model for spin d.o.f., one has to assume that the local magnetization $\langle m \rangle = 2\langle S^z \rangle$ is described well at the dynamical mean-field level, and fluctuations revealed by the system beyond EDMFT are mostly bosonic. In order to have well-defined local magnetic moment, the effective impurity model has to be considered for the spin-polarized state. For an easier description, one can transform spin variables from the $\mathbf{s} = \{x, y, z\}$ to the $\mathbf{s} = \{+, -, z\}$ basis with $S^\pm = (\rho^x \pm i\rho^y)/2$. In the spin-polarized case, charge and spin z channels are yet entangled, but the \pm spin channel can be separated in the collinear case [66,67]. Thus, for the correct description of the spin fluctuations, one may consider correlations only in the \pm spin channel, and the contribution of the z channel to the exchange interaction can later be restored from symmetry arguments. For simplicity, \pm spin labels are omitted wherever they are not crucial for understanding.

Now, one can integrate out fermionic d.o.f. in the effective action (2) and get the following spin model:

$$\mathcal{S}_{\text{spin}} = -\frac{1}{2} \sum_{\mathbf{q}, \omega} S_{\mathbf{q}\omega}^- [X_{\mathbf{q}\omega}^-]^{-1} S_{\mathbf{q}, -\omega}^+ + \text{H.c.} \quad (3)$$

A first approximation for the magnetic susceptibility $X_{\mathbf{q}\omega}$ can be obtained for the case when the interaction $W[f, \rho]$ contains only the three-point vertex $\gamma_{\nu\omega}^\pm$, as discussed above. Therefore, the expansion of the partition function of the action (2) up to the second order with respect to bosonic fields gives [62]

$$[X_{\mathbf{q}\omega}^{(2)}]^{-1} = J_{\mathbf{q}}^d + \Lambda_\omega + \chi_\omega^{-1} - \tilde{\Pi}_{\mathbf{q}\omega}^{(2)} \quad (4)$$

Here, Λ_ω and χ_ω are the bosonic hybridization function and susceptibility of the impurity problem, respectively. Also,

$$\tilde{\Pi}_{\mathbf{q}\omega}^{(2)} = \sum_{\mathbf{k}, \nu} \gamma_{\nu+\omega, -\omega}^- \tilde{G}_{\mathbf{k}+\mathbf{q}, \nu+\omega} \tilde{G}_{\mathbf{k}\nu\downarrow} \gamma_{\nu, \omega}^+ = \text{Diagram} \quad (5)$$

is the second-order polarization function [49]. Note that a conserving description of spin fluctuations is given by the two-particle ladder approximation of the magnetic susceptibility provided by the ladder DB approach [50] that accounts for the four-fermionic contribution in $W[f, \bar{\rho}]$ and treats bosonic hybridization Λ as a constant [55]

$$[X_{\mathbf{q}\omega}^{\text{ladd}}]^{-1} = J_{\mathbf{q}}^d + \Lambda + [X_{\mathbf{q}\omega}^{\text{DMFT}}]^{-1}. \quad (6)$$

Here, $X_{\mathbf{q}\omega}^{\text{DMFT}} = \chi_\omega + \chi_\omega \tilde{\Pi}_{\mathbf{q}\omega}^{\text{ladd}} \chi_\omega$ is the DMFT- [33,34], or dynamical vertex approximation (DΓA)-like [68] susceptibility written in terms of local two-particle irreducible four-point vertices and lattice Green's functions. $\tilde{\Pi}_{\mathbf{q}\omega}^{\text{ladd}}$ is the dual polarization in the ladder form [62,69] that contains $\tilde{\Pi}_{\mathbf{q}\omega}^{(2)}$ as the lowest order term. Therefore, the hybridization

Λ plays the role of the Moriyaesque λ correction that was introduced in DΓA [70] by hand similarly to the Moriya and Kawabata theory of weak itinerant magnets [71,72] and now is derived analytically.

Importantly, the expressions for magnetic susceptibility (4) and (6) can be drastically simplified to be applicable for realistic multiband calculations, for which the two-particle quantities can hardly be obtained. As was discussed above, the system with a well-defined local magnetic moment exhibits mostly bosonic fluctuations. Therefore, one can expect that local vertex functions are mostly described by the bosonic frequency ω , while the dependence on fermionic frequencies ν, ν' is negligible and can be averaged out. In order to perform this averaging consistently, it is carried out using the local Ward identities [54,55], which leads to the following approximation of a three-point vertex [62]:

$$\gamma_{\nu\omega}^+ = \gamma_{\nu+\omega, -\omega}^- \simeq \chi_\omega^{-1} + \delta\Sigma_{\nu\omega} \simeq \chi_\omega^{0-1}. \quad (7)$$

Here, $\chi_\omega^0 = \sum_\nu g_{\nu+\omega\uparrow} g_{\nu\downarrow}$ is the bare spin susceptibility, $g_{\nu\sigma}$ and $\Sigma_{\nu\sigma}$ are the full Green's function and self-energy of the impurity problem, and $\delta\Sigma_{\nu\omega} = (\Sigma_{\nu+\omega\uparrow} - \Sigma_{\nu\downarrow})/\langle m \rangle$. Therefore, exploiting the system being in the magnetic phase allows us to rewrite the complicated many-body problem (1) in a much simpler form of Eq. (2) introducing bosonic fields that correspond to the collective magnetic fluctuations. In this case, the expression for the corresponding fermion-boson coupling $\gamma_{\nu\omega}^\pm$ can be drastically simplified (7), leading to a similar expression that was recently postulated in Ref. [73] and numerically checked using brute force calculations [74].

Exact numerical solution.—In order to exemplify the above approximations, we consider the half-filled Hubbard model (1) ($V_{\mathbf{q}}, J_{\mathbf{q}}^d, \Lambda = 0$) on the hypercubic lattice in infinite dimensions. In this case, the exact result for the magnetic susceptibility is known to be given by the DMFT

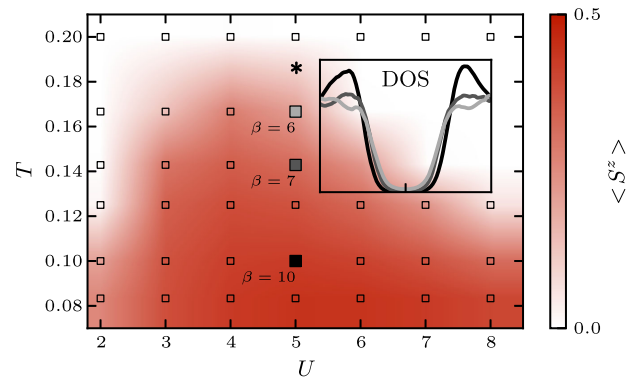


FIG. 1. The antiferromagnetic phase of the half-filled Hubbard model. Squares mark where calculations were done, the red shading depicts the magnitude of the magnetic moment $\langle S^z \rangle$, and the asterisk marks the Néel temperature $T_N \approx 0.186$. (Inset) The total DOS at $\beta = 6, 7$, and 10 for $U = 5$.

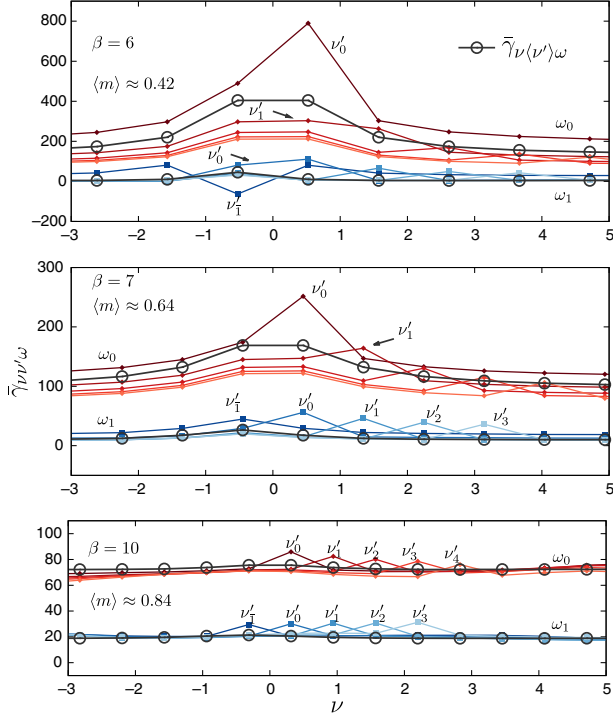


FIG. 2. Real part of the four-point vertex $\bar{\gamma}_{\nu\nu'\omega}$ in the \pm spin channel at $U = 5$ for three different temperatures (see the marked points in Fig. 1). The plot shows $\bar{\gamma}_{\nu\nu'\omega}$ as a function of ν for fixed ω and ν' . Diamonds and squares show data for $\omega = \omega_0$ and ω_1 , respectively. Red (ω_0) and blue (ω_1) lines serve as guides for the eye, whereas lighter colors indicate larger ν' . Black circles and lines show $\bar{\gamma}_{\nu(\nu')\omega}$, which does not depend on ν' .

expression (6) and can be compared to the simplified result of Eq. (4). At low temperatures this system favors antiferromagnetic (AFM) order over paramagnetism, as shown in the phase diagram in Fig. 1.

The local four-point vertex $\bar{\gamma}_{\nu\nu'\omega}$ is measured at $U = 5$ for the three temperatures marked in Fig. 1, roughly below the maximum of the AFM dome, where $T_N \approx 0.186$ is obtained using the DMFT [62]. As the temperature is lowered from $\beta = 6$ to $\beta = 10$, the magnetization $\langle m \rangle$ increases from ≈ 0.42 to 0.84 . We validate in Fig. 2 that at large magnetization the dependence of the four-point vertex $\bar{\gamma}_{\nu\nu'\omega}$ on fermionic frequencies ν, ν' is small. Consequently, one may indeed use the approximated form of the vertex $\bar{\gamma}_{\nu\nu'\omega} \approx \bar{\gamma}_{\nu(\nu')\omega}$, which leads to Eq. (7).

We evaluate Eq. (6) in the AFM phase at the $\mathbf{q} = 0$ point of the reduced Brillouin zone. The transversal susceptibility is a 2×2 matrix with the homogeneous susceptibility $X^{\text{hom}}(\omega)$ as a diagonal element [75]. Figure 3 shows $X^{\text{hom}}(\omega)$, which is real, as well as the off-diagonal element $X^{\text{off}}(\omega)$. Remarkably, despite the approximation of the vertex functions, $X^{\text{hom}}(\omega \neq 0) = 0$ and $X^{\text{off}}(\omega \neq 0) = -2i\langle m \rangle/\omega$, which are exact constraints due to global spin conservation [62], hold to very good accuracy.

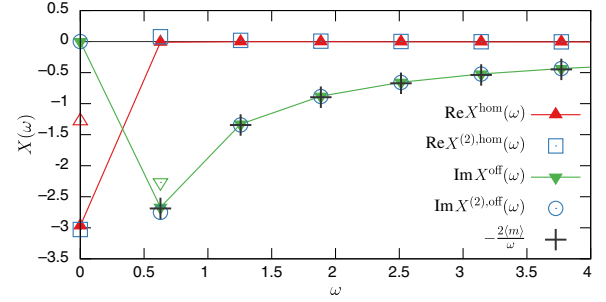


FIG. 3. Spin susceptibility components X_ω^{hom} and X_ω^{off} as a function of the Matsubara frequency (triangles). Squares and circles show the simplified form of the magnetic susceptibility (4). The single red triangles indicate expression for the magnetic susceptibility in the case of the truncated ladder (see the text). The parameters of this figure correspond to the bottom panel of Fig. 2.

At $U = 5$ the eigenvalue of the ladder equation (6) corresponding to $X^{\text{hom}}(\omega = 0)$ is large (≈ 0.715). Therefore, one can not approximate the polarization $\tilde{\Pi}_{\mathbf{q}\omega}^{\text{ladd}}$ by the second-order expression $\tilde{\Pi}_{\mathbf{q}\omega}^{(2)}$ in Eq. (6). The corresponding approximation for $\text{Re}X^{\text{hom}}(\omega = 0)$ and $\text{Im}X^{\text{off}}(\omega = 2\pi\beta)$ is marked in Fig. 3 with open triangles and is indeed clearly distinguishable from Eq. (6).

Nonetheless, the simplified expression for magnetic susceptibility $X^{(2)}$ (4) with the vertex approximation (7) shows a good agreement with X^{ladd} (6). Importantly, the approximation for the magnetic susceptibility obtained in Eq. (4) should not be confused with the truncation of the ladder equation, even though it formally uses the same quantity $\tilde{\Pi}_{\mathbf{q}\omega}^{(2)}$. The good agreement of the simplified result $X^{(2)}$ with the much more advanced ladder approximation (6) shows that the bosonic fluctuations indeed dominate in the polarized regime of the impurity model, which was assumed while deriving Eq. (4).

Classical Heisenberg Hamiltonian.—Although the action (3) is general and can be used for the description of quantum effects in terms of susceptibilities, at low temperatures it can be mapped onto an effective classical Heisenberg Hamiltonian $H_{\text{spin}} = -\sum_{\mathbf{q}} J_{\mathbf{q}} \mathbf{S}_{\mathbf{q}} \mathbf{S}_{-\mathbf{q}}$ that describes small spin fluctuations around the AFM ground state [29]. To this aim, spin variables $S_{\mathbf{q}\omega}^{\pm}$ in Eq. (3) are replaced by classical vectors $\mathbf{S}_{\mathbf{q}}$ of the length $\langle S_z \rangle$, and the contribution from the z spin channel is restored from the requirement of rotational invariance. Then, an effective exchange interaction $J_{\mathbf{q}}$ can be defined as a nonlocal part of the inverse spin susceptibility at the zero bosonic frequency [31]. Thus, the effective exchange interaction that corresponds to the simplified form of magnetic susceptibility (4) reads

$$J_{\mathbf{q}} = J_{\mathbf{q}}^d - \sum_{\mathbf{k}, \nu} \gamma_{\nu, \omega=0}^- \tilde{G}_{\mathbf{k}+\mathbf{q}, \nu \uparrow} \tilde{G}_{\mathbf{k}, \nu \downarrow} \gamma_{\nu, \omega=0}^+, \quad (8)$$

while the exchange interaction in the ladder approximation is detailed in Ref. [62]. This result is reminiscent of Anderson's idea of the superexchange interaction

[52,53]. Indeed, the first and the second term in Eq. (8) describe the direct ferromagnetic and kinetic antiferromagnetic exchange interactions, respectively. As a result, in the strongly localized regime and in the case of an antiferromagnetic dimer, the kinetic part of the exchange interaction takes the well-known form $J = -2t^2/U$ [62].

It is worth mentioning that the three-point vertex $\gamma_{\nu,\omega}$ that enters the kinetic part of the exchange interaction describes the total spin splitting. In the spin-polarized case, one can again use the simplified form of the vertex function [the first approximation in Eq. (7)]. In the strongly polarized regime, the potential contribution to the spin splitting $\delta\Sigma_{\nu,\omega}$ is much larger than the kinetic one χ_{ω}^{-1} . Therefore, the latter can be neglected and the result for the exchange interaction (8) reduces to the expression obtained in Ref. [31] that was successfully applied to the description of many realistic systems [39–44]. Note that in Ref. [31] the exchange interaction was derived assuming the existence of the collinear spin ground state, while here we show that the limit of applicability of the derived expression is much broader. If the dependence of the three-point vertex on the fermionic frequencies is fully disregarded [the second approximation in Eq. (7)], the exchange interaction reduces to the “Hartree-Fock” approximation $J_{\mathbf{q}} = \chi_{\omega=0}^{0-1} X_{\mathbf{q},\omega=0}^0 \chi_{\omega=0}^{0-1}$ [62] derived in Ref. [76].

Conclusion.—To conclude, here we derived the action for effective s - d and Heisenberg-like problems for the extended Hubbard model. We observed that, by virtue of a local Ward identity, the vertex functions of the impurity model can be well approximated, provided its weak dependence on the fermionic frequencies. Our results show that this criterion is indeed satisfied in the AFM phase of the Hubbard model in infinite dimensions when the staggered magnetization is sufficiently large. As a consequence, it is possible to obtain the magnetic susceptibility without a costly measurement of the impurity vertex functions, which is very useful for the realistic multiband calculations. For the considered parameters this approximation becomes accurate enough to reach an agreement with the global spin conservation. In finite dimensions this is of importance for a sound description of magnon spectra in accord with Goldstone’s theorem. In the classical limit, the derived spin action reduces to an effective Heisenberg Hamiltonian. In the spin-polarized case, the result for the kinetic part of the effective exchange interaction simplifies to the expression derived in Ref. [31], which is argued to be a good approximation for the case of many real materials. We believe that this approximation can be applied in different and, in particular, more realistic contexts. We further speculate that similar approximations could prove valuable in any physical regime where it can be argued that the behavior of the vertex functions is strongly dominated by the transferred momentum.

The authors thank Hugo Strand and Vladimir Antropov for the inspiring discussions. We kindly thank Igor

Krivenko for providing the solver for the stochastic optimization method for analytical continuation [77–79] used to obtain the data shown in Fig. 1. We also would like to thank Junya Otsuki for providing the continuous-time quantum Monte Carlo solver [80] that was used to obtain the data shown in Fig. 2. The work of E. A. S. was supported by Russian Science Foundation Grant No. 18-12-00185. The work of M. I. K. was supported by the Nederlandse Organisatie voor Wetenschappelijk Onderzoek (NWO) via the Spinoza Prize and by European Research Council (ERC) Advanced Grant No. 338957 FEMTO/NANO. M. H., F. K., and A. I. L. acknowledge support from the excellence cluster “The Hamburg Centre for Ultrafast Imaging—Structure, Dynamics and Control of Matter at the Atomic Scale” and the North-German Supercomputing Alliance (HLRN) under Project No. hhp00040. Also, the work was partially supported by the Stichting voor Fundamenteel Onderzoek der Materie (FOM), which is financially supported by the NWO.

-
- [1] A. Bogdanov and D. Yablonskii, *Sov. Phys. JETP* **68**, 101 (1989).
 - [2] S. Mühlbauer, B. Binz, F. Jonietz, C. Pfleiderer, A. Rosch, A. Neubauer, R. Georgii, and P. Böni, *Science* **323**, 915 (2009).
 - [3] X. Yu, Y. Onose, N. Kanazawa, J. Park, J. Han, Y. Matsui, N. Nagaosa, and Y. Tokura, *Nature (London)* **465**, 901 (2010).
 - [4] S. Heinze, K. Von Bergmann, M. Menzel, J. Brede, A. Kubetzka, R. Wiesendanger, G. Bihlmayer, and S. Blügel, *Nat. Phys.* **7**, 713 (2011).
 - [5] F. Jonietz, S. Mühlbauer, C. Pfleiderer, A. Neubauer, W. Münzer, A. Bauer, T. Adams, R. Georgii, P. Böni, R. A. Duine, K. Everschor, M. Garst, and A. Rosch, *Science* **330**, 1648 (2010).
 - [6] A. Fert, V. Cros, and J. Sampaio, *Nat. Nanotechnol.* **8**, 152 (2013).
 - [7] N. Romming, C. Hanneken, M. Menzel, J. E. Bickel, B. Wolter, K. von Bergmann, A. Kubetzka, and R. Wiesendanger, *Science* **341**, 636 (2013).
 - [8] A. Y. Kitaev, *Phys. Usp.* **44**, 131 (2001).
 - [9] A. Kitaev, *Ann. Phys. (New York)* **321**, 2 (2006).
 - [10] C. Beenakker, *Annu. Rev. Condens. Matter Phys.* **4**, 113 (2013).
 - [11] R. M. Lutchyn, J. D. Sau, and S. Das Sarma, *Phys. Rev. Lett.* **105**, 077001 (2010).
 - [12] J. D. Sau, R. M. Lutchyn, S. Tewari, and S. Das Sarma, *Phys. Rev. Lett.* **104**, 040502 (2010).
 - [13] V. Mourik, K. Zuo, S. M. Frolov, S. R. Plissard, E. P. A. M. Bakkers, and L. P. Kouwenhoven, *Science* **336**, 1003 (2012).
 - [14] S. Nadj-Perge, I. K. Drozdov, J. Li, H. Chen, S. Jeon, J. Seo, A. H. MacDonald, B. A. Bernevig, and A. Yazdani, *Science* **346**, 602 (2014).
 - [15] M. Reiher, N. Wiebe, K. M. Svore, D. Wecker, and M. Troyer, *Proc. Natl. Acad. Sci. U.S.A.* **114**, 7555 (2017).
 - [16] W. Heitler and F. London, *Z. Phys.* **44**, 455 (1927).

- [17] A. J. Freeman and R. E. Watson, *Phys. Rev.* **124**, 1439 (1961).
- [18] J. B. Goodenough, *Magnetism and the Chemical Bond*, Vol. 143 (Wiley InterScience, New York, 1964).
- [19] S. V. Vonsovskii, *Magnetism*, Vol. 2 (John Wiley & Sons, New York, 1974).
- [20] V. A. Gubanov, A. I. Liechtenstein, and A. V. Postnikov, *Magnetism and the Electronic Structure of Crystals*, Vol. 98 (Springer Science+Business Media, New York, 2012).
- [21] D. Khomskii, *Transition Metal Compounds* (Cambridge University Press, Cambridge, England, 2014).
- [22] L. Hedin and S. Lundqvist, *Solid State Phys.* **23**, 1 (1970).
- [23] R. O. Jones and O. Gunnarsson, *Rev. Mod. Phys.* **61**, 689 (1989).
- [24] J. Kübler, *Theory of Itinerant Electron Magnetism*, Vol. 106 (Oxford University Press, New York, 2017).
- [25] C. Herring, *Exchange Interactions among Itinerant Electrons: Magnetism*, Vol. 4 (Academic Press, New York, 1966).
- [26] T. Moriya, *Spin Fluctuations in Itinerant Electron Magnetism* (Springer, New York, 1985).
- [27] Y. A. Izyumov, M. I. Katsnelson, and Y. N. Skryabin, *Itinerant Electron Magnetism* (Fizmatlit, Moscow, 1994).
- [28] A. I. Liechtenstein, M. I. Katsnelson, and V. A. Gubanov, *J. Phys. F* **14**, L125 (1984).
- [29] A. Liechtenstein, M. Katsnelson, and V. Gubanov, *Solid State Commun.* **54**, 327 (1985).
- [30] A. Liechtenstein, M. Katsnelson, V. Antropov, and V. Gubanov, *J. Magn. Magn. Mater.* **67**, 65 (1987).
- [31] M. I. Katsnelson and A. I. Lichtenstein, *Phys. Rev. B* **61**, 8906 (2000).
- [32] L. V. Pourovskii, *Phys. Rev. B* **94**, 115117 (2016).
- [33] W. Metzner and D. Vollhardt, *Phys. Rev. Lett.* **62**, 324 (1989).
- [34] A. Georges, G. Kotliar, W. Krauth, and M. J. Rozenberg, *Rev. Mod. Phys.* **68**, 13 (1996).
- [35] A. Secchi, S. Brener, A. Lichtenstein, and M. Katsnelson, *Ann. Phys. (N.Y.)* **333**, 221 (2013).
- [36] M. I. Katsnelson, Y. O. Kvashnin, V. V. Mazurenko, and A. I. Lichtenstein, *Phys. Rev. B* **82**, 100403 (2010).
- [37] A. Secchi, A. Lichtenstein, and M. Katsnelson, *Ann. Phys. (N.Y.)* **360**, 61 (2015).
- [38] A. Secchi, A. Lichtenstein, and M. Katsnelson, *J. Magn. Magn. Mater.* **400**, 112 (2016).
- [39] K. Sato, L. Bergqvist, J. Kudrnovský, P. H. Dederichs, O. Eriksson, I. Turek, B. Sanyal, G. Bouzerar, H. Katayama-Yoshida, V. A. Dinh, T. Fukushima, H. Kizaki, and R. Zeller, *Rev. Mod. Phys.* **82**, 1633 (2010).
- [40] D. W. Boukhvalov, V. V. Dobrovitski, M. I. Katsnelson, A. I. Lichtenstein, B. N. Harmon, and P. Kögerler, *Phys. Rev. B* **70**, 054417 (2004).
- [41] V. V. Mazurenko, Y. O. Kvashnin, F. Jin, H. A. De Raedt, A. I. Lichtenstein, and M. I. Katsnelson, *Phys. Rev. B* **89**, 214422 (2014).
- [42] Y. O. Kvashnin, O. Grånäs, I. Di Marco, M. I. Katsnelson, A. I. Lichtenstein, and O. Eriksson, *Phys. Rev. B* **91**, 125133 (2015).
- [43] Y. O. Kvashnin, R. Cardias, A. Szilva, I. Di Marco, M. I. Katsnelson, A. I. Lichtenstein, L. Nordström, A. B. Klautau, and O. Eriksson, *Phys. Rev. Lett.* **116**, 217202 (2016).
- [44] I. V. Solovyev, I. V. Kashin, and V. V. Mazurenko, *Phys. Rev. B* **92**, 144407 (2015).
- [45] R. Logemann, A. N. Rudenko, M. I. Katsnelson, and A. Kirilyuk, *J. Phys. Condens. Matter* **29**, 335801 (2017).
- [46] M. I. Katsnelson and A. I. Lichtenstein, *J. Phys. Condens. Matter* **16**, 7439 (2004).
- [47] A. Secchi, A. I. Lichtenstein, and M. I. Katsnelson, *Phys. Rev. B* **94**, 085153 (2016).
- [48] A. Rubtsov, M. Katsnelson, and A. Lichtenstein, *Ann. Phys. (N.Y.)* **327**, 1320 (2012).
- [49] E. G. C. P. van Loon, A. I. Lichtenstein, M. I. Katsnelson, O. Parcollet, and H. Hafermann, *Phys. Rev. B* **90**, 235135 (2014).
- [50] E. A. Stepanov, E. G. C. P. van Loon, A. A. Katanin, A. I. Lichtenstein, M. I. Katsnelson, and A. N. Rubtsov, *Phys. Rev. B* **93**, 045107 (2016).
- [51] E. A. Stepanov, A. Huber, E. G. C. P. van Loon, A. I. Lichtenstein, and M. I. Katsnelson, *Phys. Rev. B* **94**, 205110 (2016).
- [52] P. W. Anderson, *Phys. Rev.* **115**, 2 (1959).
- [53] T. Yildirim, A. B. Harris, A. Aharony, and O. Entin-Wohlman, *Phys. Rev. B* **52**, 10239 (1995).
- [54] H. Hafermann, E. G. C. P. van Loon, M. I. Katsnelson, A. I. Lichtenstein, and O. Parcollet, *Phys. Rev. B* **90**, 235105 (2014).
- [55] F. Krien, E. G. C. P. van Loon, H. Hafermann, J. Otsuki, M. I. Katsnelson, and A. I. Lichtenstein, *Phys. Rev. B* **96**, 075155 (2017).
- [56] A. M. Sengupta and A. Georges, *Phys. Rev. B* **52**, 10295 (1995).
- [57] Q. Si and J. L. Smith, *Phys. Rev. Lett.* **77**, 3391 (1996).
- [58] J. L. Smith and Q. Si, *Phys. Rev. B* **61**, 5184 (2000).
- [59] R. Chitra and G. Kotliar, *Phys. Rev. Lett.* **84**, 3678 (2000).
- [60] R. Chitra and G. Kotliar, *Phys. Rev. B* **63**, 115110 (2001).
- [61] S. Biermann, F. Aryasetiawan, and A. Georges, *Phys. Rev. Lett.* **90**, 086402 (2003).
- [62] See Supplemental Material at <http://link.aps.org/supplemental/10.1103/PhysRevLett.121.037204> for explicit derivation of the bosonic action and Heisenberg Hamiltonian for spin degrees of freedom of the extended Hubbard model.
- [63] N. Dupuis and S. Pairault, *Int. J. Mod. Phys. B* **14**, 2529 (2000).
- [64] N. Dupuis, *Nucl. Phys.* **B618**, 617 (2001).
- [65] N. Dupuis, [arXiv:cond-mat/0105063](https://arxiv.org/abs/cond-mat/0105063).
- [66] N. Bickers and D. Scalapino, *Ann. Phys. (N.Y.)* **193**, 206 (1989).
- [67] M. I. Katsnelson and A. I. Lichtenstein, *J. Phys. Condens. Matter* **11**, 1037 (1999).
- [68] A. Toschi, A. A. Katanin, and K. Held, *Phys. Rev. B* **75**, 045118 (2007).
- [69] H. Hafermann, E. G. C. P. van Loon, M. I. Katsnelson, A. I. Lichtenstein, and O. Parcollet, *Phys. Rev. B* **90**, 235105 (2014).
- [70] A. A. Katanin, A. Toschi, and K. Held, *Phys. Rev. B* **80**, 075104 (2009).
- [71] T. Moriya and A. Kawabata, *J. Phys. Soc. Jpn.* **34**, 639 (1973).
- [72] T. Moriya and A. Kawabata, *J. Phys. Soc. Jpn.* **35**, 669 (1973).

- [73] M. S. Scheurer, S. Chatterjee, W. Wu, M. Ferrero, A. Georges, and S. Sachdev, Proc. Natl. Acad. Sci. U.S.A. (to be published).
- [74] W. Wu, M. S. Scheurer, S. Chatterjee, S. Sachdev, A. Georges, and M. Ferrero, *Phys. Rev. X* **8**, 021048 (2018).
- [75] The second diagonal element corresponds to $\mathbf{q} = (\pi, \dots, \pi)$ of the regular Brillouin zone and is divergent due to the rotational invariance of the Hamiltonian.
- [76] V. Antropov, *J. Magn. Magn. Mater.* **262**, L192 (2003).
- [77] I. Krivenko, <https://github.com/krivenko/som>.
- [78] A. S. Mishchenko, N. V. Prokof'ev, A. Sakamoto, and B. V. Svistunov, *Phys. Rev. B* **62**, 6317 (2000).
- [79] E. Gull, S. Isakov, I. Krivenko, A. A. Rusakov, and D. Zgid, [arXiv:1805.03521](https://arxiv.org/abs/1805.03521).
- [80] J. Otsuki, *Phys. Rev. B* **87**, 125102 (2013).

Supplemental Material for “Effective Heisenberg model and exchange interaction for strongly correlated systems”

E. A. Stepanov,¹ S. Brener,² F. Krien,² M. Harland,² A. I. Lichtenstein,² and M. I. Katsnelson¹

¹*Radboud University, Institute for Molecules and Materials, 6525AJ Nijmegen, The Netherlands*

²*Institute of Theoretical Physics, University of Hamburg, 20355 Hamburg, Germany*

EFFECTIVE SPIN PROBLEM FOR THE EXTENDED HUBBARD MODEL

Here we explicitly derive a spin problem for the extended Hubbard model and obtain magnetic susceptibility. For this reason, let us consider the following action written in momentum space

$$S = - \sum_{\mathbf{k}, \nu, \sigma} c_{\mathbf{k}\nu\sigma}^* [i\nu + \mu - \varepsilon_{\mathbf{k}}] c_{\mathbf{k}\nu\sigma} + U \sum_{\mathbf{q}, \omega} n_{\mathbf{q}\omega\uparrow} n_{-\mathbf{q}, -\omega\downarrow} + \frac{1}{2} \sum_{\mathbf{q}, \omega, \zeta} \rho_{\mathbf{q}\omega}^{*\zeta} [V_{\mathbf{q}}]_{\zeta\zeta} \rho_{\mathbf{q}\omega}^{\zeta}. \quad (1)$$

Here, $c_{\mathbf{k}\nu\sigma}^*$ ($c_{\mathbf{k}\nu\sigma}$) are Grassmann variables corresponding to creation (annihilation) of an electron with momentum \mathbf{k} , fermionic Matsubara frequency ν and spin σ . Quantities $\varepsilon_{\mathbf{k}}$ and $[V_{\mathbf{q}}]_{\zeta\zeta}$ are the Fourier transforms of the hopping amplitude and nonlocal part of an interaction written in the matrix form, respectively. The label $\zeta = \{c, s\}$ depicts the charge c and spin $\mathbf{s} = \{x, y, z\}$ degrees of freedom, so that U and $[V_{\mathbf{q}}]_{cc} = V_{\mathbf{q}}$ describe the local and nonlocal parts of the Coulomb interaction respectively, and $[V_{\mathbf{q}}]_{ss} = -J_{\mathbf{q}}^d/2$ is the nonlocal direct ferromagnetic exchange interaction. The latter ensures the following form of the Heisenberg Hamiltonian $H = -\sum_{\mathbf{q}} J_{\mathbf{q}}^d S_{\mathbf{q}} S_{-\mathbf{q}}$. Here, we also introduce bosonic variables $\rho_{\mathbf{q}\omega}^{\zeta} = n_{\mathbf{q}\omega}^{\zeta} - \langle n_{\mathbf{q}\omega}^{\zeta} \rangle$, where $n_{\mathbf{q}\omega}^{\zeta} = \sum_{\mathbf{k}\nu\sigma\sigma'} c_{\mathbf{k}\nu\sigma}^* \sigma_{\sigma\sigma'}^{\zeta} c_{\mathbf{k}+\mathbf{q}, \nu+\omega, \sigma'}$ is the charge ($\zeta = c$) and spin ($\zeta = s$) density of electrons with the momentum \mathbf{q} , bosonic frequency ω and Pauli matrices $\sigma^{\zeta} = \{\mathbb{1}, \sigma^{\zeta}\}$.

Following the standard procedure of the Dual Boson theory [1–4], the lattice action is divided into the local impurity S_{imp} and nonlocal S_{rem} parts as

$$S_{\text{imp}} = - \sum_{\nu, \sigma} c_{\nu\sigma}^* [i\nu + \mu - \Delta_{\nu}] c_{\nu\sigma} + U \sum_{\omega} n_{\omega\uparrow} n_{-\omega\downarrow} + \frac{1}{2} \sum_{\omega, \zeta} \rho_{\omega}^{*\zeta} [\Lambda_{\omega}]_{\zeta\zeta} \rho_{\omega}^{\zeta}, \quad (2)$$

$$S_{\text{rem}} = - \sum_{\mathbf{k}, \nu, \sigma} c_{\mathbf{k}\nu\sigma}^* [\Delta_{\nu} - \varepsilon_{\mathbf{k}}] c_{\mathbf{k}\nu\sigma} + \frac{1}{2} \sum_{\mathbf{q}, \omega, \zeta} \rho_{\mathbf{q}\omega}^{*\zeta} [V_{\mathbf{q}} - \Lambda_{\omega}]_{\zeta\zeta} \rho_{\mathbf{q}\omega}^{\zeta} + \sum_{\mathbf{q}, \omega, \zeta} j_{\mathbf{q}\omega}^{*\zeta} \rho_{\mathbf{q}\omega}^{\zeta}, \quad (3)$$

where we introduced fermionic Δ_{ν} and bosonic $[\Lambda_{\omega}]_{\zeta\zeta}$ hybridization functions and sources $j_{\mathbf{q}\omega}^{\zeta}$ for bosonic variables. Since here we consider a spin-polarized case of local impurity model, the fermionic hybridization function $\Delta_{\nu\sigma}$ becomes spin-dependent. The partition function of our problem is given by the following relation

$$\mathcal{Z} = \int D[c^*, c] e^{-S}, \quad (4)$$

where S is the lattice action introduced in Eq. 1. Using a matrix form of the Hubbard–Stratonovich transformation of the remainder term S_{rem} (3) one can introduce *dual* fermionic f^*, f and bosonic variables ϕ^{ζ}

$$\exp \left\{ \sum_{\mathbf{k}, \nu, \sigma} c_{\mathbf{k}\nu\sigma}^* [\Delta_{\nu\sigma} - \varepsilon_{\mathbf{k}}] c_{\mathbf{k}\nu\sigma} \right\} = D_f \int D[f^*, f] \exp \left\{ - \sum_{\mathbf{k}, \nu, \sigma} (f_{\mathbf{k}\nu\sigma}^* [\Delta_{\nu\sigma} - \varepsilon_{\mathbf{k}}]^{-1} f_{\mathbf{k}\nu\sigma} + c_{\mathbf{k}\nu\sigma}^* f_{\mathbf{k}\nu\sigma} + f_{\mathbf{k}\nu\sigma}^* c_{\mathbf{k}\nu\sigma}) \right\}, \quad (5)$$

$$\exp \left\{ \sum_{\mathbf{q}, \omega, \zeta} \frac{1}{2} \rho_{\mathbf{q}\omega}^{*\zeta} [\Lambda_{\omega} - V_{\mathbf{q}}]_{\zeta\zeta} \rho_{\mathbf{q}\omega}^{\zeta} \right\} = D_{\phi} \int D[\phi] \exp \left\{ - \sum_{\mathbf{q}, \omega, \zeta} \left(\frac{1}{2} \phi_{\mathbf{q}\omega}^{*\zeta} [\Lambda_{\omega} - V_{\mathbf{q}}]_{\zeta\zeta}^{-1} \phi_{\mathbf{q}\omega}^{\zeta} + \phi_{\mathbf{q}\omega}^{*\zeta} \rho_{\mathbf{q}\omega}^{\zeta} \right) \right\}, \quad (6)$$

where terms $D_f = \det(\Delta_{\nu\sigma} - \varepsilon_{\mathbf{k}})$ and $D_{\phi}^{-1} = \sqrt{\det[\Lambda_{\omega} - V_{\mathbf{q}}]}$ can be neglected when calculating expectation values. Rescaling fermionic fields on the Green’s function $g_{\nu\sigma}$ of impurity problem (2) as $f_{\mathbf{k}\nu\sigma}^* \rightarrow f_{\mathbf{k}\nu\sigma}^* g_{\nu\sigma}^{-1}$ and $f_{\mathbf{k}\nu\sigma} \rightarrow g_{\nu\sigma}^{-1} f_{\mathbf{k}\nu\sigma}$, and bosonic field on the susceptibility $[\chi_{\omega}]_{\zeta\zeta}$ as $\phi_{\mathbf{q}\omega}^{\zeta} \rightarrow \phi_{\mathbf{q}\omega}^{\zeta} [\chi_{\omega}]_{\zeta\zeta}^{-1}$, and shifting bosonic variables, the nonlocal part (3) of the lattice action (1)

transforms to

$$\begin{aligned} \mathcal{S}_{\text{DB}} = & - \sum_{\mathbf{k}, \nu, \sigma} f_{\mathbf{k}\nu\sigma}^* g_{\nu\sigma}^{-1} [\varepsilon_{\mathbf{k}} - \Delta_{\nu\sigma}]^{-1} g_{\nu\sigma}^{-1} f_{\mathbf{k}\nu\sigma} + \sum_{\mathbf{k}, \nu, \sigma} [c_{\mathbf{k}\nu\sigma}^* g_{\nu\sigma}^{-1} f_{\mathbf{k}\nu\sigma} + f_{\mathbf{k}\nu\sigma}^* g_{\nu\sigma}^{-1} c_{\mathbf{k}\nu\sigma}] + \sum_{\mathbf{q}, \omega, \zeta(\prime)} \phi_{\mathbf{q}\omega}^* \zeta [\chi_{\omega}]_{\zeta\zeta'}^{-1} \rho_{\mathbf{q}\omega}^{\zeta'} \\ & - \frac{1}{2} \sum_{\mathbf{q}, \omega, \zeta(\prime)} (\phi_{\mathbf{q}\omega}^* \zeta - j_{\mathbf{q}\omega}^{\zeta'} [\chi_{\omega}]_{\zeta'\zeta}) [\chi_{\omega}]_{\zeta\zeta''}^{-1} [V_{\mathbf{q}} - \Lambda_{\omega}]_{\zeta''\zeta'''}^{-1} [\chi_{\omega}]_{\zeta'''\zeta''''}^{-1} (\phi_{\mathbf{q}\omega}^{\zeta''''} - [\chi_{\omega}]_{\zeta''''\zeta'''''} j_{\mathbf{q}\omega}^{\zeta'''''}). \end{aligned} \quad (7)$$

Now, the initial degrees of freedom can be integrated out with respect to the impurity action (2) in the following way

$$\begin{aligned} & \int D[c^*, c] \exp \left\{ - \sum_i \mathcal{S}_{\text{imp}}^i - \sum_{\mathbf{k}, \nu, \sigma} [c_{\mathbf{k}\nu\sigma}^* g_{\nu\sigma}^{-1} f_{\mathbf{k}\nu\sigma} + f_{\mathbf{k}\nu\sigma}^* g_{\nu\sigma}^{-1} c_{\mathbf{k}\nu\sigma}] - \sum_{\mathbf{q}, \omega, \zeta(\prime)} \phi_{\mathbf{q}\omega}^* \zeta [\chi_{\omega}]_{\zeta\zeta'}^{-1} \rho_{\mathbf{q}\omega}^{\zeta'} \right\} = \\ \mathcal{Z}_{\text{imp}} \times & \exp \left\{ - \sum_{\mathbf{k}, \nu, \sigma} f_{\mathbf{k}\nu\sigma}^* g_{\nu\sigma}^{-1} f_{\mathbf{k}\nu\sigma} - \frac{1}{2} \sum_{\mathbf{q}, \omega, \zeta(\prime)} \phi_{\mathbf{q}\omega}^* \zeta [\chi_{\omega}]_{\zeta\zeta'}^{-1} \phi_{\mathbf{q}\omega}^{\zeta'} - \tilde{W}[f, \phi] \right\}, \end{aligned} \quad (8)$$

where \mathcal{Z}_{imp} is a partition function of the impurity problem. Here, the interaction part of the action $\tilde{W}[f, \phi]$ is presented as an infinite series of full vertex functions of impurity problem (2) as discussed in [1, 3]. The lowest order interaction terms are following

$$\tilde{W}[f, \phi] \simeq \sum_{\mathbf{k}, \mathbf{k}', \mathbf{q}} \sum_{\nu, \nu', \omega} \sum_{\sigma(\prime), \zeta(\prime)} \left(\phi_{\mathbf{q}\omega}^* \gamma_{\nu\omega}^{\zeta} f_{\mathbf{k}\nu\sigma}^* f_{\mathbf{k}+\mathbf{q}, \nu+\omega, \sigma'} - \frac{1}{4} \bar{\gamma}_{\nu\nu'\omega}^{\sigma\sigma'\sigma''\sigma'''} f_{\mathbf{k}\nu\sigma}^* f_{\mathbf{k}+\mathbf{q}, \nu+\omega, \sigma'} f_{\mathbf{k}'+\mathbf{q}, \nu'+\omega, \sigma''}^* f_{\mathbf{k}'\nu'\sigma'''} \right), \quad (9)$$

where the full three-point vertex function (and its Hermitian conjugate) is defined as

$$\begin{aligned} \gamma_{\nu\omega}^{\zeta} &= \sum_{\zeta'} [\chi_{\omega}]_{\zeta\zeta'}^{-1} \langle \rho_{\omega}^{\zeta'} c_{\nu\sigma}^* c_{\nu+\omega, \sigma'}^* \rangle_{\text{imp}} g_{\nu\sigma}^{-1} g_{\nu+\omega, \sigma'}^{-1} = \sum_{\zeta'} \langle c_{\nu\sigma}^* c_{\nu+\omega, \sigma'}^* \rho_{\omega}^{\zeta'} \rangle_{\text{imp}} [\chi_{\omega}]_{\zeta\zeta'}^{-1} g_{\nu\sigma}^{-1} g_{\nu+\omega, \sigma'}^{-1}, \\ [\gamma_{\nu\omega}^{\zeta}]^* &= \gamma_{\nu+\omega, -\omega}^{\zeta'} = \sum_{\zeta'} \langle c_{\nu+\omega, \sigma'}^* c_{\nu\sigma}^* \rho_{\omega}^{\zeta'} \rangle_{\text{imp}} [\chi_{\omega}]_{\zeta'\zeta}^{-1} g_{\nu+\omega, \sigma'}^{-1} g_{\nu\sigma}^{-1}. \end{aligned} \quad (10)$$

The full four-point vertex determined in the particle-hole channel is equal to

$$\bar{\gamma}_{\nu\nu'\omega}^{\sigma\sigma'\sigma''\sigma'''} = \langle c_{\nu\sigma}^* c_{\nu+\omega, \sigma'}^* c_{\nu'+\omega, \sigma''}^* c_{\nu'\sigma'''}^* \rangle_c \text{imp} g_{\nu\sigma}^{-1} g_{\nu+\omega, \sigma'}^{-1} g_{\nu'+\omega, \sigma''}^{-1} g_{\nu'\sigma'''}^{-1}. \quad (11)$$

Therefore, the initial lattice problem (1) transforms to the following *dual* action

$$\begin{aligned} \tilde{\mathcal{S}} = & - \sum_{\mathbf{k}, \nu, \sigma} f_{\mathbf{k}\nu\sigma}^* g_{\nu\sigma}^{-1} [\varepsilon_{\mathbf{k}} - \Delta_{\nu\sigma}]^{-1} g_{\nu\sigma}^{-1} f_{\mathbf{k}\nu\sigma} + \sum_{\mathbf{k}, \nu, \sigma} f_{\mathbf{k}\nu\sigma}^* g_{\nu\sigma}^{-1} f_{\mathbf{k}\nu\sigma} + \frac{1}{2} \sum_{\mathbf{q}, \omega, \zeta(\prime)} \phi_{\mathbf{q}\omega}^* \zeta [\chi_{\omega}]_{\zeta\zeta'}^{-1} \phi_{\mathbf{q}\omega}^{\zeta'} + \tilde{W}[f, \phi] \\ & - \frac{1}{2} \sum_{\mathbf{q}, \omega, \zeta(\prime)} (\phi_{\mathbf{q}\omega}^* \zeta - j_{\mathbf{q}\omega}^{\zeta'} [\chi_{\omega}]_{\zeta'\zeta}) [\chi_{\omega}]_{\zeta\zeta''}^{-1} [V_{\mathbf{q}} - \Lambda_{\omega}]_{\zeta''\zeta'''}^{-1} [\chi_{\omega}]_{\zeta'''\zeta''''}^{-1} (\phi_{\mathbf{q}\omega}^{\zeta''''} - [\chi_{\omega}]_{\zeta''''\zeta'''''} j_{\mathbf{q}\omega}^{\zeta'''''}). \end{aligned} \quad (12)$$

In order to come back to the original bosonic variables, one can perform the third Hubbard-Stratonovich transformation as

$$\begin{aligned} & \exp \left\{ \frac{1}{2} \sum_{\mathbf{q}, \omega, \zeta(\prime)} (\phi_{\mathbf{q}\omega}^* \zeta - j_{\mathbf{q}\omega}^{\zeta'} [\chi_{\omega}]_{\zeta'\zeta}) [\chi_{\omega}]_{\zeta\zeta''}^{-1} [V_{\mathbf{q}} - \Lambda_{\omega}]_{\zeta''\zeta'''}^{-1} [\chi_{\omega}]_{\zeta'''\zeta''''}^{-1} (\phi_{\mathbf{q}\omega}^{\zeta''''} - [\chi_{\omega}]_{\zeta''''\zeta'''''} j_{\mathbf{q}\omega}^{\zeta'''''}) \right\} = \\ D_{\bar{\rho}} \int & D[\bar{\rho}] \exp \left\{ - \sum_{\mathbf{q}, \omega, \zeta(\prime)} \left(\frac{1}{2} \bar{\rho}_{\mathbf{q}\omega}^* \zeta [V_{\mathbf{q}} - \Lambda_{\omega}]_{\zeta\zeta'}^{-1} \bar{\rho}_{\mathbf{q}\omega}^{\zeta'} - \phi_{\mathbf{q}\omega}^* \zeta [\chi_{\omega}]_{\zeta\zeta'}^{-1} \bar{\rho}_{\mathbf{q}\omega}^{\zeta'} + j_{\mathbf{q}\omega}^{\zeta'} \bar{\rho}_{\mathbf{q}\omega}^{\zeta} \right) \right\}. \end{aligned} \quad (13)$$

Comparing this expression to the Eq. 3, one can see that sources $j_{\mathbf{q}\omega}^{\zeta'}$ introduced for the initial degrees of freedom $\rho_{\mathbf{q}\omega}^{\zeta'}$ are also the sources for new bosonic fields $\bar{\rho}_{\mathbf{q}\omega}^{\zeta'}$. Therefore, fields $\bar{\rho}_{\mathbf{q}\omega}^{\zeta'}$ indeed represent initial degrees of freedom and have the same physical meaning as original *composite* bosonic variables $\rho_{\mathbf{q}\omega}^{\zeta'} = \sum_{\mathbf{k}\nu\sigma\sigma'} c_{\mathbf{k}\nu\sigma}^* \sigma_{\sigma\sigma'}^{\zeta} c_{\mathbf{k}+\mathbf{q}, \nu+\omega, \sigma'}$ - $\langle n_{\mathbf{q}\omega}^{\zeta'} \rangle$ of the lattice problem (1). Nevertheless, $\bar{\rho}_{\mathbf{q}\omega}^{\zeta'}$ can now be treated as *elementary* bosonic fields that have a well-defined propagator, since they are introduced as a decoupling fields of dual degrees of freedom $\phi_{\mathbf{q}\omega}^{\zeta'}$ and therefore, independent on fermionic variables $c_{\mathbf{k}\nu\sigma}^*$ ($c_{\mathbf{k}\nu\sigma}$). Taking

sources to zero and replacing $\bar{\rho}_{\mathbf{q}\omega}^S$ by $\rho_{\mathbf{q}\omega}^S$, dual bosonic fields can be integrated out with respect to the Gaussian bosonic part of the dual action as

$$\int D[\phi^*, \phi] \exp \left\{ - \sum_{\mathbf{q}, \omega, \zeta'} \left(\frac{1}{2} \phi_{\mathbf{q}\omega}^{*S} [\chi_{\omega}]_{\zeta\zeta'}^{-1} \phi_{\mathbf{q}\omega}^{S'} - \phi_{\mathbf{q}\omega}^{*S} [\chi_{\omega}]_{\zeta\zeta'}^{-1} \bar{\rho}_{\mathbf{q}\omega}^{S'} \right) - \tilde{W}[f, \phi] \right\} = \mathcal{Z}_\phi \times \exp \left\{ \frac{1}{2} \sum_{\mathbf{q}, \omega, \zeta'} \rho_{\mathbf{q}\omega}^{*S} [\chi_{\omega}]_{\zeta\zeta'}^{-1} \rho_{\mathbf{q}\omega}^{S'} - W[f, \rho] \right\}, \quad (14)$$

where \mathcal{Z}_ϕ is a partition function of the Gaussian part of the bosonic action. Here we restrict ourselves to the lowest order interaction terms of $\tilde{W}[f, \phi]$ shown in Eq. 9. Then, the integration of dual bosonic fields in Eq. 14 simplifies and $W[f, \rho]$ keeps an efficient dual form of $\tilde{W}[f, \phi]$ (9) with replacement of bosonic variables $\phi^S \rightarrow \bar{\rho}^S$. Also the four-point vertex becomes irreducible with respect to the full local bosonic propagator χ_ω , as can be seen from the works of [5–7], while the three-point vertex $\gamma_{\nu\omega}$ remains invariant

$$W[f, \rho] = \sum_{\mathbf{k}, \mathbf{k}', \mathbf{q}} \sum_{\nu, \nu', \omega} \sum_{\zeta'} \left(\rho_{\mathbf{q}\omega}^{*S} \gamma_{\nu\omega}^S f_{\mathbf{k}\nu\sigma}^* f_{\mathbf{k}+\mathbf{q}, \nu+\omega, \sigma'} - [\bar{\gamma} - \theta]_{\nu\nu'\omega}^{SS'} f_{\mathbf{k}\nu\sigma}^* f_{\mathbf{k}+\mathbf{q}, \nu+\omega, \sigma'} f_{\mathbf{k}'+\mathbf{q}, \nu'+\omega, \sigma''}^* f_{\mathbf{k}'\nu'\sigma''} \right). \quad (15)$$

Here,

$$\theta_{\nu\nu'\omega}^{SS'} = -\gamma_{\nu\omega}^S [\chi_\omega]_{\zeta\zeta'} [\gamma_{\nu'\omega}^{S'}]^* \quad (16)$$

is the full reducible bosonic contribution to the full local four-point vertex $\bar{\gamma}_{\nu\nu'\omega}^{SS'}$ introduced in [4] and spin labels $\sigma, \sigma', \sigma'', \sigma'''$ are fixed by the channel indices ζ, ζ' . Therefore, the problem transforms to the following action of an effective s - d model

$$\mathcal{S}_{s-d} = - \sum_{\mathbf{k}, \nu, \sigma} f_{\mathbf{k}\nu\sigma}^* \tilde{G}_0^{-1} f_{\mathbf{k}\nu\sigma} - \frac{1}{2} \sum_{\mathbf{q}, \omega, \zeta'} \rho_{\mathbf{q}\omega}^{*S} [X_E]_{\zeta\zeta'}^{-1} \rho_{\mathbf{q}\omega}^{S'} + W[f, \rho], \quad (17)$$

where $[X_E]_{\zeta\zeta'} = [\chi_\omega^{-1} + \Lambda_\omega - V_{\mathbf{q}}]_{\zeta\zeta'}^{-1}$ is the susceptibility of the extended dynamical mean-field theory. As it is shown below, when the three-point vertex function $\gamma_{\nu\omega}^S$ of impurity problem that connects two fermionic propagators and interaction is close to unity (87), the main contribution to the local four-point vertex is given by the full reducible bosonic contribution, i.e. $\bar{\gamma} \simeq \theta$, or diagrammatically

$$\square \simeq \triangleleft \text{---} \text{---} \text{---} \text{---} \triangleright. \quad (18)$$

Here, the dotted wave line depicts full local bosonic propagator and the minus sign in Eq. 16 appears due to Feynman rules [2]. Then, the interaction part of the action (17) takes the most simple form that contains only three-point vertex functions

$$W'[f, \rho] \simeq \sum_{\mathbf{k}, \mathbf{q}} \sum_{\nu, \omega} \sum_{\sigma(\zeta), \sigma'(\zeta')} \rho_{\mathbf{q}\omega}^{*S} \gamma_{\nu\omega}^S f_{\mathbf{k}\nu\sigma}^* f_{\mathbf{k}+\mathbf{q}, \nu+\omega, \sigma'}. \quad (19)$$

Transformation of spin basis

Let us consider an effective impurity model in the spin-polarized case. For easier description, one can transform spin variables from the $\mathbf{s} = \{x, y, z\}$ to the $\mathbf{s} = \{+, -, z\}$ basis as $S^\pm = (\rho^x \pm i\rho^y)/2$. In the spin-polarized case fluctuations in the charge and spin z channels are yet entangled, but the \pm spin channel can be separated in the collinear case. Thus, for a correct account for spin fluctuations, one may consider correlations only in the \pm spin channel and the contribution of the z channel to the exchange interaction can be later restored from the symmetry arguments. It is worth mentioning that the transformation $\{x, y\} \rightarrow \{+, -\}$ is very useful for calculation of physical observables, since it diagonalizes the spin susceptibility. Nevertheless, one has to remember that operators S^+ and S^- are not Hermitian. Therefore, components of bosonic operator in matrix representation in the old and new basis are defined as

$$\hat{\rho}_{\mathbf{q}\omega} = \begin{pmatrix} \rho_{\mathbf{q}\omega}^x \\ \rho_{\mathbf{q}\omega}^y \end{pmatrix}; \quad \hat{S}_{\mathbf{q}\omega} = \begin{pmatrix} S_{\mathbf{q}\omega}^+ \\ S_{\mathbf{q}\omega}^- \end{pmatrix}; \quad \hat{\rho}_{\mathbf{q}\omega}^* = (\rho_{-\mathbf{q}, -\omega}^x, \rho_{-\mathbf{q}, -\omega}^y); \quad \hat{S}_{\mathbf{q}\omega}^* = (S_{-\mathbf{q}, -\omega}^-, S_{-\mathbf{q}, -\omega}^+). \quad (20)$$

Connection between these bases can be obtained using the following matrix transformation

$$\hat{S}_{\mathbf{q}\omega}^* = \hat{\rho}_{\mathbf{q}\omega}^* \times \hat{A}, \quad \text{or} \quad (S_{-\mathbf{q}, -\omega}^-, S_{-\mathbf{q}, -\omega}^+) = (\rho_{-\mathbf{q}, -\omega}^x, \rho_{-\mathbf{q}, -\omega}^y) \times \begin{pmatrix} \frac{1}{2} & \frac{1}{2} \\ \frac{-i}{2} & \frac{i}{2} \end{pmatrix} \quad (21)$$

and

$$\hat{S}_{\mathbf{q}\omega} = \hat{B} \times \hat{\rho}_{\mathbf{q}\omega}, \quad \text{or} \quad \begin{pmatrix} S_{\mathbf{q}\omega}^+ \\ S_{\mathbf{q}\omega}^- \end{pmatrix} = \begin{pmatrix} \frac{1}{2} & \frac{i}{2} \\ \frac{1}{2} & -\frac{i}{2} \end{pmatrix} \times \begin{pmatrix} \rho_{\mathbf{q}\omega}^x \\ \rho_{\mathbf{q}\omega}^y \end{pmatrix}. \quad (22)$$

Then, all matrices \hat{M}_{xy} involved in above derivations can also be transformed to the new basis \hat{M}_{\pm} as

$$\hat{M}_{\pm} = \hat{A}^{-1} \times \hat{M}_{xy} \times \hat{B}^{-1}. \quad (23)$$

In particular, the matrix form of the nonlocal interaction $[V_{\mathbf{q}}]_{\zeta\zeta'}$ remains diagonal

$$[V_{\mathbf{q}}]_{\pm} = \hat{A}^{-1} \times \begin{pmatrix} -J_{\mathbf{q}}^d/2 & 0 \\ 0 & -J_{\mathbf{q}}^d/2 \end{pmatrix} \times \hat{B}^{-1} = \begin{pmatrix} -J_{\mathbf{q}}^d & 0 \\ 0 & -J_{\mathbf{q}}^d \end{pmatrix} \quad (24)$$

and inverse susceptibility is transformed to a diagonal form as

$$[\chi_{\omega}]_{\pm}^{-1} = \hat{A}^{-1} \times \begin{pmatrix} \chi_{\omega}^{xx} & \chi_{\omega}^{xy} \\ \chi_{\omega}^{yx} & \chi_{\omega}^{yy} \end{pmatrix}^{-1} \times \hat{B}^{-1} = \frac{1}{\chi_{\omega}^{xx}\chi_{\omega}^{yy} - \chi_{\omega}^{xy}\chi_{\omega}^{yx}} \begin{pmatrix} \chi_{\omega}^{xx} + \chi_{\omega}^{yy} + i\chi_{\omega}^{xy} - i\chi_{\omega}^{yx} & \chi_{\omega}^{xx} - \chi_{\omega}^{yy} + i\chi_{\omega}^{xy} + i\chi_{\omega}^{yx} \\ -\chi_{\omega}^{xx} + \chi_{\omega}^{yy} + i\chi_{\omega}^{xy} + i\chi_{\omega}^{yx} & \chi_{\omega}^{xx} + \chi_{\omega}^{yy} - i\chi_{\omega}^{xy} + i\chi_{\omega}^{yx} \end{pmatrix}. \quad (25)$$

Defining $\chi_{\omega}^{+-} = -\langle S_{\omega}^+ S_{-\omega}^- \rangle = \frac{1}{4}(\chi_{\omega}^{xx} + \chi_{\omega}^{yy} - i\chi_{\omega}^{xy} + i\chi_{\omega}^{yx})$ and $\chi_{\omega}^{-+} = -\langle S_{\omega}^- S_{-\omega}^+ \rangle = \frac{1}{4}(\chi_{\omega}^{xx} + \chi_{\omega}^{yy} + i\chi_{\omega}^{xy} - i\chi_{\omega}^{yx})$, and taking into account that $\chi_{\omega}^{xx} = \chi_{\omega}^{yy}$ and $\chi_{\omega}^{xy} = -\chi_{\omega}^{yx}$, one gets that $\chi_{\omega}^{xx}\chi_{\omega}^{yy} - \chi_{\omega}^{xy}\chi_{\omega}^{yx} = 4\chi_{\omega}^{+-}\chi_{\omega}^{-+}$ and

$$[\chi_{\omega}]_{\pm}^{-1} = \begin{pmatrix} [\chi_{\omega}^{+-}]^{-1} & 0 \\ 0 & [\chi_{\omega}^{-+}]^{-1} \end{pmatrix}. \quad (26)$$

Magnetic susceptibility

In order to obtain the effective problem written in terms of bosonic degrees of freedom only, one can integrate out dual fermionic degrees of freedom from the Eq. 17. Taking into account transformation of the spin basis presented above, the spin \pm part of the effective action reads

$$\mathcal{S}_{\text{spin}} = -\frac{1}{2} \sum_{\mathbf{q},\omega} S_{\mathbf{q}\omega}^- [X_{\mathbf{q}\omega}^{+-}]^{-1} S_{-\mathbf{q},-\omega}^+ - \frac{1}{2} \sum_{\mathbf{q},\omega} S_{\mathbf{q}\omega}^+ [X_{\mathbf{q}\omega}^{-+}]^{-1} S_{-\mathbf{q},-\omega}^- \quad (27)$$

The first approximation for the spin susceptibility $X_{\mathbf{q}\omega}^{+-}$ can be obtained after expanding the simplified form of interaction $W[f, \rho]$ given by Eq. 19 up to the second order with respect to bosonic fields ρ in the expression for the partition function of the action (17). This results in

$$[X_{\mathbf{q}\omega}^{(2)}]^{-1} = J_{\mathbf{q}}^d + \Lambda_{\omega} + \chi_{\omega}^{-1} - \tilde{\Pi}_{\mathbf{q}\omega}^{(2)}, \quad (28)$$

where

$$\tilde{\Pi}_{\mathbf{q}\omega}^{(2)} = \sum_{\mathbf{k},\nu} \gamma_{\nu+\omega,-\omega}^- \tilde{G}_{\mathbf{k}+\mathbf{q},\nu+\omega\uparrow} \tilde{G}_{\mathbf{k}\nu\downarrow} \gamma_{\nu,\omega}^+ \quad (29)$$

is the second order polarization function and $\chi_{\omega} = \chi_{\omega}^{+-}$ and $\Lambda_{\omega} = \Lambda_{\omega}^{-+}$ are the spin susceptibility and bosonic hybridization function of impurity problem, respectively. Hereinafter, \pm spin labels are omitted for simplicity wherever they are not crucial for understanding. The three-point vertex functions in the spin channel are defined as in Eq. 10, or explicitly as

$$\begin{aligned} \gamma_{\nu,\omega}^+ &= \langle c_{\nu\downarrow} c_{\nu+\omega\uparrow}^* S_{\omega}^- \rangle_{\text{imp}} [\chi_{\omega}^{+-}]^{-1} g_{\nu\downarrow}^{-1} g_{\nu+\omega\uparrow}^{-1}, \\ \gamma_{\nu+\omega,-\omega}^- &= \langle S_{-\omega}^+ c_{\nu+\omega\uparrow} c_{\nu\downarrow}^* \rangle_{\text{imp}} [\chi_{\omega}^{-+}]^{-1} g_{\nu+\omega\uparrow}^{-1} g_{\nu\downarrow}^{-1}. \end{aligned} \quad (30)$$

The more accurate approximation for the spin susceptibility can be found when expanding the full form of interaction $W[f, \rho]$ given by Eq. 15 up to the second order with respect to bosonic fields ρ as previously. Using the ladder approximation, one gets

$$[X_{\mathbf{q}\omega}^{\text{ladder}}]^{-1} = J_{\mathbf{q}}^d + \Lambda_{\omega} + \chi_{\omega}^{-1} - \Pi_{\mathbf{q}\omega}^{\text{ladder}}, \quad (31)$$

where the polarization function $\Pi_{\mathbf{q}\omega}^{\text{ladd}}$ expressed in the matrix form in the space of fermionic frequencies ν, ν' reads

$$\Pi_{\mathbf{q}\omega}^{\text{ladd}} = \text{Tr} \left\{ \hat{\gamma}_{\omega}^{-} \hat{X}_{\mathbf{q}\omega}^0 \left[I + (\hat{\gamma}_{\omega}^{-} - \hat{\theta}_{\omega}) \hat{X}_{\mathbf{q}\omega}^0 \right]^{-1} \hat{\gamma}_{\omega}^{+} \right\}. \quad (32)$$

Here, I is the identity matrix in the same space. Multiplication and inversion should be understood as a standard matrix operations. For simplicity, we omit the fermionic indices wherever they are not crucial for understanding. The trace is taken over the external fermionic indices. Matrix elements of the bare dual spin susceptibility $\hat{X}_{\mathbf{q}\omega}^0$ and three-point vertex function γ_{ω} are defined as $\hat{X}_{\mathbf{q}\omega; \nu\nu'}^0 = \sum_{\mathbf{k}} \tilde{G}_{\mathbf{k}+\mathbf{q}, \nu+\omega\uparrow} \tilde{G}_{\mathbf{k}\nu\downarrow} \delta_{\nu\nu'}$ and $\gamma_{\omega; \nu\nu'}^{\pm} = \gamma_{\nu\omega}^{\pm} \delta_{\nu\nu'}$, where $\gamma_{\nu\omega}^{\pm}$ are defined in Eq. 30. The four-point vertex functions $\bar{\gamma}_{\nu\nu'\omega}$ and $\theta_{\nu\nu'\omega}$ in the \pm spin channel are defined above in Eqs. 11 and (16), or explicitly as

$$\bar{\gamma}_{\nu\nu'\omega} = \bar{\gamma}_{\nu\nu'\omega}^{\uparrow\uparrow\downarrow} = \left\langle c_{\nu\downarrow} c_{\nu+\omega\uparrow}^* c_{\nu'+\omega\uparrow} c_{\nu'\downarrow}^* \right\rangle_{\text{c imp}} g_{\nu\downarrow}^{-1} g_{\nu+\omega\uparrow}^{-1} g_{\nu'+\omega\uparrow}^{-1} g_{\nu'\downarrow}^{-1}, \quad (33)$$

$$\theta_{\nu\nu'\omega} = -\gamma_{\nu\omega}^{+} \chi_{\omega} \gamma_{\nu'+\omega, -\omega}^{-}. \quad (34)$$

Substituting the above expressions to the Eq. 31, one recovers conserving result for the spin susceptibility provided by the ladder DB approach [3] in the case of the constant bosonic hybridization function Λ [8]

$$\left[X_{\mathbf{q}\omega}^{\text{ladd}} \right]^{-1} = J_{\mathbf{q}}^{\text{d}} + \Lambda + \left[X_{\mathbf{q}\omega}^{\text{DMFT}} \right]^{-1}. \quad (35)$$

Here,

$$X_{\mathbf{q}\omega}^{\text{DMFT}} = \chi_{\omega} + \chi_{\omega} \tilde{\Pi}_{\mathbf{q}\omega}^{\text{ladd}} \chi_{\omega} \quad (36)$$

and $\tilde{\Pi}_{\mathbf{q}\omega}^{\text{ladd}}$ is the dual polarization function in the ladder form [9] given by the following matrix form in the space of fermionic frequencies ν, ν'

$$\tilde{\Pi}_{\mathbf{q}\omega}^{\text{ladd}} = \text{Tr} \left\{ \hat{\gamma}_{\omega}^{-} \hat{X}_{\mathbf{q}\omega}^0 \left[I + \hat{\gamma}_{\omega}^{-} \hat{X}_{\mathbf{q}\omega}^0 \right]^{-1} \hat{\gamma}_{\omega}^{+} \right\}. \quad (37)$$

As it was already noted in [4], the difference between the lattice (32) and dual (37) polarization functions is that the first one is irreducible with respect to the (local and nonlocal parts of) EDMFT susceptibility X_{E} , while the dual one is irreducible only with respect to the bare dual susceptibility, which is identically equal to the nonlocal part of X_{E} .

Expression for the spin susceptibility (35) can be rewritten in the more convenient way. For this reason one can define the two-particle irreducible (2PI) vertex function in the \pm spin channel as

$$\hat{\gamma}_{\omega}^{\pm 2\text{PI}} = \hat{\gamma}_{\omega}^{\pm} \left[I - \hat{\chi}_{\omega}^0 \hat{\gamma}_{\omega}^{\pm} \right]^{-1}, \quad (38)$$

where the matrix elements of the bare local spin susceptibility are $\chi_{\omega; \nu\nu'}^0 = g_{\nu+\omega\uparrow} g_{\nu\downarrow} \delta_{\nu\nu'}$. Then, the spin susceptibility of the impurity problem can be expressed as

$$\chi_{\omega} = -\langle S_{\omega}^{-} S_{-\omega}^{+} \rangle = \text{Tr} \left\{ \hat{\chi}_{\omega}^0 - \hat{\chi}_{\omega}^0 \hat{\gamma}_{\omega}^{\pm} \hat{\chi}_{\omega}^0 \right\} = \text{Tr} \left\{ \hat{\chi}_{\omega}^0 \left[I + \hat{\gamma}_{\omega}^{\pm 2\text{PI}} \hat{\chi}_{\omega}^0 \right]^{-1} \right\}. \quad (39)$$

Rewriting the relation for the dual polarization function $\tilde{\Pi}_{\mathbf{q}\omega}^{\text{ladd}}$ (37) through the 2PI vertex function and using the exact relation between the three- and four-point vertex functions of impurity problem

$$\begin{aligned} \gamma_{\omega}^{+} &= \left\langle c_{\nu\downarrow} c_{\nu+\omega\uparrow}^* S_{\omega}^{-} \right\rangle_{\text{imp}} \chi_{\omega}^{-1} g_{\nu\downarrow}^{-1} g_{\nu+\omega\uparrow}^{-1} = \sum_{\nu'} \left\langle c_{\nu\downarrow} c_{\nu+\omega\uparrow}^* c_{\nu'\downarrow} c_{\nu'+\omega\uparrow} \right\rangle_{\text{imp}} \chi_{\omega}^{-1} g_{\nu\downarrow}^{-1} g_{\nu+\omega\uparrow}^{-1} \\ &= \sum_{\nu'} \left\{ \delta_{\nu\nu'} - \bar{\gamma}_{\nu\nu', \omega} g_{\nu'+\omega\uparrow} g_{\nu\downarrow} \right\} \chi_{\omega}^{-1} = \sum_{\nu'} \left[\delta_{\nu\nu'} + \bar{\gamma}_{\nu\nu', \omega}^{\text{2PI}} g_{\nu'+\omega\uparrow} g_{\nu\downarrow} \right]^{-1} \chi_{\omega}^{-1}, \end{aligned} \quad (40)$$

and the fact that in the case of zero dual self energy $\tilde{\Sigma}_{\mathbf{k}\nu} = 0$ the following relation holds

$$\tilde{X}_{\mathbf{q}\omega; \nu\nu'}^0 + \chi_{\omega; \nu\nu'}^0 = X_{\mathbf{q}\omega; \nu\nu'}^0 = \sum_{\mathbf{k}} G_{\mathbf{k}+\mathbf{q}, \nu+\omega\uparrow} G_{\mathbf{k}\nu\downarrow} \delta_{\nu\nu'}, \quad (41)$$

one finds that

$$X_{\mathbf{q}\omega}^{\text{DMFT}} = \chi_{\omega} + \chi_{\omega} \tilde{\Pi}_{\mathbf{q}\omega}^{\text{ladd}} \chi_{\omega} = \text{Tr} \left\{ \hat{X}_{\mathbf{q}\omega}^0 \left[I + \hat{\gamma}_{\omega}^{\pm 2\text{PI}} \hat{X}_{\mathbf{q}\omega}^0 \right]^{-1} \right\} \quad (42)$$

is the DMFT-like [10, 11] susceptibility written in terms of the 2PI vertex functions of impurity model and lattice Green's functions. Therefore, the spin susceptibility (35) derived within the ladder Dual Boson approach [1] can be rewritten as

$$X_{\mathbf{q}\omega}^{\text{ladd}} = \text{Tr} \left\{ \hat{X}_{\mathbf{q}\omega}^0 \left[I + \left(\hat{\gamma}_{\omega}^{\pm 2\text{PI}} + I \left[J_{\mathbf{q}}^{\text{D}} + \Lambda \right] \right) \hat{X}_{\mathbf{q}\omega}^0 \right]^{-1} \right\}. \quad (43)$$

Classical Heisenberg Hamiltonian

In order to map the initial problem onto a classical Heisenberg Hamiltonian the spin variables $S_{\mathbf{q}\omega}^{\pm}$ in Eq. (27) have to be replaced by the classical vectors $\mathbf{S}_{\mathbf{q}}$ of the length $\langle S_z \rangle$. Then, an effective exchange interaction $J_{\mathbf{q}}$ can be defined as a nonlocal part of the inverse susceptibility at zero bosonic frequency [12]. After all, the action (27) maps on an effective Heisenberg Hamiltonian

$$H_{\text{spin}} = - \sum_{\mathbf{q}} J_{\mathbf{q}} \mathbf{S}_{\mathbf{q}} \mathbf{S}_{-\mathbf{q}}, \quad (44)$$

where the contribution from the z spin channel is restored from the requirement of rotational invariance. Here, the effective exchange interaction obtained from the simplified form of magnetic susceptibility (28) is

$$J_{\mathbf{q}} = J_{\mathbf{q}}^{\text{d}} - \sum_{\mathbf{k}, \nu} \gamma_{\nu, \omega=0}^{-} \tilde{G}_{\mathbf{k}+\mathbf{q}, \nu \uparrow} \tilde{G}_{\mathbf{k}\nu \downarrow} \gamma_{\nu, \omega=0}^{+}. \quad (45)$$

and the exchange interaction in the ladder approximation obtained from the Eq. 43 reads

$$J_{\mathbf{q}} = J_{\mathbf{q}}^{\text{d}} - \tilde{\Pi}_{\mathbf{q}, \omega=0}^{\text{ladd}} \left[1 + \chi_{\omega=0} \tilde{\Pi}_{\mathbf{q}, \omega=0}^{\text{ladd}} \right]^{-1}. \quad (46)$$

Ward identity for the vertex function of impurity model

When the system exhibits mostly bosonic fluctuation, one can expect that local vertex functions of impurity problem are mostly described by the bosonic frequency ω , while the dependence on fermionic frequencies ν, ν' can be averaged. In order to account for single electronic degrees of freedom correctly, the averaging procedure over the fermionic frequencies is carried out using Ward identity for the two-particle irreducible four-point vertex function of the impurity problem [8] as

$$\Sigma_{\nu+\omega \uparrow} - \Sigma_{\nu \downarrow} = - \sum_{\nu''} \bar{\gamma}_{\nu, \nu'', \omega}^{2\text{PI}} (g_{\nu''+\omega \uparrow} - g_{\nu'' \downarrow}) \simeq - \bar{\gamma}_{\nu, \langle \nu'' \rangle, \omega}^{2\text{PI}} \left\{ \sum_{\nu''} (g_{\nu''+\omega \uparrow} - g_{\nu'' \downarrow}) \right\} = -2 \bar{\gamma}_{\nu, \langle \nu'' \rangle, \omega}^{2\text{PI}} \langle S^z \rangle. \quad (47)$$

Then, one can approximate the two-particle irreducible vertex function as

$$\bar{\gamma}_{\nu, \nu'', \omega}^{2\text{PI}} \simeq \bar{\gamma}_{\nu, \langle \nu'' \rangle, \omega}^{2\text{PI}} = - \frac{\Sigma_{\nu+\omega \uparrow} - \Sigma_{\nu \downarrow}}{2 \langle S^z \rangle} = -\delta \Sigma_{\nu\omega}. \quad (48)$$

The three-point vertex function (40) is then simplified as

$$\begin{aligned} \gamma_{\nu\omega}^{+} &= \sum_{\nu', \nu''} \left\{ \delta_{\nu, \nu'} - \bar{\gamma}_{\nu, \nu'', \omega}^{2\text{PI}} \left[\delta_{\nu'', \nu'} + g_{\nu''+\omega \uparrow} g_{\nu'' \downarrow} \bar{\gamma}_{\nu'', \nu', \omega}^{2\text{PI}} \right]^{-1} g_{\nu'+\omega \uparrow} g_{\nu' \downarrow} \right\} \chi_{\omega}^{-1} \\ &\simeq \left\{ 1 - \bar{\gamma}_{\nu, \langle \nu'' \rangle, \omega}^{2\text{PI}} \sum_{\nu', \nu''} \left\{ \left[\delta_{\nu'', \nu'} + g_{\nu''+\omega \uparrow} g_{\nu'' \downarrow} \bar{\gamma}_{\nu'', \nu', \omega}^{2\text{PI}} \right]^{-1} g_{\nu'+\omega \uparrow} g_{\nu' \downarrow} \right\} \right\} \chi_{\omega}^{-1} \\ &= \left\{ 1 - \bar{\gamma}_{\nu, \langle \nu'' \rangle, \omega}^{2\text{PI}} \chi_{\omega} \right\} \chi_{\omega}^{-1} = \chi_{\omega}^{-1} + \delta \Sigma_{\nu\omega} \simeq \chi_{\omega}^{0-1}, \end{aligned} \quad (49)$$

where $\chi_{\omega}^0 = \sum_{\nu} g_{\nu+\omega \uparrow} g_{\nu \downarrow}$. Similarly, one can show that

$$\gamma_{\nu+\omega, -\omega}^{-} \simeq \chi_{\omega}^{-1} + \delta \Sigma_{\nu\omega} \simeq \chi_{\omega}^{0-1} \quad (50)$$

and the magnetic susceptibility (28) can be written as

$$\left[X_{\mathbf{q}\omega}^{(2)} \right]^{-1} = J_{\mathbf{q}}^{\text{d}} + \Lambda_{\omega} + \chi_{\omega}^{-1} - \sum_{\mathbf{k}, \nu} \left(\chi_{\omega}^{-1} + \delta \Sigma_{\nu\omega} \right) \tilde{G}_{\mathbf{k}+\mathbf{q}, \nu+\omega, \uparrow} \tilde{G}_{\mathbf{k}, \nu, \downarrow} \left(\chi_{\omega}^{-1} + \delta \Sigma_{\nu\omega} \right) \quad (51)$$

$$= J_{\mathbf{q}}^{\text{d}} + \Lambda_{\omega} + \chi_{\omega}^{-1} - \chi_{\omega}^{0-1} \tilde{X}_{\mathbf{q}\omega}^0 \chi_{\omega}^{0-1}. \quad (52)$$

Here, we also introduce $\tilde{X}_{\mathbf{q}\omega}^0 = \sum_{\mathbf{k}, \nu} \tilde{G}_{\mathbf{k}+\mathbf{q}, \nu+\omega, \uparrow} \tilde{G}_{\mathbf{k}, \nu, \downarrow}$.

The ladder form of the magnetic susceptibility (43) can also be simplified. Taking into account that the last approximation in Eq. 50 is nothing else than averaging of the 2PI four-point vertex function (48) over the second fermionic frequency

$$\bar{\gamma}_{\nu \langle \nu' \rangle \omega}^{2\text{PI}} \simeq \bar{\gamma}_{\langle \nu \nu' \rangle \omega}^{2\text{PI}} = \chi_{\omega}^{-1} - \chi_{\omega}^{0-1}, \quad (53)$$

one gets the following RPA-like approximation for the magnetic susceptibility in the ladder approximation (43)

$$X_{\mathbf{q}\omega}^{\text{ladd}} = X_{\mathbf{q}\omega}^0 \left[1 + \left(\bar{\gamma}_{\langle\nu\nu'\rangle\omega}^{2\text{PI}} + \Lambda + J_{\mathbf{q}}^{\text{d}} \right) X_{\mathbf{q}\omega}^0 \right]^{-1}, \quad (54)$$

where the bare lattice magnetic susceptibility $X_{\mathbf{q}\omega}^0 = \sum_{\mathbf{k}\nu} G_{\mathbf{k}+\mathbf{q},\nu+\omega\uparrow} G_{\mathbf{k}\nu\downarrow}$ was introduced.

As it is shown below, in the strongly polarized regime the three-point vertex function of impurity problem $\gamma'_{\nu\omega}$ that connects two fermionic propagators and interaction is close to unity (87). Then, the local polarization function of impurity can be approximated as $\Pi_{\omega} \simeq \chi_{\omega}^0$ and the full local susceptibility in the spin channel reads

$$\chi_{\omega}^{-1} = \chi_{\omega}^0{}^{-1} - \mathcal{U}_{\omega}^{\pm}. \quad (55)$$

Here, $\mathcal{U}_{\omega}^{\pm} = -U + \Lambda$ is the bare interaction of impurity problem in the spin channel. Then, the averaged 2PI four-point vertex function (53) reads $\bar{\gamma}_{\langle\nu\nu'\rangle\omega}^{2\text{PI}} \simeq U - \Lambda$ and one finally gets the following simple expression for the magnetic susceptibility (54)

$$X_{\mathbf{q}\omega}^{\text{ladd}} = X_{\mathbf{q}\omega}^0 \left[1 + \left(U + J_{\mathbf{q}}^{\text{d}} \right) X_{\mathbf{q}\omega}^0 \right]^{-1}. \quad (56)$$

APPLICATION: THE HUBBARD MODEL ON THE HYPERCUBIC LATTICE IN INFINITE DIMENSIONS

We consider the half-filled Hubbard model

$$H = -(2d)^{-\frac{1}{2}} \sum_{\langle ij \rangle \sigma} c_{i\sigma}^{\dagger} c_{j\sigma} + U \sum_i n_{i\uparrow} n_{i\downarrow} \quad (57)$$

on the hypercubic lattice in infinite dimensions $d \rightarrow \infty$, where the summation over $\langle ij \rangle$ runs over nearest neighbors. In this limit the non-interacting density of states becomes a Gaussian, $D(\epsilon) = (2\pi)^{-1/2} e^{-\epsilon^2/2}$ [11]. At low temperatures this system favors antiferromagnetic order over paramagnetism. Within the symmetry-broken phase one has to consider two sublattices A and B of the bipartite hypercubic lattice with a staggered magnetization, $\langle m^A \rangle = -\langle m^B \rangle = \langle m \rangle$. In a bipartite ordered state the volume of the Brillouin zone (BZ) is halved, such that Fourier transforms may only be performed up to the magnetic unit cell, see, for example, [11]. In the reduced Brillouin zone (RBZ) the noninteracting Hamiltonian reads,

$$H_0 = \sum_{\mathbf{k}\sigma} \begin{pmatrix} a_{\mathbf{k}\sigma}^* & b_{\mathbf{k}\sigma}^* \end{pmatrix} \begin{pmatrix} 0 & \epsilon_{\mathbf{k}} \\ \epsilon_{\mathbf{k}} & 0 \end{pmatrix} \begin{pmatrix} a_{\mathbf{k}\sigma} \\ b_{\mathbf{k}\sigma} \end{pmatrix}, \quad (58)$$

where $a_{\mathbf{k}\sigma}^{(*)}$ and $b_{\mathbf{k}\sigma}^{(*)}$ annihilate (create) a σ -electron with momentum \mathbf{k} in sublattice A and B , respectively. $\epsilon_{\mathbf{k}}$ is the dispersion of the hypercubic lattice and \mathbf{k} a vector of the RBZ. Therefore, the Green's function becomes a two-by-two matrix $\hat{G} = (G^{AA}, G^{AB}; G^{BA}, G^{BB})$ in sublattice space. Since the Hubbard model in infinite dimensions is an exact limit of DMFT, the lattice model (57) is mapped exactly to a single-site Anderson impurity model (AIM). Therefore, the self-energy $\Sigma_{\nu\sigma}$ of $\hat{G}_{\mathbf{k}\nu\sigma}$ is local and it reads

$$\hat{G}_{\mathbf{k}\nu\sigma} = \begin{pmatrix} \zeta_{\nu\bar{\sigma}} & -\epsilon_{\mathbf{k}} \\ -\epsilon_{\mathbf{k}} & \zeta_{\nu\sigma} \end{pmatrix}^{-1}, \quad (59)$$

where $\zeta_{\nu\sigma} = i\nu + \mu - \Sigma_{\nu\sigma}$. The impurity $\hat{g}_{\nu\sigma}$ and local part of the lattice Green's function $\hat{G}_{\text{loc}} = \sum_{\mathbf{k}} \hat{G}_{\mathbf{k}}$ are tied via the following prescription

$$\hat{G}_{\text{loc},\nu\sigma} = \hat{g}_{\nu\sigma} = \int_{-\infty}^{\infty} \frac{D(\epsilon)d\epsilon}{\zeta_{\nu\sigma}\zeta_{\nu\bar{\sigma}} - \epsilon^2} \begin{pmatrix} \zeta_{\nu\bar{\sigma}} & 0 \\ 0 & \zeta_{\nu\sigma} \end{pmatrix}. \quad (60)$$

The momentum summation was rewritten as an integral over the density of states $D(\epsilon)$ of the hypercubic lattice. It was used that the off-diagonal elements of Green's function are an odd function of ϵ and thus vanish upon integration. By symmetry, an exchange of the sublattice indices $A \leftrightarrow B$ is equivalent to a flip of the spin label $\sigma \leftrightarrow \bar{\sigma}$. The prescription is satisfied by fixing the dynamical Weiss field $\mathcal{G}_{\nu\sigma}^{-1} = G_{\text{loc},\nu\sigma}^{-1} + \Sigma_{\nu\sigma}$ of the AIM self-consistently.

DMFT susceptibility of the ordered phase

In order to calculate the transversal spin susceptibility of the Hubbard model in the antiferromagnetically ordered phase we introduce the bare susceptibility. On a bipartite lattice it is in general necessary to consider two-particle quantities with four

indices a, b, c, d . The bubble is then a 4×4 matrix given by the tensor product $\hat{G}_\uparrow \otimes \hat{G}_\downarrow^T$. The locality of the irreducible vertex in DMFT allows to consider the Bethe-Salpeter equation only in a 2×2 subspace, where the bare susceptibility is given by the following point-wise product $\hat{G}_\uparrow \circ \hat{G}_\downarrow^T$

$$\begin{aligned} \hat{X}_{\mathbf{q}\omega; \nu}^0 &= \sum_{\mathbf{k}} \hat{G}_{\mathbf{k}+\mathbf{q}, \nu+\omega\uparrow} \circ \hat{G}_{\mathbf{k}\nu\downarrow}^T \\ &= \sum_{\mathbf{k}} \frac{1}{\zeta_{\nu+\omega, \uparrow} \zeta_{\nu+\omega, \downarrow} - \epsilon_{\mathbf{k}+\mathbf{q}}^2} \frac{1}{\zeta_{\nu\downarrow} \zeta_{\nu\uparrow} - \epsilon_{\mathbf{k}}^2} \begin{pmatrix} \zeta_{\nu+\omega, \downarrow} \zeta_{\nu, \uparrow} & \epsilon_{\mathbf{k}+\mathbf{q}} \epsilon_{\mathbf{k}} \\ \epsilon_{\mathbf{k}+\mathbf{q}} \epsilon_{\mathbf{k}} & \zeta_{\nu+\omega, \uparrow} \zeta_{\nu, \downarrow} \end{pmatrix} \\ &= \iint_{-\infty}^{\infty} d\epsilon_1 d\epsilon_2 \frac{D_{\mathbf{q}}(\epsilon_1, \epsilon_2)}{(\zeta_{\nu+\omega, \uparrow} \zeta_{\nu+\omega, \downarrow} - \epsilon_1^2)(\zeta_{\nu\downarrow} \zeta_{\nu\uparrow} - \epsilon_2^2)} \begin{pmatrix} \zeta_{\nu+\omega, \downarrow} \zeta_{\nu, \uparrow} & \epsilon_1 \epsilon_2 \\ \epsilon_1 \epsilon_2 & \zeta_{\nu+\omega, \uparrow} \zeta_{\nu, \downarrow} \end{pmatrix}, \end{aligned} \quad (61)$$

where \mathbf{k} and \mathbf{q} are vectors of the reduced Brillouin zone (RBZ). Here, the momentum summation leads to a double integral involving the expression $D_{\mathbf{q}}(\epsilon_1, \epsilon_2)$. This reduces to $D(\epsilon_1)D(\epsilon_2)$ for any generic wave vector \mathbf{q} . The term ‘‘generic’’ may be understood such that \mathbf{q} is a vector of the RBZ with an infinite number of random entries (see [11] and references therein). As a consequence, the integrals in Eq. (61) factorize and the bubble is given as $\hat{g}_{\nu+\omega\uparrow} \circ \hat{g}_{\nu\downarrow}$. Hence, the nonlocal bubble

$$\tilde{X}_{\mathbf{q}\omega; \nu}^{0, ab} = \sum_{\mathbf{k}} G_{\mathbf{k}+\mathbf{q}, \nu+\omega, \uparrow}^{ab} G_{\mathbf{k}\nu\downarrow}^{ba} - g_{\nu+\omega, \uparrow}^a g_{\nu\downarrow}^a \delta_{ab}, \quad (62)$$

vanishes identically at generic \mathbf{q} . In the following, we consider the non-generic vector $\mathbf{q}_0 = \mathbf{0}$ of the RBZ, where $D_{\mathbf{q}_0}(\epsilon_1, \epsilon_2) = \delta(\epsilon_1 - \epsilon_2)D(\epsilon_1)$. This may be used to eliminate one of the integrals in Eq. (61), the remaining integral is solved numerically. Vectors $\tilde{\mathbf{q}}$ of the Brillouin zone (BZ) are marked with a tilde.

From the nonlocal bubble in Eq. (62) and from the full local four-point vertex of impurity model $\bar{\gamma}_{\nu\nu'\omega}^{ab} = \bar{\gamma}_{\nu\nu'\omega}^a \delta_{ab}$ one obtains the T -matrix $F_{\mathbf{q}\omega; \nu\nu'}^{ab}$ via the Bethe-Salpeter equation (BSE),

$$\hat{F}_{\mathbf{q}\omega}^{-1} = \hat{\gamma}_{\omega}^{-1} + \hat{X}_{\mathbf{q}\omega}^0, \quad (63)$$

where $\tilde{X}_{\mathbf{q}\omega; \nu\nu'}^{0, ab} = \tilde{X}_{\mathbf{q}\omega; \nu}^{0, ab} \delta_{\nu\nu'}$ and \hat{O}^{-1} denotes a super-matrix inversion with respect to the indices (a, ν) and (b, ν') . One further calculates the dual polarization in the ladder approximation (37) as

$$\hat{\Pi}_{\mathbf{q}\omega}^{\text{ladd}} = \text{Tr}_{\nu\nu'} \left[\hat{\gamma}_{\omega} \hat{X}_{\mathbf{q}\omega}^0 (I - \text{V.C.}) \hat{\gamma}_{\omega} \right], \quad (64)$$

where $\text{Tr}_{\nu\nu'}$ denotes a trace over fermionic frequencies and V.C. indicates vertex corrections given by $\hat{F}_{\mathbf{q}\omega} \hat{X}_{\mathbf{q}\omega}^0$. Finally, the lattice susceptibility is obtained using the relation (36). Further, we consider an approximation for the magnetic susceptibility given by equation (28) in the case of Hubbard model

$$\left[X_{\mathbf{q}\omega}^{(2)} \right]^{-1} = \chi_{\omega}^{-1} - \tilde{\Pi}_{\mathbf{q}\omega}^{(2)}, \quad (65)$$

where $\tilde{\Pi}_{\mathbf{q}\omega}^{(2)}$ is obtained when neglecting vertex corrections in Eq. (64). The case of magnetic susceptibility (36) where the polarization function $\tilde{\Pi}_{\mathbf{q}\omega}^{\text{ladd}}$ is approximated by the second-order correction $\tilde{\Pi}_{\mathbf{q}\omega}^{(2)}$ is also considered. However, it does not provide a good approximation for the exact result of Eq. 64 as shown in the main text.

Numerical calculations

The numerical calculations are performed using 10^8 measurements with 50 Monte-Carlo moves between them. Aside from the segment insertion and removal we also use the shift and the double move as well as the spin-flip, a global move. We measure the Green’s function in the Legendre basis with 35 coefficients. The Hilbert-transform for the local Green’s function is done on an energy mesh of $\omega \in [-20, 20]$ with 4000 mesh points. The initial DMFT-cycle is performed with an external magnetic field, that is switched off for the following cycles. For the DMFT updates we use a mixing parameter of 0.5.

We fit the model $\langle S^z \rangle = \sqrt{T_N - T}$ to the DMFT results to estimate $T_N \approx 0.186$, see Fig. 1. This refined scan is done for $U = 5$ with a more dense temperature mesh. Only data points in proximity to the transition were taken into account and the domain of the paramagnetic region is treated by a Heaviside step-function.

For simplicity, we calculate an approximated versions (52) and (54) of the magnetic susceptibilities (28) and (35) for the Hubbard model ($V_{\mathbf{q}}, J_{\mathbf{q}}^d, \Lambda = 0$), respectively. We note that the wave vector \mathbf{q}_0 of the RBZ maps to two vectors $\tilde{\mathbf{q}}_0 = \mathbf{q}_0$ and

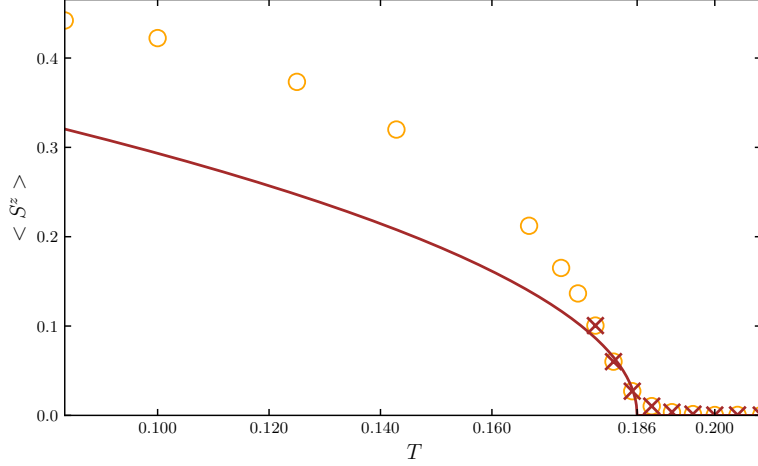


FIG. 1. The magnetic moment as a function of the temperature for the interaction value of $U = 5$. The mean-field model (solid line) fits DMFT results close to the transition (red crosses). DMFT data for lower temperatures are shown, too (circles).

$\tilde{\mathbf{q}}_\pi = (\pi, \dots, \pi)$ of the BZ. In the paramagnet this mapping diagonalizes the susceptibility matrix $\hat{X}(\mathbf{q}_0) = (X^{AA}, X^{AB}; X^{BA}, X^{BB})$, where the diagonal elements are $X(\tilde{\mathbf{q}}_\pi) = X^{AA} + X^{BB} - X^{AB} - X^{BA}$ and $X(\tilde{\mathbf{q}}_0) = X^{AA} + X^{BB} + X^{AB} + X^{BA}$. In the ordered phase the same mapping does not diagonalize \hat{X} , since the offdiagonal element $X^\pm(\tilde{\mathbf{q}}_0) = X^{AA} - X^{BB} + X^{AB} - X^{BA}$ does not vanish. Approaching T_N from above, $X(\tilde{\mathbf{q}}_\pi)$ diverges and it remains divergent in the ordered phase, signaling that the crystal is prone to a spontaneous tilt of its magnetization axis. We verified in our calculations that at $U = 5$ and $T = 0.1 < T_N$ one of the two eigenvalues of the BSE (63) is very close to unity, $|\lambda_{\mathbf{q}_\pi}| \approx 0.993$, and that this channel corresponds to $X(\tilde{\mathbf{q}}_\pi)$. We account the slight deviation of this eigenvalue from unity to our approximation of the impurity vertex γ . The second eigenvalue, however, remains smaller than one, $|\lambda_{\mathbf{q}_0}| \approx 0.715$, and belongs to the homogenous susceptibility $X(\tilde{\mathbf{q}}_0)$. In the main text we show the real and imaginary parts of the lattice susceptibility $\hat{X}(\tilde{\mathbf{q}}_0)$, which corresponds to $\Re \hat{X}(\tilde{\mathbf{q}}_0) = \Re X(\tilde{\mathbf{q}}_0)$ and $\Im \hat{X}(\tilde{\mathbf{q}}_0) = \Im X(\tilde{\mathbf{q}}_0)$.

Ward identity

We deduce two exact statements about the dynamical homogenous susceptibility $\hat{X}(\mathbf{q}_0, \omega)$ from the Ward identity of the two-particle correlation function $G_{kk'q}^{abcd} = -\langle a_{k\downarrow} b_{k+q,\uparrow}^* c_{k'+q,\uparrow} d_{k'\downarrow}^* \rangle$, where each of the operators labeled with a, b, c, d denotes either $a^{(*)}$ or $b^{(*)}$, respectively, and $k = (\mathbf{k}, \nu)$, $q = (\mathbf{q}, \omega)$ abbreviate momenta from the RBZ and Matsubara frequencies. From the equation of motion $\partial_\tau \rho_{\mathbf{q}}^a = [H, \rho_{\mathbf{q}}^a]$ of the density operator $\rho_{\mathbf{q}}^a = \sum_{\mathbf{k}} a_{\mathbf{k}\downarrow}^* a_{\mathbf{k}+\mathbf{q}\uparrow}$ one obtains the Ward identity (see, for example, [8]),

$$-i\omega \sum_{k'} (G_{kk'q}^{aaaa} + G_{kk'q}^{aabb}) + \sum_{k'} [\varepsilon_{k'+q} - \varepsilon_{k'}] (G_{kk'q}^{aaba} + G_{kk'q}^{aaab}) = G_{k+q\uparrow}^{aa} - G_{k\downarrow}^{aa}, \quad (a \neq b), \quad (66)$$

where \sum_k implies a summation over the RBZ and Matsubara frequencies. Evaluating Eq. (66) at $q_0^+ = (\mathbf{q}_0 = \mathbf{0}, \omega^+ > 0)$ the term in the second line vanishes. Upon summation over k and using that $\sum_{kk'} G_{kk'q_0^+}^{aabb} = X^{ab}(\mathbf{q}_0, \omega^+)$ it follows,

$$-i\omega^+ [X^{aa}(\mathbf{q}_0, \omega^+) + X^{ab}(\mathbf{q}_0, \omega^+)] = \langle m^a \rangle, \quad (67)$$

where it was also used that $\sum_k G_{k\sigma}^{aa} = \langle n_\sigma^a \rangle$ and $\langle m^a \rangle = \langle n_\uparrow^a \rangle - \langle n_\downarrow^a \rangle$. Adding up above relation for $a = A, b = B$ and $a = B, b = A$ it follows that

$$X(\tilde{\mathbf{q}}_0, \omega^+) = X^{AA}(\mathbf{q}_0, \omega^+) + X^{AB}(\mathbf{q}_0, \omega^+) + X^{BB}(\mathbf{q}_0, \omega^+) + X^{BA}(\mathbf{q}_0, \omega^+) = 0, \quad (68)$$

since $\langle m^A \rangle = -\langle m^B \rangle = \langle m \rangle$. Subtraction likewise leads to

$$X^\pm(\tilde{\mathbf{q}}_0, \omega^+) = X^{AA}(\mathbf{q}_0, \omega^+) + X^{AB}(\mathbf{q}_0, \omega^+) - X^{BB}(\mathbf{q}_0, \omega^+) - X^{BA}(\mathbf{q}_0, \omega^+) = \frac{2i \langle m \rangle}{\omega^+}. \quad (69)$$

Eqs. (68) and (69) follow from the equation of motion of the total spin density, $\rho_{\mathbf{q}_0}^A + \rho_{\mathbf{q}_0}^B$, and are therefore necessary criteria for global spin conservation.

SPIN POLARIZED SOLUTION OF ATOMIC PROBLEM

One can perform an exact diagonalization of a magnetically polarized single orbital Hubbard atom at the half-filling. The thermodynamic potential operator of the atom is given by

$$\hat{H} - \mu\hat{N} = \sum_{\sigma} \Delta_{\sigma} c_{\sigma}^* c_{\sigma} + U n_{\uparrow} n_{\downarrow}, \quad (70)$$

Here $\Delta_{\uparrow,\downarrow} = \pm B - \mu$ and the magnetic field B is considered much larger than the temperature $T \equiv 1/\beta$. The system has four eigenstates $|0\rangle, |\uparrow\rangle, |\downarrow\rangle$ and $|\uparrow\downarrow\rangle$ with the corresponding energies $E_0 = 0, E_{\uparrow,\downarrow} = \pm B - \mu$ and $E_{\uparrow\downarrow} = U - 2\mu$. Half-filling corresponds to $\mu = U/2$, so that $E_{\uparrow\downarrow} = 0$. Indeed, the partition function for $\mu = U/2$ is

$$Z = 2 + e^{\beta(\mu-B)} + e^{\beta(\mu+B)} \approx e^{\beta(B+\mu)}, \quad (71)$$

and the average filling is given by $(1 \times e^{\beta(\mu-B)} + e^{\beta(\mu+B)} + 2 \times 1)/Z = 1$, where we used that $B\beta \gg 1$.

The non-zero matrix elements of the creation and annihilation operators are

$$\langle \uparrow | c_{\uparrow}^* | 0 \rangle = 1; \quad \langle \downarrow | c_{\downarrow}^* | 0 \rangle = 1; \quad \langle \uparrow\downarrow | c_{\uparrow}^* | \downarrow \rangle = 1; \quad \langle \uparrow\downarrow | c_{\downarrow}^* | \uparrow \rangle = -1. \quad (72)$$

Now we use the Lehmann representation to obtain the Green's functions of the system

$$g_{v\sigma} = \frac{1}{Z} \sum_{ij} |\langle i | c_{\sigma} | j \rangle|^2 \frac{e^{-\beta E_i} + e^{-\beta E_j}}{i\nu + E_i - E_j}. \quad (73)$$

This yields

$$\begin{aligned} g_{v\uparrow} &= \frac{1}{Z} \left[|\langle 0 | c_{\uparrow} | \uparrow \rangle|^2 \frac{1 + e^{\beta(\mu-B)}}{i\nu + \mu - B} + |\langle \downarrow | c_{\uparrow} | \uparrow\downarrow \rangle|^2 \frac{1 + e^{\beta(\mu+B)}}{i\nu - \mu - B} \right], \\ g_{v\downarrow} &= \frac{1}{Z} \left[|\langle 0 | c_{\downarrow} | \downarrow \rangle|^2 \frac{1 + e^{\beta(\mu+B)}}{i\nu + \mu + B} + |\langle \uparrow | c_{\downarrow} | \uparrow\downarrow \rangle|^2 \frac{1 + e^{\beta(\mu-B)}}{i\nu - \mu + B} \right], \end{aligned} \quad (74)$$

or, using $B\beta \gg 1$,

$$g_{v\uparrow} = \frac{1}{i\nu - \mu - B} \approx \frac{1}{i\nu - U/2}, \quad g_{v\downarrow} = \frac{1}{i\nu + \mu + B} \approx \frac{1}{i\nu + U/2}. \quad (75)$$

Now we calculate the magnetic susceptibility

$$\chi_{\omega}^{-+} = -\frac{1}{Z} \int_0^{\beta} d\tau e^{i\omega\tau} \langle S^-(\tau) S^+(0) \rangle, \quad (76)$$

where $S^{\pm}(\tau)$ are Heisenberg representations of S^{\pm} operators. The non-zero matrix elements of the latter are

$$\langle \uparrow | S^+ | \downarrow \rangle = \langle \downarrow | S^- | \uparrow \rangle = 1. \quad (77)$$

Lehmann representation reads

$$\chi_{\omega}^{-+} = -\frac{1}{Z} \sum_{ij} |\langle i | S^- | j \rangle|^2 \left[\frac{(e^{-\beta E_j} - e^{-\beta E_i})(1 - \delta_{E_i, E_j})}{i\omega + E_i - E_j} + \beta \delta_{E_i, E_j} \delta_{\omega 0} \right] = \frac{1}{i\omega - 2B}. \quad (78)$$

Finally we turn to calculating of $\chi^{\uparrow\downarrow}(\tau_1, \tau_2) \equiv \langle T_{\tau} c_{\downarrow}^*(\tau_1) c_{\uparrow}(\tau_2) S^+(0) \rangle$. Unlike the previous cases, here we have to explicitly consider the time-ordering operator.

$$\chi^{\sigma\sigma' s}(\tau_1, \tau_2) = \langle c_{\sigma}^*(\tau_1) c_{\sigma'}(\tau_2) S^s(0) \rangle \theta(\tau_1 - \tau_2) - \langle c_{\sigma'}(\tau_2) c_{\sigma}^*(\tau_1) S^s(0) \rangle \theta(\tau_2 - \tau_1). \quad (79)$$

The usual trick here is to split the integration region $0 < \tau_1, \tau_2 < \beta$ in the Fourier transform integral into two parts: $\int_0^{\beta} \int_0^{\beta} d\tau_1 d\tau_2 \dots = \int_0^{\beta} d\tau_1 \int_0^{\tau_1} d\tau_2 \dots + \int_0^{\beta} d\tau_2 \int_0^{\tau_2} d\tau_1 \dots$ and swapping the integration variables in the second term. This immediately gives for

$$\chi^{\sigma\sigma' s}(\nu_1, \nu_2) \equiv \int_0^{\beta} \int_0^{\beta} d\tau_1 d\tau_2 e^{i\nu_1 \tau_1 + i\nu_2 \tau_2} \chi^{\sigma\sigma' s}(\tau_1, \tau_2) \quad (80)$$

the following Lehmann representation

$$\chi^{\sigma\sigma'\zeta}(\nu_1, \nu_2) = \frac{1}{Z} \left[\sum_{ijk} \langle i | c_{\sigma'}^* | j \rangle \langle j | c_{\sigma'} | k \rangle \langle k | S^{\zeta} | i \rangle f_{ijk}(\nu_1, \nu_2) - \sum_{ijk} \langle i | c_{\sigma'} | j \rangle \langle j | c_{\sigma'}^* | k \rangle \langle k | S^{\zeta} | i \rangle f_{ijk}(\nu_2, \nu_1) \right], \quad (81)$$

where

$$f_{ijk}(\nu_1, \nu_2) = \int_0^{\beta} d\tau_1 \int_0^{\tau_1} d\tau_2 e^{-\beta E_i} e^{i\nu_1 \tau_1 + i\nu_2 \tau_2} e^{\tau_1(E_i - E_j) + \tau_2(E_j - E_k)} \quad (82)$$

$$= \frac{(e^{-\beta E_k} - e^{-\beta E_i})(1 - \delta_{E_i, E_k})}{(i\nu_1 + i\nu_2 + E_i - E_k)(i\nu_2 + E_j - E_k)} + \frac{e^{-\beta E_j} + e^{-\beta E_i}}{(i\nu_1 + E_i - E_j)(i\nu_2 + E_j - E_k)} + \frac{\beta \delta_{E_i, E_k} \delta_{\nu_1 + \nu_2, 0}}{i\nu_2 + E_j - E_k}. \quad (83)$$

For our particular case $\sigma = \downarrow$, $\sigma' = \uparrow$ and $\zeta = +$, so $i = |\downarrow\rangle$, $k = |\uparrow\rangle$ and j can be either $|0\rangle$ for the first term in (81) or $|\uparrow\downarrow\rangle$ for the second one. Thus

$$\chi^{\uparrow\downarrow+}(\nu_1, \nu_2) = \frac{1}{Z} (f_{\downarrow,0,\uparrow}(\nu_1, \nu_2) + f_{\downarrow,\uparrow,\uparrow}(\nu_2, \nu_1)). \quad (84)$$

Using (83) and $\beta B \gg 1$ we obtain

$$\chi^{\uparrow\downarrow+}(\nu_1, \nu_2) = \left(1 - \frac{2\mu}{i\nu_1 + i\nu_2 - 2B} \right) \frac{1}{(i\nu_1 - B - \mu)(i\nu_2 - B - \mu)} \quad (85)$$

$$= -g_{\nu_1\downarrow} g_{-\nu_2\uparrow} (1 - U\chi^{-+}(\nu_1 + \nu_2)). \quad (86)$$

Let us define the three-point vertex $\gamma'_{\nu\omega}$ for the spin channel that connects two fermionic propagators and interaction in the same way as in [4] with the cut-off on the renormalization parameter $\alpha_{\omega}^{-+} = (1 + U^{-+}\chi^{-+}(\nu_1 + \nu_2)) = \mathcal{W}_{\omega}^{-+}/U^{-+}$ instead of χ_{ω}^{-+} . The difference between these two definitions is that in the case of $\gamma'_{\nu\omega}$ the full bosonic propagator of the impurity problem that is attached to the vertex is the full local susceptibility χ_{ω} , while in the case of $\gamma'_{\nu\omega}$ vertex function it is equal to the renormalized interaction of impurity problem $\mathcal{W}_{\omega}^{-+}$ in the spin channel.

Remarkably, the three-point vertex function $\gamma'_{\nu\omega}$ in the spin-polarized case is equal to unity

$$\gamma'^{-}(\nu_1, \nu_2) = \frac{-\langle c_{\downarrow}^*(\nu_1) c_{\uparrow}(-\nu_2) S^+(\nu_1 + \nu_2) \rangle}{g_{\nu_1\downarrow} g_{-\nu_2\uparrow} \alpha^{-+}(\nu_1 + \nu_2)} = 1, \quad (87)$$

because in the spin channel the bare interaction is equal to $U^{+-} = -U$. Using the relation between the three- and four-point vertices derived in [4], one gets

$$\gamma'_{\nu\omega}{}^S = \alpha_{\omega}^S{}^{-1} \sum_{\nu'} \left[1 - \bar{\gamma}_{\nu\nu'\omega}^S g_{\nu'\sigma} g_{\nu'+\omega, \sigma'} \right] \quad (88)$$

$$\gamma'_{\nu\omega}{}^S (1 + \mathcal{W}_{\omega}^S \Pi_{\omega}^S) = \sum_{\nu'} \left[1 - \bar{\gamma}_{\nu\nu'\omega}^S g_{\nu'\sigma} g_{\nu'+\omega, \sigma'} \right] \quad (89)$$

$$\gamma'_{\nu\omega}{}^S = \sum_{\nu'} \left[1 - (\bar{\gamma}_{\nu\nu'\omega}^S + \gamma'_{\nu\omega}{}^S \mathcal{W}_{\omega}^S \gamma'_{\nu'+\omega, -\omega}{}^S) g_{\nu'\sigma} g_{\nu'+\omega, \sigma'} \right], \quad (90)$$

where the Hedin expression for the polarization function of impurity problem $\Pi_{\omega} = \sum_{\nu} \gamma'_{\nu+\omega, -\omega} g_{\nu, \sigma} g_{\nu+\omega, \sigma'}$ is used. Therefore, when the three-point vertex function $\gamma'_{\nu\omega}$ is close to unity, the main contribution to the four-point vertex function is given by the following expression

$$\bar{\gamma}_{\nu\nu'\omega}^S \simeq -\gamma'_{\nu\omega}{}^S \mathcal{W}_{\omega}^S \gamma'_{\nu'+\omega, -\omega}{}^S. \quad (91)$$

Transforming back to the definition of the three-point vertex function used in this Letter $\gamma'_{\nu\omega} \rightarrow \gamma_{\nu\omega}$, one also has to replace the full local bosonic propagator as $\mathcal{W}_{\omega} \rightarrow \chi_{\omega}$. Then, the final expression for the four-point vertex reads

$$\bar{\gamma}_{\nu\nu'\omega}^S \simeq -\gamma_{\nu\omega}^S \chi_{\omega}^S \gamma_{\nu'+\omega, -\omega}^S. \quad (92)$$

APPLICATION: EXCHANGE INTERACTION IN THE STRONGLY LOCALIZED REGIME

Here, we calculate the exchange interaction for the Hubbard model in the strongly localized regime $t \ll U$. For this reason, let us find the nonlocal Green's function as the first order correction to the atomic limit solution with respect to the hopping amplitude. Then, using the definition of the Green's function, one gets

$$G_{ij\sigma} = \frac{1}{Z} \int D[c^*, c] c_{i\sigma}^* c_{j\sigma} e^{-\sum_i S_{at}^i - \sum_{i'j'\sigma'} t_{i'j'} c_{i'\sigma'}^* c_{j'\sigma'}} = \frac{1}{Z} \int D[c^*, c] c_{i\sigma}^* c_{j\sigma} e^{-\sum_i S_{at}^i} - \frac{1}{Z} \int D[c^*, c] \sum_{i'j'} t_{i'j'} c_{i'\sigma'}^* c_{j'\sigma'} e^{-\sum_i S_{at}^i}. \quad (93)$$

Since the atomic action is purely local, the contribution to the nonlocal Green's function for $i \neq j$ is given only by the second term when $i = j'$ and $j = i'$, so $\sigma = \sigma'$. Then, the nonlocal Green's function can be rewritten as

$$G_{ij\sigma} = t_{ji} \frac{1}{Z_{at}^i} \int D[c^*, c] c_{i\sigma}^* c_{i\sigma} e^{-S_{at}^i} \times \frac{1}{Z_{at}^j} \int D[c^*, c] c_{j\sigma}^* c_{j\sigma} e^{-S_{at}^j} = t g_{v\sigma}^2, \quad (94)$$

where $g_{v\sigma}$ is the local Green's function of atomic problem. Taking into account the result of Eq. 75 and that the difference of the self-energies is equal to $\Sigma_{v\uparrow} - \Sigma_{v\downarrow} = U + 2B$ and that $2\langle S^z \rangle = 1$, the exchange interaction reads

$$J_{ij} = - \sum_{\nu} \left(\chi_{\omega=0}^{-1} + \frac{\Sigma_{v\uparrow} - \Sigma_{v\downarrow}}{2\langle S^z \rangle} \right) G_{ij, \nu\uparrow} G_{ji, \nu\downarrow} \left(\chi_{\omega=0}^{-1} + \frac{\Sigma_{v\uparrow} - \Sigma_{v\downarrow}}{2\langle S^z \rangle} \right) = - \sum_{\nu} \frac{tU}{(i\nu - U/2)^2} \frac{tU}{(i\nu + U/2)^2} = - \frac{2t^2}{U}. \quad (95)$$

APPLICATION: ANTIFERROMAGNETIC DIMER

One can also perform an exact diagonalization of a two-site model with the antiferromagnetic ground state

$$\hat{H} - \mu\hat{N} = t c_{1\sigma}^* c_{2\sigma} + t c_{2\sigma}^* c_{1\sigma} + \sum_{i=1,2;\sigma} (\Delta_{i\sigma} c_{i\sigma}^* c_{i\sigma} + U n_{i\uparrow} n_{i\downarrow}), \quad (96)$$

where $\Delta_{\uparrow,\downarrow} = \pm B - \mu$ and the magnetic field B is again considered much larger than the temperature $T \equiv 1/\beta$. Using the Lehmann representation, one can obtain the nonlocal Green's functions at the low temperatures, i.e. $\beta U \gg 1$ in the strongly-correlated regime $t \ll U$ as

$$G_{ab,\sigma} = \frac{1}{Z} \sum_{ij} \langle \Psi_i | c_{a\sigma}^* | \Psi_j \rangle \langle \Psi_j | c_{b\sigma} | \Psi_i \rangle \frac{e^{-\beta E_i} + e^{-\beta E_j}}{i\nu + E_i - E_j} \quad (97)$$

Since only the low-lying energy states contribute to the Green's function at low temperatures, because the contribution of higher energy states is exponentially suppressed, we give only relevant energies and (unnormalized) eigenstates below

$E_5 = -U/2 + \sqrt{B^2 + t^2}$	$\Psi_5 = -\frac{-B - \sqrt{B^2 + t^2}}{t} \uparrow\downarrow \cdot \uparrow\rangle + \uparrow \cdot \uparrow\downarrow\rangle$
$E_4 = -U/2 + \sqrt{B^2 + t^2}$	$\Psi_4 = -\frac{-B - \sqrt{B^2 + t^2}}{t} \downarrow \cdot 0\rangle + 0 \cdot \downarrow\rangle$
$E_3 = -U/2 - \sqrt{B^2 + t^2}$	$\Psi_3 = -\frac{-B + \sqrt{B^2 + t^2}}{t} \uparrow\downarrow \cdot \uparrow\rangle + \uparrow \cdot \uparrow\downarrow\rangle$
$E_2 = -U/2 - \sqrt{B^2 + t^2}$	$\Psi_2 = -\frac{-B + \sqrt{B^2 + t^2}}{t} \downarrow \cdot 0\rangle + 0 \cdot \downarrow\rangle$
$E_1 = -U - 2B$	$\Psi_1 = \uparrow\downarrow \cdot 0\rangle - \frac{2t}{U+2B} \downarrow \cdot \uparrow\rangle - \frac{U+2B}{t} \uparrow \cdot \downarrow\rangle + 0 \cdot \uparrow\downarrow\rangle$

Then, one gets

$$G_{ab\uparrow} = \frac{1}{Z} \langle \Psi_3 | c_{a\uparrow}^* | \Psi_1 \rangle \langle \Psi_1 | c_{b\uparrow} | \Psi_3 \rangle > \frac{e^{-\beta E_3} + e^{-\beta E_1}}{iv + E_3 - E_1} + \frac{1}{Z} \langle \Psi_1 | c_{a\uparrow}^* | \Psi_2 \rangle \langle \Psi_2 | c_{b\uparrow} | \Psi_1 \rangle > \frac{e^{-\beta E_1} + e^{-\beta E_2}}{iv + E_1 - E_2} \quad (98)$$

$$+ \frac{1}{Z} \langle \Psi_5 | c_{a\uparrow}^* | \Psi_1 \rangle \langle \Psi_1 | c_{b\uparrow} | \Psi_5 \rangle > \frac{e^{-\beta E_5} + e^{-\beta E_1}}{iv + E_5 - E_1} + \frac{1}{Z} \langle \Psi_1 | c_{a\uparrow}^* | \Psi_4 \rangle \langle \Psi_4 | c_{b\uparrow} | \Psi_1 \rangle > \frac{e^{-\beta E_1} + e^{-\beta E_4}}{iv + E_1 - E_4} \quad (99)$$

$$= \frac{1}{Z} \frac{1}{N_1^2 N_{3(5)}^2} \left(-\frac{-B \pm \sqrt{B^2 + t^2}}{t} \langle \uparrow \downarrow \cdot \uparrow | + \langle \uparrow \cdot \uparrow \downarrow | \right) \left(-\frac{2t}{U + 2B} | \uparrow \downarrow \cdot \uparrow \rangle + | \uparrow \cdot \uparrow \downarrow \rangle \right) \times \\ \times \left(-\langle \uparrow \downarrow \cdot \uparrow | + \frac{U + 2B}{t} \langle \uparrow \cdot \uparrow \downarrow | \right) \left(-\frac{-B \pm \sqrt{B^2 + t^2}}{t} | \uparrow \downarrow \cdot \uparrow \rangle + | \uparrow \cdot \uparrow \downarrow \rangle \right) \frac{e^{\beta(U/2 \pm \sqrt{B^2 + t^2})} + e^{\beta(U+2B)}}{iv - (U/2 \pm \sqrt{B^2 + t^2}) + (U + 2B)} \\ + \frac{1}{Z} \frac{1}{N_1^2 N_{2(4)}^2} \left(\langle \downarrow \cdot 0 | - \frac{U + 2B}{t} \langle 0 \cdot \downarrow | \right) \left(-\frac{-B \pm \sqrt{B^2 + t^2}}{t} | \downarrow \cdot 0 \rangle + | 0 \cdot \downarrow \rangle \right) \times \\ \times \left(-\frac{-B \pm \sqrt{B^2 + t^2}}{t} \langle \downarrow \cdot 0 | + \langle 0 \cdot \downarrow | \right) \left(-\frac{2t}{U + 2B} | \downarrow \cdot 0 \rangle + | 0 \cdot \downarrow \rangle \right) \frac{e^{\beta(U/2 \pm \sqrt{B^2 + t^2})} + e^{\beta(U+2B)}}{iv + (U/2 \pm \sqrt{B^2 + t^2}) - (U + 2B)}.$$

Note that all eigenstates Ψ_i were normalized as $\frac{1}{N_i} \Psi_i$. Simplifying the previous equation one gets

$$G_{ab\uparrow} = \frac{1}{Z} \frac{1}{N_1^2 N_{3(5)}^2} \left(\frac{-2B \pm 2\sqrt{B^2 + t^2}}{U + 2B} + 1 \right) \left(\frac{-B \pm \sqrt{B^2 + t^2}}{t} + \frac{U + 2B}{t} \right) \frac{e^{\beta(U/2 \pm \sqrt{B^2 + t^2})} + e^{\beta(U+2B)}}{iv + U/2 + 2B \mp \sqrt{B^2 + t^2}} \\ + \frac{1}{Z} \frac{1}{N_1^2 N_{2(4)}^2} \left(-\frac{-B \pm \sqrt{B^2 + t^2}}{t} - \frac{U + 2B}{t} \right) \left(\frac{-B \pm \sqrt{B^2 + t^2}}{t} \frac{2t}{U + 2B} + 1 \right) \frac{e^{\beta(U/2 \pm \sqrt{B^2 + t^2})} + e^{\beta(U+2B)}}{iv - U/2 - 2B \pm \sqrt{B^2 + t^2}}. \quad (100)$$

Taking into account that

$$Z = 4 \left(1 + e^{\beta U/2} \cosh \beta B \right) \simeq e^{\beta(U+2B)} \quad (101)$$

$$N_1^2 = 2 + \left(\frac{2t}{U + 2B} \right)^2 + \left(\frac{U + 2B}{t} \right)^2 \simeq \left(\frac{U + 2B}{t} \right)^2 \quad (102)$$

$$N_{2(4)}^2 = N_{3(5)}^2 = 1 + \left(\frac{-B \pm \sqrt{B^2 + t^2}}{t} \right)^2 \quad (103)$$

one can finally get

$$G_{ab\uparrow} = \frac{t^2}{(U + 2B)^2} \frac{1}{1 + \left(\frac{-B \pm \sqrt{B^2 + t^2}}{t} \right)^2} \frac{U \pm 2\sqrt{B^2 + t^2}}{U + 2B} \frac{U + B \pm \sqrt{B^2 + t^2}}{t} \frac{1}{iv + U/2 + 2B \mp \sqrt{B^2 + t^2}} \\ - \frac{t^2}{(U + 2B)^2} \frac{1}{1 + \left(\frac{-B \pm \sqrt{B^2 + t^2}}{t} \right)^2} \frac{U + B \pm \sqrt{B^2 + t^2}}{t} \frac{U \pm 2\sqrt{B^2 + t^2}}{U + 2B} \frac{1}{iv - U/2 - 2B \pm \sqrt{B^2 + t^2}}. \quad (104)$$

If $U \gg B$ and $U \gg t$, we get

$$G_{ab\uparrow} = \sum_{\pm} \frac{t}{U} \frac{1}{1 + \left(\frac{-B \pm \sqrt{B^2 + t^2}}{t} \right)^2} \left[\frac{1}{iv + U/2} - \frac{1}{iv - U/2} \right] = \frac{t}{U} \left[\frac{1}{iv + U/2} - \frac{1}{iv - U/2} \right]. \quad (105)$$

The same result can be found for

$$G_{ba\downarrow} = \frac{t}{U} \left[\frac{1}{iv + U/2} - \frac{1}{iv - U/2} \right]. \quad (106)$$

Therefore, the exchange interaction reads

$$J_{ab} = -\frac{U^2}{\beta} \sum_{\nu} G_{ab\uparrow} G_{ba\downarrow} = \frac{t^2}{2\pi} \int_{-\infty}^{+\infty} \frac{2 dx}{(x - iU/2)(x + iU/2)} = -\frac{2t^2}{U}. \quad (107)$$

-
- [1] A. Rubtsov, M. Katsnelson, and A. Lichtenstein, *Annals of Physics* **327**, 1320 (2012).
 - [2] E. G. C. P. van Loon, A. I. Lichtenstein, M. I. Katsnelson, O. Parcollet, and H. Hafermann, *Phys. Rev. B* **90**, 235135 (2014).
 - [3] E. A. Stepanov, E. G. C. P. van Loon, A. A. Katanin, A. I. Lichtenstein, M. I. Katsnelson, and A. N. Rubtsov, *Phys. Rev. B* **93**, 045107 (2016).
 - [4] E. A. Stepanov, A. Huber, E. G. C. P. van Loon, A. I. Lichtenstein, and M. I. Katsnelson, *Phys. Rev. B* **94**, 205110 (2016).
 - [5] N. Dupuis and S. Pairault, *International Journal of Modern Physics B* **14**, 2529 (2000).
 - [6] N. Dupuis, *Nuclear Physics B* **618**, 617 (2001).
 - [7] N. Dupuis, eprint arXiv:cond-mat/0105063 (2001), cond-mat/0105063.
 - [8] F. Krien, E. G. C. P. van Loon, H. Hafermann, J. Otsuki, M. I. Katsnelson, and A. I. Lichtenstein, *Phys. Rev. B* **96**, 075155 (2017).
 - [9] H. Hafermann, E. G. C. P. van Loon, M. I. Katsnelson, A. I. Lichtenstein, and O. Parcollet, *Phys. Rev. B* **90**, 235105 (2014).
 - [10] W. Metzner and D. Vollhardt, *Phys. Rev. Lett.* **62**, 324 (1989).
 - [11] A. Georges, G. Kotliar, W. Krauth, and M. J. Rozenberg, *Rev. Mod. Phys.* **68**, 13 (1996).
 - [12] M. I. Katsnelson and A. I. Lichtenstein, *Phys. Rev. B* **61**, 8906 (2000).

4.3 Multiorbital effects

From the atomic view, the d levels are degenerate. Effects, such as crystal field splitting, can lift the degeneracy, but still the bandwidth of transition metal compounds can be similar to another so that several orbitals contribute to the low-energy physics of the system. The orbital adds the the charge and spin degrees of freedom, and it is another important aspect for the understanding of many materials [202]. The Hund's rule coupling which is mentioned in the beginning of this chapter (Sec. 4) is a result of multiorbital physics. Often the d -levels are split by the ligands of the transition metal atom. In many compounds the coordination is octahedral which splits the d -levels into e_g and t_{2g} , examples are NiO and La_2CuO_4 . However, details of this splitting depend on the individual compounds, repulsion between transition metal and ligand as well as hybridization have to be considered. Further splittings due to the crystal structure are possible and even if they are small, in strongly correlated systems they can have major effects on, e.g., the magnetic properties [203].

Magnetic exchange interactions are diverse and depend on the orbital alignment between atoms and also on their fillings. The Goodenough-Kanamori-Anderson rules explain the magnetic interactions systematically. In the case of direct exchange, if two orbitals of transition metal atoms overlap, at half-filling the exchange has to be antiferromagnetic because of the Pauli principle. In contrast, if a half-filled and an empty orbital overlap, then the Hund's coupling to a degenerate orbital adds to the exchange process and favors ferromagnetic coupling. Moreover, the Coulomb repulsion in that case would be of interorbital type. However, for a comparison one can consider the energies of the two cases, which are $J_1 \sim 2t^2/U$ for antiferromagnetic coupling and $J_2 \sim t^2 J_H/U^2$ for ferromagnetic coupling [203]. Furthermore, the parameters for $3d$ transition metals are estimated to $J_H \sim 1 \text{ eV}$ and $U = 5 - 7 \text{ eV}$ [5], which is the reason why most compounds of localized electrons tend to antiferromagnetism, whereas the ferromagnetic coupling is more likely to occur in metals. It also explains the trend for much higher Néel temperatures for the antiferromagnetism compared to the ferromagnetic transition temperatures. This picture also shows that ferromagnetic order matches well with antiferro-orbital ordering and vice versa.

A special type of exchange is the double exchange [204]. It considers localized electrons in one orbital and itinerant electrons in another orbital. The itinerant electrons minimize their kinetic energy and their mobility stems from the fact that they have been doped into the system, so that their orbitals are almost empty. The localized electrons couple antiferromagnetically to each other. The two species are coupled by Hund's coupling, i.e. ferromagnetic. Thus, the antiferromagnetism of the localized electrons competes with the itinerancy of the other electrons of the other orbital and this is mediated by the Hund's coupling [205]. This competition is described by the Kondo lattice model and realized in, for example, manganites such as $\text{La}_{1-x}\text{Sr}_x\text{MnO}_3$ in which the wide e_g bands become doped and the narrow t_{2g} bands contribute localization and local magnetic moments [206].

4.3.1 Correlations from Hund's coupling

Strong correlations occur not only in Mott insulator, or the proximity to those, but also in so-called Hund's metals [37, 207]. They are embodied by renormalized mass, high-spin

fluctuations and orbital selectivity. Despite the fact that often the bandwidth is significantly larger than the Hund's coupling, the coherence scale of the metal's quasiparticles are strongly reduced. In the extreme case the spins are "frozen" [208] and the corresponding self-energy shows non-Fermi liquid characteristics. The filling of the d -shells has been calculated to be a crucial parameter regarding the correlation effects from Hund's coupling [209]. At half-filling the Mott transition is enhanced by Hund's coupling in the sense that it occurs at smaller interactions U and with increased correlations. Away from half-filling the Mott transition is suppressed and occurs only at larger U . However, at non-half-filling the correlations effects can be enhanced in terms of the quasiparticle weight.

For the atomic t_{2g} states the Coulomb interaction can be written in the Kanamori parametrization [210, 37]

$$H = U \sum_m n_{m\uparrow} n_{m\downarrow} + U' \sum_{n \neq m} n_{m\uparrow} n_{n\downarrow} + (U' - J_H) \sum_{m < m', \sigma} n_{m\sigma} n_{m'\sigma} \quad (4.18)$$

$$- J_H \sum_{m \neq m'} c_{m\uparrow}^\dagger c_{m\downarrow} c_{m'\downarrow}^\dagger c_{m'\uparrow} + J_H \sum_{m \neq m'} c_{m\uparrow}^\dagger c_{m\downarrow}^\dagger c_{m'\downarrow} c_{m'\uparrow} \quad (4.19)$$

with fermionic creation (c^\dagger), annihilation (c) and occupation number (n) operators of spins ($\sigma \in \{\uparrow, \downarrow\}$) and orbitals (m). From rotational invariance follows $U' = U - 2J$. The first three terms are of density-density type. U describes the electronic repulsion within an orbital and U' between different orbitals. U' occurs in the second and third term of Eq. (4.18), whereas the latter is reduced by J_H for the case of ferromagnetic spin alignment between the orbitals. The last two terms of Eq. (4.18) are fluctuation terms with coefficient J_H . The spin-flip fluctuations lowers the energy, assuming positive J_H , and the pair-hopping fluctuations between orbitals raise the energy. This interaction has full charge-spin-orbital symmetry according to $U(1) \otimes SU(2) \otimes SO(3)$.

The orbital selectivity is induced by Hund's coupling gives rise to the orbital selective Mott transition [211, 212]. The orbitals are differentiated and one becomes localized while the other remains itinerant. Whereas orbital fluctuations become decoupled [213], the spin correlations are enhanced in proximity of the orbital selective phase. Finally, the model of Eq. (4.18) is also studied in the context of triplet superconductivity [214].

4.3.2 Competing orders in multiorbital dimers

Clusters, such as dimers, appear in the breaking of translational symmetry which is in the Peierls insulator the case and can be understood by the simple single-particle tightbinding theory. However, another route towards clusterformation has been suggested, which is the stepwise Mott transition which leads to molecules in solids [203]. Candidate materials can be identified by comparing the distances of the transition metal atoms in the compound with those in a pure solid. If the distance of the former is smaller, it indicates a clustering. Example materials for such transitions are $\text{NaTiSi}_2\text{O}_6$ [215] and LiVO_2 [216], for which both cases involve orbital ordering in the cluster formation.

The following study is about low-spin and high-spin configuration of dimer states in lattices of such dimers. In particular the focus lies on the dimer hopping driven transition

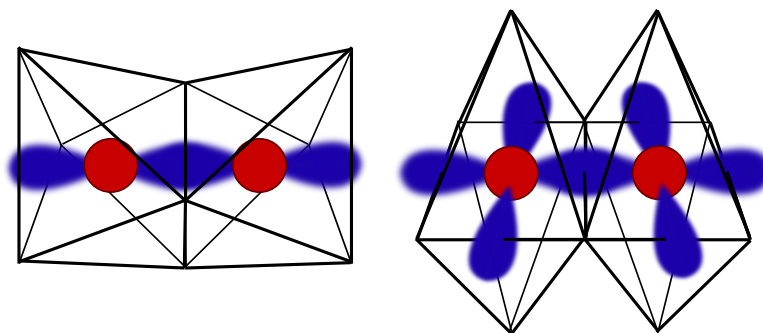


Figure 4.4: Transition metal atoms (red) surrounded by their ligands (corners of the octahedra). Left: Dimer of common-face octahedra with a_{a1} orbital of the transition metal atom (blue). Right: Dimer of common-edge octahedra with d_{xy} orbital of the transition metal atom (blue).

between the spin states, which is tuned using the hopping amplitude of the dimer. In the course of the transition intermediate states are passed through. This is interesting in the context of measurements on $\text{Ba}_5\text{AlIr}_2\text{O}_{11}$, a material with mixed valence iridium in dimer chains which has shown such intermediate spin states [217]. Since in $3d$ transition metals the d -orbitals are relatively localized, the Hund's coupling is strong enough to be treated on an atomic level, i.e. Hund's rules are unlikely to be violated due to dimer formation. In contrast, $4d$ and $5d$ transition metals have more extended d orbitals and the Hund's coupling is relatively weaker, so that competing effects, such as dimer formation, become more pronounced.

A recent reported example is the hexagonal perovskite family of $\text{Ba}_3M\text{Ru}_2\text{O}_9$ where M can be Y, In, Lu and La [218, 219]. The metal is in the configuration of M^{3+} and the Ru has valence IV and V. Ru has octahedral oxygen coordination and two Ru octahedra share a common face, see Fig. 4.4. It is the two facesharing Ru atoms which have been proposed to form a dimer [219]. Such a dimer can depending on the choice of M be in a molecular orbital state ($M=\text{Y, In, Lu}$) or in a double exchange state ($M = \text{La}$). Neutron powder diffraction on $\text{Ba}_3\text{LaRu}_2\text{O}_9$ indicates that the La of the dimers lie closer compared to other choices of M due to their atom's distances to the oxygen ligands. Thus, the bonding energy from the dimer formation is smaller. This is sketched in Fig. 4.5. The additional splitting from the t_{2g} orbitals in to the e_g^π and a_{1g} orbitals originates from the trigonal distortion of the octahedra [220], which is distortion along the axis of the a_{1g} orbital. This distortion can be imagined such that two opposing triangles (which share no common corner) of the octahedra are change in their distance.

If the splitting is small, as proposed for $M = \text{La}$, then Hund's coupling wins the competition and the antibonding $e_g^{\pi*}$ becomes doubly occupied. Both are ferromagnetically coupled to the spin in the e_g^π orbital. In opposite, if the splitting due to the trigonal distortion is large, then the bonding energy is large and molecular orbitals are formed in the e_g^π orbital, which has been proposed for $M = \text{Y, In, Lu}$. Thus, for the latter the mixed valence Ruthenium form spin-1/2 dimers that have antiferromagnetic coupling, albeit with frustration due to the triangular lattice structure. In principle, the molecular orbital formation

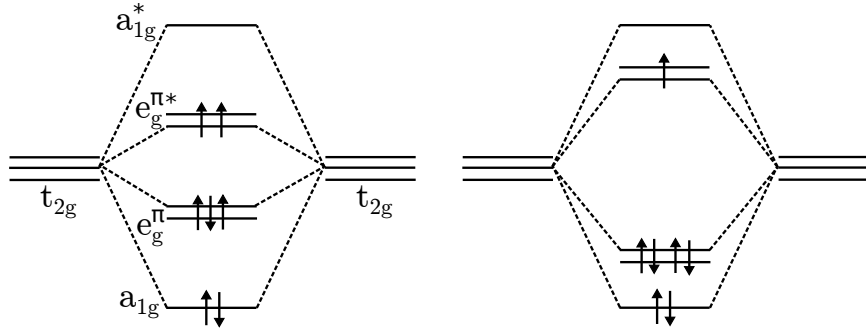


Figure 4.5: Trigonal splitting of octahedrally coordinated transition metals. The t_{2g} orbitals are split into e_g^π and a_{1g} orbitals. Left: The bonding energy of the e_g^π orbitals is small and the Hund's coupling causes ferromagnetic alignment through occupation of the antibonding $e_g^{\pi*}$ orbitals. Right: The bonding energy of the e_g^π orbitals are large and the low-spin molecular orbital state is formed.

can also be realized in compounds with edge sharing octahedra. In that case the additional t_{2g} splitting, e.g., lowers the energy of the d_{xy} orbital, and it raises the energy of d_{yz} and d_{zx} orbitals. However, the distance between the transition metal atoms in the center of the octahedra is larger. Thus, in terms of geometry the face-sharing octahedra promote dimer formation stronger than edge sharing octahedra. Corner-sharing octahedra have the ligands between the transition metal atoms which also maximizes the distance between the transition metal atoms.

The minimal model to study a system, such as it is shown in Fig. 4.5, is by considering a system of two spins (\uparrow, \downarrow), two sites (0, 1) and two orbitals (c, d) with a filling of $3/8$. Regarding the interaction, it is an approximation to neglect spin-orbit coupling, especially for the $4/5d$ compounds and the Kanamori parametrization is chosen according to the rotational invariance of the t_{2g} orbitals. The filling of $3/8$ introduces a dimer occupation describing effectively, e.g., mixed valence Ru. For such a system of a large dimer splitting for the c orbital and a more localized d orbital, the double exchange state has the energy [221]

$$E_{DE} = -t_c - J_H, \quad (4.20)$$

with the large intra-dimer hopping t_c and the Hund's coupling J_H , see also Fig. 1 of the publication below. A simplified calculation using the molecular orbital state

$$|MO\rangle = (c_{\uparrow 0}^\dagger + c_{\uparrow 1}^\dagger)(c_{\downarrow 0}^\dagger + c_{\downarrow 1}^\dagger)/2 \quad (4.21)$$

of a singlet bond with ionic contributions, the energy of the molecular orbital state is estimated as

$$E_{MO} = -2t_c - J_H/2. \quad (4.22)$$

This gives an estimate for the molecular orbital formation of such systems

$$2t_c > J_H. \quad (4.23)$$

In $3d$ transition metals Hund's coupling is about $J_H \sim 0.7 - 0.9 \text{ eV}$, which reduces to $J_H \sim 0.5 \text{ eV}$ in $4/5d$ materials. The (effective) $d - d$ exchange is about $t_c \sim 0.1 - 0.3 \text{ eV}$ [221, 203]. Therefore, according to the estimate above the molecule in solids concept seems more likely to occur in $4/5d$ transition metals. The following publication [222] studies the competition of the molecular orbital and double exchange state in dimers with regard to strong correlation effects.

Electronic correlations and competing orders in multiorbital dimers: A cluster DMFT studyMalte Harland,¹ Alexander I. Poteryaev,² Sergey V. Streltsov,^{2,3} and Alexander I. Lichtenstein^{1,3}¹*Institute of Theoretical Physics, University of Hamburg, Jungiusstraße 9, 20355 Hamburg, Germany*²*Institute of Metal Physics, S. Kovalevskoy 18, 620219 Ekaterinburg GSP-170, Russia*³*Ural Federal University, Mira St. 19, 620002 Ekaterinburg, Russia*

(Received 21 September 2018; revised manuscript received 14 December 2018; published 8 January 2019)

We investigate the violation of the first Hund's rule in $4d$ and $5d$ transition-metal oxides that form solids of dimers. Bonding states within these dimers reduce the magnetization of such materials. We parametrize the dimer formation with realistic hopping parameters and find not only regimes where the system behaves like a Fermi liquid or as a Peierls insulator, but also strongly correlated regions due to Hund's coupling and its competition with the dimer formation. The electronic structure is investigated using the cluster dynamical mean-field theory for a dimer in the two-plane Bethe lattice with two orbitals per site and $3/8$ filling, which is three electrons per dimer. It reveals dimer-antiferromagnetic order of a high-spin (double-exchange) state and a low-spin (molecular-orbital) state. At the crossover region, we observe the suppression of long-range magnetic order, fluctuation enhancement, and renormalization of electron masses. At certain interaction strengths, the system becomes an incoherent antiferromagnetic metal with well-defined local moments.

DOI: [10.1103/PhysRevB.99.045115](https://doi.org/10.1103/PhysRevB.99.045115)**I. INTRODUCTION**

A standard paradigm of strongly correlated materials involves competition between on-site Coulomb repulsion (U), which tends to localize electrons on particular sites, and band effects (characterized, e.g., by the width of a corresponding band, W), making them delocalized [1,2]. In effect, there can be a transition from a homogeneous metallic to a homogeneous insulating state. In real materials, this picture can be enriched by an unusual band topology [3–5], namely spin-orbit coupling [4,6], which is an interplay between different degrees of freedom, such as orbital, charge, spin, etc. [7–9]. However, there can be another option—a system may prefer an inhomogeneous scenario forming metallic clusters within an insulating media (molecules-in-solids conception [10]). The simplest example of such clusters is a dimer. If U is not very large, the wave function is essentially a molecular orbital with an electron delocalized over both sites. But there are also materials with other types of clusters: trimers [11,12], tetramers [13], and even heptamers [14]. The electrons can easily propagate within these clusters, but hoppings between them are suppressed.

There are two main problems in this regard. First of all, there is no general theory, which explains why some of the systems remain homogeneous while others form (spontaneous) clusters. We knew for a long time that such transitions can be induced by Peierls and spin-Peierls effects [15,16], or, more generally, by a charge-density-wave (CDW) instability due to nesting of the Fermi surface [9,17], but a complete understanding of how strong electronic correlations, spin-orbit coupling, and exchange coupling affect this transition is still lacking. Moreover, calculations for real materials show that there is no nesting in many systems, whose properties were supposed to be explained by the formation of a CDW, or that there is nesting at a wrong wave vector [18].

Another problem is a theoretical description of such inhomogeneous systems. While the homogeneous situation with a Mott-Hubbard transition was extensively investigated over the years, the physical properties of clusterized materials remain mostly unexplored. Up to now, most of the efforts were concentrated on a study of the so-called two-plane Hubbard model (known also as the dimer Hubbard model), which is the Hubbard model on the Bethe lattice composed of dimers; see also Sec. II. Most of the attention has been paid to the situation with one orbital per site in a dimer and half-filling [19–22]. This model allows us to describe the transition from a band to a Mott insulator and is particularly relevant for such materials as VO_2 , V_2O_3 , and Ti_2O_3 [23–26]. The two-orbital case has been considered for the one-dimensional chain using the dynamical mean-field theory (DMFT) [27,28]. The orbital-selective behavior has been found for different electron fillings and has been shown to strongly affect the magnetic properties of a system, since some of the electrons occupying bonding orbitals may form spin-singlets. In effect, only part of the electrons contribute to the total magnetic moment. This violates Hund's rules and may dramatically change exchange coupling between neighboring dimers [28]. However, the one-dimensional lattice is not a natural choice for the DMFT because of the small number of nearest neighbors.

Hund's coupling stems from the Coulomb interaction. It represents the intra-atomic exchange, and it has a strong influence on the electronic correlations and therefore also on the Mott transition [29–32]. It can shift the critical interaction value of the Mott transition and also diminish or promote the coherence of Fermi liquids. This depends strongly on the filling [33], i.e., for half-filling the effective Coulomb interaction is increased, and for all other fillings it is decreased. Therefore, Hund's coupling can suppress the Mott transition, but not the correlations. Thus there can be strongly correlated materials that are not close to a Mott transition, but they still

exhibit enhanced electron masses, local moments, and orbital selectivity [34].

In the present paper, the simplest model of multiorbital (two orbitals) dimers on the two-plane Bethe lattice with an odd number of electrons (three) is considered. The parameters of the model are chosen to be close to those specific parameters in real materials based on the late transition-metal ions. We not only find the transition between states with different total spin ($S = 1/2$ to $3/2$) as a function of the hopping in the dimer, but we also observe the suppression of the long-range magnetic ordering by the temperature in the crossover region near this transition. Moreover, surprisingly such a transition can be induced by the hopping in the Bethe lattice. We discuss the electronic and magnetic properties of the considered two-plane Bethe lattice model, and we identify regimes where the system behaves like a Fermi liquid, a Peierls insulator, and a correlated metal. These results not only advance our knowledge of the properties of the two-plane Bethe lattice model, but they can also be useful for the description of dimerized materials, which are presently under close examination.

II. MODEL AND METHOD

While the two-plane Hubbard model seems to be a rather natural choice in the case of VO_2 with a single electron in the $3d$ shell, for a realistic description of materials with a larger number of d electrons one needs to take into account the orbital degeneracy and possible crystal-field splitting. The latter can be due to (i) a nearest-neighbor ligand's environment (below, for the sake of simplicity, we will consider the octahedral case) and (ii) bonding with other transition-metal ions.

The dimerization occurs when two transition-metal ions are able to come close enough to each other to lower the total energy due to the formation of bonding orbitals. This is possible when ligand octahedra share their edges or faces, whereas a common corner geometry prevents dimerization because of a negatively charged ligand sitting in between two transition metals. Edge-sharing structures can be achieved, e.g., in delafossites, spinels, 213 honeycomb iridates (which are very popular at present), and ruthenates. Face-sharing is more common in one-dimensional materials such as 6H-perovskites, ZrI_3 , etc., but there are also three-dimensional corundum-like structures.

It is rather important that in addition to a trivial splitting of the d orbitals onto lower-lying t_{2g} and higher-lying e_g manifolds, there is always an additional splitting in these geometries due to neighboring transition-metal ions. The last can be effectively integrated out. In the edge-sharing octahedra, the t_{2g} orbitals turn out to be split into xy and yz/zx orbitals. The xy orbitals of neighboring metals point to each other. This results in a strong bonding-antibonding splitting, while the xz/yz orbitals may still be considered as site-localized [10]. This is especially important for the $4d$ and $5d$ transition-metal ions, since their wave functions are more spatially extended, and the corresponding bonding-antibonding splitting is much larger than for the $3d$ transition-metal ions. A similar situation occurs for face-sharing octahedra, where the a_{1g} orbitals form a bonding orbital and the e_g^π orbitals remain localized [35,36].

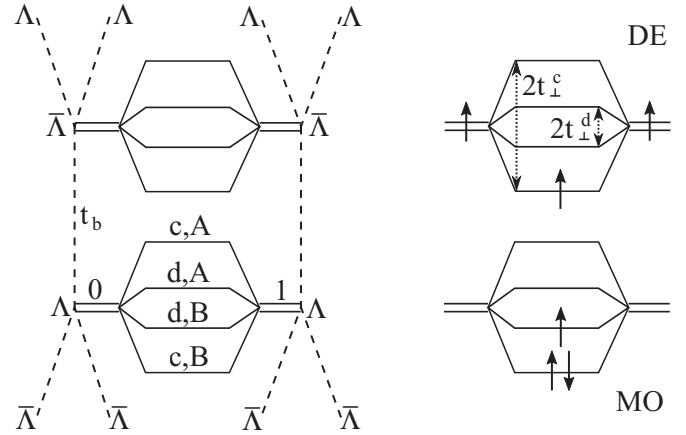


FIG. 1. Left: The two Bethe lattices with hopping t_b are interconnected by dimers of two atomic orbitals (c, d) and two sites (0,1). The Bethe lattice coordination is finite, i.e., $z = 3$, for illustrative purposes. The sites can form bonding (B) and antibonding (A) molecular orbitals. The bipartite Bethe lattice can be divided into sublattices ($\Lambda, \bar{\Lambda}$). Right: Two possible ground-state configurations in the case of $N = 3$ electrons: the molecular-orbital (MO) and the double-exchange (DE) states. Their competition is defined by Hund's exchange coupling J , screened intra- (U) and interorbital (U') Coulomb repulsion, and the dimer hoppings t_\perp^c and t_\perp^d .

Thus, in order to describe dimerized transition-metal compounds with more than one electron, one needs at least two different sets of atomic orbitals, which differ by the value of the hopping parameters. Due to computational limitations, we will restrict ourselves to the minimal model with two orbitals per site. We label the orbital forming the molecular orbital as c and the localized one as d (see Fig. 1). Corresponding intradimer hopping parameters are t_\perp^c and t_\perp^d . A dimer is considered to be a vertex of the Bethe lattice with infinite coordination. For the sake of simplicity, we assume that hoppings along the Bethe lattice, t_b , are the same for both orbitals. Spatial correlations beyond the dimer do not exist because of the infinite coordination.

The Hamiltonian of the model above is

$$\hat{H} = -t_b \sum_{\langle \lambda, \lambda' \rangle} \sum_{\sigma} \hat{c}_{\lambda\sigma}^\dagger \hat{c}_{\lambda'\sigma} + \sum_{\lambda} \hat{H}_{\lambda}^{\text{dimer}}, \quad (1)$$

where \dagger denotes a nearest-neighbor dimer, σ is a spin, $i = \{0, 1\}$ runs over sites within a dimer, and $\alpha = \{c, d\}$ is an orbital index of the t_{2g} orbitals. Therefore, the first term describes a hopping of the electron between dimers with the amplitude t_b , and the second term is responsible for the ‘‘local’’ (intradimer) interaction and can be written as

$$\begin{aligned} \hat{H}_{\lambda}^{\text{dimer}} = & \sum_{\sigma i \alpha} t_{\perp}^{\alpha} \hat{c}_{\lambda\sigma\alpha i}^\dagger \hat{c}_{\lambda\sigma\alpha i} + U \sum_{i \alpha} \hat{n}_{\lambda\uparrow\alpha i} \hat{n}_{\lambda\downarrow\alpha i} \\ & + U' \sum_{\sigma i} \hat{n}_{\lambda\sigma c i} \hat{n}_{\lambda\sigma d i} + (U' - J) \sum_{\sigma i} \hat{n}_{\lambda\sigma c i} \hat{n}_{\lambda\sigma d i} \\ & - J \sum_i (\hat{c}_{\lambda\downarrow c i}^\dagger \hat{c}_{\lambda\uparrow d i}^\dagger \hat{c}_{\lambda\downarrow d i} \hat{c}_{\lambda\uparrow c i} \\ & + \hat{c}_{\lambda\uparrow d i}^\dagger \hat{c}_{\lambda\downarrow d i}^\dagger \hat{c}_{\lambda\uparrow c i} \hat{c}_{\lambda\downarrow c i} + \text{H.c.}). \end{aligned} \quad (2)$$

The orbital differentiation (the first term) is caused by the intradimer hopping parameters, t_{\perp}^{α} , and we do not introduce crystal-field splittings (c - d). The intradimer hopping can also be written in matrix notation,

$$t_{\text{loc}} = \begin{pmatrix} -t_{\perp}^c & 0 \\ 0 & -t_{\perp}^d \end{pmatrix} \otimes \sigma_x, \quad (3)$$

where the Pauli matrix σ_x creates the off-diagonal entries of the site space. The local electron-electron interaction at each site [the last terms in Eq. (2)] is modeled via the Kanamori parametrization [37], where U, U' are intra-/interorbital Coulomb repulsions, and J is Hund's exchange coupling. We choose the interorbital Coulomb interaction by cubic symmetry as $U' = U - 2J$.

The model is solved at finite temperatures exactly using the cluster dynamical mean-field theory (CDMFT) [38–41] with a continuous-time quantum Monte Carlo impurity solver [the continuous-time hybridization expansion solver (CTHYB)] [42–45]. The solver as well as the CDMFT code have been written using the TRIQS library [46].

The dimer's degrees of freedom of our auxiliary impurity model contain two spins, two orbitals, and two sites. The Bethe lattice can be divided into two equivalent sublattices Λ and $\bar{\Lambda}$; see Fig. 1. The CDMFT self-consistency equation describes a particle of Λ fluctuating through its environment $\bar{\Lambda}$. Since we are interested in a solution of a broken spin-symmetry, we apply the antiferromagnetic condition for the construction of the Weiss field,

$$\mathcal{G}_{\sigma}^{-1}(i\omega_n) = (i\omega_n + \mu)\mathbb{1} - t_{\text{loc}} - t_b^2 G_{-\sigma}(i\omega_n), \quad (4)$$

where $\mathbb{1}$ is a unit matrix, $\mathcal{G}(i\omega_n)$ is the Weiss field, and $G(i\omega_n)$ is the local Green's function; the latter two are both matrices in spin, orbital, and site space. Note that the antiferromagnetic order described by Eq. (4) exists between the dimers (dimer antiferromagnetism) and not within them. To find CDMFT solutions of broken spin symmetry, we add a small external magnetic field to the Hamiltonian, which is switched off after a few CDMFT iterations. It is worth mentioning that there are also other interesting solutions, which allow for the coexistence of insulating behavior and ferromagnetism [47], but a study of this part of the phase diagram is beyond the scope of the present paper. We also use a diagonal basis of the site space in the block structure of the Green's function (see below), and thereby solutions of broken site symmetry within dimers are excluded, i.e., charge ordering within the dimers was forbidden by construction.

The local Green's function, which is needed to calculate the chemical potential μ in the CDMFT self-consistency, can be found using the following equation:

$$G_{\sigma}^{-1}(i\omega_n) = (i\omega_n + \mu)\mathbb{1} - t_{\text{loc}} - t_b^2 G_{-\sigma}(i\omega_n) - \Sigma_{\sigma}(i\omega_n). \quad (5)$$

This implicit equation has to be solved iteratively, which begins by setting it equal to the impurity Green's function of the last CDMFT cycle $G(i\omega_n) = g(i\omega_n)$, which is also the self-consistency condition for the CDMFT. The self-energy is calculated via the Dyson equation from the impurity quantities $\Sigma(i\omega_n) = \mathcal{G}^{-1}(i\omega_n) - g^{-1}(i\omega_n)$, and initially it is set to zero.

To make the quantum Monte Carlo impurity solver more efficient, we use a standard unitary transformation on the site space $j \in \{0, 1\}$:

$$\hat{c}_{\sigma ai} = \sum_j R_{ij} \hat{c}_{\sigma aj}, \quad R = \frac{1}{\sqrt{2}} \begin{pmatrix} 1 & 1 \\ 1 & -1 \end{pmatrix}, \quad (6)$$

transforming to the bonding (B)/antibonding (A) basis, labeled by $i \in \{A, B\}$, with corresponding creation/annihilation operators labeled by a tilde. This transformation diagonalizes the local Green's function in site space and thereby also in all single-particle orbitals.

To sum up, even taking into account all constraints and simplifications, there are still five parameters in our model ($U, J, t_{\perp}^c, t_{\perp}^d, t_b$). To reduce this number further, we will restrict ourselves by typical values met in real materials. We choose two groups of compounds with the general formulas $\text{Ba}_3\text{MeTM}_2\text{O}_9$ [48–52] and $\text{Re}_5\text{TM}_2\text{O}_{12}$ [53–55], where Re is a rare-earth ion, TM is a transition-metal ion, and Me is a rare-earth, alkali-, or transition-metal ion. There are dimers formed by two TMO_6 octahedra in these two classes of systems (sharing their faces in $\text{Ba}_3\text{MeTM}_2\text{O}_9$ and edges in $\text{Re}_5\text{TM}_2\text{O}_{12}$).

Typically, TM ions are $4d$ metals such as Ru, Re, Mo, and Os for which Hund's exchange $J \sim 0.7$ eV and Hubbard $U \sim 4.5$ eV (i.e., $U' \sim 3$ eV) [10]. Therefore, we will fix the screened Coulomb interaction and Hund's exchange to the values above. The hopping of the more localized orbital is set to $t_{\perp}^d = 0.2$ eV. The hopping parameters, t_{\perp}^c and t_b , will be varied in what follows. Based on density-functional theory calculations, we also suggest typical values of the hopping parameters in these materials: t_{\perp}^c changes from 0.7 to 1.4 eV, while $t_{\perp}^d \sim 0.2$ eV and $t_b \sim 0.2$ eV. One should also note that the electron filling per dimer will be fixed to the value of $N = 3$, i.e., $3/2$ electrons per site. This is the simplest nontrivial case with odd-number electrons in the two-orbital model (a situation with five electrons, i.e., three holes, is the same in the presence of particle-hole symmetry; one- or seven-electron filling, i.e., one hole, is trivial). Such a filling is not only interesting from the model point of view, but it also reflects the situation realized in many different transition-metal oxides with dimerized crystal structure, such as, e.g., $\text{Ho}_5\text{Mo}_2\text{O}_{12}$ [56], V_4O_7 [57,58], $\text{Nb}_2\text{O}_2\text{F}_3$ [59], and many others. Additionally, we remind the reader that the antiferromagnetic (AFM) and paramagnetic (PM) self-consistency conditions will be used throughout this study.

A. Atomic limit at $T = 0$

We start with a treatment of our model in the atomic limit, where the hopping in the Bethe planes is suppressed, i.e., $t_b = 0$. There are two possible ground states for the isolated dimer with $N = 3$ electrons and two different orbitals c and d . The first state, with one electron residing bonding c and two other electrons occupying d orbitals with the same spin, will be referred to as the double-exchange (DE) configuration, since it maximizes the total spin of the dimer. Another configuration, called the molecular-orbital (MO) state, is a state with a completely filled bonding c orbital and the remaining electron distributed over localized d orbitals (the charge ordering is forbidden by construction; see Sec. II).

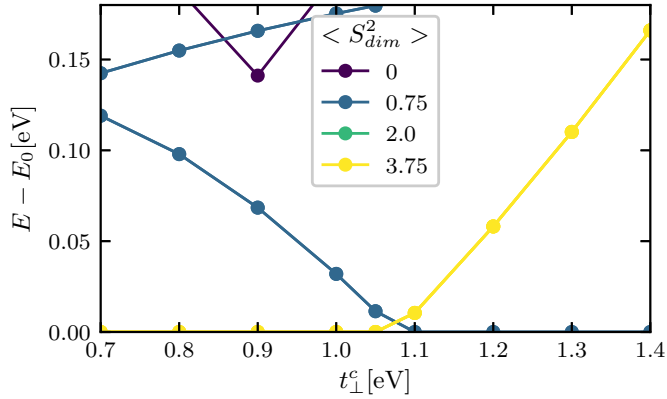


FIG. 2. Spectrum E depending on the dimer-hopping t_{\perp}^c in the atomic limit of an isolated dimer ($T = 0$). States are characterized by $\langle S_{\text{dim}}^2 \rangle$. The ground-state energy E_0 per t_{\perp}^c is subtracted from all energies.

Neglecting quantum fluctuations, one can approximate these states by their largest contribution to the wave function:

$$|\text{MO}\rangle \approx \hat{c}_{\uparrow dB}^{\dagger} \hat{c}_{\uparrow cB}^{\dagger} \hat{c}_{\downarrow cB}^{\dagger} |0\rangle, \quad |\text{DE}\rangle \approx \hat{c}_{\uparrow d0}^{\dagger} \hat{c}_{\uparrow d1}^{\dagger} \hat{c}_{\uparrow cB}^{\dagger} |0\rangle, \quad (7)$$

as illustrated in Fig. 1, which provides an understanding of the spin quantum numbers of the ground state. However, since we use a large U , the ionic and homopolar terms in the MO wave function will have somewhat different weights, and therefore a variational approach [28] would be more reasonable to estimate transition energies. In the case of $T = 0$, we can use the exact diagonalization for a Hilbert space of 256 states. The results are shown in Fig. 2. At a critical $1.05 < \tilde{t}_{\perp}^c < 1.1$ eV, we observe a ground-state crossover from a spin-quadruplet ($\langle S_{\text{dim}}^2 \rangle = 3.75$), which we identify as the DE state, to a spin-doublet ($\langle S_{\text{dim}}^2 \rangle = 0.75$), i.e., the MO state. In the considered range of t_{\perp}^c (0.7–1.4 eV), the spectrum contains only these two states within energies up to ~ 0.1 eV.

B. Noninteracting regime

To identify the effects of the interaction below, we first present the electronic structure in the noninteracting regime in Fig. 3. It is reminiscent of the simplified sketch shown in the right part of Fig. 1. The density of states in this limit is a superposition of four semicirculars with the individual bandwidth $W = 4t_b$. The bands, corresponding to the c (d) orbitals, are centered at energies of $\pm t_{\perp}^c$ ($\pm t_{\perp}^d$) in a site representation (see the upper panel of Fig. 3). A site equivalence leads to an overlay of the densities of state (DOSs) from different sites. Because in our consideration $t_{\perp}^c > t_{\perp}^d$, the c bands are always farther away from the Fermi level than the d bands. One should note that the Fermi level is not at the middle of the d band since we are not at half-filling (which would be for $N = 4$).

The transformation of the noninteracting model to the bonding-antibonding (BA) representation simplifies drastically an examination of the DOS (see the lower panel of Fig. 3). For example, in the site representation, the band of

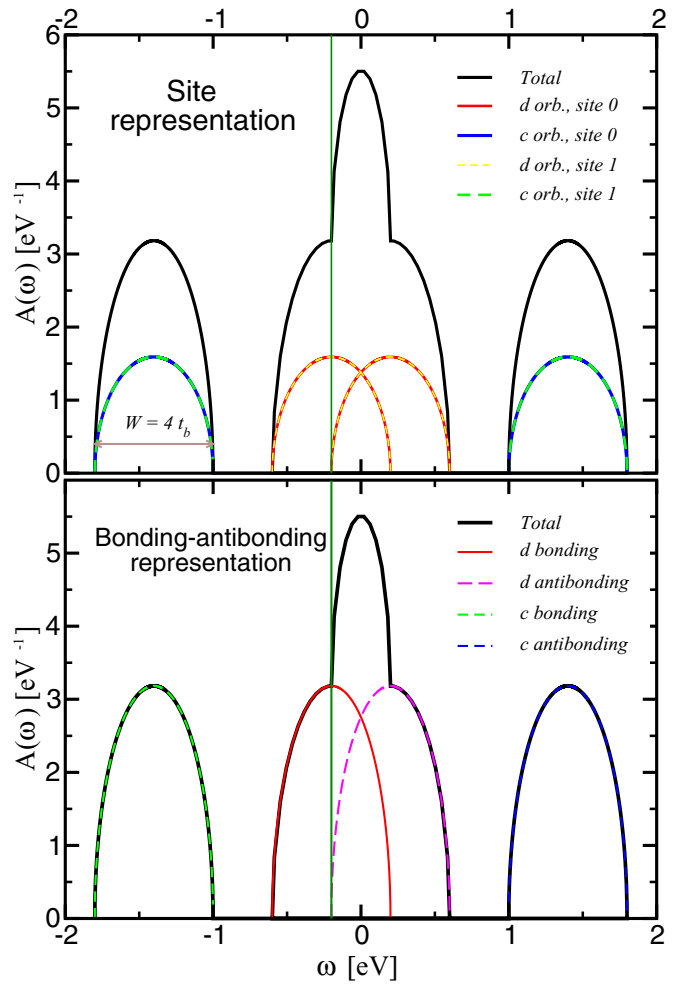


FIG. 3. The density of states in the noninteracting limit (i.e., $U = J = 0$) as a function of intradimer hopping of the c -electrons t_{\perp}^c and excitation energy ω . Hopping within the Bethe plane is chosen to be $t_b = t_{\perp}^d = 0.2$ eV.

c character at site 0 or 1 was located at $-t_{\perp}^c$ and $+t_{\perp}^c$, while after BA transformation there are two bands (instead of two sites) of pure c bonding character at $-t_{\perp}^c$ and c antibonding character at $+t_{\perp}^c$. Thus, in ascending order, one has four bands of pure character: c bonding (c, B), d bonding (d, B), d antibonding (d, A), and c antibonding (c, A). The bonding and antibonding states are separated by $2t_{\perp}^c - 4t_b$ ($2t_{\perp}^d - 4t_b$). If $t_{\perp}^c > t_{\perp}^d + 4t_b$, there is a gap between c (anti)bonding and d (anti)bonding states. Additionally, if $t_{\perp}^d > 2t_b$, there is a small gap between bonding and antibonding states of d character. The formation of these bands can be considered as a local crystal-field effect with the t_{\perp}^c (t_{\perp}^d) playing the role of crystal-field splitting.

Crystal fields are known to compete with Hund's coupling. This leads to a number of very important phenomena, such as, e.g., spin-state transitions [9,29]. Whereas intra-atomic Hund's exchange tends to the uniform orbital occupancy (strictly speaking, this can be achieved only at half-filling), the crystal field promotes orbital polarization when some of the orbitals are less occupied than others [60]. However, the interpretation of the BA splitting as an effective crystal field

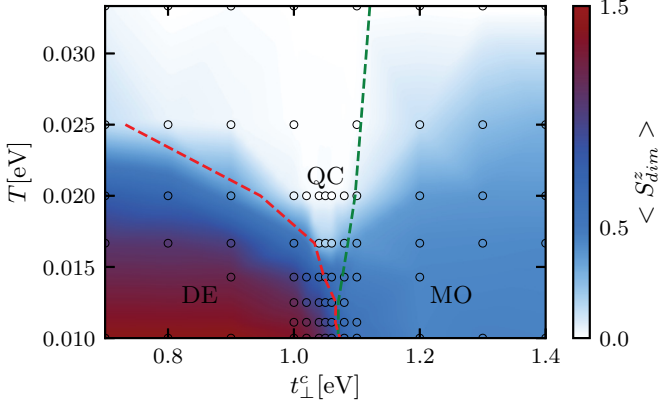


FIG. 4. The magnetic moment of the dimer ($\langle S_{\text{dim}}^z \rangle$) as a function of temperature T and intradimer hopping of the c -orbitals t_{\perp}^c for $t_{\perp}^d = t_b = 0.2$ eV. For certain temperatures, the double-exchange state (DE) and the molecular-orbital state (MO) are separated by a quantum critical region (QC). The red and green dashed lines mark the positions of local minima of the spin and orbital correlations, respectively.

also needs to take into account that the coefficients of the interaction terms also change under the BA transformation. In the next section, we discuss the phase diagram of the two-plane Bethe lattice for an intermediate situation when both intradimer hoppings and interaction (given by U and J) strength are not small.

III. PHASE DIAGRAM

Previous studies of the two-plane Bethe lattice have focused on the single-orbital case. It was found to hold not only the Mott and band insulators, but also a correlated mixed state with coherent and incoherent peaks in the local density of states. Competition between intra- and interplane exchange interactions was shown to affect the formation of the local moments [19,22,26]. We will demonstrate that substantial orbital differentiation due to different interplane hoppings, $t_{\perp}^c \gg t_{\perp}^d$, results not only in a spin-state-like transition, but also in a strong suppression of a long-range magnetic order in the critical region.

Throughout this section, we discuss the results for fixed $t_b = 0.2$ eV. Figure 4 shows the phase diagram of our model obtained by the CDMFT described in Sec. II. There are three main regions. At low temperature and for small t_{\perp}^c we find the DE state with a total spin $S_{\text{dim}}^z = \pm 3/2$ (red part of the phase diagram). All dimers are antiferromagnetically ordered, so that $\langle S_{\text{dim}}^z \rangle \sim 3/2$. This DE state transforms into the MO state with the total spin $S_{\text{dim}}^z = \pm 1/2$ upon increasing intradimer hopping t_{\perp}^c (the light blue part of the phase diagram). This can be considered as a spin-state transition for the cluster. The critical \tilde{t}_{\perp}^c is close to the value obtained in the atomic limit (see Sec. II A). At low temperatures, dimers in the MO phase are antiferromagnetically ordered and $\langle S_{\text{dim}}^z \rangle \sim 1/2$.

Increasing the temperature, we get to the last region with paramagnetic dimers (this phase can again be divided according to $\langle S_{\text{dim}}^z \rangle$ in the DE or MO parts). Interestingly, however, the temperature dependence of $\langle S_{\text{dim}}^z \rangle$ is very different in

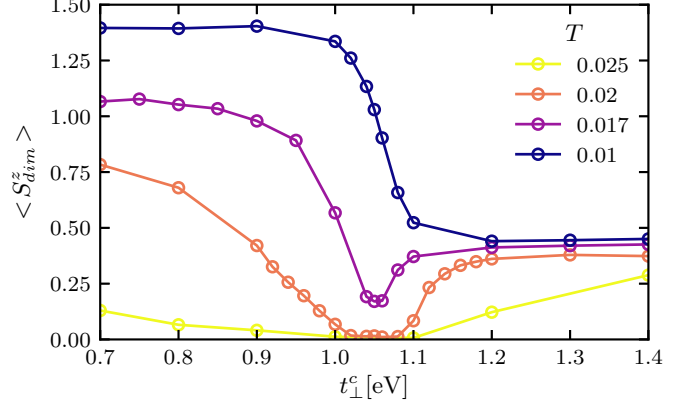


FIG. 5. The magnetic moment of the dimer ($\langle S_{\text{dim}}^z \rangle$) as a function of intradimer hopping of the c -orbitals t_{\perp}^c for $t_{\perp}^d = t_b = 0.2$ eV and temperatures T .

different parts of the phase diagram. We see that the paramagnetic phase appears at much lower temperatures in the critical region of $t_{\perp}^c \sim 1.05$ eV. The DE and MO states have different quantum numbers (different total spins), and thus in the limit of isolated dimers ($t_b = 0$) the transition between them must be discontinuous at $T = 0$. Obviously, no long-range magnetic order is possible in this situation. However, fluctuations can result in a crossover. In this crossover region, the system becomes frustrated and the paramagnetic phase is promoted by the competition of the DE and MO states forming a hybrid state (HYB) with properties that are distinct from both.

In Fig. 5 we present a selection of data of Fig. 4 in order to resolve more detailed properties of the DE/MO transition. In particular, it shows that the order parameter $\langle S_{\text{dim}}^z \rangle$ is smooth along the transition, and since furthermore no coexistence of the two phases is found, it suggests that the lattice exhibits a phase transition of second order at \tilde{t}_{\perp}^c corresponding to the ground-state crossover of the isolated dimer. The integrated occupancies

$$\begin{aligned}
 N_{\sigma} &= \sum_{\alpha \in \{c,d\}} \sum_{i \in \{B,A\}} \tilde{n}_{\sigma\alpha i}, \quad \sigma \in \{\uparrow, \downarrow\}, \\
 N_{\alpha} &= \sum_{\sigma \in \{\uparrow, \downarrow\}} \sum_{i \in \{B,A\}} \tilde{n}_{\sigma\alpha i}, \quad \alpha \in \{c, d\}, \\
 N_i &= \sum_{\sigma \in \{\uparrow, \downarrow\}} \sum_{\alpha \in \{c,d\}} n_{\sigma\alpha i}, \quad i \in \{B, A\},
 \end{aligned} \tag{8}$$

are shown in Fig. 6 (top), confirming our illustration of the DE and MO states (Fig. 1). For low temperatures, fluctuations are suppressed by AFM order and the integrated occupancy has a sharper crossover. In fact the crossover region, in close proximity to its boundaries, shows local minima of the spin and orbital correlations $\langle \delta N_x \delta N_{\bar{x}} \rangle = \langle N_x N_{\bar{x}} \rangle - \langle N_x \rangle \langle N_{\bar{x}} \rangle$ with $x = \uparrow, \downarrow$ and $x = d, c$, respectively. The physical reasoning behind this is that the fluctuations are always very strong in the vicinity of phase transitions. The temperature dependences of the $\langle \delta N_x \delta N_{\bar{x}} \rangle$ minima are shown in Fig. 4 by dashed lines.

The phase diagram shows that both originate from the DE/MO ground-state crossover, but their temperature

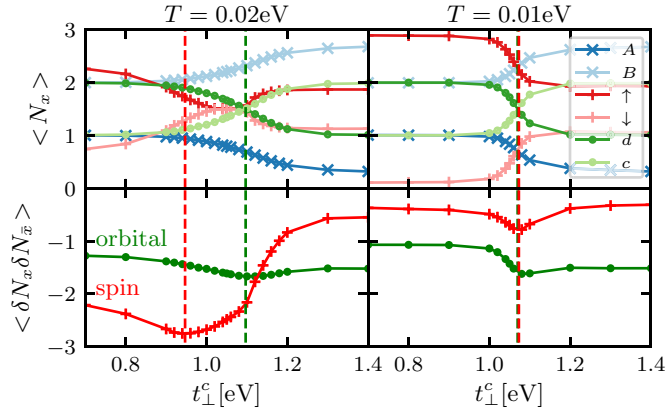


FIG. 6. Occupations (top) and correlations (bottom) of the single-particle orbitals across the t_{\perp}^c driven DE/MO transition at $T = 0.02$ eV (left) and $T = 0.01$ eV (right). N_x is the integrated occupancy. Dashed lines mark the t_{\perp}^c of the correlation's respective local minimum for the spin (red) and orbital (green) correlations.

dependence is very different. The spin correlation minimum is very close to the critical temperature of the DE state for all t_{\perp}^c . The decoupling of spins is much stronger than that of the orbitals, which is rather independent of the temperature. The comparison of the correlations at different temperatures (Fig. 6, left and right) shows that also the magnitude of spin fluctuations of the DE state depends strongly on the temperature whereas the orbital fluctuations do not. The orbital fluctuations are less temperature-dependent because of a rather large U' that suppresses them. In contrast, the main impact of the relatively small J is on the spin fluctuations, and therefore they set in at lower temperatures. A prominent feature of the ground-state crossover is also the inversion of the orbital polarization, which agrees with our estimated critical value of \tilde{t}_{\perp}^c in Sec. II A.

To estimate the evolution of quasiparticles, we use the description of renormalized quasiparticle bands [26]. The quasiparticle residue

$$Z^{-1} = 1 - \left. \frac{\partial \text{Re}\Sigma(\omega)}{\partial \omega} \right|_{\omega=0} \quad (9)$$

renormalizes the noninteracting bandwidth $W = 4t_b$ to

$$W_{\tilde{\epsilon}} = ZW, \quad (10)$$

and thereby the imaginary part of the self-energy $\Sigma(i\omega_n)$ on the Matsubara axis encodes the coherence of the quasiparticles. Additionally, the real part of the self-energy shifts the energies of the quasiparticles,

$$\tilde{\epsilon} = Z[\tilde{t}_{\text{loc}}^c - \mu + \text{Re}\Sigma(\omega = 0)]. \quad (11)$$

One can see in Fig. 7 that far from the critical region ($t_{\perp}^c \ll 1.05$ eV or $t_{\perp}^c \gg 1.05$ eV) both c and d states are (mostly) shifted from the Fermi level (by strong bond-antibonding splitting and by correlation effects). In contrast, three bands appear in the vicinity of the Fermi level close to critical t_{\perp}^c , which favors frustration effects.

In Fig. 4, we use the notion of a quantum critical (QC) region for the low-temperature ($T \sim 0.02$ eV) paramagnetic phase. It is critical in the sense that the scattering rates of all

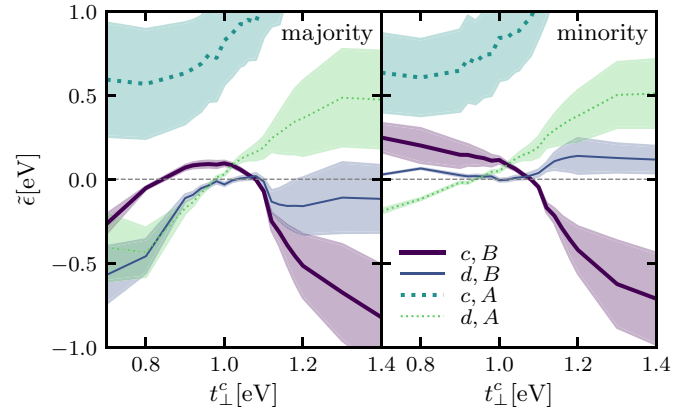


FIG. 7. Renormalized quasiparticle bands of the majority (left) and the minority (right) spin at $T = 0.02$ eV. Bonding (b) and antibonding (a) combinations of the atomic c and d orbitals. The renormalized bandwidths are represented by the colored regions.

quasiparticles in proximity to the Fermi level diverge, i.e., the quasiparticle residue and renormalized bandwidth go to zero. The mechanism behind the formation of the paramagnetic insulator for $1 < t_{\perp}^c \leq 1.1$ eV is the divergence of self-energies in several orbitals. This is distinct from interaction-induced effective field splittings encoded in the real part of the self-energies, and it is reminiscent of the Mott insulator. The QC region is bounded from below. At low temperatures, this criticality is avoided by the quasiparticles as they leave the Fermi level.

It is interesting that different molecular spin-states (such as our DE and MO) have been observed experimentally in dimerized materials mentioned in Sec. II with the general formula $\text{Ba}_3\text{MeTM}_2\text{O}_9$ depending of the choice of Me [48–50,52]. Moreover, some of these materials are characterized by a puzzling suppression of the long-range magnetic order and even a possible realization of the quantum spin-liquid phase due to frustrations [61–63].

IV. LATTICE EFFECT

The Bethe hopping parameter t_b controls the embedding of the correlated dimer into the lattice. The limits of $t_b = 0$ and $t_b \rightarrow \infty$ correspond to isolated dimers and disconnected Bethe lattices, respectively. The situation of $t_b \ll t_{\perp}^c$ corresponds to not yet disconnected dimers, but “uncorrelated” ones with the charge concentrated on the bonds rather than sites. This state corresponds to the uncorrelated Peierls insulator. Apart from that, t_b controls the strength of quantum fluctuations of the bath, because it scales the hybridization for the corresponding Anderson impurity model that CDMFT maps to.

In this section, we pick three values of $t_{\perp}^c = 0.7, 1.05,$ and 1.4 eV as representatives of the DE, HYB, and MO states, respectively, at the temperature of $T = 0.01$ eV, and we vary the Bethe-hopping t_b for each of them. The first part focuses on spin-polarized solutions and the second on paramagnetic ones.

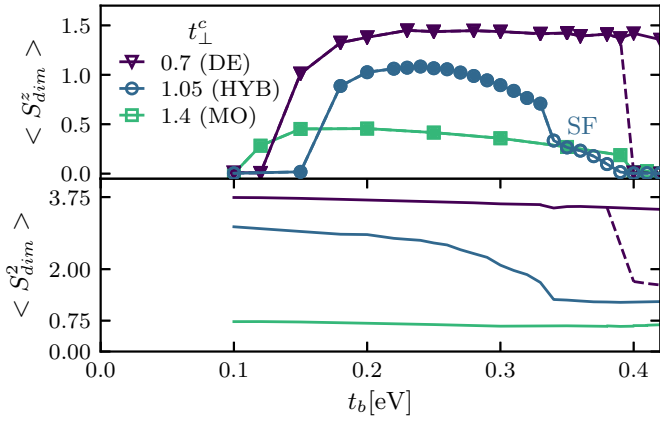


FIG. 8. Top: Dimer magnetization $\langle S_{\text{dim}}^z \rangle$ as a function of the Bethe hopping t_b for the dimer hoppings $t_{\perp}^c = 0.7$ eV (DE), 1.05 eV (HYB), and 1.4 eV (MO) at $T = 0.01$ eV. At the crossover, the spin-freezing (SF) phenomenon exists at certain t_b . Filled and empty markers present insulating and metallic states, respectively. Metallicity is determined by analytical continuation using the maximum-entropy method. Bottom: Squared total spin of the dimer $\langle S_{\text{dim}}^2 \rangle$ as a function of the Bethe hopping t_b for the dimer hoppings $t_{\perp}^c = 0.7$, 1.05, and 1.4 eV at $T = 0.01$ eV.

A. Dimer antiferromagnetism

The upper panel of Fig. 8 shows the dimer magnetization $\langle S_{\text{dim}}^z \rangle$ (for the sake of simplicity, we omit the g factor) at $T = 0.01$ eV as a function of the Bethe hopping parameter t_b in three regimes: the antiferromagnetically ordered DE ($t_{\perp}^c = 0.7$ eV) state, the crossover region ($t_{\perp}^c = 1.05$ eV), and the antiferromagnetically ordered MO ($t_{\perp}^c = 1.4$ eV) phase. One may see from this figure that there is no net magnetization in the limit of very small t_b (< 0.1 eV), which corresponds to nearly isolated dimers as for $t_b = 0.1$ eV the single-particle gap of the d -orbital opens up. In the region of intermediate t_b , both the DE and MO solutions have nearly maximal $\langle S_{\text{dim}}^z \rangle$, 3/2 and 1/2, respectively. It is interesting that the t_b range of the nonzero magnetization is smallest for $t_{\perp}^c = 1.05$ eV corresponding to the HYB state of the crossover region. Here, the fluctuations between the dimers are enhanced by the competing MO and DE states and suppress long-range magnetic order.

It is useful to compare the upper and lower panels of Fig. 8, where the square of the total spin, $\langle S_{\text{dim}}^2 \rangle$, is plotted for the same values of t_{\perp}^c . While $\langle S_{\text{dim}}^z \rangle$ measures ordered spin, $\langle S_{\text{dim}}^2 \rangle$ simply tells us what is the total spin of a configuration. The squares of the total spin [$= S(S + 1)$] for the DE and MO states in the atomic limit and at $T = 0$ are 3.75 and 0.75. Comparing Fig. 8 (top) and Fig. 8 (bottom), we first make sure that two transitions for the MO solution at $t_b = 0.1$ eV and 0.4 are due to a transition to the paramagnetic state, and the total spin per dimer is still well defined even for $t_b < 0.1$ eV and $t_b > 0.4$ eV. $\langle S_{\text{dim}}^2 \rangle$ for both the MO and DE solutions depend on t_b only weakly. Thus, the formation of spin order is not due to local moment formation, but rather to suppression of the fluctuations.

Second, we see from Fig. 8 that an increase of t_b suppresses the DE state and increases the MO contribution in the crossover region (i.e., for $t_{\perp}^c = 1.05$ eV). Using corresponding

values of $\langle S_{\text{dim}}^2 \rangle$ for these two states, one may estimate their contributions to the wave function for arbitrary t_b . If for $t_b = 0.1$ eV there is roughly a 50/50 ratio between the weights of the DE and MO states, then for $t_b = 0.35$ we have $\sim 90\%$ of the MO and only 10% of the DE state. This can be rationalized by treating it with a correction to the total energy of both states due to hopping within the Bethe lattice, i.e., t_b , using the perturbation theory.

We assume that the intradimer hopping t_{\perp}^c , Hubbard U , and Hund's exchange J are leading parameters. Then the second-order correction to the total energy due to t_b would be $\sim -t_b^2/\delta\varepsilon$, where $\delta\varepsilon$ is the energy difference between excited and ground states. Clearly, the excited energy for the MO state will be much smaller than for the DE configuration, since the transfer of the d electrons between two antiferromagnetically coupled dimers in the MO state does not cost Hund's exchange energy [there are two electrons with opposite spin projections on the bonding c orbitals in the MO state, and when transferring d electrons between dimers we keep the number of electrons (per site) with the same spin]. Neglecting spin-flip and pair-hopping terms for the sake of simplicity, we get $\delta\varepsilon_{\text{MO}} \sim U/2$. The transfer of the c electrons in the MO configuration is rather unfavorable, since it is possible only to antibonding orbitals. In contrast, one may transfer the c electrons in the DE state, which gives $\delta\varepsilon_{\text{DE}} \sim U/2 + J$, while an electron hopping via d orbitals results in $\delta\varepsilon_{\text{DE}} \sim U + J/2$ —both much larger than the energy of the excited state in the MO configuration. This explains the gradual increase of the MO weight and the decrease of $\langle S_{\text{dim}}^z \rangle$ in the crossover region with increasing t_b .

Third, there is a rather nontrivial evolution of both $\langle S_{\text{dim}}^z \rangle$ and $\langle S_{\text{dim}}^2 \rangle$ with t_b for $t_{\perp}^c = 0.7$ eV (i.e., nominally for the DE solution). In particular, for large t_b (≥ 0.4 eV) we observe the coexistence of two regimes: a conventional insulating DE solution with long-range magnetic ordering and $\langle S_{\text{dim}}^z \rangle = 3/2$, and a metallic and paramagnetic solution with suppressed $\langle S_{\text{dim}}^z \rangle \approx 2$. The value of $\langle S_{\text{dim}}^2 \rangle$ for the second solution is close to what one may expect for the spin triplet.

Figure 9 shows the local density of states in the crossover region with an increase of t_b . One can see that for $t_b =$

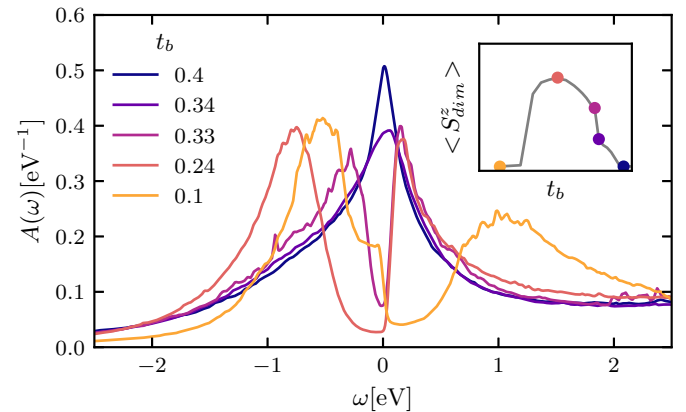


FIG. 9. The dimer density of states for different Bethe hoppings t_b at $T = 0.01$ and $t_{\perp}^c = 1.05$ obtained via the stochastic optimization method [64,65]. Inset: the corresponding dimer magnetizations $\langle S_{\text{dim}}^z \rangle$.

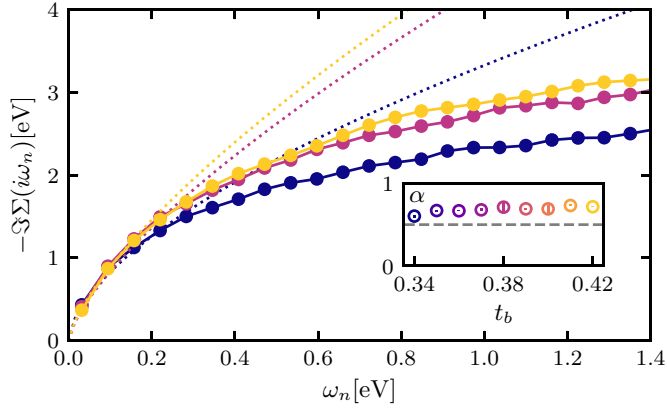


FIG. 10. Imaginary part of the self-energy (solid) on Matsubara frequencies together with a power-law low-frequency fit (dotted) for different t_b , $t_{\perp}^c = 1.05$ eV and $T = 0.01$ eV. The fitted power is shown in the inset.

0.4 eV our system is in a metallic state, characterized by a large quasiparticle peak. Reducing t_b , we arrive at the broken spin-symmetry situation, where the peak becomes less coherent (the width at half-maximum height decreases), and then eventually we observe the formation of a pseudogap for $t_b = 0.33$ eV, which corresponds to a sudden increase in the magnetization. The maximum of $\langle S_{\text{dim}}^z \rangle$ is exceeded at $t_b \approx 0.24$ eV, where the pseudogap transforms to a real gap. A further decrease of t_b results in a transition to the paramagnetic state, which is accompanied by a modification of the spectral function. In particular, for $t_b = 0.24$ eV there is a sharp edge for electron excitations, while for $t_b = 0.1$ eV we have a sharp edge for hole excitations.

In Fig. 10 we focus on the incoherent metal with local moments of $0.33 < t_b < 0.4$ eV, and we identify the underlying mechanism of spin-freezing, which has been found in a previous single-site DMFT multiorbital study [66–68] and is a property of Hund’s metals. It is a non-Fermi-liquid described by the constant spin-spin correlation function at long times and a strong enhancement of the local susceptibility [69]. It has been pointed out that the ground-state degeneracy seems to be an important component of spin-freezing. We can confirm that as our model shows the feature only in proximity to the ground-state crossover. The self-energy of that phase is non-Fermi-liquid-like, but still the system is metallic in the freezing process. Since electrons scatter at the frozen moments, the self-energy shows power-law behavior $\Sigma(i\omega_n \rightarrow 0) = (i\omega_n)^\alpha$ with $\alpha < 1$ and can be fit with a quantum critical crossover function,

$$-\text{Im}\Sigma(\omega_n)/t = C + A(\omega_n/t)^\alpha. \quad (12)$$

A minimal exponent of $\alpha = 0.5$ was found at the critical point in the original study [66]. At the magnetization jump, i.e., $t_b = 0.34$ eV, we also find a drop in α leading to a value $\alpha \approx 0.5$. The crossover region we found is very similar to that of studies that investigated a high-spin/low-spin transition driven by a crystal field [70]. In that context, one can also expect to find an instability toward spin-orbital ordering, i.e., an excitonic insulator [71]. The latter is suppressed as we do not consider interorbital hybridization in our numerical calculations.

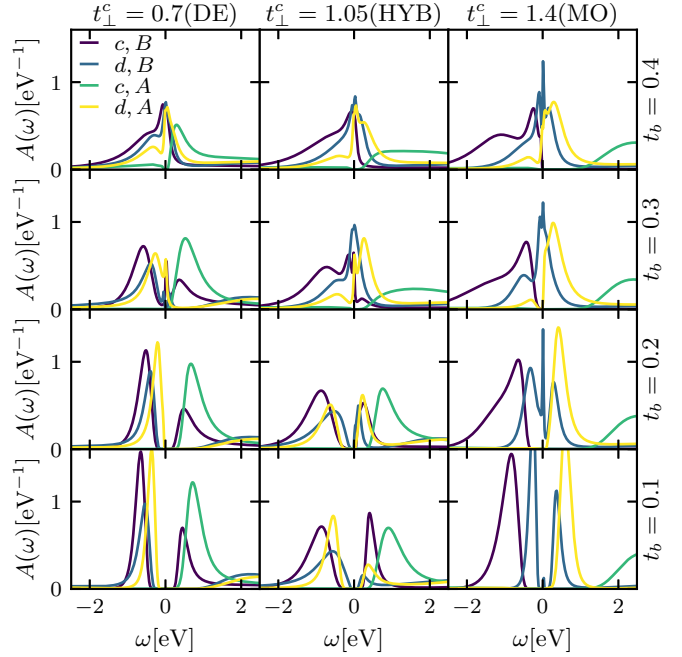


FIG. 11. Partial DOSes in BA representation as a function of intradimer hopping, t_{\perp}^c , and Bethe hopping, t_b , parameters (rows and columns, respectively). The fixed parameters are: $U = 4.5$ eV, $J = 0.7$ eV, $t_{\perp}^d = 0.2$ eV, $T = 0.01$ eV and paramagnetism is enforced. Obtained by the Maximum Entropy method.

B. Spectral properties

Even though a paramagnetic solution may only be metastable, one can enforce it to enhance scattering processes and thereby also amplify the electronic correlations. Thus, the paramagnetic solution is a tool to investigate ordering mechanisms and quasiparticles, whose diverging scattering rates eventually lead to a symmetry-broken solution.

Figure 11 presents partial DOSs in the BA representation for various values of the intradimer hopping of the c electrons, t_{\perp}^c , and the Bethe hopping, t_b , which controls the bandwidth of noninteracting states. The most comprehensible is the MO state with $t_{\perp}^c = 1.4$ eV and $t_b = 0.1$ eV (the lower-right part of Fig. 11). At these values of parameters, the bonding and antibonding c orbitals are almost completely occupied ($n_{(c,B)} = 1.78$) and empty ($n_{(c,A)} = 0.2$), respectively, and can be integrated out. Therefore, one deals with a single electron in the double-band model with crystal-field splitting defined by $2t_{\perp}^d = 0.4$ eV [72]. Such a large value of the crystal-field splitting in comparison to the bandwidth, $W = 4t_b = 0.4$ eV, results in a further lifting of the degeneracy, and finally one has a conventional Mott-Hubbard single-band insulator, which occurs for the (d, B) orbital. By increasing t_b (from bottom to top, right column of Fig. 11), this insulating state is determined to be a single-band metal at $t_b = 0.2$ eV and a three-band metal at $t_b = 0.4$ eV. The latter happens due to such factors as the bandwidth increase of (c, B) and (d, A) states and its touching of the Fermi level (see the lower panel of Fig. 12). One should note that the (c, A) state remains empty at all values of the Bethe hopping. This picture of the insulator-to-metal transition is confirmed by the renormalized quasiparticle bands, $(\tilde{\epsilon}, W_{\tilde{\epsilon}})$, and the quasiparticle residue

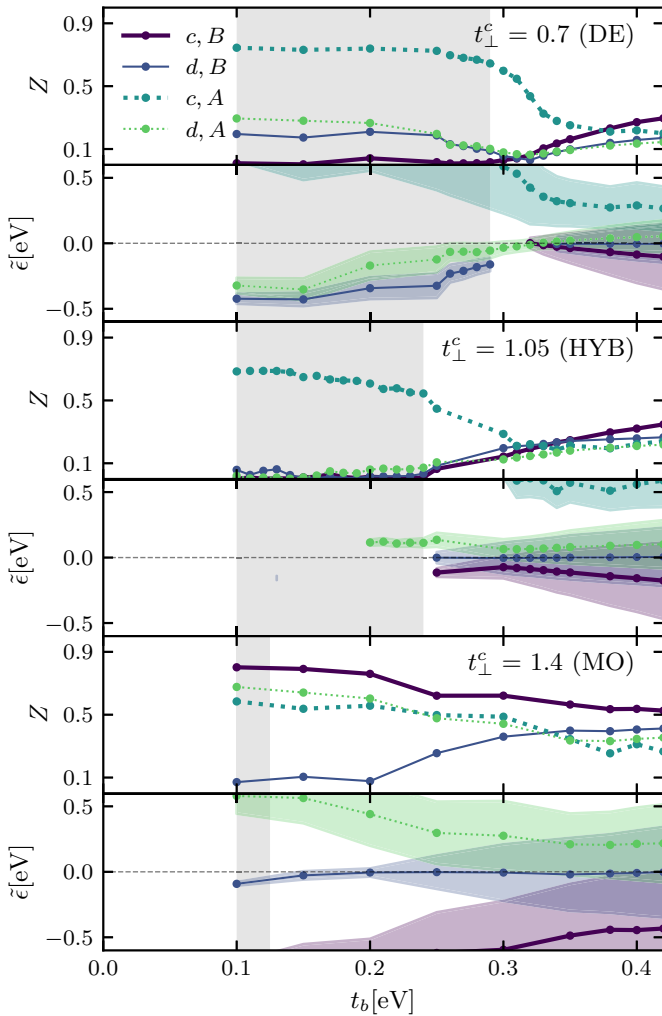


FIG. 12. Quasiparticle residues Z and renormalized quasiparticle bands ($\tilde{\epsilon}$, $W_{\tilde{\epsilon}}$) as a function of the Bethe hopping t_b . The renormalized quasiparticle bands vanish if $Z \approx 0$. The shaded area depicts insulating phases determined by analytical continuation (maximum entropy method). Paramagnetism is enforced, $T = 0.01$.

Z , shown in Fig. 12 (lower panel). The energetic order of the bands is determined by t_{loc} , i.e., bonding orbitals are lower than antibonding orbitals, and the c orbital is lower than the d orbital. At small values of t_b , all renormalized bands except (d, B) are placed far from the Fermi level. The corresponding quasiparticle residue, $Z_{(d,B)}$, is close to zero. At $t_b > 0.2$ eV, $Z_{(d,B)}$ is increased and the system becomes a correlated metal.

The spectral function of the DE state (lower-left part of Fig. 11) is also consistent with the atomic picture. The (d, B) and (d, A) states are occupied with one electron per spin orbital, $n_{(d,B)} = n_{(d,A)} = 1$, which is equivalent to a single-electron occupation of site-centered orbitals. The remaining electron is on the (c, B) state (the antibonding part is completely empty). The Coulomb interaction leads to a gap opening for these states in different ways. Although the QP bands for all these orbitals are away from the Fermi level (see the upper panel of Fig. 12), the quasiparticle residues behave differently for (c, B) and (d, B) , (d, A) states. $Z_{(c,B)}$ goes to zero at small values of t_b , while for larger t_b they have finite

values. This results in the orbital selective Mott transition at increased values of $t_b = 0.3$ eV. A further increase of t_b closes the gap in the (c, B) spectral function. One should note that the overall quasiparticle residues of the DE solution are smaller than its MO counterparts, indicating stronger electronic correlations in this regime.

The hybrid state, $t_{\perp}^c = 1.05$ eV, has an even stronger quasiparticle renormalization than the DE state for all orbitals. The (c, B) , (d, B) , and (d, A) quasiparticle residues go to zero approximately at $t_b = 0.25$ eV. This is related to the quantum critical region, which we have discussed in the context of Fig. 4. It results in the metal-to-insulator transition and gap opening in the corresponding spectral functions; see Fig. 11.

It is interesting to note that a critical value of the Bethe hopping, t_b^* , decreases with the increase of the intradimer hopping parameter t_{\perp}^c . In the MO case, there is only one active electron, which leads to an increased value of the critical Coulomb interaction for the multiband model [31], which also corresponds to a decreased value of t_b . With the decrease of the intradimer hopping, t_{\perp}^c , all of the electrons have to be regarded for a description of the model. Therefore, the effective number of electrons is increased, which results in a decreased value of the Coulomb interaction parameter, or an increased value of the critical Bethe lattice hopping, t_b .

V. CONCLUSIONS

The electronic and magnetic properties of multiorbital dimers in solids have been studied using a cluster extension of the DMFT. We used the model consisting of two orbitals per site constituting a dimer with specific filling of $3/8$ electrons per site (three per dimer). The parameter range of the model was motivated by the density-functional calculations for two large classes of materials with the general formula $\text{Ba}_3\text{MeTM}_2\text{O}_9$ (face sharing of TMO_6 octahedra) and $\text{Re}_5\text{TM}_2\text{O}_{12}$ (edge sharing of TMO_6 octahedra). We argue that already such a minimal model can be used to describe various physical phenomena observed in real materials with dimerized crystal structure. For example, the ratio of hopping parameters of strongly overlapping orbitals (t_{\perp}^c) and Hund's rule exchange (J_H) may strongly affect the value of the observed magnetic moments. These effects were indeed observed in $\text{Ba}_3\text{MeTM}_2\text{O}_9$ (through modification of the hopping parameters by lattice distortions induced by different Me ions) [52,73].

In our simplistic two-orbital model, \tilde{t}_{\perp}^c defines a critical hopping parameter, which separates the regions where the high-spin, $S = 3/2$, or low-spin, $S = 1/2$, states are realized. Close to this critical parameter, the lattice of such dimers is in a strongly correlated state, where the long-range antiferromagnetic order is substantially suppressed. This fact can be important in connection with recent findings on the formation of the spin liquid state in $\text{Ba}_3\text{ZnRu}_2\text{O}_9$ [61,63] and $\text{Ba}_3\text{ZnIr}_2\text{O}_9$ [74]. This correlated state exhibits electrons with strongly renormalized masses in both orbitals (c and d) and separates orbital decoupling from spin decoupling. Both decouplings originate from the dimer-ground-state crossover of \tilde{t}_{\perp}^c . Furthermore, the long-range spin order is more sensitive to temperature fluctuations than orbital order, and that renders the MO state more stable against temperature fluctuations.

Correlation effects could be induced by the change of the electron's itineracy within the Bethe planes (t_b) as it promotes quantum fluctuations from the lattice on the dimers. We explain the larger stability of the AFM order in the MO configuration with the exchange energy $t_b^2/(U/2)$ of the d electrons as opposed to the exchange energy of the DE state, i.e., $t_b^2/(U/2 + J)$ for the c electrons. The competition of the DE and MO states causes the formation of a new hybrid state, which exhibits qualitatively new features, e.g., an incoherent metallic spin-polarized state with a non-Fermi-liquid self-energy corresponding to the spin-freezing phenomenon.

We used the cluster DMFT to study the correlation-enhanced enforced paramagnetic calculations that unveiled the orbital selectiveness of the DE state—typical for Hund's physics. The MO state shows correlation features, but the metal-to-insulator transition is of Peierls-type instead. Finally, the hybrid state has a metal-insulator transition involving the renormalization of all d and the bonding c states around

the same value of the Bethe lattice hopping, emphasizing the large impact of competing interactions on the electronic correlations.

ACKNOWLEDGMENTS

M.H. and A.L. gratefully acknowledge financial support by the Deutsche Forschungsgemeinschaft (DFG) in the framework of the SFB 925. The work of S.V.S. and A.I.P. was supported by the Russian president science council via MD 916.2017.2 program, by the Russian ministry of science and high education via the theme "spin" AAAA-A18-118020290104-2, "electron" AAAA-A18-118020190098-5, and Contract No. 02.A03.21.0006, and by the Ural Branch of Russian Academy of Science (18-10-2-37). The computations were performed with resources provided by the North-German Supercomputing Alliance (HLRN).

-
- [1] N. F. Mott, *Proc. Phys. Soc., Sect. A* **62**, 416 (1949).
 [2] M. Imada, A. Fujimori, and Y. Tokura, *Rev. Mod. Phys.* **70**, 1039 (1998).
 [3] D. Pesin and L. Balents, *Nat. Phys.* **6**, 376 (2010).
 [4] W. Witczak-Krempa, G. Chen, Y. B. Kim, and L. Balents, *Annu. Rev. Condens. Matter Phys.* **5**, 57 (2014).
 [5] S. Streltsov, I. I. Mazin, and K. Foyevtsova, *Phys. Rev. B* **92**, 134408 (2015).
 [6] B. J. Kim, H. Jin, S. J. Moon, J.-Y. Kim, B.-G. Park, C. S. Leem, J. Yu, T. W. Noh, C. Kim, S.-J. Oh, J.-H. Park, V. Durairaj, G. Cao, and E. Rotenberg, *Phys. Rev. Lett.* **101**, 076402 (2008).
 [7] K. I. Kugel and D. I. Khomskii, *Phys. Usp.* **25**, 231 (1982).
 [8] Y. Tokura and N. Nagaosa, *Science* **288**, 462 (2000).
 [9] D. I. Khomskii, *Transition Metal Compounds* (Cambridge University Press, Cambridge, 2014).
 [10] S. V. Streltsov and D. I. Khomskii, *Phys. Usp.* **60**, 1121 (2017).
 [11] T. Takayama, A. Yaresko, A. Matsumoto, K. Ishii, M. Yoshida, J. Mizuki, and H. Takagi, *Sci. Rep.* **4**, 6818 (2014).
 [12] J. P. Sheckelton, K. W. Plumb, B. A. Trump, C. L. Broholm, and T. M. McQueen, *Inorg. Chem. Front.* **4**, 481 (2017).
 [13] P. G. Radaelli, Y. Horibe, M. J. Gutmann, H. Ishibashi, C. H. Chen, R. M. Ibberson, Y. Koyama, Y.-S. Hor, V. Kiryukhin, and S.-W. Cheong, *Nature (London)* **416**, 155 (2002).
 [14] Y. Horibe, M. Shingu, K. Kurushima, H. Ishibashi, N. Ikeda, K. Kato, Y. Motome, N. Furukawa, S. Mori, and T. Katsufuji, *Phys. Rev. Lett.* **96**, 086406 (2006).
 [15] L. N. Bulaevskii, *Phys. Usp.* **18**, 131 (1975).
 [16] S. Kagoshima, *Jpn. J. Appl. Phys.* **20**, 1617 (1981).
 [17] C.-W. Chen, J. Choe, and E. Morosan, *Rep. Prog. Phys.* **79**, 084505 (2016).
 [18] M. D. Johannes and I. I. Mazin, *Phys. Rev. B* **77**, 165135 (2008).
 [19] G. Moeller, V. Dobrosavljević, and A. E. Ruckenstein, *Phys. Rev. B* **59**, 6846 (1999).
 [20] A. Fuhrmann, D. Heilmann, and H. Monien, *Phys. Rev. B* **73**, 245118 (2006).
 [21] S. S. Kancharla and S. Okamoto, *Phys. Rev. B* **75**, 193103 (2007).
 [22] H. Hafermann, M. I. Katsnelson, and A. I. Lichtenstein, *Europhys. Lett.* **85**, 37006 (2009).
 [23] A. I. Poteryaev, A. I. Lichtenstein, and G. Kotliar, *Phys. Rev. Lett.* **93**, 086401 (2004).
 [24] S. Biermann, A. Poteryaev, A. I. Lichtenstein, and A. Georges, *Phys. Rev. Lett.* **94**, 026404 (2005).
 [25] O. Nájera, M. Civelli, V. Dobrosavljević, and M. J. Rozenberg, *Phys. Rev. B* **95**, 035113 (2017).
 [26] O. Nájera, M. Civelli, V. Dobrosavljević, and M. J. Rozenberg, *Phys. Rev. B* **97**, 045108 (2018).
 [27] S. V. Streltsov and D. I. Khomskii, *Phys. Rev. B* **89**, 161112 (2014).
 [28] S. V. Streltsov and D. I. Khomskii, *Proc. Natl. Acad. Sci. (USA)* **113**, 10491 (2016).
 [29] P. Werner and A. J. Millis, *Phys. Rev. Lett.* **99**, 126405 (2007).
 [30] P. Werner, E. Gull, and A. J. Millis, *Phys. Rev. B* **79**, 115119 (2009).
 [31] A. Georges, L. de' Medici, and J. Mravlje, *Annu. Rev. Condens. Matter Phys.* **4**, 137 (2013).
 [32] L. de' Medici, *Phys. Rev. B* **83**, 205112 (2011).
 [33] L. de' Medici, J. Mravlje, and A. Georges, *Phys. Rev. Lett.* **107**, 256401 (2011).
 [34] *The Physics of Correlated Insulators, Metals, and Superconductors*, edited by E. Pavarini, E. Koch, R. Scalettar, and R. Martin, Schriften des Forschungszentrums Jülich Reihe Modeling and Simulation Vol. 7 (Forschungszentrum Jülich GmbH Zentralbibliothek, Verlag, Jülich, 2017).
 [35] K. I. Kugel, D. I. Khomskii, A. O. Sboychakov, and S. V. Streltsov, *Phys. Rev. B* **91**, 155125 (2015).
 [36] D. I. Khomskii, K. I. Kugel, A. O. Sboychakov, and S. V. Streltsov, *J. Exp. Theor. Phys.* **122**, 484 (2016).
 [37] J. Kanamori, *Prog. Theor. Phys.* **30**, 275 (1963).
 [38] A. Georges, G. Kotliar, W. Krauth, and M. J. Rozenberg, *Rev. Mod. Phys.* **68**, 13 (1996).
 [39] G. Kotliar and D. Vollhardt, *Phys. Today* **57**(3), 53 (2004).
 [40] T. Maier, M. Jarrell, T. Pruschke, and M. H. Hettler, *Rev. Mod. Phys.* **77**, 1027 (2005).

- [41] G. Kotliar, S. Y. Savrasov, K. Haule, V. S. Oudovenko, O. Parcollet, and C. A. Marianetti, *Rev. Mod. Phys.* **78**, 865 (2006).
- [42] P. Werner and A. J. Millis, *Phys. Rev. B* **74**, 155107 (2006).
- [43] E. Gull, A. J. Millis, A. I. Lichtenstein, A. N. Rubtsov, M. Troyer, and P. Werner, *Rev. Mod. Phys.* **83**, 349 (2011).
- [44] L. Boehnke, H. Hafermann, M. Ferrero, F. Lechermann, and O. Parcollet, *Phys. Rev. B* **84**, 075145 (2011).
- [45] P. Seth, I. Krivenko, M. Ferrero, and O. Parcollet, *Comput. Phys. Commun.* **200**, 274 (2016).
- [46] O. Parcollet, M. Ferrero, T. Ayril, H. Hafermann, I. Krivenko, L. Messio, and P. Seth, *Comput. Phys. Commun.* **196**, 398 (2015).
- [47] S. Nishimoto and Y. Ohta, *Phys. Rev. Lett.* **109**, 076401 (2012).
- [48] S. A. J. Kimber, M. S. Senn, S. Fratini, H. Wu, A. H. Hill, P. Manuel, J. P. Attfield, D. N. Argyriou, and P. F. Henry, *Phys. Rev. Lett.* **108**, 217205 (2012).
- [49] M. S. Senn, S. A. J. Kimber, A. M. Arevalo Lopez, A. H. Hill, and J. P. Attfield, *Phys. Rev. B* **87**, 134402 (2013).
- [50] S. K. Panda, S. Bhowal, Y. Li, S. Ganguly, R. Valentí, L. Nordström, and I. Dasgupta, *Phys. Rev. B* **92**, 180403 (2015).
- [51] H. L. Feng and M. Jansen, *J. Solid State Chem.* **258**, 776 (2017).
- [52] D. Ziat, A. A. Aczel, R. Sinclair, Q. Chen, H. D. Zhou, T. J. Williams, M. B. Stone, A. Verrier, and J. A. Quilliam, *Phys. Rev. B* **95**, 184424 (2017).
- [53] C. Torardi, C. Fecketter, W. McCarroll, and F. DiSalvo, *J. Solid State Chem.* **60**, 332 (1985).
- [54] W. Jeitschko, D. H. Heumannska, M. S. Schriewer-pottgen, and U. C. Rodewald, *J. Solid State Chem.* **228**, 218 (1999).
- [55] L. Chi, J. F. Britten, and J. E. Greedan, *J. Solid State Chem.* **172**, 451 (2003).
- [56] A. J. Cortese, D. Abeyasinghe, B. Wilkins, M. D. Smith, and G. Morrison, *Inorg. Chem.* **54**, 11875 (2015).
- [57] A. Gossard, J. Remeika, T. Rice, H. Yasuoka, K. Kosuge, and S. Kachi, *Phys. Rev. B* **9**, 1230 (1974).
- [58] A. Heidemann, K. Kosuge, and S. Kachi, *Phys. Status Solidi A* **35**, 481 (1976).
- [59] T. T. Tran, M. Gooch, B. Lorenz, A. P. Litvinchuk, M. G. Sorolla, J. Brgoch, P. C. W. Chu, and A. M. Guloy, *J. Am. Chem. Soc.* **137**, 636 (2014).
- [60] F. Lechermann, S. Biermann, and A. Georges, *Prog. Theor. Phys. Suppl.* **160**, 233 (2005).
- [61] I. Terasaki, T. Igarashi, T. Nagai, K. Tanabe, H. Taniguchi, T. Matsushita, N. Wada, A. Takata, T. Kida, M. Hagiwara, K. Kobayashi, H. Sagayama, R. Kumai, H. Nakao, and Y. Murakami, *J. Phys. Soc. Jpn.* **86**, 033702 (2017).
- [62] J. T. Rijssenbeek, P. Matl, B. Batlogg, N. P. Ong, and R. J. Cava, *Phys. Rev. B* **58**, 10315 (1998).
- [63] T. D. Yamamoto, H. Taniguchi, and I. Terasaki, *J. Phys.: Condens. Matter* **30**, 355801 (2018).
- [64] I. Krivenko and M. Harland, [arXiv:1808.00603](https://arxiv.org/abs/1808.00603) [physics.comp-ph].
- [65] O. Goulko, A. S. Mishchenko, L. Pollet, N. Prokof'ev, and B. Svistunov, *Phys. Rev. B* **95**, 014102 (2017).
- [66] P. Werner, E. Gull, M. Troyer, and A. J. Millis, *Phys. Rev. Lett.* **101**, 166405 (2008).
- [67] K. M. Stadler, Z. P. Yin, J. von Delft, G. Kotliar, and A. Weichselbaum, *Phys. Rev. Lett.* **115**, 136401 (2015).
- [68] K. M. Stadler, G. Kotliar, A. Weichselbaum, and J. von Delft, *Annals of Physics* (2018), doi: [10.1016/j.aop.2018.10.017](https://doi.org/10.1016/j.aop.2018.10.017).
- [69] K. Haule and G. Kotliar, *New J. Phys.* **11**, 025021 (2009).
- [70] S. Hoshino and P. Werner, *Phys. Rev. B* **93**, 155161 (2016).
- [71] J. Kuneš, *Phys. Rev. B* **90**, 235140 (2014).
- [72] A. I. Poteryaev, M. Ferrero, A. Georges, and O. Parcollet, *Phys. Rev. B* **78**, 045115 (2008).
- [73] Y. Doi, K. Matsuhira, and Y. Hinatsu, *J. Solid State Chem.* **165**, 317 (2002).
- [74] A. Nag, S. Middey, S. Bhowal, S. K. Panda, R. Mathieu, J. C. Orain, F. Bert, P. Mendels, P. G. Freeman, M. Mansson, H. M. Ronnow, M. Telling, P. K. Biswas, D. Sheptyakov, S. D. Kaushik, V. Siruguri, C. Meneghini, D. D. Sarma, I. Dasgupta, and S. Ray, *Phys. Rev. Lett.* **116**, 097205 (2016).

4.4 Exotic magnetism

Competing effects may not only arise between local interactions, but also from the frustration of an interaction by the lattice geometry. One of the simplest examples is to place spins with antiferromagnetic coupling on a triangle. It is not possible to have a spin alignment on the triangle such that all spin interactions will be satisfied. Instead the space group of the triangle will produce a six-fold degenerate groundstate which can cause strong fluctuations, even at very cold temperatures the system can continue to fluctuate. The spin ices $\text{Dy}_2\text{Ti}_2\text{O}_7$ and $\text{Ho}_2\text{Ti}_2\text{O}_7$ [223, 224] are examples for materials of such degenerate states. Spins reduce the frustration by tilting, in the case of the pyrochlore lattices of coupled tetrahedra, two spins point inwards and two outwards according to the ice rule. For the Kagome and triangular lattices the spin configuration would involve relative spin alignments rotated by $2\pi/3$, i.e. 120° . Those configurations are not only studied in materials [225, 226], but also in optical lattices [227].

However, in such microscopic descriptions it is important to go beyond classical spins and consider quantum effects and superpositions. Many concepts and theories have been suggested for such a quantum spin liquid state [228, 111, 229, 230]. If spin frustration is to be avoided, the spin-singlet state of the valence bond is to be considered. In order not to break point group symmetries of the lattice the state has to be a superposition of many “resonating” valence bonds [96], otherwise it would be termed a valence bond solid. An excitation could be from a valence bond to a triplet state. Due to the frustration the spins can delocalize without changing the system’s energy. Effectively, it remains a spin-1/2 excitation without charge, the spinon, a fraction of the electron. Moreover, the spinons can form by breaking valence bonds of many sites giving rise to a continuum of these excitations which is in sharp contrast to the discrete magnon spectra. This intriguing characteristic has been measured in the Herbertsmithite $\text{ZnCu}_3(\text{OH})_6\text{Cl}_2$ [231, 232, 233] and in the triangular lattice of YbMgGaO_4 [234].

The frustration is also interesting with regard to the theory of the Mott insulator as Mottness often causes antiferromagnetic order. But antiferromagnetism can have different origins. In contrast a paramagnetic metal-insulator transition would be a strong evidence for the Mott insulator. The organics κ -(BEDT-TTF) $_2\text{Cu}_2(\text{CN})_3$ and $\text{EtMe}_3\text{Sb}[\text{Pd}(\text{dmit})_2]_2$ [235] are modeled by triangular lattice. They exhibit a rich phase diagram including a metallic, a Mott-insulating and even a superconducting phase. Magnetic ordering can be suppressed to very low temperatures.

4.4.1 Triple Bethe lattice

Geometric frustration has been studied in the framework of CDMFT extensively. However, most studies focus on the paramagnetic metal-insulator transition and investigate the effect of frustration on Mottness [236, 237, 238, 239]. The renormalized quasiparticles exist also in the Kagome lattice and geometric frustration increases the critical Hubbard interaction U_{MIT} of the Mott transition. Moreover, related works start from commensurate antiferromagnetism and suppress it by tuning in frustration using hopping parameters [132, 240]. More exotic phenomena of frustration have been addressed by studies which

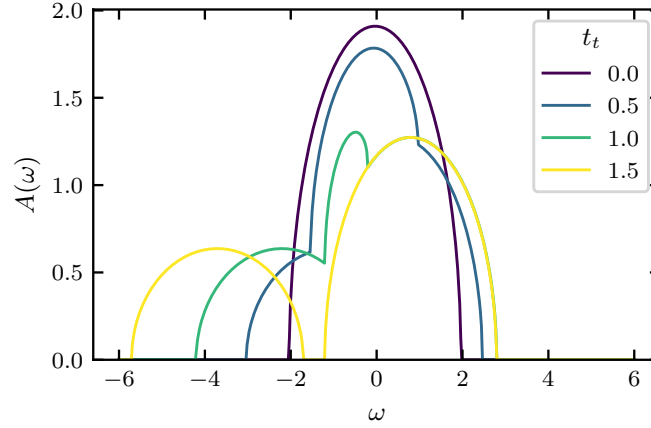


Figure 4.6: The non-interacting ($U = 0$) density of states of the triple bethe lattice for different triangle hoppings t_t .

extend the (C)DMFT, e.g. spinons at the Mott point [241] and the fractionalization of the spin degrees of freedom [242, 243]. The interesting transition from frustrated spins into the RVB-like quantum spin liquid has been investigated by means of the dual fermion method [244]. It has been found that on the triangular lattice the 120° Néel state is the groundstate for $8 < U/t < 9$ and for $9.5 < U/t < 14$ the spin liquid becomes the groundstate (bandwidth $W = 12|t|$). Since localization is suspected to have an important part on the nature of the spin liquid it is suggestive to study it based on the Hubbard model. However, effect spin models have been derived based on the Hubbard model [245].

This section introduces an minimal and exactly solvable model for geometric frustration within the framework of the CDMFT, the triple Bethe lattice. The lattice is built from three Bethe lattices with infinite coordination each. The electrons have hopping processes within the Bethe lattices described by the Bethe hopping. Equivalent sites are interconnect into triangles by intra-triangle hopping. The interaction is the local screened Coulomb repulsion U according to the Hubbard model. The full hamiltonian reads

$$H = t_b \sum_{\langle r, r' \rangle_{R\sigma}} c_{rR\sigma}^\dagger c_{r'R\sigma} + \sum_{rRR'} \underline{t}_{RR'} c_{rR\sigma}^\dagger c_{r'R\sigma} - \mu \sum_{rR\sigma} n_{rR\sigma} + U \sum_{rR} n_{rR\uparrow} n_{rR\downarrow} \quad (4.24)$$

with the sum over nearest neighbors on the Bethe lattices $\langle r, r' \rangle$, the position in a triangle R , i.e. one of the three Bethe lattices, the chemical potential μ and the hopping matrix of the triangles \underline{t} . In the following all quantities will be considered as local in the Bethe lattice, i.e. $r = \text{loc}$, and the corresponding index will be dropped.

Writing the spin and cluster degrees of freedom as matrices, the self-consistency of the triple Bethe lattice, that solves Eq. (4.24) via the CDMFT exactly, is the familiar

$$G^{-1}(i\omega_n) = (i\omega_n + \mu) \mathbb{1} + \underline{t} - t_b^2 G(i\omega_n) - \Sigma(i\omega_n), \quad (4.25)$$

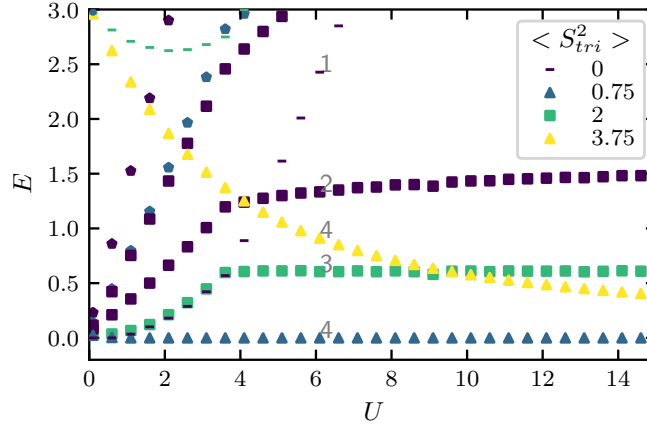


Figure 4.7: Low-energy states of the Hubbard triangle as functions of the interaction U . The colors encode $\langle S_{tot}^2 \rangle$ -values of 0, 0.75, 2 and 3.75 correspond to spin-singlet, doublet, triplet and quadruplet, respectively. The states of the particle numbers $N = 0, 1, 2, 3, 4, 5$ are represented by dots, dimers, triangles, squares and pentagons, respectively. The grey numbers label the degeneracies of the states. The inverse temperature is $\beta = 30$, half-filling ($\mu \neq U/2$) and the hopping is $t_t = 1$.

with the scalar Bethe hopping t_b and the triangle hopping

$$\underline{t} = \begin{pmatrix} 0 & -t_t & -t_t \\ -t_t & 0 & -t_t \\ -t_t & -t_t & 0 \end{pmatrix}. \quad (4.26)$$

In the following the Bethe hopping is the energy unit $t_b = 1$. The Green function $G(i\omega_n)$ and the self-energy $\Sigma(i\omega_n)$ are matrices in spin and cluster space. Further, they depend on fermionic Matsubara frequencies ω_n . The hopping \underline{t} can be diagonalized using the unitary transformation

$$T = \begin{pmatrix} \frac{1}{\sqrt{3}} & \frac{1}{\sqrt{3}} & \frac{1}{\sqrt{3}} \\ 0 & \frac{-1}{\sqrt{2}} & \frac{1}{\sqrt{2}} \\ -\sqrt{\frac{2}{6}} & \frac{1}{\sqrt{6}} & \frac{1}{\sqrt{6}} \end{pmatrix}, \quad (4.27)$$

which acts on the site degrees of freedom.

The $t_t = 0$ density of states of the non-interacting triple Bethe lattice is shown in Fig. 4.6 and resembles the well-known semicircular of bandwidth $W = 4$. Upon increasing the triangle hopping t_t two asymmetric semicirculars evolve out of the original one. Their centers in terms of ω correspond to the eigenvalues of the triangle hopping \underline{t} , which are $-2t_t$ and two-fold degenerate t_t . One of them is two-fold degenerate and thus forms a double-height semicircular. An additional peak occurs for $t_t = 1$ due to the overlap of the semicirculars.

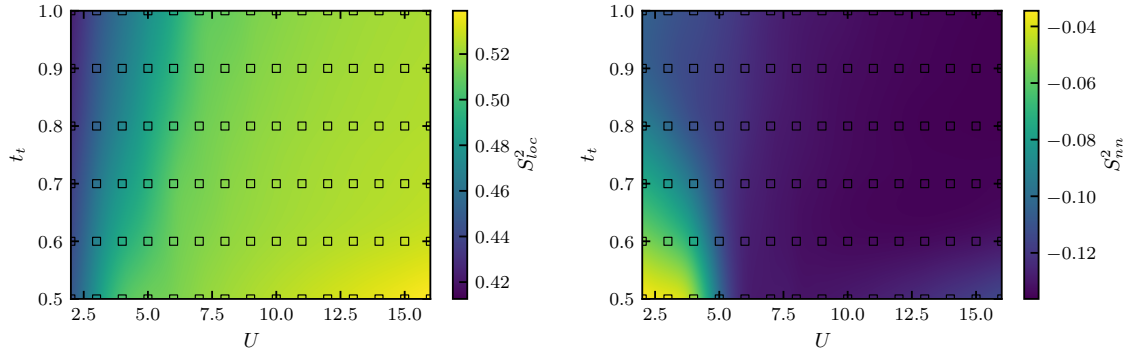


Figure 4.8: Spin correlations, local $\langle S_{loc}^2 \rangle$ (left) and triangle-nearest-neighbor $\langle S_{nn}^2 \rangle$ (right), of the triple Bethe lattice as functions for the triangle hopping t_t and the Hubbard interaction U . The breaking of symmetries is suppressed. $\beta = 30$, half-filling. The data has been obtained in a collaboration with Kristina Klafka.

Hubbard triangle

In order to understand the CDMFT on the triple Bethe lattice, it is helpful to examine the Hubbard triangle first. It is the atomic limit of the triple Bethe lattice and, moreover, the impurity of the auxiliary setup. Therefore it defines the many-body structure of the system. In Fig. 4.7 is the spectrum of the Hubbard triangle presented and how it evolves with increasing interaction. This system is not bipartite and thus $\mu \neq U/2$ for the considered half-filling.

For very small $U \sim 0$ the groundstate is a two-particle spin-singlet $|N, S\rangle = |2, 0\rangle$. But already for small $0 < U \lesssim 4t_t$ the groundstate becomes a four-fold degenerate three-particle spin-doublet $|3, 1/2\rangle$, that remains the groundstate for all larger U under consideration. Being a spin-doublet this state must have symmetries that stem from a different origin. Additional degeneracies occur due to the C_{3v} point group symmetry. In principle the states can be assigned to further sectors using the conjugacy classes of the point group symmetry. Indeed, if the frustration is released, by e.g. a hopping anisotropy, this state will split into two. The same behavior can be observed for the four-particle spin-singlet $|4, 0\rangle$, that is two-fold degenerate. $|2, 0\rangle$ is the first excitation for small U and lies very close to the 4-particle spin-triplet $|4, 1\rangle$, which becomes the first excitation at intermediate $4 \lesssim U \lesssim 10$. At large U the first excitation becomes a 3-particle spin-quadruplet $|3, 3/2\rangle$.

Metal-insulator transition of the paramagnetic state

Electronic correlations and in particular quasiparticle properties can be studied in the paramagnetic state. If the system of the corresponding parameter regime is in an ordered state, then it can still provide insight on the ordering mechanism as electronic correlations are enhanced in the paramagnetic state. In this subsection are results presented that correspond to the triple Bethe lattice for which broken-symmetry states are suppressed. The spin correlations are depicted in Fig. 4.8 and Fig. 4.9 (left). From $\langle S_{loc}^2 \rangle = \langle S_i S_i \rangle$ with

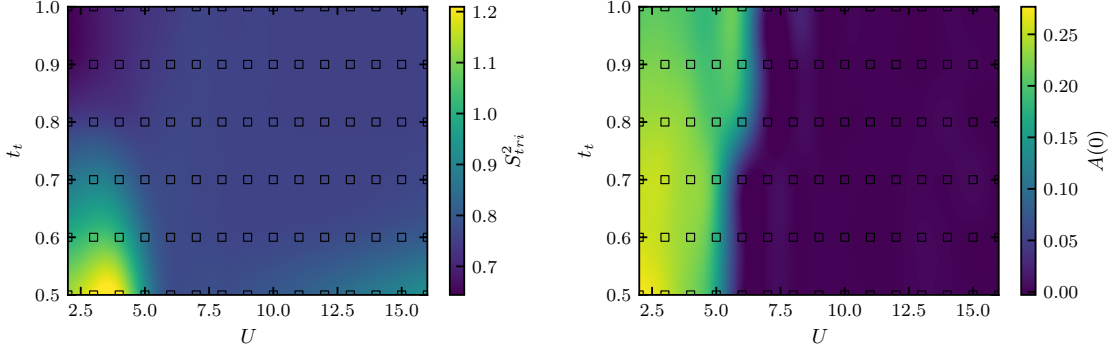


Figure 4.9: Left: Spin quantum number of a triangle $\langle S_{tri}^2 \rangle$ within the triple Bethe lattice as a function of the triangle hopping t_t and the Hubbard interaction U . Right: The local density of states $A(0)$ of the triple Bethe lattice. Both: The breaking of symmetries is suppressed. $\beta = 30$, half-filling. The data has been obtained in a collaboration with Kristina Klafka.

the vector

$$S_i = \sum_{\tau\tau'} c_{i\tau}^\dagger \vec{\sigma}_{\tau\tau'} c_{i\tau'} \quad (4.28)$$

can be read off that the local magnetic moment is most pronounced at large U and small t_t and the least pronounced at small U and large t_t for the considered range of $2 \leq U \leq 16$ and $0.5 \leq t_t \leq 1$. It's of the order of $\langle S_{loc}^2 \rangle \sim 0.5$. The intra-triangle nearest neighbor spin correlations are antiferromagnetic and of the order of $\langle S_{nn}^2 \rangle \sim -0.1$. The maximum lies at small U and small t_t and the minimum at large U and large t_t . Regarding $t_t \sim 0.5$, the nearest neighbor spin correlation exhibit a local minimum in its U dependence around $U \sim 6$.

The spin multiplet structure of the whole triangle (Fig. 4.9, left) within the triple Bethe lattice is constituted of the local and nearest-neighbor contributions. It has a local maximum in its U -dependence with a value of $\langle S_{tri}^2 \rangle \sim 1.2$ which could be explained by fluctuations of the spin-triplet $|4, 3/2\rangle$ shown in Fig. 4.7. Increasing the interaction to $U \sim 6$ leads to a spin-doublet configuration of the triangle, mostly defined by the four-fold degenerate $|3, 1/2\rangle$. Finally, at large $U \sim 15$ the spin-quadruplet increases $\langle S_{tri}^2 \rangle$. Further, at $t_t \sim 1$ and small U , $\langle S_{tri}^2 \rangle$ drops below the value of a spin-doublet, which can be caused by fluctuations through the spin-singlet states of particle numbers $N_{tri} = 2, 4$. Fig. 4.9 (right) shows the corresponding local density of states. For $t_t \leq 0.7$ the critical interaction strength lies between $5 < U_{MIT} < 6$, and for $0.8 \leq t_t$ it increases to $6 < U_{MIT} < 7$. Considering $t_t = 1$ as the fully frustrated case, then frustration increases the critical U_{MIT} for the paramagnetic metal-insulator transition of the triple Bethe lattice. A check for coexistence of the two phases has not been performed.

The full frequency dependence of the local density of states is shown in Fig. 4.10, for colder temperatures $\beta = 50$ and $t_t = 1$. The metal insulator transition occurs around $7 < U_{MIT} < 8$, which is an increase of the critical interaction strength. This is in line with CDMFT calculations on the triangular lattice [238]. With increasing interaction the

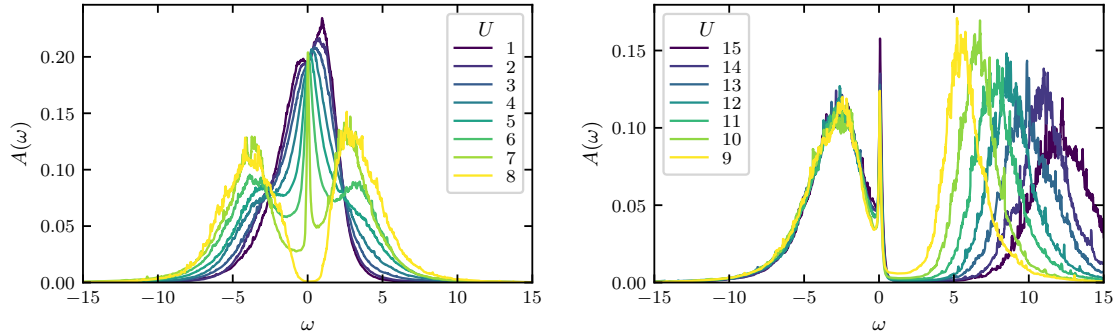


Figure 4.10: Local density of states of the enforced paramagnetic triple Bethe lattice, $t_t = 1$, $\beta = 50$. Left: Interaction driven metal-insulator transition at half-filling. Right: For $8 < U$ the filling changes continuously to a hole doping of up to $\sim 2.5\%$. The data has been obtained in a collaboration with Kristina Klafka.

system develops a heavily renormalized quasiparticle and a sharp resonance with pinning, reminiscent of the Kondo peak which has also been discussed for trimers [246, 247, 248]. The triangle exchange can suppress the Kondo resonance, but also increase the Kondo temperature and even non-Fermi liquid characteristics have been suggested. Interaction strengths above $9 \leq U$, Fig. 4.10 (right), show a peculiar convergence in the CDMFT calculations. CDMFT convergence is reached, but the algorithm for the filling fails. The system retains small hole doping which increases with U , at $U = 15$ it reaches about $\sim 2.5\%$. Moreover, a very sharp resonance develops at Fermi level which also increases with U . This behavior has been found in single-site DMFT calculations of a frustrated pyrochlore structure and has been proposed for the explanation of the heavy fermion behavior in LiV_2O_4 [249]. It is interesting that this property is stable also including the cluster correlations of a frustrated cluster.

All-in/all-out state

As the geometrically frustrated triangle is a building block of the triple Bethe lattice, it is suggesting to study exotic spin structures on this lattice. The spin structure considered here is termed all-in/all-out (AIAO) state which is already used for the spin order in the frustrated pyrochlores. The spin order is illustrated in Fig. 4.11 and in fact, it is related, but not the same as for the pyrochlores. It is probably closer related to the 120° -Néel or $\sqrt{3} \times \sqrt{3}$ orderings of the triangular or Kagome lattices. In the triple Bethe lattice, the spins of a triangle have relative angles of 120° , but the Bethe sublattice ordering is antiferromagnetic, i.e. along the Bethe hopping a translation is accompanied by 180° spin-flip according to the spin order. From that follows an A/B -sublattice ordering for which one sublattice consists of triangle-inward pointing spins and the other of triangle-outward pointing spins.

The description of spin rotations can be formalized by the general transformation

$$R_{\text{gen}}(\phi_i, \theta_i, \psi_i) = e^{-i\phi_i S^z} e^{-i\theta_i S^y} e^{-i\psi_i S^z} \quad (4.29)$$

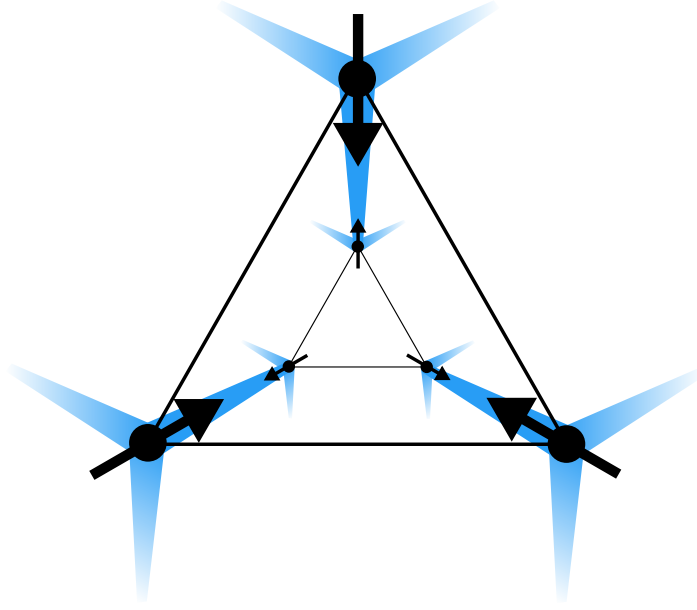


Figure 4.11: Sketch of the triple Bethe lattice with all-in/all-out spin ordering. The Bethe lattice hopping is depicted in blue and the coordination number within in each Bethe lattice is $z = 3$. Shown are two triangles representing the different sublattices that are related by a 180° -spin-flip, whereas within a triangle the spins have relative angles of 120° .

of euler angles ϕ_i, θ_i, ψ_i on site i . For in-plane rotations one angle is sufficient, so that $R(\theta_i) = R_{\text{gen}}(0, \theta_i, 0)$ allows for a description for AIAO ordering. The formalism is also used, e.g., to describe spin spirals [250], though here it is applied in real space rather than k -space. The transformed fermionic creation and annihilation operators read

$$\begin{aligned}\tilde{c}_{\sigma i}^\dagger &= \sum_{\tau} \left(e^{-i\theta_i \sigma_y / 2} \right)_{\sigma\tau} c_{\tau i}^\dagger = \sum_{\tau} c_{\tau i}^\dagger \left(e^{-i\theta_i \sigma_y / 2} \right)_{\tau\sigma}^\dagger = \sum_{\tau} c_{\tau i}^\dagger R_{\tau\sigma}^\dagger(\theta_i), \\ \tilde{c}_{\sigma i} &= \sum_{\tau} c_{\tau i} \left(e^{i\theta_i \sigma_y / 2} \right)_{\tau\sigma} = \sum_{\tau} \left(e^{-i\theta_i \sigma_y / 2} \right)_{\sigma\tau} c_{\tau i} = \sum_{\tau} R_{\sigma\tau}(\theta_i) c_{\tau i},\end{aligned}\tag{4.30}$$

which means for any quadratic term

$$\tilde{c}_{\sigma i}^\dagger \tilde{c}_{\sigma j} = \sum_{\tau\tau'} c_{\tau i}^\dagger R_{\tau\sigma}^\dagger(\theta_i) R_{\sigma\tau'}(\theta_j) c_{\tau' j} \equiv \sum_{\tau\tau'} c_{\tau i}^\dagger W_{\tau\tau'}^\sigma(\theta_i, \theta_j) c_{\tau' j},\tag{4.31}$$

where $W_{\tau\tau'}^\sigma(\theta_i, \theta_j)$ has been introduced for convenience. A triangular-local AIAO order

parameter can then be written as

$$\begin{aligned}
\phi_{\text{AIAO}} &= \sum_i \tilde{n}_{\uparrow i} - \tilde{n}_{\downarrow i} \\
&= \sum_{\tau\tau'i} c_{\tau i}^\dagger \left[W_{\tau\tau'}^\uparrow(\theta_i, \theta_i) - W_{\tau\tau'}^\downarrow(\theta_i, \theta_i) \right] c_{\tau'i} \\
&= \begin{pmatrix} c_{\uparrow 0} \\ c_{\downarrow 0} \end{pmatrix}^\dagger \begin{pmatrix} 1 & 0 \\ 0 & -1 \end{pmatrix} \begin{pmatrix} c_{\uparrow 0} \\ c_{\downarrow 0} \end{pmatrix} \\
&\quad + \begin{pmatrix} c_{\uparrow 1} \\ c_{\downarrow 1} \end{pmatrix}^\dagger \begin{pmatrix} -1/2 & -\sqrt{3}/2 \\ -\sqrt{3}/2 & 1/2 \end{pmatrix} \begin{pmatrix} c_{\uparrow 1} \\ c_{\downarrow 1} \end{pmatrix} \\
&\quad + \begin{pmatrix} c_{\uparrow 2} \\ c_{\downarrow 2} \end{pmatrix}^\dagger \begin{pmatrix} -1/2 & \sqrt{3}/2 \\ \sqrt{3}/2 & 1/2 \end{pmatrix} \begin{pmatrix} c_{\uparrow 2} \\ c_{\downarrow 2} \end{pmatrix},
\end{aligned} \tag{4.32}$$

and also serves as an expression for the numerical seed of the CDMFT, i.e. a symmetry-breaking field that is switched off after a few iterations. There are infinite many possibilities to distribute the spins with relative 120° ordering on the triangle. In fact, an AIAO spin order as the groundstate of the spin- $SU(2)$ symmetric Hubbard triangle means, that the symmetry-breaking occurs spontaneously and any global in-plane $U(1)$ rotation of the spins or Z_3 symmetry operation according to the triangle will also result in a AIAO groundstate. Here has been made the particular choice that does not introduce an imaginary part which makes the Monte-Carlo method more efficient.

The self-consistency condition that corresponds to the AIAO order of the triple Bethe lattice reads

$$G^{\text{AO}}(i\omega_n) = \left[\underbrace{(i\omega_n + \mu) \mathbb{1} - t_t - t_b^2 G^{\text{AI}}(i\omega_n)}_{(G^{\text{AO}}(i\omega_n))^{-1}} - \Sigma^{\text{AO}}(i\omega_n) \right]^{-1} \tag{4.33}$$

with triangle-local correlation functions. Thus, G^{AO} corresponds to an all-out triangle and G^{AI} corresponds to an all-in triangle. The Weiss-field is defined such that the Dyson-like equation is straightforwardly $\mathcal{G}^{-1} = G^{-1} + \Sigma$. Compared to the paramagnetic case, the matrix block structure is more complex, i.e. with off-diagonals in the spin as well as the site degrees of freedom. The Green function of an all-in triangle is related to that of an all-out triangle by

$$G^{\text{AI}}(i\omega_n) = R(\pi) G^{\text{AO}}(i\omega_n) R^\dagger(\pi), \tag{4.34}$$

where $R(\pi)$ describes the 180° spin-flip, which is performed in each Bethe lattice in the same way, see Fig. 4.11, and corresponds to antiferromagnetic coupling. In this view, $t_b \gg t_t$ releases the frustration and will bind the electrons into singlets, like a valence bond solid [251].

Results for the triple Bethe lattice in the symmetry-broken state are shown in Fig. 4.12. The triangle hopping is set to $t_t = 0.5$ and the transition is driven by the interaction U . The local density of states shows a metal-insulator transition for $3 < U_{\text{MIT}} < 4$ accompa-

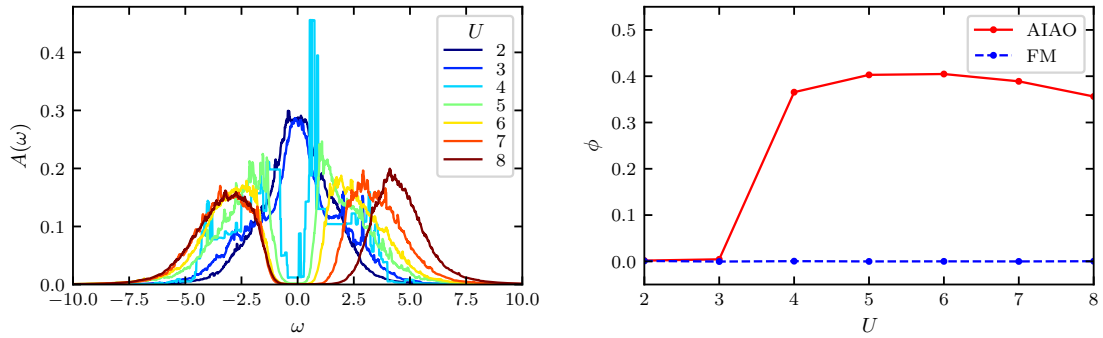


Figure 4.12: Local density of states (left) and order parameter (right) of the triple Bethe lattice for different Hubbard interactions U at $\beta = 10$, $t_t = 0.5$ and half-filling. Considered are the order parameters for all-in/all-out ϕ_{AIAO} and ferromagnetic ϕ_{FM} spin orderings.

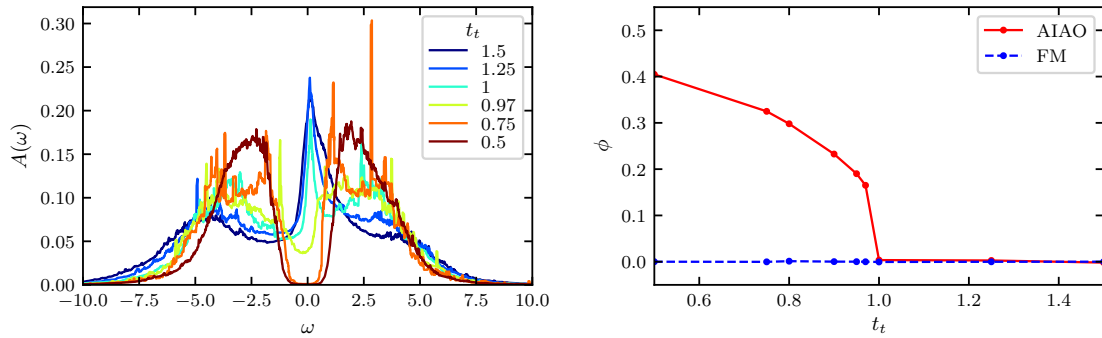


Figure 4.13: Local density of states (left) and order parameter (right) of the triple Bethe lattice for different triangle hoppings t_t at $\beta = 10$, $U = 6$ and half-filling. Considered are the order parameters for all-in/all-out ϕ_{AIAO} and ferromagnetic ϕ_{FM} spin orderings.

nied by the onset of AIAO spin ordering $3 < U_{\text{AIAO}} < 4$. The quasiparticle renormalization occurs only weakly before the transition sets in. At $U = 4$ the AIAO state has a very sharp band edge for the particle excitations, albeit the analytic continuation by the stochastic optimization method is quite noisy for this particular U . $U = 4$ is the value of the paramagnetic calculations at which the spin correlations start to turn doublet-like, see Fig. 4.9. The AIAO order parameter reaches a local maximum around $U = 5 - 6$. The ferromagnetic order parameter is also shown in Fig. 4.12 to verify that the spin order is purely AIAO. Fig. 4.13 shows the local density of states and order parameter of the triple Bethe lattice at constant $U = 6$, but for different t_t . The AIAO order sets in for $t_t < 1$ with $t_t = 1$ excluded. The AIAO order parameter is large ϕ_{AIAO} for small $t_t = 0.5$ and decreases towards $t_t = 1$ at which possibly a jump of the order parameter occurs. For $t_t = 0.97$, the local density of states $A(\omega)$ shows a finite density of states at Fermi level together with a finite values for the AIAO ordering. For $t_t = 0.75$, $A(\omega)$ has a four-peak structure reminiscent of the Slater peaks.

The 120° spin structure has been calculated successfully in the triple Bethe lattice. It is

found in a parameter regime at that the Bethe hopping is larger than the triangle hopping, but only for sufficiently large Hubbard interactions which promote the triangle many-body state of a four-fold degenerate spin-doublet which also has a degeneracy that originates from the triangular point group symmetry.

Chapter 5

Conclusion

The phenomenon of high-temperature superconductivity in copper oxides has been addressed. The isolated plaquette with Hubbard interaction has a highly degenerate point in the phase diagram of chemical potential and Hubbard interaction at 25% doping. The six plaquette many-body eigenstates of $|N, S, K\rangle = |4, 0, \Gamma\rangle$, $|3, 1/2, X/Y\rangle$ and $|2, 0, \Gamma\rangle$ cross at a single point in this phase diagram. The states support quantum superpositions of valence bonds in agreement with the resonating valence bond theory. A detailed analysis using the environments of a simple fermionic bath, the quadruple Bethe lattice and also the square lattice. The Hubbard interaction is screened by the plaquette as a whole so that the thermodynamic potential does not change if an electron is added to or removed from the plaquette. The possibility has been studied that more complex environments, which e.g. involve a full mean-field self-consistency for their solution, shift this peculiar point. Following the idea that in the square lattice plaquettes resonate and long-range plaquette modes form, the corresponding point has also been detected in the $(N_\uparrow, N_\downarrow) = (6, 6)$ -sector and $U = 7.5$ of a four-by-four lattice using signatures from critical points of quantum information theory.

The self-consistency condition for the quadruple Bethe lattice in the symmetry-broken state of antiferromagnetism and d -wave superconductivity has been formulated and solved. The model consists of Bethe lattices with infinite coordination and therefore it is solved by the CDMFT exactly. It has been identified that the system fluctuates through the plaquette eigenstates which cross at the plaquette degenerate point, when superconductivity occurs. For Bethe hopping around $t_b \sim 0.1$ The maximum of the superconducting dome lies at the optimal hole doping of 15%, as it is observed in many copper oxides. If the ordering is suppressed, then it occurs a Lifshitz transition at the optimal doping. It is indicated that two-particle processes diminish the superconductivity in the overdoped regime and the absence of free charge carriers at Fermi level, quasiparticles, in the underdoped regime. Superconductivity and antiferromagnetism coexist in this model and moreover in their coexistence regime is also a spin-triplet form of superconductivity. However, the coexistence region can be suppressed by the Bethe hopping parameter.

The study of the quadruple Bethe lattice has made extensive use of the stochastic optimization method for analytic continuation. An efficient implementation of the Mishchenko-

algorithm has been presented and benchmarked. The method's ergodicity mainly depends on the number of global updates which optimizes the configuration according to the distance measure, reasonable values are $3 \times 10^2 - 3 \times 10^4$. The number of local updates in the Metropolis-chain can also improve the result, but has not been crucial for the considered examples. Noise is reduced by the number of particular solutions which are accumulated and subsequently selected by a threshold and averaged for the final result, reasonable values are $30 - 3 \times 10^3$. The bandwidth should always be chosen too large, but with the correct order of magnitude for efficiency.

The issue of the small superfluid density in superconducting copper oxides has been addressed by the formulation of the Josephson lattice model. Since the plaquette-theory provides a local theory of Cooper pair formation, long-range effects have to be considered differently. The Josephson lattice assumes local pairs in plaquettes and describes long-range coherence effects of the plaquette pairs. It maps the Hubbard model to an effective XY model and is derived by means of the local force theorem which has been applied successfully in problems of magnetism. This opens up the possibility to study the issue of phase fluctuations in the XY model by including band structure and correlations effects. Furthermore, the continuum limit has been applied to obtain the superconducting stiffness, which allows for a comparison with experimental data for the London penetration depth and the Kosterlitz Thouless transition temperature.

The local force theorem has been studied for the magnetic case in the antiferromagnetic hypercubic lattice. It maps the Hubbard model to an effective Heisenberg model. It has been found that the reduction of the effective interaction can be reduced to single-particle correlation functions, if the local order parameter is well-defined. In the transition regime it should be used as an estimate only as vertex corrections become important. The local force theorem has been extended to a map from the Hubbard model with generic non-local interactions to an effective Heisenberg model. The antiferromagnetism in the hypercubic lattice can be differentiated into itinerant, Slater antiferromagnetism and localized, Heisenberg antiferromagnetism, which has been confirmed. The Heisenberg antiferromagnetism originates from Mottness as the gap is defined by the Hubbard interaction.

Another origin of magnetism is the Hund's coupling, intra-atomic Coulomb exchange. A violation of the Hund's rules is possible if competing effects, such as dimer formation, bind the spins into singlet states. The transition from the molecular orbital to the double exchange state has been tuned by the dimer hopping parameter in the multiorbital double Bethe lattice. Strong correlation effects have been found in the crossover regime, such as strong quasiparticle renormalization, fluctuation enhancement and spin freezing. Finally, an exotic magnetic state has been calculated in the triple Bethe lattice. It contains relative spin alignments of 120° , reminiscent of the all-in/all-out, 120° -Néel or $\sqrt{3} \times \sqrt{3}$ states in pyrochlore, triangular or Kagome lattices, respectively. It is found in a parameter regime for which the Bethe hopping is larger than the hopping within the triangles. The Hubbard interaction has to be sufficiently large, as local magnetic moments must be formed for this ordering.

Bibliography

- [1] H. Bethe. Theorie der beugung von elektronen an kristallen. *Annalen der Physik*, 392(17): 55–129, 1928. doi: 10.1002/andp.19283921704. URL <https://onlinelibrary.wiley.com/doi/abs/10.1002/andp.19283921704>.
- [2] F. Bloch. Über die quantenmechanik der elektronen in kristallgittern. *Zeitschrift für Physik*, 52(7):555–600, Jul 1929. ISSN 0044-3328. doi: 10.1007/BF01339455. URL <https://doi.org/10.1007/BF01339455>.
- [3] M. Imada, A. Fujimori, and Y. Tokura. Metal-insulator transitions. *Rev. Mod. Phys.*, 70: 1039–1263, Oct 1998. doi: 10.1103/RevModPhys.70.1039. URL <https://link.aps.org/doi/10.1103/RevModPhys.70.1039>.
- [4] Y. Tokura. Correlated-electron physics in transition-metal oxides. *Physics Today*, 56(7):50–55, 2003. doi: 10.1063/1.1603080. URL <https://doi.org/10.1063/1.1603080>.
- [5] D. I. Khomskii. *Transition Metal Compounds*. Cambridge University Press, 2014. doi: 10.1017/CBO9781139096782. URL <https://doi.org/10.1017/CBO9781139096782>.
- [6] J. Kondo. Resistance Minimum in Dilute Magnetic Alloys. *Progress of Theoretical Physics*, 32(1):37–49, 07 1964. ISSN 0033-068X. doi: 10.1143/PTP.32.37. URL <https://doi.org/10.1143/PTP.32.37>.
- [7] G. R. Stewart. Heavy-fermion systems. *Rev. Mod. Phys.*, 56:755–787, Oct 1984. doi: 10.1103/RevModPhys.56.755. URL <https://link.aps.org/doi/10.1103/RevModPhys.56.755>.
- [8] N. F. Mott. The basis of the electron theory of metals, with special reference to the transition metals. *Proceedings of the Physical Society. Section A*, 62(7):416–422, Jul 1949. doi: 10.1088/0370-1298/62/7/303. URL <https://doi.org/10.1088/0370-1298/62/7/303>.
- [9] N. Cabrera and N. F. Mott. Theory of the oxidation of metals. *Reports on Progress in Physics*, 12(1):163–184, Jan 1949. doi: 10.1088/0034-4885/12/1/308. URL <https://doi.org/10.1088/0034-4885/12/1/308>.
- [10] V. I. Anisimov and O. Gunnarsson. Density-functional calculation of effective coulomb interactions in metals. *Phys. Rev. B*, 43:7570–7574, Apr 1991. doi: 10.1103/PhysRevB.43.7570. URL <https://link.aps.org/doi/10.1103/PhysRevB.43.7570>.
- [11] I. V. Solovyev and M. Imada. Screening of coulomb interactions in transition metals. *Phys. Rev. B*, 71:045103, Jan 2005. doi: 10.1103/PhysRevB.71.045103. URL <https://link.aps.org/doi/10.1103/PhysRevB.71.045103>.
- [12] S. L. Dudarev, G. A. Botton, S. Y. Savrasov, C. J. Humphreys, and A. P. Sutton. Electron-energy-loss spectra and the structural stability of nickel oxide: An lsd+u study. *Phys. Rev. B*, 57:1505–1509, Jan 1998. doi: 10.1103/PhysRevB.57.1505. URL <https://link.aps.org/>

doi/10.1103/PhysRevB.57.1505.

- [13] A. Fujimori, I. Hase, H. Namatame, Y. Fujishima, Y. Tokura, H. Eisaki, S. Uchida, K. Takegahara, and F. M. F. de Groot. Evolution of the spectral function in mott-hubbard systems with d^1 configuration. *Phys. Rev. Lett.*, 69:1796–1799, Sep 1992. doi: 10.1103/PhysRevLett.69.1796. URL <https://link.aps.org/doi/10.1103/PhysRevLett.69.1796>.
- [14] H. A. Kramers. L'interaction Entre les Atomes Magnétogènes dans un Cristal Paramagnétique. *Physica*, 1:182–192, 1934. doi: 10.1016/S0031-8914(34)90023-9. URL [https://doi.org/10.1016/S0031-8914\(34\)90023-9](https://doi.org/10.1016/S0031-8914(34)90023-9).
- [15] J. Hubbard. Electron Correlations in Narrow Energy Bands. *Proceedings of the Royal Society of London Series A*, 276:238–257, November 1963. doi: 10.1098/rspa.1963.0204. URL <https://royalsocietypublishing.org/doi/10.1098/rspa.1963.0204>.
- [16] P. W. Anderson. More is different. *Science*, 177(4047):393–396, 1972. ISSN 0036-8075. doi: 10.1126/science.177.4047.393. URL <https://science.sciencemag.org/content/177/4047/393>.
- [17] E. Dagotto. Complexity in strongly correlated electronic systems. *Science*, 309(5732):257–262, 2005. ISSN 0036-8075. doi: 10.1126/science.1107559. URL <https://science.sciencemag.org/content/309/5732/257>.
- [18] E. Dagotto. Correlated electrons in high-temperature superconductors. *Rev. Mod. Phys.*, 66:763–840, Jul 1994. doi: 10.1103/RevModPhys.66.763. URL <https://link.aps.org/doi/10.1103/RevModPhys.66.763>.
- [19] H. Bethe. Zur theorie der metalle. *Zeitschrift für Physik*, 71(3):205–226, Mar 1931. ISSN 0044-3328. doi: 10.1007/BF01341708. URL <https://doi.org/10.1007/BF01341708>.
- [20] A. Georges, G. Kotliar, W. Krauth, and M. J. Rozenberg. Dynamical mean-field theory of strongly correlated fermion systems and the limit of infinite dimensions. *Rev. Mod. Phys.*, 68:13–125, Jan 1996. doi: 10.1103/RevModPhys.68.13. URL <https://link.aps.org/doi/10.1103/RevModPhys.68.13>.
- [21] A. Georges. Strongly correlated electron materials: Dynamical mean-field theory and electronic structure. *AIP Conference Proceedings*, 715(1):3–74, 2004. doi: 10.1063/1.1800733. URL <https://aip.scitation.org/doi/abs/10.1063/1.1800733>.
- [22] N. D. Mermin and H. Wagner. Absence of ferromagnetism or antiferromagnetism in one- or two-dimensional isotropic heisenberg models. *Phys. Rev. Lett.*, 17:1133–1136, Nov 1966. doi: 10.1103/PhysRevLett.17.1133. URL <https://link.aps.org/doi/10.1103/PhysRevLett.17.1133>.
- [23] J. M. Kosterlitz and D. J. Thouless. Ordering, metastability and phase transitions in two-dimensional systems. *Journal of Physics C: Solid State Physics*, 6(7):1181–1203, Apr 1973. doi: 10.1088/0022-3719/6/7/010. URL <https://doi.org/10.1088/0022-3719/6/7/010>.
- [24] J. G. Bednorz and K. A. Müller. Possible hightc superconductivity in the balacuo system. *Zeitschrift für Physik B Condensed Matter*, 64(2):189–193, Jun 1986. ISSN 1431-584X. doi: 10.1007/BF01303701. URL <https://doi.org/10.1007/BF01303701>.
- [25] W. Meissner and R. Ochsenfeld. Ein neuer effekt bei eintritt der supraleitfähigkeit. *Naturwissenschaften*, 21(44):787–788, Nov 1933. ISSN 1432-1904. doi: 10.1007/BF01504252. URL <https://doi.org/10.1007/BF01504252>.

- [26] J. Bardeen, L. N. Cooper, and J. R. Schrieffer. Theory of superconductivity. *Phys. Rev.*, 108:1175–1204, Dec 1957. doi: 10.1103/PhysRev.108.1175. URL <https://link.aps.org/doi/10.1103/PhysRev.108.1175>.
- [27] D. J. Scalapino. A common thread: The pairing interaction for unconventional superconductors. *Rev. Mod. Phys.*, 84:1383–1417, Oct 2012. doi: 10.1103/RevModPhys.84.1383. URL <https://link.aps.org/doi/10.1103/RevModPhys.84.1383>.
- [28] M. K. Wu, J. R. Ashburn, C. J. Torng, P. H. Hor, R. L. Meng, L. Gao, Z. J. Huang, Y. Q. Wang, and C. W. Chu. Superconductivity at 93 k in a new mixed-phase y-ba-cu-o compound system at ambient pressure. *Phys. Rev. Lett.*, 58:908–910, Mar 1987. doi: 10.1103/PhysRevLett.58.908. URL <https://link.aps.org/doi/10.1103/PhysRevLett.58.908>.
- [29] G. Kotliar and J. Liu. Superexchange mechanism and d-wave superconductivity. *Phys. Rev. B*, 38:5142–5145, Sep 1988. doi: 10.1103/PhysRevB.38.5142. URL <https://link.aps.org/doi/10.1103/PhysRevB.38.5142>.
- [30] A. I. Lichtenstein and M. I. Katsnelson. Antiferromagnetism and d-wave superconductivity in cuprates: A cluster dynamical mean-field theory. *Phys. Rev. B*, 62:R9283–R9286, Oct 2000. doi: 10.1103/PhysRevB.62.R9283. URL <https://link.aps.org/doi/10.1103/PhysRevB.62.R9283>.
- [31] T. Senthil, Ashvin V., L. Balents, S. Sachdev, and M. P. A. Fisher. Deconfined quantum critical points. *Science*, 303(5663):1490–1494, 2004. ISSN 0036-8075. doi: 10.1126/science.1091806. URL <https://science.sciencemag.org/content/303/5663/1490>.
- [32] P. A. Lee, N. Nagaosa, and X.-G. Wen. Doping a mott insulator: Physics of high-temperature superconductivity. *Rev. Mod. Phys.*, 78:17–85, Jan 2006. doi: 10.1103/RevModPhys.78.17. URL <https://link.aps.org/doi/10.1103/RevModPhys.78.17>.
- [33] B. Keimer, S. A. Kivelson, M. R. Norman, S. Uchida, and J. Zaanen. From quantum matter to high-temperature superconductivity in copper oxides. *Nature*, 518:179 EP –, Feb 2015. URL <http://dx.doi.org/10.1038/nature14165>.
- [34] V. J. Emery, S. A. Kivelson, and H. Q. Lin. Phase separation in the t-j model. *Phys. Rev. Lett.*, 64:475–478, Jan 1990. doi: 10.1103/PhysRevLett.64.475. URL <https://link.aps.org/doi/10.1103/PhysRevLett.64.475>.
- [35] J. Spalek. t-J Model Then and Now: a Personal Perspective from the Pioneering Times. *Acta Physica Polonica A*, 111(4):409, Apr 2007.
- [36] P. W. Anderson. Antiferromagnetism. theory of superexchange interaction. *Phys. Rev.*, 79:350–356, Jul 1950. doi: 10.1103/PhysRev.79.350. URL <https://link.aps.org/doi/10.1103/PhysRev.79.350>.
- [37] A. Georges, L. de’ Medici, and J. Mravlje. Strong correlations from hund’s coupling. *Annual Review of Condensed Matter Physics*, 4(1):137–178, 2013. doi: 10.1146/annurev-conmatphys-020911-125045. URL <https://doi.org/10.1146/annurev-conmatphys-020911-125045>.
- [38] P. Hohenberg and W. Kohn. Inhomogeneous electron gas. *Phys. Rev.*, 136:B864–B871, Nov 1964. doi: 10.1103/PhysRev.136.B864. URL <https://link.aps.org/doi/10.1103/PhysRev.136.B864>.
- [39] W. Kohn and L. J. Sham. Self-consistent equations including exchange and correlation effects. *Phys. Rev.*, 140:A1133–A1138, Nov 1965. doi: 10.1103/PhysRev.140.A1133. URL <https://link.aps.org/doi/10.1103/PhysRev.140.A1133>.

[//link.aps.org/doi/10.1103/PhysRev.140.A1133](https://link.aps.org/doi/10.1103/PhysRev.140.A1133).

- [40] V. I. Anisimov, J. Zaanen, and O. K. Andersen. Band theory and mott insulators: Hubbard u instead of stoner i. *Phys. Rev. B*, 44:943–954, Jul 1991. doi: 10.1103/PhysRevB.44.943. URL <https://link.aps.org/doi/10.1103/PhysRevB.44.943>.
- [41] V. I. Anisimov, F. Aryasetiawan, and A. I. Lichtenstein. First-principles calculations of the electronic structure and spectra of strongly correlated systems: the LDA+U method. *Journal of Physics: Condensed Matter*, 9(4):767–808, Jan 1997. doi: 10.1088/0953-8984/9/4/002. URL <https://doi.org/10.1088/0953-8984/9/4/002>.
- [42] G. Kotliar, S. Y. Savrasov, K. Haule, V. S. Oudovenko, O. Parcollet, and C. A. Marianetti. Electronic structure calculations with dynamical mean-field theory. *Rev. Mod. Phys.*, 78:865–951, Aug 2006. doi: 10.1103/RevModPhys.78.865. URL <https://link.aps.org/doi/10.1103/RevModPhys.78.865>.
- [43] E. Pavarini, E. Koch, A. Lichtenstein, and D. (Eds.) Vollhardt. *The LDA+DMFT approach to strongly correlated materials*, volume 1 of *Schriften des Forschungszentrums Jülich : Modeling and Simulation*. Forschungszentrum Jülich GmbH Zentralbibliothek, Verlag, 2011. URL <http://juser.fz-juelich.de/record/17645>. Record converted from VDB: 12.11.2012.
- [44] E. Gull, A. J. Millis, A. I. Lichtenstein, A. N. Rubtsov, M. Troyer, and P. Werner. Continuous-time monte carlo methods for quantum impurity models. *Rev. Mod. Phys.*, 83:349–404, May 2011. doi: 10.1103/RevModPhys.83.349. URL <https://link.aps.org/doi/10.1103/RevModPhys.83.349>.
- [45] O. Parcollet, M. Ferrero, T. Ayril, H. Hafermann, I. Krivenko, L. Messio, and P. Seth. Triqs: A toolbox for research on interacting quantum systems. *Computer Physics Communications*, 196:398 – 415, 2015. ISSN 0010-4655. doi: <http://dx.doi.org/10.1016/j.cpc.2015.04.023>. URL <http://www.sciencedirect.com/science/article/pii/S0010465515001666>.
- [46] S. R. White. Density matrix formulation for quantum renormalization groups. *Phys. Rev. Lett.*, 69:2863–2866, Nov 1992. doi: 10.1103/PhysRevLett.69.2863. URL <https://link.aps.org/doi/10.1103/PhysRevLett.69.2863>.
- [47] A.F. Albuquerque, F. Alet, P. Corboz, P. Dayal, A. Feiguin, S. Fuchs, L. Gamper, E. Gull, S. Gürtler, A. Honecker, R. Igarashi, M. Körner, A. Kozhevnikov, A. Läuchli, S.R. Manmana, M. Matsumoto, I.P. McCulloch, F. Michel, R.M. Noack, G. Pawłowski, L. Pollet, T. Pruschke, U. Schollwöck, S. Todo, S. Trebst, M. Troyer, P. Werner, and S. Wessel. The alps project release 1.3: Open-source software for strongly correlated systems. *Journal of Magnetism and Magnetic Materials*, 310(2, Part 2):1187 – 1193, 2007. ISSN 0304-8853. doi: <https://doi.org/10.1016/j.jmmm.2006.10.304>. URL <http://www.sciencedirect.com/science/article/pii/S0304885306014983>. Proceedings of the 17th International Conference on Magnetism.
- [48] G. Carleo and M. Troyer. Solving the quantum many-body problem with artificial neural networks. *Science*, 355(6325):602–606, 2017. ISSN 0036-8075. doi: 10.1126/science.aag2302. URL <https://science.sciencemag.org/content/355/6325/602>.
- [49] V. L. Ginzburg and L. D. Landau. *On the Theory of Superconductivity*, pages 113–137. Springer Berlin Heidelberg, Berlin, Heidelberg, 2009. ISBN 978-3-540-68008-6. doi: 10.1007/978-3-540-68008-6_4. URL https://doi.org/10.1007/978-3-540-68008-6_4.
- [50] U. Schollwöck. The density-matrix renormalization group. *Rev. Mod. Phys.*, 77:259–315, Apr 2005. doi: 10.1103/RevModPhys.77.259. URL <https://link.aps.org/doi/10.1103/RevModPhys.77.259>.

- RevModPhys.77.259.
- [51] T. Plefka. Convergence condition of the TAP equation for the infinite-ranged ising spin glass model. *Journal of Physics A: Mathematical and General*, 15(6):1971–1978, Jun 1982. doi: 10.1088/0305-4470/15/6/035. URL <https://doi.org/10.1088/0305-4470/15/6/035>.
- [52] A. Georges and J. S. Yedidia. How to expand around mean-field theory using high-temperature expansions. *Journal of Physics A: Mathematical and General*, 24(9):2173–2192, May 1991. doi: 10.1088/0305-4470/24/9/024. URL <https://doi.org/10.1088/0305-4470/24/9/024>.
- [53] G. Kotliar and D. Vollhardt. Strongly correlated materials: Insights from dynamical mean-field theory. *Physics Today*, 57(3):53–59, 2004. doi: 10.1063/1.1712502. URL <https://doi.org/10.1063/1.1712502>.
- [54] *DMFT at 25: Infinite Dimensions*, volume 4 of *Modeling and Simulation*, Jülich, Sep 2014. Autumn School on Correlated Electrons, Jülich (Germany), 15 Sep 2014 - 19 Sep 2014, Forschungszentrum Jülich Zentralbibliothek, Verlag. ISBN 978-3-89336-953-9. URL <http://juser.fz-juelich.de/record/155829>.
- [55] J. M. Luttinger and J. C. Ward. Ground-state energy of a many-fermion system. ii. *Phys. Rev.*, 118:1417–1427, Jun 1960. doi: 10.1103/PhysRev.118.1417. URL <https://link.aps.org/doi/10.1103/PhysRev.118.1417>.
- [56] G. Baym and L. P. Kadanoff. Conservation laws and correlation functions. *Phys. Rev.*, 124:287–299, Oct 1961. doi: 10.1103/PhysRev.124.287. URL <https://link.aps.org/doi/10.1103/PhysRev.124.287>.
- [57] F. Krien. *Conserving dynamical mean-field approaches to strongly correlated systems*. PhD thesis, Universität Hamburg, Von-Melle-Park 3, 20146 Hamburg, 2018. URL <http://ediss.sub.uni-hamburg.de/volltexte/2018/9182>.
- [58] R. O. Jones and O. Gunnarsson. The density functional formalism, its applications and prospects. *Rev. Mod. Phys.*, 61:689–746, Jul 1989. doi: 10.1103/RevModPhys.61.689. URL <https://link.aps.org/doi/10.1103/RevModPhys.61.689>.
- [59] W. Metzner and D. Vollhardt. Correlated lattice fermions in $d = \infty$ dimensions. *Phys. Rev. Lett.*, 62:324–327, Jan 1989. doi: 10.1103/PhysRevLett.62.324. URL <https://link.aps.org/doi/10.1103/PhysRevLett.62.324>.
- [60] J.W. Negele and H. Orland. *Quantum many-particle systems*. Frontiers in physics. Addison-Wesley Pub. Co., 1988. ISBN 9780201125931.
- [61] H. A. Bethe and W. L. Bragg. Statistical theory of superlattices. *Proceedings of the Royal Society of London. Series A - Mathematical and Physical Sciences*, 150(871):552–575, 1935. doi: 10.1098/rspa.1935.0122. URL <https://royalsocietypublishing.org/doi/abs/10.1098/rspa.1935.0122>.
- [62] T. Maier, M. Jarrell, T. Pruschke, and M. H. Hettler. Quantum cluster theories. *Rev. Mod. Phys.*, 77:1027–1080, Oct 2005. doi: 10.1103/RevModPhys.77.1027. URL <https://link.aps.org/doi/10.1103/RevModPhys.77.1027>.
- [63] C. Gros and R. Valentí. Cluster expansion for the self-energy: A simple many-body method for interpreting the photoemission spectra of correlated fermi systems. *Phys. Rev. B*, 48:418–425, Jul 1993. doi: 10.1103/PhysRevB.48.418. URL <https://link.aps.org/doi/10.1103/PhysRevB.48.418>.

-
- [64] D. Sénéchal, D. Perez, and M. Pioro-Ladrière. Spectral weight of the hubbard model through cluster perturbation theory. *Phys. Rev. Lett.*, 84:522–525, Jan 2000. doi: 10.1103/PhysRevLett.84.522. URL <https://link.aps.org/doi/10.1103/PhysRevLett.84.522>.
- [65] D. Sénéchal and A.-M. S. Tremblay. Hot spots and pseudogaps for hole- and electron-doped high-temperature superconductors. *Phys. Rev. Lett.*, 92:126401, Mar 2004. doi: 10.1103/PhysRevLett.92.126401. URL <https://link.aps.org/doi/10.1103/PhysRevLett.92.126401>.
- [66] G. Biroli, O. Parcollet, and G. Kotliar. Cluster dynamical mean-field theories: Causality and classical limit. *Phys. Rev. B*, 69:205108, May 2004. doi: 10.1103/PhysRevB.69.205108. URL <https://link.aps.org/doi/10.1103/PhysRevB.69.205108>.
- [67] M. H. Hettler, A. N. Tahvildar-Zadeh, M. Jarrell, T. Pruschke, and H. R. Krishnamurthy. Nonlocal dynamical correlations of strongly interacting electron systems. *Phys. Rev. B*, 58:R7475–R7479, Sep 1998. doi: 10.1103/PhysRevB.58.R7475. URL <https://link.aps.org/doi/10.1103/PhysRevB.58.R7475>.
- [68] E. Gull, M. Ferrero, O. Parcollet, A. Georges, and A. J. Millis. Momentum-space anisotropy and pseudogaps: A comparative cluster dynamical mean-field analysis of the doping-driven metal-insulator transition in the two-dimensional hubbard model. *Phys. Rev. B*, 82:155101, Oct 2010. doi: 10.1103/PhysRevB.82.155101. URL <https://link.aps.org/doi/10.1103/PhysRevB.82.155101>.
- [69] *Many-Body Physics: From Kondo to Hubbard*, volume 5 of *Modeling and Simulation*, Jülich, Sep 2015. Autumn School on Correlated Electrons, Jülich (Germany), 21 Sep 2015 - 25 Sep 2015, Forschungszentrum Jülich GmbH Zentralbibliothek, Verlag. ISBN 978-3-95806-074-6. URL <http://juser.fz-juelich.de/record/205123>.
- [70] P. Staar, T. Maier, and T. C. Schulthess. Dynamical cluster approximation with continuous lattice self-energy. *Phys. Rev. B*, 88:115101, Sep 2013. doi: 10.1103/PhysRevB.88.115101. URL <https://link.aps.org/doi/10.1103/PhysRevB.88.115101>.
- [71] G. Biroli and G. Kotliar. Cluster methods for strongly correlated electron systems. *Phys. Rev. B*, 65:155112, Apr 2002. doi: 10.1103/PhysRevB.65.155112. URL <https://link.aps.org/doi/10.1103/PhysRevB.65.155112>.
- [72] S. Sakai, G. Sangiovanni, M. Civelli, Y. Motome, K. Held, and M. Imada. Cluster-size dependence in cellular dynamical mean-field theory. *Phys. Rev. B*, 85:035102, Jan 2012. doi: 10.1103/PhysRevB.85.035102. URL <https://link.aps.org/doi/10.1103/PhysRevB.85.035102>.
- [73] T. D. Stanescu and G. Kotliar. Fermi arcs and hidden zeros of the green function in the pseudogap state. *Phys. Rev. B*, 74:125110, Sep 2006. doi: 10.1103/PhysRevB.74.125110. URL <https://link.aps.org/doi/10.1103/PhysRevB.74.125110>.
- [74] J. Vučković, N. Wentzell, M. Ferrero, and O. Parcollet. Practical consequences of the luttinger-ward functional multivaluedness for cluster dmft methods. *Phys. Rev. B*, 97:125141, Mar 2018. doi: 10.1103/PhysRevB.97.125141. URL <https://link.aps.org/doi/10.1103/PhysRevB.97.125141>.
- [75] Potthoff, M. Self-energy-functional approach to systems of correlated electrons. *Eur. Phys. J. B*, 32(4):429–436, 2003. doi: 10.1140/epjb/e2003-00121-8. URL <https://doi.org/10.1140/epjb/e2003-00121-8>.

- [76] E. Pavarini, E. Koch, F. Anders, and M. (Eds.) Jarrell. *Correlated electrons: from models to materials*, volume 2 of *Schriften des Forschungszentrums Jülich. Reihe Modeling and simulation*. Forschungszentrum Jülich GmbH, Jülich, 2012. ISBN 9783893367962. URL <http://juser.fz-juelich.de/record/136393>. Record converted from JUWEL: 18.07.2013.
- [77] D. Bergeron and A.-M. S. Tremblay. Algorithms for optimized maximum entropy and diagnostic tools for analytic continuation. *Phys. Rev. E*, 94:023303, Aug 2016. doi: 10.1103/PhysRevE.94.023303. URL <https://link.aps.org/doi/10.1103/PhysRevE.94.023303>.
- [78] J. Schött, E. G. C. P. van Loon, I. L. M. Locht, M. I. Katsnelson, and I. Di Marco. Comparison between methods of analytical continuation for bosonic functions. *Phys. Rev. B*, 94:245140, Dec 2016. doi: 10.1103/PhysRevB.94.245140. URL <https://link.aps.org/doi/10.1103/PhysRevB.94.245140>.
- [79] O. Goulko, A. S. Mishchenko, L. Pollet, N. Prokof'ev, and B. Svistunov. Numerical analytic continuation: Answers to well-posed questions. *Phys. Rev. B*, 95:014102, Jan 2017. doi: 10.1103/PhysRevB.95.014102. URL <https://link.aps.org/doi/10.1103/PhysRevB.95.014102>.
- [80] J. Otsuki, M. Ohzeki, H. Shinaoka, and K. Yoshimi. Sparse modeling approach to analytical continuation of imaginary-time quantum Monte Carlo data. *Phys. Rev. E*, 95:061302, Jun 2017. doi: 10.1103/PhysRevE.95.061302. URL <https://link.aps.org/doi/10.1103/PhysRevE.95.061302>.
- [81] K. S. D. Beach, R. J. Gooding, and F. Marsiglio. Reliable padé analytical continuation method based on a high-accuracy symbolic computation algorithm. *Phys. Rev. B*, 61:5147–5157, Feb 2000. doi: 10.1103/PhysRevB.61.5147. URL <https://link.aps.org/doi/10.1103/PhysRevB.61.5147>.
- [82] J. Schött, I. L. M. Locht, E. Lundin, O. Grånäs, O. Eriksson, and I. Di Marco. Analytic continuation by averaging padé approximants. *Phys. Rev. B*, 93:075104, Feb 2016. doi: 10.1103/PhysRevB.93.075104. URL <https://link.aps.org/doi/10.1103/PhysRevB.93.075104>.
- [83] C. Lawson and R. Hanson. *Solving Least Squares Problems*. Society for Industrial and Applied Mathematics, 1995. doi: 10.1137/1.9781611971217. URL <https://epubs.siam.org/doi/abs/10.1137/1.9781611971217>.
- [84] M. Jarrell and J.E. Gubernatis. Bayesian inference and the analytic continuation of imaginary-time quantum monte carlo data. *Physics Reports*, 269(3):133 – 195, 1996. ISSN 0370-1573. doi: [https://doi.org/10.1016/0370-1573\(95\)00074-7](https://doi.org/10.1016/0370-1573(95)00074-7). URL <http://www.sciencedirect.com/science/article/pii/0370157395000747>.
- [85] R. K. Bryan. Maximum entropy analysis of oversampled data problems. *European Biophysics Journal*, 18(3):165–174, Apr 1990. ISSN 1432-1017. doi: 10.1007/BF02427376. URL <https://doi.org/10.1007/BF02427376>.
- [86] A. W. Sandvik. Stochastic method for analytic continuation of quantum monte carlo data. *Phys. Rev. B*, 57:10287–10290, May 1998. doi: 10.1103/PhysRevB.57.10287. URL <https://link.aps.org/doi/10.1103/PhysRevB.57.10287>.
- [87] K. S. D. Beach. Identifying the maximum entropy method as a special limit of stochastic analytic continuation. *arXiv e-prints*, art. cond-mat/0403055, Mar 2004.
- [88] I. Krivenko and M. Harland. Triqs/som: Implementation of the stochastic optimization

- method for analytic continuation. *Computer Physics Communications*, 2019. ISSN 0010-4655. doi: <https://doi.org/10.1016/j.cpc.2019.01.021>. URL <http://www.sciencedirect.com/science/article/pii/S0010465519300402>.
- [89] P. Werner, S. Hoshino, and H. Shinaoka. Spin-freezing perspective on cuprates. *Phys. Rev. B*, 94:245134, Dec 2016. doi: 10.1103/PhysRevB.94.245134. URL <https://link.aps.org/doi/10.1103/PhysRevB.94.245134>.
- [90] J. L. Wagner, B. A. Hunter, D. G. Hinks, and J. D. Jorgensen. Structure and superconductivity of $\text{HgBa}_2\text{Ca}_2\text{Cu}_3\text{O}_{8+\delta}$. *Phys. Rev. B*, 51:15407–15414, Jun 1995. doi: 10.1103/PhysRevB.51.15407. URL <https://link.aps.org/doi/10.1103/PhysRevB.51.15407>.
- [91] J. L. Tallon, R. G. Buckley, P. W. Gilberd, M. R. Presland, I. W. M. Brown, M. E. Bowden, L. A. Christian, and R. Goguel. High- T_c superconducting phases in the series $\text{Bi}_2.1(\text{Ca}, \text{Sr})_n\text{Cu}_n\text{O}_{2n+4+d}$. *Nature*, 333(6169):153–156, 1988. ISSN 1476-4687. doi: 10.1038/333153a0. URL <https://doi.org/10.1038/333153a0>.
- [92] J. P. Franck, S. Harker, and J. H. Brewer. Copper and oxygen isotope effects in $\text{La}_{2-x}\text{Sr}_x\text{CuO}_4$. *Phys. Rev. Lett.*, 71:283–286, Jul 1993. doi: 10.1103/PhysRevLett.71.283. URL <https://link.aps.org/doi/10.1103/PhysRevLett.71.283>.
- [93] V. J. Emery. Theory of high- T_c superconductivity in oxides. *Phys. Rev. Lett.*, 58:2794–2797, Jun 1987. doi: 10.1103/PhysRevLett.58.2794. URL <https://link.aps.org/doi/10.1103/PhysRevLett.58.2794>.
- [94] F. C. Zhang and T. M. Rice. Effective hamiltonian for the superconducting Cu oxides. *Phys. Rev. B*, 37:3759–3761, Mar 1988. doi: 10.1103/PhysRevB.37.3759. URL <https://link.aps.org/doi/10.1103/PhysRevB.37.3759>.
- [95] J. Zaanen, G. A. Sawatzky, and J. W. Allen. Band gaps and electronic structure of transition-metal compounds. *Phys. Rev. Lett.*, 55:418–421, Jul 1985. doi: 10.1103/PhysRevLett.55.418. URL <https://link.aps.org/doi/10.1103/PhysRevLett.55.418>.
- [96] P. W. Anderson. The resonating valence bond state in La_2CuO_4 and superconductivity. *Science*, 235(4793):1196–1198, 1987. ISSN 0036-8075. doi: 10.1126/science.235.4793.1196. URL <https://science.sciencemag.org/content/235/4793/1196>.
- [97] K. P. Daly, W. D. Dozier, J. F. Burch, S. B. Coons, R. Hu, C. E. Platt, and R. W. Simon. Substrate step-edge $\text{YBa}_2\text{Cu}_3\text{O}_7$ rf squids. *Applied Physics Letters*, 58(5):543–545, 1991. doi: 10.1063/1.104581. URL <https://doi.org/10.1063/1.104581>.
- [98] C. C. Tsuei and J. R. Kirtley. Pairing symmetry in cuprate superconductors. *Rev. Mod. Phys.*, 72:969–1016, Oct 2000. doi: 10.1103/RevModPhys.72.969. URL <https://link.aps.org/doi/10.1103/RevModPhys.72.969>.
- [99] Y. Wang, L. Li, and N. P. Ong. Nernst effect in high- T_c superconductors. *Phys. Rev. B*, 73:024510, Jan 2006. doi: 10.1103/PhysRevB.73.024510. URL <https://link.aps.org/doi/10.1103/PhysRevB.73.024510>.
- [100] K. Behnia and H. Aubin. Nernst effect in metals and superconductors: a review of concepts and experiments. *Reports on Progress in Physics*, 79(4):046502, Mar 2016. doi: 10.1088/0034-4885/79/4/046502. URL <https://doi.org/10.1088/0034-4885/79/4/046502>.
- [101] X. Zhou, D. C. Peets, B. Morgan, W. A. Huttema, N. C. Murphy, E. Thewalt, C. J. S. Truncik, P. J. Turner, A. J. Koenig, J. R. Waldram, A. Hosseini, Ruixing Liang, D. A. Bonn, W. N. Hardy, and D. M. Broun. Logarithmic upturn in low-temperature electronic transport

- as a signature of d -wave order in cuprate superconductors. *Phys. Rev. Lett.*, 121:267004, Dec 2018. doi: 10.1103/PhysRevLett.121.267004. URL <https://link.aps.org/doi/10.1103/PhysRevLett.121.267004>.
- [102] O. Cyr-Choinière, R. Daou, F. Laliberté, C. Collignon, S. Badoux, D. LeBoeuf, J. Chang, B. J. Ramshaw, D. A. Bonn, W. N. Hardy, R. Liang, J.-Q. Yan, J.-G. Cheng, J.-S. Zhou, J. B. Goodenough, S. Pyon, T. Takayama, H. Takagi, N. Doiron-Leyraud, and L. Taillefer. Pseudogap temperature T^* of cuprate superconductors from the nernst effect. *Phys. Rev. B*, 97:064502, Feb 2018. doi: 10.1103/PhysRevB.97.064502. URL <https://link.aps.org/doi/10.1103/PhysRevB.97.064502>.
- [103] T. Timusk and B. Statt. The pseudogap in high-temperature superconductors: an experimental survey. *Reports on Progress in Physics*, 62(1):61–122, Jan 1999. doi: 10.1088/0034-4885/62/1/002. URL <https://doi.org/10.1088/0034-4885/62/1/002>.
- [104] A. Damascelli, Z. Hussain, and Z.-X. Shen. Angle-resolved photoemission studies of the cuprate superconductors. *Rev. Mod. Phys.*, 75:473–541, Apr 2003. doi: 10.1103/RevModPhys.75.473. URL <https://link.aps.org/doi/10.1103/RevModPhys.75.473>.
- [105] W. Wu, M. S. Scheurer, S. Chatterjee, S. Sachdev, A. Georges, and M. Ferrero. Pseudogap and fermi-surface topology in the two-dimensional hubbard model. *Phys. Rev. X*, 8:021048, May 2018. doi: 10.1103/PhysRevX.8.021048. URL <https://link.aps.org/doi/10.1103/PhysRevX.8.021048>.
- [106] I. M. Vishik. Photoemission perspective on pseudogap, superconducting fluctuations, and charge order in cuprates: a review of recent progress. *Reports on Progress in Physics*, 81(6):062501, Apr 2018. doi: 10.1088/1361-6633/aaba96. URL <https://doi.org/10.1088/1361-6633/aaba96>.
- [107] E. Fradkin, S. A. Kivelson, and J. M. Tranquada. Colloquium: Theory of intertwined orders in high temperature superconductors. *Rev. Mod. Phys.*, 87:457–482, May 2015. doi: 10.1103/RevModPhys.87.457. URL <https://link.aps.org/doi/10.1103/RevModPhys.87.457>.
- [108] M. R. Norman, H. Ding, M. Randeria, J. C. Campuzano, T. Yokoya, T. Takeuchi, T. Takahashi, T. Mochiku, K. Kadowaki, P. Guptasarma, and D. G. Hinks. Destruction of the fermi surface in underdoped high- t_c superconductors. *Nature*, 392(6672):157–160, 1998. ISSN 1476-4687. doi: 10.1038/32366. URL <https://doi.org/10.1038/32366>.
- [109] S. Sachdev. *Quantum Phase Transitions*. Cambridge University Press, 2 edition, 2011. doi: 10.1017/CBO9780511973765.
- [110] L. Savary and L. Balents. Quantum spin liquids: a review. *Reports on Progress in Physics*, 80(1):016502, Nov 2016. doi: 10.1088/0034-4885/80/1/016502. URL <https://doi.org/10.1088/0034-4885/80/1/016502>.
- [111] L. Balents. Spin liquids in frustrated magnets. *Nature*, 464:199 EP –, Mar 2010. URL <https://doi.org/10.1038/nature08917>.
- [112] C. M. Varma, P. B. Littlewood, S. Schmitt-Rink, E. Abrahams, and A. E. Ruckenstein. Phenomenology of the normal state of cu-o high-temperature superconductors. *Phys. Rev. Lett.*, 63:1996–1999, Oct 1989. doi: 10.1103/PhysRevLett.63.1996. URL <https://link.aps.org/doi/10.1103/PhysRevLett.63.1996>.
- [113] J. Zaanen. Planckian dissipation, minimal viscosity and the transport in cuprate strange metals. *SciPost Phys.*, 6:61, 2019. doi: 10.21468/SciPostPhys.6.5.061. URL <https://>

scipost.org/10.21468/SciPostPhys.6.5.061.

- [114] M. Platé, J. D. F. Mottershead, I. S. Elfimov, D. C. Peets, R. Liang, D. A. Bonn, W. N. Hardy, S. Chiuzaian, M. Falub, M. Shi, L. Patthey, and A. Damascelli. Fermi surface and quasiparticle excitations of overdoped $\text{t}_2\text{ba}_2\text{cuo}_{6+\delta}$. *Phys. Rev. Lett.*, 95:077001, Aug 2005. doi: 10.1103/PhysRevLett.95.077001. URL <https://link.aps.org/doi/10.1103/PhysRevLett.95.077001>.
- [115] R. Comin, A. Frano, M. M. Yee, Y. Yoshida, H. Eisaki, E. Schierle, E. Weschke, R. Sutarto, F. He, A. Soumyanarayanan, Y. He, M. Le Tacon, I. S. Elfimov, J. E. Hoffman, G. A. Sawatzky, B. Keimer, and A. Damascelli. Charge order driven by fermi-arc instability in $\text{bi}_2\text{sr}_2\text{-xlaxcuo}_6+\hat{\text{I}}\hat{\text{Z}}$. *Science*, 343(6169):390–392, 2014. ISSN 0036-8075. doi: 10.1126/science.1242996. URL <https://science.sciencemag.org/content/343/6169/390>.
- [116] H.-C. Jiang and T. P. Devereaux. Superconductivity in the Hubbard model and its interplay with charge stripes and next-nearest hopping t' . *arXiv e-prints*, art. arXiv:1806.01465, June 2018.
- [117] H. Bragança, S. Sakai, M. C. O. Aguiar, and M. Civelli. Correlation-driven lifshitz transition at the emergence of the pseudogap phase in the two-dimensional hubbard model. *Phys. Rev. Lett.*, 120:067002, Feb 2018. doi: 10.1103/PhysRevLett.120.067002. URL <https://link.aps.org/doi/10.1103/PhysRevLett.120.067002>.
- [118] E. Pavarini, I. Dasgupta, T. Saha-Dasgupta, O. Jepsen, and O. K. Andersen. Band-structure trend in hole-doped cuprates and correlation with t_{cmax} . *Phys. Rev. Lett.*, 87:047003, Jul 2001. doi: 10.1103/PhysRevLett.87.047003. URL <https://link.aps.org/doi/10.1103/PhysRevLett.87.047003>.
- [119] O. Nájera, M. Civelli, V. Dobrosavljević, and M. J. Rozenberg. Multiple crossovers and coherent states in a mott-peierls insulator. *Phys. Rev. B*, 97:045108, Jan 2018. doi: 10.1103/PhysRevB.97.045108. URL <https://link.aps.org/doi/10.1103/PhysRevB.97.045108>.
- [120] M. J. Rozenberg, R. Chitra, and G. Kotliar. Finite temperature mott transition in the hubbard model in infinite dimensions. *Phys. Rev. Lett.*, 83:3498–3501, Oct 1999. doi: 10.1103/PhysRevLett.83.3498. URL <https://link.aps.org/doi/10.1103/PhysRevLett.83.3498>.
- [121] P. Seth, I. Krivenko, M. Ferrero, and O. Parcollet. Triqs/cthyb: A continuous-time quantum monte carlo hybridisation expansion solver for quantum impurity problems. *Computer Physics Communications*, 200:274 – 284, 2016. ISSN 0010-4655. doi: <http://dx.doi.org/10.1016/j.cpc.2015.10.023>. URL <http://www.sciencedirect.com/science/article/pii/S001046551500404X>.
- [122] L. Boehnke, H. Hafermann, M. Ferrero, F. Lechermann, and O. Parcollet. Orthogonal polynomial representation of imaginary-time green’s functions. *Phys. Rev. B*, 84:075145, Aug 2011. doi: 10.1103/PhysRevB.84.075145. URL <https://link.aps.org/doi/10.1103/PhysRevB.84.075145>.
- [123] E. Pavarini, S. Biermann, A. Poteryaev, A. I. Lichtenstein, A. Georges, and O. K. Andersen. Mott transition and suppression of orbital fluctuations in orthorhombic $3d^1$ perovskites. *Phys. Rev. Lett.*, 92:176403, Apr 2004. doi: 10.1103/PhysRevLett.92.176403. URL <https://link.aps.org/doi/10.1103/PhysRevLett.92.176403>.
- [124] O. Parcollet, G. Biroli, and G. Kotliar. Cluster dynamical mean field analysis of the mott transition. *Phys. Rev. Lett.*, 92:226402, Jun 2004. doi: 10.1103/PhysRevLett.92.226402. URL <https://link.aps.org/doi/10.1103/PhysRevLett.92.226402>.

- [125] H. Park, K. Haule, and G. Kotliar. Cluster dynamical mean field theory of the mott transition. *Phys. Rev. Lett.*, 101:186403, Oct 2008. doi: 10.1103/PhysRevLett.101.186403. URL <https://link.aps.org/doi/10.1103/PhysRevLett.101.186403>.
- [126] E. Gull, P. Werner, X. Wang, M. Troyer, and A. J. Millis. Local order and the gapped phase of the hubbard model: A plaquette dynamical mean-field investigation. *EPL (Europhysics Letters)*, 84(3):37009, 2008. URL <http://stacks.iop.org/0295-5075/84/i=3/a=37009>.
- [127] M. Harland, M. I. Katsnelson, and A. I. Lichtenstein. Plaquette valence bond theory of high-temperature superconductivity. *Phys. Rev. B*, 94:125133, Sep 2016. doi: 10.1103/PhysRevB.94.125133. URL <http://link.aps.org/doi/10.1103/PhysRevB.94.125133>.
- [128] M. Harland, S. Brener, M. I. Katsnelson, and A. I. Lichtenstein. Exactly solvable model of strongly correlated d -wave superconductivity. *arXiv e-prints*, art. arXiv:1905.12610, May 2019.
- [129] Y. Z. Zhang and Masatoshi Imada. Pseudogap and mott transition studied by cellular dynamical mean-field theory. *Phys. Rev. B*, 76:045108, Jul 2007. doi: 10.1103/PhysRevB.76.045108. URL <https://link.aps.org/doi/10.1103/PhysRevB.76.045108>.
- [130] N. Doiron-Leyraud, C. Proust, D. LeBoeuf, J. Levallois, J.-B. Bonnemaison, R. Liang, D. A. Bonn, W. N. Hardy, and L. Taillefer. Quantum oscillations and the fermi surface in an underdoped high- t_c superconductor. *Nature*, 447:565 EP –, May 2007. URL <http://dx.doi.org/10.1038/nature05872>.
- [131] S. Sachdev. Emergent gauge fields and the high-temperature superconductors. *Philosophical Transactions of the Royal Society A: Mathematical, Physical and Engineering Sciences*, 374(2075):20150248, 2016. doi: 10.1098/rsta.2015.0248. URL <https://royalsocietypublishing.org/doi/abs/10.1098/rsta.2015.0248>.
- [132] B. Kyung, S. S. Kancharla, D. Sénéchal, A.-M. S. Tremblay, M. Civelli, and G. Kotliar. Pseudogap induced by short-range spin correlations in a doped mott insulator. *Phys. Rev. B*, 73:165114, Apr 2006. doi: 10.1103/PhysRevB.73.165114. URL <https://link.aps.org/doi/10.1103/PhysRevB.73.165114>.
- [133] O. Gunnarsson, T. Schäfer, J. P. F. LeBlanc, E. Gull, J. Merino, G. Sangiovanni, G. Rohringer, and A. Toschi. Fluctuation diagnostics of the electron self-energy: Origin of the pseudogap physics. *Phys. Rev. Lett.*, 114:236402, Jun 2015. doi: 10.1103/PhysRevLett.114.236402. URL <https://link.aps.org/doi/10.1103/PhysRevLett.114.236402>.
- [134] M. Civelli, M. Capone, A. Georges, K. Haule, O. Parcollet, T. D. Stanescu, and G. Kotliar. Nodal-antinodal dichotomy and the two gaps of a superconducting doped mott insulator. *Phys. Rev. Lett.*, 100:046402, Jan 2008. doi: 10.1103/PhysRevLett.100.046402. URL <https://link.aps.org/doi/10.1103/PhysRevLett.100.046402>.
- [135] E. Gull and A. J. Millis. Quasiparticle properties of the superconducting state of the two-dimensional hubbard model. *Phys. Rev. B*, 91:085116, Feb 2015. doi: 10.1103/PhysRevB.91.085116. URL <https://link.aps.org/doi/10.1103/PhysRevB.91.085116>.
- [136] E. Gull, O. Parcollet, and A. J. Millis. Superconductivity and the pseudogap in the two-dimensional hubbard model. *Phys. Rev. Lett.*, 110:216405, May 2013. doi: 10.1103/PhysRevLett.110.216405. URL <https://link.aps.org/doi/10.1103/PhysRevLett.110.216405>.
- [137] G. Sordi, P. Sémon, K. Haule, and A.-M. S. Tremblay. Strong coupling superconductivity,

- pseudogap, and mott transition. *Phys. Rev. Lett.*, 108:216401, May 2012. doi: 10.1103/PhysRevLett.108.216401. URL <https://link.aps.org/doi/10.1103/PhysRevLett.108.216401>.
- [138] G. Sordi, K. Haule, and A.-M. S. Tremblay. Finite doping signatures of the mott transition in the two-dimensional hubbard model. *Phys. Rev. Lett.*, 104:226402, Jun 2010. doi: 10.1103/PhysRevLett.104.226402. URL <https://link.aps.org/doi/10.1103/PhysRevLett.104.226402>.
- [139] L. Fratino, P. Sémon, G. Sordi, and A.-M. S. Tremblay. Pseudogap and superconductivity in two-dimensional doped charge-transfer insulators. *Phys. Rev. B*, 93:245147, Jun 2016. doi: 10.1103/PhysRevB.93.245147. URL <https://link.aps.org/doi/10.1103/PhysRevB.93.245147>.
- [140] T. Ying, R. Mondaini, X. D. Sun, T. Paiva, R. M. Fye, and R. T. Scalettar. Determinant quantum monte carlo study of d -wave pairing in the plaquette hubbard hamiltonian. *Phys. Rev. B*, 90:075121, Aug 2014. doi: 10.1103/PhysRevB.90.075121. URL <https://link.aps.org/doi/10.1103/PhysRevB.90.075121>.
- [141] E. Arrigoni, E. Fradkin, and S. A. Kivelson. Mechanism of high-temperature superconductivity in a striped hubbard model. *Phys. Rev. B*, 69:214519, Jun 2004. doi: 10.1103/PhysRevB.69.214519. URL <https://link.aps.org/doi/10.1103/PhysRevB.69.214519>.
- [142] M. J. Lawler, K. Fujita, Jhinhwan Lee, A. R. Schmidt, Y. Kohsaka, Chung Koo Kim, H. Eisaki, S. Uchida, J. C. Davis, J. P. Sethna, and Eun-Ah Kim. Intra-unit-cell electronic nematicity of the high- T_c copper-oxide pseudogap states. *Nature*, 466:347 EP –, Jul 2010. URL <https://doi.org/10.1038/nature09169>.
- [143] L. Nie, G. Tarjus, and S. A. Kivelson. Quenched disorder and vestigial nematicity in the pseudogap regime of the cuprates. *Proceedings of the National Academy of Sciences*, 111(22):7980–7985, 2014. ISSN 0027-8424. doi: 10.1073/pnas.1406019111. URL <https://www.pnas.org/content/111/22/7980>.
- [144] S. S. Kancharla, B. Kyung, D. Sénéchal, M. Civelli, M. Capone, G. Kotliar, and A.-M. S. Tremblay. Anomalous superconductivity and its competition with antiferromagnetism in doped mott insulators. *Phys. Rev. B*, 77:184516, May 2008. doi: 10.1103/PhysRevB.77.184516. URL <http://link.aps.org/doi/10.1103/PhysRevB.77.184516>.
- [145] A. Foley, S. Verret, A.-M. S. Tremblay, and D. Sénéchal. Coexistence of superconductivity and antiferromagnetism in the hubbard model for cuprates. *Phys. Rev. B*, 99:184510, May 2019. doi: 10.1103/PhysRevB.99.184510. URL <https://link.aps.org/doi/10.1103/PhysRevB.99.184510>.
- [146] L. Fratino, P. Sémon, G. Sordi, and A.-M. S. Tremblay. An organizing principle for two-dimensional strongly correlated superconductivity. *Scientific Reports*, 6:22715–, March 2016. URL <http://dx.doi.org/10.1038/srep22715>.
- [147] E. Altman and A. Auerbach. Plaquette boson-fermion model of cuprates. *Phys. Rev. B*, 65:104508, Feb 2002. doi: 10.1103/PhysRevB.65.104508. URL <https://link.aps.org/doi/10.1103/PhysRevB.65.104508>.
- [148] K. Haule and G. Kotliar. Avoided criticality in near-optimally doped high-temperature superconductors. *Phys. Rev. B*, 76:092503, Sep 2007. doi: 10.1103/PhysRevB.76.092503. URL <http://link.aps.org/doi/10.1103/PhysRevB.76.092503>.

- [149] M. Ferrero, P. S. Cornaglia, L. De Leo, O. Parcollet, G. Kotliar, and A. Georges. Pseudogap opening and formation of fermi arcs as an orbital-selective mott transition in momentum space. *Phys. Rev. B*, 80:064501, Aug 2009. doi: 10.1103/PhysRevB.80.064501. URL <https://link.aps.org/doi/10.1103/PhysRevB.80.064501>.
- [150] J. Merino and O. Gunnarsson. Pseudogap and singlet formation in organic and cuprate superconductors. *Phys. Rev. B*, 89:245130, Jun 2014. doi: 10.1103/PhysRevB.89.245130. URL <https://link.aps.org/doi/10.1103/PhysRevB.89.245130>.
- [151] O. Gunnarsson, J. Merino, T. Schäfer, G. Sangiovanni, G. Rohringer, and A. Toschi. Complementary views on electron spectra: From fluctuation diagnostics to real-space correlations. *Phys. Rev. B*, 97:125134, Mar 2018. doi: 10.1103/PhysRevB.97.125134. URL <https://link.aps.org/doi/10.1103/PhysRevB.97.125134>.
- [152] L. Liu, H. Yao, E. Berg, S. R. White, and S. A. Kivelson. Phases of the infinite u hubbard model on square lattices. *Phys. Rev. Lett.*, 108:126406, Mar 2012. doi: 10.1103/PhysRevLett.108.126406. URL <https://link.aps.org/doi/10.1103/PhysRevLett.108.126406>.
- [153] K. Haule and G. Kotliar. Strongly correlated superconductivity: A plaquette dynamical mean-field theory study. *Phys. Rev. B*, 76:104509, Sep 2007. doi: 10.1103/PhysRevB.76.104509. URL <https://link.aps.org/doi/10.1103/PhysRevB.76.104509>.
- [154] E. Demler, W. Hanke, and S.-C. Zhang. $SO(5)$ theory of antiferromagnetism and superconductivity. *Rev. Mod. Phys.*, 76:909–974, Nov 2004. doi: 10.1103/RevModPhys.76.909. URL <https://link.aps.org/doi/10.1103/RevModPhys.76.909>.
- [155] U. Fano. Effects of configuration interaction on intensities and phase shifts. *Phys. Rev.*, 124:1866–1878, Dec 1961. doi: 10.1103/PhysRev.124.1866. URL <https://link.aps.org/doi/10.1103/PhysRev.124.1866>.
- [156] Y. S. Joe, A. M. Satanin, and C. S. Kim. Classical analogy of fano resonances. *Physica Scripta*, 74(2):259–266, Jul 2006. doi: 10.1088/0031-8949/74/2/020. URL <https://doi.org/10.1088/0031-8949/74/2/020>.
- [157] E. Gull and A. J. Millis. Pairing glue in the two-dimensional hubbard model. *Phys. Rev. B*, 90:041110, Jul 2014. doi: 10.1103/PhysRevB.90.041110. URL <https://link.aps.org/doi/10.1103/PhysRevB.90.041110>.
- [158] A. Reymbaut, M. Charlebois, M. F. Asiani, L. Fratino, P. Sémon, G. Sordi, and A.-M. S. Tremblay. Antagonistic effects of nearest-neighbor repulsion on the superconducting pairing dynamics in the doped mott insulator regime. *Phys. Rev. B*, 94:155146, Oct 2016. doi: 10.1103/PhysRevB.94.155146. URL <https://link.aps.org/doi/10.1103/PhysRevB.94.155146>.
- [159] P. Coleman and A. J. Schofield. Quantum criticality. *Nature*, 433(7023):226–229, 2005. ISSN 1476-4687. doi: 10.1038/nature03279. URL <https://doi.org/10.1038/nature03279>.
- [160] S. Sachdev and B. Keimer. Quantum criticality. *Physics Today*, 64(2):29–35, 2011. doi: 10.1063/1.3554314. URL <https://doi.org/10.1063/1.3554314>.
- [161] L. Amico, R. Fazio, A. Osterloh, and V. Vedral. Entanglement in many-body systems. *Rev. Mod. Phys.*, 80:517–576, May 2008. doi: 10.1103/RevModPhys.80.517. URL <https://link.aps.org/doi/10.1103/RevModPhys.80.517>.
- [162] M. A. Nielsen and I. L. Chuang. *Quantum Computation and Quantum Information: 10th Anniversary Edition*. Cambridge University Press, 2010. doi: 10.1017/CBO9780511976667.

-
- [163] A. Osterloh, L. Amico, G. Falci, and R. Fazio. Scaling of entanglement close to a quantum phase transition. *Nature*, 416(6881):608–610, 2002. ISSN 1476-4687. doi: 10.1038/416608a. URL <https://doi.org/10.1038/416608a>.
- [164] G. Vidal, J. I. Latorre, E. Rico, and A. Kitaev. Entanglement in quantum critical phenomena. *Phys. Rev. Lett.*, 90:227902, Jun 2003. doi: 10.1103/PhysRevLett.90.227902. URL <https://link.aps.org/doi/10.1103/PhysRevLett.90.227902>.
- [165] B. Groisman, S. Popescu, and A. Winter. Quantum, classical, and total amount of correlations in a quantum state. *Phys. Rev. A*, 72:032317, Sep 2005. doi: 10.1103/PhysRevA.72.032317. URL <https://link.aps.org/doi/10.1103/PhysRevA.72.032317>.
- [166] M. A. Valdez, D. Jaschke, D. L. Vargas, and L. D. Carr. Quantifying complexity in quantum phase transitions via mutual information complex networks. *Phys. Rev. Lett.*, 119:225301, Nov 2017. doi: 10.1103/PhysRevLett.119.225301. URL <https://link.aps.org/doi/10.1103/PhysRevLett.119.225301>.
- [167] B. Sundar, M. A. Valdez, L. D. Carr, and K. R. A. Hazzard. Complex-network description of thermal quantum states in the ising spin chain. *Phys. Rev. A*, 97:052320, May 2018. doi: 10.1103/PhysRevA.97.052320. URL <https://link.aps.org/doi/10.1103/PhysRevA.97.052320>.
- [168] A. A. Bagrov, M. Danilov, S. Brener, M. Harland, A. I. Lichtenstein, and M. I. Katsnelson. Detecting the quantum critical point in high-temperature superconducting cuprates via complex network theory. *arXiv e-prints*, art. arXiv:1904.11463, Apr 2019. URL <https://arxiv.org/abs/1904.11463>.
- [169] V. J. Emery and S. A. Kivelson. Importance of phase fluctuations in superconductors with small superfluid density. *Nature*, 374:434 EP –, Mar 1995. URL <http://dx.doi.org/10.1038/374434a0>.
- [170] A. A. Abrikosov. On the magnetic properties of superconductors of the second group. *Sov. Phys. JETP*, 5:1174–1182, 1957. URL <https://ci.nii.ac.jp/naid/10029655993/en/>.
- [171] C. C. Homes, S. V. Dordevic, M. Strongin, D. A. Bonn, Ruixing Liang, W. N. Hardy, Seiki Komiya, Yoichi Ando, G. Yu, N. Kaneko, X. Zhao, M. Greven, D. N. Basov, and T. Timusk. A universal scaling relation in high-temperature superconductors. *Nature*, 430:539 EP –, Jul 2004. URL <https://doi.org/10.1038/nature02673>.
- [172] L. Benfatto, C. Castellani, and T. Giamarchi. Kosterlitz-thouless behavior in layered superconductors: The role of the vortex core energy. *Phys. Rev. Lett.*, 98:117008, Mar 2007. doi: 10.1103/PhysRevLett.98.117008. URL <https://link.aps.org/doi/10.1103/PhysRevLett.98.117008>.
- [173] Richard P. (Richard Phillips) 1918-1988 Feynman. *The Feynman lectures on physics*. Reading, Mass. : Addison-Wesley Pub. Co., c1963-1965., 1965 1963. URL <https://search.library.wisc.edu/catalog/999468136802121>. Vol. 2 has subtitle: The electromagnetic field; 3 has subtitle: Quantum mechanics.;Includes bibliographical references and indexes.
- [174] Royal Swedish-Academy. Topological phase transitions and topological phases of matter. *Scientific Background on the Nobel Prize in Physics 2016*, 2016. URL <https://www.nobelprize.org>.
- [175] N. Nagaosa and S. Heusler. *Quantum Field Theory in Condensed Matter Physics*. Texts and monographs in physics. Springer, 1999. ISBN 9783540655374. URL <https://doi.org/10.1007/978-3-540-65537-4>.

- 1007/978-3-662-03774-4.
- [176] D. R. Nelson and J. M. Kosterlitz. Universal jump in the superfluid density of two-dimensional superfluids. *Phys. Rev. Lett.*, 39:1201–1205, Nov 1977. doi: 10.1103/PhysRevLett.39.1201. URL <https://link.aps.org/doi/10.1103/PhysRevLett.39.1201>.
- [177] D. J. Bishop and J. D. Reppy. Study of the superfluid transition in two-dimensional ^4He films. *Phys. Rev. Lett.*, 40:1727–1730, Jun 1978. doi: 10.1103/PhysRevLett.40.1727. URL <https://link.aps.org/doi/10.1103/PhysRevLett.40.1727>.
- [178] G. Blatter, M. V. Feigel'man, V. B. Geshkenbein, A. I. Larkin, and V. M. Vinokur. Vortices in high-temperature superconductors. *Rev. Mod. Phys.*, 66:1125–1388, Oct 1994. doi: 10.1103/RevModPhys.66.1125. URL <https://link.aps.org/doi/10.1103/RevModPhys.66.1125>.
- [179] M. R. Beasley, J. E. Mooij, and T. P. Orlando. Possibility of vortex-antivortex pair dissociation in two-dimensional superconductors. *Phys. Rev. Lett.*, 42:1165–1168, Apr 1979. doi: 10.1103/PhysRevLett.42.1165. URL <https://link.aps.org/doi/10.1103/PhysRevLett.42.1165>.
- [180] Y. J. Uemura, G. M. Luke, B. J. Sternlieb, J. H. Brewer, J. F. Carolan, W. N. Hardy, R. Kadono, J. R. Kempton, R. F. Kiefl, S. R. Kreitzman, P. Mulhern, T. M. Riseman, D. Li. Williams, B. X. Yang, S. Uchida, H. Takagi, J. Gopalakrishnan, A. W. Sleight, M. A. Subramanian, C. L. Chien, M. Z. Cieplak, Gang Xiao, V. Y. Lee, B. W. Statt, C. E. Stronach, W. J. Kossler, and X. H. Yu. Universal correlations between T_c and $\frac{n_s}{m^*}$ (carrier density over effective mass) in high- T_c cuprate superconductors. *Phys. Rev. Lett.*, 62:2317–2320, May 1989. doi: 10.1103/PhysRevLett.62.2317. URL <https://link.aps.org/doi/10.1103/PhysRevLett.62.2317>.
- [181] F. Mahmood, X. He, I. Božović, and N. P. Armitage. Locating the missing superconducting electrons in the overdoped cuprates $\text{La}_{2-x}\text{Sr}_x\text{CuO}_4$. *Phys. Rev. Lett.*, 122:027003, Jan 2019. doi: 10.1103/PhysRevLett.122.027003. URL <https://link.aps.org/doi/10.1103/PhysRevLett.122.027003>.
- [182] B.D. Josephson. Possible new effects in superconductive tunnelling. *Physics Letters*, 1(7): 251 – 253, 1962. ISSN 0031-9163. doi: [https://doi.org/10.1016/0031-9163\(62\)91369-0](https://doi.org/10.1016/0031-9163(62)91369-0). URL <http://www.sciencedirect.com/science/article/pii/0031916362913690>.
- [183] X.G. Wen. *Quantum Field Theory of Many-Body Systems: From the Origin of Sound to an Origin of Light and Electrons: From the Origin of Sound to an Origin of Light and Electrons*. Oxford Graduate Texts. OUP Oxford, 2004. ISBN 9780198530947. URL <https://www.oxfordscholarship.com/view/10.1093/acprof:oso/9780199227259.001.0001/acprof-9780199227259>.
- [184] M. Harland, S. Brener, A. I. Lichtenstein, and M. I. Katsnelson. Josephson lattice model for phase fluctuations of local pairs in copper oxide superconductors. *Phys. Rev. B*, 100:024510, Jul 2019. doi: 10.1103/PhysRevB.100.024510. URL <https://link.aps.org/doi/10.1103/PhysRevB.100.024510>.
- [185] A. L. Solovjov, E. V. Petrenko, L. V. Omelchenko, R. V. Vovk, I. L. Goulatis, and A. Chroneos. Effect of annealing on a pseudogap state in untwinned $\text{YBa}_2\text{Cu}_3\text{O}_{7-d}$ single crystals. *Scientific Reports*, 9(1):9274, 2019. ISSN 2045-2322. doi: 10.1038/s41598-019-45286-w. URL <https://doi.org/10.1038/s41598-019-45286-w>.
- [186] S. Rajasekaran, E. Casandruc, Y. Laplace, D. Nicoletti, G. D. Gu, S. R. Clark, D. Jaksch, and A. Cavalleri. Parametric amplification of a superconducting plasma wave. *Nature Physics*, 12:1012 EP –, Jul 2016. URL <https://doi.org/10.1038/nphys3819>.

-
- [187] J. Okamoto, A. Cavalleri, and L. Mathey. Theory of enhanced interlayer tunneling in optically driven high- T_c superconductors. *Phys. Rev. Lett.*, 117:227001, Nov 2016. doi: 10.1103/PhysRevLett.117.227001. URL <https://link.aps.org/doi/10.1103/PhysRevLett.117.227001>.
- [188] F. Hund. Zur deutung verwickelter spektren, insbesondere der elemente scandium bis nickel. *Zeitschrift für Physik*, 33(1):345–371, Dec 1925. ISSN 0044-3328. doi: 10.1007/BF01328319. URL <https://doi.org/10.1007/BF01328319>.
- [189] Weiss, P. L’hypothèse du champ moléculaire et la propriété ferromagnétique. *J. Phys. Theor. Appl.*, 6(1):661–690, 1907. doi: 10.1051/jphystap:019070060066100. URL <https://doi.org/10.1051/jphystap:019070060066100>.
- [190] A. I. Lichtenstein, M. I. Katsnelson, and G. Kotliar. Finite-temperature magnetism of transition metals: An ab initio dynamical mean-field theory. *Phys. Rev. Lett.*, 87:067205, Jul 2001. doi: 10.1103/PhysRevLett.87.067205. URL <https://link.aps.org/doi/10.1103/PhysRevLett.87.067205>.
- [191] C. G. Shull and J. S. Smart. Detection of antiferromagnetism by neutron diffraction. *Phys. Rev.*, 76:1256–1257, Oct 1949. doi: 10.1103/PhysRev.76.1256.2. URL <https://link.aps.org/doi/10.1103/PhysRev.76.1256.2>.
- [192] J. C. Slater. Magnetic effects and the hartree-fock equation. *Phys. Rev.*, 82:538–541, May 1951. doi: 10.1103/PhysRev.82.538. URL <https://link.aps.org/doi/10.1103/PhysRev.82.538>.
- [193] T. Pruschke and R. Zitzler. From slater to mott–heisenberg physics: the antiferromagnetic phase of the hubbard model. *Journal of Physics: Condensed Matter*, 15(46):7867–7879, Nov 2003. doi: 10.1088/0953-8984/15/46/006. URL <https://doi.org/10.1088/0953-8984/15/46/006>.
- [194] A.I. Liechtenstein, M.I. Katsnelson, V.P. Antropov, and V.A. Gubanov. Local spin density functional approach to the theory of exchange interactions in ferromagnetic metals and alloys. *Journal of Magnetism and Magnetic Materials*, 67(1):65 – 74, 1987. ISSN 0304-8853. doi: [https://doi.org/10.1016/0304-8853\(87\)90721-9](https://doi.org/10.1016/0304-8853(87)90721-9). URL <http://www.sciencedirect.com/science/article/pii/0304885387907219>.
- [195] E. Pavarini, E. Koch, and U. Schollwöck, editors. *Emergent Phenomena in Correlated Matter*, volume 3 of *Modeling and Simulation*. Forschungszentrum Jülich Zentralbibliothek, Verlag, Jülich, Sep 2013. ISBN 978-3-89336-884-6. URL <http://juser.fz-juelich.de/record/137827>.
- [196] M. I. Katsnelson and A. I. Lichtenstein. First-principles calculations of magnetic interactions in correlated systems. *Phys. Rev. B*, 61:8906–8912, Apr 2000. doi: 10.1103/PhysRevB.61.8906. URL <https://link.aps.org/doi/10.1103/PhysRevB.61.8906>.
- [197] H. A. Mook and R. M. Nicklow. Neutron scattering investigation of the magnetic excitations in iron. *Phys. Rev. B*, 7:336–342, Jan 1973. doi: 10.1103/PhysRevB.7.336. URL <https://link.aps.org/doi/10.1103/PhysRevB.7.336>.
- [198] R. Chitra and G. Kotliar. Effect of long range coulomb interactions on the mott transition. *Phys. Rev. Lett.*, 84:3678–3681, Apr 2000. doi: 10.1103/PhysRevLett.84.3678. URL <https://link.aps.org/doi/10.1103/PhysRevLett.84.3678>.
- [199] M. Schüler, M. Rösner, T. O. Wehling, A. I. Lichtenstein, and M. I. Katsnelson. Optimal hubbard models for materials with nonlocal coulomb interactions: Graphene, silicene, and

- benzene. *Phys. Rev. Lett.*, 111:036601, Jul 2013. doi: 10.1103/PhysRevLett.111.036601. URL <https://link.aps.org/doi/10.1103/PhysRevLett.111.036601>.
- [200] E. A. Stepanov, S. Brener, F. Krien, M. Harland, A. I. Lichtenstein, and M. I. Katsnelson. Effective heisenberg model and exchange interaction for strongly correlated systems. *Phys. Rev. Lett.*, 121:037204, Jul 2018. doi: 10.1103/PhysRevLett.121.037204. URL <https://link.aps.org/doi/10.1103/PhysRevLett.121.037204>.
- [201] A.N. Rubtsov, M.I. Katsnelson, and A.I. Lichtenstein. Dual boson approach to collective excitations in correlated fermionic systems. *Annals of Physics*, 327(5):1320 – 1335, 2012. ISSN 0003-4916. doi: <https://doi.org/10.1016/j.aop.2012.01.002>. URL <http://www.sciencedirect.com/science/article/pii/S0003491612000164>.
- [202] Y. Tokura and N. Nagaosa. Orbital physics in transition-metal oxides. *Science*, 288(5465):462–468, 2000. ISSN 0036-8075. doi: 10.1126/science.288.5465.462. URL <https://science.sciencemag.org/content/288/5465/462>.
- [203] S. V. Streltsov and D. I. Khomskii. Orbital physics in transition metal compounds: new trends. *Physics-Uspokhi*, 60(11):1121–1146, Nov 2017. doi: 10.3367/ufne.2017.08.038196. URL <https://doi.org/10.3367/ufne.2017.08.038196>.
- [204] C. Zener. Interaction between the d -shells in the transition metals. ii. ferromagnetic compounds of manganese with perovskite structure. *Phys. Rev.*, 82:403–405, May 1951. doi: 10.1103/PhysRev.82.403. URL <https://link.aps.org/doi/10.1103/PhysRev.82.403>.
- [205] S. Nishimoto and Y. Ohta. Double exchange ferromagnetism in the peierls insulator state. *Phys. Rev. Lett.*, 109:076401, Aug 2012. doi: 10.1103/PhysRevLett.109.076401. URL <https://link.aps.org/doi/10.1103/PhysRevLett.109.076401>.
- [206] Y. Tokura and Y. Tomioka. Colossal magnetoresistive manganites. *Journal of Magnetism and Magnetic Materials*, 200(1):1 – 23, 1999. ISSN 0304-8853. doi: [https://doi.org/10.1016/S0304-8853\(99\)00352-2](https://doi.org/10.1016/S0304-8853(99)00352-2). URL <http://www.sciencedirect.com/science/article/pii/S0304885399003522>.
- [207] E. Pavarini, E. Koch, R. Scalettar, and R. Martin, editors. *The Physics of Correlated Insulators, Metals, and Superconductors*, volume 7 of *Schriften des Forschungszentrums Jülich Reihe Modeling and Simulation*. Forschungszentrum Jülich GmbH Zentralbibliothek, Verlag, Jülich, Sep 2017. ISBN 978-3-95806-224-5. URL <http://juser.fz-juelich.de/record/837488>.
- [208] P. Werner, E. Gull, M. Troyer, and A. J. Millis. Spin freezing transition and non-fermi-liquid self-energy in a three-orbital model. *Phys. Rev. Lett.*, 101:166405, Oct 2008. doi: 10.1103/PhysRevLett.101.166405. URL <https://link.aps.org/doi/10.1103/PhysRevLett.101.166405>.
- [209] L. de’ Medici, J. Mravlje, and A. Georges. Janus-faced influence of hund’s rule coupling in strongly correlated materials. *Phys. Rev. Lett.*, 107:256401, Dec 2011. doi: 10.1103/PhysRevLett.107.256401. URL <https://link.aps.org/doi/10.1103/PhysRevLett.107.256401>.
- [210] J. Kanamori. Electron correlation and ferromagnetism of transition metals. *Progress of Theoretical Physics*, 30(3):275–289, 1963. doi: 10.1143/PTP.30.275. URL <http://dx.doi.org/10.1143/PTP.30.275>.
- [211] V. I. Anisimov, I. A. Nekrasov, D. E. Kondakov, T. M. Rice, and M. Sigrist. Orbital-selective mott-insulator transition in $\text{Ca}_2\text{-xSr}_x\text{RuO}_4$. *The European Physical Journal B - Condensed*

- Matter and Complex Systems*, 25(2):191–201, Jan 2002. ISSN 1434-6036. doi: 10.1140/epjb/e20020021. URL <https://doi.org/10.1140/epjb/e20020021>.
- [212] L. de’ Medici, S. R. Hassan, M. Capone, and X. Dai. Orbital-selective mott transition out of band degeneracy lifting. *Phys. Rev. Lett.*, 102:126401, Mar 2009. doi: 10.1103/PhysRevLett.102.126401. URL <https://link.aps.org/doi/10.1103/PhysRevLett.102.126401>.
- [213] L. de’ Medici. Hund’s coupling and its key role in tuning multiorbital correlations. *Phys. Rev. B*, 83:205112, May 2011. doi: 10.1103/PhysRevB.83.205112. URL <https://link.aps.org/doi/10.1103/PhysRevB.83.205112>.
- [214] S. Hoshino and P. Werner. Electronic orders in multiorbital hubbard models with lifted orbital degeneracy. *Phys. Rev. B*, 93:155161, Apr 2016. doi: 10.1103/PhysRevB.93.155161. URL <https://link.aps.org/doi/10.1103/PhysRevB.93.155161>.
- [215] M. Isobe, E. Ninomiya, A. N. Vasil’ev, and Y. Ueda. Novel phase transition in spin-1/2 linear chain systems: Natisi2o6 and litisi2o6. *Journal of the Physical Society of Japan*, 71(6):1423–1426, 2002. doi: 10.1143/JPSJ.71.1423. URL <https://doi.org/10.1143/JPSJ.71.1423>.
- [216] N. Katayama, M. Uchida, D. Hashizume, S. Niitaka, J. Matsuno, D. Matsumura, Y. Nishihata, J. Mizuki, N. Takeshita, A. Gauzzi, M. Nohara, and H. Takagi. Anomalous metallic state in the vicinity of metal to valence-bond solid insulator transition in LiV_2O_5 . *Phys. Rev. Lett.*, 103:146405, Oct 2009. doi: 10.1103/PhysRevLett.103.146405. URL <https://link.aps.org/doi/10.1103/PhysRevLett.103.146405>.
- [217] J. Terzic, J. C. Wang, F. Ye, W. H. Song, S. J. Yuan, S. Aswartham, L. E. DeLong, S. V. Streltsov, D. I. Khomskii, and G. Cao. Coexisting charge and magnetic orders in the dimer-chain iridate $\text{Ba}_5\text{AlIr}_2\text{O}_{11}$. *Phys. Rev. B*, 91:235147, Jun 2015. doi: 10.1103/PhysRevB.91.235147. URL <https://link.aps.org/doi/10.1103/PhysRevB.91.235147>.
- [218] M. S. Senn, S. A. J. Kimber, A. M. Arevalo Lopez, A. H. Hill, and J. P. Attfield. Spin orders and lattice distortions of geometrically frustrated 6h-perovskites $\text{Ba}_3\text{B}'\text{Ru}_2\text{O}_9$ ($\text{B}' = \text{La}^{3+}$, Nd^{3+} , and Y^{3+}). *Phys. Rev. B*, 87:134402, Apr 2013. doi: 10.1103/PhysRevB.87.134402. URL <https://link.aps.org/doi/10.1103/PhysRevB.87.134402>.
- [219] D. Ziat, A. A. Aczel, R. Sinclair, Q. Chen, H. D. Zhou, T. J. Williams, M. B. Stone, A. Verrier, and J. A. Quilliam. Frustrated spin- $\frac{1}{2}$ molecular magnetism in the mixed-valence antiferromagnets $\text{Ba}_3\text{mRu}_2\text{O}_9$ ($m = \text{In}, \text{Y}, \text{Lu}$). *Phys. Rev. B*, 95:184424, May 2017. doi: 10.1103/PhysRevB.95.184424. URL <https://link.aps.org/doi/10.1103/PhysRevB.95.184424>.
- [220] K. I. Kugel, D. I. Khomskii, A. O. Sboychakov, and S. V. Streltsov. Spin-orbital interaction for face-sharing octahedra: Realization of a highly symmetric $\text{su}(4)$ model. *Phys. Rev. B*, 91:155125, Apr 2015. doi: 10.1103/PhysRevB.91.155125. URL <https://link.aps.org/doi/10.1103/PhysRevB.91.155125>.
- [221] S. V. Streltsov and D. I. Khomskii. Covalent bonds against magnetism in transition metal compounds. *Proceedings of the National Academy of Sciences*, 113(38):10491–10496, 2016. ISSN 0027-8424. doi: 10.1073/pnas.1606367113. URL <https://www.pnas.org/content/113/38/10491>.
- [222] M. Harland, A. I. Poteryaev, S. V. Streltsov, and A. I. Lichtenstein. Electronic correlations and competing orders in multiorbital dimers: A cluster dmft study. *Phys. Rev. B*, 99:045115, Jan 2019. doi: 10.1103/PhysRevB.99.045115. URL <https://link.aps.org/doi/10.1103/PhysRevB.99.045115>.

- [223] A. P. Ramirez, A. Hayashi, R. J. Cava, R. Siddharthan, and B. S. Shastry. Zero-point entropy in 'spin ice'. *Nature*, 399(6734):333–335, 1999. ISSN 1476-4687. doi: 10.1038/20619. URL <https://doi.org/10.1038/20619>.
- [224] S. T. Bramwell and M. J. P. Gingras. Spin ice state in frustrated magnetic pyrochlore materials. *Science*, 294(5546):1495–1501, 2001. ISSN 0036-8075. doi: 10.1126/science.1064761. URL <https://science.sciencemag.org/content/294/5546/1495>.
- [225] D. Grohol, K. Matan, J.-H. Cho, S.-H. Lee, J. W. Lynn, D. G. Nocera, and Y. S. Lee. Spin chirality on a two-dimensional frustrated lattice. *Nature Materials*, 4(4):323–328, 2005. ISSN 1476-4660. doi: 10.1038/nmat1353. URL <https://doi.org/10.1038/nmat1353>.
- [226] A. Zorko, M. Pregelj, M. Gomilsek, M. Klanjsek, O. Zaharko, W. Sun, and J. X. Mi. Negative-vector-chirality 120° spin structure in the defect- and distortion-free quantum kagome antiferromagnet $\text{YCu}_3(\text{OH})_6\text{Cl}_3$. *arXiv e-prints*, art. arXiv:1907.07489, Jul 2019.
- [227] J. Struck, C. Ölschläger, R. Le Targat, P. Soltan-Panahi, A. Eckardt, M. Lewenstein, P. Windpassinger, and K. Sengstock. Quantum simulation of frustrated classical magnetism in triangular optical lattices. *Science*, 333(6045):996–999, 2011. ISSN 0036-8075. doi: 10.1126/science.1207239. URL <https://science.sciencemag.org/content/333/6045/996>.
- [228] F. Mila. Quantum spin liquids. *European Journal of Physics*, 21(6):499–510, Nov 2000. doi: 10.1088/0143-0807/21/6/302. URL <https://doi.org/10.1088/0143-0807/21/6/302>.
- [229] P. A. Lee. Quantum spin liquid: a tale of emergence from frustration. *Journal of Physics: Conference Series*, 529:012001, Aug 2014. doi: 10.1088/1742-6596/529/1/012001. URL <https://doi.org/10.1088/1742-6596/529/1/012001>.
- [230] M. Vojta. Frustration and quantum criticality. *Reports on Progress in Physics*, 81(6):064501, May 2018. doi: 10.1088/1361-6633/aab6be. URL <https://doi.org/10.1088/1361-6633/aab6be>.
- [231] J. S. Helton, K. Matan, M. P. Shores, E. A. Nytko, B. M. Bartlett, Y. Yoshida, Y. Takano, A. Suslov, Y. Qiu, J.-H. Chung, D. G. Nocera, and Y. S. Lee. Spin dynamics of the spin-1/2 kagome lattice antiferromagnet $\text{ZnCu}_3(\text{OH})_6\text{Cl}_2$. *Phys. Rev. Lett.*, 98:107204, Mar 2007. doi: 10.1103/PhysRevLett.98.107204. URL <https://link.aps.org/doi/10.1103/PhysRevLett.98.107204>.
- [232] T.-H. Han, J. S. Helton, S. Chu, D. G. Nocera, J. A. Rodriguez-Rivera, C. Broholm, and Y. S. Lee. Fractionalized excitations in the spin-liquid state of a kagome-lattice antiferromagnet. *Nature*, 492:406 EP –, Dec 2012. URL <https://doi.org/10.1038/nature11659>.
- [233] M. R. Norman. Colloquium: Herbertsmithite and the search for the quantum spin liquid. *Rev. Mod. Phys.*, 88:041002, Dec 2016. doi: 10.1103/RevModPhys.88.041002. URL <https://link.aps.org/doi/10.1103/RevModPhys.88.041002>.
- [234] Y. Shen, Y.-D. Li, H. Wo, Y. Li, S. Shen, B. Pan, Q. Wang, H. C. Walker, P. Steffens, M. Boehm, Y. Hao, D. L. Quintero-Castro, L. W. Harriger, M. D. Frontzek, L. Hao, S. Meng, Q. Zhang, G. Chen, and J. Zhao. Evidence for a spinon fermi surface in a triangular-lattice quantum-spin-liquid candidate. *Nature*, 540:559 EP –, Dec 2016. URL <https://doi.org/10.1038/nature20614>.
- [235] B. J. Powell and R. H. McKenzie. Quantum frustration in organic mott insulators: from spin liquids to unconventional superconductors. *Reports on Progress in Physics*, 74(5):056501, Apr 2011. doi: 10.1088/0034-4885/74/5/056501. URL <https://doi.org/10.1088/0034-4885/>

74/5/056501.

- [236] T. Ohashi, N. Kawakami, and H. Tsunetsugu. Mott transition in kagomé lattice hubbard model. *Phys. Rev. Lett.*, 97:066401, Aug 2006. doi: 10.1103/PhysRevLett.97.066401. URL <https://link.aps.org/doi/10.1103/PhysRevLett.97.066401>.
- [237] Y. Furukawa, T. Ohashi, Y. Koyama, and N. Kawakami. Mott transition in the hubbard model on the anisotropic kagome lattice. *Phys. Rev. B*, 82:161101, Oct 2010. doi: 10.1103/PhysRevB.82.161101. URL <https://link.aps.org/doi/10.1103/PhysRevB.82.161101>.
- [238] H. T. Dang, X. Y. Xu, K.-S. Chen, Z. Y. Meng, and S. Wessel. Mott transition in the triangular lattice hubbard model: A dynamical cluster approximation study. *Phys. Rev. B*, 91:155101, Apr 2015. doi: 10.1103/PhysRevB.91.155101. URL <https://link.aps.org/doi/10.1103/PhysRevB.91.155101>.
- [239] M. Udagawa and Y. Motome. Entanglement spectrum in cluster dynamical mean-field theory. *Journal of Statistical Mechanics: Theory and Experiment*, 2015(1):P01016, Jan 2015. doi: 10.1088/1742-5468/2015/01/p01016. URL <https://doi.org/10.1088/1742-5468/2015/01/p01016>.
- [240] S. Acheche, A. Reymbaut, M. Charlebois, D. Sénéchal, and A.-M. S. Tremblay. Mott transition and magnetism on the anisotropic triangular lattice. *Phys. Rev. B*, 94:245133, Dec 2016. doi: 10.1103/PhysRevB.94.245133. URL <https://link.aps.org/doi/10.1103/PhysRevB.94.245133>.
- [241] T.-H. Lee, S. Florens, and V. Dobrosavljević. Fate of spinons at the mott point. *Phys. Rev. Lett.*, 117:136601, Sep 2016. doi: 10.1103/PhysRevLett.117.136601. URL <https://link.aps.org/doi/10.1103/PhysRevLett.117.136601>.
- [242] J. Yoshitake, J. Nasu, and Y. Motome. Fractional spin fluctuations as a precursor of quantum spin liquids: Majorana dynamical mean-field study for the kitaev model. *Phys. Rev. Lett.*, 117:157203, Oct 2016. doi: 10.1103/PhysRevLett.117.157203. URL <https://link.aps.org/doi/10.1103/PhysRevLett.117.157203>.
- [243] J. Yoshitake, J. Nasu, Y. Kato, and Y. Motome. Majorana dynamical mean-field study of spin dynamics at finite temperatures in the honeycomb kitaev model. *Phys. Rev. B*, 96:024438, Jul 2017. doi: 10.1103/PhysRevB.96.024438. URL <https://link.aps.org/doi/10.1103/PhysRevB.96.024438>.
- [244] A. E. Antipov, A. N. Rubtsov, M. I. Katsnelson, and A. I. Lichtenstein. Electron energy spectrum of the spin-liquid state in a frustrated hubbard model. *Phys. Rev. B*, 83:115126, Mar 2011. doi: 10.1103/PhysRevB.83.115126. URL <https://link.aps.org/doi/10.1103/PhysRevB.83.115126>.
- [245] H.-Y. Yang, A. M. Läuchli, F. Mila, and K. P. Schmidt. Effective spin model for the spin-liquid phase of the hubbard model on the triangular lattice. *Phys. Rev. Lett.*, 105:267204, Dec 2010. doi: 10.1103/PhysRevLett.105.267204. URL <https://link.aps.org/doi/10.1103/PhysRevLett.105.267204>.
- [246] Yu. B. Kudasov and V. M. Uzdin. Kondo state for a compact cr trimer on a metallic surface. *Phys. Rev. Lett.*, 89:276802, Dec 2002. doi: 10.1103/PhysRevLett.89.276802. URL <https://link.aps.org/doi/10.1103/PhysRevLett.89.276802>.
- [247] B. Lazarovits, P. Simon, G. Zaránd, and L. Szunyogh. Exotic kondo effect from magnetic trimers. *Phys. Rev. Lett.*, 95:077202, Aug 2005. doi: 10.1103/PhysRevLett.95.077202. URL

<https://link.aps.org/doi/10.1103/PhysRevLett.95.077202>.

- [248] V. V. Savkin, A. N. Rubtsov, M. I. Katsnelson, and A. I. Lichtenstein. Correlated adatom trimer on a metal surface: A continuous-time quantum monte carlo study. *Phys. Rev. Lett.*, 94:026402, Jan 2005. doi: 10.1103/PhysRevLett.94.026402. URL <https://link.aps.org/doi/10.1103/PhysRevLett.94.026402>.
- [249] R. Arita, K. Held, A. V. Lukoyanov, and V. I. Anisimov. Doped mott insulator as the origin of heavy-fermion behavior in LiV_2O_4 . *Phys. Rev. Lett.*, 98:166402, Apr 2007. doi: 10.1103/PhysRevLett.98.166402. URL <https://link.aps.org/doi/10.1103/PhysRevLett.98.166402>.
- [250] M. Fleck, A. I. Lichtenstein, A. M. Oleś, L. Hedin, and V. I. Anisimov. Dynamical mean-field theory for doped antiferromagnets. *Phys. Rev. Lett.*, 80:2393–2396, Mar 1998. doi: 10.1103/PhysRevLett.80.2393. URL <https://link.aps.org/doi/10.1103/PhysRevLett.80.2393>.
- [251] H. Hafermann, M. I. Katsnelson, and A. I. Lichtenstein. Metal-insulator transition by suppression of spin fluctuations. *EPL (Europhysics Letters)*, 85(3):37006, Feb 2009. doi: 10.1209/0295-5075/85/37006. URL <https://doi.org/10.1209/0295-5075/85/37006>.

List of publications

1. M. Harland, M. I. Katsnelson, and A. I. Lichtenstein. Plaquette valence bond theory of high-temperature superconductivity. *Phys. Rev. B*, 94:125133, Sep 2016. doi: 10.1103/PhysRevB.94.125133. URL <http://link.aps.org/doi/10.1103/PhysRevB.94.125133>

The author of this thesis wrote the exact diagonalization and the CDMFT codes and he performed the calculations for data corresponding to those methods. He participated in the writing of the manuscript, he contributed the figures 1. and 5.

2. E. A. Stepanov, S. Brener, F. Krien, M. Harland, A. I. Lichtenstein, and M. I. Katsnelson. Effective heisenberg model and exchange interaction for strongly correlated systems. *Phys. Rev. Lett.*, 121:037204, Jul 2018. doi: 10.1103/PhysRevLett.121.037204. URL <https://link.aps.org/doi/10.1103/PhysRevLett.121.037204>

The author of this thesis implemented the DMFT of the hypercubic lattice. Further, he ran the analytic continuation calculations and wrote code for the calculation of bubble diagrams. He wrote the section “Numerical calculations” of the manuscript and contributed figure 1. of the main part and also figure 1. of the supplemental material.

3. M. Harland, A. I. Poteryaev, S. V. Streltsov, and A. I. Lichtenstein. Electronic correlations and competing orders in multiorbital dimers: A cluster dmft study. *Phys. Rev. B*, 99:045115, Jan 2019. doi: 10.1103/PhysRevB.99.045115. URL <https://link.aps.org/doi/10.1103/PhysRevB.99.045115>

The author of this thesis ran calculations with his CDMFT code and wrote a whole preliminary version of the manuscript, which remained the main part of the publication. He performed the analytic continuation and all other post-processings, such as the quasiparticle evaluation. He wrote the main part of the correspondence with the editor and referees in the publication process. He contributed the figures 1., 2. and 4.-12. .

4. I. Krivenko and M. Harland. Triqs/som: Implementation of the stochastic optimization method for analytic continuation. *Computer Physics Communications*, 2019. ISSN 0010-4655. doi: <https://doi.org/10.1016/j.cpc.2019.01.021>. URL <http://www.sciencedirect.com/science/article/pii/S0010465519300402>

During the development stage the author of this thesis used the Python interface to implement the test framework and also compared the results with other methods, that are available. He contributed the figures 2-6. and wrote section 5. Further he helped to improve content and text of the remaining part.

5. M. Harland, S. Brener, A. I. Lichtenstein, and M. I. Katsnelson. Josephson lattice model for phase fluctuations of local pairs in copper oxide superconductors. *Phys. Rev. B*, 100:024510, Jul 2019. doi: 10.1103/PhysRevB.100.024510. URL <https://link.aps.org/doi/10.1103/PhysRevB.100.024510>

The author of this thesis participated in the derivation of the equations. He implemented the CDMFT, the calculation of the effective Josephson exchange and stiffness. He contributed the 13 figures, and he wrote the main part of the manuscript and of the correspondence with the editor and referees in the publication process.

6. A. A. Bagrov, M. Danilov, S. Brener, M. Harland, A. I. Lichtenstein, and M. I. Katsnelson. Detecting the quantum critical point in high-temperature superconducting cuprates via complex network theory. *arXiv e-prints*, art. arXiv:1904.11463, Apr 2019. URL <https://arxiv.org/abs/1904.11463>

The author of this thesis contributed benchmarks from the ED-solver which he developed, and also from the quadruple Bethe lattice of his CDMFT implementation. Furthermore, he helped in the debugging process of the implementation of the four-by-four cluster. He contributed to the discussion of the manuscript. The manuscript is currently under consideration for publication in Nature Communications Physics.

7. M. Harland, S. Brener, M. I. Katsnelson, and A. I. Lichtenstein. Exactly solvable model of strongly correlated d -wave superconductivity. *arXiv e-prints*, art. arXiv:1905.12610, May 2019

The author of this thesis performed the calculations for the presented data using his implementations. He wrote a preliminary version of the manuscript, which remained the main part of the (preprint-)publication. Furthermore, he participated in the derivation of the equations. He contributed the 19 figures. The manuscript is currently under consideration for publication in Phys. Rev. B.

The CDMFT code has been written using an existing impurity solver. Moreover, the author of this thesis contributed to the proposals for computational resources that were required for all projects. The CDMFT, ED, Josephson lattice and mutual entanglement codes are available at <https://github.com/mharland>.

List of Figures

2.1	Cayley trees	16
2.2	Non-interacting Bethe lattice $A(\omega)$ for different z	18
2.3	Cluster description of the square lattice.	19
2.4	Illustration of the CDMFT mapping.	20
2.5	SOM algorithm and parameters	27
3.1	YBa ₂ Cu ₃ O ₇ structure	48
3.2	Cuprate phase diagram	49
3.3	Tightbinding Fermi surface of the square lattice	50
3.4	Electronic band structure of the Square lattice.	52
3.5	Mott transition of the simple Bethe lattice (LDOS)	54
3.6	Mott transition of the simple Bethe lattice (self-energy)	55
3.7	Slater-Mott transition of the quadruple Bethe lattice (LDOS)	56
3.8	Particle number and spin correlations of plaquette eigenstates	60
3.9	Plaquette degenerate point	60
3.10	Pseudoparticle spectral function of the plaquette	61
3.11	Real-space spectral function of the plaquette	62
3.12	Quantum mutual information of the two-by-two plaquette depending on μ .	89
3.13	Quantum mutual information of the two-by-two plaquette depending on U .	90
4.1	Non-interacting density of states of the hypercubic lattice. Obtained through the Padé method of analytic continuation.	133
4.2	LDOS and self-energies of the hypercubic lattice.	135
4.3	Paramagnetic metal-insulator transition of the hypercubic lattice	136
4.4	Face-sharing and edgesharing octahedra	162
4.5	Trigonal splitting of octahedrally coordinated transition metals	163
4.6	The non-interacting ($U = 0$) density of states of the triple bethe lattice for different triangle hoppings t_t	177
4.7	Spectrum of the Hubbard triangle	178
4.8	Spin correlations $\langle S_{loc}^2 \rangle$ and $\langle S_{nn}^2 \rangle$ of the paramagnetic triple Bethe lattice .	179
4.9	$\langle S_{tri}^2 \rangle$ and $A(0)$ of the paramagnetic triple Bethe lattice	180
4.10	LDOS for the U driven metal-insulator transition of the paramagnetic triple Bethe lattice	181

4.11 All-in/all-out spin structure of the triple Bethe lattice	182
4.12 LDOS and order parameters of the symmetry-broken triple Bethe lattice (U -dependence)	184
4.13 LDOS and order parameters of the symmetry-broken triple Bethe lattice (t_t -dependence)	184

Acknowledgements

Hereby I want to thank the people who supported me during my research for this work. It has been a very exciting and enjoyable time. I thank Alexander Lichtenstein for giving me the chance to participate in interesting scientific projects and for sharing many inspiring ideas, explanations and advice. I thank Michael Potthoff for his evaluation of this thesis. For many discussions and a great time in the office, I thank my colleagues Burkhard Sachs, Lewin Boehnke, Erik van Loon, Frank Lechermann, Friedrich Krien, Daniel Hirschmeier, Igor Krivenko, Arthur Huber, Sergey Brenner, Maria Bandelmann, Oleg Kristanovski, Viktor Valmispild, Roberto Mozara, Viktor Harkov, Andre Lehmann, Hristiana Atanasova, Patryk Kubiczek, Yusuf Mohammed, Mikhail Danilov, Matteo Vandelli, Zhenya Stepanov and Georg Rohringer. Further, I thank Tim Berberich, Kristina Klafka and Eduard Belsch for their research in close collaboration with me for the purpose of their thesis. I thank the coauthors of the papers I contributed to, Mikhail Katsnelson, Alexander Poteryaev, Sergey Streltsov and Andrey Bagrov. I thank the physnet-team for their IT support and the teaching-staff of the TUHH-Praktikum, especially Katrin Groth and Afsaneh Farhadi. Finally, my deepest thanks I want to express to my parents and girlfriend for their great support in every aspect of my life, Jörn, Susanne and Louisa.

Eidesstattliche Versicherung

Hiermit erkläre ich an Eides statt, dass ich die vorliegende Dissertationsschrift selbst verfasst und keine anderen als die angegebenen Quellen und Hilfsmittel benutzt habe.

Hamburg, den

Unterschrift